IDŐJÁRÁS

QUARTERLY JOURNAL

OF THE HUNGARIAN METEOROLOGICAL SERVICE

Special Issue of the COST-ES0601 (HOME) ACTION: Advances in homogenization methods of climate series: an integrated approach

Guest Editors: **Mónika Lakatos** and **Tamás Szentimrey**

CONTENTS

Editorial I

Ralf Lindau and *Victor Venema*: On the multiple breakpoint problem and the number of significant breaks in homogenization of climate records 1

José A. Guijarro: Climatological series shift test comparison on running windows........... 35

Olivier Mestre, Peter Domonkos, Franck Picard, Ingeborg Auer, Stéphane Robin, Emilie Lebarbier, Reinhard Böhm, Enric Aguilar, Jose Guijarro, Gregor Vertachnik, Matija Klancar, Brigitte Dubuisson, and *Petr Stepanek*: HOMER: a homogenization software – methods and applications 47

Luís Freitas, Mário Gonzalez Pereira, Liliana Caramelo, Manuel Mendes, and *Luís Filipe Nunes:* Homogeneity of monthly air temperature in Portugal with HOMER and MASH... 69

Peter Domonkos: Measuring performances of homogenization methods 91

Tamás Szentimrey: Theoretical questions of daily data homogenization.......................... 113

Petr Štěpánek, Pavel Zahradníček and *Aleš Farda*: Experiences with data quality control and homogenization of daily records of various meteorological elements in the Czech Republic in the period 1961–2010..... 123

Mónika Lakatos, Tamás Szentimrey, Zita Bihari, and *Sándor Szalai*: Creation of a homogenized climate database for the Carpathian region by applying the MASH procedure and the preliminary analysis of the data 143

****

http://www.met.hu/Journal-Idojaras.php

VOL. 117* NO. 1 * JANUARY – MARCH 2013

IDŐJÁRÁS

Quarterly Journal of the Hungarian Meteorological Service

Editorial Office: Kitaibel P.u. 1, H-1024 Budapest, Hungary
P.O. Box 38, H-1525 Budapest, Hungary
E-mail: journal.idojaras@met.hu
Fax: (36-1) 346-4669

Indexed and abstracted in Science Citation Index Expanded™ and Journal Citation Reports/Science Edition
Covered in the abstract and citation database SCOPUS®

Subscription by

mail: IDŐJÁRÁS, P.O. Box 38, H-1525 Budapest, Hungary
E-mail: journal.idojaras@met.hu

Editorial

Special Issue of the COST-ES0601 (HOME) Action: Advances in homogenization methods of climate series: an integrated approach

Long term instrumental climate records are the basis of climate research. However, these series are usually affected by inhomogeneities (artificial shifts), due to changes in the measurement conditions (relocations, instrumentation). As the artificial shifts often have the same magnitude as the climate signal, such as long-term variations, trends, or cycles, a direct analysis of the raw data series can lead to wrong conclusions about climate change. In order to deal with this crucial problem, many statistical homogenization procedures have been developed for detection and correction of these inhomogeneities.

The large number of different homogenization methods and the need for a realistic comparative study was the reason to start a coordinated European initiative, the COST Action ES0601: Advances in Homogenization Methods of Climate Series: an integrated approach (HOME). Its main objective was to review and improve common homogenization methods, and to assess their impact on climate time series. As one of the high importance achievements of the Action a benchmark dataset was generated for comparing monthly homogenization algorithms. The main results of this examination were published in the journal Climate of the Past.

The COST HOME Action ended in October 2011. The final meeting of the Management Committee was organized in Budapest together with the 7th Seminar for Homogenization and Quality Control in Climatological Databases. The Homogenization Seminars are traditionally held in Budapest and hosted by the Hungarian Meteorological Service from 1996. The jointly organized Seminar and the final MC meeting was a good occasion for conversation between the participants of the HOME Action and other researchers of the homogenization community. During this meeting, publishing a special issue of the COST HOME Action was suggested. It is a pleasure for us that this publication has been realized at the Quarterly Journal of the Hungarian Meteorological Service as a Special Issue of the Action.

This Special Issue includes eight papers which are covering wide range of topics on homogenization. The first five articles are connected mainly with the homogenization on monthly scale, while the other three ones focus rather on the homogenization of daily series. In both cases, theoretical aspects and practical applications are discussed and presented alike.

We are very grateful to the Editor–in-Chief of IDŐJÁRÁS supporting the progress on the field of homogenization, thank to the authors of the articles for their high scientific level work, and also to the reviewers supporting the improvement of papers with their critical comments and recommendations keeping the high standards of the Journal. We have to underline the hard work of the Executive Editor of the Journal, therefore, we express our thanks together with the authors for that.

Tamás Szentimrey and *Mónika Lakatos*
Guest Editors

IDŐJÁRÁS

Quarterly Journal of the Hungarian Meteorological Service
Vol. 117, No. 1, January–March 2013, pp. 1-34

On the multiple breakpoint problem and the number of significant breaks in homogenization of climate records

Ralf Lindau* and **Victor Venema**

Meteorological Institute, University of Bonn
Auf dem Hügel 20, D-53121 Bonn, Germany

**Corresponding author E-mail: rlindau@uni-bonn.de*

(Manuscript received in final form November 8, 2012)

Abstract—Changes in instrumentation and relocations of climate stations may insert inhomogeneities into meteorological time series, dividing them into homogeneous subperiods interrupted by sudden breaks. Such inhomogeneities can be distinguished from true variability by considering the differences compared to neighboring stations. The most probable positions for a given number of break points are optimally determined by using a multiple-break point approach. In this study the maximum external variance between the segment averages is used as decision criterion and dynamic programming as optimization method. Even in time series without breaks, the external variance is growing with any additionally assumed break, so that a stop criterion is needed. This is studied by using the characteristics of a random time series. The external variance is shown to be beta-distributed, so that the maximum is found by solving the incomplete beta function. In this way, an analytical function for the maximum external variance is derived. In its differential form our solution shows much formal similarities to the penalty function used in *Caussinus* and *Mestre* (2004), but differs numerically and exhibits more details.

Key words: Climate records, homogenization, multiple break point detection, stop criterion for search algorithms, dynamic programming, penalty term.

1. Introduction

Multiple-century long instrumental datasets of meteorological variables exist for Europe (*Brunetti et al.*, 2006; *Bergström* and *Moberg*, 2002; *Slonosky et al.*, 2001). Such series provide invaluable information on the evolution of the climate. However, between the Dutch Golden Age, the French and the industrial revolution, the rise and the fall of communism, and the start of the internet age, inevitably many changes have occurred in climate monitoring practices (*Aguilar et al.*, 2003; *Trewin*, 2010). The typical size of temperature jumps due to these changes is similar to the global warming in the 20th century, and the average length of the periods between breaks in the climate records is 15 to 20 years (*Auer et al.*, 2007; *Menne* and *Williams*, 2009). Clearly, such changes interfere with the study of natural variability and secular trends (*Rust et al.*, 2008; *Venema et al.*, 2012).

Technological progress and a better understanding of the measurement process have led to the introduction of new instruments, screens, and measurement procedures (*MeteoSchweiz*, 2000). In the early instrumental period, temperature measurements were often performed under open shelters or in metal window screens on a North facing wall (*Brunetti et al.*, 2006), which were replaced by Montsouri (*Brunet et al.*, 2011), Wild, and various Stevenson screens (*Nordli et al.*, 1997; *Knowles Middleton*, 1966), and nowadays more and more by labor-saving automatic weather stations (*Begert et al.*, 2005). Every screen differs in their protection against radiation, wetting, as well as their quality of ventilation (*Van der Meulen* and *Brandsma*, 2008). Initially many precipitation observations were performed on roofs. As it was realized that many hydrometeors do not enter the gauge due to wind and turbulence, especially in case of snow, the observations were taken nearer the ground, and various types of wind shields were tested leading to deliberate inhomogeneities (*Auer et al.*, 2005). Due to the same effect, any change in the geometry of a rain gauge can lead to unintended inhomogeneities.

Inhomogeneities are frequently caused by relocations, either because the voluntary observer changed, because the observer had to move or because the surrounding was no longer suited for meteorological observations. Changes in the surrounding can lead to gradual or abrupt changes, for example gradual increases in urbanization or growing vegetation or fast changes due to cutting of vegetation, buildings that disrupt the flow or land-use change.

Changes in the observations should be documented in the station history. It is recommended to perform several years of parallel measurements in case of changes (*Aguilar et al.*, 2003). However, it is not guaranteed that metadata is complete, thus statistical homogenization should always be performed additionally. The dominant approach to homogenize climate networks is the relative homogenization method. This principle states that nearby stations are exposed to almost the same climate signal, and thus, the differences between nearby stations can be utilized to detect inhomogeneities (*Conrad* and *Pollack*, 1950). By computing the difference time series, the interannual weather noise, decadal variability, and secular trends are strongly reduced. Consequently, a jump in single station becomes much more salient.

The two fundamental problems of homogenization are that the nearby stations are also inhomogeneous and that typically more than one break is present. Recent intercomparison studies by *Domonkos* (2011a) and *Venema et al.* (2012) showed that the best performing algorithms are the ones that attack these two problems directly. This study will focus on the multiple-breakpoint problem.

Traditionally the multiple-breakpoint problem is solved by applying single-breakpoint algorithms multiple times. Either a cutting algorithm is applied: the dataset is cut at the most significant break and the subsections are investigated individually until no more breaks are found or the section become too short; see, e.g., *Easterling* and *Peterson* (1995). A variation on this theme is a semi-hierarchical algorithm, in which potential breakpoints are found using the cutting algorithm, but before correcting a potential break its significance is tested anew (*Alexanderson* and *Moberg*, 1997). According to *Domonkos* (2011a), this improvement has a neutral effect on the efficiency of homogenization.

The first algorithms solving the multiple-breakpoint problem directly are MASH (*Szentimrey*, 1996, 1999) and PRODIGE (*Caussinus* and *Mestre*, 1996, 2004). MASH solves the problem with a computationally expensive exhaustive search (*Szentimrey*, 2007). PRODIGE solves the problem in two steps. First, the optimal position of the breaks for a given number of breaks is found using a computationally fast optimization approach called dynamic programming (*Bellman*, 1954; *Hawkins*, 1972). Second, the number of breaks is determined by minimizing the internal variance within the subperiods between two consecutive breaks plus a penalty for every additional break (*Caussinus* and *Lyazrhi*, 1997). The penalty term aims to avoid adding insignificant breaks.

Recently, *Domonkos* (2011b) expanded ACMANT, which is based on the generic PRODIGE algorithm, by searching for common breaks in the annual mean and the size of the annual cycle. *Picard et al.* (2011) developed an alternative version, in which not only pairs, but all data in the network are jointly taken into account for optimization. ACMANT, PRODIGE, and the joint detection method of *Picard et al.* (2011) are implemented in the software package HOMER (*Mestre et al.*, 2012). *Nemec et al.* (2012) used PRODIGE with three different criteria for the assessment of the number of breaks. Beyond dynamic programming, genetic algorithms (e.g., *Li* and *Lund*, 2012; *Davis et al.*, 2012) and simulated annealing (*Lavielle*, 1998) are alternatively used for reducing the computational demand.

Not all inhomogeneities are abrupt changes, some changes are more gradual (*Lindau*, 2006). Such trends are explicitly considered by some homogenization algorithms (*Vincent*, 1998; *Menne* and *Williams*, 2009). Using the HOME benchmark dataset in which 10% of the stations contained a local trend inhomogeneity, a blind experiment with two versions of PRODIGE has been performed (*Venema et al.*, 2012). In the main version only breaks have been used for homogenization, and in the alternative version multiple breaks in one direction are combined into a slope correction. These two versions have a very similar performance. One of the reasons may be that not many local trends had to be introduced. Still this suggests that trend inhomogeneities can be reasonably well modeled by multiple breaks. Consequently, this paper will only consider break inhomogeneities.

To characterize breaks within a time series, it is helpful to decompose the total variance of the time series into two terms: the internal and the external variance. Consider a time series with k breaks dividing it into $k + 1$ subperiods (*Fig. 1*). In this concept, the variance within the subperiods is referred to as the internal variance, whereas the variance between the means of different subperiods is the external variance. The decomposition with the maximum external variance defines the optimum positions of breaks for a given number of breaks.

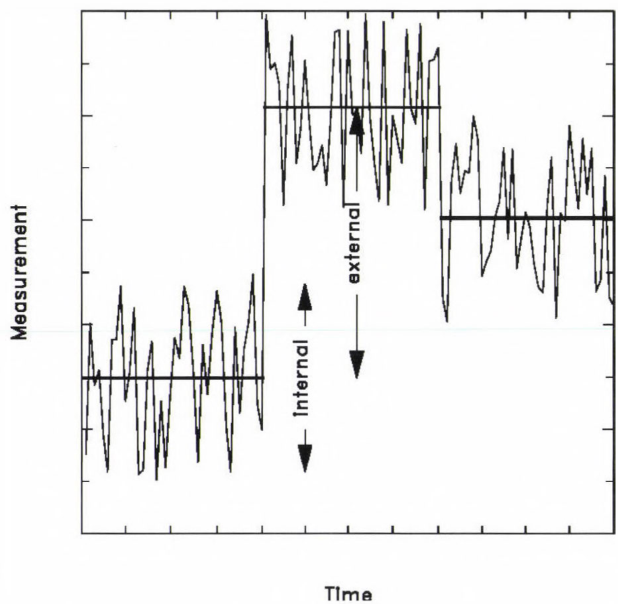

Fig. 1. Sketch to illustrate the occurrence of breaks in climate records and the related expressions, internal and external variance.

As we use internal and external variance as the basic concept to characterize breaks, an exact quantitative formulation is necessary. *Lindau* (2003) discussed the decomposition of variance and showed that the total variance of a time series can be divided into three parts:

$$\frac{1}{n-1}\sum_{i=1}^{N}\sum_{j=1}^{n_j}\left(x_{ij}-\bar{x}\right)^2 = \frac{1}{n}\sum_{i=1}^{N} n_i(\bar{x}_i-\bar{x})^2 + \frac{1}{n}\sum_{i=1}^{N}\sum_{j=1}^{n_j}\left(x_{ij}-\bar{x}_i\right)^2$$

$$+\frac{1}{n(n-1)}\sum_{i=1}^{N}\sum_{j=1}^{n_j}(x_{ij}-\bar{x})^2 \quad . \tag{1}$$

In Eq. (1), the variance of a time series of length n is considered. It contains N subperiods, each comprising n_i members. Individual members are denoted by x_{ij}, where i specifies the subperiod and j the temporal order within the respective subperiod. The mean of the ith subperiod is denoted by $\bar{x}_i$ and the overall mean of the entire time series by $\bar{x}$, without any index. The total variance on the left hand side is decomposed into the three parts on the right hand side of Eq. (1). These are equal to the external and the internal variance plus, as third term, the error of the total mean. As the last term is constant for a given time series, the sum of internal and external variance is constant, too. Consequently, we can formulate an alternative criterion for the optimum decomposition of a time series into subsegments being a minimum internal variance.

However, two problems arise. The first is of practical nature. The number of possible decompositions is normally too large for a simple test of all permutations. The second is rather fundamental. For a fixed number of breaks, the maximum external variance is actually a reasonable criterion for the optimum decomposition. However, it is obvious that for zero breaks, the entire variance is internal, whereas it is fully external for n–1 breaks. During the transition from 0 to n–1 breaks, more and more variance is converted from internal to external, so that the internal variance is a monotonously falling function of the break number k. Consequently, we need a second criterion for the optimum *number* of breaks. As this is the critical problem for any multiple-breakpoint detection algorithm, the discussion and proposed solution of this problem built the major part of this paper. However, initially also the first minor problem and its solution are shortly described in the following.

There exists a large number of possibilities to decompose a time series of length n into a fixed number of N subsegments: it is equal to $\binom{n-1}{N-1}$. Even for a moderate length of $n = 100$ and ten subsegments, there are already more than 10^{12} combinations, so that the testing of all permutations is mostly not feasible. This problem is already solved by the so-called dynamic programming method, firstly inspired by *Bellman* (1954). Originally designed for economic problems, this method is by now established in many different disciplines, in climate research (*Caussinus* and *Mestre*, 2004) as well as in biogenetics (*Picard et al.*, 2005). As we will also use dynamic programming later on, we describe shortly how we applied this technique.

2. *Dynamic programming*

We begin with the optimum solution for a single break point. In this case, simple testing of all possibilities is still feasible as only n–1 permutations exist. Afterwards, the best break position together with its respective internal variance is known. The basic idea is now to find an optimum decomposition not only for the entire time series, but also for all truncated variants of any length l. There exist n–1 variants, all beginning with the first time point. The first variant ends at the second time point, the second at the third time point, and the last variant is equal to the entire time series. For each of these variants an optimum position of a single breakpoint is searched and stored together with the criterion on which the decision is made, i.e., its internal variance. In the next step we consider what happens if the truncated variants are filled up to the original length n. In this case the internal variance consists of two contributions: that of the truncated variant, plus that of the added rest. For this step, it is, of course, necessary that the used criterion is additive, which is fulfilled for variances. Consequently, we can test a number of n–1 filled-up variants. That variant, where the combined internal variance is minimal, is then the optimum solution for two break points. The first break is situated within the truncated time series; the second is equal to the length l of the truncated series itself, because here is the break between the two combined time series.

To expand the method from two to three and more breaks, some more work is necessary already at the beginning. So far the truncated variants are always filled up to the entire length n. But the starting point for the proceeding from one to two breaks are, as described above, known previous solutions for all lengths. Consequently, to proceed from two to three breaks, we need not only the best two-break solution for the entire length n, but the solutions for every length. Thus, also all shorter fillings are performed so that we obtain the optimum two-break solution not only for the final time series length n, but also for every shorter length between 2 and n. This set of solutions is then used accordingly as basis to find the three-break solution. Filling up the time series to the full length would be sufficient if we want to stop at three breaks. However, if the method should be continued to higher break numbers, again a full set of three-break solutions is needed.

Thus, the solution for k breaks is found by testing only n–1 truncated and refilled optima, where the truncated part contains already the optimum distribution of k–1 breaks. To perpetuate the method for k+1 breaks, each truncated optimum has to be refilled to all possible length so that a number of cases in the order of n^2 has to be calculated. This reduces the number of cases from the order of $\binom{n}{k}$ to n^2, which facilitates a much faster processing.

3. Outline of the paper

In the above described way, the optimum positions for a given number of breaks can be calculated. Minimum internal variance is serving as criterion, and dynamic programming avoids a time consuming exhaustive search. However, as mentioned above, there is still a problem left. The absolute minimum of internal variance being equal to zero would be attained by inserting n–1 breaks into the time series, which is obviously not the optimum solution. Instead, we need to define which number of breaks is appropriate.

A state-of-the-art method for detecting breaks is PRODIGE (*Caussinus* and *Mestre*, 2004). Although using a log-likelihood method, it is based on the minimization of the internal variance and does not differ essentially from the procedure described here so far. PRODIGE uses a penalty term to ensure that the search stops at a reasonable number of breaks. This penalty term is adopted from *Caussinus* and *Lyazrhi* (1997). Similar to PRODIGE, *Picard et al.* (2005) applied a log-likelihood method to minimize the internal variance, but developed a specific penalty term. Before, they discussed different commonly used penalty terms, such as the Information Criteria AIC and BIC, based on *Akaike* (1973), and found that these penalty terms suffer from different weaknesses.

In the remaining part of this study, we derive an alternative stop criterion based on the idea that the external variance is the key parameter, which defines the optimum solutions. We will use the characteristics of a random standard normal distributed time series as reference. Only if the optimum solution for an additionally inserted break gains significantly more external variance than the expected amount for a random time series, an increased break number is justified. Thus, it is necessary to describe mathematically how the external variance of random data increases with increasing number of breaks, so that it can be used as reference for real data.

In a first step, we derive the statistical distribution that can be expected for the external variance v. In Section 4, we show theoretically that the χ^2 distribution would be a good candidate. In Section 5, we show by empirical tests that the related Beta distribution is even better suited to describe the external variance. To identify the optimum solution for the decomposition, we use, as mentioned, the maximum external variance. Consequently, we have to find the maximum value within a Beta distribution, identical to its exceeding probability, which is performed in Section 6. For that purpose, the definite integral of the Beta distribution, known as the incomplete Beta function, has to be solved. From this formulation, the rate of change of the external variance v for growing break numbers k is derived in Section 7. This derivative dv/dk is then integrated and a formulation for $v(k)$ is presented.

In its differential form our solution shows much formal similarities to the penalty function used in *Caussius* and *Mestre* (2004), but it differs numerically and exhibits more details. In Section 8 we discuss these differences and propose finally a revision.

4. *Theoretical characteristics of random data*

Consider a random standard normal distributed time series $N(0,1)$ with k breaks inserted, so that the number of segments N is:

$$N = k + 1 \ . \tag{2}$$

According to Eq. (1) the external variance v is:

$$v = \frac{1}{n}\sum_{i=1}^{N} n_i(\overline{x_i} - \bar{x})^2 \ . \tag{3}$$

As standard normal distributed data is considered, $\bar{x}=0$ and $\sigma_x=1$. Furthermore, we are interested here in the statistics of external variance for many realizations as produced by $\binom{n-1}{k}$ permutations of break positions for a fixed number of breaks. Averages over these permutations are denoted by brackets, whereas averages over individual data points within a time segment are overlined.

$$[v] = \left[\frac{1}{n}\sum_{i=1}^{N} n_i \, \overline{x_i}^2\right] \ . \tag{4}$$

Consider now the segment averages $\overline{x_i}$, which are the critical constituents of $[v]$ in Eq. (4). Their expected mean is equal to zero, since random data with $\bar{x} = 0$ is assumed. Only the finite number of segment members causes the segment means to scatter randomly around zero. As the members of a segment are standard normal distributed, the standard deviation of any segment mean is equal to $1/\sqrt{n_i}$.

$$\overline{x_i} \sim N\left(0, \frac{1}{n_i}\right) \ . \tag{5}$$

If the segment means are multiplied by the square root of the number of segment members (Eq. (6)), the distribution is broadened in such a way that a standard normal distribution is obtained. These modified means can be defined as to y_i.

$$y_i := \sqrt{n_i}\,\bar{x}_i \sim N(0,1) \quad . \tag{6}$$

Inserting this definition into Eq. (4) leads to:

$$[v] = \left[\frac{1}{n}\sum_{i=1}^{N} {y_i}^2\right] = \frac{N-1}{n} = \frac{k}{n} \quad . \tag{7}$$

The second equal sign in Eq. (7) follows, because the squared sum over standard normal distributed data is N–1, which is directly evident from the definition of standard deviation. Furthermore, the brackets can be omitted as both the total length of the time series n and the number of segments N are constants for all permutations subsumed under the brackets. The last equal sign follows from Eq. (2), which just states that there is always one segment more than breaks.

From Eq. (7), we can conclude the following. The average external variance increases linearly with the number of inserted breaks k. Such a linear increase of v could be expected if one of the $\binom{n-1}{k}$ segmentation possibilities for a given number of breaks is chosen randomly. However, actually we select always the optimum segmentation as given by the above described dynamic programming. Consequently, we are less interested in the expected mean, but in the best of several attempts. In order to conclude such an extreme, the distribution has to be known.

For this purpose, let us go back to Eq. (3) where we insert again Eq. (6). It follows the same relationship as given in Eq. (7), but without averaging brackets, according to:

$$v = \frac{1}{n}\sum_{i=1}^{N} {y_i}^2 \quad . \tag{8}$$

It is striking that Eq. (8) is nearly identical to the definition of a χ^2 distribution, which is as follows: N values are randomly taken out of a standard normal distribution, which are then squared and added up. By repeating this procedure several times, these square sums form a χ^2 distribution with N being the number of degrees of freedom. Remembering that y_i is standard normal distributed, it becomes obvious that Eq. (8) reproduces this definition. The difference is that we divide finally by n. But, hereby, no substantial change is performed, as n is a constant equal to the length of the considered time series.

Consequently, we can conclude that v (actually nv), must be χ^2 distributed with k being the degree of freedom, according to:

$$f(x) = \frac{x^{\frac{k-2}{2}} e^{-\frac{x}{2}}}{2^{\frac{k}{2}} \Gamma\left(\frac{k}{2}\right)} \quad . \qquad (9)$$

However, there is an important restriction of this rule. As v is normalized, it is confined between 0 and 1, whereas normal distributed data have no upper limit. The number of breaks k is inversely proportional to the number of segment members n_i. Therefore, the standard deviation of segment averages (Eq. (5)), is small compared to 1 for low break numbers. In this case the normal distribution is a good approximation for $\overline{x_k}$. However, with increasing break number, n_i decreases so that the standard deviation is approaching 1. Assume, e.g., a time series of length 100 with 25 breaks. n_i is then in the order of 4, so that the standard deviation of the $\overline{x_k}$ becomes 0.5 (Eq. (5)). Assuming still a normal distribution is no longer appropriate, as the true frequency for $\overline{x_k}$=1 is zero by definition, whereas the normal distribution at 2 standard deviations is not exactly zero. For the distribution of v it means that we have to expect a kind of confined χ^2 distribution, which is defined exclusively between zero and one. In the next chapter, we will show empirically that this is a Beta distribution. For this purpose, we verify in the following our theoretical considerations by practical tests with random data.

5. Empirical tests with random data

Typical climate time series contain at least 100 data points, which is preventing in general the explicit calculation of the entire distribution as discussed above. However, for n=20, this is still possible and carried out in the following to check our theoretical conclusions. *Fig. 2* shows the development of the external variance v as a function of the number of inserted breaks k.

To obtain statistical quantities, 100 repetitions have been performed. The mean amount of v increases linearly with k, as stated in Eq. (7). Additionally, the minimum and maximum are given for each number of breaks. In realistic cases, i.e., for larger n, the maximum can only be determined by dynamic programming; here the entire distribution could be explicitly calculated. In the following, it is our aim to find a mathematical function determining how the maximum external variance is growing with increasing number of breaks. A first approximation of this solution is already visible in *Fig. 2*. Three estimates are given for the maximum external variance. The central one, where an exponent of 4 is assumed, is in good agreement with the data. Obviously, the external variance v is connected to the break number k by the approximate function:

$$1 - v = \left(1 - \frac{k}{n-1}\right)^4 \quad . \qquad (10)$$

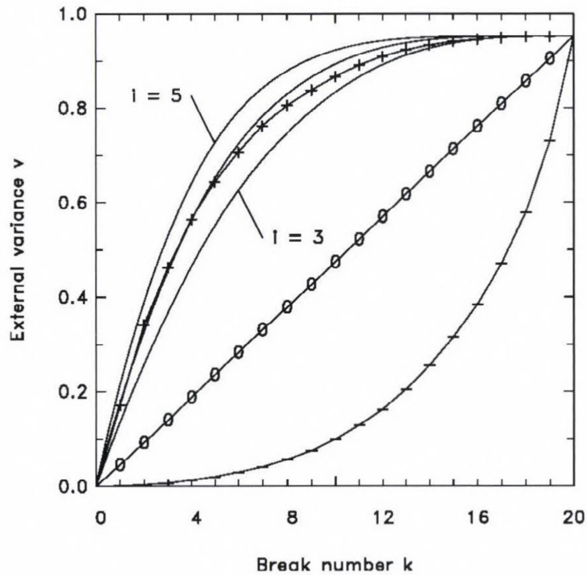

Fig. 2. Mean (0), maximum (+), and minimum (–) external variance as a function of inserted breaks for an $n = 21$ year random time series. For the maximum, three estimates are given: $1-v=(1-k^*)^i$, for $i=3, 4, 5$, where $k^* = k/(n-1)$ is the normalized break number. For 20 breaks, v reaches not 1, but 0.95, because a fraction of $1/(n-1)$ is covered by the error of the total mean, as given in Eq. (1).

For each break number, *Fig. 2* gives minimum and maximum of the external variance for 100 repetitions. Between these extremes we expect a kind of confined χ^2 distribution. As the shown result is based on numerical calculations, we are able to check our theory. *Fig. 3* shows exemplarily the distribution as obtained from a Monte Carlo experiment for 7 breaks. Differences to the corresponding χ^2 distribution are not large, but noticeable, especially at the tail of the distribution, where the maximum value, we are interested in, occurs. In contrast, the Beta distribution with 7 degrees of freedom is in good agreement with the data. Confirmed by tests with further break numbers, we assume in the following that the external variance is generally Beta distributed. The Beta distribution is formally given by:

$$p(v) = \frac{v^{\frac{k}{2}-1}(1-v)^{\frac{n-1-k}{2}-1}}{B\left(\frac{k}{2}, \frac{n-1-k}{2}\right)} \ , \tag{11}$$

with p denoting the probability density, v the external variance, and B the Beta function defined as:

$$B(a,b) = \frac{\Gamma(a)\,\Gamma(b)}{\Gamma(a+b)} \ , \tag{12}$$

with Γ denoting the Gamma function.

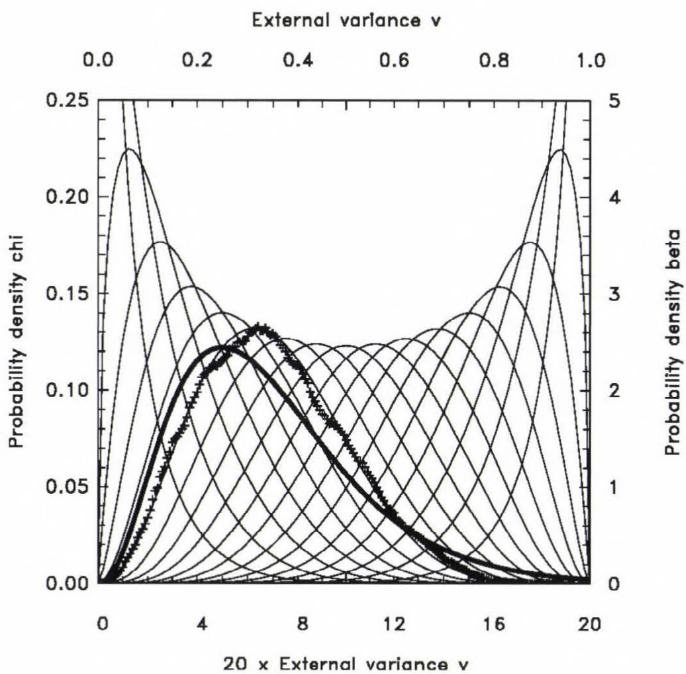

Fig. 3. Probability density for the χ^2 distribution, as given in Eq. (9) for k=7 (thick line). Furthermore, the 20 Beta distributions (thin), and the distribution of random data (crosses) are given. As expected, the data deviates slightly from the χ^2–7 and fits well to the Beta–7 curve. The lower abscissa and the left ordinate is valid for the χ^2 distribution. The upper v-abscissa and the right ordinate are valid for the Beta distribution and the normalized random data.

6. The incomplete Beta function

By Eq. (11) we are so far able to describe the distribution of the external variance v depending on length n and break number k. However, it is the maximum of v, which defines the optimum decomposition. Therefore, we need to find the maximum value of Eq. (11), or in other words, the exceeding probability of the Beta distribution, as given by:

$$P(v) = 1 - \int_0^v p dv \quad , \tag{13}$$

where the definite integral over a Beta distribution has to be solved, which is referred to as the incomplete Beta function $B(a,b,v)$. With this substitution Eq. (13) reads:

$$P(v) = 1 - \frac{B\left(\frac{k}{2}, \frac{n-1-k}{2}, v\right)}{B\left(\frac{k}{2}, \frac{n-1-k}{2}\right)} \quad . \tag{14}$$

For whole numbers the incomplete Beta function is obviously solvable by integration by parts, and the solution is:

$$\frac{B(i, m-i+1, v)}{B(i, m-i+1)} = \sum_{l=i}^{m} \binom{m}{l} v^l (1-v)^{m-l} \quad . \tag{15}$$

By comparing the arguments of the Beta function in Eq. (14) with those in Eq. (15), it follows:

$$i = \frac{k}{2} \quad , \tag{16}$$

and

$$\frac{n-1-k}{2} = m - i + 1 \quad . \tag{17}$$

Inserting Eq. (16) in Eq. (17) we have:

$$m = \frac{n-3}{2} \quad . \tag{18}$$

Since the variables i and m are defined as integers, Eq. (14) is solvable for even k and odd n. Replacing n and k in Eq. (14) by i and m, it follows:

$$P(v) = 1 - \frac{B(i, m-i+1, v)}{B(i, m-i+1)} \quad . \tag{19}$$

Using Eq. (15), the solution is:

$$P(v) = 1 - \sum_{l=i}^{m} \binom{m}{l} v^l (1-v)^{m-l} \quad . \tag{20}$$

Now we are aiming to replace the 1 in Eq. (20) by using the binomial definition, which is as follows:

$$\sum_{l=0}^{m} \binom{m}{l} a^l b^{m-l} = (a+b)^m \quad . \tag{21}$$

With a being v and b being 1- v it follows:

$$\sum_{l=0}^{m} \binom{m}{l} v^l (1-v)^{m-l} = \big(v + (1-v)\big)^m = 1 \quad , \tag{22}$$

so that it is actually possible to replace the 1 in Eq. (20) by a sum from zero to m:

$$P(v) = \sum_{l=0}^{m} \binom{m}{l} v^l (1-v)^{m-l} - \sum_{l=i}^{m} \binom{m}{l} v^l (1-v)^{m-l} \quad . \tag{23}$$

Calculating the sum from zero to m minus the sum from i to m, the sum from zero to i–1 is remaining:

$$P(v) = \sum_{l=0}^{i-1} \binom{m}{l} v^l (1-v)^{m-l} \quad . \tag{24}$$

Eq. (24) gives the exceeding probability as a function of external variance for any even break number k=2i. Let us again check the obtained equation numerically by a Monte Carlo computation. For this purpose we create a random time series of the length n=21 and search for the combination of 4 breaks that produces the maximum external variance. Fig. 4 shows the result as obtained by 1000 repetitions. As each individual time series contains $\binom{n-1}{k}=\binom{20}{4}=4845$ possibilities of decomposition, we are dealing with a sample size of 4,845,000. Two conclusions can be drawn. First, the data is in good agreement with Eq. (24). Second, the effective number of combinations is much smaller than the nominal.

To the first conclusion: In *Fig. 4*, vertical lines from ln(0)=1 are drawn down to the exceeding probability that is found in the numerical test data. Thus, the edge of the shaded area gives the probability function for a certain maximum external variance. The according theoretical function as derived from Eq. (24) is given alternatively as a curve. The chosen numbers of n=21 and k=4 can be transformed by Eqs. (16) and (18) to m=9 and i=2. Inserted into Eq. (24) it follows for the depicted example:

$$P(v) = (1-v)^9 + 9v(1-v)^8 \quad . \tag{25}$$

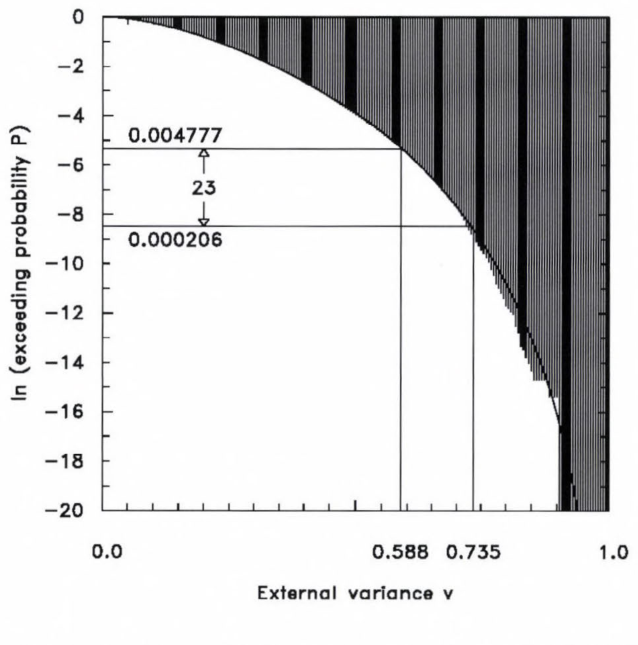

Fig. 4. Logarithmic exceeding probability as a function of external variance for 4 breaks within a 21-year time series. Vertical lines are drawn down from ln(0)=1 to the probability found for random data. The theoretical probability as generally given in Eq. (24) and specified in Eq. (25) is given by a curve. Two special data pairs are indicated, which are discussed in the text.

Fig. 4 shows that the data fits well to Eq. (25) if the probability is not too extreme. For such low probability it is not surprising that the limited Monte Carlo dataset shows more scatter and randomly deviates from the theory.

To the second conclusion: Two reading examples are given in *Fig. 4*. One starts from the exceeding probability of 2.064×10^{-4} (ln (0.0002) = –8.5). This value is equal to $\binom{20}{4}^{-1}$, the reciprocal of the nominal number of combinations for n=21 and k=4. If all combinations were independent, we could expect a maximum external variance of 0.7350. However, this is not the actually true value, which is already determined as 0.5876 (*Fig. 2*). But we can draw the reverse conclusion: What must be the effective number of combinations for the known external variance? We obtain a value of 4.777×10^{-3}, which is 23 times larger than the starting point. The conclusion is that the effective number of combinations for this special case (n=21, k = 4) is 23 times smaller than the nominal one, which is equal to $\binom{20}{4}$. The dependency of different solutions is reasonable. Shifting only one break position by one time step creates already a new break combination. However, its external variance will not deviate much from the original.

7. The relative change of variance as a function of increased break number

After confirming Eq. (24) by test data, we can assume its general validity and turn towards more realistic lengths. *Fig. 5* shows the graphs of Eq. (24) for n=101 and all even k from 2 to 20. As in *Fig. 4,* the number of independent combinations is estimated by a reversal conclusion from the known results of the maximum external variance. (In this case the results stem from a dynamic programming search as the length of n = 101 is too large for an explicit all-permutations-search of the maximum as it was possible for n = 21.)

The following question arises: What is the rate of change of the variance, if the number of breaks is increased? Obviously, there are two contributions. First, we skip from the graph in *Fig. 5* valid for k breaks to the next one valid for k+2. This causes a certain increase in the external variance, even if the number of combinations would remain constant. Second, there *is* certainly an increased number of permutations, although we showed that the effective number is always smaller than the nominal one.

Fig. 6 gives a sketch of the situation to illustrate how the mathematical formulations for the two components are derived in detail. The exceeding probability P for two arbitrary even break numbers is depicted. To determine the first contribution, we need to know the distance between two neighboring curves in v-direction for a fixed P ($v1– v0$ in *Fig. 6*).

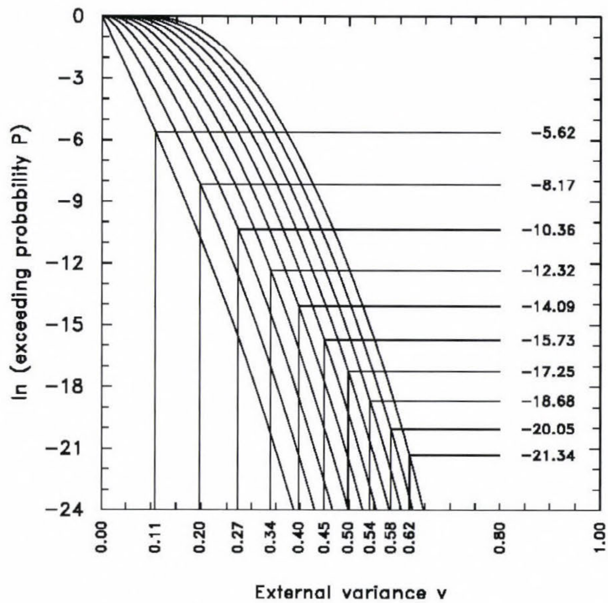

Fig. 5. As *Fig. 4*, but for a 101-year time series and for the ten different break numbers from 2, 4, 6, … , 20. The known external variances for each break number are retranslated into the observed effective exceeding probabilities given as the column at the right edge.

As Eq. (24) is difficult to solve for *v*, we estimate the *v* -distance by the *P*-distance, which is divided by the slope *s*:

$$\left(\frac{dv}{di}\right)_1 = v1 - v0 = \frac{ln(P1) - ln(P2)}{s} \quad . \tag{26}$$

Using the respective *i*-indices for *P1* and *P0* (see *Fig. 6*) we can rewrite:

$$\left(\frac{dv}{di}\right)_1 = \frac{\Big(ln\big(P_i(v)\big) - ln\big(P_{i+1}(v)\big)\Big)_{v=const}}{s} \quad . \tag{27}$$

This first part of *dv/di* arises because different functions of *P(v)* has to be used. We introduce C_f and refer to it the following as the function contribution:

$$C_f = \Big(ln\big(P_{i+1}(v)\big) - ln\big(P_i(v)\big)\Big)_{v=const} \quad , \tag{28}$$

so that Eq. (27) can be rewritten:

$$\left(\frac{dv}{di}\right)_1 = -\frac{C_f}{s} \quad . \tag{29}$$

The second contribution is the increase of v due to the total decrease of P ($v2 - v1$ in *Fig. 6*). Geometrically, this can be perceived as a walk down the respective curve.

$$\left(\frac{dv}{di}\right)_2 = v2 - v1 = \frac{ln(P2) - ln(P1)}{s} \quad . \tag{30}$$

Using i-indices for $P2$ and $P1$, it follows:

$$\left(\frac{dv}{di}\right)_2 = \frac{ln\big(P_{i+1}(v)\big) - ln\big(P_i(v)\big)}{s} \quad . \tag{31}$$

This second part of dv/di depends on the increased number of decomposing permutations with growing i. Consequently, we refer to the numerator as number contribution C_n, according to:

$$C_n = ln\big(P_{i+1}(v)\big) - ln\big(P_i(v)\big) \quad , \tag{32}$$

and it follows:

$$\left(\frac{dv}{di}\right)_2 = \frac{C_n}{s} \quad . \tag{33}$$

In both cases, changes in P are translated into v by the slope of the curves. This is appropriate if the curvatures are small and the slopes remain nearly constant. For the relevant parts of the curves this is a good approximation (*Fig. 5*).
Finally, we can summarize Eq. (29) and Eq. (33) to:

$$\frac{dv}{di} = \left(\frac{dv}{di}\right)_2 + \left(\frac{dv}{di}\right)_1 = \frac{C_n - C_f}{s} \quad . \tag{34}$$

To determine dv/di, we obviously need three terms, the slope s, the function contribution C_f, and the number contribution C_n. These three terms are derived in the following subsections.

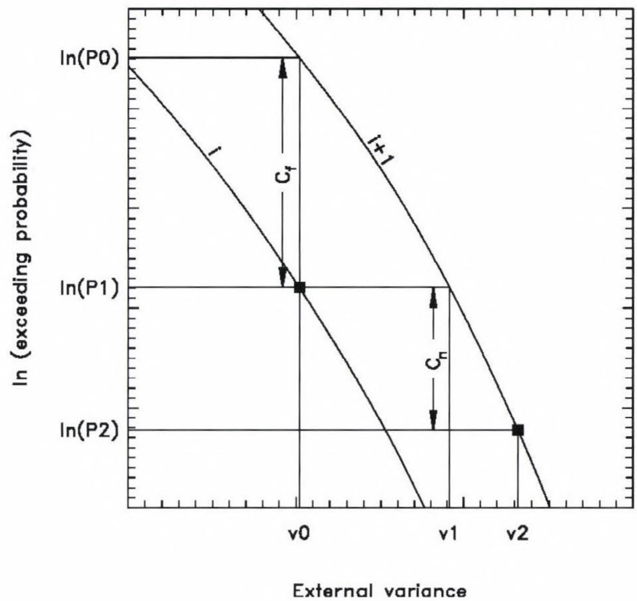

Fig. 6. Sketch to illustrate the total gain of external variance from v0 to v2, when the number of breaks k is increased by 2, i.e., from i to i+1. The first contribution ($v1-v0$) depends on the horizontal distance of the two curves. This contribution is derived in the text by the vertical distance C_f and the slope of the curve. The second contribution ($v2-v1$) occurs due to the increase of possible combinations when the break number is increased. As for the first contribution, it is translated from C_n by using the slope of the depicted curves.

7.1. The slope

The slope s of the logarithm of Eq. (24) as it is depicted in *Figs. 5* and *6* is equal to:

$$s = \frac{d}{dv}\Big(ln\big(P(v)\big)\Big) = \frac{1}{P(v)}\frac{dP(v)}{dv} \quad . \tag{35}$$

With Eq. (13) it follows:

$$s = -\frac{p(v)}{P(v)} \quad . \tag{36}$$

Replacing n and k by m and i and using the result of Appendix A we can rewrite Eq. (11) to:

$$p(v) = v^{i-1}(1-v)^{m-i}(m-i+1)\binom{m}{i-1} \quad . \tag{37}$$

Inserting Eq. (24) and Eq. (37) into Eq. (36), it follows:

$$s = -\frac{v^{i-1}(1-v)^{m-i}(m-i+1)\binom{m}{i-1}}{\sum_{l=0}^{i-1}\left(\binom{m}{l}v^l(1-v)^{m-l}\right)} \quad . \tag{38}$$

In Appendix B we show that the last summand is a good approximation for the sum occurring in the denominator and it follows:

$$s = -\frac{v^{i-1}(1-v)^{m-i}(m-i+1)\binom{m}{i-1}}{\binom{m}{i-1}v^{i-1}(1-v)^{m-i+1}} \quad , \tag{39}$$

which can be reduced to:

$$s = -\frac{m-i+1}{1-v} \quad . \tag{40}$$

After replacing again *m* and *i* by *n* and *k* it follows:

$$s = -\frac{n-1-k}{2(1-v)} \quad . \tag{41}$$

7.2. *The function contribution*

With Eq. (24) the vertical distance between two neighboring curves as given in *Fig. 6* is:

$$C_f = ln(P_{i+1}) - ln(P_i) = ln\left(\frac{\sum_{l=0}^{i}\binom{m}{l}v^l(1-v)^{m-l}}{\sum_{l=0}^{i-1}\binom{m}{l}v^l(1-v)^{m-l}}\right). \tag{42}$$

We use again Appendix B and approximate the sums by their last summand:

$$C_f = ln\left(\frac{\binom{m}{i}v^i(1-v)^{m-i}}{\binom{m}{i-1}v^{i-1}(1-v)^{m-i+1}}\right) \quad , \tag{43}$$

which can be reduced to:

$$C_f = ln\left(\frac{\binom{m}{i}\, v}{\binom{m}{i-1}\,(1-v)}\right) \quad . \tag{44}$$

The ratio of consecutive binomial coefficients is equal to $(m\text{-}i\text{+}1)/i$:

$$C_f = ln\left(\frac{(m-i+1)\, v}{i\,(1-v)}\right) \quad . \tag{45}$$

Replacing m and i again by n and k, it follows:

$$C_f = ln\left(\frac{(n-1-k)\, v}{k\,(1-v)}\right) \quad . \tag{46}$$

7.3. The number contribution

The nominal number of combinations grows with growing k from $\binom{n-1}{k}$ to $\binom{n-1}{k+1}$. This corresponds to a factor of $(n\text{–}1\text{–}k)/k$. However, in *Fig. 4* we show exemplarily for $k = 4$ that the effective number of combinations is lower. In *Fig. 5* the decrease of $\ln(P(v))$ due to the increase of the effective number of combinations is given in a column at right edge for the even k from 2 to 20. From these numbers we derived the actual decreasing factor $C_n = \Delta\ln(P(v))$ and compared it with the nominal (*Table 1*). The nominal decreasing factor for $\Delta k = 1$ is equal to the reciprocal of the growth of combinations $\frac{\binom{n-1}{k}}{\binom{n-1}{k+1}} = \frac{k}{n-1-k}$. Here we need its logarithm; and as the effective decreasing factor is only available for every second k, $nom = -2\ln((n\text{–}1\text{–}k)/k)$ is the proper reference.

From *Table 1* we can extract that the ratio between the effective and nominal factor is rather constant with $r \approx 0.4$, but slightly growing with increasing break number. The growth will be discussed in detail in Appendix C, for the time being we can summarize:

$$C_n = r\ nom = -2r\, ln\left(\frac{n-1-k}{k}\right) \quad . \tag{47}$$

Table 1. From *Fig. 5*, C_n, the effective decrease of $\ln(P(v))$ for the transition from k to k+2 is taken. It is compared to the nominal decrease equal to $-2\ \ln((n-1-k)/k)$. Finally, the ratio r between the effective and nominal factor is given

k_1	k_2	k	eff = Δ ln (P(v))	nom = –2 ln((n–1–k)/k)	r = eff/nom
2	4	3	–2.552	–6.952	0.367
4	6	5	–2.186	–5.889	0.371
6	8	7	–1.963	–5.173	0.379
8	10	9	–1.765	–4.627	0.381
10	12	11	–1.645	–4.181	0.393
12	14	13	–1.514	–3.802	0.398
14	16	15	–1.435	–3.469	0.414
16	18	17	–1.363	–3.171	0.430
18	20	19	–1.292	–2.900	0.446

7.4. *The differential equation and its solution*

The rate of change of v with regard to k is only half of that with regard to i (compare Eq. (16)):

$$\frac{dv}{dk} = \frac{dv}{di}\frac{di}{dk} = \frac{1}{2}\frac{dv}{di} \quad . \tag{48}$$

Using Eq. (34) it follows:

$$\frac{dv}{dk} = \frac{1}{2}\frac{C_n - C_f}{s} \quad . \tag{49}$$

Inserting our findings for the slope s (Eq. (41)) and for the two contributions C_f and C_n (Eqs. (46) and (47)), the growth of v with growing k is given by:

$$\frac{dv}{dk} = \frac{1-v}{n-1-k}\left(2r\ ln\left(\frac{n-1-k}{k}\right) + ln\left(\frac{(n-1-k)\ v}{k\ (1-v)}\right)\right) . \tag{50}$$

Reducing the fractions under the logarithms by n–1 leads to the normalized break number k^*, defined as:

$$k^* = \frac{k}{n-1} \quad . \tag{51}$$

At the same time, the differential dk has to be replaced by:

$$dk = (n-1)\, dk^* \quad , \tag{52}$$

so that Eq. (50) may be rewritten in normalized form:

$$\frac{dv}{dk^*} = \frac{1-v}{1-k^*}\left(2r\, ln\left(\frac{1-k^*}{k^*}\right) + ln\left(\frac{(1-k^*)\, v}{k^*\,(1-v)}\right)\right) \quad . \tag{53}$$

The final main question is now: What is the solution of Eq. (53)? Let us make a first approach to the solution by a very rough estimate for small k^*.

$$\frac{1-k^*}{1-v}\frac{dv}{dk^*} = 2r\, ln\left(\frac{1-k^*}{k^*}\right) + ln\left(\frac{(1-k^*)\, v}{k^*\,(1-v)}\right) = \alpha = -C_n + C_f \ . \tag{54}$$

The first logarithm constituting α, i.e., $-C_n$, is for small k^* in the order of $\ln(n)$ and it decreases with increasing k^*. The second, C_f, is in the order of $\ln(v/k^*)$. Because we know already the approximate solution being $1-v \approx (1-k^*)^4$, we can estimate the second term to about $\ln(4)$ (compare Eq. (78) in Appendix B). In contrast to the first term, this term increases with increasing k^* (see Appendix C), because $1-v$ is decreasing faster than $1-k^*$. Assuming $n = 101$, an estimate for α is:

$$\alpha \approx 2r\, ln(n) + ln(4) \approx 2 \cdot 0.4\, \ln(100) + ln(4) = 5.07 \ . \tag{55}$$

If α were actually constant, the integration of Eq. (54) would be easy:

$$\frac{1}{1-v}\, dv = \frac{\alpha}{1-k^*}\, dk^* \quad , \tag{56}$$

$$-\,ln(1-v) = -\,\alpha\, ln(1-k^*) \quad , \tag{57}$$

$$1-v = (1-k^*)^\alpha \quad , \tag{58}$$

which is rather similar to the already known approximate solution (Eq. (10)), except that the exponent found in Eq. (55) is higher. This already shows that the assumptions made to estimate s, C_f, and C_n were reasonable.

For a more accurate solution let us go back to the performance of the random data that we already used above to verify our theory. By these data we can check how well the rough estimate of a constant α is fulfilled in reality. *Fig. 7* shows that such an estimate is actually not too bad, which is the reason for Eq. (58) being rather close to the true solution. For a more precise solution, we fit a function to $\alpha(k^*)$ and obtain:

$$\frac{1-k^*}{1-v}\frac{dv}{dk^*} = \frac{1-k^*}{2}\,ln\left(\frac{1-k^*}{k^*}\right) + 2\,ln(5) \quad . \qquad (59)$$

Eq. (59) may be rewritten as:

$$\frac{1}{1-v}\,dv = \left(\frac{1}{2}\,ln\left(\frac{1-k^*}{k^*}\right) + \frac{2\,ln(5)}{1-k^*}\right) dk^* \quad , \qquad (60)$$

which is easy to integrate. Its solution is:

$$1-v = (1-k^*)^a \left(\frac{1-k^*}{k^*}\right)^{bk^*} \quad , \qquad (61)$$

with $a = 2\ \ln(5) + 1/2$ and $b = -1/2$.

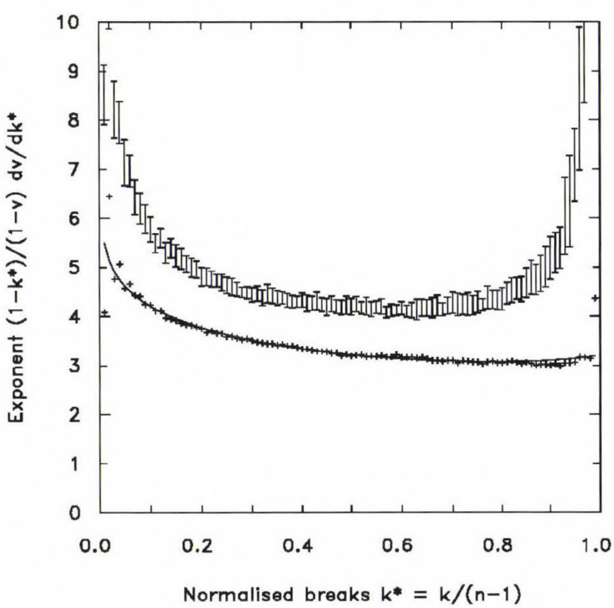

Fig. 7. Exponent α as given in Eq. (54) as a function of the normalized break number k^* for random data (crosses). These data consists of 1000 random 101-year time series. The vertical bars connect the 90 and 95 percentiles. The thin line is giving the function according to Eq. (59).

In *Fig. 7*, the function for the exponent α as given in Eq. (59) fits well to the results derived from random data. However, the relative gain of external variance is larger for even values compared to their uneven neighbors, especially for low values. This feature is reasonable, as it needs always a pair of breaks to isolate a subsegment. To produce the data, we performed 1000 repetitions, mainly to reduce the scatter. However, the repetitions can also be exploited to derive the variability of the solution. Consequently, not only the mean, but also the 90 and 95 percentiles are given. The average exponent starts for low normalized break numbers at about 5. This means that the external variance grows at the beginning 5 times faster than the normalized break number. This behavior is found for random data. When such a variance growth will occur in real data, we can be rather sure that no true break is present as it is normal for random data which has by definition no real break. The 95 percentile is for the first breaks as large as nearly 10. Thus, in only 5% of the cases, the external variance grows by a factor of more than 10 times faster than k^*. Hence, this value can be used as limit to distinguish true from spurious breaks. For the first break numbers it reaches nearly 10, decreasing rapidly to about 5 for $k^* = 0.1$.

8. Discussion of the penalty term

Within the homogenization algorithm PRODIGE (*Caussinus* and *Mestre*, 2004), the following expression is minimized to estimate the number of predicted breaks.

$$C_k(Y) = \ln\left(1 - \frac{\sum_{j=1}^{k+1} n_j\left(\bar{Y}_j - \bar{Y}\right)^2}{\sum_{i=1}^{n}(Y_i - \bar{Y})^2}\right) + \frac{2\,(k+l)}{n-1}\,ln(n) = \min \quad . \qquad (62)$$

The numeric value of $C_k(Y)$ depends on the data Y and the number of breaks k and consists of two opposite contributions. Firstly, the logarithm of the normalized internal variance, and secondly, a penalty term, originally proposed by *Caussinus* and *Lyazrhi* (1997). Whereas the first is decreasing with larger k, the second is increasing. Using our notations for the same terms, Eq. (62) can be rewritten as:

$$\ln(1 - v) + \frac{2k}{n-1}\,ln(n) = \min \quad . \qquad (63)$$

In Eq. (63), we combined k and l, the number of breaks and the number of outliers to a single number. Splitting off an outlier is identical to the separation of a subperiod of length 1. Consequently, it is not necessary to treat outliers separately. If we further use the normalized break number k^* according to Eq. (51) instead of k, we can rewrite:

$$\ln(1-v) \; + \; 2k^* \, ln(n) \; = \; \min \quad . \tag{64}$$

To find the break number k^* for which the expression is minimal, the first derivative with respect to k^* is set to zero:

$$-\frac{1}{1-v}\frac{dv}{dk^*} + 2\,ln(n) \; = \; 0 \quad , \tag{65}$$

which can be rewritten to:

$$\frac{1}{1-v}\frac{dv}{dk^*} \; = \; 2\,ln(n) \quad . \tag{66}$$

For a given time series, the length n is constant. Consequently, we can conclude from Eq. (66), that PRODIGE uses a fixed number, equal to 2 $\ln(n)$, as stop criterion. If the relative gain of the external variance falls below that constant, no further breaks are added and the final break number is reached. However, from Eq. (59) we know the function for the relative gain of external variance in detail; it just has to be divided by $1-k^*$.

$$\frac{1}{1-v}\frac{dv}{dk^*} \; = \; \frac{1}{2}\,ln\left(\frac{1-k^*}{k^*}\right) + \frac{2\,ln(5)}{1-k^*} \quad . \tag{67}$$

Fig. 8 shows this function for a time series of length 101. Additionally, six exceeding values for probabilities from 1/4 to 1/128 are given, based on 5000 repetitions. These curves are approximately equidistant. For comparison, the constant as proposed by *Caussinus* and *Mestre* (2004) and rewritten in Eq. (66) is given, which is about 9 (exactly 2 ln(101)) for $n = 101$.

As the exceeding values are computed for random data, they can be interpreted as error probability. The 1% error line (exactly 1/128) at the upper end of the family of curves in *Fig. 8* starts at a variance gain of about 15, and reaches, for $k^* = 0.1$, a value of about 8.

In the climatologically interesting range of small k^*, the numeric value of the mean variance gain (lowest line in *Fig. 8*) is equal to about 5 and can be interpreted as following. For random data, which contains no break by definition, the relative external variance grows on average with each additionally inserted break 5 times faster than expected by a simple linear approach. Such a linear approach just supposes that each break adds the same amount of external variance. For $n = 101$ this would be one percent per break. In reality, the data contains larger jumps just by chance, comprising not only 1%, but 5% of the remaining variance. In seldom cases, these highest jumps contain even 15% of the remaining variance, but the probability for that is only about 1% (uppermost line in *Fig. 8*). As the number of tentatively inserted breaks is growing, the highest jumps are already used before, so that the amount of the remaining decreases. Increasing the break number from 9 to 10 ($k^* = 0.1$) gains in average still 5%, as for the lowest break numbers, but the maximum value, exceeded in 1% of the cases, drops from 15% to 8%.

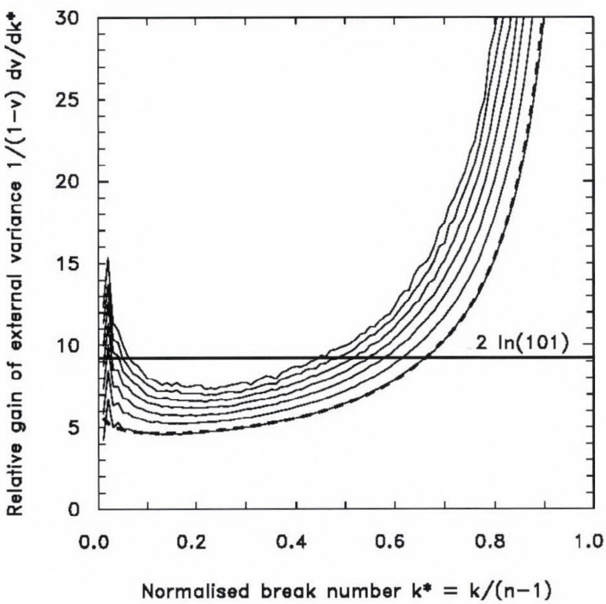

Fig. 8. Relative gain of external variance as a function of normalized breaks k^* for a time series length of $n = 101$. The dashed fat curve denotes the theoretical value as given by Eq. (67). The solid thin curves are showing the data results as obtained by 5000 repetitions. The lowest indicates the mean, which is largely congruent with the theory. The upper ones give the exceeding value for probabilities from $2^{-2}, 2^{-3}, \ldots, 2^{-7}$. For comparison, the constant 2 ln(n) proposed as stop criterion by *Caussinus* and *Lyazrhi* (1997) is given by the horizontal line.

The Lyazrhi constant of 2 ln(n) as proposed by *Caussinus* and *Mestre* (2004) is equal to about 9 for $n = 101$. At the beginning, i.e. for one break, this value lies in the middle of the family of error curves in *Fig. 8*. Thus, it corresponds here to an error of about 5%. At $k^* = 0.08$, i.e. for 8 breaks, the horizontal line is leaving the area covered by error curves. Thus, the error level decreases below 1%. Assuming continued equidistance, the horizontal line will reach areas with errors of less than 0.1% at $k^* = 0.15$. Thus, for low break numbers, PRODIGE accepts breaks, even if the error is relatively high (about

5%). In contrast, higher break numbers are effectively suppressed. Only breaks are accepted that add an amount of variance, which would occur randomly with a probability of less than 1%.

The choice of the Lyazrhi constant appears to be rather artful. For the first breaks, it allows errors of about 5%, which is a widely accepted error margin. However, for more than 8 breaks (within a time series of 101 data points), the method is much more rigid. Obviously, the preexisting knowledge is used that such high numbers of breaks are per se unlikely, so that a suppression is reasonable.

In *Fig. 9*, the corresponding features for shorter time series (n = 21) are given. Compared to n = 101, the average variance gain remains unchanged, showing that Eq. (67) is universally valid. However, the exceeding values increase, and the distances between the error curves grow by a factor of 5. This indicates that the growing factor is inversely proportional to the time series length n. In contrast, the Lyazrhi constant even decrease, although only slightly due to its logarithmic form. The direction of change of the Lyazrhi constant for different time series length is contradicting our findings for random data and should be studied further. However, instrumental climate records comprise often about 100 data points, and for such lengths the constant is chosen rather well.

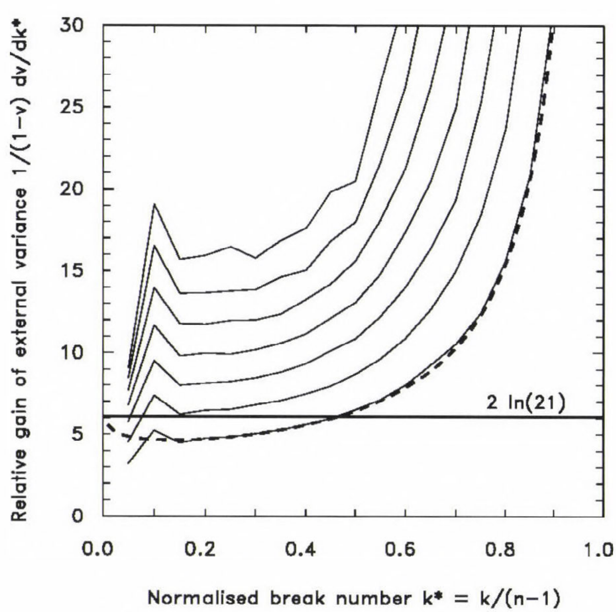

Fig. 9. As *Fig. 8*, but for n = 21. The average variance gain remains unchanged compared to *Fig. 8*, because Eq. (67) is universally valid. However, the exceeding values increase inversely proportional to n. In contrast, the constant of *Caussinus* and *Lyzrhi* (1997) decreases with decreasing n.

9. *Conclusions*

The external variance, defined as the variance of the subperiods' means, is shown to be the key parameter to detect breaks in climate records. Maximum external variance indicates the most probable combination of break positions. We analyzed the characteristics of the external variance occurring in random data and derived a mathematical formulation (Eq. (61)) for the growth of its maximum with increasing number of assumed breaks. As random data includes by definition no break, this knowledge can be used as null hypothesis to separate true breaks in real climate records more accurately from noise. In this way, it helps to enhance the valuable information from historical data.

Acknowledgement—We are grateful for advice from *Peter Domonkos* and *Tamas Szentimrey*. This work has been performed within the project Daily Stew supported by the Deutsche Forschungsgemeinschaft DFG (VE 366/5).

Appendix A

Consider the Beta function in Eq. (11):

$$B\left(\frac{k}{2},\frac{n-1-k}{2}\right) = B(i\,,m-i+1) = \frac{\Gamma(i)\,\Gamma(m-i+1)}{\Gamma(i+m-i+1)} = \frac{(i-1)!\;(m-i)!}{m!} \quad . \tag{68}$$

Multiplication of both the numerator and denominator with $m–i+1$ leads to:

$$B\left(\frac{k}{2},\frac{n-1-k}{2}\right) = \frac{(i-1)!\;(m-i+1)!}{(m-i+1)\,m!} \quad . \tag{69}$$

Remembering the definition of binomial coefficients being $\binom{n}{k} = \frac{n!}{k!\,(n-k)!}$, we can write:

$$B\left(\frac{k}{2},\frac{n-1-k}{2}\right) = \left((m-i+1)\binom{m}{i-1}\right)^{-1} \quad . \tag{70}$$

Appendix B

Consider the individual summands of the sum as defined in Eq. (24). The factor of change f between a certain summand and its successor is:

$$f = \frac{\binom{m}{l_i} v}{\binom{m}{l_i - 1}(1 - v)} \quad , \tag{71}$$

where l_i runs from zero to i. The ratio of consecutive binomial coefficients can be replaced, and it follows:

$$f = \frac{(m - l_i + 1)\, v}{l_i(1 - v)} \quad . \tag{72}$$

m and i can be replaced by n and k:

$$f = \frac{(n - 1 - l_k)\, v}{l_k(1 - v)} \quad . \tag{73}$$

Inserting k instead of l_k is a lower limit for f because $(n-1-l_k)/l_k$, the rate of change of the binomial coefficients, is decreasing monotonously with k:

$$f > \frac{(n - 1 - k)\, v}{k(1 - v)} \quad . \tag{74}$$

Normalize k by $1/(n-1)$:

$$f > \frac{(1 - k^*)\, v}{k^*(1 - v)} \quad . \tag{75}$$

The approximate solution is known with $1-v = (1-k^*)^4$, see Eq. (10).

$$f > \frac{(1 - k^*)\ (1 - (1 - k^*)^4)}{k^*(1 - k^*)^4} \quad , \tag{76}$$

$$f > \frac{1 - (1 - k^*)^4}{k^*(1 - k^*)^3} \quad , \tag{77}$$

for $k \to 0$:

$$f > \frac{1 - (1 - 4k^*)}{k^*(1 - 3k^*)} = \frac{4k^*}{k^*(1 - 3k^*)} = \frac{4}{1 - 3k^*} = 4 \quad , \tag{78}$$

for $k \rightarrow 1$:

$$f > \frac{(1-k^*)^{-3} - (1-k^*)^4}{k^*} = \frac{\infty - 0}{1} = \infty \quad . \tag{79}$$

We can conclude that each element of the sum given in Eq. (24) is by a factor f larger than the prior element. For small k^* the factor f is greater than about 4 and grows to infinity for large k^*. Consequently, we can approximate the sum by its last summand according to:

$$P(v) = \sum_{l=0}^{i-1} \binom{m}{l} v^l (1-v)^{m-l} \approx \binom{m}{i-1} v^{i-1} (1-v)^{m-i+1} \quad . \tag{80}$$

Appendix C

Once the solution for $v(k^*)$ is available (Eq. (61)), a more accurate estimation of the function contribution C_f is possible. So far, we approximated the sum given in Eq. (24) by its last summand, as discussed in Appendix B. Now we are able to check the impact of this approximation. Using the known solution, we calculated two versions of C_f. First, by taking into account only the last summand as in Eq. (43) and alternatively the complete term, as given in Eq. (42). *Fig. 10* shows these two estimates of C_f as dashed lines. The upper one denotes the full solution, the lower the approximation. Their difference remains limited, which confirms our findings in Appendix B. As discussed in Eq. (55), C_f starts for low k^* at about ln(4) and rises to infinity for high k^*.

Concerning the number contribution C_n, we applied so far only a rough estimate as given in Eq. (47), assuming a constant ratio between effective and nominal combination growths. Actual values for C_n are listed in *Table 1* for low break numbers. However, they are numerically computable up to about $k^* = 0.75$. In *Fig. 10*, these values for C_n are given as crosses. They are multiplied by -1, as $-C_n$ contributes to the exponent α. We fitted a function of the form:

$$(ak^* + b)\, ln\left(\frac{1-k^*}{k^*}\right) + c \quad , \tag{81}$$

to the data, which is depicted by the lower full curve in *Fig. 10*, and obtained for the coefficients:

$$a_l = 0.5, \qquad b_l = 0.55, \qquad c_l = 0.4 \quad .$$

A similar fit to C_f is given by the upper full curve in *Fig. 10*. Here the coefficients are:

$$a_2 = -1.0, \quad b_2 = -0.15, \quad c_2 = 2.7 \quad .$$

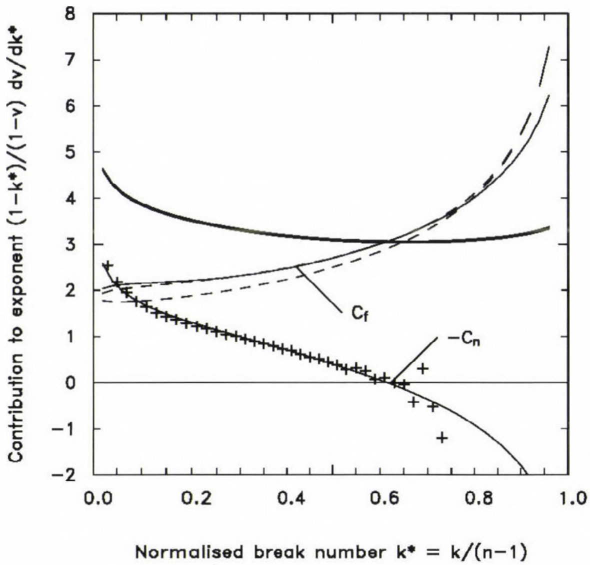

Fig. 10. Contributions of C_f and $-C_n$ to the exponent $= \frac{1-k^*}{1-v}\frac{dv}{dk^*}$. The two dashed lines are reconstructions of C_f from the known solution of $v(k^*)$, as given in Eq. (61). The solid line gives a fitted function for C_f. Crosses denote data for C_n connected likewise by a fitted curve. The sum of the two contributions is given by the fat line.

The sum of two curves yields then an alternative estimation for the exponent α. It is depicted as a fat line in *Fig. 10* and characterized by the sum of the coefficients:

$$a_3 = -0.5, \quad b_3 = 0.4, \quad c_3 = 3.1 \quad .$$

This alternative estimate is in good agreement (please compare *Fig. 7* lowest line with *Fig. 10* uppermost fat line) with the solution derived directly from the data as given in Eq. (59), where the coefficients are:

$$a_4 = -0.5, \quad b_4 = 0.5, \quad c_4 = 2\ \ln(5) = 3.2 \quad .$$

We see that Eq. (59), so far directly based on a fit to the data, is as well understandable from the theory as the sum of the two contributions C_f and $-C_n$.

References

Aguilar, E., Auer, I., Brunet, M., Peterson, T.C., and *Wieringa, J.,* 2003: Guidelines on climate metadata and homogenization. World Meteorological Organization, *WMO-TD No. 1186*, WCDMP No. 53, Geneva, Switzerland, 55 pp.

Akaike, H., 1973: Information theory and an extension of the maximum likelihood principle, In *2nd International Symposium on Information Theory*, Akademiai Kiado, Budapest, 267–281.

Alexandersson, H. and *Moberg, A.*, 1997: Homogenization of Swedish temperature data. 1. Homogeneity test for linear trends. *Int. J. Climatol. 17*, 25–34.

Auer, I., Böhm, R., Jurkovic, A., Orlik, A., Potzmann, R., Schöner, W., Ungersböck, M., Brunetti, M., Nanni, T., Maugeri, M., Briffa, K., Jones, P., Efthymiadis, D., Mestre, O., Moisselin, J.M., Begert, M., Brazdil, R., Bochnicek, O., Cegnar, T., Gajic-Capkaj, M., Zaninovic, K., Majstorovic, Z., Szalai, S., Szentimrey, T., and *Mercalli, L.*,2005: A new instrumental precipitation dataset for the Greater Alpine Region for the period 1800–2002, *Int. J. Climatol. 25*, 139–166.

Auer, I., Böhm, R., Jurkovic, A., Lipa, W., Orlik, A., Potzmann, R., Schöner, W., Ungersböck, M., Matulla, C., Briffa, K., Jones, P., Efthymiadis, D., Brunetti, M., Nanni, T., Maugeri, M., Mercalli, L., Mestre, O., Moisselin, J.M., Begert, M., Müller-Westermeier, G., Kveton, V., Bochnicek, O., Stastny, P., Lapin, M., Szalai, S., Szentimrey, T., Cegnar, T., Dolinar, M., Gajic-Capka, M., Zaninovic, K., Majstorovic, Z., and *Nieplova, E.*, 2007: HISTALP – historical instrumental climatological surface time series of the Greater Alpine Region, *Int. J. Climatol.* 27, 17–46.

Begert, M., Schlegel, T. and *Kirchhofer, W.*, 2005: Homogeneous temperature and precipitation series of Switzerland from 1864 to 2000. *Int. J. Climatol. 25*, 65–80.

Bellman, R., 1954: The Theory of Dynamic Programming, *Bull. Am. Math. Soc. 60*, 503–516. doi: 10.1090/S0002-9904-1954-09848-8, MR 0067457.

Bergström, H. and *Moberg, A.*, 2002: Daily air temperature and pressure series for Uppsala (1722–1998). *Climatic Change, 53*, 213–252.

Brunet, M., Asin, J., Sigro, J., Banon, M., Garcıa, F., Aguilar, E., Esteban Palenzuela, J., Peterson, T.C., and *Jones, P.*, 2011: The minimization of the screen bias from ancient Western Mediterranean air temperature records: an exploratory statistical analysis. *Int. J. Climatol. 31*, 1879–1895.

Brunetti, M., Maugeri, M., Monti, F., and *Nannia, T.*,2006: Temperature and precipitation variability in Italy in the last two centuries from homogenised instrumental time series. *Int. J. Climatol. 26*, 345–381.

Caussinus H. and *Lyazrhi, F.*,1997: Choosing a linear model with a random number of change-points and outliers. *Ann. Inst. Stat. Math. 49*, 761–775.

Caussinus, H. and *Mestre, O.*, 1996: New mathematical tools and methodologies for relative homogeneity testing. *Proc. First Seminar for Homogenization of Surface Climatological Data*, Budapest, Hungary, Hungarian Meteorology Service, 63–72.

Caussinus, H. and *Mestre, O.*, 2004: Detection and correction of artificial shifts in climate series. *Appl. Statist. 53*, part 3, 405–425.

Conrad, V. and *Pollak. C.*, 1950: *Methods in climatology*, Harvard University Press, Cambridge, MA, 459 pp.

Davis R.A.,. Lee, T.C.M., and *Rodriguez-Yam, G.A.*, 2012: Structural break estimation for nonstationary time series models. *J. Am.. Stat. Assoc. 101*, 223–239.

Domonkos, P., 2011a: Efficiency evaluation for detecting inhomogeneities by objective homogenization methods. *Theor. Appl. Climatol. 105*, 455–467.

Domonkos, P., 2011b: Adapted Caussinus-Mestre Algorithm for Networks of Temperature Series (ACMANT). *Int. J. Geosci. 2*, 293–309.

Easterling, D.R. and *Peterson, T.C.*, 1995: A new method for detecting undocumented discontinuities in climatological time series. *Int. J. Climatol., 15*, 369–377.

Hawkins, D.M., 1972: On the choice of segments in piecewise approximation. *J. Inst. Maths. Applics., 9*, 250–256.

Knowles Middleton, W.E., 1966: A history of the thermometer and its use in meteorology. The John Hopkin Press, Baltimore, Maryland. 249 pp.

Lavielle, M., 1998: Optimal segmentation of random processes. *IEEE Trans. Signal Processing, 46*, 1365–1373.
Li, S. and *Lund, R.*, 2012: Multiple Changepoint Detection via Genetic Algorithms. *J. Climate 25*, 674–686.
Lindau, R., 2003: Errors of Atlantic Air-Sea Fluxes Derived from Ship Observations., *J. Climate, 16*, 783–788.
Lindau, R., 2006: The elimination of spurious trends in marine wind data using pressure observations. *Int. J. Climatol.* 26, 797–817.
Menne M.J. and *Williams Jr., C.N.*, 2009: Homogenization of temperature series via pairwise comparisons. *J. Climate, 22*, 1700–1717.
Mestre O., Domonkos, P., Picard, F., Auer, I., Robin, S., Lebarbier, E., Böhm, R., Aguilar, E., Guijarro, J., Vertachnik, G., Klancar, M., Dubuisson, B., and *Stepanek, P.*, 2012: HOMER: homogenisation software in R –methods and applications. *Időjárás 117*, 47–67.
MeteoSchweiz, 2000: Alte meteorologische Instrumente (Old meteorological instruments). Bundesamt für Meteorology und Klimatologie (MeteoSchweiz), Zürich, 190 p.
Nemec J., Gruber, G., Chimani, B., and *Auer, I.*, 2012: Trends in extreme temperature indices in Austria based on a new homogenized dataset. *Int. J. Climatol.*, DOI: 10.1002/joc.3532.
Nordli, P.O., Alexandersson, H., Frich, P., Förland, E.J., Heino, R., Jonsson, T., Tuomenvirta, H., and Tveito, O.E., 1997: The effect of radiation screens on Nordic time series of mean temperature. Int. J. Climatol. 17, 1667–1681.
Picard, F., Robin, S., Lavielle, M., Vaisse, C., and Daudin, J.-J., 2005: A statistical approach for array CGH data analysis, BMC Bioinformatics 6, 27.
Picard F., Lebarbier, E., Hoebeke, M., Rigaill, G., Thiam, B., and *Robin, S.*, 2011: Joint segmentation, calling, and normalization of multiple CGH profiles. *Biostatistics 12*, 413–428.
Rust, H.W., Mestre, O., and *Venema, V.K.C.*, 2008: Less jumps, less memory: homogenized temperature records and long memory. *J. Geophys. Res. Atmos. 113*, D19110.
Slonosky, V.C., Jones, P.D. and *Davies, T.D.*, 2001: Instrumental pressure observations and atmospheric circulation from the 17th and 18th centuries: London and Paris, *Int. J. Climatol. 21*, 285–298.
Szentimrey, T., 1996: Statistical procedure for joint homogenisation of climatic time series. *Proceedings of the First seminar of homogenisation of surface climatological data*, Budapest, Hungary, 6–12 October 1996, 47–62.
Szentimrey, T., 1999: Multiple Analysis of Series for Homogenization (MASH). *Proceedings of the second seminar for homogenization of surface climatological data*, Budapest, Hungary; WMO, WCDMP-No. 41, 27–46.
Szentimrey, T., 2007: Manual of homogenization software MASHv3.02. Hungarian Meteorological Service, 65 p.
Trewin, B., 2010: Exposure, instrumentation, and observing practice effects on land temperature measurements. *WIREs Clim. Change, 1*, 490–506.
Van der Meulen, J.P. and *Brandsma, T.*, 2008: Thermometer screen intercomparison in De Bilt (The Netherlands), part I: Understanding the weather-dependent temperature differences. *Int. J. Climatol. 28*, 371–387.
Venema, V., Mestre, O., Aguilar, E., Auer, I., Guijarro, J.A., Domonkos, P., Vertacnik, G., Szentimrey, T., Stepanek, P., Zahradnicek, P., Viarre, J., Müller-Westermeier, G., Lakatos, M., Williams, C.N., Menne M.J., Lindau, R., Rasol, D., Rustemeier, E., Kolokythas, K., Marinova, T., Andresen, L., Acquaotta, F., Fratianni, S., Cheval, S., Klancar, M., Brunetti, M., Gruber, Ch., Prohom Duran, M., Likso, T., Esteban, P., and *Brandsma, Th.*, 2012: Benchmarking homogenization algorithms for monthly data. *Clim. Past 8*, 89–115.
Vincent, L.A., 1998: A technique for the identification of inhomogeneities in Canadian temperature series. *J. Climate 11*, 1094–1104.

IDŐJÁRÁS
Quarterly Journal of the Hungarian Meteorological Service
Vol. 117, No. 1, January–March 2013, pp. 35-45

Climatological series shift test comparison on running windows

José A. Guijarro

State Meteorological Agency, Moll de Ponent s/n, Portopí,
07015-Palma de Mallorca, Spain
jguijarrop@aemet.es

(Manuscript received in final form October 3, 2012)

ABSTRACT–The detection and correction of inhomogeneities in the climate series is of paramount importance for avoiding misleading conclusions in the study of climate variations. One simple way to address the problem of multiple shifts in the same series is to apply the tests on windows running along the series of anomalies. But it is not clear which of the available tests works better. 500 Monte Carlo simulations have been done for the ideal case of a 600 normally distributed terms (a 50 years series of monthly differences), with a single shift in the middle and magnitudes of 0 to 2 standard deviations (s) in steps of 0.2 s. The compared tests have been: 1) classical t-test; 2) standard normal homogeneity test; 3) two-phase regression; 4) Wilcoxon-Mann-Whitney test; 5) Durbin-Watson test (lag-1 serial correlation), and 6) squared relative mean difference (simpler than t-test and hence faster to compute). The criterion for qualifying the performance of each test was the ability to detect shifts without false alarms and to locate them at the correct point. Results indicate that, under these precise simulated conditions, the best test are the classical t-test, Alexandersson's SNHT and SRMD, with almost identical results, followed by the Wilcoxon-Mann-Whitney test, while two phase regression and Durbin-Watson performances are very poor.

Key-words: homogenization, shift tests comparison, climatological series.

1. Introduction

Climatological series are very important for studying climate variability at all scales, but the climate signal is too often merged with unwanted variations due to changes in the type or exposure of the instruments, methods of observation, relocations of the stations, or changes in their surroundings.

Many methodologies have been proposed so far to detect and correct these inhomogeneities, which commonly appear as either sudden shifts or smooth trends in relative series. These relative series are usually computed as difference or ratio series between the problem series and a reference, that can be an observed trusted homogeneous series or a synthetic one compiled from a selection of the nearest or more correlated stations. Reviews of the different methods can be seen in *Easterling* and *Peterson* (1992), *Peterson et al.* (1998), *Aguilar et al.* (2003), and *Beaulieu et al.* (2008).

Several comparisons of shift detection methods have been undertaken so far (*Easterling* and *Peterson*, 1995; *Bosshard* and *Baudenbacher*, 1997; *Ducre-Robitaille et al.*, 2003; *Beaulieu et al.*, 2008), their results being influenced by the type (shifts and/or local trends), number and position of the simulated inhomogeneities, differences in station variance and between-station correlation structure, series length, autocorrelation, and nonstationarity.

The frequent concurrence of several jumps in the same series makes their detection problematic. One simple way to address this problem is to apply the test on time moving windows. During the development of an automated homogenization function for the CLIMATOL R contributed package (*Guijarro*, 2011a), the chosen approach for the detection of multiple change points was the application of a two-sample t-test for equal means to windows running along the series of anomalies (differences between the tested series and a synthetic reference series computed from neighboring stations). At this point, the question whether there were better detection tests emerged, but the available reviews are not fully conclusive, since the performance of the tests depends on the particular settings of the simulations and the significance threshold values chosen in each case, as it happens in the differing results of *Ducre-Robitaille et al.* (2003) and *Beaulieu et al.* (2008).

Therefore, new Monte Carlo experiments were designed to test the sensitivity and correctness of several algorithms in detecting and locating a shift in repeated series of white noise that simulate the ideal case of series of differences between a tested series with a single abrupt change in the mean and a homogeneous well correlated reference series. In this way we avoid the problems of simulating networks of observation or pairs of tested and reference stations as in the aforementioned evaluation exercises. Moreover, no a priori level of significance will be imposed, and location errors of the break point will be studied with no established thresholds of good/bad location. Next sections will explain this methodology, and the results of the tested algorithms will be discussed.

2. Methodology

500 series of 600 normally distributed terms (equivalent to tested minus reference monthly series of 50 years) were generated with the help of the *R*

function *rnorm* (*R Development Core Team*, 2010). Single shifts were added to all of them just in the middle (from term 301) with magnitudes from 0 to 2 standard deviations (s) in steps of 0.2 s, yielding a total of 5500 testing series. Six shift detection algorithms were applied on them, but not over the whole series, but on fixed width windows running along them. Different sample sizes were tried, from n=1 to 5 years (12 to 60 terms in steps of 12), and since two samples were involved in the shift tests, window widths of 2, 4, 6, 8, and 10 years were used. In this way, for n years sample size, every algorithm was tested $600–24 \cdot n+1$ times in each of the 5500 series (from 577 times with 1 year samples to 481 for samples of 5 years). *Fig. 1* shows an example series with a 0.8 s shift.

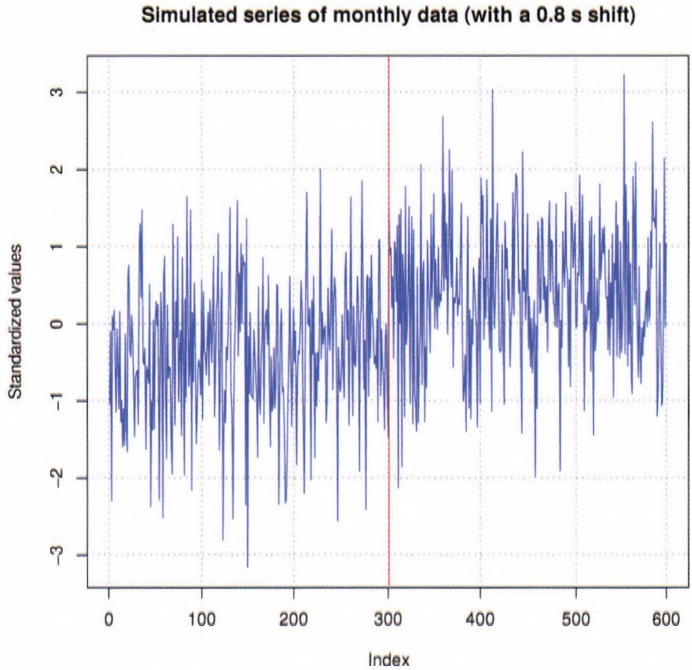

Fig. 1. Example of white noise difference series of 600 terms with a shift of 0.8 standard deviations in term 301.

The six algorithms tested were the following:

1. t-test: the classical test of mean differences of two samples.
2. SNHT: *Alexandersson*'s (1986) algorithm, but modified to test the middle point of the window only.

3. TPR: two-phase regression, as formulated by *Easterling* and *Peterson* (1995).

4. WMW: Wilcoxon-Mann-Whitney test, which is similar to the Wilcoxon rank sums applied by *Karl* and *Williams* (1987) but as formulated by *Gérard-Marchant* and *Stooksbury* (2008), and divided by the number of terms to make it less dependent on the sample size.

5. DW: lag-1 Durbin-Watson test for serial correlation.

6. SRMD (squared relative mean difference): $z = [\,(m_1\text{-}m_2)\cdot s^{-1}]^2$, where m_1 and m_2 are the sample means and s is the standard deviation of the whole window.

The reference values of DW and t-test were their returned p-values, but $\log_{10}$ transformed and sign reversed to allow more friendly figures (they are called *pV*, by analogy with the alkalinity index *pH* used in chemistry). *Fig. 2* displays the values returned by the six algorithms after being applied to a series similar to that in *Fig. 1* on running windows of 10 years (sample sizes of 5 years, i.e., 60 terms). Only the maximum value reached along the series, and its location (the middle point of the window giving that value) were retained for the statistical analysis of the results.

3. Results and discussion

The frequencies of the maximum values returned by the tests on each series and the errors of their corresponding locations (diagnosed break term minus 301) were analyzed statistically, and the results are shown graphically in form of boxplots, where each box summarizes 500 results. *Fig. 3* shows the influence of window size on the results yielded by the t-Test. It is clear that sample sizes of 12 terms are too small to allow the detection of shifts. If we take the value of the top whisker of the first box (homogeneous series) as a reasonable threshold to avoid false break detection, only roughly half of the 2 *s* shifts would be identified. With wider windows the power of detection improves: the half of the breaks detection reference is achieved with 0.8 and 0.6 *s* shifts for samples of 3 and 5 years respectively. (The intermediate 4 year sample graph can be seen in Figure 4). These results are in accordance with those of *Beaulieu et al.* (2008), who found that shifts under 1 *s* were difficult to identify, while all techniques tested by them worked well for breaks greater than 2 *s*.

The performance of the six tests with samples of 4 years can be seen in *Fig. 4*. As every test has its own metric, the units displayed in the vertical axis are all different, but it is easy to see that some tests reach higher values quicker than others as the shift magnitude increases, showing their greater power of detection.

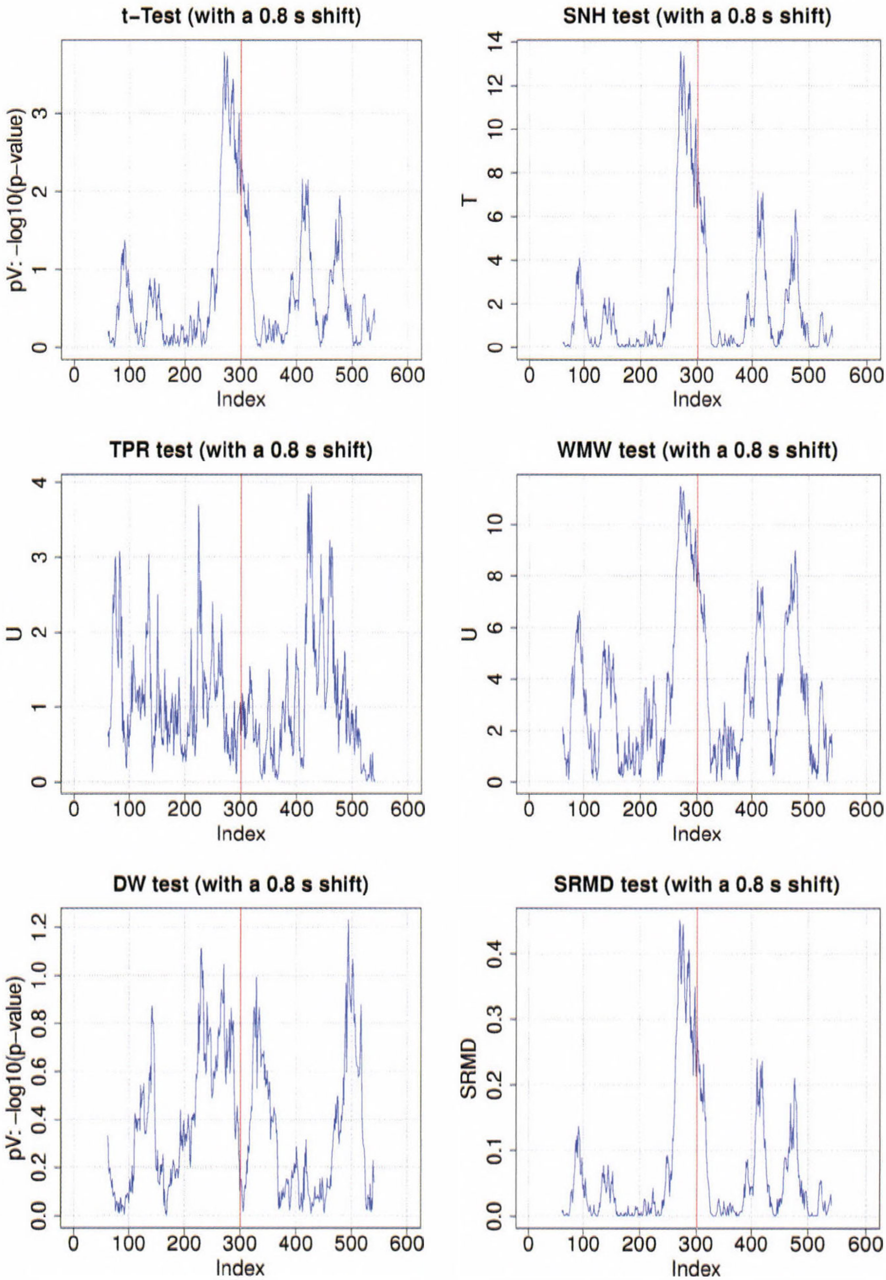

Fig. 2. Graphs of the values returned by the tests when applied to a series similar to that in *Fig 1* on running windows of 120 terms (two samples of 5 years). The vertical bar in the middle of the series indicates the true possition of the shift.

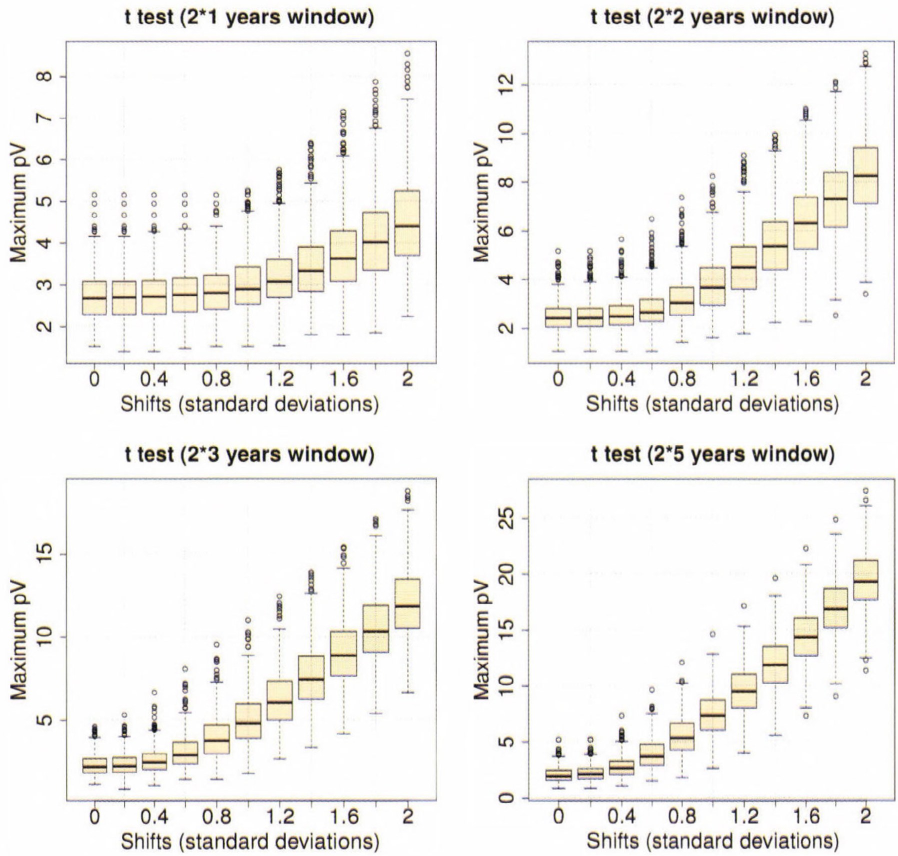

Fig. 3. Influence of window size on the results yielded by the t-test.

Table 1 presents the percentage of shift detection of every algorithm for each shift, for the 5 years samples, when the threshold detection is placed: a) at the maximum value obtained with the homogeneous series (no false detection is allowed); b) at the 99 percentile of the homogeneous values (permitting 1% of false detection). The best performances correspond to t-test, SNHT and SRMD, that give almost identical results, showing that they belong to the same family of tests. WMW follows, with good results form 1 *s* shift onwards, while DW and TPR both yield similar discouraging scores. Note that the thresholds of any test applied hundreds of times on every series through such a running window procedure, must be higher than their corresponding significant levels when applied only once on each series. E.g., the 14.23 of SNHT allowing 1% of false detection is higher than the 13.813 published by *Khaliq* and *Ouarda* (2007) for a 99% confidence level and sample size of 600 values (the whole simulated series).

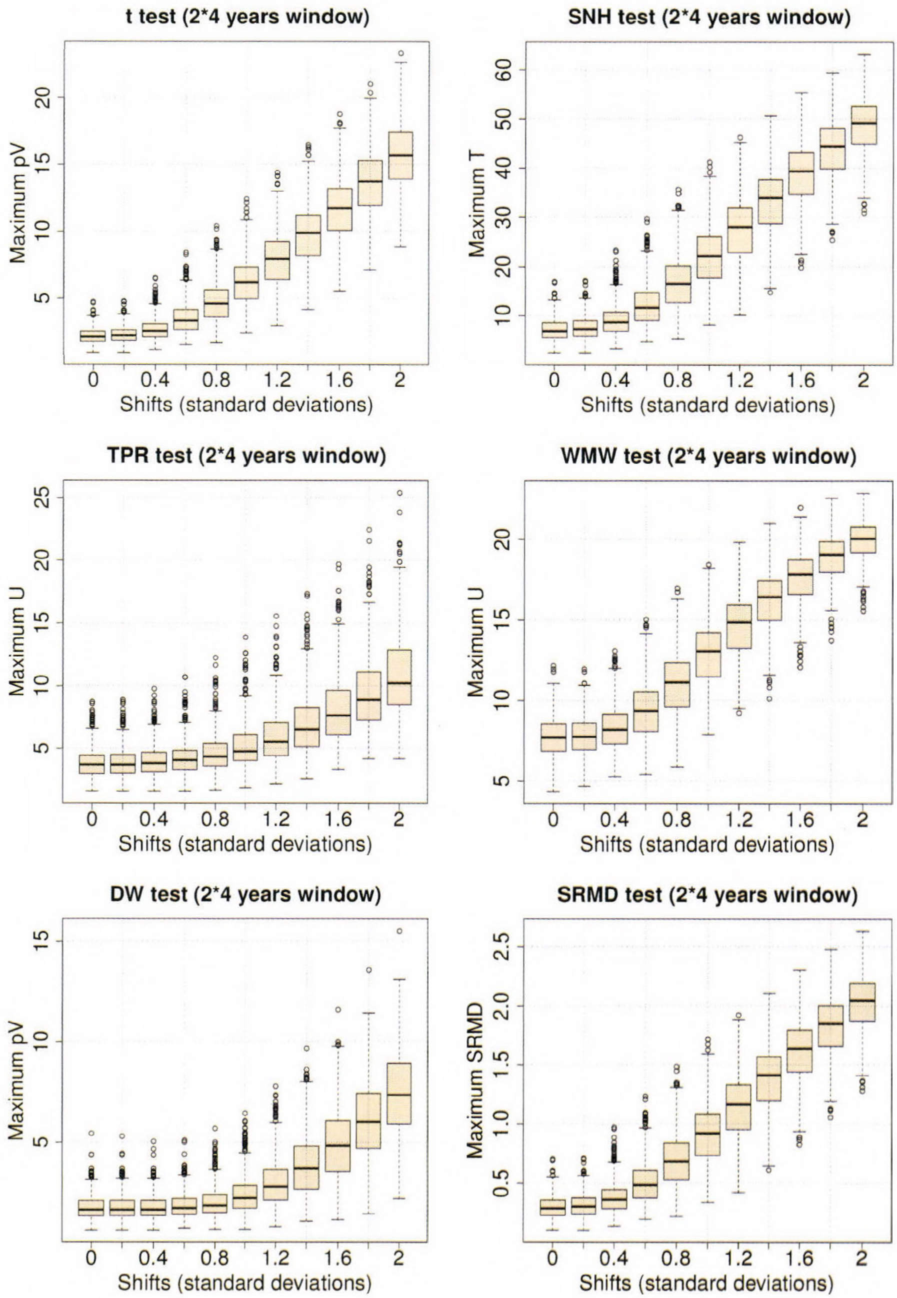

Fig. 4. Values of the six algorithms for shifts ranging from 0 to 2 standard deviations.

Table 1. Threshold values and percentage of shift detection in the cases of no false detection and allowing 1% of false detections, for a 5 years sample size (running windows of 10 years, i.e., 120 terms)

		Shift (standard deviations)									
Test	Thresh.	0.2	0.4	0.6	0.8	1.0	1.2	1.4	1.6	1.8	2.0
		No false detection:									
t-test	5.22	0.0	2.4	16.6	54.4	88.8	98.8	100.0	100.0	100.0	100.0
SNHT	19.06	0.0	2.4	16.8	54.6	88.8	98.8	100.0	100.0	100.0	100.0
TPR	8.69	0.0	0.6	1.6	2.8	7.8	16.6	34.4	55.0	74.8	88.4
WMW	13.78	0.0	2.0	12.6	47.4	82.8	98.4	100.0	100.0	100.0	100.0
DW	4.98	0.0	0.0	0.0	0.6	3.6	14.8	37.8	65.2	86.0	95.8
SRMD	0.635	0.0	2.4	16.6	54.4	88.8	98.8	100.0	100.0	100.0	100.0
		1% false detection:									
t-test	3.96	2.2	13.2	44.6	81.4	97.8	100.0	100.0	100.0	100.0	100.0
SNHT	14.23	2.4	13.2	44.4	81.4	97.8	100.0	100.0	100.0	100.0	100.0
TPR	6.87	1.6	3.0	4.6	11.6	20.4	41.0	62.2	79.4	91.0	97.4
WMW	12.04	0.8	8.6	35.0	73.4	95.2	99.8	100.0	100.0	100.0	100.0
DW	3.59	1.0	1.2	1.8	5.4	17.4	41.2	66.4	87.0	96.4	99.6
SRMD	0.474	2.4	13.2	44.4	81.4	97.8	100.0	100.0	100.0	100.0	100.0

With respect to the location errors, *Fig. 5* shows the corresponding box plots for the 4 years sample size (running windows of $2 \cdot 4 \cdot 12 = 96$ terms). Again, the t-test family (including SNHT and SRMD) reaches the best results, with small location errors for shifts greater than 0.6 standard deviations. Location errors of WMW are only slightly higher, but those of DW and specifically TPR are very big.

As CLIMATOL must apply the chosen test many times in iterative runs during the homogenization of a climatological network, computing efficiency is also important, and therefore, the time used by each of the tests was accounted for. Those adjusting regression models (TPR and DW) were the most time consuming using the R *lm* function. The R implementation of the t-test is much faster, but at the same time much slower than SNHT, probably due to its higher complexity and the inherent computation of p-values and other statistical parameters. This is why SRMD was introduced, achieving identical results as SNHT (in this two sample version), but at 20% higher speed. If TPR or DW had given better results, rewriting the regression algorithm to shorten their computing time would have been explored.

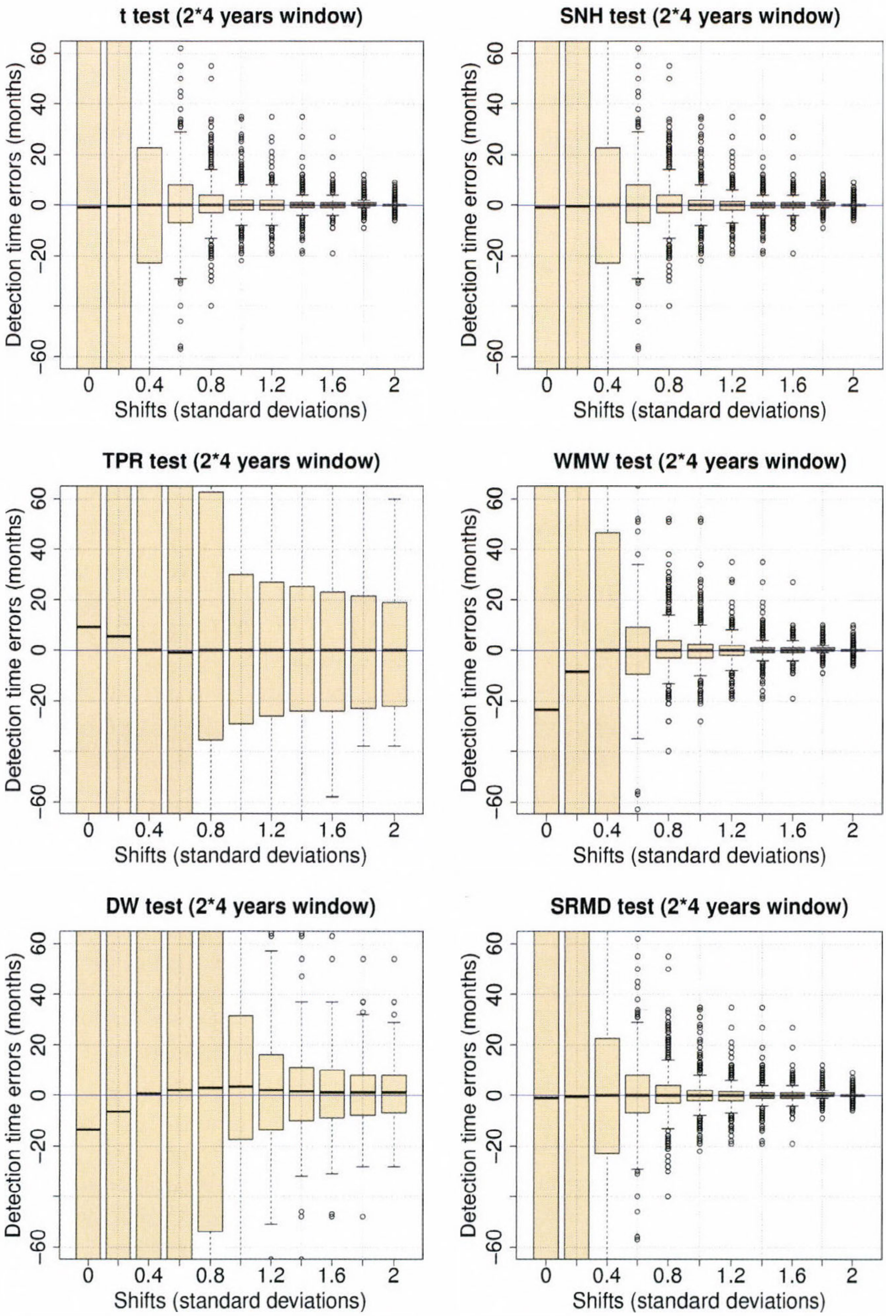

Fig. 5. Location errors of the six algorithms for shifts ranging from 0 to 2 standard deviations.

The combination of several of these tests was also tried, but when the best algorithm is used, there is no advantage in adding the results of any others. Therefore, CLIMATOL 2.0 implemented SRMD on running windows (4 years samples by default). Nevertheless, practical applications of that version showed that clear inhomogeneities spanning less than 3 years are common in real climatological series, and they were difficult to correct automatically due to the constraint of the minimum 3 years sample size required by the algorithm. Hence, the following 2.1 version dropped SRMD in favor of the popular and well tested SNTH which, freed from the window size restriction, is able to resolve close shifts. To avoid possible masking effects when multiple shifts are present in the same series, this test was implemented in two stages. In the first stages SNHT is applied on shifted windows of user defined width, and when significant shifts detected in this way have been corrected, SNHT is applied to the whole series in the second stage (*Guijarro*, 2011b).

4. Conclusions

The results of the simulations performed in this work indicate that, under these precise conditions of detection of a single shift in the middle of the series by means of fixed width windows running along the series, the best tests are the classical t-test and SNHT. SMRD is a simple derivative of the t-test with the same performance. The Wilcoxon-Mann-Whitney test yields acceptable results, but the two-phase regression and Durbin-Watson performances are very poor (although they can be better in other situations, e.g., in detecting local trends).

Nonetheless, windows need to have a minimum width of 6 years (two samples of 3 years), and that restrains the time resolution at which two close shifts can be identified. As a result, the t-test procedure of comparing the means of two samples was abandoned in favor of the standard formulation of SNHT, applied on stepped windows to avoid misleading results in the presence of multiple breaks in a first stage, then followed by an application on the whole series.

References

Aguilar, E., Auer, I., Brunet, M., Peterson, T.C., and *Wieringa, J.,* 2003: *Guidelines on climate metadata and homogenization*. WCDMP-No. 53, WMO-TD No. 1186. World Meteorological Organization, Geneve.

Alexandersson, H., 1986: A homogeneity test applied to precipitation data. *J. Climatol., 6,* 661–675.

Beaulieu, C., Seidou, O., Ouarda, T.B.M.J., Zhang, X., Boulet, G., and *Yagouti, A.,* 2008: Intercomparison of homogenization techniques for precipitation data. *Water Resour. Res, 44,* 20.

Bosshard, W. and *Baudenbacher, M.,* 1997: Evaluation of various homogeneity tests by simulation of climatological time series. In: *Proceedings of the First Seminar for Homogenization of Surface Climatological Data*, Budapest, 6–12 October 1996, Hungarian Meteorological Service, 19–34.

Ducré-Robitaille, J.F., Vincent, L.A., and *Boulet, G.*, 2003: Comparison of techniques for detection of discontinuities in temperature series. *Int. J. Climatol. 23*, 1087–1101.

Easterling, D.R. and *Peterson, T.C.*, 1992: Techniques for detecting and adjusting for artificial discontinuities in climatological time series: a review. *5th International Meeting on Stat. Climatology*, June 22–26, 1992, Toronto.

Easterling, D.R. and *Peterson, T.C.*, 1995: A new method for detecting undocumented discontinuities in climatological time series. *Int. J. Climatol. 15*, 369–377.

Gérard-marchant, P.G.F. and *Stooksbury, D.E.*, 2008: Methods for Starting the Detection of Undocumented Multiple Changepoints. *J. Climate 21*, 4887–4899.

Guijarro, J.A., 2011a: http://cran.r-project.org/web/packages/climatol/index.html.

Guijarro, J.A., 2011b: User's guide to Climatol. 40 pp. http://webs.ono.com/climatol/climatol-guide.pdf

Karl, T.R. and *Williams, C.N.*, 1987: An approach to adjusting climatological time series for discontinuous inhomogeneities. *J. Clim. Appl. Meteor. 26*, 1744–1763.

Khaliq, M.N. and *Ouarda, T.B.M.J.*, 2007: On the critical values of the standard normal homogeneity test (SNHT). *Int. J. Climatol. 27*, 681–687.

Peterson, T.C., Easterling, D.R., Karl, T.R., Groisman, P., Nicholls, N., Plummer, N., Torok, S., Auer, I., Boehm, R., Gullett, D., Vincent, L., Heino, R., Tuomenvirta, H., Mestre, O., Szentimrey, T., Salinger, J., Fřrland, E., Hanssen-bauer, I., Alexandersson, H., Jones, P., and *Parker, D.*, 1998: Homogeneity Adjustments of „In Situ" Atmospheric Climate Data: A Review. *Int. J. Climatol. 18*, 1493–1518.

R Development Core Team, 2010: *R: A language and environment for statistical computing*. R Foundation for Statistical Computing, Vienna, Austria. ISBN 3-900051-07-0, URL http://www.R-project.org/.

IDŐJÁRÁS
Quarterly Journal of the Hungarian Meteorological Service
Vol. 117, No. 1, January–March 2013, pp. 47-67

HOMER : a homogenization software – methods and applications

Olivier Mestre[1]*, Peter Domonkos[2], Franck Picard[3], Ingeborg Auer[4], Stéphane Robin[5,6], Emilie Lebarbier[5,6], Reinhard Böhm[4], Enric Aguilar[7], Jose Guijarro[8], Gregor Vertachnik[9], Matija Klancar[9], Brigitte Dubuisson[1], and **Petr Stepanek[10]**

[1]*Meteo-France, Direction de la Production, 42 avenue Coriolis, 31057 Toulouse cedex, France*

[2]*Center for Climate Change, Univ. Rovira i Virgili, Av. Remolins, 13-15, 43500-Tortosa, Spain*

[3]*UCB Lyon 1, UMR 5558, Villeurbanne, France*

[4]*Zentralanstalt für Meteorologie und Geodynamik, Wien, Austria*

[5]*AgroParisTech, UMR 518, Paris, France*

[6]*INRA, UMR 518, Paris, France*

[7]*Center for Climate Change, Univ. Rovira i Virgili, Tarragona, Spain*

[8]*Agencia Estatal de Meteorologia, Palma de Mallorca, Spain*

[9]*Environmental Agency of the Republic of Slovenia, Meteorology, Ljubljana, Slovenia;*

[10]*Czech Hydrometeorological Institute, Brno, Czech Republic*

Corresponding author E-mail: Olivier.Mestre@meteo.fr

(Manuscript received in final form October 24, 2012)

Abstract–Between 2007–2011, the European COST Action ES0601 called HOME project was devoted to evaluate the performance of homogenization methods used in climatology and produce a software that would be a synthesis of the best aspects of some of the most efficient methods. HOMER (HOMogenizaton softwarE in R) is a software for homogenizing essential climate variables at monthly and annual time scales. HOMER has been constructed exploiting the best characteristics of some other state-of-the-art homogenization methods, i.e., PRODIGE, ACMANT, CLIMATOL, and the recently developed joint-segmentation method (*cghseg*). HOMER is based on the methodology of optimal segmentation with dynamic programing, the application of a network-wide two-factor model both for detection and correction, and some new techniques in the coordination of detection processes from multiannual to monthly scales. HOMER also includes a tool to assess trend biases in urban temperature series (UBRIS). HOMER's approach to the final homogenization results is iterative. HOMER is an interactive method, that takes advantage of metadata. A practical application of HOMER is presented on temperature series of Wien, Austria and its surroundings.

Key-words: Homogenization, optimal segmentation, joint segmentation, ANOVA, temperature, precipitation, urban trend bias

1. Introduction

The accuracy of climatic observations is often affected by inhomogeneities due to changes in the technical or environmental conditions of the measurements (station relocations, changes of the type, height or sheltering of the instruments, etc., *Aguilar et al.*, 2003, *Auer et al.*, 2005). Most of such changes cause sudden shifts (change-points) in the series of local climatic data, while some others (particularly urban development) result in gradually increasing biases from the real macroclimatic characteristics. Correction of inhomogeneities before any climate variability analyses is highly desirable, and for this purpose, a large number of homogenization methods have been developed in the recent decades (*Peterson et al.*, 1998; *Ducre-Robitaille et al.*, 2003; *Beaulieu et al.*, 2008; among others).

HOMER is a recently developed method for homogenizing monthly and annual temperature and precipitation data. It includes the best features of some other state-of-the-art methods, namely PRODIGE (*Caussinus* and *Mestre*, 2004), ACMANT (*Domonkos*, 2011), and *cghseg* a joint segmentation method that was developed originally by bio-statisticians in the context of DNA segmentation (*Picard et al.*, 2011). PRODIGE and ACMANT have the same theoretical base regarding the optimal segmentation with dynamic programming DP (*Hawkins*, 2001), an information theory based formula for determining the number of segments in time series (hereafter: C&L criterion, *Caussinus* and *Lyazrhi*, 1997), and a network-wide unified correction model (ANOVA, *Caussinus* and *Mestre*, 2004). The results of blind test experiments conducted during COST Action ES0601 (*Venema et al.*, 2012) validates these approaches, since PRODIGE and ACMANT rank among the best methods for homogenizing monthly and annual climate data (*cghseg* and HOMER were not tested during the HOME action). The joint segmentation is an extension of the optimal segmentation for finding network-wide optima by means of an iterative procedure, a modified BIC criterion being used for determining the number of changes (*Zhang* and *Siegmund*, 2007; *Picard et al.*, 2011).

HOMER is an interactive semi-automatic method. In applying HOMER, users may choose between the *cghseg* detection results whose generation is fully automatic on the one hand, and a partly subjective pairwise comparison technique that is adapted from PRODIGE on the other hand. This freedom allows users to add subjective decisions based on metadata or research experiences. HOMER includes also some innovations of ACMANT in the coordination of working on different time scales. Basic quality control and network analysis are adapted from CLIMATOL (*Guijarro*, 2011).

Our paper is organized as follows: first, Section 2 describes the main models and procedures of HOMER. The methodology of characterizing urban trends (UBRIS) and the main properties of ACMANT are also presented there, together with a discussion. An application of HOMER on Wien temperature series is then shown in Section 3.

2. *HOMER main procedures*

In this section, we will focus on functions used during the homogenization process: statistical tools for pairwise detection (2.1), two factor model for joint detection and correction (2.2), UBRIS model for urban trend bias assessment (2.3), ACMANT functions (2.4). Usefulness of each task is discussed in 2.5, and a workflow of tasks is provided.

2.1. Detection of changes in pairwise series (univariate detection)

2.1.1. Model

Let Y be the annual or seasonal difference between two series. We model Y_i, i=1,...,n as a series of Gaussian variables of constant variance σ^2, but with varying mean μ from sub-period to subperiod. The number and positions of change-points are unknown.

Let k the number of changes and $\tau_1, \tau_2, ..., \tau_k$ their positions. We denote $K=\{\tau_1,\dots,\tau_k\}$ the set of changes in the series. At most cases old data are adjusted relative to the modern data, and for simplicity τ_o=0 is fixed at $\tau_{k+1}=n$. Further notations are:

$$\overline{Y} = \frac{1}{n}\sum_{i=1}^{n} Y_i \,,$$

$$\overline{Y}_j = \frac{1}{n_j} \sum_{\tau_{j-1}+1}^{\tau_j} Y_i \,,$$

where $n_j = \tau_j - \tau_{j-1} + 1$; $j = 1, \dots, k+1$,

$$\overline{Y}_{hm} = \frac{1}{m-h+1} \sum_{i=h+1}^{m} Y_i \,,$$

$$W_{hm} = \sum_{i=h+1}^{m} \left(Y_i - \overline{Y}_{hm}\right)^2.$$

Changes in the mean are $\mathrm{IE}[Y_i] = \nu_j$ for $\tau_{j-1} + 1 < i < \tau_j$

Maximum likelihood estimates of the ν_j's are straightforwardly given by $\hat{\nu}_j = \overline{Y}_j$. For a given number k, we wish to maximize the likelihood, which is equivalent to minimize deviance D:

$$D_k = \frac{\sum_{j-1}^{k+1} \sum_{\tau_{j-1}+1}^{\tau_j} \left(Y_i - \overline{Y}_j\right)^2}{\sigma^2} + 2n \log\left(\sqrt{2\pi}\,\sigma\right) \quad . \tag{1}$$

2.1.2. Dynamic programming

The naive way to minimize deviance D is to consider every combination of the position of the change-points. But the number of hypotheses rises very fast with n, the length of the series, and k, the number change-points. When detection is performed for change-points in a normal sample, a DP algorithm can be used (*Lavielle*, 1998; *Hawkins*, 1972, 2001; etc.). Computation time then becomes only linear in k and quadratic in n. It is based on a recursion between optimal k and k–1 solutions. DP allows us to find an optimal solution without computing all possibilities. For k changes, the problem is to minimize:

$$Q = \sum_{j=1}^{k+1} \sum_{i=\tau_{j-1}+1}^{\tau_j} \left(Y_i - \overline{Y}_j\right)^2 = \sum_{j=1}^{k+1} W_{\tau_{j-1}\,\tau_j} \,. \tag{2}$$

The solution is given by the following recursion:

- $F_{1,m} = W_{0m}$ for $m = 1, n$,

- for each $r = 2, \dots k+1$, let us compute
  $F_{r,m} = \mathrm{MIN}_{0<h<m}\lfloor F_{r-1,h} + W_{h,m}\rfloor$ for $m = 1, n$,

- for each $F_{r,m}$ value, let us keep in table $H_{r,m}$ the h value that corresponds to the minimum of $F_{r,m}$,

- the change-point estimates are given by: $\tau_{k+1} = n$, and for $r = k, k-1, \dots, 1$ we get $\hat{\tau}_r = H_{r+1,\tau_{r+1}}$.

2.1.3. Selecting the number of changes.

The fit of the change-point model increases monotonously with k ($Q = 0$ for $k = n$). The model selection is guided finding the most parsimonious model that gives a "good" explanation of data vector Y. Several penalized likelihood criteria can be found in the literature. In the latest version of HOMER, we take the advantage of the uniseg procedure from the R package which uses the modified BIC criterion of *cghseg*. As in *Schwarz*'s BIC (1978), *Zhang* and *Siegmund* approach this problem by deriving an asymptotic approximation of the Bayes factor, using a uniform prior on change-points location (among other hypotheses).

The procedure is as follows: for each value of k, DP allows us to select the optimal position for the k change-points $\{0, \hat{\tau}_1, \hat{\tau}_2, \dots, \hat{\tau}_k, n\}$. For each k value, *MBIC*(Y; k) is computed:

$$MBI(Y;k) = \left(\frac{n-k+1}{2}\right)\log\left[1 - \frac{\sum_{j=1}^{k+1} n_j\left(\bar{Y}_j - \bar{Y}\right)^2}{\sum_{i=1}^{n}(Y_i - \bar{Y})^2}\right] + \log\left[\frac{\Gamma\left(\frac{n-k+1}{2}\right)}{\Gamma\left(\frac{n+1}{2}\right)}\right]$$

$$+\frac{k}{2}\log\left[\sum_{i=1}^{n}(Y_i - \bar{Y})^2\right] - \frac{1}{2}\log\left[\sum_{i=1}^{n}\left(\bar{Y}_i - \bar{Y}\right)^2\right] \tag{3}$$

$$-\frac{1}{2}\sum_{j=1}^{k+1}\log(n_j) + \left(\frac{1}{2} - k\right)\log(n) ,$$

where Γ denotes the Gamma function. The model selection consists in selecting the number of change-points k that minimizes $MBIC$:

$$\text{select } k^* \text{ such that } k^*=\text{Argmin}_k(MBIC_k(Y;k)). \tag{4}$$

This criterion is more complex than the classical BIC or C&L criteria used in PRODIGE, but does not require any user-chosen shrinkage parameters like in *Tibshirani* (1996), *Birgé* and *Massart* (2001) or *Gu* and *Wang* (2003). The first term in Eq. (3) corresponds to a likelihood ratio term, the subsequent ones are the penalty. One has to note that the penalty depends on n, k, but also on the closeness of the changes via the sum of $\log(n_j)$ term: close change-points are more penalized. Simulations (not shown here) show that $MBIC$ criterion is slightly less powerful than the C&L, but less sensitive to small autocorrelation that still might be present in the pairwise comparisons.

Standard deviation of the residuals is then estimated by:

$$\hat{\sigma}^* = \sqrt{\frac{1}{n-k^*}\sum_{j=1}^{k^*+1}\sum_{i=\hat{\tau}_{j-1}+1}^{\hat{\tau}}\left(Y_j - \bar{Y}_j\right)^2} = \sqrt{\frac{1}{n-k^*}\sum_{j=1}^{k^*+1} W_{\hat{\tau}_{j-1}\hat{\tau}_j}}\ . \tag{5}$$

We will see in practice that this estimation of noise is very useful, since detection power is directly related to the signal (i.e., amplitude of changes) to noise ratio. Smaller values of noise ensure more accurate detection.

2.2. ANOVA: a two-factor model for joint-detection and correction

2.2.1. Model

Let us consider p series belonging to the same climate area in such a way that all the series are affected by the same climatic conditions at the same time. This assumption is realistic when considering monthly or annual observations of the same geographical region. We assume that each series of observations is the sum of a climatic effect, a station effect, and random white noise. This is a simple two-factor analysis of variance model without interaction, and we will denote it by ANOVA in the following.

Let X be a matrix of n observations X_{ij} on p series where $i=1,...,n$ is the time index and $j=1,...,p$ is the station index. Let k_j be the number of change-points, let $\tau_{1,j}, \tau_{2,j},\ldots, \tau_{k_j,j}$ be the positions of these k_j change-points. Let $K_j=(\tau_{1,j},\ldots, \tau_{k_j,j})$ be the set of change-points for series j. To simplify the notation, we set again $\tau_{o,j}=0$, and $\tau_{k_{j+1},j} = n$, so that K_j becomes $K_j = \left(0, \tau_{1,j}, \dots, \tau_{k_j,j}, n\right)$.

The station effect is constant if the series is homogeneous. If not, the station effect is constant between two shifts. In the following, level denotes a homogeneous sub-period between two discontinuities of a given series. For a series j with k_j breaks, let L_{jh} be the hth level ($h=1,\dots,k_j+1$), thus L_{jh} is the interval: $\left[\tau_{h-1,j} + 1, \tau_{h_j,j}\right]$. Note that the level h for the observation X_{ij} depends both on time i and station j: when necessary it will be written $h(i,j)$.

Let μ_i be the climate effect at time i and ν_{jh} the station effect of station j for level L_{jh}. If there are no outliers, the data are described by the linear model:

$$\mathrm{IE}(X_{ij}) = \mu_1 + \nu_{jh(i,j)} \ , \quad \mathrm{Var}(X) = \sigma^2 I_{np} \ . \tag{6}$$

One parameter of the model can be freely chosen and it is done with introducing the condition$\sum_{i=1}^{n} \mu_i = 0$, so that μ_i are defined as climate anomalies.

The number of independent parameters of the model without discontinuities is $n+p-1$.

Examples:

- No break in series 1: $\mathrm{IE}(X_{i1}) = \mu_i + \nu_1 \quad ,$
- One break at i_o for series 2: $\begin{cases} \mathrm{IE}(X_{i2}) = \mu_i + \nu_{21} \ , & \text{for } i \leq i_0 \\ \mathrm{IE}(X_{i2}) = \mu_i + \nu_{22} \ , & \text{for } i > i_0 \end{cases}$.

Some further characteristics of the model:

a) Estimation can be performed with missing data with the following conditions: there should be at least one non-missing value per year on the whole network (estimation of the μ's) and one non-missing value between two breaks for each subperiod on each series.

b) Climate signal is treated as a fixed parameter so that no assumption is made about the shape of this signal.

c) Conditionally to the climate signal, the disturbances are considered independent.

d) Local variabilities are very similar, which leads to the expression of Var(X).

Note that conditions c) and d) are approximately true within the same climatic region. Small spatial autocorrelation may be observed in the residuals.

So far, this model has been used in PRODIGE and ACMANT mainly for correction purposes – although *Caussinus* and *Mestre* (2004) propose some clue to use it for detection. It has been shown that the inclusion of ANOVA correction improves significantly the results of other methods participated in HOME blind test experiments (*Domonkos et al.*, 2012b). Using HOME benchmark and the set of break-points detected using for example standard normal homogeneity test (SNHT), correcting the inhomogeneities by ANOVA allowed a much better homogenization than the standard SNHT correction method. We will see below that this model can be used for detection as well, allowing for joint detection of a whole set of series.

2.2.2. Joint-detection

The change-point model Eq. (6) can theoretically be used for joint detection of the changes on the whole set of series. However, due to the introduction of factor μ, the classical DP algorithm cannot be applied (*Caussinus* and *Mestre*, 2004) and until recently, joint segmentation was considered computationally intractable. Adapted algorithms allow us to solve this problem in a reasonable computing time. *Picard et al.* (2011) rely on two "computational tricks". The first one solves the problems caused by segmentation of multiple series. Let us set all $\mu_i = 0$. Since DP complexity is quadratic with the size of the data, just considering segmentation of the ν factor may become problematic when considering multiple series. *Picard et al.* (2011) propose a "two-stage" DP algorithm that significantly reduces the computation time. Briefly, the first stage consists in finding all optimal solutions for each ν_j factor separately, from $k = 1$ to $kmax_j$. The second stage uses outputs from the first stage to optimally allocate the number of segments to each factor $\nu_1, \ldots, \nu_p$, in order to maximize the overall fit. The model selection is provided by a multivariate version of *Zhang* and *Siegmund* criterion derived in *Picard et al.* (2011).

The second strategy consists in iteratively estimating μ_i and the segmentation of factor ν: at step $(s+1)$, μ_i is estimated by:

$$\hat{\mu}_i^{(s+1)} = \frac{1}{p}\sum_{j=1}^{p} Y_{ij} - \hat{\nu}_{jh(i,j)}^{(s)} \quad , \tag{7}$$

where the segmentation of factor ν is updated using two-stage DP on $X_{ij} - \hat{\mu}_i^{(s+1)}$.

2.2.3. *Correction and reconstitution of missing data*

Once segmentation has been achieved, correction can be computed. Estimates $\hat{v}_{jh(i,j)}$ are used in the following way: let L_{jk_j} be the last level of series j, and $\hat{v}_{jk_j}$ the corresponding estimation of the station effect. Then, for every $X_{ij} \in L_{jh}$ $(1 \leq h \leq k_j + 1)$, corrected X_{ij} (denoted by X_{ij}^*) is given by:

$$X_{ij}^* = X_{ij} - \hat{v}_{jh(i,j)} + \hat{v}_{j,k_j+1} \,. \tag{8}$$

Note that the model allows the imputation of missing data and the correction of outliers. For any missing data or outlier (i,j), the imputation is naturally given by $\hat{X}_{ij} = \hat{\mu}_i + \hat{v}_{jh(i,j)}$. Since the two-factor model takes into account the change-points in the series, this allows an unbiased reconstitution of missing values, contrary to classical regression or interpolation methods.

2.3. *Characterization of urban trends: UBRIS*

UBRIS (urban bias remaining in series) procedure allows us to characterize artificial trends – in most cases related to urbanization, which are sometimes present in the climate series. UBRIS works jointly analyzing time series with potential artificial trends ("urban") and without potential artificial trends ("rural"). This is an improvement compared to traditional urban trend characterization, where rural and urban series are homogenized separately, before being compared (*Peterson*, 2003 for example). This requires a large set of both rural and urban series, which may be problematic on earlier periods for example.

UBRIS relies on an extension of model Eq. (6). Let us assume that the $j < m < p$ series are free of urban trends, and that for $m \leq j \leq p$, an additional trend may affect the series.

$$\begin{aligned}
\mathrm{IE}(X_{ij}) &= \mu_i + v_{jh(i,j)}\,, && \text{for} \quad 1 \leq j < m < p\,, \\
\mathrm{IE}(X_{ij}) &= \mu_i + v_{jh(i,j)} + \beta_j i\,, && for \quad m \leq j \leq p\,, \\
\mathrm{Var}(X) &= \sigma^2 I_{np}\,. &&
\end{aligned} \tag{9}$$

Practically, UBRIS model is slightly more complicated than Eq. (9), since trend may not affect the whole period of the series. For computation, at least one series has to be free of trend, otherwise there is no unique solution when estimating climate factor μ and trend term β. Estimation is performed via ordinary least squares. Standard student t-test allows us to test significance of the trends (β_j). UBRIS ensures a posterior estimation of those additional trends.

Prior to UBRIS analysis, HOMER has to be run in order to detect abrupt changes.

UBRIS relies on the knowledge of climatologists who decide *a priori* which series may or may not be affected by urban trends. This human expertise is important. If series corrupted by artificial trends enter the "rural" group, they will bias the estimates of climate factor μ and trend term β.

2.4. ACMANT

ACMANT (adapted caussinus mestre algorithm for homogenizing networks of monthly temperature data, *Domonkos*, 2011) was developed from PRODIGE during the HOME period. However, in contrast with PRODIGE and HOMER, ACMANT is fully automatic and it applies reference series built from composites for time series comparisons. The other main novelties of ACMANT are i) it applies pre-homogenization in a way that the double use of the same spatial connection is excluded, ii) it coordinates the operations on different time scales (from multiannual to monthly) in a unique way.

2.4.1. ACMANT bivariate detection

Observed temperature data often have inhomogeneities with significant seasonal cycles in the resulted bias (*Drogue et al.*, 2005; *Brunet et al.*, 2011; etc.). Therefore, change-points are searched by fitting step-functions to two annual characteristics, i.e., to annual means (Y) and to the range of the seasonal cycle (R) in relative time series, that is, candidate series minus reference series. In HOMER, the reference series are the climate signals (μ coefficients in ANOVA model) or, with other words, the reference series for ACMANT detection are always pre-homogenized. Adapting notations of Section 2.1. to R series, ACMANT detection procedure aims at minimizing:

$$Q_{YR} = \sum_{j=1}^{k+1} \sum_{i=\tau_{j-1}+1}^{\tau_j} \left(Y_i - \bar{Y}_j\right)^2 + \frac{1}{2}\left(R_j - \bar{R}_j\right)^2 . \tag{10}$$

The ½ factor in Eq. (10) was chosen empirically. Solutions with common timings of change-points on Y and R are considered only, so that the standard DP algorithm applies the cost function Q_{YR}. In order to set the number of changes, the C&L criterion is used both in original ACMANT and in its adaptation to HOMER:

$$C_0(Y,R) = 0 \quad \text{and}$$

$$C_k(Y,R) = \log\left[1 - \frac{\sum_{j=1}^{k+1} n_j\left[\left(\bar{Y}_j - \bar{Y}\right)^2 + \frac{1}{2}\left(\bar{R}_j - \bar{R}\right)^2\right]}{\sum_{i=1}^{n}(Y_i - \bar{Y})^2 + \frac{1}{2}(R_i - \bar{R})^2}\right] + \frac{2k}{n-1}\ln(n) \quad . \quad (11)$$

The selection rule is: select k^* such that $k^*=\text{Argmin}_k(C_k(Y))$. In many cases, this procedure will allow us to detect changes hardly noticeable in annual means.

2.4.2. Month of change specification

Another feature of ACMANT that has been included in HOMER is its procedure for finding the most likely month of a change-point. If the precise month of the change is not known, since detection is mainly performed on annual indices, the default is to validate the break at the end of the year. At the end of the homogenization procedure, a more precise detection is made, using the monthly series serially (that is, the sequence of January, February, March, etc, for each year). Both candidate monthly series and reference series (computed from monthly μ factors) are deseasonalized; when analyzing change τ_j, standard DP algorithm is run on series of differences on interval $[\tau_{j-1}, \tau_{j+1}]$. Algorithm allows us to change the position of the change in a range of +/–2 years (in the original ACMANT the range is +/–12 months). Alternatively, the monthly precision can be determined by metadata. In HOMER, a flag marks whether a detected break is validated by metadata or not.

2.5. Discussion

The different methods contributing to the operation of HOMER have their own strengths and weaknesses. PRODIGE relies on a pairwise strategy for detection of the changes. A candidate series is compared to its neighbors in the same climatic area by computing series of differences. These difference series are then tested for discontinuities. On such a difference series without metadata, the detected changes may have been caused by the candidate or the neighbor. But, if a detected change-point remains constant throughout the set of comparisons of a candidate station with its neighbors, it can be attributed to this candidate station: this is called "attribution phase". There are two advantages in this approach. First, we avoid creating composite reference series averaging non-homogeneous series. Second, detection relies on an efficient univariate detection procedure whose level and power are well controlled. But, because of the randomness of the difference series, the change-points of weak amplitude will lead to less accurate detection and sometimes no detection at all for some comparisons (in particular in the case of simultaneous breaks). At most cases, however, the induced ambiguity can be removed by considering the whole set of comparisons and using the metadata archives of the climate stations when available, as well as the knowledge of climatologists. This break-points detection phase has been considered the main drawback of PRODIGE, since it has to be performed manually, a process which may be tedious and time consuming, thus very difficult to apply to a large dataset and requiring a high level of regional climate knowledge and homogenization expertise.

To overcome the detection problem, an alternative approach is obtained by using the overall two-factor model, that allows the analysis and correction of a whole set of series (Section 2.2.). The *multiseg* (*cghseg* package) function determines the proper number of change-points using the MBIC criterion. This detection process with DP is quick and automatic. However model selection in a multivariate framework is a complex task, and the power of this procedure is sometimes lower than expected. In HOMER, function *multiseg* allows the automate attribution of the changes to a large extent, and in some cases the pairwise detection allows us to put into evidence changes that were not detected by *multiseg*.

ACMANT helps finding changes with a strong seasonal behavior in temperature series. In many cases, changes in observation conditions (location, sheltering, etc.) may have effects of opposing signs regarding the seasons, for example a positive effect in summer and a negative effect in winter. Such inhomogeneities are often hardly detectable on annual means, but clearly detectable with the ACMANT bivariate detection. A useful additional feature of ACMANT is the detection with monthly preciseness. The structure of HOMER has built in a way that it intends to exploit optimally the positive characteristics of the contributing methods. The tasks flow chart of HOMER is given in *Fig. 1*.

Detection is an iterative process. The initial detection phase usually reveals the most obvious changes which are corrected. Analyzing the result of this correction allows us to create an updated set of detected changes on a network. The joint detection is accompanied by the pairwise detection for allowing the use of metadata and for checking the results. The ACMANT detection follows the first cycle of detection and correction, since ACMANT detection needs pre-homogenized reference series. Note that correction is always performed on the initial data, simply by updating the set of the validated change-points before running ANOVA.

The process ends, whenever pairwise, joint-detection, and ACMANT bivariate detection find no additional changes on corrected series. In practice, the user may tolerate some pairwise comparisons still exhibiting unattributed isolated breaks, probably due to 1st kind errors.

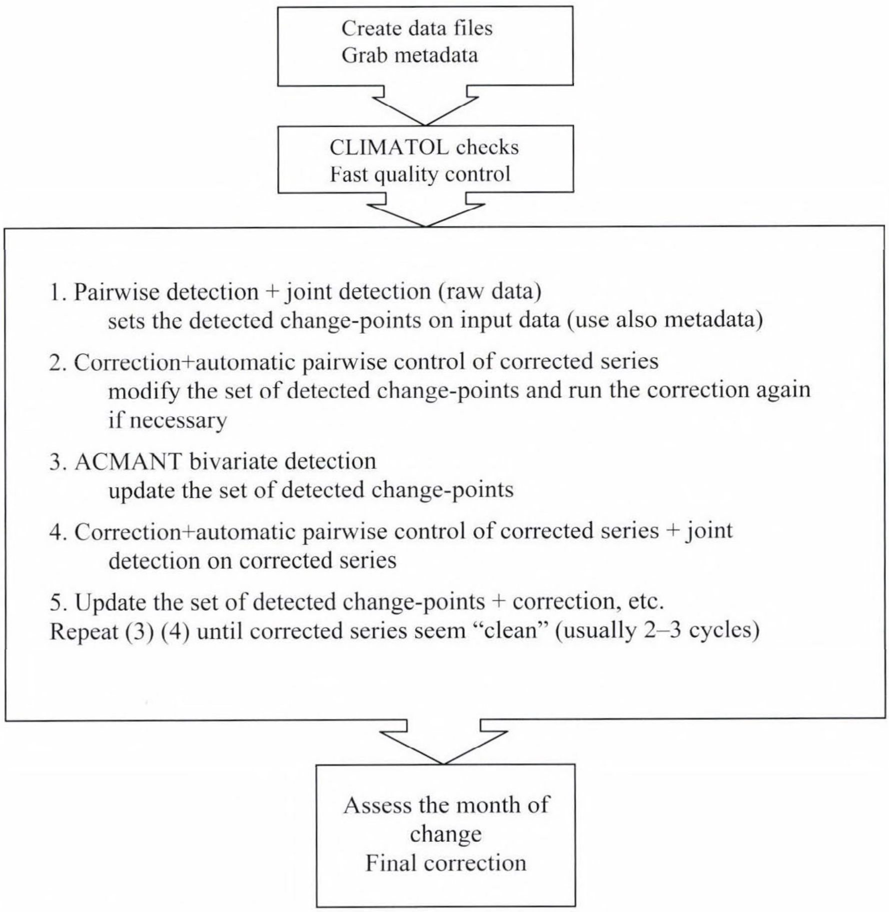

Fig. 1. Tasks flow chart of HOMER.

3. *Case study*

3.1. Homogenization using HOMER

A set of 13 series from Wien, Austria and its surroundings is provided by Zentralanstalt für Meteorologie und Geodynamik (ZAMG). Stations marked with (r) are considered rural: Fuchsenbigl$^{(r)}$, Gross-Enzersdorf$^{(r)}$, Klosterneuburg, Langenlebern$^{(r)}$, Schwechat, Wien-Innere-Stadt, Wien-Laaerberg, Wien-Mariabrunn$^{(r)}$, Rosenhügel, Rathauspark, Stadlau, Wien-Unterlaa, Wien-Hohe-Warte (*Fig. 2*).

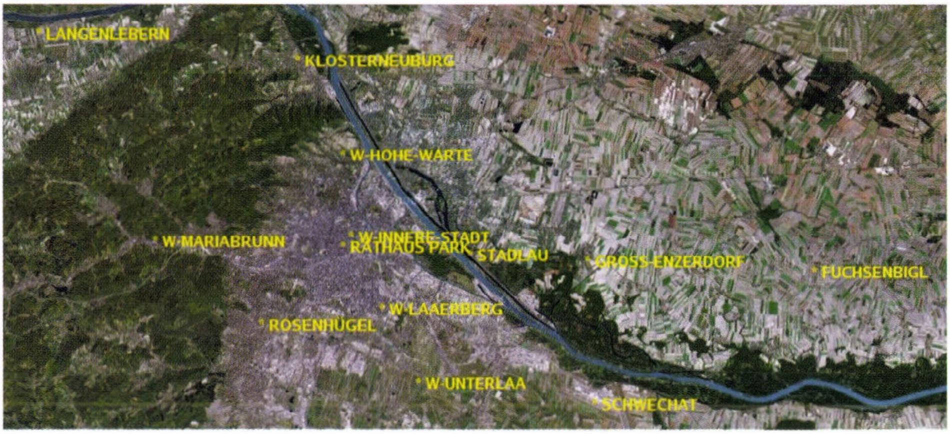

Fig. 2. Map of Wien series

Let us take Stadlau as an example: results of pairwise detection are given in *Fig. 3*. A quick examination of pairwise comparisons puts into evidence changes in 1969 or 1970, 1984, 2001 or 2002, and potential additional changes in 1953, and 1979.

The second step consists in running *cghseg* joint-detection (*multiseg* function). Combining pairwise and joint detection allows a quick attribution of the changes: 1954, 1969, 1984, and 2002 (*Fig. 4*). Note also the good agreement in the amplitudes of the changes detected in pairwise comparisons (triangles are black for breaks detected on pairwise annual series, blue for winter, and red for summer) and joint detection (green ⊕). However, the automatic joint-detection is not perfect. On Wien series, *multiseg* tends to detect a change around 1985-1987, which is not supported at all by pairwise comparisons, and thus, it is rejected manually by the user (large red cross in the same year). During estimation of μ and segmentation ν, *multiseg* iterative algorithm has wrongly attributed a climatic feature to the ν factor. Furthermore, the rather obvious change in 1979 (when considering pairwise comparisons) was not detected by *multiseg*. User has to validate it manually using the graphical user interface. When clicking on the window, the user adds red crosses to remove or validate breaks. The y axis is not important, only the date (x axis) is taken into account. Clicking on a date selected by *multiseg* (symbol ⊕ is present) removes the corresponding date, while clicking elsewhere validates a new change-point. Metadata allow us to validate changes in 1980 (relocation of the weather station) and 2002 (changes in instrumentation). There are also sufficient statistical clues to validate the other changes, even if metadata are lacking.

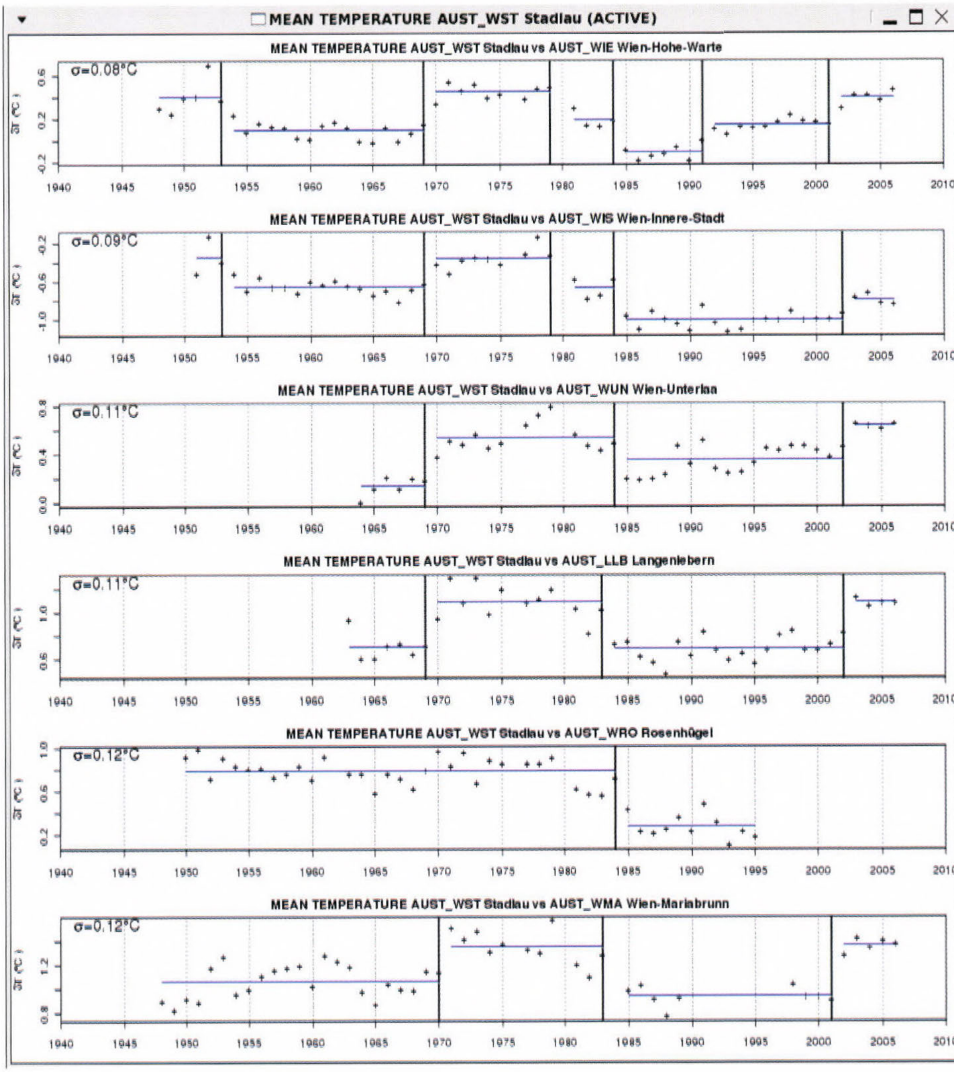

Fig. 3. Screen capture of HOMER outputs: Stadlau series compared to its neighbours. Pairwise comparison are sorted according to the increasing values of the noise standard deviation (upper left corner of each plot), computed using Eq. (5). For clarity reasons, only 6 comparisons with the smallest noise are shown.

After a correction step, ACMANT bivariate detection confirms the selected changes on Stadlau series (not shown). The raw and corrected Stadlau series after the final correction are shown in *Fig. 5* (upper panel for the raw, lower panel for the corrected series).

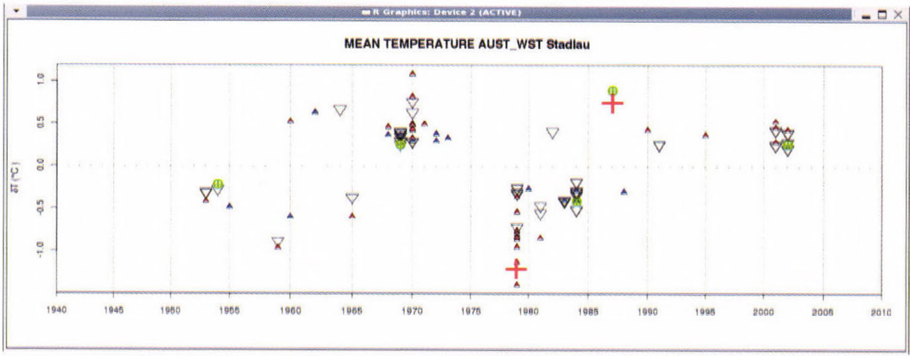

Fig. 4. Screen capture of HOMER outputs: date (x axis) and amplitude (y axis) of change-points detected on the whole set of pairwise comparisons: annual comparisons (black), winter (blue) and summer (red) triangles. Joint detection results are pointed as green ⊕ symbols. Red crosses mark user's interventions.

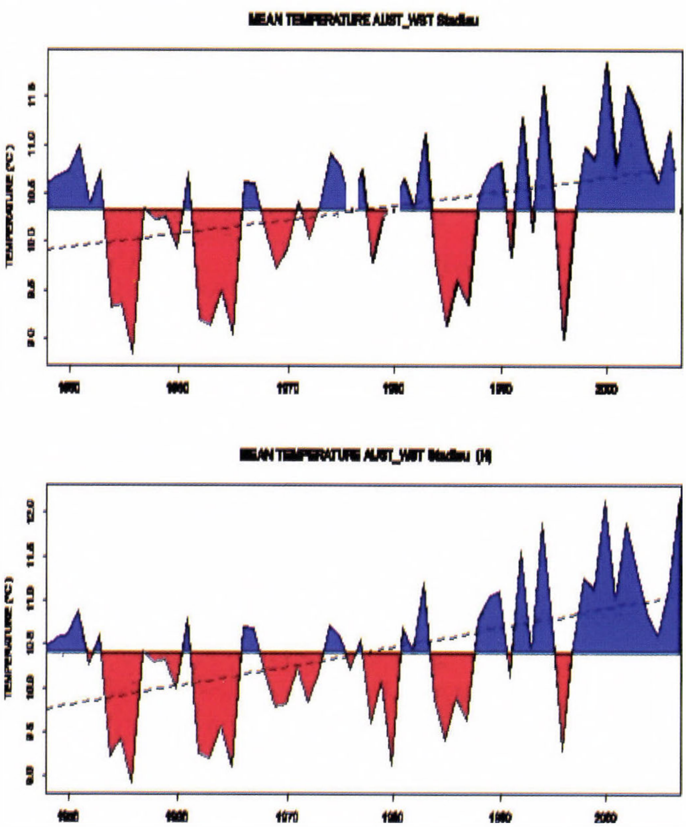

Fig. 5. Raw (up) and corrected (down) series of Stadlau.

Pairwise comparison of corrected series is characteristic of a good homogenization (*Fig. 6*).

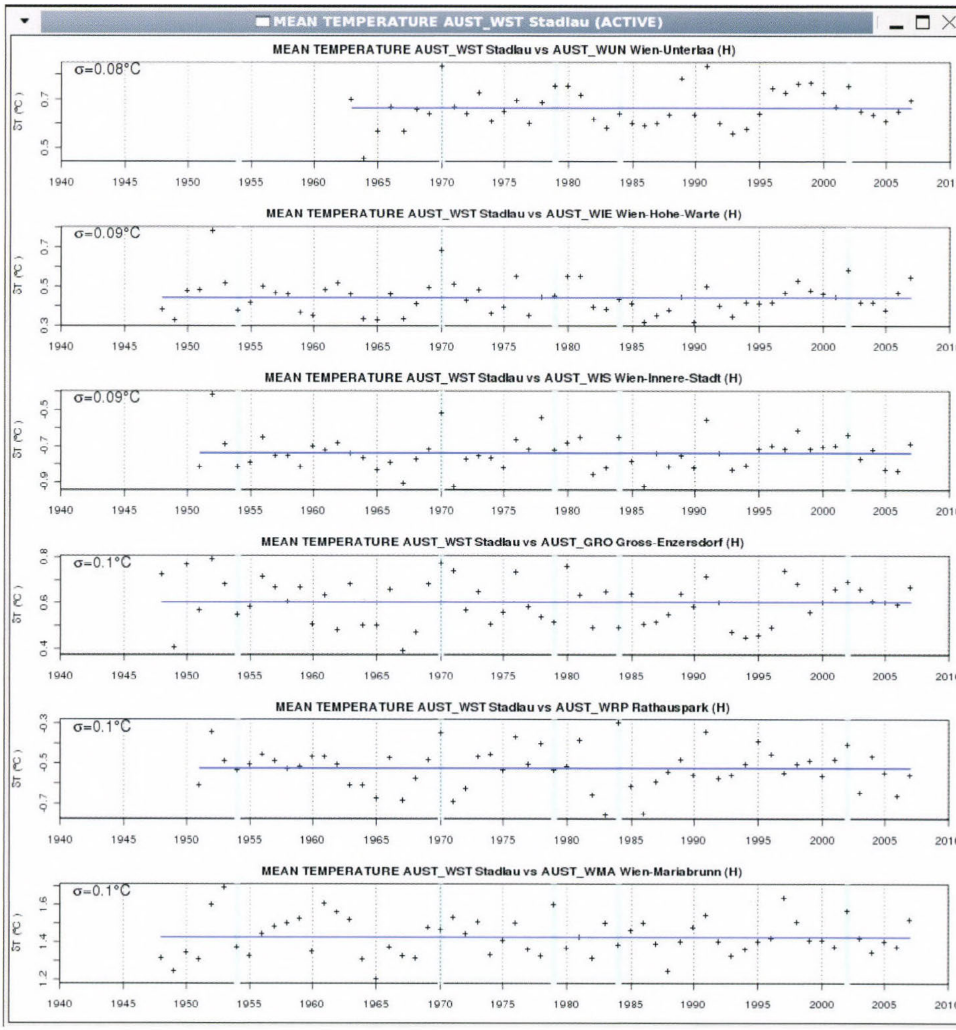

Fig. 6. The same as *Fig. 3*, but for the corrected Stadlau series compared to its corrected neighbors. The list of pairwise comparisons changed a little bit, since estimates of noise standard deviation slightly varied.

Another example of the effect of correction is shown for Rathauspark series (*Fig. 7* upper panel for the raw, lower panel for the corrected series).

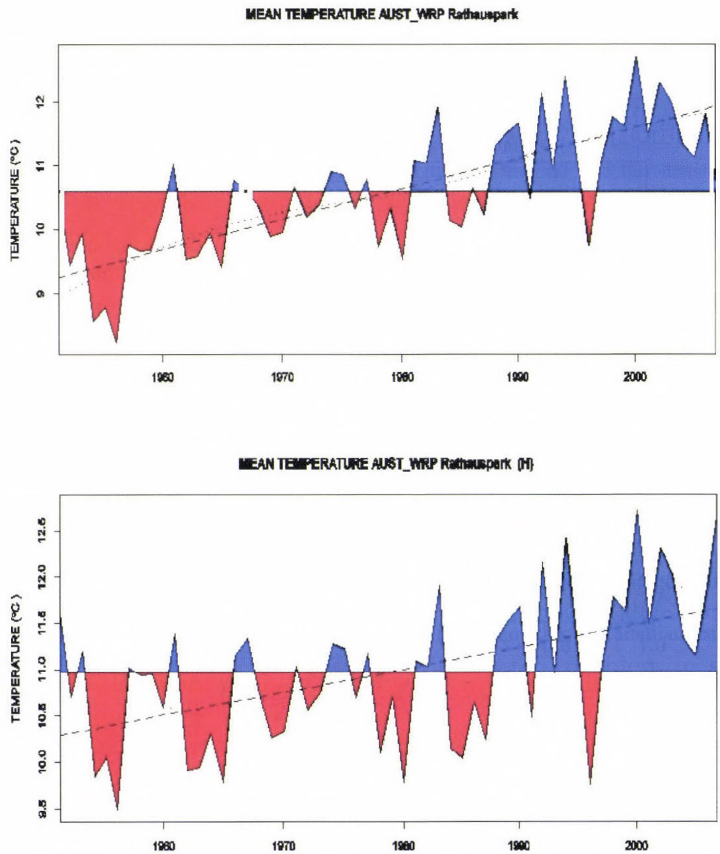

Fig. 7. Raw (up) and corrected (down) series of Rathauspark.

3.2. UBRIS characterization of urban trends

Running UBRIS allowed us to estimate jointly the effect of abrupt changes and the potentially significant urban trends on Wien series. UBRIS procedure is run in the following way: a first estimation allows us to put into evidence some urban series having no additional trend (large p values of the Student t-test for corresponding β). Those series are included into the rural set, and trends are re-estimated. At the end of the process, central temperature series exhibit no significant urban trends at level 0.05. Only suburban series (Wien Laaerberg, +0.10°C/decade, Rosenhügel +0.08°C/decade) exhibit significant positive trends (with student t-test p values lower than 10e–4). Corrected series of Laaerberg, with and without urban trend, is shown in *Fig. 8*.

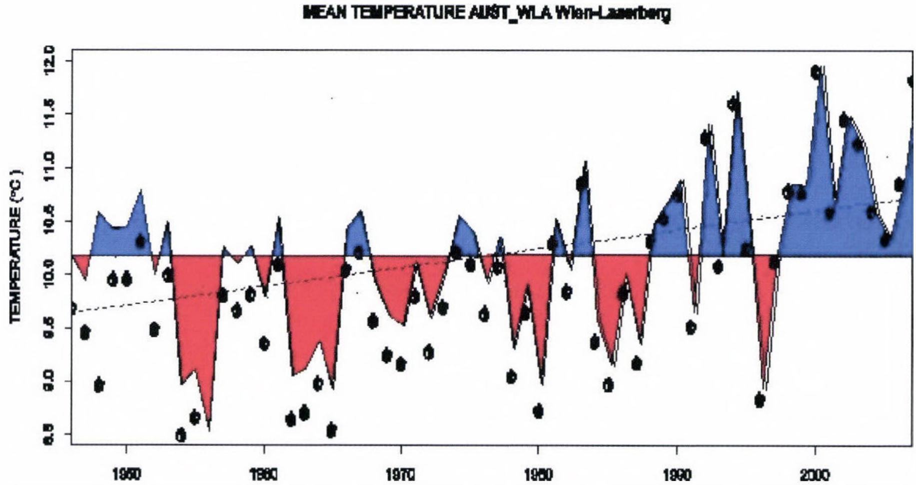

Fig. 8. Homogenized series of annual mean temperature of Laaerberg, with urban trend (series of ⊕ symbols) and removed urban trend(solid line).

These results are consistent with those obtained by *Böhm* (1998), who used a more traditional homogenization technique, and analyzed the trends of the series of differences of central series minus mean of the rural series. Note that those conclusions may not apply to other cities, since Wien population is remarkably stable since 1950 for example. UBRIS model should be run on each case study.

Additionally, Klosterneuburg series (not shown here) exhibits a remarkable feature, a highly significant decreasing trend for summer months (−0.02°C/decade). This site should be investigated for a potential shadowing effect.

4. Conclusion and perspectives

This paper presents a set of homogenization procedures integrated in the new software package HOMER (available at www.homogenization.org). This package was built relying on the results of the 4-year long COST-HOME project, so it implements the most significant findings achieved by its different working groups. The evolution of PRODIGE, combined with ACMANT and CLIMATOL procedures and supported by the R-package *cghseg* into HOMER provides a state-of-the-art homogenization tool for monthly to annual data applicable to most essential climate variables. However, HOMER shall not be considered as an automatic method, since manual input is still required in order to control the homogenization process.

HOMER is recommended by the COST Action ES0601, together with *Craddock* (1979), MASH (*Szentimrey*, 2007), USHCN (*Menne* and *Williams*, 2005), ACMANT (2011) software that got valuable results during COST benchmark experiments (*Venema et al.*, 2012).

The addition of UBRIS procedures adds value to the package since artificial trends have remained a problematic issue in homogenization.

Further development planned in this work is using a generalized least squares estimation for the correction model, in order to take into account the spatial dependency of the residuals. Although this technique is expected to have a weak effect on the correction estimates themselves, it may provide more accurate confidence intervals. A Bayesian criterion for automatic attribution of changes detected in pairwise comparison is also in development.

Acknowledgements–HOMER has been developed with support of the European Union, through the COST Action ES0601 – Advances in Homogenization Methods of Climate Series: an Integrated Approach (HOME).

References

Aguilar, E., Auer, I., Brunet, M., Peterson, T.C. and *Wieringa, J.*, 2003: WMO Guidelines on climate metadata and homogenization. WCDMP-No. 53, WMO-TD No 1186, WMO, Geneva.

Auer, I., Böhm, R., Jurkovic', A., Orlik, A., Potzmann, R., Schöner, W., Ungersböck, M., Brunetti, M., Nanni, T., Maugeri, M., Briffa, K., Jones, P., Efthymiadis, d., Mestre, O., Moisselin, J.M., Begert, M., Bradzil, R., Bochnicek, O., Cegnar, T., Gagić-Ĉapka, M., Zaninović, K., Majstorović, Z., Szalai, S.,Szentimrey, T. and *Mercalli M.*, 2005: A new instrumental precipitation dataset for the greater Alpine region for the period 1800–2002. *Int. J. Climatol. 25*, 139–166.

Beaulieu, C., Seidou, O., Ouarda, T.B.M.J., Zhang, X., Boulet, G. and *Yagouti, A.*, 2008: Intercomparison of homogenization techniques for precipitation data. *Water Resour. Res. 44*, W02425, doi:10.1029/2006WR005615.

Birgé, L. and *Massart, P.*, 2001: Gaussian model selection. *J. Eur. Math. Soc. 3*, 203–268.

Böhm, R. 1998: Urban bias in temperature time series – a case study for the city of Vienna, Austria. *Climatic Change, 38*, 113–128.

Brunet, M., Asin, J., Sigró, J., Bañon, M., García, F., Aguilar, E., Palenzuela, J.E., Peterson, T.C., and *Jones, P.*, 2011: The minimization of the screen bias from ancientWestern Mediterranean air temperature records: an exploratory statistical analysis, *Int. J.Climatol. 31*, 1879–1895.

Caussinus, H. and *Lyazrhi, F.*, 1997: Choosing a linear model with a random number of change-points and outliers. *Ann. Inst. Statist. Math., 49*, 761–775.

Caussinus, H. and *Mestre, O.*, 2004: Detection and correction of artificial shifts in climate series. *J. Roy. Stat. Soc. Series C53*, 405–425.

Craddock, J.M., 1979: Methods of comparing annual rainfall records for climatic purposes. *Weather 34*, 332–346.

Domonkos, P., 2011: Adapted Caussinus-Mestre Algorithm for Networks of Temperature series (ACMANT). *Int. J. Geosci. 2*, 293–309.

Domonkos, P., Venema, V., Auer, I., Mestre, O., and *Brunetti, M.*, 2012a: The historical pathway towards more accurate homogenization. *Adv. Sci. Res. 8*, 45–52.

Domonkos, P., Venema, V., and *Mestre, O.*, 2012b: Efficiencies of homogenization methods: our present knowledge and its limitation. *Proceedings of the 7th Seminar for Homogenization and Quality Control in Climatological Databases* in press.

Drogue, G., Mestre, O., Hoffmann, L., Iffly, J-F., and *Pfister, L.*, 2005: Recent warming in a small region with semi-oceanic climate, 1949–1998: what is the ground truth? *Theor.Appl. Climatol. 81*, 1–10.

Ducré-Robitaille, J-F., Vincent, L.A., and *Boulet, G.*, 2003: Comparison of techniques for detection of discontinuities in temperature series. *Int. J. Climatol. 23*, 1087–1101.

Gu, C. and *Wang, J.*, 2003: Penalized likelihood density estimation: Direct cross-validation and scalable approximation. *Statistica Sinica 13*, 811–826.

Guijarro, J.A., 2011: User's guide to CLIMATOL. http://www.meteobal.com/climatol/climatol-guide.pdf

Hawkins, D.M., 1972: On the choice of segments in piecewise approximation. *J. Inst. Math. Appl. 9,* 250–256.

Hawkins, D.M., 2001: Fitting multiple change-points to data. *Comput. Statist. Data Anal. 37*, 323–341.

Lavielle, M., 1998: Optimal segmentation of random processes. *IEEE Trans. on Signal Proc. 46*, 1365–1373.

Menne, M. J. and *Williams, C.N.Jr.*, 2005: Detection of undocumented changepoints using multiple test statistics and composite reference series. *J. Climate 18*, 4271–4286.

Peterson, T.C., Easterling, D.R., Karl, T.R., Groisman, P., Nicholls, N., Plummer, N., Torok, S., Auer, I., Böhm, R., Gullett, D., Vincent, L., Heino, R., Tuomenvirta, H., Mestre, O., Szentimrey, T., Salinger, J., Førland, E. J., Hanssen-Bauer, I., Alexandersson, H., Jones, P., and *Parker, D.*, 1998: Homogeneity adjustments of in situ atmospheric climate data: a review. *Int. J. Climatol. 18*, 1493–1517.

Peterson, T.C., 2003: Assessment of Urban Versus Rural In Situ Surface Temperatures in the Contiguous United States: No Difference Found. *J. Climate 16,* 2941–2959.

Picard, F., Lebarbier, E., Hoebeke, M., Rigaill, G., Thiam, B. and *Robin, S.*, 2011: Joint segmentation, calling and normalization of multiple CGH profiles. *Biostatistics 12*, 413–428.

Schwartz, G., 1978: Estimating the dimension of a model. *Ann. Statist. 6*, 2745–2756.

Szentimrey, T., 2007: Manual of homogenization software MASHv3.02, Hungarian Meteorological Service.

Tibshirani, R., 1996: Regression shrinkage and selection via the lasso. *JRSS Series B 58*, 267–288.

Venema, V., Mestre, O., Aguilar, E., Auer, I., Guijarro, J.A., Domonkos, P., Vertacnik, G., Szentimrey, T., Štěpánek, P., Zahradnicek, P., Viarre, J., Müller-Westermeier, G., Lakatos, M., Williams, C.N., Menne, M., Lindau, R., Rasol, D., Rustemeier, E., Kolokythas, K., Marinova, T., Andresen, L., Acquaotta, F., Fratianni, S., Cheval, S., Klancar, M., Brunetti, M., Gruber, C., Duran, M.P., Likso, T., Esteban, P. and *Brandsma,T.*, 2012: Benchmarking monthly homogenization algorithms, *Climate of the Past 8*, 89–115.

Zhang, N.R. and *Siegmund, D.O.*, 2007: A Modified Bayes Information Criterion with Applications to the Analysis of Comparative Genomic Hybridization Data. *Biometrics 63*, 22–32.

IDŐJÁRÁS
Quarterly Journal of the Hungarian Meteorological Service
Vol. 117, No. 1, January–March 2013, pp. 69–90

Homogeneity of monthly air temperature in Portugal with HOMER and MASH

Luís Freitas[1]*, **Mário Gonzalez Pereira**[1,2], **Liliana Caramelo**[1], **Manuel Mendes**[3], and **Luís Filipe Nunes**[4]

[1] *Centre for Research and Technology of Agro-Environment and Biological Sciences (CITAB), University of Trás-os-Montes and Alto Douro, Apartado 1013, 5001-801 Vila Real, Portugal*

[2] *Instituto Dom Luiz – Universidade de Lisboa, Faculdade de Ciências da Universidade de Lisboa, Campo Grande, Edifício C8, Piso 3, 1749-016 Lisboa, Portugal*

[3] *Instituto de Meteorologia, IM, I.P., Rua C, Aeroporto de Lisboa, 1749-077 Lisboa, Portugal*

[4] *Laboratory for Systems, Instrumentation and Modeling in Science and Technology for Space and the Environment, Faculty of Sciences of University of Lisbon, Campo Grande, Edifício C1, Gabinetes 1.4.21 e 1.4.39, P-1749-016 Lisboa, Portugal*

**Corresponding author E-mail: pedro-fafe@hotmail.com*

(Manuscript received in final form November 25, 2012)

Abstract–In this paper we focus on the homogeneity of Portuguese monthly mean air temperature with two purposes: i) to detect and correct eventual inhomogeneities in the dataset; and, ii) to compare the homogenized time series with different methods. The dataset used in this study comprises time series of minimum (TN) and maximum (TX) monthly mean air temperature recorded in weather stations located in the northern region of the continental part of Portugal, from 1941 to 2010. MASH and HOMER were the methods used in this study to homogenize the Portuguese air temperature database. The former was selected for being one of the most widely used by the homogenization community, while the latter was selected because it is one of the most recent homogenization methods, and the combination of detection methods resulted in that, along with MASH, HOMER exhibited the best results in the comparative analysis performed within the COST Action ES0601 (HOME). A high number of break points were identified in both minimum and maximum air temperature time series, but differences in the number, size and temporal location of the breaks detected by both methods must be underlined. The homogenization process was assessed by comparing results obtained with correlation, trend, and principal component analysis using non-homogenized (NH) and homogenized datasets with both methods. Correlation analysis reveals a higher increase in the similarity in homogenized TX than in TN in relation with NH time series. Decrease in the amplitude of the tendencies and in the number of statistically significant trends is higher in homogenized TX than in TN, independently of the homogenization method. On the other hand, the number of statistically significant principal components tend to decrease with the application of homogenization procedures, while the explained variance by the first principal components of homogenized datasets is tendentiously higher than for non-homogenized datasets.

Key-words: Homogenization, temperature, MASH, HOMER, Portugal.

1. Introduction

The existence of long and reliable instrumental climate records registered in a sufficiently dense network is fundamental to assess climate variability and climate change and to validate climate models. Climate research results are also dependent on the quality of the datasets, in particular on its homogeneity (*Venema et al.*, 2012). A homogeneous climate time series can be defined as the one whose variability is only caused by changes in weather and climate (*Aguilar et al.*, 2003). However, long instrumental records are rarely homogeneous because they include non-climatic signals which must be removed. Results from the homogenization of Western Europe climate records points to the existence of inhomogeneities in mean temperature series every 15 to 20 years (*Venema et al.*, 2012). In fact, any weather observation network, that operates for a long period of time, undergoes changes in its functioning due, for example, to instrumentation failure or damage, changes on its surrounding (e.g., urbanization), relocation and substitution of weather stations. For these reasons, it is expected that the Portuguese maximum and minimum air temperature datasets present heterogeneities that need to be detected and corrected.

In the last decades, inhomogeneity detection techniques have been developed based on classical statistical tests (*Alexandersson*, 1986; *Gullett et al.*, 1990), regression models (*Vincent*, 1998), or Bayesian approaches (*Perreault et al.*, 2000). More recently, new procedures were particularly developed to detect and correct multiple change-points using reference series (*Szentimrey*, 1999; *Mestre*, 1999; *Caussinus* and *Mestre*, 2004; *Menne* and *Williams*, 2005) and changes in the mean and variance (*Toreti et al.*, 2012). Review papers and comparison studies of homogenization methods have been published regularly (*Peterson et al.*, 1998; *Ducré-Robitaille*, 2003, *Reeves et al.*, 2007, *Venema et al.*, 2012). Some authors have been focusing their interest in specific aspects of the homogenization procedure such as the cause of inhomegeneities (*Trewin*, 2010), use of reference series (*Menne* and *Willians*, 2005, *Domonkos, et al.*, 2012), ability of homogenization methods (*Menne* and *Willians*, 2005), or to test automatic homogenization methods by the introduction of perturbed parameter experiments (*Williams et al.*, 2012).

The inventory and evaluation of existing detection and correction methods and the need of an objective comparative analysis to assess their performance was included in the scientific programme of the COST Action HOME ES0601: Advances in Homogenization Methods of Climate Series: an integrated approach (HOME). HOME results include the publication of a comparison study, based on 25 blind contributions and 22 contributions made after knowing the location and size of the heterogeneities, performed with a large number of different versions of 9 main methods (*Venema et al.*, 2012). This study was based on a benchmark dataset of monthly air temperature and precipitation and on different error metrics to assess the performance of the methods. Results of this comparison suggests that: (i) the assessment of the methods is dependent on the error metric considered; (ii) in general, all relative methods contribute to homogenized temperature data; but, (iii) only the methods with best performance are able to improve the quality of precipitation datasets; and, (iv) the list of methods with better performance includes Craddock (*Craddock*, 1979), PRODIGE (*Caussinus* and *Mestre*, 2004), MASH (*Szentimerey*, 2007), ACMANT (*Domonkos*, 2011), and USHCN methods (*Menne* and *Williams*, 2009).

HOME main objective was to develop a general homogenization method for homogenizing climate and environmental datasets which was accomplished in 2011 with the release of a free software package (HOMER), implemented in R language (*HOME*, 2011). It should be noted that ACMANT is a modified and automated version of PRODIGE, and that HOMER integrates PRODIGE, ACMANT, and USHCN.

Consequently, the purpose of this study is twofold: (i) to analyze the homogeneity of minimum and maximum air temperatures in northern Portugal; and, (ii) to compare the homogenized maximum and minimum air temperatures Portuguese datasets with HOMER and MASH. A review of the main characteristics of the procedures used to control the quality of the data and methods of homogenization will be undertaken in order to justify the options taken in this study and to highlight the methodological differences between MASH and HOMER.

2. *Dataset description*

The dataset that we analyze here is representative of the monthly mean maximum and minimum air temperature fields (hereafter TX and TN, respectively) in the northern region of the continental part of Portugal for the 1941–2010 period. Monthly time series were calculated from daily values, following the WMO directives in what concerns to the existence of missing values in daily time series. Specifically, a monthly value should only be computed if no more than five consecutive daily values or less than ten daily values throughout the month are missing (*WMO*, 2011).

Daily values of TX and TN were recorded at weather stations managed by the Portuguese Meteorological Institute (IM). Location and characteristics of these weather stations are presented in *Fig. 1* and *Table 1*, respectively. This network comprises both classical weather stations (CWS), collecting data since the mid-1800s, and automatic weather stations (AWS), installed in the end of the 20th century. In cases where AWS were installed in approximately the same location of the CWS, the time series from both weather stations were merged, the type of station in *Table 1* was set to CWS/AWS, and the date of the fusion was stored as metadata. Maximum distance between an AWS and CWS used to produce the merged time series was 4.7 km (in Vila Real), which is a much lower distance than those used in previous studies (*Stepanek* and *Mikulova*, 2008; *Vicente-Serrano et al.*, 2010).

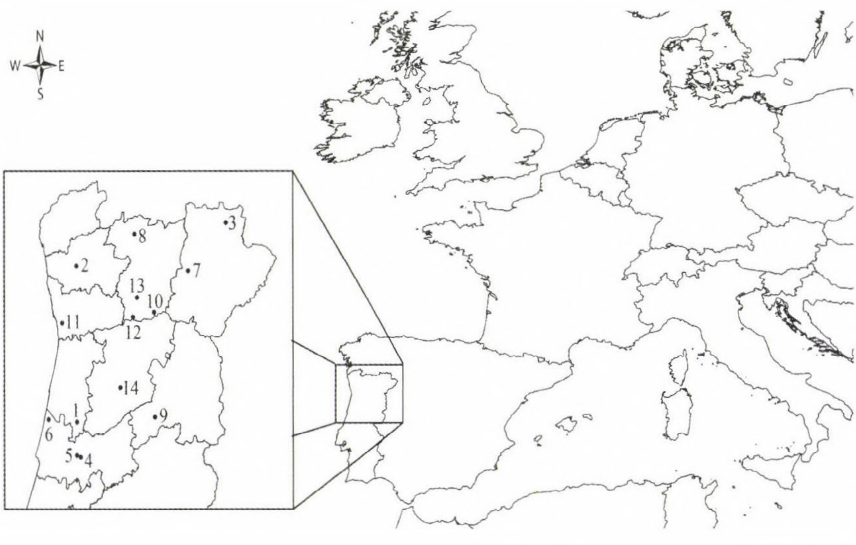

Fig. 1. Location of the weather stations of the Portuguese Institute of Meteorology (IM) network, in northern Portugal. Addition characteristics of these stations are provided in *Table 1*.

In this network, weather stations are well distributed and located both in low and high altitude (ranging from 14 m to 1380 m), in densely populous coastal areas and sparsely populated inner regions within the country territory (*Fig. 1*). The northern Portugal is characterized for being the region with the highest density of mountains and river basins in the country as well as by a diverse land use/occupation (*Freitas et al.*, 2012). Independently of the proximity to the Atlantic Ocean or the altitude, all weather stations considered in this study are located in a region of C_s type of climate, which is a temperate climate with dry period in summer (*AEMET-IM*, 2011). In more detail, the climate of this northern region is essentially of C_{sb} type, which corresponds to a temperate climate with dry or temperate summer, except a small part, in the northeast, which is of type C_{sa}, also temperate but with dry or hot summer. The recently published Iberian Climate Atlas (*AEMET-IM*, 2011) provides a brief history of the complete IM network and additional description and characteristics of the temperature dataset. Results of the exploratory preliminary statistical analysis of minimum and maximum air temperature datasets for the 1941–2010 period are presented and discussed in *Freitas et al.* (2012).

Table 1. Characteristics of the weather stations of the Portuguese Institute of Meteorology (IM) network, located in northern Portugal including: identification code (ID); stations name; station type; altitude (m); start and ending dates; and, amount of missing values (in %), accounted for the 1941–2010 period. When the entire time series results from measurements from a CWS (or AWS), the type is simply CWS (or AWS); in the cases where a CWS was replaced by a AWS, the type is CWS/AWS

ID	Station Name	Type	Altitude (m)	Start year	End year
1	Anadia (AN)	AWS	45	1941	2010
2	Braga (BR)	CWS/AWS	65	1931	2010
3	Bragança (BG)	CWS	690	1932	2010
4	Coimbra B. (CB)	CWS	35	1941	2010
5	Coimbra G. (CG)	CWS	141	1864	1996
6	Dunas Mira (DM)	CWS	14	1935	2005
7	Mirandela (MI)	CWS/AWS	250	1926	2010
8	Montalegre (MO)	CWS/AWS	1050	1880	2010
9	Penhas D. (PD)	CWS/AWS	1380	1932	2010
10	Pinhão (PI)	CWS/AWS	130	1941	2010
11	Porto S.P. (PS)	CWS	93	1863	2005
12	Régua (RE)	CWS	56	1933	2010
13	Vila Real (VR)	CWS/AWS	561	1928	2010
14	Viseu (VI)	CWS/AWS	443	1925	2010

3. *Methodological procedures*

This section is devoted to the description of the methods used to perform the quality control of the data, the homogeneity analysis and to compare the homogenized datasets with those methods. The quality control of the datasets comprises a preliminary exploratory statistical analysis to characterize the potential and limitations of the datasets as well as to identify and correct missing values and outliers. Main technical features of the procedures used in this study will be briefly discussed to validate the followed methodology and to underline the major differences between the approaches of the two selected methods to homogenize the Portuguese air temperature dataset.

3.1. Quality control with homogenization methods packages

In this study two homogenization methods were used: (i) the most recent version of MASH, (Version MASHv3.03), initially developed in the Hungarian Meteorological Service by *Szentimrey* (1994, 1999); and, (ii) HOMER, developed in the framework of COST Action ES0601 (*HOME*, 2011). We start with presenting the homogenization methods because, in addition to being able to detect and correct inhomogenieties, these softwares comprise additional functions to perform fast quality control. On this subject, with MASH it is obligatory to use available functionalities to fill the missing values and perform automatic correction of outliers. On the other hand, HOMER provides a fast quality control of the data, which includes functions of the CLIMATOL R package (*Guijarro*, 2011), which allow the user to perform/estimate station density, correlogram, histograms, boxplots, and cluster analysis. With respect to the detection of heterogeneities, MASH relies on multiple references series while HOMER combines three detection algorithms: pairwise – univariate detection (*Caussinus* and *Lyazrhi*, 1997), joint detection (*Picard et al.*, 2011), and ACMANT – bivariate detection (*Domonkos et al.*, 2012). To correct the datasets, MASH uses multiple comparison techniques whereas HOMER uses ANOVA. MASH is provided with a user guide, while a brief description of HOMER can be found in *Mestre* and *Aguilar* (2011) or in *Freitas et al.* (2012).

3.2. Outlier detection

It is recommended to use different methods for outlier detection because, in general, one single method/criteria is not sufficient to identify real outliers nor to exclude false detections (*Stepanek et al.*, 2009). Consequently, in this study, abnormal high and low values were only classified as outliers if two criteria were simultaneously verified: (i) values above/below the upper/lower thresholds defined as the upper/lower quartiles plus/minus the interquartile range times a coefficient (usually equal to 1.5 to detect outliers and equal to 3.0 to detect extreme values); and, (ii) pairwise comparison which is based on the difference time series between candidate and best neighbor time series, which can be defined as the closer stations and/or those presenting higher correlation (*Stepanek et al.*, 2009; *Syrakova* and *Stefanova*, 2009). This latter procedure can be performed in HOMER by visual inspection of the plots of the difference between candidate and best neighbor time series. As mentioned in the previous section, in addition to this analysis, MASH has an independent and automatic procedure to detect and correct outliers that is executed before detection procedures.

3.3. *Missing values correction*

The existence of missing data in climate time series can be solved with temporal interpolation, using data of the same time series before and after the data gap, or with spatial interpolation, using data from nearby weather stations (*WMO*, 2011). Complex estimation methods, such as weighted averages, spline functions, linear regression, and kriging, which take into account the correlations with other elements, can also be used to complete the time series. *Brunetti et al.*, (2006) adopted a procedure to fill the gaps on monthly precipitation and temperature Italian time series, with estimates based on the highest correlated reference series. For temperature, this method is based on the differences between incomplete and reference temperature series. *Staudt et al.* (2007), replace the missing values on monthly time series of Spanish minimum and maximum temperatures by weighted means of the best-correlated synchronous data. The method used by *Syrakova* and *Stefanova* (2009) to fill the gaps in Bulgarian monthly temperature is based on the stability of the differences between the time series at neighboring highly correlated stations. More recently, *Vicente-Serrano et al.* (2010) tested three different procedures to fill missing data in daily precipitation time series: (i) the nearest neighbor, (ii) inverse distance weighted interpolation; and, (iii) linear regression methods, concluding that the nearest-neighbor method provided the best results. Both homogenization methods used in this study (MASH and HOMER) have corrected databases as final result with respect to inhomogeneities and missing values using multiple comparison and ANOVA, respectively.

3.4. *Reference time series*

Reference series or reference sections are used in detection procedures in many homogenization methods, such as ACMANT, AnClim/ProClimDB, Climatol, RHTestV3, and MASH (*WMO*, 2011). Reference series are also used to assess the quality of the homogenization (*Kuglitsch et al.*, 2009). These reference series do not need to be homogeneous (*Szentimrey*, 1999; *Zhang et al.*, 2001; *Causinus* and *Mestre*, 2004), but must encompass the same climatic signal as the candidate series (*Della-Marta* and *Wanner*, 2006) and, in this sense, are usually produced as weighted averages of the time series from surrounding stations

(*Peterson* and *Easterling*, 1994; *Sahin* and *Cigizoglu*, 2010). *Stepanek* and *Mikulova* (2008) discuss the advantages and disadvantages producing weighted reference series based on the distance between stations or on the correlation between candidate and potential time series, while *Della-Marta* and *Wanner* (2006) argue about the benefits of using weighted reference series in comparison with a single reference station. The selection procedure of the surrounding stations to produce the reference series can be based on the distance between stations or on the correlation between candidate and potential time series. Both criteria present advantages and disadvantages that must be underlined. Distance-based methods preserve the geographical vicinity, but time series from near stations with different climatic signals (e.g., due to altitude) can be selected. Using high correlated neighbor time series, both the candidate and reference series present similar variability (which reduces differences/ratios time series variability), but stations affected with similar/coincident inhomogeneities with the candidate can be selected (*Stepanek* and *Mikulova*, 2008). Weighted reference series are considered more representative of the climatic region and, for being less prone to potential inhomogeneities in the neighbor series than single reference station, are more characteristic of the climate variability at smaller scale (*Della-Marta* and *Wanner*, 2006).

In this study, reference time series are used in the detection procedure, because this is the methodology adopted in MASH and ACMANT, and to assess the quality of the homogenized time series. For the reasons presented before, weighted reference series were produced with AnClim software (*Stepanek*, 2008) using difference series to evaluate the correlation coefficients as suggested in *Alexandersson* and *Molberg* (1997), *Peterson et al.* (1998), *Stepanek* and *Mikulova* (2008), and *Domonkos et al.* (2012). Since our database is affected by only a few number of missing values and the objective is to assess the quality of the homogenization process not of the data completion process, reference series were produced to present the same data gaps than the uncorrected time series. This is achieved by using uncorrected time series (with the data gaps) and neighbor time series without missing values (in order to exclude neighbor time series missing value in the reference series).

3.5. Homogenization methods performance assessment

In contrast to comparative studies performed with synthetic databases, when type, size, and location of inhomogeneities are known a priori (as in *Venema et al.*, 2012), the homogenization methods performance assessment must be executed with real data, by comparing the results obtained with different techniques using non-homogenized (hereafter NH) and homogenized data with MASH (hereafter HM) and HOMER (hereafter HH). This section is devoted to present the methodology used to assess the quality of the corrected dataset and, consequently, methods used in the homogenization process.

i. Correlation analysis

The main objective of correlation analysis is to evaluate the strength of the temporal linear relationship through the computation of the Spearman correlation coefficient, SCC (*Pereira et al.*, 2011). In this sense, to assess potential improvement in the similarity between time series before and after the homogenization process, correlation analysis was applied to annual time series to compute: (i) the correlation matrix between time series of non-homogenized and homogenized time series with MASH and with HOMER datasets; and, (ii) the SCC between each candidate and corresponding reference series. Since our objective is to assess the quality of the homogenization process, and not of the interpolation procedures used in MASH and HOMER to fill the data gaps, SCC was computed between time series with the same missing values than in NH datasets.

ii. Trend analysis

The existence of trends is in the basis of climate change studies (*Raj* and *Azeez*, 2012). In this study, the Mann-Kendal non-parametric test is used to estimate the existence, magnitude and statistical significance of potential trends in the NH, HM, and HH time series, in order to assess the impacts of homogenization methods. This test is suggested for trend analysis by the WMO (*Sneyers*, 1990) and has been used in many published works on climate change and climate variability (e.g., *Moberg* and *Jones*, 2004; *Brunetti et al.*, 2006; *Rodrigo* and *Trigo*, 2007).

iii. Principal component analysis (PCA)

When PCA is applied on a dataset, a new set of time series is produced as linear combination of the original ones. The new time series are the so-called principal components (PC), while the coefficients used to compute them are the elements of the empirical orthogonal functions (EOF). From the mathematical point of view, EOFs are the eigenvectors of the variance-covariance or the correlation matrix of the original dataset, the PCs are obtained by projecting the original time series into the EOF, and the eigenvalues are a measure of the explained variance, i.e., the proportion of the total variance explained by each PC. Obtained PCs are uncorrelated and sorted by decreasing order of variance, while EOFs are orthogonal to each other and constitute a vector base. There are different versions of this multivariate statistical technique, but it is easy to find their description/characteristics (*Jolliffe*, 2005; *Wilks*, 2011). PCA has multidisciplinary applications and is used in data analysis as an exploratory tool (for outlier detection, cluster identification, data visual examination, and interpretation), data preprocessing (dimensionality and noise reduction), modeling, and to identify spatial and temporal patterns and modes of variability such as NAO and ENSO (*Wold et al.*, 1987; *Jolliffe*, 2005; *Pozo-Vazquez et al.*, 2005). PCA results are dependent on the scaling of the original matrix (*Wold et al.*, 1987; *Jolliffe*, 2005), but statistical significance can be assessed, e.g., with cross-validation, bootstrap, or jackknifing techniques (*Romanazzi*, 1993; *Jolliffe*, 2005). PCA outputs, in particular the amount of explained variance by each PC, are dependent on the similarity of the time series (*Jolliffe*, 2005). This characteristic of PCA will be used in this study to assess homogenization results.

4. Obtained results

Preliminary exploratory statistical analysis reveals the existence of a very small number of missing values. Time series most affected by this problem present multiple consecutive missing values or their last record (end date) is before 2010. Results for maximum temperature are very similar to that for minimum temperature. The great majority of the low number of outliers detected above and below the defined thresholds based on the quartiles of their own time series was not confirmed with pairwise comparison with neighboring time series. The final number of outliers considered in HOMER for minimum and maximum temperatures were 10 and 11, respectively, which corresponds to 0.1% of total number of monthly values in each dataset or to less than 1 missing values per time series in each dataset. As mentioned in Section 3.2, MASH has an automatic procedure to detect and correct outliers which is not controlled by the user.

Temporal location and size of the breaks detected in minimum and maximum air temperature time series with MASH and HOMER are shown in *Table 2*. It should be pointed out that breaks marked with a star (*), noticeable only in the detection list of MASH, correspond to shifts of equal value but opposite sign in two consecutive years, that will most likely be an annual outlier than a break point and, from this point forward, will not be considered as breaks. Consequently, the number of breaks detected with HOMER (39 in TN and 32 in TX) is higher than with MASH (32 in TN and 24 in TX). Since the original data only have one significant decimal digit, the physical meaning of a great number of these breaks can be questioned. The number of shifts smaller than 0.1°C detected with MASH is much higher (12 breaks in TN and 19 in TX) than with HOMER (5 breaks in TN and 1 in TX). On the other hand, the number of coincident breaks detected in TN with both methods is 18 (which corresponds to 56% and 46% of total number of breaks detected with MASH and HOMER, respectively) and 9 in TX (37% of MASH and 28% of HOMER total breaks, respectively). If the analysis is restricted to breaks with shifts greater or equal to 0.1°C, the number of coincident breaks in TN is 14 (which corresponds to 70% and 41% of total number of breaks detected with MASH and HOMER, respectively) and 5 in TX (100% of MASH and 16% of HOMER total number of detected breaks, respectively). These results suggest that MASH could be able to detect smaller shifts but an overall small number of break points.

Table 2. Location (and magnitude) of break points detected on minimum and maximum air temperature during 1941-2010 period, with MASH and HOMER. Coincident detections with both methods, defined with utmost 18 months apart are presented in bold. Detections in two consecutive years with symmetrical shifts are marked with a star (*)

ID	Minimum air temperature (TN) MASH	HOMER	Maximum air temperature (TX) MASH	HOMER
1	**1963**(0.11), 1996(0.12)	1944(-0.08), 1950(0.04), **1964**(-0.45), 1970(0.49), 1984(0.29)	1944*(0.12)	1977(-0.22)
2	-	1963(-0.37), 1987(0.24) 1992 (0.53)	**1949**(0.14)	**1950**(-0.76), 1959(-0.49) 1971(-0.27), 1981(0.23)
3	1947*(0.17), 1972(0.08), **1980**(0.14)	1962(0.27), **1980**(-0.49)	1962(-0.05), 1969(-0.14), 1977(-0.03)	1965 (0.27) 1972(0.39) 1993 (0.45)
4	**1979**(-0.31)	1966(-0,18), **1979**(0,78)	1943*(0.46), 1949(-0.03), 1961(0.06), 1963(0.01), 1988*(-0.03), 2000*(0.14)	1953(-0.26), 1992(0.42)
5	**1982**(-0.04)	1950(-0.41), 1967(0.19) **1982**(0.14)	1969(-0.06), **1971**(0.15)	1949(-0,35), **1971**(-0,51)
6	1965(0.15), **1971**(0.15), 1976 (0.09), **1979**(0.26), 1985*(0.39), **1993**(0.05), 1996 (-0.07)	**1969**(-0.75), **1980**(-1.21), 1987(1.26), **1994** (-0.20)	1949*(0.09), 1986*(-0.16)	-
7	1951(-0.28), **1966**(0.21)	**1967**(-0.60), 1989(0.31), 1998(-1.54)	-	-
8	-	1950(-0.67)	**1953**(-0.14), 1976(-0.02), 1979(-0.04), 1994*(-0.18), 1996*(-0.16), 1998*(0.08)	**1951**(0.41), 1974(0.25) 19992(0.35)
9	1963*(-0.128)	-	-	1972(0.12), 1988(0.40)
10	**2003**(-0.54), 2007(0.16)	1958(-0.33) **2004**(1.11)	**1953**(0.04), 1965*(0.06), 1977*(0.12), 1995(0.06), **1998**(-0.27), 2000(-0.12), 2003(0.09)	**1951**(-0.01), 1974(-0.59), 1991(-0.39), **1996**(1.14)
11	-	1986(0.12), 1990(0.32)	-	1951(0.40), 1955(0.19), 1973(-0.42), 1990(0.41)
12	1968(0.11), **1977**(-0.05), 1980(-0.17), **1984**(-0.12), **1986***(-0.12), 1996(-0.03)	**1978**(0.56), **1984**(-0.03), **1987**(0.80), 2000 (0.28)	-	1995 (0,52)
13	**1943***(-0.28), 1948(-0.06), 1966 (0.07), **1974**(0.12), **1986**(-0.09)	**1944**(0.81), 1946(0.45), **1973**(-0.49), **1986** (0.04), 1993 (0.04)	**1954**(0.09), 2000(0.15)	**1953**(-1.22), 1959(0.25), 1991(-0.41)
14	1955(-0.21), **1958**(-0.42), 1969 (0.11), **1982**(-0.58), **1994**(0.80), 1996(-0.08), 1999(-0.08)	**1957**(0.88), **1982**(0.27), **1994**(0.90)	1950(0.05), **1978**(-0.08), **1981**(-0.06), 1992*(0.26), **1994** (0.45)	**1977**(0.29), **1982**(0.35), **1994**(-1.70)

Correlation matrices between non-homogenized time series of maximum (minimum) air temperature, TXNH (TNNH), as well as between homogenized time series with MASH, TXHM (TNHM) and with HOMER, TXHH (TNHH) were computed. Boxplots of the Spearman correlation coefficient (SCC) values obtained for homogenized time series with HOMER are higher having lower dispersion in relation to non-homogenized and homogenized with MASH (*Fig. 2*). In general, SCC values between homogenized TX and TN time series is higher than those obtained between non-homogenized times series. Median value of the difference between TXHH and TXNH correlation matrix is higher (0.09, which corresponds to an increase of 9%) than the difference between TXHM and TXNH correlation matrix (0.02, which corresponds to a general increase of 2%). For minimum temperature, the median of the difference between TNHH and TNNH is equal to 0.13, while between TNHM and TNNH it is equal to 0.05.

Spearman correlation coefficient values obtained between reference series and non-homogenized and homogenized with MASH and HOMER corresponding time series (*Fig. 3*) reveals: (i) higher SCC values between reference and homogenized time series with MASH in every stations and for both TX and TN than between reference and non-homogenized time series; (ii) higher SCC values between reference and homogenized time series with HOMER for TX than between reference and non-homogenized time series but lower values for TN in 6 weather stations. Median of the SCC values obtained for maximum and minimum air temperature homogenized time series with HOMER are similar (94.3% and 89.3%) to those obtained with MASH (91.8% and 88.8%) but higher than for non-homogenized time series (88.2% and 86.4%), in particular for maximum air temperature. At this respect, the increase in the SCC can be underlined computed between the reference and one of the corresponding series: (i) TXHM and TXHH time series in Vila Real and Viseu (of 14.7% and 13.0%, respectively); and, (ii) TNHH and TNHM time series in Vila Real (of 13.7% and 8.4%, respectively).

Trend analysis for TN performed with Mann-Kendal test assuming a statistical significance level of 99% (Table 3) reveals that: (i) only a small number of non-homogenized times series presents statistically significant trends (5 in TNNH and TNHM datasets and only 1 in TNHH dataset); (ii) almost all time series present positive trends except Mirandela and Dunas de Mira; (iii) a reduction in the number of statistical significant trends is only verified for TNHH dataset; and, (iv) with the homogenization procedures, the trend of two time series, after being homogenized, became statistically significant (time series of Bragança, with MASH and of Montalegre with HOMER). Results obtained for TX shows that: (i) there is a lower number of statistically significant trends (2 in TXNH and only 1 in TXHM); (ii) the number of non-homogenized and homogenized time series with negative and positive trends are similar; but, (iii) all statistically significant trends are positive; and, (iv) homogenization procedures lead the loss of statistical significance of the trends in one homogenized time series with MASH and in two homogenized time series with HOMER.

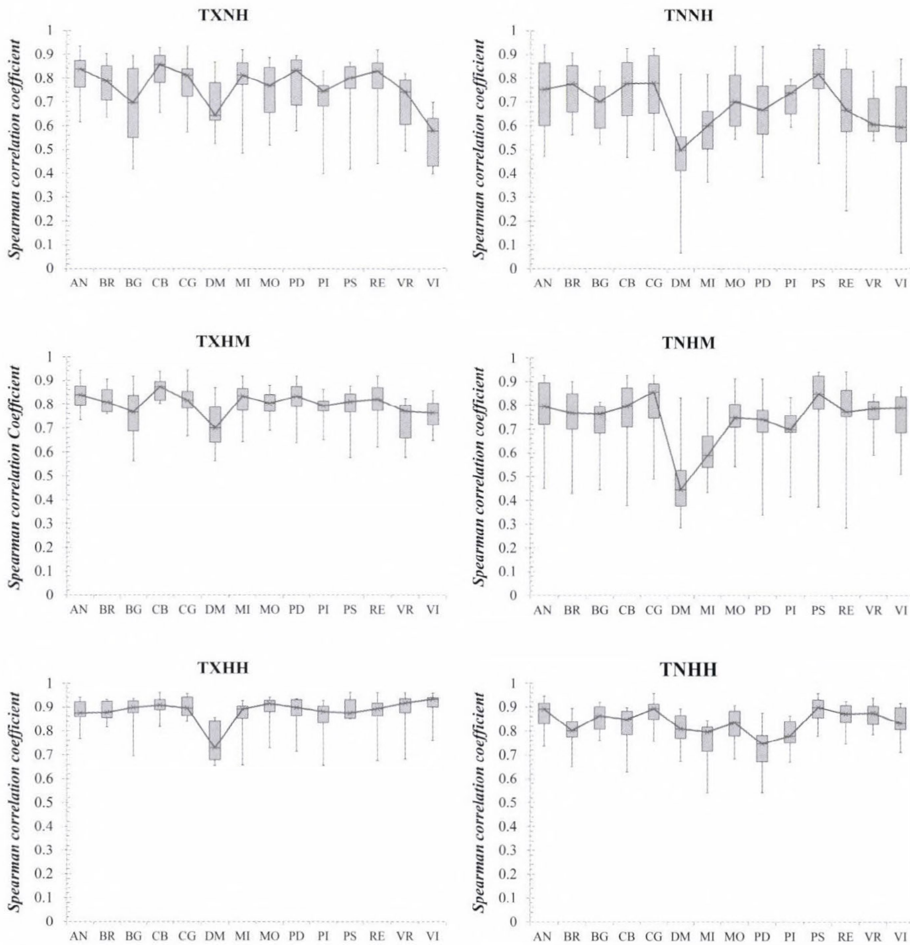

Fig. 2. Boxplot of Spearman correlation coefficient (SCC) between annual time series of non-homogenized (NH), homogenized with MASH (HM) and with HOMER (HH) maximum (top panel) and minimum air temperatures (bottom panel), from weather stations located in northern part of the continental Portugal (*Table 1* and *Fig. 1*), for 1941–2010 period. SCC was evaluated taking into account missing values of NH time series. The bottom/top indicates the lower/upper quartiles, and the band near the middle of the box is the median. The lower/upper end of the whiskers represents the minimum/maximum values.

Results obtained with PCA performed on non-homogenized and homogenized datasets (Table 3) can be summarized as follows: (i) only a small number of PCs are statistical significances (1 PC for TXHM, TXHH, and TNHH and 2 PCs for TNNH, TXNH, and TNHM); (ii) the explained variance by the first PC of homogenized datasets is greater than the explained variance by the first PC of non-homogenized ones; (iii) explained variance of first PC are higher for homogenized datasets with HOMER than with MASH.

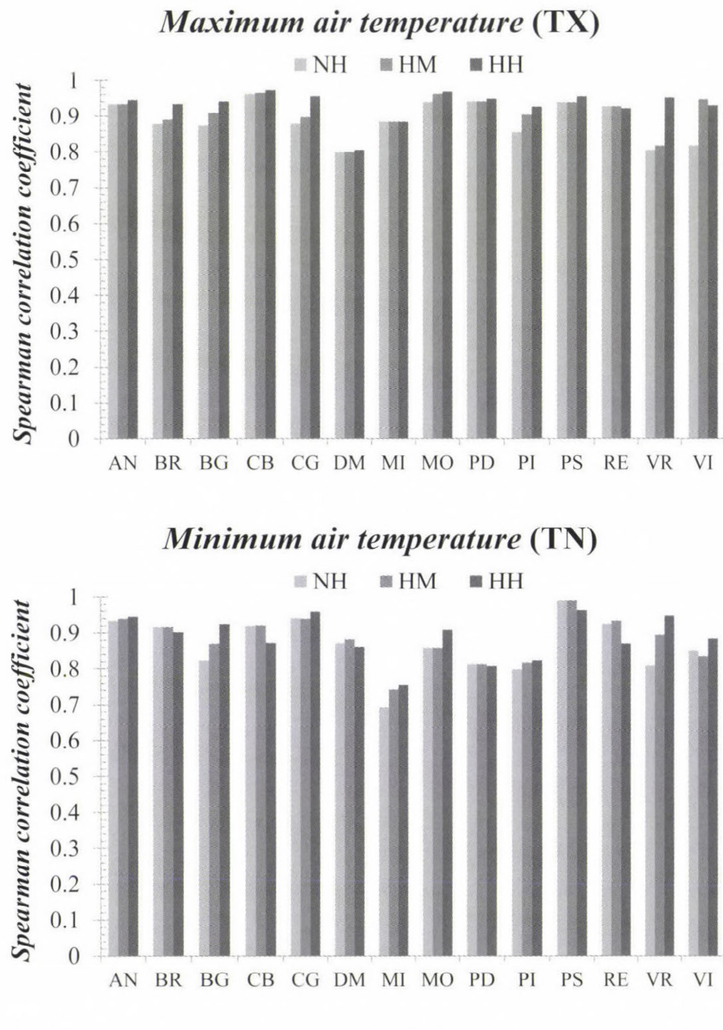

Fig. 3. Spearman correlation coefficient (SCC) between annual reference series and time series of non-homogenized (NH), homogenized with MASH (HM) and HOMER (HH) of maximum air temperature (top panel) and minimum air temperature (bottom panel), for the 1941–2010 period.

5. Discussion and conclusions

The IM network analyzed here includes stations located near the coast and a few meters above sea level and inland stations at higher altitude. Moreover, all weather stations are located in the same climatic region (temperate with dry and hot summer), which is a necessary condition to perform homogenization analysis. Results of the preliminary exploratory data analysis reveals time series with no extremes and only a small amount of outliers and missing values except in cases where times series does not cover the entire analysis period of 1941–2010. This is an important characteristic of the dataset, because missing values can have profound impact on reference series and, consequently, in the detection procedures (*Menne* and *Williams*, 2005; *Syrakova* and *Stefanova*, 2009). In addition, since missing values are treated differently in MASH and HOMER, a small number of data gaps cannot be associated with potential significant differences between homogenized datasets with both methods. On the other hand, heterogeneities are to be expected in TX and TN datasets, since this network is in operation for a long time, and during this period experienced adjustments were carried out on its structure (e.g., replacement of instruments), on its type (changes from classical to automatic sensors), and spatial distribution (e.g., relocation, cessation, and installation of new stations). For these reasons, we may conclude that maximum and minimum air temperature datasets in northern Portugal are examples of databases in good position to be analyzed for homogeneity.

MASH and HOMER were the methods used to perform the homogeneity analysis of TX and TN datasets. The selection criterion was, primarily, the high performance shown by these two methods during the comparison study performed in the framework of the COST Action HOME, using monthly temperature benchmark databases but also the large methodological differences between these two methods, discussed in previous sections. In fact, HOMER was not compared with other methods in *Venema et al.* (2012), because it became available later, but its results from the combination of the methods had the best performance. Craddock method was also included in the list of algorithms with best performance, but because it is a subjective method (uses visual detection of breaks), was not used in this study.

Time series were corrected with both methods from the most recent observations to the oldest. This procedure is consistent with the general believe that current sensors and data acquisition systems are more reliable than previous ones. Both methods uses interpolation to produce homogenized time series without missing values, but MASH also uses extrapolation to fill the data gaps in the extremes of the time series. MASH identifies the location of the break with the year of the shift, while HOMER is able to estimate the month of the change also (not shown in *Table 2*).

The total number of breaks detected in TN with both methods is higher than in TX, and the number of breaks detected with HOMER is higher than with MASH, in both climatic elements. The same conclusion is supported by considering the number of breaks with amplitudes above increasing thresholds. In addition, the amplitude of the breaks detected with HOMER is, in general, higher than the amplitude of the breaks detected with MASH (*Table 2*). The weather stations of Vila Real and Coimbra B were selected as examples of inland and coastal weather stations, located at higher and lower altitudes, respectively (*Fig. 4* and *Fig. 5*), to illustrate the differences between the non-homogenized and homogenized time series with MASH and HOMER. It should also be mentioned that maximum air temperature time series in Mirandela is the only one without inhomogeneities.

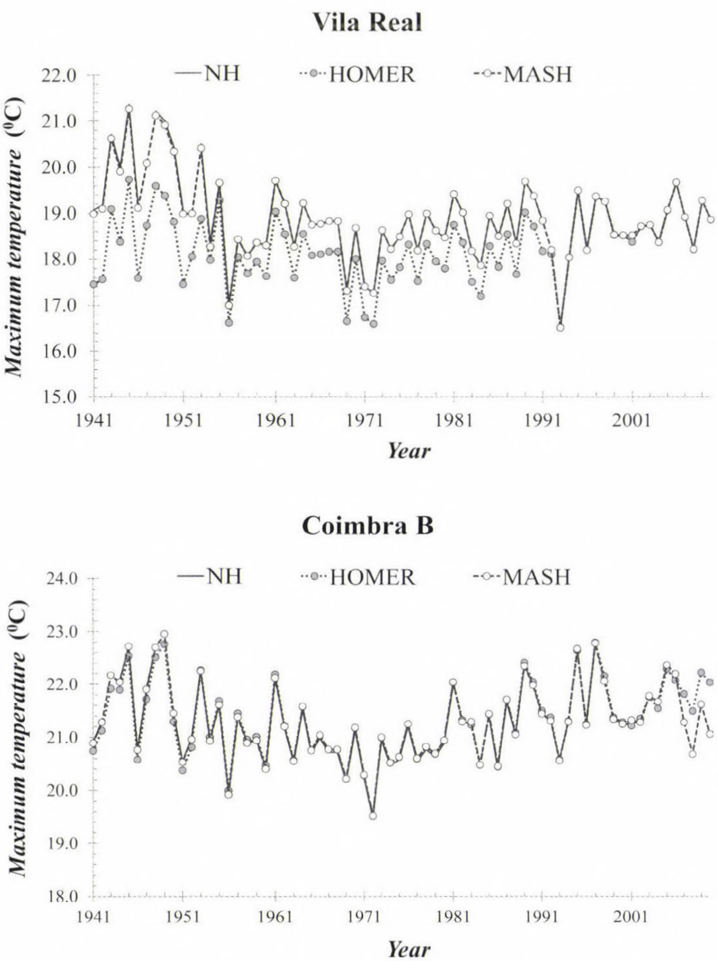

Fig. 4. Non-homogenized (NH) and homogenized time series (with HOMER and MASH) of maximum air temperature (TX) recorded in Vila Real and Coimbra B weather stations. Coimbra B is an example of weather station located in near the coast at low altitude, while Vila Real is an example of weather station located at mountainous region of the interior.

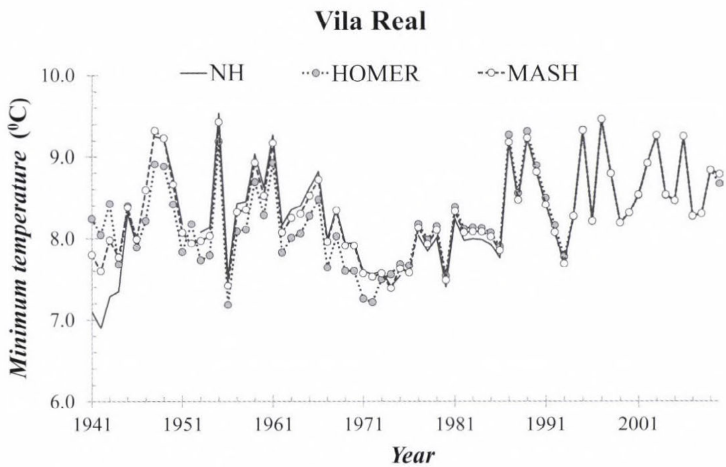

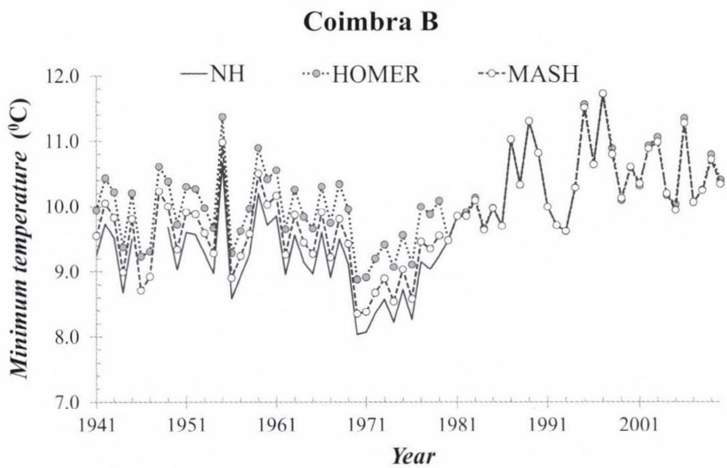

Fig. 5. As in *Fig. 4*, but for minimum air temperature (TN).

Correlation, trend, and principal component analysis were used to assess the homogenization process performance by comparing the results obtained with using non-homogenized and homogenized datasets. Boxplots of the Spearman correlation coefficient (SCC) statistical values obtained between homogenized time series with HOMER are higher and have much lower dispersion than those obtained between homogenized with MASH and non-homogenized time series (*Fig. 2*). For maximum air temperature, the homogenized time series of Dunas de Mira weather station (with both methods) presents the lowest values of the statistics, and it is responsible for the high dimension of the lower whisker. This result is more perceptible in homogenized time series with HOMER than with

MASH as boxplots for other time series are much more alike. For TN, the dispersion is much higher than for TX, and Dunas de Mira time series is also among those presenting lower statistics values. Results obtained with correlation analysis between reference, non-homogenized, and homogenized time series are also consistent with the increase of the similarity of the datasets with the application of both homogenization procedures. Values of SCC increases for all homogenized time series with MASH, but for a few time series (both in TX and TN), SCC values obtained for homogenized time series with HOMER are smaller than for non-homogenized. Notwithstanding this fact, an overall small increase in the median SCC values is conspicuous.

Trend analysis performed on TX and TN time series reveals a small reduction in the number of statistically significant tendencies after homogenization, but a general decrease in the slope, more significant for homogenized time series with HOMER than with MASH, must be underlined. Results obtained using different statistical significance levels (97.5% and 95%) are similar except for the expected higher number of statistically significant trends.

Results from PCA are consistent with those previously obtained with other methodologies and also suggests that homogenization leads to an increase of the resemblance in the spatial and temporal variability of both TN and TX. This behavior is more evident for TX than for TN. In general, the first EOF presents elements with equal sign, which reflects similar behavior in the entire region. Then, the following EOF represents small scale features of variability (e.g., contrast between north and south or between east and west). The magnitude of each feature can be measured by the explained variance of the corresponding mode of variability. In this study, the explained variance by the first PC is higher for homogenized than for non-homogenized datasets, independently of the climatic element (*Table 3*). This difference is higher for homogenized time series with HOMER than with MASH.

Table 3. Explained variance of the statistically significant principal components of non-homogenized (NH), homogenized with MASH (HM) and with HOMER (HH) minimum and maximum air temperature datasets, for the 1941–2010 period

	N	NH	HM	HH
Maximum temperature	1	78.6%	81.0%	89.4%
	2	8.6%	–	–
Minimum temperature	1	75.2%	76.3%	84.8%
	2	9.7%	8.3%	–

In resume, the most important conclusion from this study is that both methods contribute to correcting the inhomogeneities detected in both TN and TM datasets, and that there is no clear evidence of the better performance of one method relative to one another. Results obtained from the correlation analysis, trend analysis and principal component analysis point to a general increase on the spatial and temporal similarity of the time series as should be expected in datasets of the same climatic region. Apparently, these results are independent of the location and altitude of the weather stations. However, these conclusions should be taken with caution, because earlier studies reveal that the evaluation of methods performance is dependent on the metrics used for this purpose (*Venema et al.*, 2012) and on the quality and characteristics of databases (*Freitas et al.*, 2012).

Finally, it should be noted that, to the best of our knowledge, this study is the first effort to compare HOMER with other homogenization methods using observed datasets. The other known study assessing HOMER performance was recently presented in the 7th seminar for homogenization and quality control on climatological databases, but using the HOME benchmark datasets (*Domonkos*, 2012). Furthermore, besides the study of *Freitas et al.* (2012), to assess HOMER potential and limitations, this is the first consistent attempt to homogenize maximum and minimum air temperature Portuguese datasets, using more than one method, MASH and HOMER in particular. The other known homogenization study performed with Portuguese data, was performed by *Soares* and *Costa* (2009), which used precipitation data from stations located in the southern part of the country, as a case study, to compare the potential advantages of geostatistical techniques. As a final point, it should also be emphasized the number of different methods/measures used to compare the homogenized Portuguese air temperature datasets.

References

AEMET, IM, 2011: Iberian Climate Atlas. Closas-Orcoyen S.L, Madrid.

Aguilar E, Auer I, Brunet M, Peterson T.C, Wieringa J., 2003. *Guidelines on Climate Metadata and Homogenization*. World Meteorological Organization: *WMO–TD No. 1186, WCDMP No. 53*, Switzerland, Geneva.

Alexandersson, A., 1986: A homogeneity test applied to precipitation data. *J. Climatol., 6*, 661–675.

Alexandersson, H. and *Moberg, A.*, 1997: Homogenization of Swedish temperature data. 1. Homogeneity test for linear trends. *Int. J. Climatol. 17*, 25–34.

Brunetti M., Maugeri M., Monti F., Nanni T., 2006: Temperature and precipitation variability in Italy in the last two centuries from homogenized time series. *Int. J. Climatol. 26, 345–381* .

Caussinus H. and *Lyazrhi F.*,1997: Choosing a linear model with a random number of change-points and outliers. *Ann. Inst. Statist. Math. 49*, 761–775.

Caussinus, H. and *O. Mestre*, 2004: Detection and correction of artificial shifts in climate series. *Appl. Statist. 53*, 405–425.

Craddock, J.M., 1979: Methods of comparing annual rainfall records for climatic purposes. *Weather 34*, 332–346.

Della-Marta, P.M. and *Wanner, H.*, 2006: A Method of Homogenizing the Extremes and Mean of Daily Temperature Measurements. *J. Climate 19*, 4179–4197.

Domonkos, P., 2011: Adapted Caussinus-Mestre Algorithm for Networks of Temperature series (ACMANT). *Int. J. Geosci. 2*, 293–309.

Domonkos, P., Venema, V., Auer, I., Mestre, O., and *Brunetti, M.*, 2012: The historical pathway towards more accurate homogenisation. *Adv. Sci. Res. 8, 45–52*

Ducré-Robitaille, J-F., Vincent, L.A., and *G. Boulet*, 2003: Comparison of techniques for detection of discontinuities in temperature series. *Int. J. Climatol. 23*, 1087–1101.

Freitas,L., Pereira M.G., Amorim L., Caramelo L., Mendes M., and *Nunes F.L*, 2012: Portuguese temperature dataset homogeneity with HOMER *(submitted to WMO serial World Climate Data and Monitoring Program)*

Guijarro, J.A., 2011: Climatol version 2.0, an R contributed package for homogenization of climatological series. State Meteorological Agency, Balearic Islands Office, Spain, http://webs.ono.com/climatol/climatol.html

Gullet, D.W., Vincent, L., and *Sajecki, P.J.F.*, 1990: Testing for Homogeneity in Temperature Time Series at Canadian Climate Stations. CCC Report No. 90-4, *Atmospheric Environment Service, Downsview, Ontario.*

HOME, 2011: Homepage of the COST Action ES0601 - *Advances in Homogenisation Methods of Climate Series: an Integrated Approach* (HOME), http://www.homogenisation.org.

Jolliffe, I.T , 2005:Principal component analysis. In (B.S. Everitt and D.C. Howell) *Encyclopedia of Statistics in Behavioral Science, vol. 3,* Wiley, New York, 1580–1584.

Kuglitsch, F.G., Toreti, A., Xoplaki, E., Della-Marta, P.M., Luterbacher, J., and *Wanner, H.,* 2009: Homogenization of daily maximum temperature series in the Mediterranean, *JGR 114*, 1–6.

Menne, M.J. and *Williams Jr., C.N.*, 2009: Homogenization of temperature series via pairwise comparisons. *J. Climate 22*, 1700–1717.

Menne, M.J. and *Williams jr. C.N.*, 2005: Detection of undocumented changepoints using multiple test statistics and composite reference series. *J. Climate 18*, 4271–4286.

Mestre O., 1999. Step-by-step procedures for choosing a model with change-points. In *Proceedings of the second seminar for homogenisation of surface climatological data*, Budapest, Hungary, *WCDMP-No.41, WMO-TD No.962*, 15–26.

Mestre, O. and *Aguilar E.*, 2011: Homogenization (personal communication). COST ES0601 Training School, 5–7th of October, Tarragona.

Moberg, A. and *Jones, P.D.*, 2004: Regional Climate Models simulations of daily maximum and minimum near-surface temperatures across Europe compared with observed station data for 1961-1990. *Clim. Dynamics 23*, 695–715.

Pereira, M.G., Caramelo, L., Gouveia, C., Gomes-Laranjo, J., and *Magalhaes, M.* 2011: Assessment of weather-related risk on chestnut productivity. *NHESS,* 2729–2739.

Perreault L., Bernier J., Bobée B., and *Parent E.*, 2000. Bayesian change-point analysis in hydrometeorological time series. Part. 1. The Normal model revisited. *J. Hydrol. 235*, 221–241.

Peterson, T.C. and *Easterling, D.R*, 1994: Creation of homogeneous composite climatological reference series, *Int. J. Climatol. 14*, 671–679.

Peterson T.C., Easterling, D.R., Karl, T.R., Groisman, P., Nicholls, N., Plummer, N., Torok, S., Auer, I., Boehm, R., Gullett, D., Vincent, L., Heino, R., Tuomenvirta, H., Mestre, O., Szentimrey, T., Salinger, J., Førland, E.J., Hanssen-Bauer, I., Alexandersson, H., Jones, P. and *Parker, D.*,1998: Homogeneity adjustments of in situ atmospheric climate data: A review. *Int. J. Climatol. 18*, 1493–1517.

Peterson, T.C., Easterling, D.R., Karl, T.R., Groismanm P., Nicholls, N., Plummer, N., Torok, S., Auer, I., Boehm, R., Gullett, D., Vincent, L., Heino, R., Tuomenvirta, H., Mestre, O., Szentimrey, T., Salinger, J., Forland, E.J., Hanssen-Bauer, I., Alexandersson, H., Jones, P., and *Parker, D.*, 1998: Homogeneity adjustments of in situ atmospheric climate data: A review. *Int. J. Climatol. 18*, 1493–1517.

Picard, F., Lebarbier, E., Hoebeke, M., Rigaill, G., Thiam B., and *Robin, S.*, 2011: Joint segmentation, calling, and normalization of multiple CGH profiles. *Biostatistics.* doi:10.1093/biostatistics/kxq076

Pozo-Vazquez, D., Gamiz-Fortis, S.R., Tovar-Pescador, J., Esteban- Parra, M.J., Castro-Dıez, Y., 2005: North Atlantic winter SLP anomalies based on the autumn ENSO state. *J. Climatol. 18*, 97–103.

Raj, P.P.N. and *Azeez, P.A.*, 2012: Trend analysis of rainfall in Bharathapuzha River basin, Kerala, India. *Int. J. Climatol. 32,* 533–539.
Reeves, J., Chen, J., Wang, X.L., Lund, R., and *Lu, Q.*, 2007: A review and comparison of changepoint detection techniques for climate data. *J. Appl. Meteorol. Climatol. 46,* 900–915.
Rodrigo, F.S. and *Trigo, R.M.*, 2007: Trends in daily rainfall in the Iberian Peninsula from 1951 to 2002. *Int. J. Climatol. 27,* 513–529.
Romanazzi, M., 1993: Jackknife estimation of the eigenvalues of the covariance matrix. *Comput. Statist. Data Anal. 15,* 179–198.
Sahin, S. and *Cigizoglu, H.K.*, 2010: Homogeneity analysis of Turkish meteorological data set. *Hydrol. Process. 24,* 981–992.
Sneyers, R., 1990: On the statistical analysis of series of observations., WMO *Tech. Note 143, 145,* Geneva, Switzerland.
Staudt, M., Esteban-Parra, M.J., and *Castrı-Diez, Y.*, 2007: Homogenization of long-term monthly Spanish temperature data. *Int. J. Climatol. 27,* 1809–1823.
Štěpánek, P., 2008: AnClim – software for time series analysis (for windows). *Dept. of Geography, Fac. of Natural Sciences*, MU, Brno. http://www.climahom.eu/AnClim.html.
Štěpánek, P. and *Mikulová, K.*, 2008: Homogenization of air temperature and relative humidity monthly means of individual observation hours in the area of the Czech and Slovak Republic. In: *5th Seminar for Homogenization and Quality Control in Climatological Databases.* Hungarian Met. Service, Budapest, Hungary, 147–163.
Štěpánek, P., Zahradniéek, P., and *Skalák, P.*, 2009: Data quality control and homogenization of the air temperature and precipitation series in the Czech Republic in the period 1961–2007, *Adv. Sci. Res. 3,* 23–26.
Syrakova, M. and *Stefanova, M.*, 2009: Homogenization of Bulgarian temperature series. *Int. J. Climatol. 29,* 1835–1849.
Szentimrey, T., 1994: Statistical problems connected with the homogenization of climatic time series. In *Proceedings of the European Workshop on Climate Variations*, Kirkkonummi, Finland, *Publications of the Academy of Finland, 3/94,* 330–339.
Szentimrey, T., 1999: Multiple Analysis of Series for Homogenization (MASH). *Proceedings of the Second Seminar for Homogenization of Surface Climatological Data,* Budapest, Hungary, WMO, *WCDMP-No. 41,* 27–46.
Szentimrey, T., 2007: Manual of homogenization software MASHv3.02", Hungarian Meteorological Service.
Toreti, F.G., Kuglitsch, A., Xoplaki, E., and. Luterbacher, J., 2012: A Novel Approach for the Detection of Inhomogeneities Affecting Climate Time Series. *J. Appl. Meteorol. Climatol.,vol. 51,* 317–326.
Trewin, B., 2010: Exposure, instrumentation, and observing practice effects on land temperature measurements. *WIREs Clim. Change, 1,* 490–506.
Venema, V., Mestre, O., Aguilar, E., Auer, I., Guijarro, J.A., Domonkos, P., Vertacnik, G., Szentimrey, T., Stepanek, P., Zahradnicek, P., Viarre, J., Müller-Westermeier, G. Lakatos, M., Williams, C.N., Menne, M., Lindau, R., Rasol, D., Rustemeier, E., Kolokythas, K., Marinova, T., Andresen, L., Acquaotta, F., Fratianni, S., Cheval, S., Klancar, M., Brunetti, M., Gruber, C., Duran, M.P., Likso, T., Esteban, P., and Brandsma, T., 2012: Benchmarking monthly homogenization algorithms. *Climate of the Past 8*, 89–115.
Vicente-Serrano, S., Begueria, S., Lopez-Moreno, J.I., García-Verac, M.A., and *Stepanek, P.*, 2010: A complete daily precipitation database for northeast Spain: reconstruction, quality control, and homogeneity. *Int. J. Climatol. 30,* 1146–1163.
Vincent, L.A., 1998: A technique for the indentification of inhomogeneities in Canadian temperature series. *J. Clim. 11,* 1094–1104.
Wilks, D.S., 2011. Statistical Methods in the Atmospheric Sciences, vol 100, 3rd Edition,*International Geophysics 100.* Academic Press, Oxford, UK
Williams, C.N., Menne, M.J., and *Thorne, P.W.*, 2012:. Benchmarking the performance of pairwise homogenization of surface temperatures in the United States. *J. Geophys. Res.-Atmos. 117, D05116.*

Wold, S., Geladi, P., Esbesen, K. and *Ohman, J.*, 1987: Multi-way principal components- and PLS-analysis. *J. Chemometrics 1*, 41–56.

World Meteorological Organization, 2011: Guide to Climatological Practices, WMO/No. 100., Geneva.

Zhang, X.B., Vincent, L.A., Hogg, W.D., and *Niitsoo, A.*, 2001: Temperature and precipitation trends in Canada during the 20th century, *Atmos. Ocean 38*, 395–429.

IDŐJÁRÁS
Quarterly Journal of the Hungarian Meteorological Service
Vol. 117, No. 1, January–March 2013, pp. 91-112

Measuring performances of homogenization methods

Peter Domonkos

University Rovira i Virgili, Centre for Climate Change, Campus Terres de l'Ebre, Av. Remolins, 13-15, 43500-Tortosa, Spain,
peter.domonkos@urv.cat

(Manuscript received in final form October 8, 2012)

Abstract–Climatologists apply various homogenization methods to eliminate the non-climatic biases (the so-called inhomogeneities) from the observed climatic time series. The appropriateness of the homogenization methods is varied, therefore, their performance must be examined. This study reviews the methodology of measuring the efficiency of homogenization methods. The principles of reliable efficiency evaluations are: (i) Efficiency tests need the use of simulated test datasets with similar properties to real observational datasets; (ii) The use of root mean squared error (RMSE) and the accuracy of trend-estimations must be preferred instead of the skill in detecting change-points; (iii) The evaluation of the detection of inhomogeneities must be clearly distinguished from the evaluation of whole homogenization procedures; (iv) Evaluation of homogenization methods including subjective steps needs blind tests. The study discusses many other details of the efficiency evaluation, recalls the results of the blind test experiment of the COST action ES0601 (HOME), summarizes our present knowledge about the efficiencies of homogenization methods, and describes the main tasks ahead the climatologist society in the examinations of the efficiency of homogenization methods.

Key words: time series homogenization, efficiency, surface climatic observations, upper air climatic observations

1. Introduction

Homogenization is a procedure to improve the quality of data. During homogenization, the temporal constancy of some characteristics is tested and the degree of constancy is a quality indicator. In contrast with the common data quality control, homogenization examines the characteristics of segments of data instead of those of individual pieces of data. Homogenization is applied in several branches of science, e.g., economics, information systems, neurology, etc. (see some references in *Toreti et al.* 2012), but homogenization tasks often have peculiarities according to research fields and the variables examined.

In climatology, homogenization examines and adjusts temporal biases of climatic variables, caused by non-climatic factors. Various technical changes may cause non-climatic biases in observed surface climate (*Aguilar et al.*, 2003; *Auer et al.*, 2005; *Menne et al.*, 2009, etc.) and in radiosonde data (*Lanzante et al.*, 2003, *Gruber* and *Haimberger*, 2008; *Dai et al.*, 2011, etc.), and a large number of methods are applied for their correction. The purpose of homogenization is to obtain observed climatic datasets of the best possible quality for climate variability investigations. Relative homogenization, named also innovation of time series (*Haimberger*, 2007), examines the series of the differences or ratios of the observed data (relative time series hereafter) instead of examining directly the raw data (absolute homogenization). Relative homogenization is preferred when the spatial density and coherence of the observed data allows it, because in relative time series the climatic fluctuation that is common for the examined region does not appear. Note, however, that absolute homogenization is also applicable under certain conditions. Different homogenization methods often have markedly different efficiencies in finding and correcting the non-climatic biases. The objective interpretation of climate change and climate variability, assessment of risks of extreme climatic events, modeling of spatial and temporal evolution of weather and climate events all need accurate input data fields; therefore, the climatological community is interested in finding the best homogenization methods. The selection of the most appropriate methods requires the application of objective efficiency tests.

The COST action "Advances in homogenization methods of climate series: an integrated approach" (2007–2011) accelerated the progress of the methodological development of homogenization and its reliable testing in several ways. We refer to the COST action with its acronym "HOME", to its benchmark dataset for the surrogate European surface temperature dataset with "Benchmark", and often to its closing study written by the HOME group (*Venema et al.*, 2012). Under HOME, 25 versions of 9 statistical homogenization algorithms were subjected to blind tests, and their results were evaluated with 13 efficiency measures. Nevertheless, the scope of this paper is much wider than the analysis of HOME products. We review the contemporary methodology of tests applied in the efficiency evaluations for homogenization procedures in a wide range of homogenization tasks. The problems related to the choice of efficiency measure and the construction or selection of test datasets are widely discussed. Reliable efficiency tests must be based on test datasets whose statistical properties mimic well the properties of observational datasets. In this respect the study has limitations, i.e., we do not deal with the peculiarities of individual homogenization tasks apart from some examples. We do not deal with the particularities of daily data homogenization either.

The organization of the paper is as follows. In the next section, the problems related to setting up efficiency evaluation methods with general reliability are listed and discussed. In Section 3, the efficiency measures and their properties are described. In Section 4, various kinds of efficiency tests with their different objectives are presented, while Section 5 deals with the problem of constructing realistic test datasets. Finally, the tasks for the future are discussed in Section 6.

2. *Difficulties in producing reliable efficiency evaluations*

As the most frequent type of inhomogeneities is the sudden shift in the means (referred also as change-points), e.g., for station relocations, change in the instrumentation, etc., the evaluation of efficiency might not seem to be a complicated task: the simplest assessment is to calculate the ratio of correctly identified change-points relative to all change-points (the so-called hit rate), since higher hit rate generally indicates better performance of homogenization method. However, this simple approach often fails and its causes are discussed in this section, grouping the problematic aspects into four subsections.

2.1. Complexity of homogenization methods

Homogenization is a complex procedure. It generally includes at least 3 segments (*Gruber* and *Haimberger*, 2008), they are:

(i) time series comparison,
(ii) detection of inhomogeneities,
(iii) adjustments of the detected biases.

Each segment can be objective (i.e., based on pure statistics) or subjective. Detection and adjustments may be partly or fully based on metadata. Note that in absolute homogenization segment (i) is missing. On the other hand, any segments or even all segments can be included multiple times in one homogenization procedure, because several procedures are iterative with the cyclically repeated application of their segments. From the point of view of efficiency evaluation, the problem is that a certain detection method can be applied with various time series comparisons, adjustments, and iteration techniques. When, for instance, the hit rate is calculated, the result depends on all the segments and even on each of the parameters included in the procedure. For example, *Moberg* and *Alexandersson* (1997) presented the application of the standard normal homogeneity test (SNHT) through the homogenization of Swedish temperatures. They built reference series from 8 series of the neighbourhood with the highest spatial correlations for the increment (first difference) series, applying the cutting algorithm by *Easterling* and *Peterson* (1995) until the subsections had at least 10 years length, etc. A problem of testing the performance of homogenization methods is that the details of the methods, as for instance the ones cited from *Easterling* and *Peterson* (1995) and particularly the parameters are only recommendations, and some of the proposed details cannot even be applied for all homogenization tasks. However, the performance depends on all the particularities of the procedure.

A further problem is that most homogenization procedures include subjective steps that make the objective evaluation of the performance difficult (Section 4.3).

2.2. Indication of good performance

The simplest evaluation of performance is the calculation of the hit rate. The problem with hit rate (and with more advanced related metrics, e.g., detection skill, see Section 3) is that the accuracy of homogenized time series only partly depends on it. When the Hit rate is high, but some large shifts fail to be detected, the variability of the homogenised time series may substantially differ from the true climatic variability. By contrast, if the largest shifts are detected well, the final result of homogenization might be fair in spite of a relatively low hit rate. Note that the accumulated effect of inhomogeneities on the bias of variability characteristics is even more important than the shift-magnitudes at individual change-points (an example will be shown in Section 3). As the aim of homogenization is to have the climatic time series in the appropriate state for deriving climate variability characteristics with high accuracy, the best way is to use efficiency measures which directly evaluate the quality of homogenized time series from this point of view. Yet, there are two more problems. One is that a homogenization result may be excellent for the examinations of some climatic characteristics (e.g., linear trend, low frequency variability of the mean values, etc.), but might be poor for some other examinations (e.g., standard deviation, extreme events, etc.). For this reason, the use of one efficiency measure cannot be sufficient to evaluate the general performances of homogenization procedures. Another problem is that often the objective parts of homogenization methods are evaluated only (we consider homogenization procedures or their certain segments objective when subjective decisions by homogenisers are not allowed in them). Evaluations are often restricted to the examination of the detection of change-points with statistical tests (*DeGaetano*, 2006; *Gerard-Marchant et al.*, 2008; *Bealieu et al.*, 2008; etc.). However, if one would like to know the connection between the skill in detecting change-points and the final quality of homogenization product, the inclusion of other segments of the homogenization procedure is necessary for the evaluation. A suggested solution will be described in Section 4.1.

2.3. Station effects: true or false?

Even if all time series are ideally homogeneous in a network of the same climatic region, some statistical properties of time series are still distinct for each individual time series due to the peculiarities of the observing station (e.g., exposure, land use, natural vegetation, etc.). Therefore, when the aim of homogenization is transformed to an exact mathematical task, it should include the elimination of change-points, but should exclude the cancellation of true station effects. In relative homogenization, temporally constant station effects can be preserved only, since relative homogenization is based on the equalization of differences or ratios of time series. The accuracy of mean station effects can hardly be controlled by efficiency tests, because a) there is no objective method for the estimation of mean station effects, b) it seems to be a challenge to construct test datasets with pre-defined realistic mean station effects.

The most usual way of determining station effects in homogenization procedures is to keep the last homogeneous section (the section between the change-point detected with the latest date and the end of the series) unchanged and adjust all the other parts of the series to that section. This assumption is correct when all the technical, personal, and environmental conditions were good to provide high quality observations in the last period of the series, but false in the opposite case. Especially, when only the late part of a time series is influenced by urbanization, that urban effect will be included for the whole homogenized time series if the adjustments are made relative to the last homogeneous section of the series. Note however, that from the point of view of macroclimatic examinations, the temporal changes of urban effect are undesired inhomogeneities, thus their elimination by homogenization is correct.

In the homogenization of surface climatic data, the assessment of mean station effect could be considered a task that is out of the scope of homogenization, since a series can be perfectly homogeneous in term of mathematical homogeneity in spite of the average station effect is false. An example for the latter case is when each value of the series of ideally accurate observational values is shifted with a constant error-term mimicking an erroneous mean station effect: the trends remain in line with the macroclimate, but the distribution function and its statistical characteristics would be false. We incorporate this problem into the homogenization task, because with the expression "homogenized time series" climatologists mean high quality data that are applicable well for climate variability analyses. Note that large errors in the assessment of mean station effects in the principal surface climate variables are rare, therefore, the problem of their correct treatment is basically theoretical with relatively little practical importance.

In upper air measurements, the origin of true station effect is restricted to the geographical coordinates, as there is no particular effect from exposure, surface type, natural vegetation, etc. However, systematic local errors can be larger due to the more serious problems of instrumentation than in surface observations. In accordance with these facts, the homogenization of upper air time series includes the optimization of the spatial differences of data (*Haimberger*, 2007).

2.4. Dependence on the properties of test dataset

True observational time series cannot be used for evaluating efficiency, because we never know the exact characteristics of non-climatic biases. Even with the best homogenization methods, only a part of the inhomogeneities can be identified, and even false detections sometimes occur (*Venema et al.*, 2012). Therefore, artificial test datasets are needed with known positions and magnitudes of inhomogeneities for measuring the efficiency of homogenization methods. These test datasets should resemble the true climatic time series as much as it is possible, because otherwise the observed efficiencies in test experiments may not be valid in the real world. We illustrate the seriousness of this problem with the description of two experiments. Detection skill (see its definition in Section 3) was examined for 6 widely used change-point detection methods (*Fig. 1*). In the first experiment, one change-point was inserted into 100 years long stationary white noise processes. The shift-magnitude was 3 times larger than the standard deviation of the white noise. In the second experiment the only difference was that further four change-points were inserted with half-size shifts relative to the one large shift inserted earlier. The positions and directions of the small shifts were random. In both experiments, the detection skill for the one large shift was evaluated only. The difference between the obtained efficiencies is striking: while in the first experiment the efficiencies are between 88–96% for the five best methods (out of the examined six in *Fig. 1*), the values drop to 59–75% when 4 more change-points are present in the time series. We underline that the detection skill of small change-points did not contribute directly to the results shown, but small shifts generally act as a kind of noise, which substantially worsens the detection skill of large shifts.

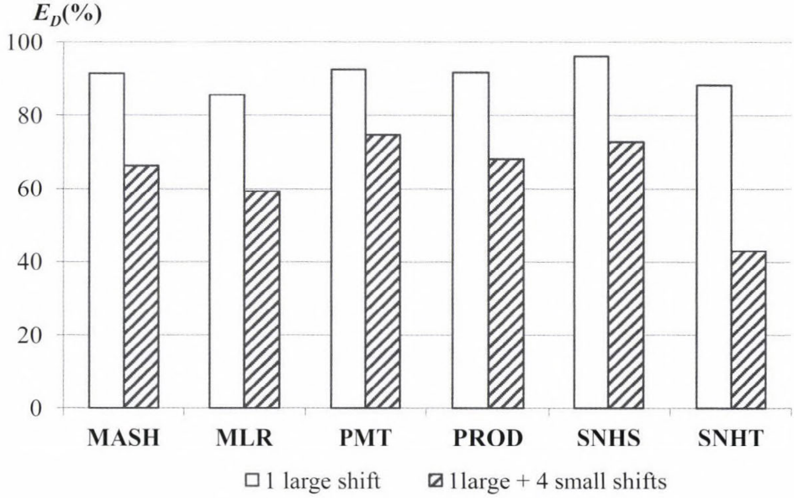

Fig. 1. Detection skill (E_D) of large shifts with the background of white noise and with that of white noise plus four small shifts. PMT – Penalized maximum t-test (*Wang et. al.*, 2007); PROD – PRODIGE, SNHS – SNHT for shifts only (*Alexandersson*, 1986); the explanation of other denotations is in the text.

For constructing realistic test datasets, we should know the statistical properties of inhomogeneities in the target climatic time series. There are two problems related to this point: a) We cannot learn the exact properties of inhomogeneities, because small inhomogeneities often cannot be detected with any kind of method; b) Even if we could determine the exact characteristics of some real climatic time series, that characteristics would not be projected without control to new homogenization tasks, since the properties for different time series, networks, and climatic variables are obviously diverse.

3. Efficiency measures

For characterizing the appropriateness of homogenization methods to make the climatic time series more suitable for accurate climate variability examinations, efficiency measures must evaluate the mean progress in the accuracy of the variability of homogenized time series. The root mean squared error (RMSE) is a known tool for characterizing skills and remaining errors:

$$\mathrm{RMSE}(\mathbf{X}) = \sqrt{\frac{1}{n}\sum_{i=1}^{n}(x_i - t_i)^2} \,. \qquad (1)$$

It can be formed to an efficiency measure at which 1 means perfect skill and 0 means neutrality (no improvement, neither destruction):

$$E = \frac{\mathrm{RMSE}(\mathbf{Z}) - \mathrm{RMSE}(\mathbf{X})}{\mathrm{RMSE}(\mathbf{Z})} \,, \qquad (2)$$

where **Z**, **X**, **T** stand for raw, homogenized, and true (fully homogeneous) time series, respectively, n is the sample size, and E is the efficiency.

The RMSE can be calculated for various time units of the observed series. For instance, *Venema et al.* (2012) applied month, year, and decade time units. With RMSE of long time units, the evaluation is focused on the accuracy in long-term variability, while the meaning of RMSE of short time units is more general. Especially, the detection of seasonality of non-climatic biases can be evaluated with the comparison of monthly and annual RMSE results.

Venema et al. (2012) introduced a modified version of RMSE (centered RMSE, CRMSE), it calculates the RMSE of the anomalies relative to the mean bias:

$$\mathrm{CRMSE}(\mathbf{X}) = \sqrt{\frac{1}{n}\sum_{i=1}^{n}\left(x_i - t_i - \overline{\mathbf{X} - \mathbf{T}}\right)^2} \,, \qquad (3)$$

where the upper stroke means arithmetical average. The motivation of using CRMSE instead of RMSE in HOME was to eliminate the effect of unknown mean station effects, because the HOME tests did not incorporate this specific problem in any form.

In the evaluation of the accuracy of linear trends in homogenized time series, RMSE is also applicable to the comparison of trend slopes in **X** and **T** (*Venema et al.*, 2012; *Domonkos*, 2011a). Linear trend estimations and their accuracy have enhanced importance in climate studies, since linear trends indicate the sign and degree of mean systematic change of the climate variable under study over the period examined. Note that the RMSE of trend biases is not impacted by the possible errors in the estimation of mean station effects.

All RMSE and CRMSE characteristics described can be applied in the evaluations of entire time series or sections of time series. The accuracy of network-mean values is particularly important in the assessment of past climate changes, and a novelty of HOME was that RMSE was calculated also for the series of network-means (*Venema et al.*, 2012). We mention that apart from RMSE or CRMSE, mean absolute error or rank order are also applicable (the latter is only for the comparison of performances, see, e.g., *Titchner et al.*, 2009).

The most frequently used efficiency measures for the homogenization of climatic time series are hit rate (S_R, referred also as detection power), false alarm rate (S_F) and their various combinations (*Buishand*, 1982; *Easterling* and *Peterson*, 1995, *Reeves et al.* 2007, etc.). Hit rate (false alarm rate) shows the ratio of correctly (falsely) detected change-points relative to the total number of change-points (S) that are present in time series. Large S_R and small S_F indicate good skill in detecting change-points, while the opposite case indicates poor skill. With detection skill (E_D, Eq. (4)), S_R and S_F can be examined jointly (*Menne* and *Williams*, 2005; *Domonkos*, 2011a).

$$E_D = \frac{S_R - S_F}{S} \quad . \tag{4}$$

Although hit rate and detection skill are the most traditional efficiency measures, there are several problems with their applications. Their main deficiency is that S_R and E_D do not indicate confidently the accuracy of homogenized time series and the appropriateness of time series for climate variability analysis. *Fig. 2* presents the imaginary results of a time series homogenization. The series consists of 100 years, and it contains three change-points in years 30, 50 and 70. The shift-magnitudes in years 30 and 70 are slightly larger than in year 50. The sign of the shift in year 30 is the opposite of the sign of the other two shifts. In the homogenization labelled with Y1, only the shift of year 70 was detected and corrected, while in Y2 two shifts, i.e.,the ones in years 30 and 70 (*Fig. 2*). It is clear that the hit rate and detection skill are better for Y2 than for Y1 (namely 1/3 for Y1 and 2/3 for Y2). However, the RMSE and remaining trend-bias are better for Y1 than for Y2. The RMSE (remaining trend bias for the entire series) are 1.45 (0.54/100yr) for Y1 and 2.12 (4.50/100yr) for Y2. We have these seemingly contradictory results in spite of the two largest shifts were detected in Y2, the time-lapses of the detected change-points are zero, no false detection occurred, and the assessment of shift-magnitudes is perfect for the detected shifts. The only thing that favored for Y1 is that the accumulated effect of inhomogeneities in the first 30 years section of the series is smaller if the bias of year 70 is corrected.

Another problem is that during the practical use of hit rate and detection skill, subjectively-set parameters are often applied. First, because a certain time lapse in the detection is usually accepted as correct detection, otherwise the evaluation could be too strict and unrealistic (*Ducré-Robitaille et al.*, 2003; *Bealieu et al.*, 2008; etc.). Second, because the detection of small size biases is often not evaluated, and third, if test series include other kinds of inhomogeneities than sudden shifts (e.g., gradually increasing biases), even the calculation of S may need the incorporation of parameterized definition (*Domonkos*, 2011a). The thresholds for the allowed time lapse, minimum size of shift, and criterions for change-point in temporally irregular station effects all need subjective decisions which reduce the power and comparability of tests with hit rate and detection skill. On the other hand, these statistics must be considered as indications about the operation of the homogenization procedure, which indications may be important both for the users and constructors of the methods. Note that from hit rate and false alarm rate not only detection skill can be derived, but also several other scores that characterize the success of change-point detection in various ways (*Menne* and *Williams*, 2005; *Venema et al.*; 2012).

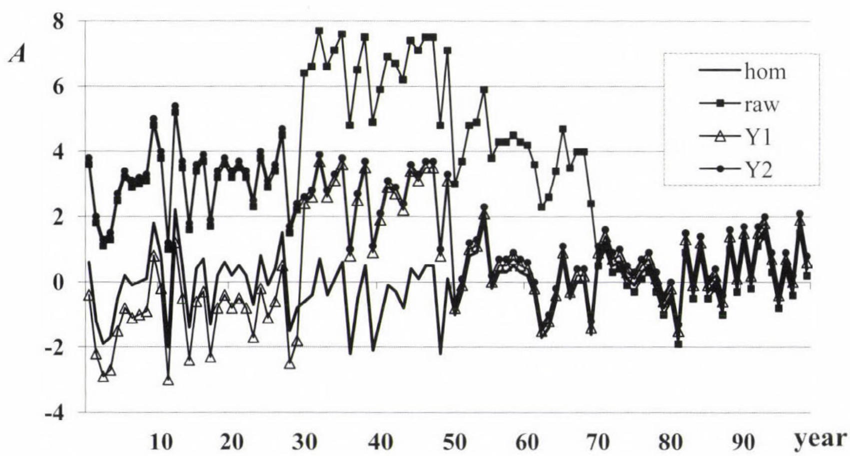

Fig. 2. Example of homogenization results. The raw time series is a 100 years long white noise with shifts in years 30, 50, and 70, whose magnitudes are +4, –3, –4, respectively. The unit of the values (A) is the standard deviation of white noise. hom = homogenous data, raw = "raw" (simulated) data, Y1 and Y2 are the results of partly successful homogenization. In Y1 only the shift of year 70, while in Y2 two shifts, i.e., the shifts in years 30 and 70 are detected and corrected. Hit rate and detection skill are better for Y2, but the RMSE and mean trend bias are better for Y1.

The skill of detection can also be characterized in other ways than with versions or combinations of hit rate and false alarm rate. Such indicators are the ratio of experiments in which the exact number of change-points are detected (*Caussinus* and *Mestre*, 2004; *Bealieu et al.* 2009; etc.), the mean squared temporal distance between true change-points and detected change-points (*Bealieu et al.*, 2008, 2009), and the ratio of correctly chosen models in the detection process (*Reeves et al.*, 2007). Their connection with the method performance is similar to that of hit rate, i.e. they serve useful information about the operation of homogenization methods, but they cannot be applied directly for characterizing efficiency. In connection with the model selection during detection process, it has to be noted that there is no evidence that the use of more complex or more flexible models in the detection process would result in higher efficiency than the use of step function. In reality, *Domonkos* (2011a) found just the opposite relation when he compared the performances of Multiple Linear Regression (MLR, *Vincent*, 1998) and the second version of SNHT (*Alexandersson* and *Moberg*, 1997) with detection methods applying always step function model, namely with Multiple Analysis of Series for Homogenization (MASH, *Szentimrey*, 1999) and PRODIGE (*Caussinus* and *Mestre*, 2004). The likely explanation is that the selection of model type and its parameters is problematic from noisy, finite, and inhomogeneous samples, like true observed climatic time series.

4. Kinds of efficiency tests

Efficiency tests can be sorted at least into two groups according to their goals. One type is for measuring the performance of complete homogenization procedures and another type is when a particular segment of homogenization procedures is tested only. Both types of tests are important: while the tests of complete procedures inform us about the practical appropriateness of a method, the separated investigation of segments helps to reveal the positive features and deficiencies of the methods, and thus it may give suggestions for further, methodological developments. In this section we define more than two kinds of tests, but we admit that the classification is partly subjective.

4.1. Tests for detection methods

We have mentioned in Section 3 that mostly the detection parts of homogenization methods are tested only, and it is often the case even when studies promise tests for entire homogenization procedures. This inexactness in the use of terms might arise from the fact that a particular detection method is often paired with indefinite characteristics in the other segments of the homogenization procedure (some examples were mentioned in Section 2.1), and thus, often only the detection part is common in the different versions of the method. Another possible explanation is that the detection segment might be expected to be the most influential part of homogenization procedure to the final efficiency. Note that the latter expectation is often not true, the comparison of efficiency results by *Venema et al.* (2012) and *Domonkos* (2011a) proves that the major error source is often in other segments of homogenization procedures than the detection part.

A seeming difficulty of finding the real effectiveness for detection methods is that hit rate, false alarm rate, and the characteristics that are derived from these two do not show the true efficiency accurately. On the other hand, the calculation of RMSE error needs the incorporation of the other segments of homogenization procedures. This problem can be solved with the application of standard procedures in all segments except for the detection part (*Domonkos*, 2011a). The idea is not new, since for calculating relative time series and shift magnitudes, standard procedures had been applied in earlier studies (*Ducré-Robitaille et al.*, 2003; *DeGaetano*, 2006). Recent examinations show that the most effective detection methods apply a relatively simple model, namely the step-function, and they select the most probable parameters of this model by the examination of all possible combination of change-point positions. Such detection segments are included in MASH, PRODIGE, Applied Caussinus-Mestre Algorithm for homogenizing Networks of Temperature series (ACMANT, *Domonkos*, 2011b), and HOMER (*Mestre et al.*, 2012). Note, however, that when the signal to noise ratio is small or when the frequency of change-points is very low, the advantage of the highlighted detection methods ceases.

4.2. Tests for specific segments others than the detection of inhomogeneities

There are three main kinds of time series comparisons: a) for each candidate series, building one reference series from composite series, b) using multiple reference comparisons for each candidate series, c) using multiple comparisons without defining which are the candidate and the reference. Their testing is problematic, because this segment contains subjective steps in many procedures. For fully objective procedures the testing would be straightforward with the inclusion of standardised detection and correction segments, but according to our knowledge such tests never have been done.

Objective correction methods can generally be tested applying the same logic as described for the testing of detection methods and time series comparisons. We know about one example of testing correction segment, i.e., the test of ANOVA (*Domonkos et al.*, 2012a). The testing of ANOVA is much easier than making any other segment-specific tests, because the input field of ANOVA is the list of change-point positions detected. Once such lists are available from different test experiments, there is no need of constructing test dataset, applying standard procedures for other segments than the target segment, etc. HOME provided the required lists from different homogenization procedures and homogenizers, and these data are freely available for the climatologist community. The tests showed that the application of ANOVA always results in improvement in the final results of homogenization. It means that the performance of any homogenization procedures (at least, which were participating in this test) could be improved with the inclusion of ANOVA. This finding is in accordance with the fact that ANOVA provides the optimal estimation of correction terms when the climate is uniform in the network and when the detected change-point positions are correct (*Caussinus* and *Mestre*, 2004). Considering the contemporary homogenization methods, PRODIGE, ACMANT and HOMER include ANOVA. Note that MASH was one of the most successful methods of HOME and although MASH does not include ANOVA, there was no experiment of adding ANOVA to MASH, because MASH did not produce a usable list of change-point positions.

4.3. Tests for complete homogenization procedures

Testing whole procedures might not seem to be more challenging than testing selected segments only: it needs the use of a reliable test dataset and the calculation of some efficiency measures. However, most procedures contain subjective steps, which make it difficult to produce objective comparative tests for wide range of homogenization methods.

The testing of fully automatic procedures is relatively easy: Running an automatic program is simple, and nowadays, the computational time is usually fairly short. The results are objective, impersonal, and they can be reconstructed at any time. Although the application of appropriate test dataset is a critical point of the methodology, the doubts and difficulties can be fairly treated by the use of some variety of test datasets (*McCarthy et al.*, 2008; *Titchner et al.*, 2009). Note that the same works also when detection segments are tested only (*Ducré-Robitaille et al.*, 2003; *Domonkos*, 2011a; etc.); moreover, tests with moving parameters of the test dataset may clarify the roles of selected dataset characteristics in the performance of the examined methods (*DeGaetano*, 2006). The easy application of tests for automatic methods favors their development, since large number of variants of the same homogenization procedure can be executed with relatively little effort. Tests with moving parameters of the examined method show the sensitivity of the performance to changes in its parameters (*Gruber* and *Haimberger*, 2008; *Domonkos*, 2008, 2012), while ensemble experiments with random selection of parameter sets indicate the general stability of method performance (*McCarthy et al.*, 2008; *Titchner et al.*, 2009; *Williams et al.*, 2012).

The main problem with testing subjective or partly subjective methods is that the evaluation might be affected from the known truth, both in the construction of test datasets and in the execution of tests. This influence can be unintentional, and it questions the objectivity of the test results. Further problems of subjective methods are that the test results are homogenizer dependent and usually cannot be reconstructed. Finally, the subjective homogenization of large datasets is sometimes very tiring, practically unmanageable.

One conclusion could be that the use of automatic homogenization procedures should be encouraged, because their performance is more easily controllable. However, even when automatic methods will be much better developed than at present, the best statistical homogenization will still need expert decisions at least in two cases: a) when the number of comparable time series or their spatial correlations are relatively low, b) in the use of certain kinds of metadata.

4.4. Blind tests

The most correct tool for the evaluation of homogenization procedures including subjective steps is the blind test, i.e., when homogenizers do not know the properties of the test series. Naturally, automatic methods may also be incorporated in such tests, and thus, the performances of various homogenization methods are objectively comparable. An appropriate test dataset is not only blind for homogenizers, but also realistic, which means that its properties are similar to the general properties (or at least to the properties of certain kinds) of true data in observational networks and time series. The development of such comparative tests needs wide cooperation of dataset developers, method developers, and homogenizers. In the blind tests of HOME in homogenizing the benchmark, large number of researchers worked together, and thus, HOME substantially improved our knowledge about the performances of homogenization methods. The results are particularly valuable in the homogenization of monthly and annual surface temperature data and in the homogenization of precipitation totals. The HOME tests proved that a) among objective and semi-objective methods the most sophisticated ones based on simple model structure, provide the best performance, namely MASH, PRODIGE, and ACMANT; b) the predominantly subjective homogenization with Craddock-test (*Craddock*, 1979) can compete with any objective method considering the mean performance, but not in the amount of accomplished tasks. Another important finding was that the United States Historical Climate Network homogenization (USHCN, *Menne* and *Williams*, 2009) produced the lowest rate of unnecessary adjustments, while its general performance was only slightly lower than the other best methods. The other methods participated in the HOME tests had significantly poorer performance than MASH, PRODIGE, ACMANT, Craddock and USHCN, therefore, in the final conclusions of *Venema et al.* (2012), these five methods are recommended for practical use. Note that the recently developed

HOMER likely has at least as good performance as the highlighted five, because HOMER adapts the best segments of PRODIGE and ACMANT and applies them in a sophisticated way. Note also that in specific tasks, the enhanced methods do not always show the best performance, e.g. in the example of *Fig. 1* (detection skill for one large shift) the early version of SNHT and PMT perform best.

Naturally, one set of blind tests as it was done under HOME could not answer all questions related to effective homogenization, because the kinds of homogenization tasks are diverse and not restricted to the homogenization of monthly surface temperature and precipitation data. The tasks ahead for the method developers will be discussed in Section 6.

5. Datasets for efficiency examinations

The numerical results of efficiency tests are most meaningful when they are based on the full understanding of the homogenization problem and the nature of inhomogeneities in the climate data, therefore, the use of test datasets of realistic properties is essential. In this section we deal with the construction, selection, and application of appropriate datasets for testing efficiencies. The appropriateness largely depends on the type of the homogenization task, but here some general aspects will be discussed only. In the first part of this section, some general problems of creating realistic test datasets and the properties of benchmark are discussed. In the second part, some examples are shown in which the test datasets do not contain simulated data.

5.1. Datasets of simulated time series

The simulation of time series for surface climatic variables is based on the constructors' knowledge of climatic and non-climatic properties of observed time series. By contrast, in the simulation of upper air data, general circulation models (GCM) are used, since GCM products provide more reliable data for the upper air conditions than for the surface climate. Both ways of dataset construction have advantages and weak points.

It is obvious that the more similar the test dataset to the real observational data, the more reliable conclusions can be drawn from its use. The problem is that we do not know exactly the properties of observed datasets. The last statement might sound strange, because thousands of studies have been devoted to examine and quantify the climatic and non-climatic characteristics (trends, low- and high-frequency variability, change-points, etc.) of observed data. However, the problem is not with the possible lack of scrutiny, but with the nature of data. In nature, magnitudes of inhomogeneities can be either small or relatively large, and it seems to be a realistic approach that their distribution is normal with 0 mean (*Menne* and *Williams*, 2005; *Venema et al.*, 2012). However, small inhomogeneities cannot be detected (*Fig. 3*). The ratio of detected biases is particularly low for small and medium-size platform-shaped biases, i.e. when the duration of biases is limited (*Fig. 3b*). *Fig. 3* proves that the detection results of homogenization procedures do not provide realistic information neither about the rate of very small biases, nor about the rate of platform-shaped biases.

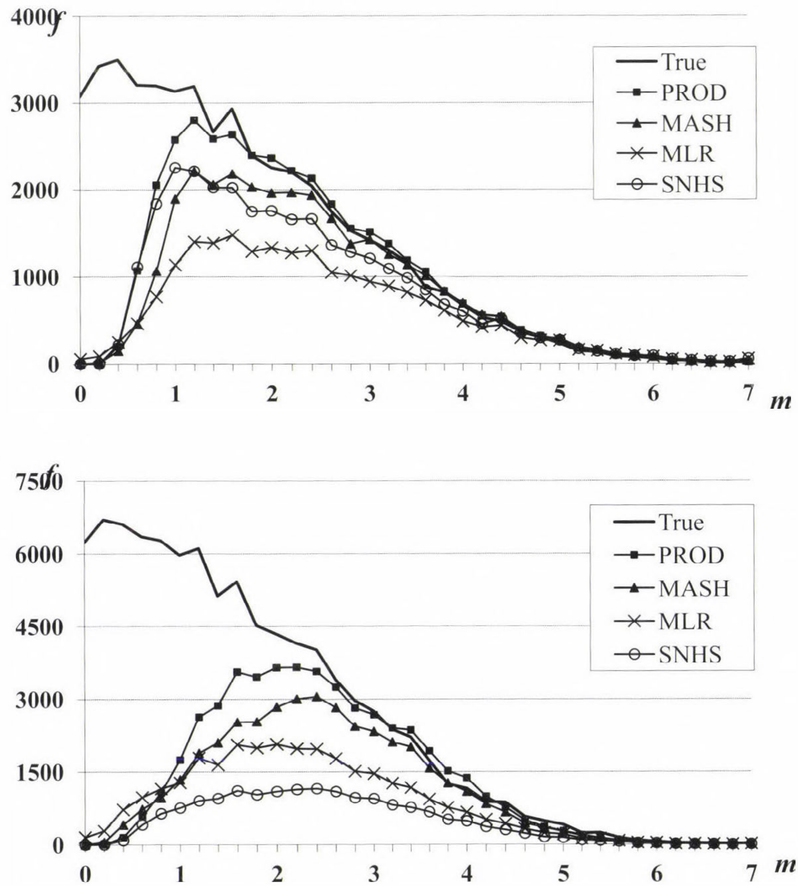

Fig. 3. Frequency (*f*) of detected change-points as a function of shift-magnitudes (*m*), when 5 shifts with random positions (top panel) and 5 platforms (pair of shifts with the same *m* and opposite directions, bottom panel) with random positions are inserted into 100 years long white noise process. The duration of platforms is evenly distributed between 1 and 10 year. *m* is shown in the ratio to the standard deviation of the background noise, while the unit of *f* is arbitrary.

Domonkos (2011a) presented an experiment in which the detection results for true and simulated observational datasets were empirically approached for large number of detection methods and surprisingly high rate of platforms, especially platforms of short duration was reported for the best approach achieved. However, the direct application of that structure of inhomogeneities for construction of test datasets is not recommended, because i) the results are valid for a specific temperature dataset (of Hungary), ii) small, persistent anomalies of short duration in the spatial gradients of a climatic variable may be components of the true climate, even when data of the same climatic region is examined, so that platform-like biases of relative time series may have climatic origin, iii) the mode of generating reference series applied by *Domonkos* (2011a) might have contributed to the amount of apparent small biases for the candidate series. In spite of the uncertainties related to the lately described experiment, it is very likely that the amount of short-term platform-shaped biases in observational time series is much larger than that exists in a simulated test dataset with randomly positioned shifts. This thesis also has non-statistical reasoning: a non-climatic shift and/or its technical cause is often realized after some periods have passed and thereafter, the bias does not appear in the time series, due to the elimination of the technical problem (see also *Rienzner* and *Gandolfi*, 2011; *Domonkos*, 2011a). However, with resetting the technical conditions, observed data are usually not corrected backwards, and even if they are corrected, they might still have systematic bias. We think that the described phenomenon and its consequences on time series properties are general for all observed climatic variables, although the frequency and intensity of platform-shaped biases as well as their impact on the quality of observed time series may substantially differ. Note that the test datasets generated by *Domonkos* (2008, 2011a; etc.) directly mimic relative time series instead of generating raw time series and their differences. This simplification is allowed only when detection segments are tested.

The properties of test datasets may have crucial impact on the observed efficiencies in test experiments (*Caussinus* and *Mestre*, 2004; *Titchner et al.*, 2009; *Domonkos*, 2011a; etc.). Unfortunately, the test dataset properties are often far from the real world in climatological studies, even sometimes the natural spread of shift-magnitudes is missing. In HOME, the benchmark was constructed in a way that it includes realistic climatic signal, the statistical momentums, spatial correlations, and low frequency fluctuations mimic the natural variability of surface temperature and precipitation data in Europe (*Venema et al.*, 2012). The statistical characteristics of inhomogeneities were established with expert decisions of some HOME participants, thus, the frequency and magnitude distributions of biases are likely realistic. However, the frequency of platform-shaped biases in the benchmark is lower than what would follow from the arguments of *Rienzner* and

Gandolfi (2011) and *Domonkos* (2011a). We emphasise that the necessity of inclusion of realistic amount of small biases and platform-shaped biases in test datasets is not because we should be able to detect such inhomogeneities, but because they influence the detection results for the larger and more persistent biases, as it is illustrated in *Fig. 1*.

5.2. Test datasets composed of real data

It was mentioned that the true positions and magnitudes of non-climatic shifts are not exactly known in real observed time series, therefore, efficiency tests usually need the use of simulated datasets. However, under specific conditions, there are some other options for testing efficiencies. The performance of an automatic homogenization method can be tested against a good quality real dataset that has been homogenized with a dense network and/or metadata (*Begert et al.*, 2008). The use of satellite data in the validation of radiosonde data homogenization method has been reported by *Sherwood et al.* (2008), although it must be noted that the homogeneity of satellite data is doubtful due to small temporal biases and calibration problems (*Mears et al.*, 2003). Metadata can be valuable either in the accomplishment or in the validation of homogenization procedures (*Auer et al.*, 2005; *Brunet et al.*, 2006; *Sherwood et al.*, 2008; etc.). Note, however, that sizes of non-climatic biases cannot be quantified from metadata, with few exceptions. This fact reduces the usability of metadata in making quantitative evaluations. Finally, we mention that in testing ANOVA, lists of the timings of detected change-points have been used as test datasets (*Domonkos et al.*, 2012a and Section 4.2. of this study).

6. Tasks for the future

The HOME blind test experiments showed that the differences between the efficiencies of homogenization methods are larger than that was thought earlier when detection parts were examined only. Although most efficiencies obtained in the HOME experiments are positive, some results show the opposite. Consequently, the impact of statistical homogenization on the final quality of observed climatic datasets is often significantly positive, but sometimes nearly neutral or negative. The success depends on the signal to noise ratio (*Ducré-Robitaille et al.*, 2003; *Caussinus* and *Mestre*, 2004; *DeGaetano*, 2006; etc.) and the homogenization method applied (*Venema et al.*, 2012). The blind tests of HOME have brought a large number of valuable new results. Supplying the test results with the details of the historical methodological development of homogenization methods (*Domonkos et al.*, 2012b), our knowledge has become more complete about some fundamental rules of homogenization. Yet, there are still a large number of open questions that indicate the tasks ahead the developers of homogenization methods.

- We have limited knowledge about the method performances when the signal to noise ratio is not high. HOME results showed the best resistance for USHCN against applying spurious adjustments, but, on the other hand, certain segments of USHCN are suboptimal. These two facts together show that we have not found yet the most appropriate method for treating the cases of moderate signal to noise ratio.
- In HOME, only surface temperature data and precipitation total data were homogenized, and even for these two variables, daily scale homogenization was not included apart from some sporadic examinations.
- Several widely used methods were not tested by HOME, e.g., MLR, the method of *Easterling* and *Peterson* (1995), the family of Bayes methods (*Perreault et al.*, 2000a,b), etc. Most of them have similar statistical structures to the tested methods, therefore, the appearance of substantially new, highly efficient homogenization methods is not envisaged at present. However, some of the methods which were found to be the best in the HOME tests are still under development. ACMANT and Climatol (www.climatol.eu) have newer versions than that were tested in HOME, and the availability of a fully automated MASH version has been reported (www.homogenization.org). HOMER has been developed after the HOME experiments, thus it had not been subjected to the blind tests of HOME. There are promising experiments with developing the detection segment of PRODIGE and HOMER to a network-wide joint segmentation algorithm (*Picard et al.*, 2011). The strategy of USHCN against applying unnecessary adjustments should likely be combined with segments of other homogenization methods of better general performance.

New blind test experiments could produce the largest amount of new and objective information about the performance of homogenization methods. However, blind test experiments such that accomplished under HOME are not economic in costing time, money, and human effort. Perhaps an alternative could be producing an automatic version for each promising homogenization method with subjective steps in a way that default options would be included in them at steps that may incorporate subjective decisions. Its advantage would be that with tests for the automated versions one could easily filter the possible false expectations and common software errors. The weak point of this idea is that it is a challenge to find relatively simple but intelligent defaults (otherwise, there would no need to subjective steps). Note that at present, the International Surface Temperature Initiative works on developing a benchmark dataset for surface temperature data of all over the world (www.surfacetemperatures.org).

Testing automatic methods is much simpler and more productive than organizing and performing blind tests. On the other hand, the development of homogenization methods is worth some investment. The observed climatic datasets is of huge value to the human society. This value has been accumulated during decades and centuries. The costs of gaining as-optimal-as-possible climatic information from the data via their homogenization are much lower than the costs of many other steps in producing and archiving reliable climatic data.

Acknowledgements–The research was supported by the projects COST ES0601 and EURO4M FP7-SPACE-2009-1/242093. The author thank Constanta Boroneant and Dimitrios Efthymiadis for their contribution to finding the final form of the paper.

References

Aguilar, E., Auer, I., Brunet, M., Peterson, T.C., and *Wieringa, J.*, 2003: WMO Guidelines on climate metadata and homogenization. WCDMP-No. 53, WMO-TD.No:1186, WMO, Geneva.

Alexandersson, H. and *Moberg, A.*, 1997: Homogenization of Swedish temperature data. Part I: Homogeneity test for linear trends, *Int. J. Climatol. 17*, 25–34.

Auer, I., Böhm, R., Jurković, A., Orlik, A., Potzmann, R., Schöner, W., Ungersböck, M., Brunetti, M., Nanni, T., Maugeri, M., Briffa, K., Jones, P., Efthymiadis, D., Mestre, O., Moisselin, J.- M., Begert, M., Brazdil, R., Bochnicek, O., Cegnar, T., Gajić-Čapka, M., Zaninović, K., Majstorović, Ž., Szalai, S., Szentimrey, T., and Mercalli, L., 2005: A new instrumental precipitation dataset for the greater Alpine region for the period 1800–2002. *Int. J. Climatol. 25*, 139–166.

Beaulieu, C., Seidou, O., Ouarda, T.B.M.J., Zhang, X., Boulet, G., and *Yagouti, A.*, 2008: Intercomparison of homogenization techniques for precipitation data. *Water Resour. Res. 44*, W02425.

Beaulieu, C., Seidou, O., Ouarda, T.B.M.J. and *Zhang, X.*, 2009: Intercomparison of homogenization techniques for precipitation data continued: Comparison of two recent Bayesian change point models. *Water Resour. Res. 45*, W08410, pp15.

Begert, M., Zenklusen, E., Häberli, C., Appenzeller, C., and *Klok, L.*, 2008: An automated procedure to detect discontinuities; performance assessment and application to a large European climate data set. *Meteorol. Z. 17*, 663–672.

Brunet, M., Saladié, O., Jones, P., Sigró, J., Aguilar, E., Moberg, A., Lister, D., Walther, A., Lopez, D., and *Almarza, C.*, 2006: The development of a new dataset of Spanish daily adjusted temperature series (SDATS) (1850–2003). *Int. J. Climatol. 26*, 1777–1802.

Buishand, T.A., 1982: Some methods for testing the homogeneity of rainfall records. *J. Hydrology 58*, 11–27.

Caussinus, H. and *Mestre, O.*, 2004: Detection and correction of artificial shifts in climate series, *J. Roy. Stat. Soc. Series C53*, 405–425.

Craddock, J.M., 1979: Methods of comparing annual rainfall records for climatic purposes, *Weather 34*, 332–346.

Dai, A., Wang, J., Thorne, P.W., Parker, D.E., Haimberger, L., and *Wang, X.L.*, 2011: A new approach to homogenize daily radiosonde humidity data. *J. Climate 24*, 965–991.

DeGaetano, A.T., 2006: Attributes of several methods for detecting discontinuities in mean temperature series. *J. Climate 19*, 838–853.
Domonkos, P., 2008: Testing of homogenization methods: purposes, tools and problems of implementation. In *Proceedings of the 5th Seminar and Quality Control in Climatological Databases*, WCDMP-No. 71, WMO-TD 1493, WMO, Geneva, 126–145.
Domonkos, P., 2011a: Efficiency evaluation for detecting inhomogeneities by objective homogenization methods, *Theor. Appl. Climatol. 105*, 455–467.
Domonkos, P., 2011b: Adapted Caussinus-Mestre Algorithm for Networks of Temperature series (ACMANT). *Int. J. Geosci. 2*, 293–309.
Domonkos, P., 2012: ACMANT: Why is it efficient? In *Proceedings of the 7th Seminar and Quality Control in Climatological Databases*. WMO-HMS, www.c3.urv.cat/publicacions/publicacions2012.html
Domonkos, P., Venema, V. and *Mestre, O.*, 2012a: Efficiencies of homogenization methods: our present knowledge and its limitation. In *Proceedings of the 7th Seminar for Homogenization and Quality Control in Climatological Databases* in press, www.c3.urv.cat/publicacions/publicacions2012.html
Domonkos, P., Venema, V., Auer, I., Mestre, O. and *Brunetti, M.*, 2012b: The historical pathway towards more accurate homogenization. *Adv. Sci. Res. 8*, 45–52.
Ducré-Robitaille, J-F., Vincent, L.A. and *Boulet, G.*, 2003: Comparison of techniques for detection of discontinuities in temperature series. *Int. J. Climatol. 23*, 1087–1101.
Easterling, D.R. and *Peterson, T.C.*, 1995: A new method for detecting undocumented discontinuities in climatological time series. *Int. J. Climatol. 15*, 369–377.
Gérard-Marchant, P.G.F., Stooksbury, D.E. and *Seymour, L.*, 2008: Methods for starting the detection of undocumented multiple changepoints. *J. Climate 21*, 4887–4899.
Gruber, C. and *Haimberger, L.*, 2008: On the homogeneity of radiosonde wind time series. *Meteorol. Z. 17*, 631–643.
Haimberger, L., 2007: Homogenization of radiosonde temperature time series using innovation statistics. *J. Climate 20*, 1377–1403.
Lanzante, J.R., Klein, S.A. and *Seidel, D.J.*, 2003: Temporal homogenization of monthly radiosonde temperature data. Part I: Methodology. *J. Climate 16*, 224–240.
McCarthy, M.P., Titchner, H.A., Thorne, P.W., Tett, S.F.B., Haimberger, L., and *Parker, D.E.*, 2008: Assessing bias and uncertainty in the HadAT adjusted radiosonde climate record. *J. Climate 21*, 817–832.
Mears, C.A., Schabel, M.C. and *Wentz, F.J.*, 2003: A reanalysis of the MSU channel 2
tropospheric temperature record. *J. Climate, 16*, 3650-3664.
Menne, M.J. and *Williams Jr., C.N.*, 2005: Detection of undocumented changepoints using multiple test statistics and composite reference series. *J. Climate 18*, 4271–4286.
Menne, M.J. and *Williams Jr., C.N.*, 2009: Homogenization of temperature series via pairwise comparisons. *J. Climate, 22*, 1700–1717.
Mestre, O., Domonkos, P., Picard, F., Auer, I., Robin, S., Lebarbier, E., Böhm, R., Aguilar, E., Guijarro, J., Vertacnik, G., Klancar, M., Dubuisson, B., and *Stepanek, P.* 2013: HOMER: homogenization software in R – methods and applications, *Időjárás 117*, 47–67.
Moberg, A. and *Alexandersson, H.*, 1997: Homogenization of Swedish temperature data. Part II: Homogenized gridded air temperature compared with a subset of global gridded air temperature since 1861. *Int. J. Climatol. 17*, 35–54.
Perreault, L., Bernier, J., Bobée, B., and *Parent, E.* 2000a: Bayesian change-point analysis in hydrometeorological time series. Part 1. The normal model revisited. *J. Hydrology 235*, 221–241.
Perreault, L., Bernier, J., Bobée, B., and *Parent, E.* 2000b: Bayesian change-point analysis in hydrometeorological time series. Part 2. Comparison of chage-point models and forecasting. *J. Hydrology 235*, 242–263.

Picard, F., Lebarbier, E., Hoebeke, M., Rigaill, G., Thiam, B., and *Robin, S.*, 2011: Joint segmentation, calling and normalization of multiple CGH profiles. *Biostatistics 12*, 413–428.

Reeves, J., Chen, J., Wang, X.L., Lund, R. and *Lu, X.*, 2007: A review and comparison of change-point detection techniques for climate data. *J. Appl. Meteor. Climatol. 46*, 900–915.

Rienzner, M. and *Gandolfi, C.*, 2011: A composite statistical method for the detection of multiple undocumented abrupt changes in the mean value within a time series. *Int. J. Climatol. 31*, 742–755.

Sherwood, S.C., Meyer, C.L., Allen, R.J., and *Titchner, H.A.*, 2008: Robust tropospheric warming revealed by iteratively homogenized radiosonde data. *J. Climate 21*, 5336–5352.

Szentimrey, T., 1999: Multiple Analysis of Series for Homogenization (MASH). In *Second Seminar for Homogenization of Surface Climatological Data (Eds.: Szalai, S., Szentimrey, T. and Szinell, Cs.) WCDMP 41, WMO-TD 962*, WMO, Geneva, 27–46.

Titchner, H.A., Thorne, P.W., McCarthy, M.P., Tett, S.F.B., Haimberger, L., and *Parker, D.E.*, 2009: Critically reassessing tropospheric temperature trends from radiosondes using realistic validation experiments. *J. Climate 22*, 465–485.

Toreti, A., Kuglitsch, F.G., Xoplaki, E., and *Luterbacher, J.*, 2012: A novel approach for the detection of inhomogeneities affecting climate time series. *J. Appl. Meteor. Climatol. 51*, 317–326.

Venema, V., Mestre, O., Aguilar, E., Auer, I., Guijarro, J.A., Domonkos, P., Vertacnik, G., Szentimrey, T., Stepanek, P., Zahradnicek, P., Viarre, J., Müller-Westermeier, G. Lakatos, M., Williams, C.N., Menne, M., Lindau, R., Rasol, D., Rustemeier, E., Kolokythas, K., Marinova, T., Andresen, L., Acquaotta, F., Fratianni, S., Cheval, S., Klancar, M., Brunetti, M., Gruber, C., Duran, M.P., Likso, T., Esteban, P., and *Brandsma, T.*, 2012: Benchmarking monthly homogenization algorithms. *Climate of the Past 8*, 89–115.

Vincent, L.A., 1998: A technique for the identification of inhomogeneities in Canadian temperature series. *J. Climate 11*, 1094–1104.

Williams, C.N., Menne, M.J. and *Thorne, P.W.*, 2012: Benchmarking the performance of pairwise homogenization of surface temperatures in the United States. *J. Geoph. Res. Atmos. 117, D5.*

IDŐJÁRÁS

Quarterly Journal of the Hungarian Meteorological Service
Vol. 117, No. 1, January–March 2013, pp. 113-

Theoretical questions of daily data homogenization

Tamás Szentimrey

Hungarian Meteorological Service,
P.O. Box 38, H-1525 Budapest, Hungary
E-mail: szentimrey.t@met.hu

(Manuscript received in final form December 10, 2012)

Abstract—The so-called variable correction methods form a special type of methods developed for daily data homogenization. Their common assumption is that in case of daily data series, the corrections for inhomogeneity have to vary according to the meteorological situation of each day in order to represent the extremes. In this paper we express our objections to these variable correction methods, especially to their underlying principles. Since the exact theoretical mathematical formulation of the question of daily data homogenization is generally neglected, we also try to formulate and analyze this problem in accordance with mathematical conventions.

Key-words: daily data series, homogenization, climate extremes, higher-order moments, distribution, mathematical formulation

1. Introduction

During the last years, the interest to the daily data series homogenization has increased dramatically. The main reason of this tendency is that daily data are essential for studying extremes of weather and climate, for example, computing extreme climate indices requires reliable daily data series. However, according to numerous climatologists homogenization of daily data is still in its infancy and is much more difficult problem than homogenization at monthly or annual scales. The essence of this argumentation is that the correction in mean is sufficient for monthly and annual series, but in case of daily data series, the corrections should vary according to the meteorological situation of each day in order to represent the extremes. This idea was published in the paper by *Trewin* and *Trevitt* (1996), where parallel measurements were examined and compared to each other. Since then on the basis of the ideas formulated in the paper, a number of variable correction methods have been developed with the declared aim of being capable of correcting the daily data not only in mean (first moment) but also in the higher order moments. For example, we mention the following methods: higher order moments (HOM) method by *Della-Marta* and *Wanner* (2006) and spline daily homogenization (SPLIDHOM) method by *Mestre et al.* (2011), and there are numerous other similar methods applied in practice. But unfortunately, in this paper we have to make a criticism about these variable correction methods, especially about their underlying principles. In our humble opinion, during the examinations only some physical experiences were considered without any exact theoretical, mathematical formulation of the problem. The empiric interpretation and formulation seem to be a misunderstanding. Moreover, there are some mathematical statements at the description of the methods – e. g., capability to correct the higher order moments – but without any proof, and this practice is of course contrary to the mathematical conventions.

2. Examination of parallel measurements

2.1. Examinations by Trewin and *Trevitt (1996)*

First here is a quotation from the paper of *Della-Marta* and *Wanner* (2006): "One of the most robust methods capable of adjusting the higher-order moments of daily temperature data is that of *Trewin* and *Trevitt* (1996)." *Trewin* and *Trevitt* (1996) intended to homogenize daily data series in order to create composite temperature records. The following sentences are from their paper: "It is therefore necessary to make use of climatological records with inhomogeneities, and to develop a means of removing or minimizing the impact of inhomogeneities on these records. One way of doing this is by adjusting all parts of a record to be comparable with some 'reference period'. Standard procedures for such adjustments in mean temperatures have relied on the implicit assumption that, if two neighbouring stations both have homogeneous records over some period of time, the difference in daily maximum (or minimum) temperature between them will be a constant for any day in a given month of the year. This implies that the difference in monthly means will be a constant for that month from year to year." In general it is not true of course, but after some examination of real station data series they obtained the following result: "This is observed at Armidale (P. Burr, pers. comm.), ..,where the difference in minimum temperature between the town centre site used in this study and a second site approximately 2 km to the east, in the outer part of the town, has a mean value of 1.5 to 2 °C , but can increase to 4 °C on cold, clear nights. The assumption that the temperature difference between any two nearby sites is always constant must therefore be questioned."

The above conclusion was all right, but the next conclusion is a little bit surprising for us: "The relationship between the temperature characteristics of the two sites in each pair was examined, with the aim of determining an appropriate method for use in extrapolating records at one site to records at the other."

Probably here is the origin of the methods that apply varying corrections per days, and at this step a regression or interpolation problem was obtained for homogenization instead of the adequate distribution problem. Three interpolation techniques were considered by *Trewin* and *Trevitt* (1996) namely: the 'traditional' constant-difference approach, the 'regression' method, and the frequency distribution matching. The methods will be detailed in Section 4.1.

2.2. *Mathematical examinations of parallel measurements*

What was the reason of the development of the variable correction methods? Essentially, an observed phenomenon at the extremes, namely the differences of parallel measurements are larger in case of extremes. In our opinion, this observed phenomenon has a simple and logical reason, and it is superfluous to look for some complicated physical explanation for the inhomogeneity. The simple reason is that the extremes may be expected at different moments in case of parallel measurements, or in other words, there may be systematic biases in rank order! It is a natural phenomenon, and for illustration a trivial example is presented according to the probability theory.

Example 2.2

Let $Y_1(t) \in N(0,1)$, $Y_2(t) \in N(0,1)$ $(t = 1,2,..,n)$ be standard normally distributed series with expected values $\mathrm{E}(Y_1(t)) = \mathrm{E}(Y_2(t)) = 0$, with standard deviations $\mathrm{D}(Y_1(t)) = \mathrm{D}(Y_2(t)) = 1$, and with correlation between the series $\mathrm{corr}(Y_1(t), Y_2(t)) = \rho$ $(t = 1,2,..,n)$.

Then the mean difference $\mathrm{E}(Y_1(t) - Y_2(t)) = 0$ of course, however, the difference $Y_1(t) - Y_2(t)$ is not independent from the elements $Y_1(t)$, $Y_2(t)$ if $\rho \neq 1$, and, e.g., the conditional expectation of difference $Y_1(t) - Y_2(t)$ given $Y_1(t)$, or equivalently the regression of difference $Y_1(t) - Y_2(t)$ on $Y_1(t)$ is $\mathrm{E}(Y_1(t) - Y_2(t) | Y_1(t)) = (1 - \rho) \cdot Y_1(t)$.

Consequently, the difference $Y_1(t) - Y_2(t)$ is an expectedly monotonous increasing function of $Y_1(t)$ if $\rho \neq 1$. This is the theory, but it can be demonstrated in practice too. We generated such standard normal series by the Monte Carlo method with parameters $\rho = 0.9$, $n = 1000$. In this case,

$E(Y_1(t) - Y_2(t) | Y_1(t)) = 0.1 \cdot Y_1(t)$ and the difference series $Y_1(t) - Y_2(t)$ as a function of series $Y_1(t)$ is plotted in *Fig. 1*.

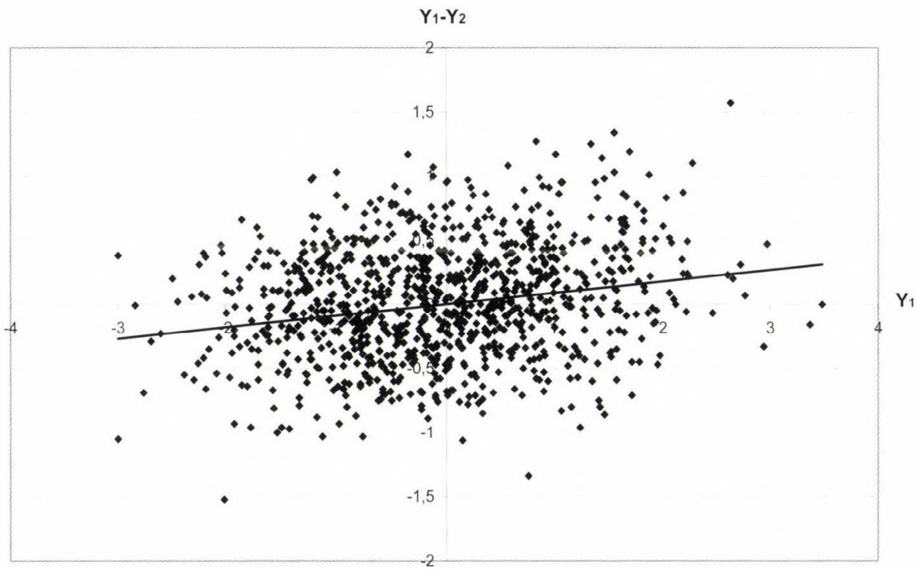

Fig. 1. Difference series $Y_1(t) - Y_2(t)$ as a function of series $Y_1(t)$

It is evident that the conditional expectation of difference $Y_1(t) - Y_2(t)$ is monotonous increasing function of $Y_1(t)$, consequently the difference may be larger mainly in the case of extreme values. It is a general phenomenon not only observed for meteorological measurements. Presumably this experience is the reason for the idea that the correction of daily data should vary according to the meteorological situation of each day, in particular on the basis of some regression models. But it is a misunderstanding of the homogenization problem.

3. Mathematical formulation of the daily data homogenization

Unfortunately, the exact theoretical, mathematical formulation of the problem of homogenization is generally neglected in meteorological studies. Therefore, we try to formulate this problem in accordance with mathematical conventions. First of all it is necessary to emphasize that homogenization is a distribution problem and not a regression one.

Notation

Let us assume we have daily data series:
$Y_1(t)$ $(t=1,2,..,n)$: candidate time series of the new observing system.
$Y_2(t)$ $(t=1,2,..,n)$: candidate time series of the old observing system.
$1 \leq T < n$: change-point, series $Y_2(t)$ $(t=1,2,..,T)$ can be used before and series $Y_1(t)$ $(t=T+1,..,n)$ can be used after the change-point.

Definition

The aim of homogenization is the adjustment or correction of values $Y_2(t)$ $(t=1,2,..,T)$ in order to have the corrected values $Y_{1,2h}(t)$ $(t=1,2,..,T)$ with the same distribution as the elements of series $Y_1(t)$ $(t=1,2,..,T)$, i.e.:

$$\mathrm{P}(Y_{1,2h}(t)<y)=\mathrm{P}(Y_1(t)<y), \quad y \in (-\infty,\infty)\ ,\ t=1,2,..,T\ . \tag{1}$$

Eq. (1) means the equality in distribution: $Y_{1,2h}(t) \stackrel{d}{=} Y_1(t)$ $(t=1,2,..,T)$.

Consequence

Within the same climate area, if the variables $Y_1(t), Y_2(t)$ $(t=1,2,..,T)$ have identical distribution, i.e., $Y_2(t) \stackrel{d}{=} Y_1(t)$ $(t=1,2,..,T)$, then the merged series $Y_2(t)$ $(t=1,2,..,T)$, $Y_1(t)$ $(t=T+1,..,n)$ is homogeneous.

Example

Let us assume we have parallel measurements $Y_1(t)$, $Y_2(t)$ $(t=1,2,..,n)$ within the same climate area with distance 50 m between the locations. Then, as a consequence of micrometeorological processes, the series are probably different, $Y_2(t) \neq Y_1(t)$ $(t=1,2,..,n)$, but they may be equal in distribution, $Y_2(t) \stackrel{d}{=} Y_1(t)$ $(t=1,2,..,n)$. In this case, the mixed series $Y_2(t)$ $(t=1,2,..,T)$, $Y_1(t)$ $(t=T+1,..,n)$ can be taken as a homogeneous series. This mixed series is equivalent with the homogeneous series $Y_1(t)$ $(t=1,2,..,n)$ also in respect of the distribution of extremes.

Returning to the general question, we have to see clearly that the aim of homogenization is to correct the distribution of $Y_2(t)$ according to $Y_1(t)$, instead of the estimation or regression of $Y_1(t)$ on $Y_2(t)$! Moreover, the correction of distribution is equivalent in essence with the correction or adjustment of the moments. The aim of the homogenization expressed in k^{th} moments:

$$m_k = \mathrm{E}\left((Y_{1,2h}(t))^k\right) = \mathrm{E}\left((Y_1(t))^k\right) \quad k = 1,2,\ldots\ ;\ t = 1,2,\ldots,T\ , \tag{2}$$

where E is the usual notation of the expected value or mean equivalently. Some remarkable formulas for the moments:

$$E = m_1,\ \ D^2 = m_2 - m_1^2 \tag{3}$$

where E denotes the expected value or mean, and D denotes the standard deviation.

In practice, numerous methods indicate the capability to correct the higher order moments but without any exact proof.

4. The variable correction methods

We return to the methods suggested by *Trewin* and *Trevitt* (1996) which was mentioned in Section 2.1. Essentially, the underlying principles of the variable correction procedures developed later were formulated based on these methods. We do not agree with these principles as explained by our argument in Sections 2.1 and 3, but let us see some details and properties of the mathematical consequences.

4.1. The Trewin and Trevitt (1996) methods for parallel measurements

The short description is cited word for word again from the paper of *Della-Marta* and *Wanner* (2006):

"Trewin and Trevitt (1996) present three different methods to build a composite daily temperature series. Essential to the methods is the existence of simultaneous (in time) observations from the *new* and *old* observing system. These parallel measurements had been taken based on the recommendations of Karl et al. (1995), who suggest that a minimum of a 2-yr overlap between the new and old observing systems be made. In Australia, for example, this practice has only become routine since around 1993 and so many inhomogeneities needed to be adjusted using the traditional constant difference techniques with neighboring reference stations. In this way, Trewin (2001) created a homogenized daily temperature dataset that has subsequently been used by Collins et al. (2000) to assess trends in the frequency of extreme temperature events in Australia.

The three methods they intercompared were constant difference, linear regression, and frequency distribution matching.

The constant difference approach simply adjusted the older data with the newer data using the mean of the daily differences in the simultaneous (parallel) measurements.

The linear regression method fitted a linear model to the difference in daily simultaneous measurements between the two observing systems and the temperature at the older station. This model could then be used to adjust daily temperatures at the older station differentially depending on the temperature, thereby adjusting the higher-order moments.

Their third method determines the frequency distribution of each site during the simultaneous measurement period. The adjustment for each desired percentile is calculated simply as the difference between the two percentiles. This method assumes that there is no systematic bias in the rank order of the temperatures at the two sites.

They show that both the regression method and the frequency distribution matching technique have certain advantages; however, if the homogenization of extreme events is most needed, then their frequency distribution matching technique is more accurate."

Our mathematical comments to the methods are as follows.

4.1.1. Constant difference approach

Yes, this approach is correct if the inhomogeneity is in mean or expected value or first moment, which are the same with different names.

4.1.2. Linear regression method

This procedure is absolutely wrong for homogenization. To demonstrate the problem, a trivial counter-example is presented.

Theorem

Let us assume that the different series $Y_1(t)$, $Y_2(t)$ $(t=1,2,..,n)$ have identical distribution, with expected values $\mathrm{E}(Y_1(t))=\mathrm{E}(Y_2(t))=0$, standard deviations $\mathrm{D}(Y_1(t))=\mathrm{D}(Y_2(t))=1$, and correlation between the series $\mathrm{corr}(Y_1(t),Y_2(t))=\rho$ $(t=1,2,..,n)$.

(i) Then the linear regression of difference $Y_1(t)-Y_2(t)$ on $Y_2(t)$ is $(\rho-1)\cdot Y_2(t)$, consequently, the homogenized series after the suggested adjustment, $Y_{1,2h}(t)=Y_2(t)+(\rho-1)\cdot Y_2(t)=\rho\cdot Y_2(t)$ and $\rho\cdot Y_2(t)$ is just the linear regression of $Y_1(t)$ on $Y_2(t)$.

(ii) Moreover, since the expected values $\mathrm{E}(Y_{1,2h}(t))=\mathrm{E}(Y_1(t))=\mathrm{E}(Y_2(t))=0$, therefore – using Eq. (3) – , the second moment of $Y_{1,2h}(t)$ is equal to the variance $\mathrm{D}^2(Y_{1,2h}(t))=\delta^2<1$, while the common second moment of $Y_1(t)$,

$Y_2(t)$ is equal to the variances $D^2(Y_1(t)) = D^2(Y_2(t)) = 1$. Therefore, the second moment was decreased from 1 to $\delta^2 < 1$ during the regression.

Summing up, according to (i) this procedure is equivalent with the simple linear regression of $Y_1(t)$ on $Y_2(t)$. Furthermore, according to (ii) the following statement about the method is absolutely false: "This model could then be used to adjust daily temperatures at the older station differentially depending on the temperature, thereby adjusting the higher-order moments." The truth is just the opposite, since the correct second moment was damaged at our counter-example.

4.1.3. Frequency distribution matching technique

The main problem is the following assumption which is the fundament of the method: "This method assumes that there is no systematic bias in the rank order of the temperatures at the two sites."

Unfortunately, the reality and the mathematics are much more complicated, and the above assumption cannot be accepted as it is demonstrated in *Fig. 1.* The bias in rank order depends on the stochastic connection, and there may be systematic bias, since $Y_1(t)$, $Y_2(t)$ are not monotonous increasing functions of each others. At this method, the adjusted $Y_{1,2h}(t)$ is obtained essentially by a simple exchange $Y_2(t)$ for $Y_1(t)$ according to the rank orders. Why? For example, if $Y_1(t)$, $Y_2(t)$ were equal in distribution then such an exchange would not be necessary.

4.2. The general type of variable correction methods applied in the practice

On the basis of the former principles described in Sections 4.1.2 and 4.1.3 (regression and frequency distribution matching), a number of variable correction methods have been developed during the last years. The new improvement of these methods is that they do not need overlap observations, instead of this they use information from nearby reference stations, for example higher order moments (HOM) method by *Della-Marta* and *Wanner* (2006) and spline daily homogenization (SPLIDHOM) method by *Mestre et al.* (2011). We do not want to criticize the details of these methods however, we express again our skepticism on their common fundamental principles which were based on a pseudo problem demonstrated in *Example 2.2*. Moreover, we repeat the following sources of errors for consideration.

- The assumption of the frequency distribution matching technique, i.e., there is no systematic bias in the rank, cannot be accepted.

- The regression methods are not adequate to correct the higher order moments.

Our last remark is connected also with the higher order moments. In general, the papers about these methods indicate the capability to correct the higher order moments, but this statement is always without any exact mathematical proof. We are skeptic, however if somebody could send us a nice proof, we would be grateful for it.

5. Some remarks about the homogenization in the higher-order moments

We suggest to consider the following remarks when developing homogenization methods with the capability to correct also the higher order moments.

Remark 1

There is a common assumption that the correction in mean is sufficient for monthly and annual series, and that the correction of higher order moments is necessary only in the case of daily data series. In general, it is tacitly assumed that the averaging is capable to filter out the inhomogeneities in the higher order moments. However, this assumption is false, for example, if there is an inhomogeneity in the standard deviation of daily data, we may have the same inhomogeneity in monthly data.

Proof

Daily data are $X(t)\ (t = 1,2,..,30)$, monthly average is $\overline{X} = \frac{1}{30}\sum_{t=1}^{30} X(t)$.

Let us introduce an inhomogeneity in the standard deviation for the daily data:
$X_{ih}(t) = \alpha \cdot (X(t) - \mathrm{E}(X(t))) + \mathrm{E}(X(t)),\ (t = 1,2,..,30)$.
The expected value is unchanged: $\mathrm{E}(X_{ih}(t)) = \mathrm{E}(X(t))$, but the standard deviation has changed: $\mathrm{D}(X_{ih}(t)) = \alpha \cdot \mathrm{D}(X(t))$.

Let us see the new monthly average: $\overline{X}_{ih} = \frac{1}{30}\sum_{t=1}^{30} X_{ih}(t)$.

The expected value is unchanged: $\mathrm{E}(\overline{X}_{ih}) = \mathrm{E}(\overline{X})$, but the standard deviation changed with the same measure:

$$\mathrm{D}(\overline{X}_{ih}) = \mathrm{D}\left(\frac{1}{30}\sum_{t=1}^{30} X_{ih}(t)\right) = \mathrm{D}\left(\frac{1}{30}\sum_{t=1}^{30} \alpha \cdot X(t)\right) = \alpha \cdot \mathrm{D}\left(\frac{1}{30}\sum_{t=1}^{30} X(t)\right) = \alpha \cdot \mathrm{D}(\overline{X}).$$

Remark 2

The correction in the first two moments or, equivalently, in mean and standard deviation can be formulated by using the notations defined in Section 3 as follows:

$$Y_{1,2h}(t) = E_1(t) + \frac{D_1(t)}{D_2(t)}(Y_2(t) - E_2(t)) \quad (t = 1,2,..,T), \tag{4}$$

where $E_1(t) = \mathrm{E}(Y_1(t))$, $E_2(t) = \mathrm{E}(Y_2(t))$ are the means, and $D_1(t) = \mathrm{D}(Y_1(t))$, $D_2(t) = \mathrm{D}(Y_2(t))$ are the standard deviations. Then $\mathrm{E}(Y_{1,2h}(t)) = E_1(t)$, $\mathrm{D}(Y_{1,2h}(t)) = D_1(t)$.

In general, the detection of the change points and the estimation of correction factors are suggested to be based on the examination of monthly data series because of the larger signal to noise ratio.

Remark 3

If the joint distribution of the series is normal, $Y_1(t) \in N(E_1(t), D_1(t))$, $Y_2(t) \in N(E_2(t), D_2(t))$ $(t = 1,2,..,n)$ and $Y_{1,2h}(t)$ $(t = 1,2,..,T)$, calculated according to Eq. (4), then $Y_{1,2h}(t), Y_1(t)$ $(t = 1,2,..,T)$ have identical distribution: $Y_{1,2h}(t) \stackrel{d}{=} Y_1(t)$ $(t = 1,2,..,T)$. Consequently, the mixed series $Y_{1,2h}(t)$ $(t = 1,2,..,T)$, $Y_1(t)$ $(t = T+1,..,n)$ is homogeneous, that means it is sufficient to correct only the first two moments in case of joint normal distribution.

Proof

Owing to Remark 2 and the joint normal distribution, $Y_{1,2h}(t) \in N(E_1(t), D_1(t))$ $(t = 1,2,..,T)$.

6. Conclusion

It is necessary to define the exact mathematical theory for homogenization of climate data series. Homogenization is a probability distribution problem, and the methods applied in practice should be theoretically evaluated in this respect.

References

Della-Marta, P.M. and *Wanner, H.*, 2006: A Method for homogenizing the extremes and mean of daily temperature measurements. *J. Climate 19*, 4179–4197.

Mestre, O., Gruber, C., Prieur, C., Caussinus, H., and *Jourdain, S.*, 2011: Splidhom: a method for homogenization of daily temperature observations. *J. Appl. Meteor. Climatol. 50*, 2343–2358.

Szentimrey, T., 2008: Development of MASH homogenization procedure for daily data, *Proceedings of the Fifth Seminar for Homogenization and Quality Control in Climatological Databases,* Budapest, Hungary, 2006; *WCDMP-No. 68, WMO-TD NO. 1434*, 116–125.

Trewin, B.C. and *Trevitt, A.C.F.*, 1996: The development of composite temperature records. *Int. J. Climatol. 16*, 1227–1242.

IDŐJÁRÁS
Quarterly Journal of the Hungarian Meteorological Service
Vol. 117, No. 1, January–March 2013, pp. 123–141

Experiences with data quality control and homogenization of daily records of various meteorological elements in the Czech Republic in the period 1961–2010

Petr Štěpánek[1,2] *, **Pavel Zahradníček**[1,2] and **Aleš Farda**[2]

[1]*Czech Hydrometeorological Institute, regional office, Kroftova 43, 616 67 Brno, Czech Republic*

[2]*Global Change Research Centre AS CR, v.v.i, Bělidla 986/4a, 603 00 Brno, Czech Republic*

Corresponding author E-mail: petr.stepanek@chmi.cz

(Manuscript received in final form December 14, 2012)

Abstract–Quality control and homogenization has to be undertaken prior to any data analyses in order to eliminate any erroneous values and non-climatic biases in time series. In recent years, considerable attention was paid to daily data since it can serve, among other conventional climatological analyses, as non-biased input into extreme value analysis, correction of RCM outputs, etc. In this work, we describe and then apply our own approach to data quality control of station measurements, combining several methods: (i) by analyzing difference series between candidate and neighboring stations, (ii) by applying limits derived from interquartile ranges, and (iii) by comparing the series values tested with "expected" values – technical series created by means of statistical methods for spatial data (e.g., IDW, kriging). Because of the presence of noise in series, statistical homogeneity tests render results with some degree of uncertainty. In this work, the use of various statistical tests and reference series made it possible to increase considerably the number of homogeneity test results for each series and, thus, to assess homogeneity more reliably. Inhomogeneities were corrected on a daily scale. In the end, missing values were filled applying geostatistical methods; thus, the so-called technical series for stations were constructed, which can finally be used as quality input into further time series analysis. These methodological approaches are applied to daily data, for various meteorological elements within the area of the Czech Republic in the period 1961–2010, which allows demonstrate their usefulness. Series were processed by means of the developed ProClimDB and AnClim softwares (http://www.climahom.eu).

Key-words: data quality control, homogenization, statistical correction of inhomogeneities, daily data processing, climatological time series

1. Introduction

For any meaningful climate analysis, investigated time series should be homogeneous, which means that their variations are caused solely by variations in weather and climate (*Conrad* and *Pollak*, 1950). Thus, prior to any analyses, the need to homogenize data and check their quality arises. Unfortunately, most of the climatological series that span from decades to centuries, contain inhomogeneities caused by station relocations, change of observers, changes in the vicinity of the stations (e.g., urbanization), changes in instruments, observing practices (e.g., different formulas for calculating daily means, different observation times), etc. (*Aguilar et al.*, 2003). Another important requirement for climatological analyses is the quality of the individual values, where series should be free of errors and have a low number of missing values (*Vicente-Serrano et al.*, 2010).

In the Czech Republic, this topic has been a focus of interest for several years. The first studies devoted to the homogenization of long series of air temperature, precipitation, and relative humidity for individual stations (e.g., *Macková*, 1997; *Brázdil* and *Štěpánek*, 1998; *Brázdil et al.*, 1996, 2000, 2001), which makes their use difficult (their availability, purpose of the given study, etc.). Later, studies devoting to the whole county have emerged (*Štěpánek*, 2003; *Štěpánek* and *Mikulová*, 2009; *Štěpánek et al.*, 2009), and this interest has continued up to the time of this study dealing with all the basic climatological characteristics throughout the whole territory of the Czech Republic. In recent years, considerable attention has also been devoted to the analysis of daily data (e.g., *Klein Tank et al.*, 2002; *Vincent et al.*, 2002; *Wijngaard et al.*, 2003; *Brunet et al.*, 2006; *Brandsma* and *Können*, 2006; *Della-Marta* and *Wanner*, 2006; *Vicente-Serano et al.*, 2010), which then may be used for various analyses, including those that were not possible to apply when homogenizing only monthly data, like the analysis of extreme value (*Sacré et al.*, 2007; *Kyselý* and *Picek*, 2007; *Costa* and *Soares*, 2009).

The organization of meteorological observations (i.e., maintaining the station network) and administration of collected data belong among the main duties of the Czech Hydrometeorological Institute (CHMI). The climatological database CLIDATA (*Tolasz*, 2008) serves very well for the usual quality control of the collected data (using GIS), but for the historical records, we face a lack of human resources, since the system requires user input. The software tools ProClimDB and AnClim (*Štěpánek*, 2010a, 2010b) allow automation of the process for quality control, homogenization, and filling of missing data but, at the same time, give the user a variety of outputs from which he can easily read what happened during the data processing and can track back all the important changes made to data, and also he can change the parameters and re-run the calculation. Thus, the ProClimDB and AnClim complement the aforementioned CHMI database system very well. However, it can also be used as a stand-alone application.

The general scheme of data processing that we advise being performed before any analyses includes the detection, verification, and possible correction of outliers (at the sub-daily scale – using the measured values), creation of reference series, homogeneity testing applying various statistical tests to better account for uncertainties in the results, determination of inhomogeneities in the light of test results and metadata (in monthly, seasonal and annual scale), adjustment of inhomogeneities (in daily scale) and, finally, the filling of missing values (see *Fig. 1*). We applied this approach to various meteorological elements available in our area in the period 1961–2010: mean, maximum and minimum air temperature, precipitation totals, water vapor pressure, wind speed and sunshine duration.

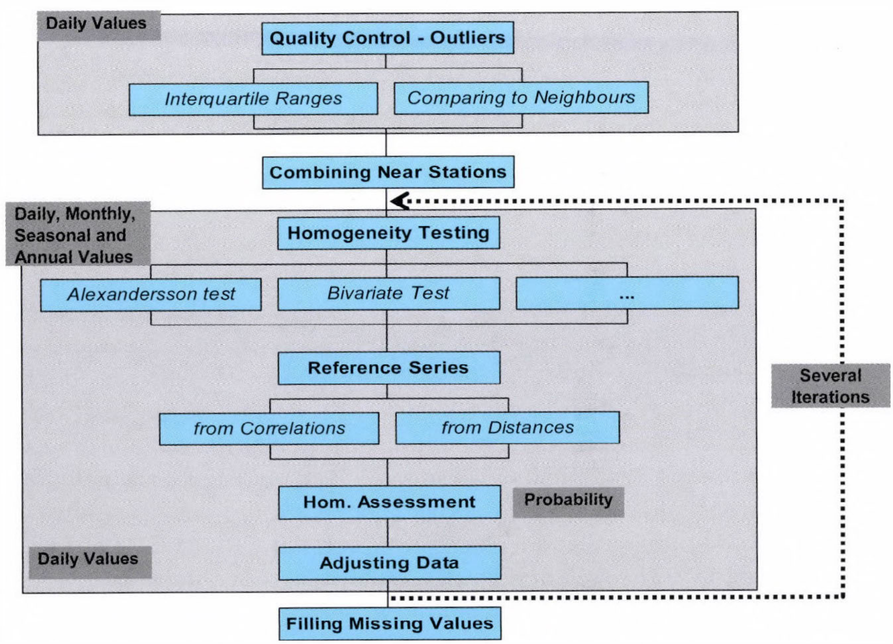

Fig. 1. Scheme of data processing – data quality control and homogenization.

2. Data Quality control

There is a lack of a generally accepted methodology for data quality control (contrary to homogenization). But, without outliers being properly treated, homogenization and analysis may render misleading results. Therefore, we devoted considerable attention to the methodology of outlier detection, to something that could, moreover, be automated to process large datasets of daily/sub-daily values (whole country dataset). This quality control was then applied to historical records which had not yet been processed by the methods used nowadays (using GIS and user interaction).

In our approach, data quality control is carried out by combining several methods:

(i) analyzing series of differences between candidate and neighboring stations (i.e. pairwise comparisons);

(ii) applying limits derived from interquartile ranges (either to individual series, i.e. absolutely, or better, to series of the difference between candidate and reference series, i.e. relatively); and

(iii) comparing the series of tested values with "expected" (theoretical) values – "technical" series created by means of statistical methods for spatial data (e.g. IDW, kriging).

Neighboring stations (method, (i)) or reference series (method, (ii)) may be selected either by correlations or distances (in the case of temperature, the results are different, while for precipitation, the selection coincides). Correlation coefficients can be applied either to raw series or to series of first differences (see, e.g., *Peterson*, 1998). In our case, for comparison with neighbor stations, up to six of the nearest stations were selected, with significant correlation coefficients, a distance limit of 400 km and an altitude difference restricted to 500 m. The distance limit was set with the help of a preceding analysis about how correlation coefficients drop with distance and change in altitude.

A method for outlier detection that could be automated to the greatest extent was a priority, since millions of values had to be processed for each meteorological element. Such a method was finally found and successfully applied. It utilizes a combination of several characteristics and their limits are based on the methods mentioned above (details on the quality control process may also be found in the documentation for the ProClimDB software, see *Štěpánek*, 2010b). No method on its own was found adequate; only their combination leads to satisfying results, i.e. the discovery of real outliers and suppression of false alarms. Parameters (settings appropriate to methods) had to be individually found for each meteorological element. The setting of parameters for outlier detection was validated using stations selected within different parts of the Czech Republic and also representing different altitudes.

As for the number of found suspicious values, the wind speed seems to be the most problematic variable, while air temperature has a relatively low number of problematic values (see *Fig. 2*). The number of outliers has a clear annual cycle. For most of the elements (e.g., air temperature), a higher number of outliers was detected in the summer months than in the winter months (larger spatial differences in summer are related to the increased influence of radiation factors compared to winter patterns, prevailingly influenced by circulation factors). More outliers were detected in the morning (7:00 local mean time –

LMT) and evening (19:00 LMT) observation terms compared to 14:00 LMT (associated with steeper gradients in the former case). For precipitation, there are two maxima per year: in the summer months and in December–January (this pertains to problems with solid precipitation measurements in winter), while during spring and autumn, a lower number of outliers were detected. The number of detected outliers also changes with time. The higher number of temperature outliers since the late 1990s coincides well with the transition to automatic measurements. Our explanation is that all values coming from automatic measurements (including errors) are stored directly into the database, while in the case of manual measurements, the observer revises the measured values before sending them to CHMI. In the last years, the number of outliers is again lower, owing to improved data quality control in the database. Conversely, in the case of precipitation, no increase of errors after automation was encountered (*Fig. 3*).

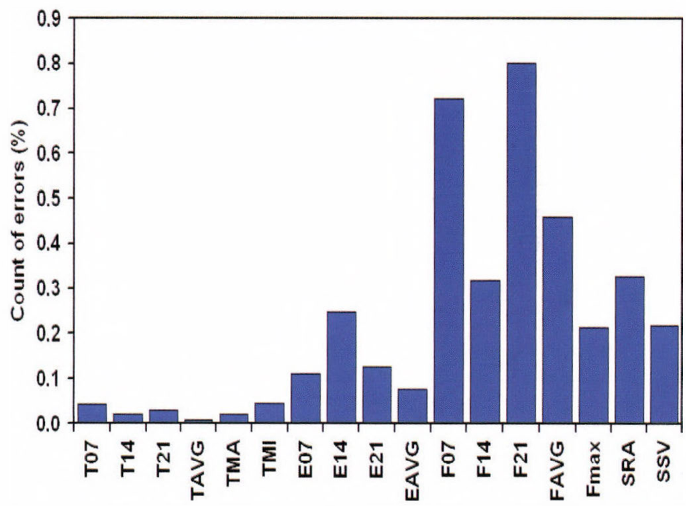

Fig. 2. Percentage portions of the number of errors detected in the total number of tested values for meteorological stations in the territory of the Czech Republic in the 1961–2009 period. Explanations: T – air temperature (T07, T14, T21 – observation terms, TAVG – daily mean), TMA – daily maximum air temperature, TMI – daily minimum air temperature, E – water vapor pressure (E07, E14, E21 – observation terms, EAVG – daily mean), F – wind speed (F07, F14, F21 – observation terms, FAVG – daily mean), Fmax – maximum daily wind gust, SRA – daily precipitation total, SSV – daily sunshine duration.

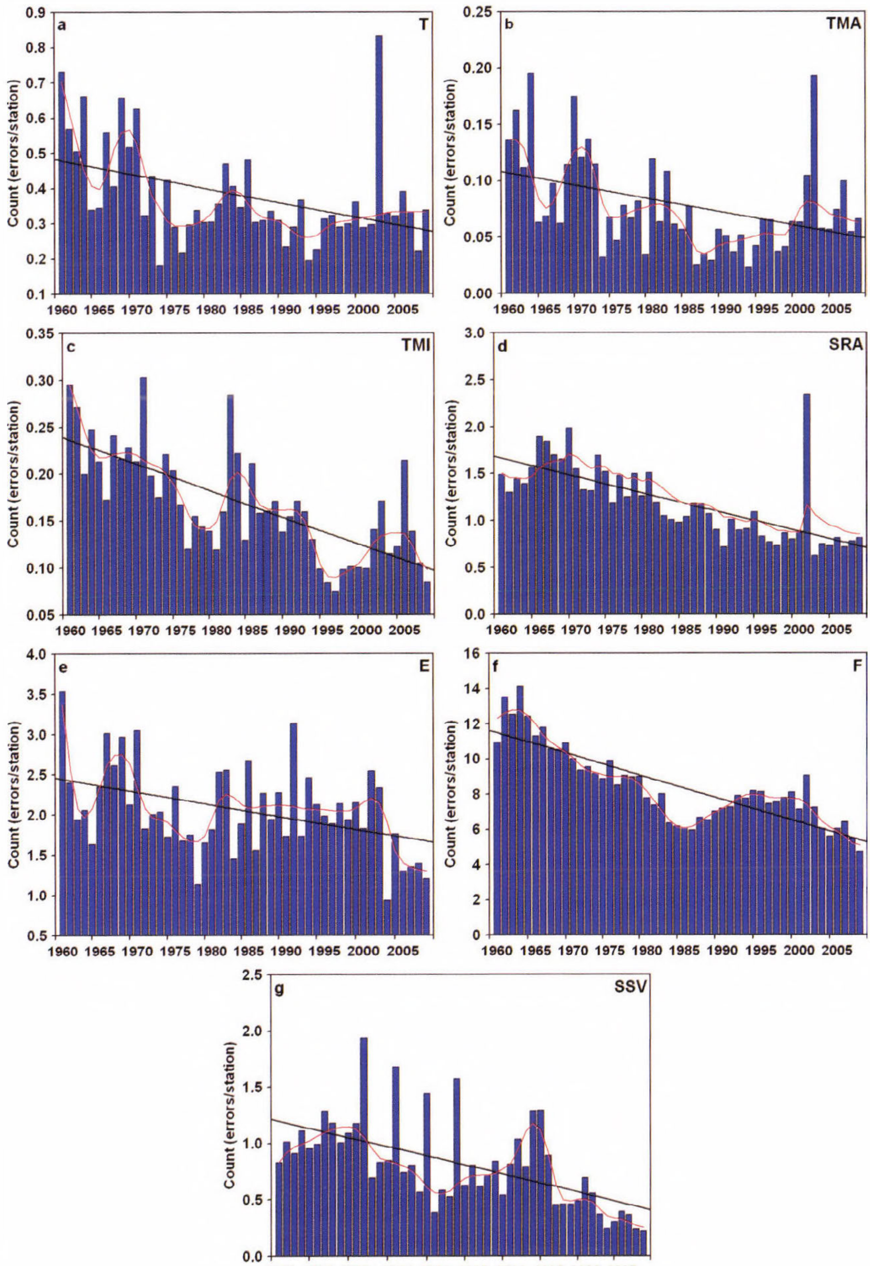

Fig. 3. Number of detected problematic values re-calculated per one meteorological station in the territory of the Czech Republic in the individual years of the 1961–2009 period: a) air temperature (observation terms and daily mean), b) maximum air temperature, c) minimum air temperature, d) precipitation total, e) water vapor pressure (observation terms and daily mean), f) wind speed (observation terms and daily mean), g) sunshine duration. The values are smoothed with a low-pass Gaussian filter for 10 years (red line) and complemented by the linear trend.

3. *Methodology of homogenization*

The general steps to be taken during homogenization consist of reference series creation (serving for comparison with tested series; this is a principal point of relative homogenization, see, e.g., *Conrad* and *Pollak*, 1950), applying statistical tests for testing the homogeneity of candidate series, homogenization (correction of inhomogeneities detected) and filling missing values (some prefer to fill missing values before homogenization). The individual steps are discussed, e.g., in *Štěpánek et al.* (2012), including a comparison of the results for various parameter settings (methods of weighting, number of stations used, individual statistical tests applied, method of correlation calculation for selection of neighbors, etc.)

Because of noise in time series, statistical homogeneity tests render results with some degree of uncertainty (see *Fig. 4*). In this work, the use of various statistical tests, types of reference series and time frames (monthly, seasonal, and annual series) allowed a considerable increase in the number of homogeneity test results for each series tested and thus to assess the homogeneity more reliably.

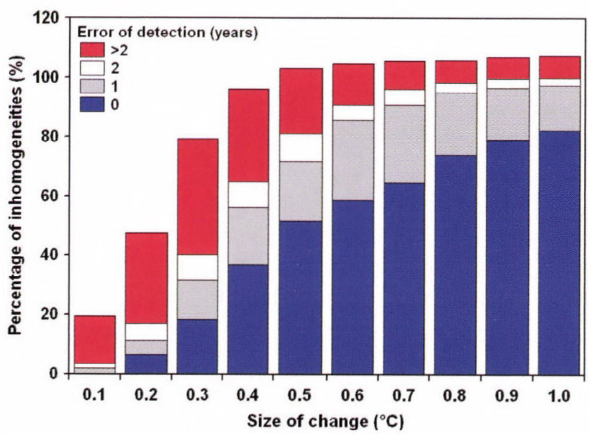

Fig. 4. The relative proportion (%) of the number of detected inhomogeneities of various sizes in the theoretically possible number of all inhomogeneities detected by the Alexandersson's SNHT test for the significance level of $\alpha = 0.05$. Generated series shorter than 50 years with annual standard deviation were used. Zero false detection (blue) corresponds to the exact inhomogeneity estimation in the given year; further false detections are given for 1, 2, or more years apart (grey, white, and red). A total of 180 series were used for each category of the inhomogeneity size in mean (shift). The proportion of inhomogeneities exceeding 100% is due to dividing series into more parts during the testing.

The relative homogeneity tests applied were as follows: the standard normal homogeneity test [SNHT] (*Alexandersson*, 1986, 1995), the Maronna and Yohai bivariate test (*Potter*, 1981), and finally, the Easterling and Peterson test (*Easterling* and *Peterson*, 1995). Reference series were calculated as weighted means from the five nearest stations (measuring within the same period as the candidate series, they were also newly applied individually), with statistically significant correlations, a distance limit of 300 km, and an altitude difference limit of 500m. The weight (inverse distance) for temperature was taken as one and for precipitation as three. Neighbouring station values were standardized to the mean and standard deviation of the candidate station. The detection of inhomogeneities was performed for series divided into a maximum duration of 40 years, with an overlap for two consecutive periods of 10 years (due to requirements of SNHT to test only one shift in a series). The tests were applied for series of monthly, as well as seasonal and annual means (totals in the case of precipitation and sunshine duration).

The main criterion for determining a year of inhomogeneity was the probability of detection of a given year, i.e., the ratio between the count of detections for a given year from all test results for a given station (using type of reference series, range of tests applied, monthly, seasonal, and annual series) and the count of all theoretically possible detections (for more details of reference series creation and testing, see *Štěpánek et al.*, 2012).

After the evaluation of detected breaks and a comparison with metadata, a final decision on the correction of inhomogeneities was made. Data were corrected on a daily scale. The adjustment of such inhomogeneities was addressed by means of a reference series calculated in a similar way as described above.

We created our own correction method, an adaptation of a method for the correction of regional climate model outputs by *Déqué* (2007), itself based on assumptions similar to those implicit in methods described by *Trewin* and *Trevitt* (1996) and *Della-Marta* and *Wanner* (2006), which apply variable correction according to individual percentiles (or deciles). Our process is based on a comparison of percentiles (empirical distribution) of differences (or ratios) between candidate and reference series before and after a break. Percentiles are estimated from candidate and references series separately (not for the same date). Each month is processed individually, but the values of adjacent months before and after are also taken into account to ensure smoother passage from one month to another. Differences of candidate and reference series for individual percentiles are treated before and after a break and smoothed by low-pass filter to obtain a final adjustment based on a given percentile (see *Fig. 5* for illustration). Values before a break are then adjusted in such a way that we find a value for the candidate series before a break (interpolating between two percentile values if needed) and the corresponding correction factor, which is then applied to the values to be adjusted. Special treatment is needed for extremes at the ends of distribution. A comparison of the DAP approach and the "classic" one using monthly values is shown in *Fig. 6*.

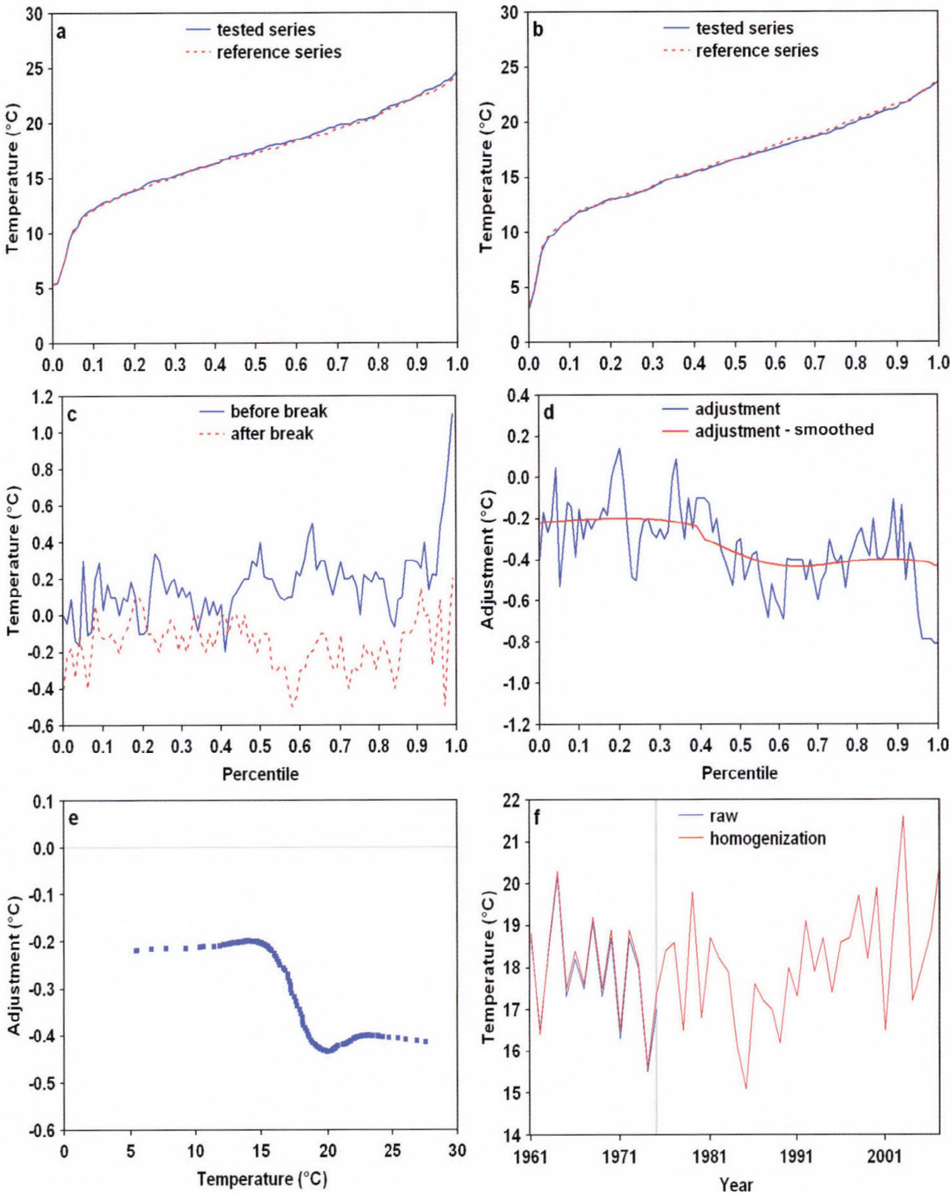

Fig. 5. Adjustment of series of daily mean air temperatures from the Velké Pavlovice station with an inhomogeneity detected in April 1975: a) quantiles (empirical distribution) of tested and reference series before the break, b) quantiles (empirical distribution) of tested and reference series after the break, c) the difference between tested and reference series for quantiles before and after the break, d) values of adjustments for quantiles (difference of tested and reference series differences before and after the break) and their smoothing by low-pass filter (final value of adjustments), e) adjustment values for a specific air temperature, f) original and homogenized series (monthly means).

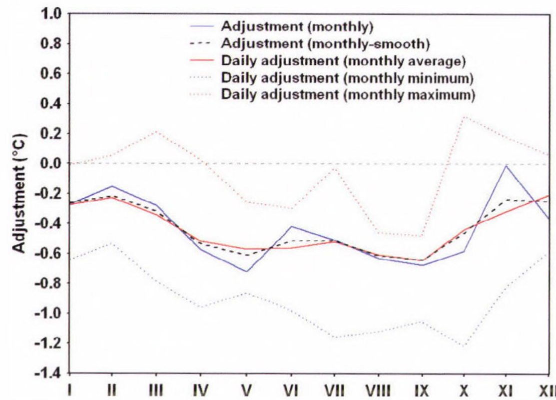

Fig. 6. Example of the series adjustment for inhomogeneity applying the classic approach with use of monthly data (solid blue line; smoothed corrections: dashed black line) and monthly means of daily corrections using DAP – distribution adjusting by percentiles method (solid red line; dotted red (blue) lines show the monthly maxima (minima) from daily corrections). The series is mean daily air temperature measured at station Bystřice pod Hostýnem with inhomogeneity on Januar 1, 1985.

Various characteristics were analyzed before applying the adjustments: the increment of correlation coefficients between candidate and reference series after adjustments; any change of standard deviation in differences before and after the change; the presence of linear trends, etc. In the event of any doubt, the adjustments were not applied.

Homogeneity testing, evaluation and correction of inhomogeneities detected were performed by several iterations, in which more precise results are gradually obtained. Missing values were filled after the homogenization and adjustment of inhomogeneities in the series. This means that the new values filled are estimated from data which are not influenced by possible shifts in the series. Filling missing data before homogenization may negatively influence inhomogeneity detection.

A preference for testing individual observation term series, if available, belongs among the recommendations for further homogenization improvement, since inhomogeneities are manifested in a different way in them (see *Fig. 7*). Further improvement can potentially be achieved by grouping values into categories, e.g., using weather types and testing individual categories alone.

Within the COST Action ES0601 ("Advances in homogenization methods of climate series: an integrated approach – HOME", 2006–2011), parameter settings used in this work were verified (at least for creation of reference series and detection of inhomogeneities that were run in the monthly mode) for air temperature and precipitation. The best parameter settings for air temperature were achieved applying a probability of detection equal to 20%, using correlations for neighbors selection calculated from the first differenced series, pairwise comparison with neighbors, and running several iterations of homogeneity testing and correction. The second and third iterations improved the series the best, while further iterations meant only negligible improvement. As for precipitation parameter settings, the best results were gained applying probability of detection equal to 10%, using correlations for neighbors selection calculated from the first differenced series, and pairwise comparison with neighbors; however, improvement of statistical characteristics of the series after homogenization was not as profound as in the case of air temperature. These settings will be applied in the follow-up work dealing with historical records (before 1961).

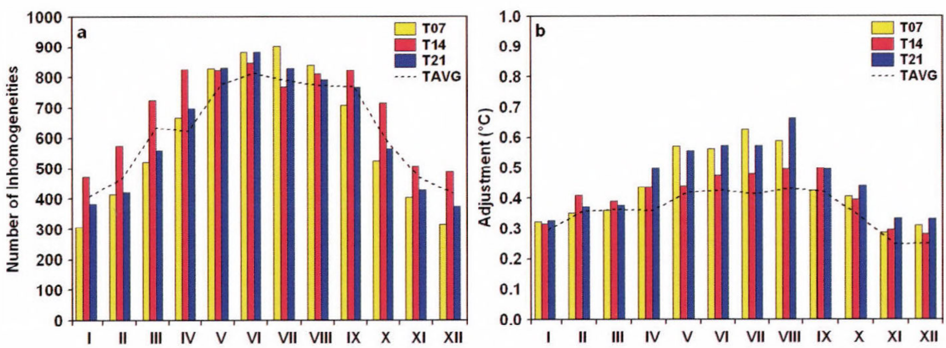

Fig. 7. a) Annual variation of the number of statistically significant inhomogeneities detected in air temperature series of observation terms (T07, T14, T21) and daily mean (TAVG) (Alexandersson's test – SNHT, bivariate test, reference series calculated using distances and correlations); b) annual variation of the size of corrections for individual observation terms and daily mean. Data refer to 230 stations analyzed in the Czech Republic and Slovak Republic in the 1961–2005 period.

4. Homogenization results for the Czech Republic

In the 1961–2007 period, 1750 series of seven climatological characteristics were tested and some inhomogeneities were found in 42% of them (*Table 1*). This value is underestimated, due to the low number of detections in precipitation series, in which breaks were detected in only 15% of series. For all other characteristics, this number is above 50%. The number of detected inhomogeneities varies according to the meteorological element (*Fig. 8*). For homogenization, just as for data quality control, the most problematic meteorological element is wind speed, where 75% of series were detected as inhomogeneous. Wind speed is a very specific meteorological element because, before automation, which took place since about 2000, it was estimated subjectively by observers using the Beaufort wind force scale.

Table 1. Number of breaks detected at meteorological stations in the Czech Republic in the 1961–2007 period for selected characteristics of meteorological variables: T – mean air temperature, TMA – maximum air temperature, TMI – minimum air temperature, SRA – precipitation total, E – mean water vapor pressure, F – mean wind speed, SSV – sunshine duration.

Meteorological element	Number of series	Number of series with break	Ratio (%)	Number of breaks in series 0	1	2	3
T	181	100	55,2	81	77	21	2
TMA	178	122	68,5	56	88	32	2
TMI	179	92	51,4	87	68	23	1
SRA	761	117	15,4	644	110	7	0
E	173	123	71,1	50	83	34	6
F	176	132	75,0	44	85	39	8
SSV	102	55	53,9	47	49	5	1
Total	1750	741	42,3	1009	560	161	20

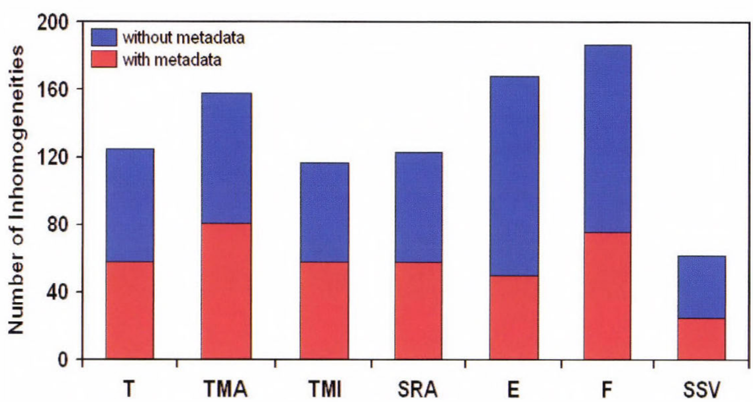

Fig. 8. Number of corrected inhomogeneities of selected characteristics of meteorological variables at stations in the territory of the Czech Republic in the 1961–2007 period: T – mean air temperature, TMA – maximum air temperature, TMI – minimum air temperature, SRA – precipitation total, E – mean water vapor pressure, F – mean wind speed, SSV – sunshine duration (the number of series tested for the individual characteristics is given in *Table 1*). Explanations for inhomogeneities: red – clarified by metadata, blue – no metadata.

For monthly values of air temperature and precipitation over the Czech Republic, the correlation coefficients between candidate and reference series are very high (median above 0.95 or 0.90, respectively; note that the rain-gauge station network is much denser than the climatological one). Along with mean wind speed, correlations are also very high in the case of the other characteristics.

As for inhomogeneity detection itself, more breaks occur in the summer months for air temperature and sunshine duration (the influence of relocation and other artificial changes is greater, resulting from the influences of the active surface, such as prevailing radiation factors and increased volume of vegetation), while for precipitation, it appears in the winter months (mainly due to problems associated with the measurement of solid precipitation). Water vapor pressure and wind speed do not show such a clear annual cycle (*Fig. 9*).

An annual variation is also clearly manifested in the correction of inhomogeneities. Considering the absolute values of corrections, the number of adjustments was higher during the summer months for temperature characteristics and water vapor pressure. After corrections, air temperature correlation coefficients increased mainly in the summer months and those for precipitation in the winter months. The largest increase in correlation coefficient after homogenization was observed in the case of wind speed.

The knowledge of metadata is an import factor for the proper correction of detected inhomogeneities. Out of all corrected breaks, 44% can be explained by metadata (*Fig 8*). There are some differences in the size of corrections according to the causes of the inhomogeneity: the size of correction was higher for inhomogeneities explained by metadata for all characteristics except minimum temperature and sunshine duration, where the mean size of corrections was similar to the case of missing metadata, and for precipitation, where it is even lower (however, for precipitation, only a small percentage of breaks can be detected). As it is evident from the results, the automation of measurements had a very strong influence on the homogeneity of series, as well as on the occurrence of outliers: for mean and maximum temperature and water vapor pressure, the size of the corrections was higher in the case of automatic measurements than the mean of over-all corrections. For example, the inhomogeneities in the series of maximum air temperature caused by automation are higher on average by 0.1°C than breaks not confirmed by metadata. Because the automation of measurements was introduced in the CHMI station network successively from the mid-1990s (see *Fig. 10*), it was possible to detect and make corrections without major problems.

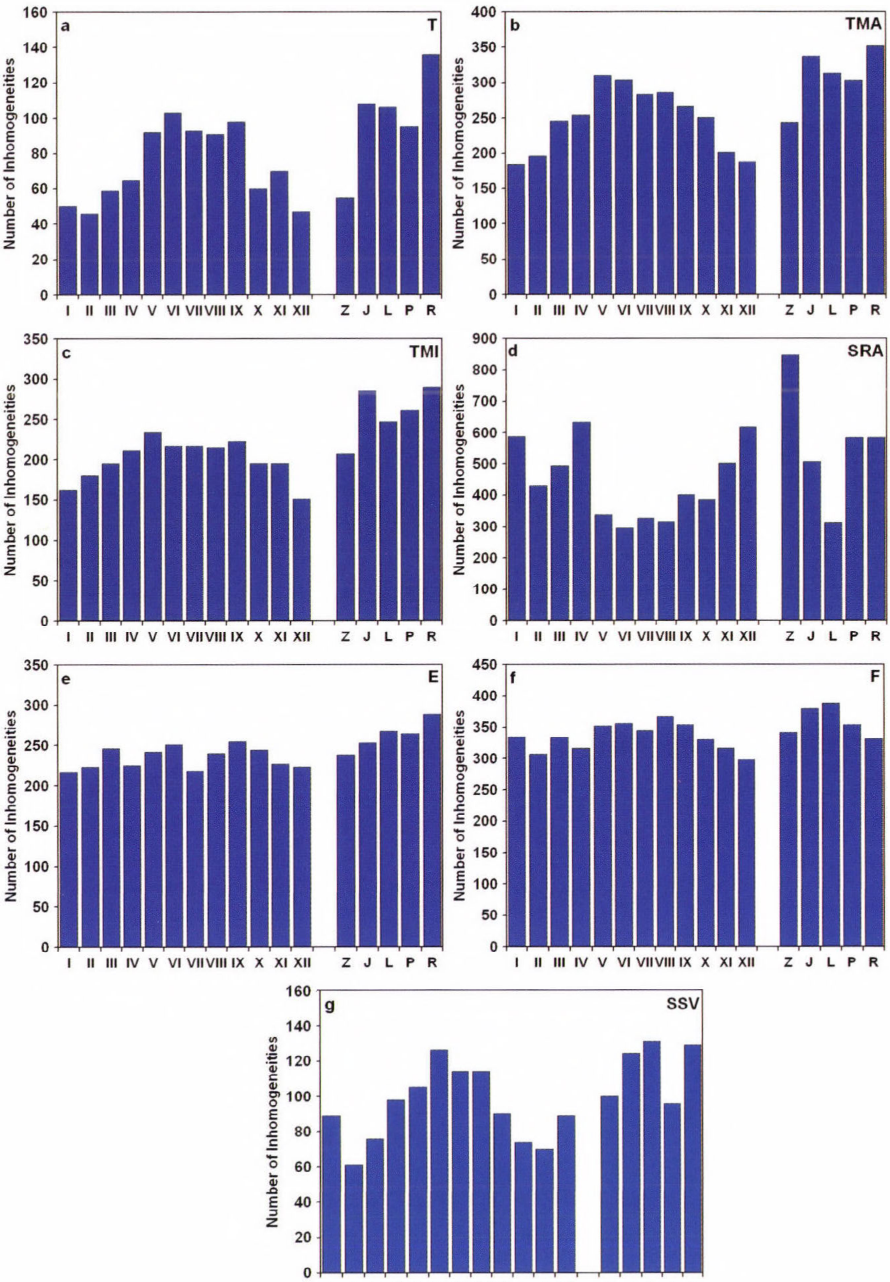

Fig. 9. Annual variation in the number of detected statistically significant inhomogeneities ($\alpha = 0.05$) for selected climatological and rain-gauge stations in the territory of the Czech Republic in the 1961–2007 period: a) mean air temperature, b) maximum air temperature, c) minimum air temperature, d) precipitation total, e) mean water vapor pressure, f) mean wind speed, g) sunshine duration (Z – winter, J – spring, L – summer, P – autumn; R – year).

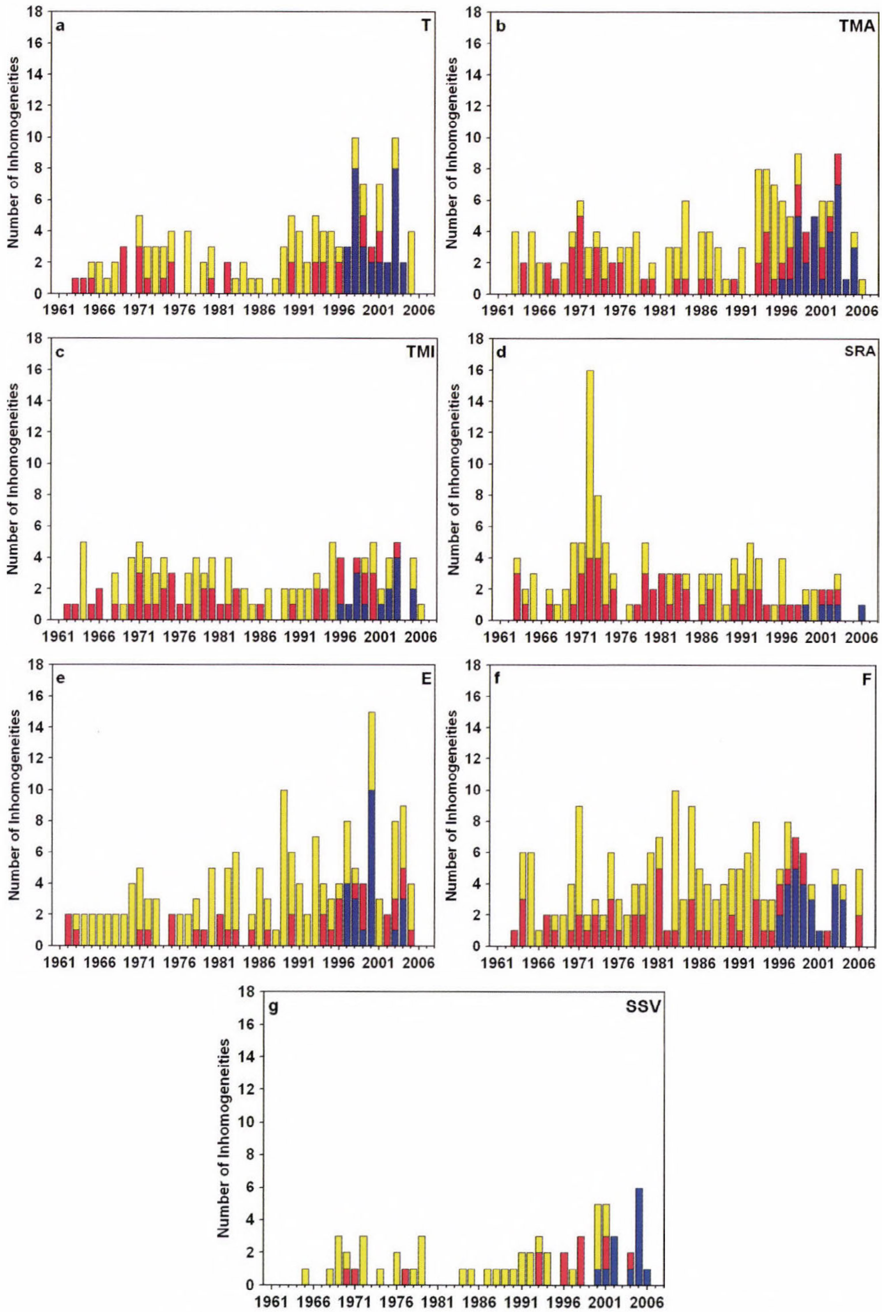

Fig. 10. Number of inhomogeneities detected in the series of climatological and rain-gauge stations in the territory of the Czech Republic in the 1961–2007 period: a) mean air temperature, b) maximum air temperature, c) minimum air temperature, d) precipitation total, e) mean water vapor pressure, f) mean wind speed, g) sunshine duration (yellow – break without metadata, red – break with metadata, blue – break with automation of measurements); AMS express a change to automatic measurements.

5. *Technical series*

Data quality control, homogenization and filling missing values lead to the creation of the so-called "technical" series for mean, maximum and minimum temperatures, precipitation totals, sums of sunshine duration, mean water vapor pressure, and wind speed. Such series may be used for further data analysis, because their values are consistent and complete over a given period. They were calculated for 268 climatological and 787 rain-gauge stations of the CHMI network in the 1961–2010 period, and actual values are continually added. Despite the fact that a smaller number of stations were available for some of the studied climatological characteristics (e.g. 196 stations for sunshine duration or 257 stations for water vapor pressure), "technical" series were completely calculated (for arbitrary station location or regular gridded network). In this way, we have a complex set of meteorological variables for each position of climatological stations, which can easily be further used (e.g., for evapo-transpiration calculation).

The possibility of calculating "technical" series for new positions, either in irregular or regular network, e.g. for grid points of regional climate model (RCM) outputs, allow their use for validation and correction of RCM outputs in each grid point. In the case of the RCM ALADIN-Climate/CZ (*Farda et al.*, 2010), series were calculated with 10x10 km resolution, specifically for 789 grid points over the Czech Republic (*Fig. 11*). The method for the "technical" series calculation is similar to the calculation of theoretical values during the data quality control (for more details, see, e.g., *Štěpánek et al.*, 2011).

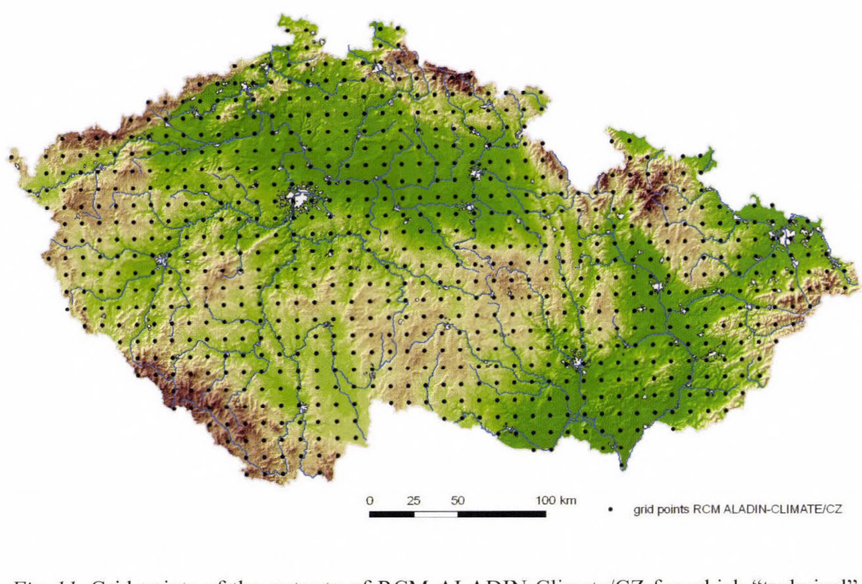

Fig. 11. Grid points of the outputs of RCM ALADIN-Climate/CZ for which "technical" series for the 1961–2009 period were calculated.

6. Conclusions

In the Czech Republic, experience with data quality control and homogenization has existed for several years. For data processing, software packages AnClim (*Štěpánek*, 2010a), LoadData and ProClimDB (*Štěpánek*, 2010b) were created. They offer complex solution, from tools for handling databases, through data quality control to homogenization of time series, as well as time series analyses, extreme value evaluation, and model output verification.

In this work, we summarize the effort and methodology behind outlier detection, series homogenization, and interpolation techniques for various climatological characteristics in the territory of the Czech Republic in the 1961–2010 period. In total, over 62 million values were data quality checked, for which the automation of the process was crucial. The final results are acceptable only because of the combination of several methods. The approach became part of the ProClimDB software (*Štěpánek*, 2010b). For correct outlier detection, it is necessary to work directly with measured values in the standard observing terms (e.g. 7:00, 14:00, 21:00 LMT), since possible errors can be masked in the "aggregated" values (daily means, monthly means, or sums).

Similar to the quality control, the aim of the created software for homogenization was to provide the user with support information for making quick, efficient, and correct decisions. Thanks to the COST Action ES0601 benchmark dataset, various parameter settings were checked in the software and recommended: finding neighbor stations using correlations of series of the first differences, performing homogeneity testing individually with each of the neighbors (pairwise comparison), weighting of the number of detected inhomogeneities for the homogeneity evaluation (weights of five for annual values, two for seasonal values, and one for monthly values). The correction of inhomogeneities was performed on a daily basis using our own approach (DAP –distribution adjusting by percentiles).

Quality control and correction of inhomogeneities have been performed on a daily (sub-daily) basis for all key meteorological variables over the territory of the Czech Republic in the 1961–2010 period. The homogenization of data before 1961 has only been carried out on the monthly basis so far (*Štěpánek*, 2003).

Due to the "technical" series calculated in both station and various regular grid point locations, we have gained a sufficiently large number of climatological series for subsequent analysis. These series are free of detectable outliers and inhomogeneities, have had their gaps filled, and are being applied to research in various projects in climatology and hydrology. From the "technical" series, we have also created maps for various meteorological variables for each month and day in the period of 1961–2010 (i.e., more than 130,000 maps).

Further steps will lead to the processing of series of individual observation terms and daily historical records before 1961, as well.

Acknowledgement–This paper was prepared with financial support from the Grant Agency of the Czech Republic for project No. P209/10/0605. The present work was also supported by the CzechGlobe project – the Centre for Global Climate Change Impacts Studies, Reg.No. Cz. 1.05/1.1.00/02.0073.

References

Alexandersson, A., 1986: A homogeneity test applied to precipitation data. *J. Climatol. 6*, 661–675.

Alexandersson, A., 1995: Homogenity testing, multiple breaks and trends. In: *Proceedings of the 6th International Meeting on Statistical Climatology*, Galway, Ireland, 439–441.

Aguilar, E., Auer, I., Brunet, M., Peterson, T.C., and *Wieringa, J.*, 2003: Guidelines on Climate Metadata and Homogenization. WCDMP-No. 53, WMO-TD No. 1186. World Meteorological Organisation, Geneva.

Brandsma, T. and *Können, G.P.*, 2006: Application of nearest-neighbour resampling for homogenizing temperature records on a daily to sub-daily level. *Int. J. Climatol. 26*, 75–89.

Brázdil, R. and *Štěpánek, P.*, 1998: Kolísání teploty vzduchu v Brně v období 1891–1995. *Geografie – Sborník České geografické společnosti 103*, 13–30, (in Czech).

Brázdil, R., Štěpánek, P., and *Budíková, M.*, 1996: Homogenized air temperature series in Brno, 1891–1994. Zeszyty Naukowe Uniwersytetu Jagiellońskiego, MCLXXXXVI, *Prace Geograficzne 102*, 85–91.

Brázdil, R., Štěpánek, P., and *Květoň, V.*, 2000: Air temperature fluctuation in the Czech Republic in the period 1961–1999. Instytut Geografii UJ – *Prace Geograficzne 107*, 173–178.

Brázdil, R., Štěpánek, P., and *Květoň, V.*, 2001: Temperature series of the Czech Republic and its relation to Northern Hemisphere temperatures in the period 1961–1999. In: *Detecting and Modelling Regional Climate Change*(eds.: Brunet India, M., López Bonillo, D.), Springer, Berlin, 69–80.

Brunet, M., Saladie, O., Jones, P., Sigro, J., Aguilar, E., Moberg, A., Lister, D., Walther, A., Lopez, D., and *Almarza, C.*, 2006: The development of a new dataset of Spanish Daily Adjusted Temperature Series (SDATS) (1850–2003). *Int. J. Climatol. 26*, 1777–1802.

Conrad, V., Pollak, L.W.,1950: Methods in Climatology. Harvard University Press, Cambridge.

Costa, A.C. and *Soares, A.*, 2009: Trends in extreme precipitation indices derived from a daily rainfall database for the south of Portugal. *Int. J. Climatol. 29*, 1956–1975.

Della-Marta, P.M. and *Wanner, H.*, 2006: A method of homogenizing the extremes and mean of daily temperature measurements. *J. Climate 19*, 4179–4197.

Déqué, M., 2007: Frequency of precipitation and temperature extremes over France in an anthropogenic scenario: model results and statistical correction according to observed values. *Global Planet. Change 57*, 16–26.

Easterling, D.R. and *Peterson, T.C.*, 1995: A new method for detecting undocumented discontinuities in climatological time series. *Int. J. Climatol. 15*, 369–377.

Farda, A., Déqué, M., Somot, S., Horányi, A., Spiridonov, V., and *Tóth, H.* ,2010: Model ALADIN as Regional Climate Model for Central and Eastern Europe. *Studia Geophysica et Geodetica 54*, 313–332.

Klein Tank, A. M. G., Wijngaard, J. B., Können, G. P., Böhm, R., Demarée, G., Gocheva, A., Mileta, M., Pashiardis, S., Hejkrlik, L., Kern-Hansen, C., Heino, R., Bessemoulin, P., Müller-Westermeier, G., Tzanakou, M., Szalai, S., Pálsdóttir, T., Fitzgerald, D., Rubin, S., Capaldo, M., Maugeri, M., Leitass, A., Bukantis, A., Aberfeld, R., van Engelen, A. F. V., Forland, E., Mietus, M., Coelho, F., Mares, C., Razuvaev, V., Nieplova, E., Cegnar, T., López, J. A., Dahlström, B., Moberg, A., Kirchhofer, W., Ceylan, A., Pachaliuk, O., Alexander, L. V., and *Petrovic, P.*, 2002: Daily dataset of 20th-century surface air temperature and precipitation series for the European Climate Assessment. *Int. J. Climatol 22*, 1441–1453.

Kyselý, J. and *Picek, J.*, 2007: Regional growth curves and improved design value estimates of extreme precipitation events in the Czech Republic. *Climate Res. 33*, 243–255.

Macková, J., 1997: Homogenizace dlouhých teplotních řad v České republice. Geografický projekt. Katedra geografie PřF MU, Brno. (in Czech)

Peterson, T.C., Easterling, D.R., Karl, T.R., Groisman, P., Nicholls, N., Plummer, N., Torok, S., Auer, I., Boehm, R., Gullett, D., Vincent, L., Heino, R., Tuomenvirta, H., Mestre, O., Szentimrey, T., Salinger, J., Førland, E. J., Hanssen-Bauer, I., Alexandersson, H., Jones, P., and *Parker, D.*, 1998: Homogeneity adjustments of in situ atmospheric climate data: A review. *International J. Climatol. 18*, 1493–1517.

Potter, K.W., 1981: Illustration of a new test for detecting a shift in mean in precipitation series. *Mon. Weather Rev. 109*, 2040–2045.

Sacré, C., Moisselin, J.M., Sabre, M., Floria, J.P., and *Dubuisson, B.*, 2007: A new statistical approach to extreme wind speeds in France. *J. Wind Engineer. Indust. Aerodyn. 95*, 1415–1423.

Štěpánek, P., 2003: Homogeneización de las series de temperatura del aire en la República Checa durante el período instrumental. *Geographicalia 43*, 5–24.

Štěpánek P., 2010a: AnClim – software for time series analysis. Department of Geography, Faculty of Natural Sciences, MU, Brno, 1.47 MB (http://www.climahom.eu/AnClim.html).

Štěpánek, P., 2010b: ProClimDB – software for processing climatological datasets. CHMI, regional office Brno (http://www.climahom.eu/ProcData.html).

Štěpánek, P. and *Mikulová, K.*, 2009: Homogenization of air temperature and relative humidity monthly means of individual observation hours in the area of the Czech and Slovak Republic. In: (Eds: Lakatos, M., Szentimrey, T., Bihari, Z., Szalai, S.) *Proceedings of the Fifth Seminar for Homogenization and Quality Control in Climatological Databases* (Budapest, Hungary, 29 May – 2 June 2006). WCDMP-No. 71. World Meteorological Organization, Geneva, 149–164.

Štěpánek, P., Řezníčková, L., and *Brázdil, R.*, 2009: Homogenization of daily air pressure and temperature series for Brno (Czech Republic) in the period 1848–2005. In: (Eds: Lakatos, M., Szentimrey, T., Bihari, Z., Szalai, S.) *Proceedings of the Fifth Seminar for Homogenization and Quality Control in Climatological Databases* (Budapest, Hungary, 29 May – 2 June 2006). WCDMP-No. 71. World Meteorological Organization, Geneva, 107–122.

Štěpánek, P., Zahradníček, P., and *Huth, R.*, 2011: Interpolation techniques used for data quality control and calculation of technical series: an example of Central European daily time series. *Időjárás 115*, 87–98.

Štěpánek, P., Zahradníček, P., Brázdil, R., and *Tolasz, R.*, 2012: *Metodologie kontroly a homogenizace časových řad v klimatologii* (Methodology of quality control and homogenisation of time series in climatology - in Czech). ČHMÚ (in print) (in Czech)

Tolasz, R., 2008: *Databázové zpracování klimatologických dat.* Sborník prací ČHMÚ 52. Český hydrometeorologický ústav, Praha. (in Czech)

Trewin, B.C. and *Trevitt, A.C.F.*, 1996: The development of composite temperature records. *International Journal of Climatology, 16*, 1227–1242.

Vicente-Serrano, S., Beguería, S., Lopez-Moreno, J. I., García-Verac, M. A., and *Stepanek, P.*, 2010: A complete daily precipitation database for northeast Spain: reconstruction, quality control, and homogeneity. *Int. J. Climatol. 30*, 1146–1163.

Vincent, L.A., Zhang, X., Bonsal, B.R., and *Hogg, W.D.*, 2002: Homogenization of daily temperatures over Canada. *J. Climate 15*, 1322–1334.

Wijngaard, J.B., Klein Tank, A.M.G., and *Können, G.P.*, 2003: Homogeneity of 20th century European daily temperature and precipitation series. *Int. J. Climatol. 23*, 679–692.

AIDŐJÁRÁS

Quarterly Journal of the Hungarian Meteorological Service
Vol. 117, No. 1, January–March 2013, pp. 143–158

Creation of a homogenized climate database for the Carpathian region by applying the MASH procedure and the preliminary analysis of the data

Mónika Lakatos[1]*, **Tamás Szentimrey**[1], **Zita Bihari**[1], and **Sándor Szalai**[2]

[1]*Hungarian Meteorological Service,*
P.O. Box 38, H-1525 Budapest, Hungary

[2]*Department on Soil Sciences and Agrochemistry,*
Szent István University,
Páter Károly utca 1, H-2100 Gödöllő, Hungary

**Corresponding author E-mail:lakatos.m@met.hu*

(Manuscript received in final form December 12, 2012)

Abstract–Homogenization of the long term observation series is essential in climate change studies. The most important achievements of the COST Action ES0601 (HOME) are survey and the comparison of the available homogenization methods. A benchmark test was performed in the Action to choose the best recent methods. The MASH (Multiple Analysis of Series for Homogenization; Szentimrey) procedure which was developed at the Hungarian Meteorological Service (OMSZ) produced good results. The Short Term Scientific Missions (STSMs) supported by the COST established the wide usage of MASH in the neighboring countries. This is the main reason why MASH became the common homogenization method used to fulfil the Climate of the Carpathian Region tender service. The aim of the project is to improve the climate data source and data access in the Carpathian Region by creating a daily harmonized gridded dataset during the period between 1961 and 2010. The homogenization process executed and the verification of the homogenization along with the quality control results are introduced in this paper. Preliminary results of trend analysis carried out on the harmonized database are also presented.

Key-words: COST Action ES0601, homogenization, Climate of the Carpathian Region Project, climate indices

1. Introduction

Climate change is expected to result in significant changes in the Carpathian region to affect ecosystems and human activities *(UNEP, 2007)*. Investigation of the recent tendencies in the regional climate conditions is essential for coping with the consequences. It is essential that studying the spatio-temporal changes can be implemented through the analysis of the observations which are representative both in time and space. Climate change studies require long term, quality controlled, homogenized, high quality climate data series.

The COST (European Cooperation in Science and Technology) Action ES0601 titled "Advances in homogenization methods of climate series: an integrated approach (HOME)" focused on investigation of the homogenization methods and testing the recent used applications. Hungary contributed to the success of the COST HOME action with the experiences of the MASH (Multiple Analysis of Series for Homogenization; *Szentimrey*, 2011) homogenization procedure, which was developed at the Hungarian Meteorological Service. The main features of MASH are illustrated in this paper by its application in the framework of the "Climate of the Carpathian Region Project" (CarpatClim).

As result of a Hungarian initiative on creation a high quality dataset covering the Carpathian basin, the JRC (European Commission Joint Research Centre) Institute for Environment and Sustainability launched a tender call in 2010 for supplying the data demand of its Desert Action activity (*JRC,* 2010). The consortium lead by the Hungarian Meteorological Service together with 10 partner organizations from 9 countries in the Carpathians region is supported by the Joint Research Centre.

The main aim of the CarpatClim project is to improve a joint climate data source and data access in the Carpathian region for application such kind of regional climate studies like drought monitoring. The CarpatClim project investigates fine temporal and spatial structures of the climate in the Carpathian Mountains and the Carpathian basin with unified methodology. The results are 0.1°(~10 × 10 km) resolution gridded daily time series of various meteorological parameters from 1961 to 2010. The target area is partly includes the territory of Czech Republic, Slovakia, Poland, Ukraine, Romania, Serbia, Croatia, Austria, and Hungary (*Fig. 1*). Uniform process of data homogenization is crucial due to the fact that significant differences might be occurred between the measurements and data handling of participant countries during the examined fifty-year-long period.

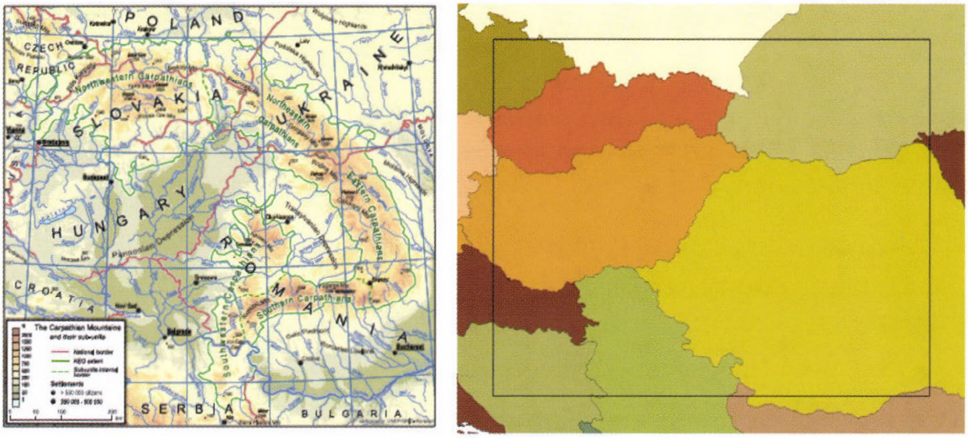

Fig. 1. The target area of the CarpatClim between latitudes 50°N and 44°N, and longitudes 17°E and 27°E approximately (left), and the political boundaries (right).

The project plan consists of three modules. Module 1 focuses on improving the availability and accessibility of homogeneous and spatially representative time series of climate data for the Carpathian Region through data rescue, quality control, and data homogenization. The activities in Module 2 ensure data harmonization with special emphasis on cross-border harmonization and production of gridded values for each country. A digital Climate Atlas as a basis for climate assessment and further applied climatological studies are developed in Module 3. The final outcome of the CarpatClim are the quality controlled, homogenized, in-situ daily time series and gridded data per country and the whole region as well, including a metadata catalogue with the documentation of the existing homogenized datasets. The daily grids with the metadata will be freely accessible for scientific purposes.

The consortium members agreed that the commonly used method for data homogenization and quality control in the project will be the MASH procedure. Using MASH is advantageous, because the COST HOME Action monthly benchmark results denoted that the MASH is one of the best monthly homogenization methods (*Venema et al,* 2012). Furthermore, several COST HOME delegates from the Carpathian region became familiar with the MASH software during STSMs supported by the COST.

The CarpatClim project is a well-accomplished cooperation for applying a single homogenization method in a region fragmented by boundaries and a pioneer work for countervailing against differences in measuring practice and strict data policies. The main features of MASH and the steps of the homogenization process along with the evaluation of the homogenization performed in Module 1 are presented in this study.

2. *Methodology*

The original MASH (*Szentimrey*, 1999) procedure was developed for homogenization of monthly series. The present version: MASHv3.03 (*Szentimrey*, 2011) has been expanded for daily series as well. The main features of the applied procedure to fulfil the tender service are summarized here.

The MASHv3.03 (*Szentimrey*, 2011) software consists of two parts.
Part 1: Quality control, missing data completion, and homogenization of monthly series:

- Relative homogeneity test procedure.
- Step by step procedure: the role of series (candidate or reference series) changes step by step in the course of the procedure.
- Additive (e.g., temperature) or multiplicative (e.g., precipitation) model can be used depending on the climate elements.
- Providing the homogeneity of the seasonal and annual series as well.
- Metadata (probable dates of break points) can be used automatically.
- Homogenization and quality control (QC) results can be evaluated on the basis of verification tables generated automatically during the procedure.

Part 2: Homogenization of daily series:

- Based on the detected monthly inhomogeneities.
- Including quality control (QC) and missing data completion for daily data. The quality control results can be evaluated by test tables generated automatically during the procedure.

These attributes are favorable to achieve the project goals in CarpatClim. The time resolution of variables is daily, the upgraded version of MASH is able to homogenize and control these daily data as well. Certain recently used daily homogenization methods take the monthly results for daily homogenization similarly to MASH (*Vincent*, 2002; *Szentimrey*, 2008). The excellent COST HOME monthly benchmark results and promising outcomes of the daily tests guarantee the high quality of times series got through the MASH procedure.

It has to underline that MASH is an automatically working software. Application of manual homogenization methods would be exceptionally labor intensive in handling huge data series. Moreover, the MASH is able to use the metadata (the date of moving of stations for example) automatically during the break point detection. This facility allows the effective usage of the existing metadata. We note that metadata were not used in CarpatClim.

Furthermore, the test results of the homogenization and quality control (e.g., detected errors, degree of inhomogeneity of the series system, number of break points, estimated corrections, and certain verification results) are documented in automatically generated tables during the homogenization process. Summary results of quality control and the homogenization performed in the project can be followed up and reported based on these tables. Verification statistics can be added to the homogenized series as the newly created metadata.

3. *Homogenization process in the CarpatClim*

The tasks in Module 1 are the data rescue, the digitization of the analogue datasets of climate observations, quality checking, including the data gap elimination of the existing climate time series, and homogenization of the data series. Completing the digitization of the measurements using MASHv3.03 is a proper way to perform the homogenization and the data quality control.

According to the tender specification, the elements listed in *Table 1* have to be homogenized in the period of 1961–2010. The chosen homogenization model is depending on the distribution of given element. Additive model is used except in case of precipitation and wind speed, where the appropriate model is multiplicative.

Table 1. Set of meteorological variables in daily temporal resolution to be homogenized (JRC, 2010)

Variable	Description	Units
T_a	2 m mean daily air temperature	°C
T_{min}	Minimum air temperature from 18:00 to 06:00	°C
T_{max}	Maximum air temperature from 06:00 to 18:00	°C
p	Accumulated total precipitation from 06:00 to 06:00	mm
DD	10 m wind direction	0°-360°
VV	10 m horizontal wind speed	m/s
Sunshine	Sunshine duration	hours
cc	Cloud cover	tenths
R_{global}	Global radiation	MJ/m^2
RH	Relative humidity	%
p_{vapour}	Surface vapour pressure	hPa
p_{air}	Surface air pressure	hPa

To ensure the most possible station usage, each contributor executed the necessary work phases individually. The cross border harmonization is guaranteed by bilateral data exchange. As the MASH is a relative homogenization method, the candidate series have to be compared to reference series which are in the nearby, within a given distance.

3.1. Steps of creation of the homogenized station data series in the CarpatClim

I. Compilation of the raw station data series of each country.

1. Selection of the stations (with the help of spherical coordinates: φ, λ).
2. Collecting the daily station data series (missing data are allowed) and the metadata per countries. Exchange of the near border raw data series and the existing metadata between the neighboring countries.

II. Homogenization, quality control, data completion of the station data series by MASH v3.03 on national level, using near border data.

1. Derivation of monthly station data series from the daily station data series collected in step I.2. Homogenization, quality control, data completion of the monthly station data series. Metadata (probable dates of break points) can be used automatically.
2. Daily station data series (step I.2): homogenization, quality control, data completion. This procedure is based on the results of step II.1.
3. Exchange of the near border homogenized data for cross-border harmonization and for gridding (Module 2 of the project: modeling, interpolation).
4. Evaluation of the verification results of the homogenization and quality control. Controlling of the cross-border harmonization of the data series. Note that further cross-border harmonization is achieved after the modeling part of the gridding procedure in Module 2.

Summary of the main steps of homogenization of daily data series with quality control and missing data completion in CarpatClim are as follows:

1. Monthly series derivation from daily series.
2. MASH homogenization procedure for monthly series, estimation of monthly inhomogeneities. (Metadata can be used automatically.)
3. Smooth estimation of daily inhomogeneities on the basis of estimated monthly inhomogeneities.
4. Automatic correction of daily series.
5. Automatic quality control (QC) of homogenized daily data.

6. Automatic missing daily data completion.
7. Monthly series derivation from the homogenized, quality controlled, and completed daily data.
8. Test of homogeneity for the new monthly series with using the automatic verification results.

The original time series of the variables listed in *Table 1* were homogenized, completed, and quality controlled by the participants individually. The automatically generated verification results were gathered and reported to the supporter. The following chapter is an overview of the evaluation of the implemented homogenization process.

4. Verification of the homogenization

Validation is an essential part of the process, to make sure that the data quality increased as a result of homogenization. Hence a verification part is integrated into the MASH system for interpretation of the outcomes, it makes the evaluation of the different phases of the homogenization possible from the initial to the final stage. The basic conception of the verification test is that the confidence in the homogenization may be increased by the joint comparative mathematical examination of the original and the homogenized data series.

Two types of outcomes of the MASH software can be separated. The first type of output is the files containing the homogenized, controlled, and completed series, inhomogeneity series, detected breaks, and detected errors. The second type of output is the files containing the test results and verification tables in order to evaluate the homogenization. The verification tables contain the test statistics values before and after homogenization, measures to characterize the modification of series, the spatial representativity of the station network, and the evaluation of metadata. The quality control results for the daily data are also included.

The verification procedure based on hypothesis test results. The null hypothesis is that examined series are homogeneous. The test statistics can be compared to the critical value before and after homogenization. The critical values belong to different significance levels are built in the MASH software (it is 20.86 on the 0.05 significance level in our case). The homogenization is successful if the test statistics after homogenization is low. The theoretical background and more details of the derivation of the verification statistics can be found in MASH manual (*Szentimrey*, 1999).

The test statistics before (TSb) and after homogenization (TSa) and characteristics of the modified series are presented in this paper. Annual statistics are examined here; though all of them are produced automatically on the monthly and seasonal scales altogether. *Tables 2* to *4* contain the average measures for maximum and minimum temperatures and precipitation for each of the station systems and the QC results alike. Number of the partners in the header lines is as follows: Hungary and Croatia with their jointly handled dataset (1), Serbia (2), Romania (3), Ukraine (4), Slovakia (5), Poland (6), Czech Republic (7). The representativity is about 50 km for climate stations and 25 km for precipitation stations, respectively. Participants have contributed to the project with data of 415 climate stations and 904 precipitation stations in all.

The TSa has to be near to the critical value or much less than the TSb if the homogenization is acceptable. Moreover, the measures of the relative modification are expected to be in accordance with the relative change of the test statistics: (TSb-TSa)/TSb. The applied statistics for the measure of the relative modification is in fact the ratio of the RMSE (root mean square error) and the standard deviation. If the significant modification of series induces weak decreasing in the degree of inhomogeneity, overdrawing the series is unnecessary and erroneous. *Tables 2–4* containing the summary statistics and the complementary diagrams in *Figs. 2–4* support the evaluation of homogenization.

The degree of inhomogeneity of the raw minimum temperatures *(Table 3.)* is substantially higher for Serbia (2) and much higher for the Hungarian and Croatian (1) dataset than in case of the maximum temperatures. The relative modification (42%) for the Hungarian and Croatian (1) series is achieved the most, although the largest improvement (*Fig. 3.*). The Serbian (2) system has been upgraded in the same rate by less relative modification. The Slovakian (5) system is near to homogeneous after processing. Relative changes of the test statistics are small in the Romanian (3) and Ukrainian (4) series, in accordance with the low value of relative modification. At the Czech Republic (7), the degree of homogeneity increased with relatively high modification. It can be found that MASH reduced the inhomogeneity of all systems, but less than in the case of maximum temperatures. The QC results relating the minimum temperatures show that the number of erroneous data per station is the largest in the Ukrainian (4) system. The Romanian (3) and Ukrainian (4) series contained more than 400 (°C) negative error and almost 100 (°C) positive errors in the data. The smallest correction has to be performed in the Czech (7) system, although it is a minor system with 18 stations.

Table 2. Average test statistics and quality control (QC) results for maximum temperature

Maximum temperature							
No. of station system	1	2	3	4	5	6	7
Number of stations	68	39	140	53	59	38	18
Verification results of homogenization							
TS after homog. (TSa)	23.6	55.7	39.0	23.7	26.4	24.8	26.7
TS before homog. (TSb)	190.7	186.2	72.9	154.0	175.6	150.6	184.3
Relative modification (%)	21	14	9	13	23	21	29
Quality control results							
Total number of errors	6307	3811	10241	5444	4542	3288	1400
Maximal positive error (°C)	10.9	13.5	996.6	107.7	11.3	22.7	10.4
Minimal negative error (°C)	–2.3	–7.5	–21.0	–22.0	–14.5	–26.3	–6.2

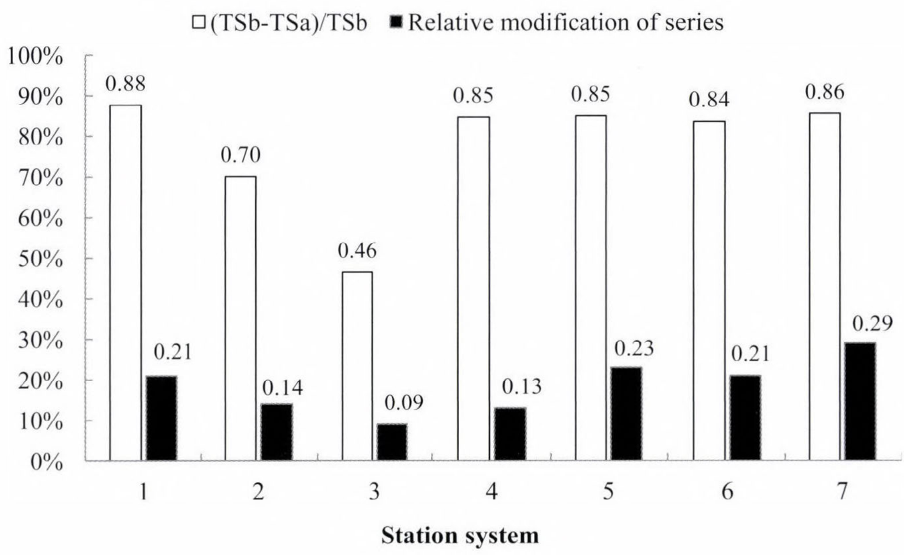

Fig. 2. Verification results for maximum temperature.

Table 3. Average test statistics and quality control (QC) results for minimum temperature

Station Sytem	1	2	3	4	5	6	7
Number of stations	68	39	140	53	59	38	18
TS after homog. (TSa)	24.3	52.5	52.5	51.9	28.5	43.5	37.8
TS before homog. (TSb)	227.5	484.7	128.3	120.3	179.7	141.3	93.9
Relative modification (%)	42	28	14	13	22	23	21
Total number of errors	4110	2161	6689	4111	3197	2592	375
Maximal positive error (°C)	23.7	11.8	95.1	79.3	14.9	15.9	0.7
Minimal negative error (°C)	–9.7	–8.0	–416.6	–417.6	–9.9	–10.0	–1.1

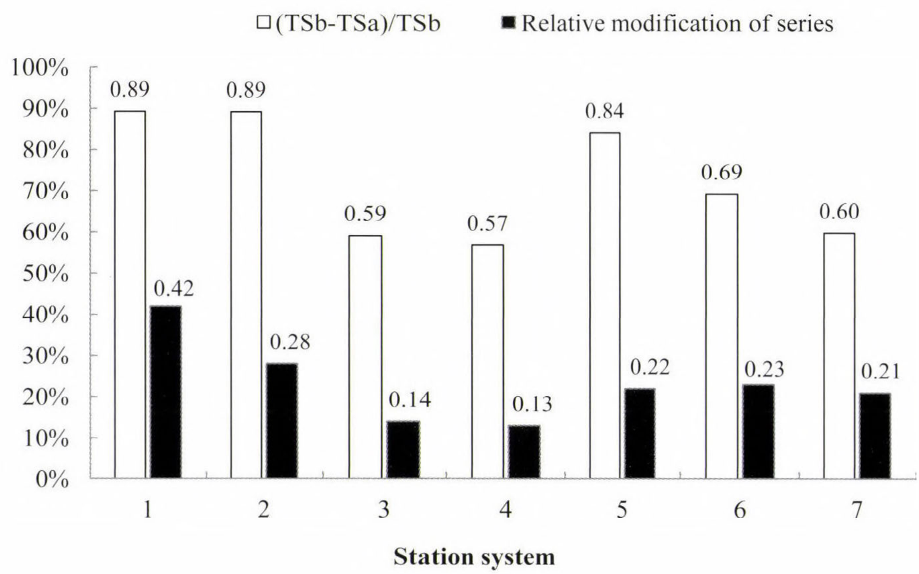

Fig. 3. Verification results for minimum temperature.

Analyzing the precipitation results, we have to take into consideration that the MASH procedure carefully detects the break points. Lower inhomogeneity arose for the precipitation series than for temperatures *(Table 4)*. During the homogenization, all of the networks became more homogeneous; nevertheless, the modification was precautious. The test statistics indicates that the Polish (6) system was the most inhomogeneous, and the improvement is also little afterward, although the similar relative modification caused higher improvement than in the Romanian (3) system *(Fig. 4.)*. The Slovakian (5) dataset passed through the most advance, at the expense of remarkable modifications of the series comparing to the others. Resulting from the QC numerous errors were detected, about in the rate of the amount of contributed stations. The amplitude of the errors in several systems is higher towards extremely heavy precipitations.

Table 4. Average test statistics and quality control (QC) results for precipitation

Station sytem	1	2	3	4	5	6	7
Number of stations	233	114	182	57	165	102	51
TS after homog. (TSa)	21.6	31.27	28.09	25.61	21.89	38.97	35.53
TS before homog. (TSb)	27.93	34.73	31.88	28.98	38.17	46.29	39.77
Relative modification (%)	4	5	6	3	10	5	4
Total number of errors	1531	672	975	313	803	408	223
Maximal positive error (mm)	71.94	230.27	10.27	179.46	94.29	93.36	60.38
Minimal negative error (mm)	23.24	–36.87	–1.52	–5.68	–59.46	–25.47	–11.41

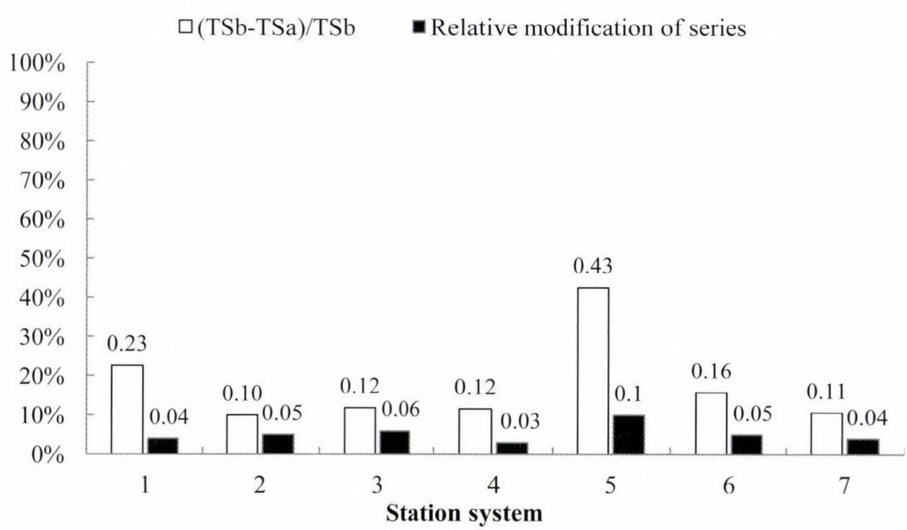

Fig. 4. Verification results for precipitation

Verification results for all the 12 elements can be followed up in the project deliverables related to the issues of the homogenization process *(D1.12)*. The data rescue and digitization activity in Module 1, and the data homogenization and QC performed by applying MASH procedure guarantee the availability of the high quality daily time series for the basic climate elements in the Carpathian region in the period of 1961–2010.

5. *Analysis of the climate trends on the harmonized gridded dataset*

The final outcome of the CarpatClim tender service is a ~10 × 10 km resolution gridded dataset on daily scale for elements listed in *Table 1*. Interpolation of the homogenized time series is carried out by applying the MISH (Meteorological Interpolation based on Surface Homogenized data basis; *Szentimrey* and *Bihari*, 2007) method. The MISH method was developed for interpolation of meteorological data, and an adequate mathematical background was also developed (*Szentimrey et al.*, 2011) for the purpose of efficient use of all the valuable meteorological and auxiliary model information. The main difference between MISH and the usual geostatistical interpolation methods is the application of the meteorological data series for modeling. In geostatistics (*Cressie*, 1991), the sample for modeling is only the predictor data, which is a single realization in time, while in meteorology there are data series, i.e., a sample in time and space as well.

5.1. Data harmonization with the homogenized data exchange

The cross border harmonization is essential in the project to avoid breaks at the boundaries on climate maps based on the gridded data. It can be ensured by the changes of the homogenized series across the borders as it was in case of the raw data exchange. The cross border harmonization is acceptable if some improvement appears in test statistics (*D2.5*). The gridding of the harmonized series was executed on national level by applying MISH, and the merging of the separate but harmonized grid parts followed up in the end.

5.2. Trend estimation based on the created dataset

Investigation of the climate extremes, observed trends, changes in frequency and intensity could contribute to the establishment of the adaptation strategies in the region. Climate indices are used in several projects on climate change as prevailing indicators of changes in extremes. Spatial interpolation of indices values for station locations is a difficult task, as the distribution functions of the several derived values are unknown. However, the basic variables, such as temperature and precipitation can be gridded by the knowledge of their statistical properties, thus higher quality gridded datasets can be constructed for further analysis, as it was created in CarpatClim (*Lakatos et al.*, 2010). The gridded database produced in daily temporal resolution provides relevant outcomes for studying extremes.

One temperature and one precipitation index was chosen to show the first results of the trend analysis based on the high quality dataset covering the region. These are the number of hot days per year (daily maximum ≥ 30 °C) and the number of days with heavy rainfall (daily precipitation amount >20 mm).The changes obtained from the linear trend estimation are demonstrated on the grid defined in the specification (*JRC*, 2010). The maps indicate the changes in the examined period, i.e., the slope of the estimated linear trend multiplied with the length of the changing period.

Fig. 5 strengthens the warming trend in the entire region. The changes are in strong correspondence with the orography. The growth is less at higher mountains than at lower altitudes. More hot days occur in the basin, especially in the territory between Danube and Tisza rivers, by 18–22 days from 1961 to 2010. The Transylvanian basin shows fewer rises. The region is lying under the south and east Carpathians turned up the largest growing in the number of hot days (over 24) during the examined period.

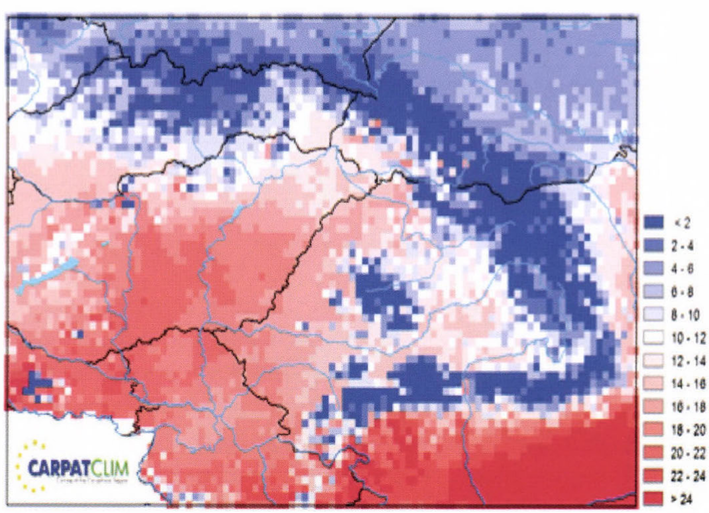

Fig. 5. Change in the number of hot days per year (daily maximum ≥ 30 °C) in the Carpathian region in the period of 1961–2010.

Fig. 6 visualizes the changes in the days above 20 mm precipitation during the whole 50 years period. The estimated changes indicated varied spatial distribution. The topographical effects are not so evident than in hot day's changes. The changes are between –2 and 3 days in the extended area of the region. More intense decreasing or increasing was found mostly on small territories. The highest increase was indicated in the northeast Carpathians and the Bihor Mountains with 7 days.

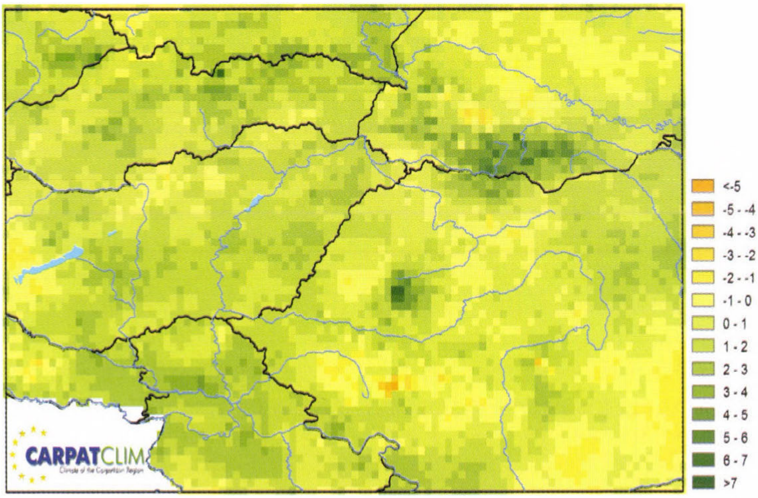

Fig. 6. Change in the number of days with heavy rainfall (daily sum > 20 mm) in the Carpathian region during the period from 1961 to 2010

6. *Conclusion*

The COST HOME Action had drawn the attention to the importance of data homogenization and recent methods. The monthly benchmark results of COST HOME denoted that MASH is one of the best monthly homogenization methods. The COST participants from the Carpathian region started the work with MASH during the STSMs supported by the COST. These STSMs established a common project for creating a homogenized dataset covering the region.

There are many advantageous attributes of MASH. Due to the automatic execution it allows performing the data homogenization, quality control, and data completion for the entire Carpathian region within a reasonable time. The MASH was used for numerous stations, 1319 climate and precipitation stations together, and 12 elements for a fifty-year long period in the Climate of the Carpathian Region tender service. The consortium members implemented the homogenization separately by the common procedure. The cross border harmonization was guaranteed by near border data exchange. The automatically generated verification results presented in this paper confirm that the quality of the data highly improved during the homogenization and quality control procedure.

The Climate of the Carpathian Region Project contributes to the availability of a set of homogeneous and spatially representative data to prepare climate change studies relevant in the region. The warming trend is obvious on the harmonized, gridded data in the period of 1961–2010 as indicated from the preliminary trend analysis. The changes in the number of days with precipitation above 20 mm show significant decrease or increase only on small areas of the region in the examined 50-year long period.

Acknowledgements–This work was supported by the COST (European Cooperation in Science and Technology) Action ES0601 titled "Advances in homogenization methods of climate series: an integrated approach (HOME)" (2007–2011) and by JRC Desert Action in the framework of the "Climate of the Carpathian Region (CarpatClim)" Project. The authors take this opportunity to thank the following members of the CarpatClim Homogenization and Interpolation Group for data homoginization:
Austria: Ingeborg Auer, Johann Hiebl
Croatia: Janja Milković
Czech Republic: Pavel Zahradníček, Petr Štěpánek, Radim Tolasz
Hungary: Tamás Szentimrey, Zita Bihari, Mónika Lakatos, Tamás Kovács, Ákos Németh, Sándor Szalai
Poland: Piotr Kilar, Robert Pyrc, Danuta Limanowka
Romania: Sorin Cheval, Monica Matei
Serbia: Dragan Mihic, Predrag Petrovic, Tatjana Savic
Slovakia: Peter Kajaba, Gabriela Ivanakova, Oliver Bochnicek, Pavol Nejedlik, Pavel Šastný
Ukraine: Oleg Skrynyk, Yurii Nabyvanets, Natalia Gnatiuk,
and Annamari Marton for depection of maps.

References

Cressie, N., 1991: Statistics for Spatial Data. Wiley, New York.

D1.12: Final report on quality control and data homogenization measures applied per country, including QC protocols and measures to determine the achieved increase in data quality. http://www.carpatclim-eu.org/pages/deliverables/

D 2.5: Report with final results of the data harmonization procedures applied, including all protocols, per country. http://www.carpatclim-eu.org/pages/deliverables/

JRC, 2010: Climate of the Carpathian Region. Technical Specifications (Contract Notice OJEU 2010/S 110-166082 dated 9 June 2010). http://desert.jrc.ec.europa.eu/action/php/index.php?action=view&id=550

Lakatos, M., Szentimrey, T., and *Bihari, Z.*, 2010: Application of gridded daily data series for calculation of extreme temperature and precipitation indices in Hungary. *Időjárás 115*, 99–109.

Szentimrey, T., 1999: Multiple Analysis of Series for Homogenization (MASH). Proceedings of the Second Seminar for Homogenization of Surface Climatological Data, Budapest, Hungary; WMO, WCDMP-No. 41, 27–46.

Szentimrey, T. and *Bihari, Z.*, 2007: Mathematical background of the spatial interpolation methods and the software MISH (Meteorological Interpolation based on Surface Homogenized Data Basis). Proceedings from the Conference on Spatial Interpolation in Climatology and Meteorology, Budapest, Hungary, 2004, COST Action 719, COST Office, 17–27.

Szentimrey, T., 2008: Development of MASH homogenization procedure for daily data. Proceedings of the Fifth Seminar for Homogenization and Quality Control in Climatological Databases, Budapest, 2006; WCDMP-No. 71, WMO/TD-NO. 1493, 2008, 123–130.
Szentimrey, T., 2011: Manual of homogenization software MASHv3.03. Hungarian Meteorological Service.
Szentimrey, T., Bihari, Z., Lakatos, M., and *Szalai, S.*, 2011: Mathematical, methodological questions concerning the spatial interpolation of climate elements. Proceedings from the Second Conference on Spatial Interpolation in Climatology and Meteorology, Budapest, Hungary, 2009, Időjárás 115, 1–2, 1–11.
UNEP, 2007: Carpathians Environment Outlook. Geneva. http://www.grid.unep.ch.
Venema, V., Mestre, O., Aguilar, E., Auer, I., Guijarro, J.A., Domonkos, P., Vertacnik, G., Szentimrey, T., Štěpánek, P., Zahradnicek, P., Viarre, J., Müller-Westermeier, G., Lakatos, M., Williams, C.N., Menne, M., Lindau, R., Rasol, D., Rustemeier, E., Kolokythas, K., Marinova, T., Andresen, L., Acquaotta, F., Fratianni, S., Cheval, S., Klancar, M., Brunetti, M., Gruber, C., Duran, M.P., Likso, T., Esteban, P. and *Brandsma,T.*, 2012: Benchmarking monthly homogenization algorithms. *Climate of the Past 8*, 89–115.
Vincent, LA, Zhang, X, Bonsal, BR, and *Hogg, WD.*, 2002: Homogenization of daily temperatures over Canada. *J. Climate 15*, 1322–1334.

INSTRUCTIONS TO AUTHORS OF *IDŐJÁRÁS*

The purpose of the journal is to publish papers in any field of meteorology and atmosphere related scientific areas. These may be

- research papers on new results of scientific investigations,
- critical review articles summarizing the current state of art of a certain topic,
- short contributions dealing with a particular question.

Some issues contain "News" and "Book review", therefore, such contributions are also welcome. The papers must be in American English and should be checked by a native speaker if necessary.

Authors are requested to send their manuscripts to

Editor-in Chief of IDŐJÁRÁS
P.O. Box 38, H-1525 Budapest, Hungary
E-mail: journal.idojaras@met.hu

including all illustrations. MS Word format is preferred in electronic submission. Papers will then be reviewed normally by two independent referees, who remain unidentified for the author(s). The Editor-in-Chief will inform the author(s) whether or not the paper is acceptable for publication, and what modifications, if any, are necessary.

Please, follow the order given below when typing manuscripts.

Title page: should consist of the title, the name(s) of the author(s), their affiliation(s) including full postal and e-mail address(es). In case of more than one author, the corresponding author must be identified.

Abstract: should contain the purpose, the applied data and methods as well as the basic conclusion(s) of the paper.

Key-words: must be included (from 5 to 10) to help to classify the topic.

Text: has to be typed in single spacing on an A4 size paper using 14 pt Times New Roman font if possible. Use of S.I. units are expected, and the use of negative exponent is preferred to fractional sign. Mathematical formulae are expected to be as simple as possible and numbered in parentheses at the right margin.

All publications cited in the text should be presented in the *list of references*, arranged in alphabetical order. For an article: name(s) of author(s) in Italics, year, title of article, name of journal, volume, number (the latter two in Italics) and pages. E.g., *Nathan, K.K.*, 1986: A note on the relationship between photo-synthetically active radiation and cloud amount. *Időjárás 90,* 10-13. For a book: name(s) of author(s), year, title of the book (all in Italics except the year), publisher and place of publication. E.g., *Junge, C.E.*, 1963: *Air Chemistry and Radioactivity.* Academic Press, New York and London. Reference in the text should contain the name(s) of the author(s) in Italics and year of publication. E.g., in the case of one author: *Miller* (1989); in the case of two authors: *Gamov* and *Cleveland* (1973); and if there are more than two authors: *Smith et al.* (1990). If the name of the author cannot be fitted into the text: *(Miller,* 1989); etc. When referring papers published in the same year by the same author, letters a, b, c, etc. should follow the year of publication.

Tables should be marked by Arabic numbers and printed in separate sheets with their numbers and legends given below them. Avoid too lengthy or complicated tables, or tables duplicating results given in other form in the manuscript (e.g., graphs).

Figures should also be marked with Arabic numbers and printed in black and white or color (under special arrangement) in separate sheets with their numbers and captions given below them. JPG, TIF, GIF, BMP or PNG formats should be used for electronic artwork submission.

Reprints: authors receive 30 reprints free of charge. Additional reprints may be ordered at the authors' expense when sending back the proofs to the Editorial Office.

More information for authors is available: journal.idojaras@met.hu

Published by the Hungarian Meteorological Service

Budapest, Hungary

INDEX 26 361

HU ISSN 0324-6329

IDŐJÁRÁS

QUARTERLY JOURNAL
OF THE HUNGARIAN METEOROLOGICAL SERVICE

CONTENTS

Ernő Führer, Anikó Jagodics, István Juhász, György Marosi, and *László Horváth:* Ecological and economical impacts of climate change on Hungarian forestry practice 159

Attila Trájer, János Bobvos, Katalin Krisztalovics, and *Anna Páldy:* Regional differences between ambient temperature and incidence of Lyme disease in Hungary 175

István Matyasovszky: Estimating red noise spectra of climatological time series 187

István Faragó, Ferenc Izsák, and *Tamás Szabó*: An IMEX scheme combined with Richardson extrapolation methods for some reaction-diffusion equations 201

Viktória Blanka, Gábor Mezősi, and *Burghard Meyer*: Projected changes in the drought hazard in Hungary due to climate change 219

****

http://www.met.hu/Journal-Idojaras.php

VOL. 117* NO. 2 * APRIL – JUNE 2013

IDŐJÁRÁS

Quarterly Journal of the Hungarian Meteorological Service

Editorial Office: Kitaibel P.u. 1, H-1024 Budapest, Hungary
P.O. Box 38, H-1525 Budapest, Hungary
E-mail: journal.idojaras@met.hu
Fax: (36-1) 346-4669

Indexed and abstracted in Science Citation Index Expanded™ and Journal Citation Reports/Science Edition
Covered in the abstract and citation database SCOPUS®

Subscription by mail:
IDŐJÁRÁS, P.O. Box 38, H-1525 Budapest, Hungary
E-mail: journal.idojaras@met.hu

IDŐJÁRÁS

Quarterly Journal of the Hungarian Meteorological Service
Vol. 117, No. 2, April – June, 2013, pp. 159–174

Ecological and economical impacts of climate change on Hungarian forestry practice

Ernő Führer[1], **Anikó Jagodics**[1], **István Juhász**[1], **György Marosi**[1], and **László Horváth**[2*]

[1]*Hungarian Forest Research Institute, Paprét 17, 9400 Sopron, Hungary*

[2]*Hungarian Meteorological Service, Gilice tér 39, 1181 Budapest, Hungary, and Plant Ecology Research Group of Hungarian Academy of Sciences at Institute of Botany and Ecophysiology, Szent István University, Páter K. utca 1, 2100 Gödöllő, Hungary*

**Correspondent author E-mail: horvath.l@met.hu*

(Manuscript received in final form March 12, 2013)

Abstract–As the result of the predicted climate change, not only the ecological circumstances but the profitability of forested areas will also change in the future in Hungary. The aim of this case study is to evaluate the expected ecological an economical impacts of a climate change scenario (REMO A1B) for three forest regions of Transdanubian Mountains (Bakony) for four climate indicator tree species (beech, hornbeam, sessile oak, and Turkey oak). According to this scenario, precipitation and air temperature increase by 5 percent and 1.3 °C, respectively in the spring months (March to May), while in summer (June to August) the precipitation decreases by 9 percent together with a higher temperature increase of 2.1 °C between the period of 2036 and 2065 compared to reference years (1961–2010). As a result of the forecasted climate change, a drift expected in forest climate classes towards the drier and warmer climate categories in Hungary, resulting in parallel decrease in production capacity of stands. We expect a significant area decrease in good forest yield classes together with an increase in poor categories. Hence, the annual revenues for the four indicator species will be lower by 9.4 percent compared to the reference period. The decrease in yield is caused by decrease of lumbered wood volume and more valuable wood assortments, as well. In case of the predicted climate scenario, the highest decay in production capacity will be expected for Turkey oak (12 percent), while the lowest for beech (7.5 percent).

Key-words: forest ecosystem, climate change, production capacity, forest yield classes, forest annual revenues

1. Introduction

The profitability of forestry practice is basically determined by ecological conditions beside the selection of tree species, the forestry practice applied, and the actual marketing circumstances (*Führer* and *Járó*, 1992). Namely, organic matter production of forests strongly depends on soil, hydrological, and climatic circumstances. While the quality of the first two site parameters can be considered as constant on short time basis, the climate, especially the magnitude and temporal variation of climate parameters show significant variability. Moreover, nowadays the change of climate can obviously be detected in Hungary, namely the climate becomes more and more warmer and drier as forecasted by *Bartholy et al.* (2009), *Faragó et al.* (2010), *Pieczka et al.* (2011), *Gálos et al.* (2007, 2012). In the forthcoming 50 years, frequency and strength of weather anomalies will be increasing. The evident, unfavorable changes in species composition, vitality, and growth of the forest ecosystems can be attributed to these changes according to numerous Hungarian forestry experts (*Berki et al.*, 2009; *Csóka*, 1996, 1997; *Csóka et al.*, 2007, 2009; *Czúcz et al.*, 2011; *Führer*, 1995; *Führer et al.*, 2011a,b; *Hirka* and *Csóka*, 2010; *Manninger*, 2004; *Mátyás*, 2010; *Mátyás* and *Czimber*, 2000, 2004; *Mátyás et al.*, 2010a,b, 2011; *Molnár* and *Lakatos*, 2009; *Solymos*, 2009; *Somogyi*, 2009; *Rasztovits et al.*, 2012).

Forestry, in practice, uses special climate categories represented by different tree species (*Járó*, 1972; *Führer*, 2010). These categories indicate different growing potential, therefore, any change in the area of climate categories accompanies with variation of organic matter production of the forest ecosystem (*Führer et al.*, 2011a,b). The forecasted warmer and drier climate in growing season would result in evident growth-loss of forest trees in Hungary; furthermore, a species composition change can also be expected on long-term time basis. The growth-loss can be indicated by the decrease in wood volume of an area unit. Considering that cost of logging are determined mainly by the actual marketing circumstances independently on climate change; final consequence of the loss in production will be the decrease of revenues and profitability of forestry practice.

The aim of this case study is to evaluate the expected ecological an economical impacts of a predicted climate change scenario for three forested regions of Transdanubian Mountains (Bakony) in Hungary (*Fig. 1*). In this work we investigate the climate of these state owned forests, the yield circumstances and potential revenues of climate indicator species, and the change of them as a result of climate change.

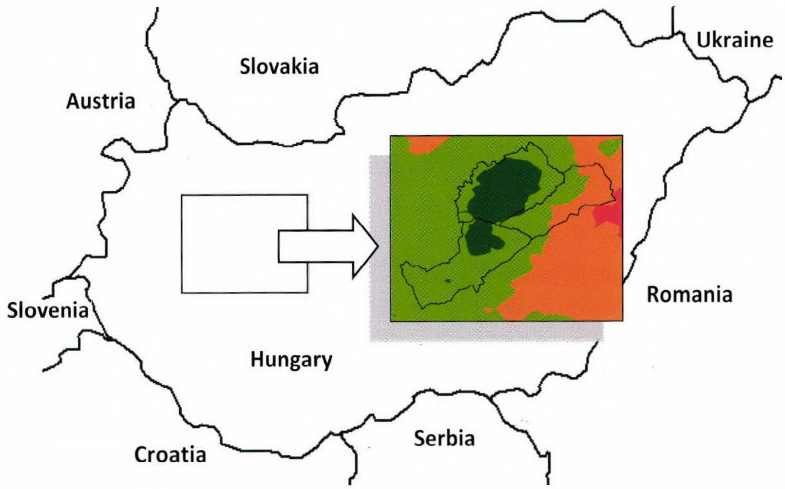

Fig. 1. Location of the three investigated forested regions in Hungary.

2. *Methodology*

The three forested test regions aimed in this study, in close connection each other, are the High-, South- and East-Bakony. Tough these areas are part of the same geographical region (Mountains), they can be characterized by a variety of ecological (pedology, hydrology, climate) circumstances. Altitude of these areas varies within 150 and 700 meters above sea level influencing among others the climate.

In the High-Bakony, the ratio of forested area is 53 percent (35,711 ha). Ridges of High-Bakony heighten over 600 m above sea level, however, nearly 48 percent of forests are located between altitudes of 350–450 m. Rate of forests between 450–550 meters is 15 percent, and above 550 m only 3.5 percent of forest can be found. Rate of forests below the altitude of 350 m above sea level mostly lies between 250 and 350 m; below that the share of forest does not reach the 3 percent. Dominant species are: beech (39 percent), hornbeam (15 percent), Turkey oak (14 percent), and sessile oak (4 percent).

In South-Bakony, the ratio of forests is 48 percent (31,989 ha). Forests can dominantly be found between altitudes of 150 and 450 m. Altitude distribution of forests are as follows, 150–250 m: 29 percent, 250–350 m: 34 percent, 350–450 m: 33 percent, and >450 m: 4 percent. Dominant species are: beech (12 percent), hornbeam (12 percent), Turkey oak (40 percent), and sessile oak (5 percent).

In the lower East-Bakony, the ratio of forested area is only 38 percent (18,132 ha). 42 percent of the forests lie between 250 and 350 m, accordingly to the lower altitude of this region. The ratios of forests below 250 m and above 350 m are 22 and 36 percent, respectively. Dominant species are: beech (9 percent), hornbeam (7 percent), Turkey oak (29 percent), sessile oak (8 percent), downy oak (12 percent), and European black pine (11 percent).

These data clearly show that the share of climate sensitive test species (as beech, hornbeam, Turkey oak, and sessile oak) is the highest in High-Bakony (72 percent), while the ratios of these in South-Bakony and East-Bakony are only 69 and 53 percent, respectively. In latter forest region, drought tolerant tree species (as downy oak, European black pine) significantly appear. While the share of beech (preferring highland, cool, moist climate) is the highest in High-Bakony (39 percent) and lowest in lower East-Bakony (9 percent), the pattern of sessile oak (preferring hilly, warmer climate) is just the opposite.

Respecting that the three regions range from 150 m up to 700 m above sea level, climate categories are definitely separated, caused by vertical changes. In the first stage of our evaluation we have characterized the climate of the regions mentioned above and the stands according to forestry climate classification methods (*Führer*, 2010; *Führer et al.*, 2011a, b) taking into account the growing circumstances of trees. The evaluation is based on precipitation and temperature data in those summer months when physiological processes are in intensive phase and 80–90 percent of organic matter production is realized (May to July) and in those (July, August) when growth of trees are limited by weather extremes. On the basis of meteorological data interpolated to the points of a Hungarian survey aiming the observation of forest stands growing (*Kolozs*, 2009) on a 2.8×2.8 km^2 grid, covering the regions, we have determined the distribution of different climate categories appeared in the examined forest regions by means of *forestry aridity index*, *FAI* (*Führer*, 2010; *Führer et al.*, 2011a) calculated from meteorological parameters in main growth cycle (May-July) and in critical months (July-August). *FAI* can be derived as:

$$FAI = 100 \times \frac{t_{VII-VIII}}{(p_{V-VII} + p_{VII-VIII})} \ , \qquad (1)$$

where $t_{VII-VIII}$ is the mean air temperature in critical months (July and August, °C), p_{V-VII} is the precipitation sum (mm) in the period from May to July, and $p_{VII-VIII}$ is the precipitation sum (mm) in the warmest (critical) months (July and August).

Then, we have collected the production capacities (from 1st to 6th forest yield classes) of state owned forests in different climate categories from the National Forest Database of Hungary, and we have evaluated the potential organic matter production in different climate categories. Test species representing the forestry climate classes were involved in the evaluation, namely the beech (*Fagus sylvatica* L.), hornbeam (*Carpinus betulus* L.), sessile oak (*Quercus petraea* (Matt.) Liebl.), and Turkey oak (*Quercus cerris* L.).

Each forest yield class can be characterized by an annual average yield at the cutting age depending on tree species and actual marketing conditions. The change in yield of wood production and wood marketing is a suitable index for quantification of the economic impact of climate change. For this reason, in the economical evaluation we have determined the estimated yield of the test stands for each yield classes. Principle of the estimation was the yield of timber during wood harvesting operations in cutting cycle. Hence, revenues depend on the species, amount and quality of timber, and assortment composition. Respecting the available data for size and assortment composition of yield, separated for the target stands and for forest yield classes for the whole cutting cycle on the basis of previous investigations (*Márkus* and *Mészáros*, 2000; *Marosi et al.*, 2005), we have calculated the expected revenues. Annual rate of this parameter gives the mean revenues of the given yield class.

The economical influence of spatial realignment of the investigated stands, as a consequence of climate change, can be calculated by the method described above. Consequently, the product of the average annual yield of yield classes and area of the stand give the average yield of the given investigated forest stand.

We can estimate the change of this index in estimating the expected variation in area of different climate categories and the potential production capacity taking into account the climate scenarios. We have calculated with a climate change scenario, where the predicted changes in climate parameters to the reference climate period (1961–1990) are given for the period of 2036–2065. The scenario describes the expected changes in the investigated regions according to the A1B emission scenario of the REMO regional climate model (*Gálos et al.*, 2007). Hence, in the spring months (March to May) the precipitation and air temperature increase by 5 percent and 1.3 °C, respectively, while in summer (June to August) the precipitation decreases by 9 percent together with higher temperature increase of 2.1 °C compared to the period 1961–2010.

3. Results and discussion

3.1. Climate of studied forest stands

The Transdanubian Mountains (Bakony) have temperate cool and wet climate with prevailing wind of NW. In Hungary, forestry practice - depending highly on weather conditions - uses special climate classes; hence the different climate categories are represented by climate indicator test species. Accordingly, the coolest/most humid and warmest/most arid climates are represented by beech and forest-steppe climate, respectively. In the middle there are hornbeam-oak climate close to *beech*, and sessile oak-Turkey oak close to forest-steppe climate. The yearly precipitation of originally treeless forest-steppe climate zones is not enough for production of native species, while sessile oak-Turkey oak climate is represented by these two species either together or separately. Precipitation and temperature characteristics of different climate categories are described in details by *Führer et al.* (2010, 2011a). On the basis of homogenized and interpolated meteorological data, the climate and the expected changes in different regions of Bakony can be characterized as follows.

In High-Bakony region the average yearly precipitation and the annual mean air temperature were 737 mm and 8.8 °C, respectively, between 1961 and 1990. Both are in the interval representative for beech climate (752±31 mm, 8.8±0.9 °C). The average temperature in the main growing period (16.1°C, May-July) and in critical months (18.0 °C, July-August) are lower than the averages of beech climate categories (16.6±0,8 and 18.5±0,8 °C). Precipitation amount for the same period (226 and 158 mm) are 10 and 5 percent lower than representative value for beech climate (259±13 and 167±9 mm). The main *FAI* for this region is 4.69 close to the upper limit of beech climate category (FAI_B: ≤4.75). On the basis of *FAI* calculated for the climate reference period (1961–1990) a total of 59 percent of this region lies in beech climate, while remaining part can be represented by hornbeam-oak climate (*Fig. 2*). In case of climate change according to the predicted scenario, the mean of *FAI* increases up to 5.59 hence there will be no longer beech climate in that region, moreover, 13 percent of the High-Bakony will be represented by sessile oak-Turkey oak climate.

beech *FAI*: ≤ 4.75 | hornbeam-oak *FAI*: 4.75–6.00 | sessile oak-Turkey oak *FAI*: 6.00–7.25 | forest steppe *FAI*: > 7.25

Fig. 2. Distribution of climate classes according to *FAI* in the examined forest regions; left: in the reference years (1961–1990), right: in case of the predicted scenario.

In the South-Bakony region, the average yearly precipitation and the annual mean air temperature were 693 mm and 9.4 °C, respectively, between 1961 and 1990 corresponding to the averages of hornbeam-oak climate (663±55 mm, 9.4±0.7 °C). Average temperature in the main growing period (May-July) is 16.7°C, while in the critical months it is 18.6 °C, i.e., temperature circumstances are representative rather for the cooler *beech* climate. However, precipitation data in the same period (219 and 150 mm) is representative again for hornbeam-oak climate (218±15 and 139±13 mm). For this region the *FAI*, as an overall index, is 5.03 refering to the hornbeam-oak climate (4.75–6.00). The share the climate classes here is 20 percent beech and 80 percent hornbeam-oak. In case of climate change scenario, the predicted average *FAI* increases up to 5.98, which is practically at the borderline between the hornbeam-oak and the sessile oak-Turkey oak climates. In this case, 44 percent of the region would be representative for hornbeam-oak and the remaining part to the sessile oak-Turkey oak climate. On the basis of this prediction, total extinction of beech zone is expected (*Fig. 2*).

In the East-Bakony region, the average yearly precipitation and the annual mean air temperature were 634 mm and 9.3 °C, respectively, between 1961 and 1990. These values are close to hornbeam-oak climate (663±55 mm, 9.4±0.7 °C), similarly to the average temperature in main growing period (17.3 °C) and in critical months (19.4 °C). On the other hand, the precipitation amount in these months are lower (198 and 132 mm) than favorable for hornbeam-oak climate (218±15 and 139±13 mm). Average *FAI* in this region is 5.88 close to the borderline between the hornbeam-oak and sessile oak-Turkey oak climates (6.00). The share of the beech, hornbeam-oak, and sessile oak-Turkey oak climates in this region is 2, 51, and 47 percent, respectively (*Fig. 2*). In case of the predicted climate scenario, the average *FAI* changes to 6.95 and the share of different climate categories would change to hornbeam oak: 9, sessile oak-Turkey oak: 51, and forest steppe: 9 percent ratios.

Average *FAI* for the total areas of the three regions (High-, South-, and East-Bakony) in the reference years is 5.09, lying in the favorable side of hornbeam-oak climate (close to the beech climate). This value would change to 6.05 (nearly by one *FAI* unit) in case of the predicted climate scenario. It means that, in the area of the three regions, 30 percent of beech climate would disappear, the share of hornbeam-oak climate would decrease from 58 to 52 percent; the ratio of sessile oak-Turkey oak climate would increase from 12 to 32 percent, while forest steppe climate would appear sharing 10 percent in the region.

The total surface area of the three Bakony regions is 179,621 ha; ratio of forested areas is 48 percent (85,752 ha). In our study only the state owned forests (64,957 ha) are involved, where the share of beech, hornbeam-oak, and sessile oak-Turkey oak climates are 36, 57, and 7 percent, respectively. Classification of the Forest Database (*MGSZH*, 2008) based on climate indicator tree species differsfrom our results: the share of the climate is 41 percent beech, 33 percent hornbeam-oak, and 26 percent sessile oak-Turkey oak climate (*Table 1*).

Table 1. Distribution of forest yield classes according to the forest management plan and the *FAI* for state owned forests in the examined regions (in percent)

climate classes	High-Bakony		South-Bakony		East-Bakony		Bakony	
	plan	*FAI*	plan	*FAI*	plan	*FAI*	plan	*FAI*
beech	78	67	17	23	15	3	41	36
hornbeam-oak	21	33	44	77	36	70	33	57
sessile oak-Turkey oak	1	0	39	0	49	27	26	7

Regarding this distribution in lower scale, the differences are higher. In High-Bakony, 78 percent of the state owned forest are in beech zone, followed by hornbeam-oak climate (21 percent) and the ratio of sessile oak-Turkey oak climate is only 1 percent. In contrast in South-Bakony, hornbeam-oak climate is the dominant (44 percent), while ratio of sessile oak-Turkey oak and beech climates is 40 and 16 percent, respectively. In the East-Bakony region, the share of climate zones is: 49 percent of sessile oak-Turkey oak, 36 percent of hornbeam-oak, and only 15 percent of beech.

Classification according to forestry aridity index (FAI, Eq. 1) differs from figures above. Taking into account the period of 1961-1990 as reference, the ratio of the beech climate in High-Bakony, South-Bakony, and East-Bakony are 67, 21, and 2 percent respectively. The ratio of the hornbeam-oak climate is highest in South-Bakony (77 percent), a little lower in East-Bakony (71 percent), while in High-Bakony it is only 33 percent. Significant share of sessile oak-Turkey oak climate can be found in East-Bakony (27 percent).

It seems that the difference between the two classifications is lower for High-Bakony with cooler and wet climate, compared to the other two drier and warmer Bakony regions (*Table 1*). Remarkable, that for latter regions the sessile oak-Turkey oak climate shares significant areas according to the forest management classification plan (South-Bakony 39; East-Bakony 49 percent). Explanation for this is that in forestry practice, the sessile oak-Turkey oak climate was classified according solely to the Turkey oak species. In contrast, nowadays, owing to the appropriate forestry practice the majority of Turkey oak trees can be found in hornbeam-oak climate zones. Reasons can be traced back to the practice in the 19th and 20th centuries, when two of the main aims were to satisfy the rapidly increasing firewood demand and the utilization of rich acorn yield as mast (rearing of pigs).

The difference between the two classifications underlines the necessity that the data in Forest Database – possible subjects of modification according to the actual species selection policy – must be supervised in the future. It is also important, since the reference basis in evaluation of impact of expected climate change in connection to tree species may have high influences to the outcome, i.e., the measure of changes.

3.2. Composition of production capacity of regions and its change according to the predicted climate scenario in state owned forests

3.2.1. Production capacity of tree species of different regions

Wood production capacity of a given site is characterized by the sum of annual average growth calculated up to the critical cutting age, and it can be classified into good (1st and 2nd), medium (3rd and 4th), and poor (5th and 6th) classes. On the basis of the Forest Database, the investigated regions can be characterized as follows, good: 24, medium: 40, and poor: 36 percent (MGSZH 2008) (*Fig. 3*). More favorable conditions are in High-Bakony, where share of classes 1st and 2nd is 46 percent, in contrast with other two regions where only 8–9 percent of trees are in the good classes. In East-Bakony, 65 percent of trees are in the poor category, where circumstances for production are less favorable mainly due to the unfavorable, climate for the given species composition. In South-Bakony, the majority of stand belongs to the medium (48 percent) and poor (43 percent) categories.

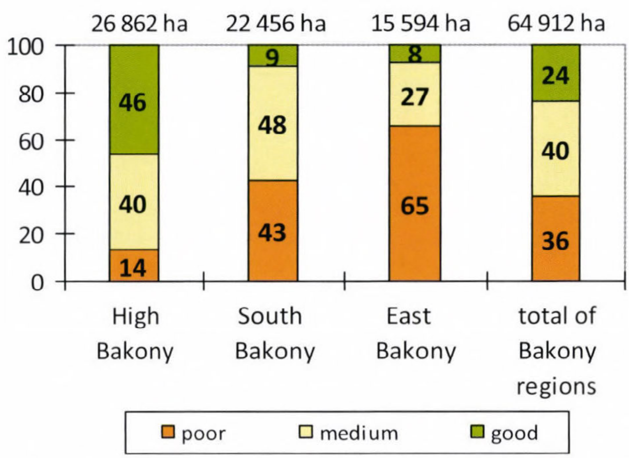

Fig. 3. Distribution of forest yield classes in the *Bakony* regions (in percent).

On the basis of distribution of forest yield classes (from 1st to 6th), the calculated average production capacity index (average of area weighted yield classes) in High-Bakony is 3.1, in South-Bakony its value is 4.2 due to the more unfavorable ecological conditions, and it is the worst in East-Bakony (4.9), as a consequence of most unfavorable conditions in this region. It is evident, because the share of different climate categories differs for the different regions (*Table 2*), and the production capacities of climate categories are also different (beech climate: 2.9, hornbeam-oak climate: 4.3, and Turkey oak- sessile oak climate: 5.1).

Respecting the large differences among the climate conditions for the different investigated regions, we have examined whether these differences appear in production capacity of test species. Area covered by test species in the state owned forests is 44,884 ha, with largest share of Turkey oak (17,941 ha), followed by beech (15,459 ha), hornbeam (7,516 ha), and sessile oak (3,968 ha).

It is evident, that among the three regions the structure of forest yield classes of test species is most favorable in High-Bakony, where the share of good class is the highest, while poor categories represent the lowest area (*Fig. 4*). Conversely, the worst conditions are in East-Bakony. Average production capacity index for beech is 2.5, 3.1, and 3.3 in High-, South-, and East-Bakony, respectively. Difference among regions is higher in case of Turkey oak, where indices for the regions above are 3.3, 4.3, and 5.0. For all of four test species the difference is larger between High- and South-Bakony than between South- and East-Bakony, showing that climate of latter two regions are closer and highly differs from that of High-Bakony. Average tree production capacity index for the group of three regions is the lowest for beech (2.6), followed by hornbeam (3.5), sessile oak (4.0), and Turkey oak (4.2).

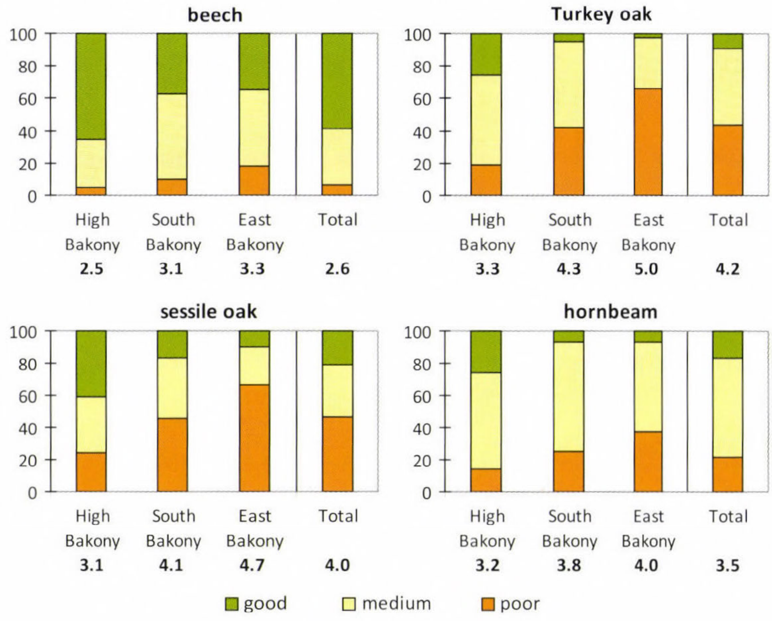

Fig. 4. Structure of forest yield classes in the examined regions (in percent).

3.2.2. Expected change in production capacity of test species for the examined regions

As it was mentioned above, four test species only in areas of state owned forests were involved in evaluating the change of area of climate classes according to the predicted climate scenario. Share of state owned forests in the three regions is 52 percent. On the basis of evaluation, the ratio of good yield classes decrease in the direction from beech to sessile oak-Turkey oak climate for four test species (*Fig. 5*). Ratio of stands in poor categories is considerably increased for hornbeam, sessile oak, and Turkey oak. For beech in Turkey oak climate, even the ratio of medium category remarkably increases as well. Certainly, the effect of climate involving the effectiveness of precipitation is influenced by the properties of underlying soil in high extent. E.g., there are stands in poor class in soils with thin organic layer or with wrong mechanical parameters even in favorable climate conditions; and vice versa, stands over deeper and better structured soils can utilize the precipitated water effectively, increasing the organic matter production.

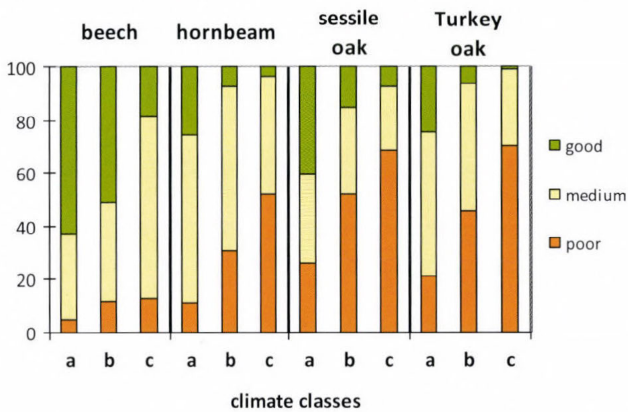

Fig. 5. Distribution of climate indicator tree species in the climate classes according to forest yield classes (in percent). Climate classes: a= beech, b=hornbeam-oak, c=sessile oak-Turkey oak.

By means of the aridity index (*FAI*), we can predict that majority of *beech* climate –calculated using the basic climate reference period (1961–1990) – will be moved to hornbeam-oak climate as a consequence of even a minor summer temperature increase at the examined three Bakony regions. According to the predicted scenario, when higher temperature increase and minor decrease in precipitation amount can be expected in summer season, the beech climate completely disappears, all of them will be moving towards hornbeam-oak climate. In turn, half area of former hornbeam-oak climate will be dominated by Turkey oak climate. Accordingly, the climate dependent tree production capacity most likely changes; pattern of forest yield class of beech climate declines to hornbeam-oak, while latter declines to sessile oak-Turkey oak climate (*Fig. 6*). Namely, we can expect a decrease in production capacity of stands, even at constant soil properties; i.e., area of good production capacity decreases from 12,781 to 5,058 ha, together with an increase of poor area from 12,339 to 21,401 ha.

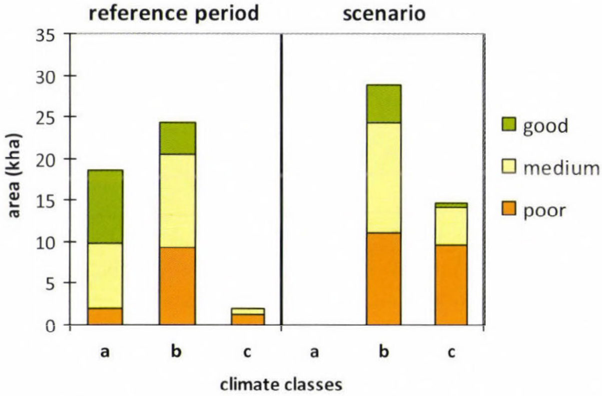

Fig. 6. Distribution of forest yield classes in climate classes in the reference period (1961–1990) and in case of predicted scenario. Climate classes: a= beech, b=hornbeam-oak, c=sessile oak-Turkey oak.

3.2.3. Yield indices of test species and their change in the investigated forest regions

It can be clearly seen from the specific revenues of forest yield classes calculated for the four climate indicator tree species (beech, hornbeam, Turkey oak, and sessile oak), that revenues for beech and sessile oak in good (1st and 2nd) classes is remarkably higher than that of for hornbeam and Turkey oak (*Marosi et al.*, 2005) (*Table 2*).

Table 2. Average revenues of forest yield classes for each climate indicator tree species (in kHUF ha^{-1} $year^{-1}$) (*Marosi et al.*, 2005)

yield classes	beech	hornbeam	sessile oak	Turkey oak
1st	129	55	129	62
2nd	108	46	108	53
3rd	77	37	83	42
4th	62	29	68	35
5th	43	21	51	25
6th	29	16	37	19

From the point of view of wood industry, the beech and oak are much more valuable than the hornbeam and Turkey oak, however the difference is continuously decreasing to the direction of less favorable ecological circumstances, more in case of beech and less for sessile oak. As previous investigations in Hungary have shown, stands in poor yield classes (5th and 6th) still do not produce any profitability.

For the 45 kha of state owned forests in the three Bakony regions, based on revenues concerning to different yield classes, we have estimated the expected economical effect of the climate change according to the forecasted scenario. As it has already been demonstrated, the expected climate change reduces the production capacity of forests. In practice, it appears in the change of the ratio of different forest yield classes. Area of good classes significantly decreases with parallel increase of poor classes, hence, available revenues decreases accordingly, as lumbered wood volume and the ratio of more valuable wood assortments decrease as well (*Fig. 6*). Specific expenses of forest management do not change significantly hence the fewer revenues appear in the decrease of profitability. In this study we disregard the case when ecological changes require the change (replace) of tree species. Naturally, in this case as a consequence of further increase of expenses, profitability would be even less depending on kind of tree species and on the technology applied.

Referring the average change of revenues to ha unit, it is highest for sessile oak (7.893 kHUF ha^{-1}, followed by beech (6.941 kHUF ha^{-1}), hornbeam (4.098 kHUF ha^{-1}), and Turkey oak (3.920 kHUF ha^{-1}) (*Fig. 7*).

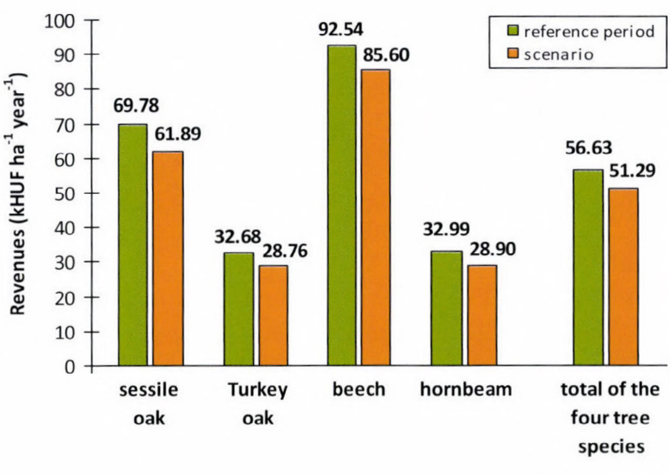

Fig. 7. Average annual revenues of test species in the examined forest regions in the reference period (1961–1990) and in case of the predicted scenario.

Calculating with the scenario predicted, the revenues will be lower by 9.4 percent for the four test species. It means that the state forest companies expect only 2.302 billion HUF (10.56 million USD) instead of 2.542 billion HUF (11.66 million USD) in the 45 kha area for the middle of this century, at the present price level. This rate of deficit may query the profitability of forest management. The four test species respond to the climate changes in different extent; highest deficit can be expected for Turkey oak and lowest for beech.

4. Conclusions

The predicted climate change probably influences the profitability of forest management besides the ecological circumstances of forested areas. We have estimated the expected changes to the A1B climate scenario for the case of test species locating in a group of Hungarian forest regions (High-, South-, and East-Bakony). The average measure of the predicted scenario between years of 2036–2065 compared to the reference period (1961–1990) is the follows: in the spring months (March-May) the precipitation decreases by 5 percent, the air temperature increases by 1.3 °C, while in the summer months (June-August) the precipitation decreases by 9 percent parallel with a dramatic temperature increase of 2.1 °C.

The average calculated forestry aridity index (*FAI*) for the three investigated Bakony regions in the reference period (1961–1990) is 5.09 favoring to hornbeam-oak climate. In these areas the dominating climate zones are *beech* (36 percent), hornbeam-oak (57 percent), and sessile oak-Turkey oak (7 percent) (*Fig. 2*).

On the basis of the predicted scenario, *FAI* increases to 6.05 extremely enlarging the share of sessile oak-Turkey oak zones dominating in East-Bakony, while hornbeam-oak climate will be representative in High-Bakony. In South-Bakony, hornbeam-oak and sessile oak climates will equally be characteristic.

As to the productivity we find the best conditions in High-Bakony (*Fig. 3*), where the ratio of good yield classes is higher, in contrast with the two other regions, where good classes share the lowest ratio of areas. Two-third of East-Bakony areas belong to the poor yield classes.

According to the assessment of climate, classes the ratio of good classes definitely decreases from beech to sessile oak climate in case of four climate indicator species (*Fig. 4*). At the same time, the share of poor yield classes significantly increases for hornbeam, sessile oak, and Turkey oak.

As a response to climate change – according to the scenario discussed – we expect a shift in climate classes resulting in decay in production capacity even at constant soil conditions, i.e., share of good classes decreases with parallel increase of poor classes.

For the four climate indicator tree species, the annual average revenues will be lower by 9.4 percent compared to the reference period in the forecasted interval (*Fig. 7*). There are two reasons of that, on one hand the volume of yield, and on the other, the ratio of valuable assortments will also be lower.

The respond of four species are different. In the case of predicted climate scenario, the highest decay in production capacity will be expected for Turkey oak (12 percent), while the lowest for the beech (7.5 percent).

Expected unfavorable ecological effect of climate change can be a high risk for forest management. Today, the conservation of forests can be financed exclusively by revenues of selling wood products on the market. If the revenues decrease as calculated above and there will not be other available sources to finance then the steady maintenance of forests will be questionable in lack of profitability of forest management.

Acknowledgements–our research was supported by NKTH-OTKA_A_08-2-2009-0054 (80305-80335) and by the TÁMOP-4.2.2/08/1-2008-0020 projects.

Refrences

Bartholy, J., Pongrácz, R., Torma, Cs., Pieczka, I., Kardos, P., and *Hunyady, A.*, 2009: Analysis of regional climate change modelling experiments for the Carpathian basin. *Int J Glob Warming 1*, 238–252.

Berki, I., Rasztovits, E., Móricz, N., and *Mátyás, Cs.*, 2009: Determination of the drought tolerance limit of beech forests and forecasting their future distribution in Hungary. *Cereal Res. Commun. 37*, 613–616.

Czúcz., B., Gálhidy, L., and *Mátyás, Cs.*, 2011: Present and forecasted xeric climatic limits of beech and sessile oak distribution at low altitudes in Central Europe. *Ann. For. Sci. 68*, 99–108.

Csóka, Gy., 1996: Aszályos évek – fokozódó rovarkárok erdeinkben. *Növvéd 32*, 541–551.(in Hungarian)

Csóka, Gy., 1997: Increased insect drought impact damage in Hungarian forests under drought impact. *Biologia 52*, 159–162.

Csóka, Gy., Koltay, A., Hirka, A., and *Janik, G.*, 2007: Az aszályosság hatása kocsánytalan tölgyeseink és bükköseink egészségi állapotára. In (*Mátyás Cs., Vig P.* (Eds.)), Proceedings of the 5th Forests and Climate Conference, Nyugat-Magyarországi Egyetem, Sopron, 229–239.

Csóka Gy., Koltay A., Hirka A., and *Janik G.*, 2009: Az aszályosság hatása kocsánytalan tölgyeseink egészségi állapotára. *„KLÍMA-21" Füzetek 57*, 64–73. (in Hungarian)

Faragó T., Láng I., and *Csete L.* (Eds.) 2010: Climate Change and Hungary: Mitigating the Hazard and Preparing for the Impacts (the „VAHAVA" Report http://www.unisdr.org/files/18582_thevahavareport08dec2010.pdf

Führer E., 1995: Az idôjárás változásának hatása az erdők fatermő képességére és egészségi állapotára. *Erd Lapok 130*, 176–178. (in Hungarian)

Führer, E., 2010: A fák növekedése és a klíma. *„KLÍMA-21" Füzetek 61*, 98–107. (in Hungarian)

Führer, E. and *Járó, Z.*, 1992: Auswirkungen der Klimaänderung auf die Waldbestände Ungarns. *Österreichische Forstztg 9*, 25–27.

Führer, E., Mátyás, Cs., Csóka, Gy., Lakatos, F., Bordács, S., Nagy, L., and *Rasztovits, E.*, 2010: Current status of European beech (*Fagus sylvatica* L.) genetic resources in Hungary. *Communicationes Instituti Forestalis Bohemicae 25*, 152–163.

Führer, E., Horváth, L., Jagodics, A., Machon, A., and *Szabados, I.*, 2011a: Application of a new aridity index in Hungarian forestry practice. *Időjárás 115*, 103–118.
Führer, E., Marosi, Gy., Jagodics, A., and *Juhász, I.* 2011b: A klímaváltozás egy lehetséges hatása az erdőgazdálkodásban. *Erdtud. Közl. 1*, 17–28. (in Hungarian)
Gálos, B., Lorenz, Ph., and *Jacob, D.*, 2007: Will dry events occur more often in Hungary in the future? *Envir Res Lett 2*, 034006.
Gálos, B., Mátyás, Cs., and *Jacob, D.*, 2012: Az erdőtelepítés szerepe a klímaváltozás hatásának mérséklésére. *Erdtud Közl 2*, 35–45. (in Hungarian)
Hirka, A. and *Csóka, Gy.*, 2010: Abiotikus károk Magyarország erdeiben. *Növvéd. 46*, 513–517.
Járó, Z., 1972: Az erdészeti termőhelyértékelés rendszere. In (*Danszky, I.* (Ed.)) Erdőművelés. Mezőgazdasági Kiadó, Budapest, 47–256. (in Hungarian)
Kolozs, L., (Ed.) 2009: *Erdővédelmi Mérő- és Megfigyelő Rendszer (Emmre) 1988–2008*. MGSZH Központ Erdészeti Igazgatóság, Budapest, Hungary, 1–161. (in Hungarian)
Manninger, M., 2004: Erdei fák éves és korszaki növekedésmenete és kapcsolódása egyes ökológiai tényezôkhöz In (*Mátyás, Cs.* and *Vig, P.*, (Eds.)), Proceedings of the 4th Forests and Climate Conference, Nyugat-Magyarországi Egyetem, Sopron, 151–162.
Márkus, L., and *Mészáros, K.*, 2000: Erdőérték-számítás. Mezőgazdasági Szaktudás Kiadó, Budapest. (in Hungarian)
Marosi, Gy., Solymos, R., Rédei, K., Führer, E., Molnár, S., Pásztory, Z., and *Juhász, I.*, 2005: A fatermesztés és faanyaghasznosítás modelljeinek kidolgozása célállományonként.. In (*Molnár, S.*, (Ed.)) Erdő-fa hasznosítás Magyarországon. Nyugat-Magyarországi Egyetem, Faipari Mérnöki Kar, Sopron, 377–386. (in Hungarian)
Mátyás, Cs., 2010: Forecasts needed for retreating forests. *Nature 464*, 1271.
Mátyás, Cs. and *Czimber, K.*, 2000: Zonális erdőtakaró mezoklíma szintű modellezése: lehetőségek a klímaváltozás hatásainak előrejelzésére. In (*Tar, K.*, (Ed.)) Proceedings of the 3rd Forests and Climate Conference, Debreceni Egyetem, Debrecen, 83–97. (in Hungarian)
Mátyás, Cs. and *Czimber, K.*, 2004: A zonális alsó erdôhatás klímaérzékenysége Magyarországon – előzetes eredmények. In (*Mátyás, Cs.* and *Vig, P.* (Eds.)) Proceedings of the 4th Forests and Climate Conference. Nyugat-Magyarországi Egyetem, Sopron, 35–44.
Mátyás, Cs., Berki, I., Czúcz, B., Gálos, B., Móricz, N., and *Rasztovits, E.*, 2010a: Future of beech in Southeast Europe from the perspective of evolutionary ecology. *Acta Silvatica et Lignaria Hungarica 6*, 91–110.
Mátyás, Cs., Führer, E., Berki, I., Csóka, Gy., Drüszler, Á., Lakatos, F., Móricz, N., Rasztovits, E., Somogyi, Z., Veperdi, G., Vig, P., and *Gálos, B.* 2010b: Erdők a szárazsági határon. *„KLÍMA-21" Füzetek 61*, 84–97. (in Hungarian)
Mátyás, Cs., Berki, I., Czúcz, B., Gálos, B., Móricz, N., and *Rasztovits, E.* 2011: Assessment and projection on climate change impacts in SE European forests. a case study of common beech (*Fagus sylvatica* L.). *Revija za Lesno Gospodarstvo 63*,142–153.
MGSZH, 2008: Országos erdőadattár 2006. 01. 01. állapot. MGSZH Központ Erdészeti Igazgatóság, Budapest, Hungary (CD-ROM edition). (in Hungarian)
Molnár, M. and *Lakatos, F.*, 2009: A bükkpusztulás Zala megyében – klímaváltozás? *„KLÍMA-21" Füzetek 57*, 74–82. (in Hungarian)
Pieczka, I., Pongrácz, R., and *Bartholy, J.*, 2011: Comparison of simulated trends of regional climate change in the Carpathian Basin for the 21st century using three different emission scenarios. *Acta Silvatica et Lignaria Hungarica 7*, 9–22.
Rasztovits, E., Móricz, N., Berki, I., Pötzelsberger, E., and *Mátyás, Cs.*, 2012: Evaluating the performance of stochastic distribution models for European beech at low-elevation xeric limits. *Időjárás 116*, 173–194.
Solymos, R., 2009: A klímaváltozás hatása az erdők fanövedékére. *„Klíma-21" Füzetek 56*, 43–47. (in Hungarian)
Somogyi, Z., 2009: A klíma, a klímaváltozás és a fanövekedés néhány összefüggése. *„Klíma-21" Füzetek 56*, 48–56. (in Hungarian)

IDŐJÁRÁS

Quarterly Journal of the Hungarian Meteorological Service
Vol. 117, No. 1, April–June 2013, pp. 175–186

Regional differences between ambient temperature and incidence of Lyme disease in Hungary

Attila Trájer[1*], **János Bobvos**[2], **Katalin Krisztalovics**[3], and **Anna Páldy**[2]

[1*]*Semmelweis University, Budapest, Hungary*
1085 Budapest, Üllői str. 26.

[2]*National Institute of Environmental Health, Budapest, Hungary*
1097 Budapest, Gyáli str. 2–6.

[3]*National Centre of Epidemiology, Budapest, Hungary*
1097 Budapest, Gyáli str. 2–6.

**Corresponding author E-mail: trajer.attila@oki.antsz.hu*

(Manuscript received in final form December 18, 2012)

Abstract–The regional climate impacts on Lyme borreliosis (LB) or Lyme disease have not been studied yet in Hungary. By this study we want to contribute the assessment of the impact of climate change on vector-borne diseases. Our aim was to assess the influence of regional spatial-temporal differences of annual temperature conditions, as well as the start of the vegetation season on LB. We created climatic contrast by selecting three southwestern (Zala, Somogy, Baranya; henceforth: SW) and two northeastern (Nógrád and Borsod-Abaúj-Zemplén: NE) counties in Hungary. Weekly LB data and the site of infection on county level for 1998–2010 were gained from the National Epidemiologic and Surveillance System. The temperature data were retrieved from the European Climate Assessment and Dataset. The regional differences of the weekly LB incidence were studied in relation to regional temperature differences. Descriptive statistics, linear and polynomial regression models were applied.

We observed a 1.6 °C difference in the mean winter temperatures between the two regions: the mean winter temperature of the NE counties was under 0 °C, in the SW counties it was more than 1 °C. In the SW counties spring warming started 2 weeks earlier, and there were only 3 weeks in the year, when the weekly mean temperature sank below 0 °C by few tenths of a degree. In the NE counties, this period lasted for 8 weeks continuously.

The first day with mean temperature of 10 °C followed by days with mean temperature >8 °C was chosen as start of spring. Based on this criterion and according of a linear regression model, in 2010 spring started by 2.5 weeks earlier in the two NE counties, less than 1 week earlier in the three SW counties compared to the beginning year of 1998. A difference of 3 weeks was observed in the detection of 10 cases of LB per week between the 2 NE and 3 SW counties, and there was a 3-4 weeks difference between the annual LB maxima. Comparing the periods of 1998–2003 and 2005–2010, the peak of the LB season sifted from the 28th to the 29th weeks in the NE counties, while in the SW counties this shift did not reach one week difference. In the NE counties, the cumulative LB incidence showed a 25.68 % increase in periods 1999–2004 and 2005–2010 in the SW counties the same increase was 30.55%.

Key-words: Lyme borreliosis, regional climatic differences, *Ixodes ricinus,* indicator species, vector-borne disease, climate change

1. Introduction

Lyme borreliosis (LB) is one of the most common vector-borne diseases in Europe. Due to the environmental sensitivity of the species of the *Ixodes* genus, these organisms and tick-borne diseases are one of the most useful climate or climate change indicators for the Northern Hemisphere (*Brownstein et al.*, 2005*; Donnelly et al.*, 2004; *English et al.*, 2009*; Kovats*, 2003; *Lindgren* and *Jaenson*, 2006;). The arthropod vectors and consequently, the vector-borne diseases are also sensitive to climatic conditions (*Rogers* and *Randolph*, 2006).

Lyme borreliosis (LB) is the most common arthropod-borne human infection in Hungary. The geographic distribution is a very important characteristic of the host and vector populations and the human transmission of LB (*James et al.*, 2010). *Stafford et al.* (1998) found that the incidence of Lyme disease positively correlated with tick abundance which showed an increasing tendency since the 1990's in Europe (*Randolph* , 2004; *Confalonieri*, 2007). In Hungary, as in Western Europe, *Ixodes ricinus* Linnaeus (1758) is the main vector of LB, but *Dermacentor reticulatus* Fabricius (1794) is a common vector tick as well (*Földvári et al.*, 2007).

As a kind of external parasites, the complex three-stage onthogeny of *Ixodes* ticks occurs in the environment, the spatial-temporal distribution of ticks in the nature depends on climatic and ecologic conditions (*Estrada-Pena,* 2008). *Kalluri et al.* (2007) discovered a strong seasonal association between the time of the annual maximum of weekly LB incidences occurring during the summer and fall months, when the nymphs are most active and the seasonal temperature and precipitation change. *Duffy* and *Campbell* (1994) found that 4 °C was the threshold of the activity of *Ixodes scapularis* Say (1821) in the milder winter days. According to *Lindgren* and *Gustafson* (2001), the threshold temperature of questing (food-seeking) tick activity was at 7–8 °C, *Perret et al.* (2000) came to a very similar conclusion (between 6.6 and 8 °C). Ambient temperature is one of the most important factors of the tick activity mainly in spring (when the relative humidity and soil moisture are appropriate for the ticks), but to explain the absolute annual LB case number, the ambient temperature is insufficient.

For the prediction of the expected effects of the future climate change on LB, it is essential to study the existing geographical differences in the LB seasons to investigate the weekly, cumulative LB incidence rates based on the present regional climate differences, and to observe the probable different seasonality of LB by regions. In our study we aimed at these observations.

2. Data and methods

2.1. Data and statistics

The weekly data of LB for 1998–2010 were retrieved from the National Epidemiologic and Surveillance System. The daily temperature data in 25 km grids are from the European Climate Assessment and Dataset (*Tank et al.*, 2002; *Haylock et al.*, 2008). Regional differences in the weekly LB incidence were studied in two northeastern and three southwestern counties in Hungary. In our study we used descriptive statistics, and the associations were analyzed by linear and polynomial regression models using SPSS 10.0 software.

2.2. Selection of the studied counties

We selected counties with similar level of forestation, number of inhabitants, and order of LB incidence. The cumulative number of population of the three southwestern (SW) counties (Zala, Somogy, Baranya) was 1,002,977 inhabitants in 2010 and the number of population of the northeastern (NE) counties (Nógrád, Borsod-Abaúj-Zemplén) was 897,688 inhabitants (*KSH*, 2010) in the same year (2010). To calculate the LB incidences we used the population numbers of 2010. The population ratio of the NE/SW counties was 0.895 – a slight difference (10.5%) exists between the two study regions.

The mean forestation of the 3 SW counties (27.74%) and the forest cover of the 2 NE counties (32.70%) are very similar, only a 15.16% difference exists (*Komarek*, 2005).

The difference between the cumulative LB incidences in period 1998–2010 of the 2 regions is not too high (NE counties: 298.99/100.000 and SW counties: 244.73/100.000), 18.2% difference exists. So, the difference of the mean forestations and the cumulative LB incidences was similar: 15.16% – 18.2% for the 13-year period.

3. Results

3.1. Differences between the weekly ambient temperatures

The comparison of the monthly mean temperature of the 3 southwestern and 2 northeastern counties (*Fig. 1*) in period 1998–2010 showed differences mainly in winter, early spring, and autumn seasons. The biggest difference was that in the southwestern counties, the January mean temperature did not exceed the 0 °C limit (*Fig. 2*). In the case of Zala, Baranya, and Somogy counties (SW), the winter was milder than in the NE counties. While in the SW counties the mean weekly temperature of winter months fluctuated near 0 °C, in the NE counties it sank to between –1 and –2 °C. The two curves met at the 13th week of the year. The mean summer temperatures were the same in both regions, althought the autumn was milder in the SW counties. From November to the end of March, the weekly mean temperature differences of the examined 13 years reached 1 °C.

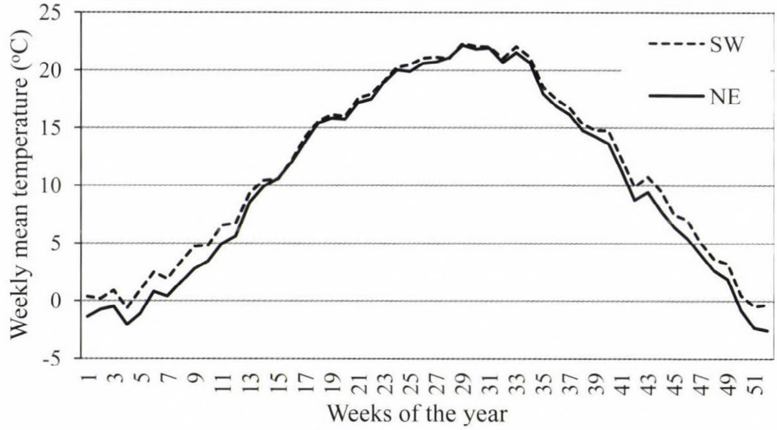

Fig. 1. Weekly mean ambient temperatures in the SW and NE counties in Hungary, in 1998–2010.

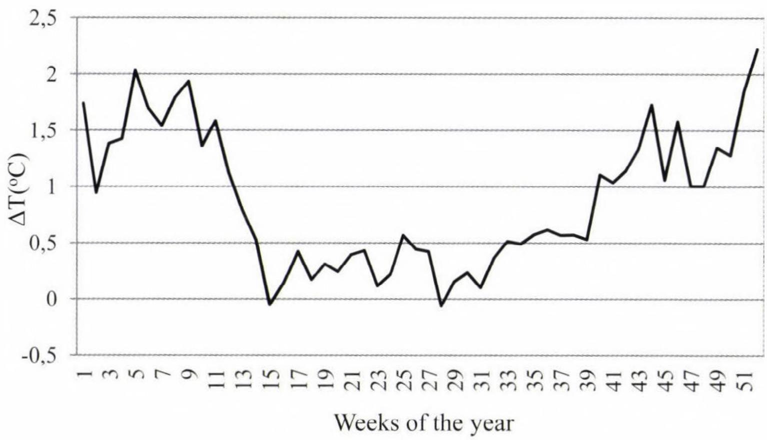

Fig. 2. Differences in the weekly mean temperatures between the SW and NE counties in Hungary, in 1998–2010.

The mean winter temperature was 1.2 °C in the 3 southwestern counties in period 1998–2010, respectively it was –0.3 °C in the 2 NE counties, the difference was 1.6 °C with a dispersion of 1.1 °C (*Fig. 3*). Due to the similar climatic influence and the small geographical distance (the nearest distance is about 100 km and the greatest distance is about 400 km), the correlation between the mean winter temperatures of the two regions was very strong ($R^2=0.9554$, $P<0.0001$; *Fig. 4*).

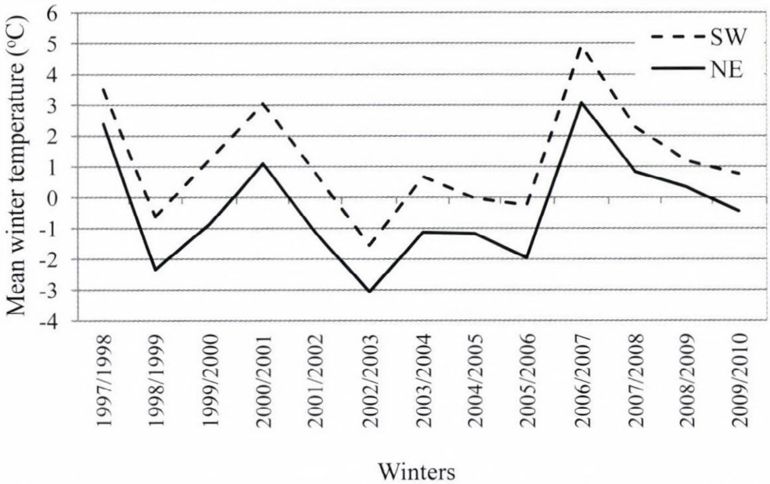

Fig. 3. Mean winter temperatures in the SW and NE counties in Hungary, in 1998–2010.

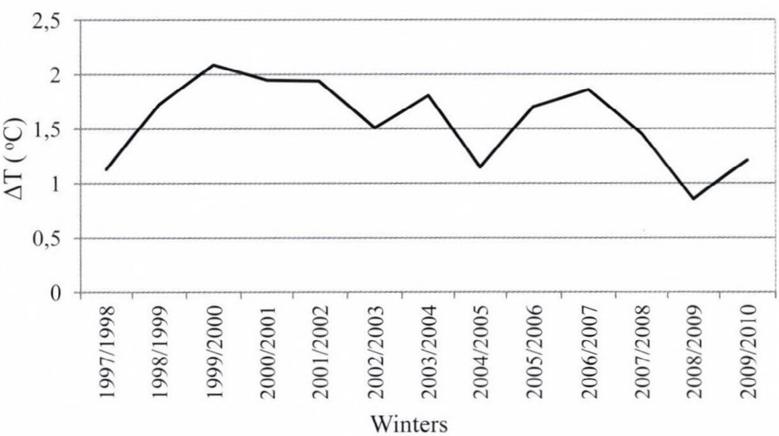

Fig. 4. Differences in the mean winter temperatures between the SW and NE counties in Hungary, in 1998–2010.

3.2. *The shift of the start of the LB season*

Our previous observations showed that the incidence rate of 0.1/100.000 is a good indicator of the onset of LB season, and usually coincides with the first stable spring week with a mean temperature of 10 °C, followed by a week with mean temperature equal or more than 7–8 °C. Therefore we used this criterion as the onset of spring. During 1998–2010, this indicator week shifted from the 16.5th week to the 14th week of the year defined by the linear regression model (P=0.0172), in the case of the NE counties. However, this shift was not significant in the SW counties, where the indicator week shifted from the 14.2nd week to the 13.6th week of the year (*Fig. 5*).

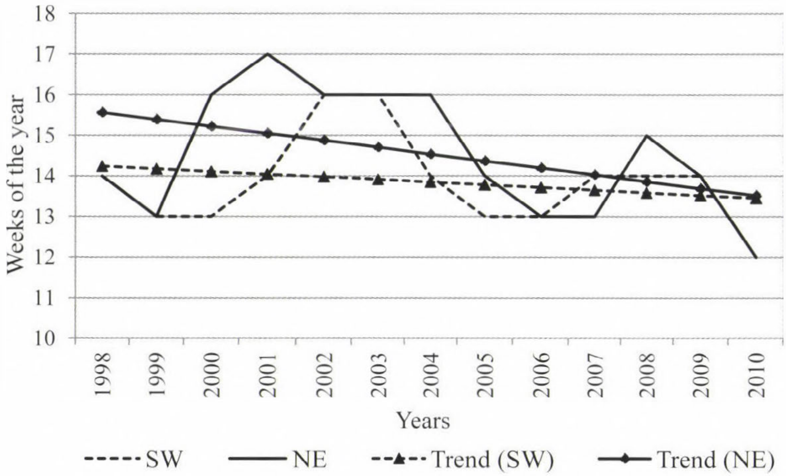

Fig. 5. Shift of the start of the vegetation period based on the temperature> 7–8°C requirement of the questing activity of *Ixodes* ticks in the SW and NE counties in Hungary, in 1998–2010.

3.3. Differences and trends in the regional LB incidences

In periods 1998–2004 and 2005–2010, the percent increase of the cumulative LB incidences showed very heterogenous trends in the different Hungarian counties (*Fig. 6*). In both regions a growing trend could be seen, with P=0.0065 and 0.0471 in the SW and NE counties, respectively. From 1998 to 2010, the trend was consistent in the 3 SW counties, however, no trend could be observed in the 2 NE counties before 2007, and each trend had borderline signficance.

The observations showed that LB incidence rate started to increase rapidly after reaching the weekly rate of 0.1/100.000 from the 16th week and reached the peak period in the 23–25th weeks. Regional differences could be observed in the onset and peak of the LB incidence. In case of the 3 SW counties the weekly LB incidence reached 0.1/100.000 rate in the 11th week and in case of the 2 NE counties, in the 14th week. The LB incidence rate was more than 0.2/100.000 in the SW counties from the 15th week and in the NE counties from the 17th week, the start of LB season showed a 2–3 weeks difference. Aside the above described slight differences, the shape of the increasing part of the seasons in the two regions were very similar. (*Fig. 7*). The peak of the annual LB curves reached its annual maximum in the 25th week in the SW counties, while in the case of the NE counties, this was observed on the 28th or 29th week, showing a 3-4 weeks difference in the peaks of the LB season by regions. The run of the later summer decreasing part of the LB season showed a more marked 4-5 weeks difference between the SW and NE regions.

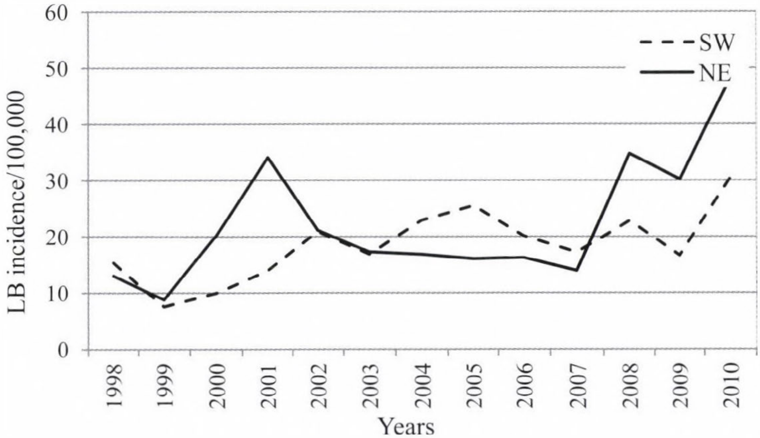

Fig. 6. The annual cumulative LB incidence in the two studied regions (SW and NE), in 1998–2010.

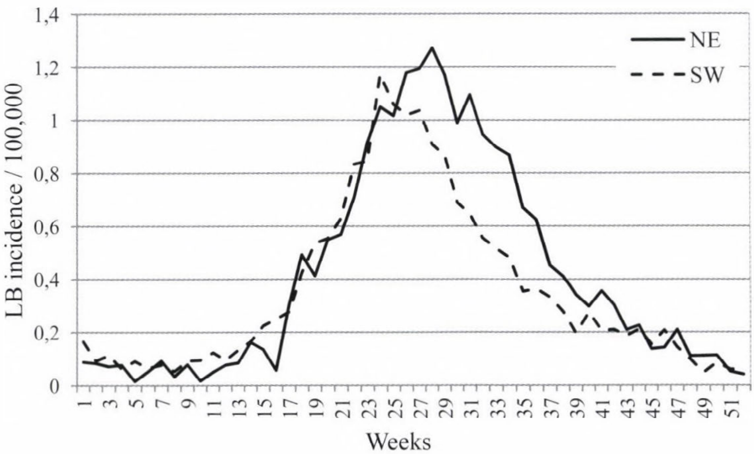

Fig. 7. The average weekly LB incidences of the SW and NE counties in Hungary, in 1998–2010.

While 13 years can not be divided into 2 periods of equal lenght, we compared the periods of 1999–2004 and 2005–2010. Comparing the periods by a polynomial regression model, the peak of the LB season shifted from the 28th to the 29th weeks in the NE counties, while in the SW counties this shift did not reach a one week difference. In the SW counties, the cumulative LB incidence was 118.3/100.000 in period 1998–2003 and 159.18/100.000 in period 2004–2010 (30.55% increase; *Fig. 8*). In the NE counties, the cumulative LB incidence was 92.22 per 100.000 in period 1999–2004 and 132.8/100.000 in period 2005–2010 (25.68% increase; *Fig. 9*).

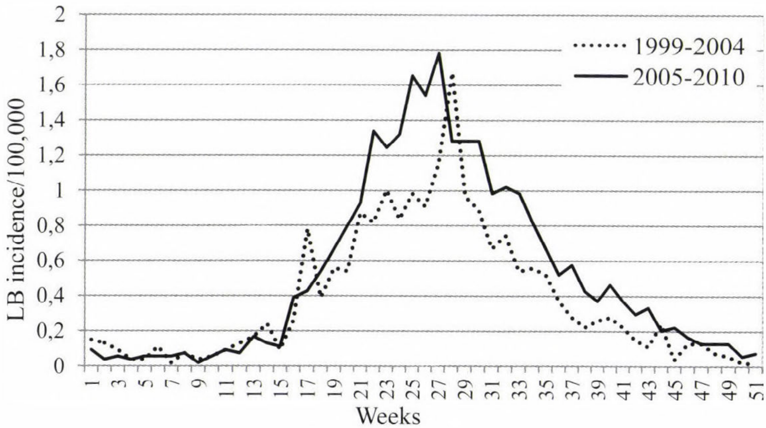

Fig. 8. Average weekly LB incidences of the NE counties in Hungary, in periods 1999–2004 and 2005–2010.

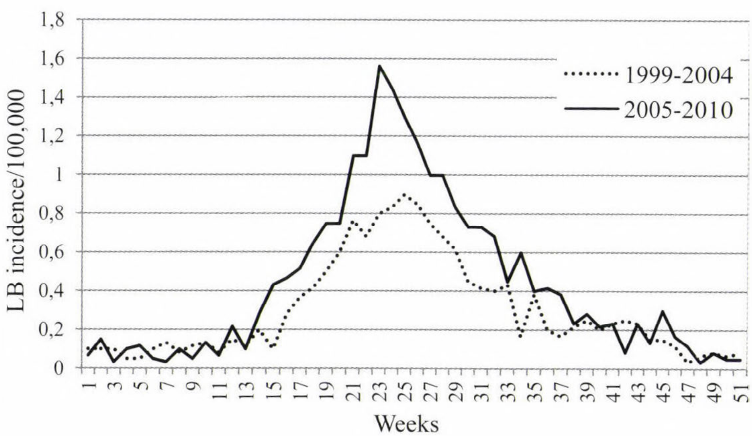

Fig. 9. Average weekly LB incidences of the SW counties in Hungary, in periods 1999–2004 and 2005–2010.

4. *Discussion*

LB is the most common vector-borne disease in Europe – more common than e.g. the tick-borne encephalitis. Although the disease is not-notificable at the European Community-level, about 85,000 cases are estimated to occur in Europe each year and only in the neighboring country Austria, the annual number of the new LB cases reaches the 14,000–24,000 value (*Lindgren* and *Jaenson*, 2006). With great certainty this amount may be highly underestimated, while it is reported only in few endemic countries. In some countries mainly the complications are reported, not the primary cases with the well recognizable symptom of erythema migrans. The follow-up of the seasonal, monthly, or weekly changes of LB incidence may be more informative than changes in annual incidence with respect to changing climate and the vector, host and pathogen biology. More information can be gained if monthly or weekly changes of the incidence are correlated with meteorological factors.

For routine purposes, temperature is the easiest accessible variable; therefore it seemed to be a first-level aim of the study to investigate whether a relationship between weekly incidence and weekly temperature can be revealed in different climatic regions within a country. This assumption was supported by several studies. LB has been positively correlated with higher summer temperatures in the UK, with a greater number being reported in southwestern regions than in northern areas (*Subak*, 1999).

As a first step, we analyzed the association of temperature and LB at regional level. Although the selected two Hungarian regions have a good contrast concerning the annual mean temperatures mainly in the colder half-year, the sums of annual precipitation of these regions are similar (550–700 mm or more; in period 1970–2000). In the centre of the Hungarian Great Plain, where the annual precipitation sum is the lowest in the Carpathian Basin (550–500 mm or less than 500 mm/year; in period 1970–2000), the annual LB incidences are too low to compare with the wetter Transdanubia region, even in the early summer period. For example, in period 1998–2010 the annual LB incidences in the western part of Transdanubia were 4–10 times higher than in the southern part of the Great Plain. For these reasons we could not make contrast between the wetter and drier Hungarian counties. We observed a 1.6 °C difference in the mean winter temperatures between the northeastern and southwestern regions. Ecologically it may be more important that the mean winter temperature of the NE counties was under 0 °C, while it was above 1 °C in the SW counties. In addition, spring warming started 2 weeks earlier in the SW counties, and there were only 3 weeks of the year in the SW counties, when the weekly mean ambient temperature dropped below 0 °C by a few tenths of a degree. This period lasted for 8 weeks continuously (the main part of the winter) in the NE region.

We did not find a significant correlation between the mean temperature of winter and the following annual LB incidence, which is consistent with

Schauber et al. (2005), who found that the mean temperatures for the prior winter showed weak or inconsistent correlations with Lyme disease incidence. In the period of 1998–2010, LB showed a significant increasing trend in the analyzed NE and SW counties, in the latter region the trend was nearly steadily increasing during the entire period, while in the NE counties this trend was detectable only in the last 4 years. In the colder counties characterized by colder winters, the onset of spring can be detected 1–2 weeks earlier compared to the warmer counties. Although in the analyzed 2 NE counties the onset of spring shifted from the 16.5th week to the 14th week significantly, the peak of the LB season shifted from the 28th to 29th weeks.

Our findings are consistent with *Széll et al.* (2006), who found that *I. ricinus* ticks are most active between April and June. In the 3 SW counties, this indicator week shifted from the 14.2nd to the 13.6th week non-significantly, and the peak of the LB season shifted less than one week. The differences between the onset and the peak of the weekly LB incidence curves can be explained by the regional differences of climate such as the different mean winter and autumn temperatures, since the peak activity of *I. ricinus* is influenced by their local environment (*Hornok* and *Farkas*, 2009).

As described above, in the NE counties the increasing trend of LB incidence started later, but the shifting trend of the spring to the earlier weeks was more rapid than in the SW counties. It remains still open, why a significant shifting trend of the start of spring was not visible in the SW counties, why a slow, but significant increasing trend was observed in the LB incidence rate. It is also at issue what caused the observed 4–5 weeks difference in the decreasing summer part of the LB seasons if the summer precipitation and the temperature conditions were so similar.

On the basis of the results we can conclude, that even a slight difference of 1.6 °C in the mean winter temperatures and 1–2 weeks difference of the start of the vegetation season may influence significantly the features of the LB season.

According to some authors, the monthly mean summer precipitation, the number of summer days with relative humidity more than 85% (*Bennet et al.*, 2006; *Walsh-Haehle*, 2010), or the soil moisture in summer (*Ashley* and *Meentemeyer*, 2004) and the Palmer drought index (*Schauber et al.*, 2005) are as important predictors of LB incidence as the monthly mean summer temperatures.

According to *Bartholy* and *Pongrácz* (2010) and *Schröter et al.* (2005), the total annual precipitation is not expected to change significantly in Hungary, but the seasonal precipitation sums can change by the end of the 21st century. The scenarios showed that summer precipitation would very likely decrease, but the projected precipitation changes would have relatively wide dispersion between 33% and 10%. Based on the seasonal standard deviation values, the largest uncertainty of precipitation change is expected in summer, when LB has the highest incidence values during the year.

Our further aim is to study the expected correlation between the summer precipitation and LB in Hungary, which would be an important additional factor to predict the future of the annual profile of LB incidence in Hungary.

References

Ashley, S.T., Meentemeyer, V., 2004: Climatic analysis of Lyme disease in the United States. *Clim. Res. 27*,177–184.

Bartholy, J. and *Pongrácz, R.*, 2010: Climate change scenarios for the Carpathian Basin. In (Eds. *Faragó, T. et al.*.)"VAHAVA" report – Climate change and Hungary: mitigating the hazard and preparing for th impacts Budapest, 12–21.

Bennet, L., Halling, A., and *Berglund, J.*, 2006: Increased incidence of Lyme borreliosis in southern Sweden following mild winters and during warm, humid summers. *Eur. J. Clin. Microbiol. 7*, 426–432.

Brownstein, J.S., Holford, T.R., and *Fish, D.*, 2005: Effect of climate change on Lyme disease risk in North America. *EcoHealth 2*, 38–46.

Confalonieri, U., Menne, B., Akhtar, R., Ebi, K.L., Hauengue, M,, Kovats, R.S.,Revich, B., and *Woodward, A.*, 2007: Human health. In (*Parry et al.* eds.) Climate Change 2007: Impacts, Adaptation and Vulnerability. Contribution of Working Group II to the Fourth Assessment Report of the Intergovernmental Panel on Climate Change, Cambridge University Press, Cambridge, UK, 391–431.

Chauvin, A., Moreau, E., Bonnet, S., Plantard, O., Malandrin, L,. 2009: Babesia and its hosts: adaptation to long-lasting interactions as a way to achieve efficient transmission. Veterinary research, 40(2), 37–37.

Donnelly, A., Jones, MB., and *Sweeney, J.*, 2004: A review of indicators of climate change for use in Ireland. *Int. J. Biometeorol. 49*, 1–12.

Duffy, D.C. and *Campbell, S.R.*, 1994: Ambient air temperature as a predictor of activity of adult Ixodes scapularis (Acari: Ixodidae). *J. Med. Entomol. 31*, 178–180.

English, P.B., Sinclair, A,H,, Ross, Z., Anderson, H., Boothe, V., Davis, C,, Ebi, K., Kagey, B., Malecki, K., Shultz, R., and *Simms, E.*, 2009: Environmental Health Indicators of Climate Change for the United States: Findings from the State Environmental Health Indicator Collaborative. *Environ. Health Perspect. 117*, 1673–1681.

Estrada-Pena, A., 2008: Climate, niche, ticks, and models: what they are and how we should interpret them. *Parasitol. Res. 103*, 87–95.

Földvári, G., Márialigeti, M., Solymosi, N., Lukács, Z., Majoros, G., Kósa, J.P., and *Farkas R.*, 2007. Hard Ticks Infesting Dogs in Hungary and their Infection with *Babesia* and *Borrelia* Species. *Parasitol. Res. 101*, 25–34

Haylock, M.R., Hofstra, N., Klein, A.M.G., Tank, E.J., Klok, P.D., Jones, and *New, M.*, 2008: A European daily high-resolution gridded dataset of surface temperature and precipitation. *J. Geophys. Res. 113*, D20119.

Hornok, S. and *Farkas, R.*, 2009: Influence of biotope on the distribution and peak activity of questing ixodid ticks in Hungary. *Med. Vet. Entomol. 23*, 41–46.

James, N.M., Gage, K.L., and *Khan, A.S.*, 2010: Potential Influence of Climate Change on Vector-Borne and Zoonotic Diseases: A Review and Proposed Research Plan. *Environ. Health Perspect. 118*, 1507–1514.

Kalluri, S., Gilruth, P., Rogers, D., and *Szczur, M.*, 2007: Surveillance of arthropod vector-borne infectious diseases using remote sensing techniques: A review. *PLoS Pathog. 3*, 1361–1371.

Komarek, L., 2005: Magyarország erdősültségének időbeni és területi alakulása. In: (*Puskás J.*, ed.) 4th International Conference on Application of Natural-, Technological and Economical Sciences. Szombathely, Hungary, 28/05/2005 1–6. (in Hungarian)

Kovats, S., Ebi, K., and *Menne, B.*, 2003: Methods of Assessing Human Health Vulnerability and Public Health Adaptation to Climate Change. Health and global environmental change series

No.1 2003 World Health Organization Regional Office for Europe, Copenhagen *KSH*, 2010. január 1. http://portal.ksh.hu/pls/ksh/docs/hun/hnk/Helysegnevkonyv_adattar_2010.xls. Last accessed: 2012.08.02.

Lindgren, E. and *Gustafson, R.*, 2001: Tick-borne encephalitis in Sweden and climate change. *The Lancet. 358,* 16–18.

Lindgren, E. and *Jaenson, T.G.T.*, 2006: Lyme borreliosis in Europe: influences of climate and climate change, epidemiology, ecology and adaptation measures. World Health Organization, Regional Office for Europe, Copenhagen, (http://www.euro.who.int/document/E89522.pdf).

Perret, J.L., Guigoz, E., Rais, O., and *Gern, L.*, 2000: Influence of saturation deficit and temperature on Ixodes ricinus tick questing activity in a Lyme borreliosis-endemic area (Switzerland). *Parasitol. Res. 86*, 554–557.

Randolph, S.E., 2009: Epidemiological consequences of the ecological physiology of ticks. *Adv. Insect Physiol.* 37, 297–339.

Randolph, S.E., 2004: Evidence that climate change has caused 'emergence' of tick-borne diseases in Europe? *Int. J. Med. Microbiol. 293*, 5–15.

Rogers, D.J. and *Randolph, S.E.*, 2006: Climate change and vector-borne diseases. *Adv. Parasitol. 62*, 345–381.

Schauber, E.M., Ostfeld, R.S., and *Evans, A.S. Jr3*, 2005: What is th ebest predictor of annual Lyme disease incidence: Weather, mice or acorns? *Eco. Soc. Am. 2*, 575–586.

Schröter, D., Cramer, W., Leemans, R., Prentice, I.C., Araujo, M.B.; Arnell, N.W., Bondeau, A., Bugmann, H., Carter, T.R., Gracia, C.A., Vega-Leinert, A.C.dl, Erhard, M., Ewert, F., Glendining, M., House, J. I., Kankaanpää, S., Klein, R.J.T., Lavorel, S., Lindner, M., Metzger, M. J., Meyer, J., Mitchell, T.D., Reginster, I., Rounsevell, M., Sabaté, S., Sitch, S., Smith, B., Smith, J., Smith, P., Sykes, M. T., Thonicke, K., Thuiller, W., Tuck, G.;,Zaehle, S., and *Zierl, B.*, 2005: Changes in annual precipitation for the IPCC A2 scenario (2071–2100 compared with 1961–1990) for four different climate models. Ecosystem Service Supply and Vulnerability to Global Change in Europe. Science 310, 13331337.

Széll, Z., Streter-Lancz, Z., Márialigeti, K., and *Streter, T.,* 2006: Temporal distribution of *Ixodes ricinus, Dermacentor reticulatus and Haemaphysalis concinna* in Hungary. *Vet. Parasitol. 141*, 377–379.

Stafford, K.C. III, Cartter, M.L., Magnarelli, L.A., and *Starr-Hope, E., Mshar, P.A.,* 1998: Temporal Correlations between Tick Abundance and Prevalence of Ticks Infected with *Borrelia burgdorferi* and Increasing Incidence of Lyme Disease. *J. Clin. Microbiol. 36*, 1240–1244.

Subak, S,. 1999: Incidence of lyme disease in humans. In: (*Cannell M.G.R. et al.* eds.) Indicators of climate change in the UK. Centre for Ecology and Hydrology, Huntingdon, UK, 38–39.

Tank, K., Wijngaard, A. M. G., Können, J. B., Böhm, G. P., Demarée, R., Gocheva, and *Petrovic, P.*, 2002: Daily dataset of 20th-century surface air temperature and precipitation series for the European Climate Assessment. *Int. J. Climatol. 22*, 1441–1453.

Walsh-Haehle, S., 2010: Vectors, hosts, and the weather: Exploring connections between Lyme disease and climate in the state of Minnesota. *Masters Abstracts Int. 49*, 117.

IDŐJÁRÁS

Quarterly Journal of the Hungarian Meteorological Service
Vol. 117, No. 2, April – June 2013, pp. 187–200

Estimating red noise spectra of climatological time series

István Matyasovszky

Department of Meteorology, Eötvös Loránd University,
Pázmány Péter sétány 1/A, H-1117 Budapest, Hungary
E-mail: matya@caesar.elte.hu

(Manuscript received in final form December 13, 2012)

Abstract–Spectral densities of climatological time series can be generally well approximated by red noise spectra. A common way of the spectral analysis is therefore based on a comparison of the periodogram with a red noise spectrum model. The red noise spectrum is described with the spectral density of a first order autoregressive (AR(1)) model. However, red noise characterized by spectral densities monotone increasing to low frequencies represents a much wider class of processes. The paper provides a concept of estimating red noise spectra without assuming any analytical form of the spectral density. The method, called isotonic regression, is based on robust regression of periodogram elements against frequencies under monotonic constraint of the regression curve. The technique is applied to SOI (Southern Oscillation Index) data from 1866 to 2011, reconstructed NAO (North Atlantic Oscillation) index data from 1659 to 2000, and the Northern Hemisphere temperature proxy data, AD 200–1995. The question of how the isotonic regression performs compared to the traditional AR(1) modeling is discussed.

Key-words: red noise, spectra, autoregressive model, isotonic regression, robust regression

1. Introduction

The task of the spectral analysis is to identify a finite number of discrete frequencies contributing to the discrete spectrum (if exists) and to estimate the spectral density characterizing the continuous spectrum. Spectral densities of climatological time series can be generally well approximated by red noise spectra. A common way of the spectral analysis is therefore to calculate the periodogram and then to fit a red noise spectrum to model the continuous spectrum. When periodogram exceeds some threshold at a frequency or a range of frequencies, the spectrum is said to differ from the red noise. The threshold depends on the red noise and the significance level selected. The red noise spectrum is generally described with the spectral density

$$f(\lambda)=(\sigma_e^2/\pi)\big/(1+a^2-2a\cos(\lambda)), \quad \sigma_e^2=\sigma^2(1-a^2) \tag{1}$$

of a first order autoregressive (AR(1)) process with substituting the autoregressive parameter a and variance σ^2 with their consistent estimates $\hat{a}$ and $\hat{\sigma}^2$. This approach is used in such an extent that red noise and AR(1) spectra are seldom used as synonyms. But red noise characterized by spectral densities monotone increasing to low frequencies represents a much wider class of processes than the AR(1) processes.

The purpose of this paper is to provide a general concept of estimating red noise spectra. The method described in Section 2 is based on isotonic regression of the periodogram against frequencies without assuming any analytical form of the spectral density. Isotonic regression includes regression under a monotonic constraint of the regression curve. The technique is applied to SOI data from 1866 to 2011, reconstructed NAO index data from 1659 to 2000, and the Northern Hemisphere temperature proxy data, AD 200–1995 in Section 3. Finally, a section for discussion and conclusions is provided.

2. *Methodology*

2.1. Isotonic regression

Let $x_1,...,x_n$ be a time series observed at $t_1,...,t_n$ as $x_i=g(t_i)+e_i$, where e_i has expectation zero and variance σ^2 for each *i*, and the sequence $\{e_i\}$ is weakly dependent (*Zhao* and *Woodroofe*, 2012). The task is to provide an estimate $\hat{g}(t)$ for the trend function $g(t)$ under the constraint $\hat{g}(t)\le\hat{g}(s), \quad t<s$. For simplicity, assume that *t* takes values equidistantly on the interval $[0,1]$. The solution of the least square (LS) problem

$$min\left\{\sum_{k=1}^{n}(x_k-\hat{g}(t_k))^2\right\}, \quad \hat{g}(t_k)\le\hat{g}(t_l), k<l \tag{2}$$

is

$$\hat{g}(t_k) = \max_{i \le k} \min_{k \le j} \frac{x_i + \ldots + x_j}{j - i + 1}$$

for $k = 1,\ldots,n$ and $\hat{g}(t)$ is left-continuous otherwise. The asymptotic behavior of $\hat{g}(t)$ for $t \in (0,1)$ can be written as

$$\hat{g}(t) = g(t) + \frac{2}{n^{1/3}} \left(\frac{1}{2} \sigma^2 g'(t) \right)^{1/3} \cdot \eta, \tag{3}$$

where $g'(t)$ is the derivative of $g(t)$ and η is a random variable following the Chernoff's distribution (*Groeneboom* and *Wellner*, 2001).

Having a time series $y_1,\ldots,y_N$, estimation of the red noise spectra can be performed with the isotonic regression (IR) with substitutions $t = (\pi - \lambda)/\pi$, $x_i = I(\lambda_{n-i+1})$, and $g((\pi - \lambda)/\pi) = f(\lambda)$, where $f(\lambda)$ is the spectral density, and

$$I(\lambda_i) = \frac{1}{\pi N} \left[\left(\sum_{j=1}^{N} y_j \cos(\lambda_i j) \right)^2 + \left(\sum_{j=1}^{N} y_j \sin(\lambda_i j) \right)^2 \right]$$

is the periodogram at frequencies $\lambda_i = (2\pi i)/N, i = 1,\ldots,n$, where n is the largest integer not larger than $N/2$. However, behavior of periodogram elements at frequencies close to the discrete frequencies substantially differs from the behavior of the majority of periodogram elements. Thus, periodogram elements at such frequencies should be taken as outliers, and an IR robust against outliers has to be found. Fortunately, *Álvarez* and *Yohai* (2011) placed the IR in a general framework covering both the ordinary and robust cases. Specifically, note that Eq. (2) is a particular case of

$$\min \left\{ \sum_{k=1}^{n} \rho((x_k - \hat{g}(t_k))/\sigma) \right\}, \quad \hat{g}(t_k) \le \hat{g}(t_l), k < l$$

with $\rho(u) = (\sigma u)^2$, and other suitable choices of $\rho(u)$ can deliver robust estimations for $g(t)$. Namely:

$$\hat{g}(t_k) = \max_{u \le k} \min_{k \le v} \{\hat{m}(u,v)\},$$

where $\hat{m}(u,v)$ is the solution of

$$\sum_{j \in C(u,v)} \psi\left((x_i - m)/\sigma\right) = 0 \tag{4}$$

under $C(u,v) = \{j; 1 \le j \le n, u \le t_j \le v\}$, and $\psi(u) = \rho'(u)$. Eq. (3) is then modified by substituting σ^2 with $r\sigma^2$, where

$$r = \frac{E\left[\psi^2(e/\sigma)\right]}{\left(E\left[\psi'(e/\sigma)\right]\right)^2},$$

and e is a random variable that generates $\{e_i\}$. (Note that $r=1$ for Eq. (2).) When estimation of the spectral density $f(\lambda)$ is in question the periodogram $I(\lambda_i)$ is asymptotically $f(\lambda_i)\xi_i$, where ξ_i has standard exponential distribution. Hence σ is not constant but $\sigma_i = f(\lambda_i)$. Therefore, Eq. (4) is modified as

$$\sum_{j \in C(u,v)} \psi\left(x_i / m - 1\right) = 0$$

with $\psi(u)$ based on the function $\psi_H(u) = max\{-c, min\{c,u\}\}$ (*Huber*, 1981) as $\psi(u) = (1 - e^{-1})\psi_H(u), u < 0$, $\psi(u) = \psi_H(u), u \ge 0$ with choosing $c=1$ (*Matyasovszky*, 2010). The asymptotic behavior of $\hat{f}(\lambda)$ with $\lambda \in (0,\pi)$ is written as

$$\hat{f}(\lambda) = f(\lambda) + \frac{2}{n^{1/3}}\left(-\frac{\pi}{2} f^2(\lambda) f'(\lambda) r\right)^{1/3} \cdot \eta \qquad \text{or}$$

$$f(\lambda) = \hat{f}(\lambda) - \frac{2}{n^{1/3}}\left(-\frac{\pi}{2} f^2(\lambda) f'(\lambda) r\right)^{1/3} \cdot \eta. \tag{5}$$

2.2. Confidence band

In order to detect frequencies where the spectrum differs from red noise, a confidence band for periodogram elements is needed. Therefore, the Chernoff's distribution of η and quantities in Eq. (5) yet unknown should be evaluated. The Chernoff's distribution can be well-approximated by a normal distribution of expectation zero and standard deviation 0.52, but the exact distribution can be found in *Groeneboom* and *Wellner* (2001). The quantity r for the function $\psi(u)$ selected above is $r=0.75$, and the squared spectral density $f^2(\lambda)$ can be substituted by its estimate $\hat{f}^2(\lambda)$. An estimate of $f'(\lambda)$ can be obtained using a nonparametric regression technique as follows. A data set $y_i = n/(2\pi)\cdot(\hat{f}(\lambda_i) - \hat{f}(\lambda_{i+1}))$, $i = 1,...,n-1$ is constructed as a finite difference approximation to $f'(\lambda_i)$, $i = 1,...,n-1$. The derivative $f'(\lambda)$ is then estimated with the Nadaraya-Watson estimator defined as

$$\hat{f}'(\lambda) = \sum_{j=1}^{n-1} y_j K\left(\frac{\lambda_j - \lambda}{h}\right) \Bigg/ \sum_{j=1}^{n-1} K\left(\frac{\lambda_j - \lambda}{h}\right), \tag{6}$$

where $K(u)$ is a so-called kernel function and h is the bandwidth. The Epanechnikov kernel is used here that is given by $K(u) = 3/4(1-u^2)$ within [-1, 1] and zero otherwise. The bandwidth having a crucial role in the resulting shape of $\hat{f}'(\lambda)$ can be estimated by minimizing the quantity

$$CV(h) = \sum_{i=1}^{n-1} (y_i - \hat{f}_i'(\lambda_i))^2$$

with respect to h, where $\hat{f}_i'(\lambda_i)$ is calculated by Eq. (6) at $\lambda = \lambda_i$ but with omitting data $y_j, |j-i| \leq 1$ from the summation. Note that Eq. (6) is one of the possible solutions of non-parametric curve fitting problems. For further details, see, e.g., *Simonoff* (1996).

The following procedure to give confidence bands for the periodogram is proposed now. 1. Simulate a spectral density $f(\lambda_i)$, $i = 1,...,n$ using Eq. (5). 2. Simulate a periodogram by generating n independent random numbers having exponential distributions with parameters $1/f(\lambda_i)$, $i = 1,...,n$. 3. Repeat steps 1 and 2 10,000 times. 4. Select the $(1-\varepsilon)$th quantile of the simulated periodograms obtained from step 3 at every λ_i. These quantiles provide the critical values for the periodogram calculated from observed data. When periodogram exceeds the critical value determined above at a frequency, the spectrum is said to differ from the red noise at a significance level $(1-\varepsilon)100\%$.

Another basic question is to identify and estimate discrete frequencies. Under general conditions, the limiting probability distribution function of $max_{1\leq i\leq L}\{\xi_i\} - ln n$ is the standard Gumbel distribution function that makes it possible to test the null-hypothesis of lacking discrete frequencies with substituting ξ_i by $I(\lambda_i)/\hat{f}(\lambda_i)$. When the null-hypothesis is rejected at a certain significance level, the second maximum is tested using its asymptotic distribution, and the procedure continues until significant frequencies are found. Evidently, an existing discrete frequency does not coincide with a detected frequency λ_k, and thus, an improvement of its estimate is needed. A straightforward method is to use the value $\hat{\lambda}_k$ maximizing the periodogram in some neighborhood of λ_k. Consistency and further properties of this technique are discussed in *Chen et al.* (2000).

3. *Examples*

3.1. Monthly SOI from 1866 to 2011

Monthly values of the Southern Oscillation Index (SOI) are taken from Climate Analysis Section (CAS) of Climate Global Dynamics Division (CGD) at NCAR (http://www.cgd.ucar.edu/cas/catalog/climind/soi.html). The example is chosen intentionally, because SOI does not have red noise but does have colored noise spectrum (e.g., *Chen*, 1982).

The procedure described in Section 2.2 detects three discrete cycles of lengths 12, 6, and 4 months at any reasonable significance level (above the 99.9% significance level). Note that these latter two cycles correspond to integer multiple frequencies of the annual frequency indicating a substantial asymmetry of the annual course. *Fig. 1* demonstrates necessity of the robust IR, because the shape (jumps) of the non-robust isotonic spectral density adapts to discrete cycles, while its robustified version removes the effect of these discrete frequencies. The AR(1) spectral density slightly underestimates the role of high and low frequencies and overestimates the contribution of moderate frequencies (from 4 months to 3.2 years) as compared to the robust isotonic spectral density. However, both techniques recognize a spectral density peak between 2.9-6.5 years (*Fig. 2*). The procedure of *Chen et al.* (2000) to improve the estimation of these cycle lengths results in the highest periodogram value at 6.4 years, but two other local maxima are obtained at 2.9 and 3.5 years. Each of them is significant at the 99% level and is in good agreement with previous several studies (e.g., *Gaucherel*, 2010). The confidence band for the AR(1) spectral density is determined as that for the IR spectral density except for step 1 of Section 2.2. Here the spectral density $f(\lambda_i), i=1,\dots,n$ is computed from Eq. (1) with random parameter a that is distributed normally with expectation $\hat{a}$ and variance $(1-\hat{a}^2)/n$ (*Priestley*, 1981).

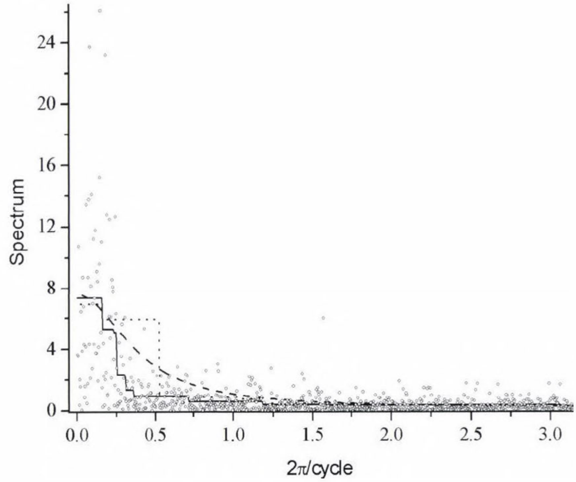

Fig. 1. Periodogram (dot) and spectral density of SOI (1866–2011) estimated by robust isotonic regression (solid), isotonic regression (dotted), and AR(1) model (dashed).

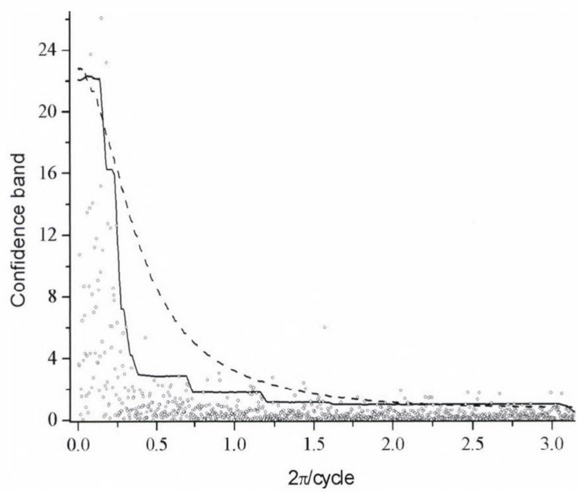

Fig. 2. Upper 95% confidence band of the periodogram (dot) under red noise assumption on the spectral density of SOI (1866–2011) corresponding to the robust isotonic regression (solid) and the AR(1) (dashed) model.

3.2. Reconstructed NAO index from 1659–2000

NAO index values reconstructed by *Luterbacher et al.* (1999; 2002) using instrumental and proxy data from Eurasia are available from 1659 (http://www.esrl.noaa.gov/psd/gcos_wgsp/Timeseries/RNAO/).

A half annual cycle and an annual cycle are detected to be significant at level 91%. The existence of these cycles is ambiguous due to their low significance levels, but an earlier study of *Matyasovszky* (2010) performed with substantially shorter observational data did not find discrete periods at these frequencies. As the contribution of the amplitude of a discrete cycle to the periodogram is proportional to data length and the earlier examination with relatively short data set did not show, but the present study performed with longer data set does show indication for discrete periods at these frequencies, we argue that weak annual and half annul cycles really exist. The third largest periodogram element meets a 65.4-year cycle. This should not be considered as a discrete frequency, but the true spectral density deviates from the red noise spectrum at a 98% significance level corresponding to previous findings. Specifically, dominant 50–70-year periods have been detected in several climatic or climate induced data series (*Loehle* and *Scafetta*, 2011) such as in NAO index (*Mazzarella* and *Scafetta*, 2012). Omitting frequencies close to annual and half annual frequencies a 5.4-year spectral peak significant at a 99% level is notable (*Figs. 3* and *4*) such as in *Box* (2002). Additionally, many other periodogram elements exceed the confidence band at higher frequencies showing the difficulty of detecting deviations from a model spectral density. Namely, assume that the underlying time series has no discrete frequencies and the spectral density is exactly known. Around $\varepsilon \cdot 100\%$ of periodogram elements exceed the $(1-\varepsilon)100\%$ upper confidence band although there are no deviations from the known spectral density at all.

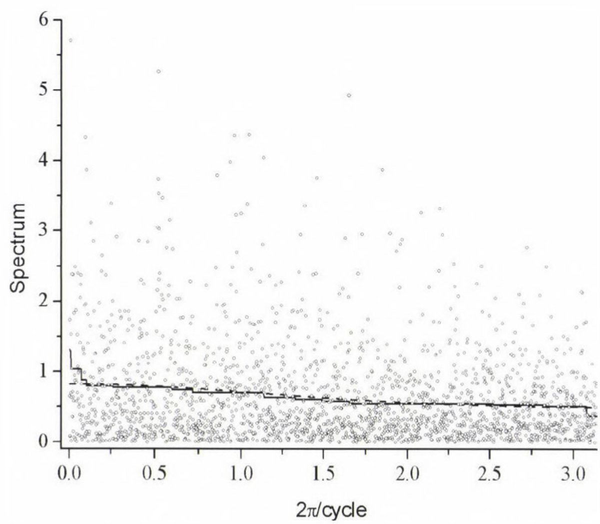

Fig. 3. Periodogram (dot) and spectral density of NAO index (1659–2000) estimated by robust isotonic regression (solid) and AR(1) model (dashed).

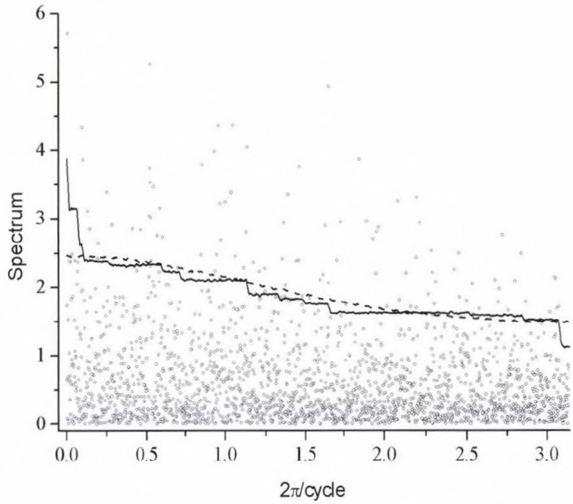

Fig. 4. Upper 95% confidence band of the periodogram (dot) under red noise assumption on the spectral density of NAO index (1659–2000) corresponding to the robust isotonic regression (solid) and the AR(1) (dashed) model.

3.3. Northern Hemisphere temperature from proxy data, AD 200–1995

Annual mean Northern Hemisphere temperatures reconstructed using instrumental and high resolution climate proxy data sources as well as climate modeling studies for the period AD 200–1995 are analyzed. Data are adjusted to the same decadal standard deviation as the instrumental record over the period 1856–1995 (*Jones* and *Mann*, 2004).

As the spectral density is characterized by a sharp peak at low frequencies and a wide flat region at moderate and high frequencies, only cycles longer than 60 years are shown in *Fig. 5*. The AR(1) spectral density seems to be radically overestimated at low frequencies as compared to the IR spectral density. Based on the AR(1) density, the spectrum differs from red noise at cycle lengths around 114, 81, 23, and 11 years at least at the 95% significance level. These cycles are clearly related to the periodicities of solar activity (*Damon* and *Sonett,* 1991). However, the 81-year and 11-year cycles are not reinforced when using the IR spectral density, but further periodicities of 33 and 38 years are detected by both the AR(1) and IR densities (*Fig. 6*). These peaks can be attributed to Atlantic Multidecadal Oscillation (AMO). Although the AMO is generally known as a phenomenon having periodicities 50–70 years (see Section 3.2), other proxy records and model simulations show a more complex structure of periodicities ranging from 30 to 100 years (*Knight et al.*, 2005).

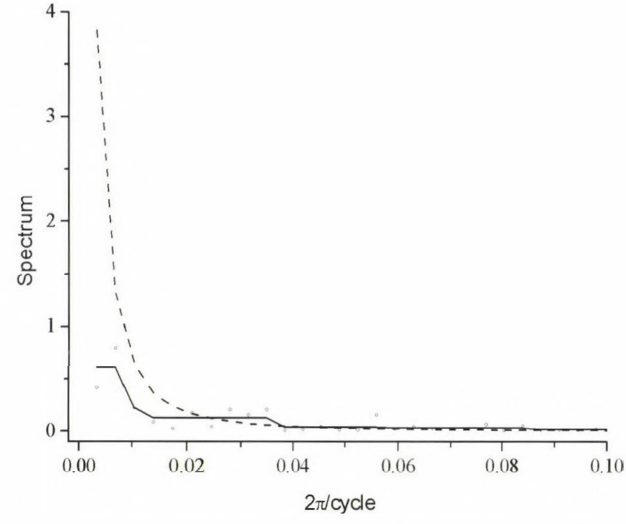

Fig. 5. Periodogram (dot) and spectral density of Northern Hemisphere temperature from proxy data (AD 200-1995) estimated by robust isotonic regression (solid) and AR(1) model (dashed)

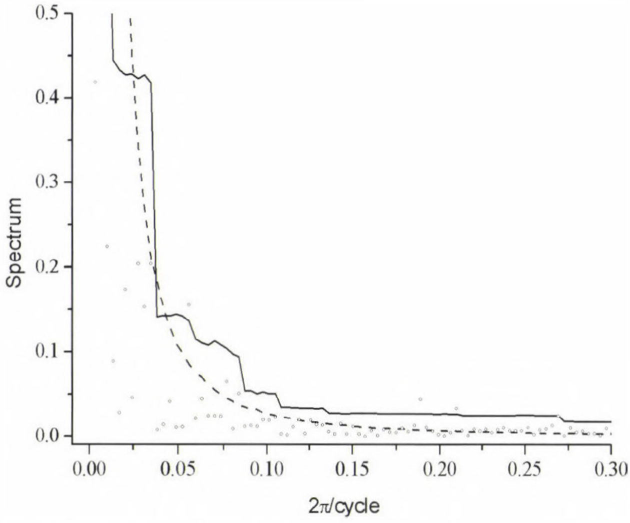

Fig. 6. Upper 95% confidence band of the periodogram (dot) under red noise assumption on the spectral density of Northern Hemisphere temperature from proxy data (AD 200–1995) corresponding to the robust isotonic regression (solid) and AR(1) (dashed) model

4. Discussion

A methodology (robust IR) to estimate red noise spectra has been introduced without any assumption on the analytical form of the spectral density. Although the shape of the spectral densities obtained with the IR method and AR(1) modeling is more or less different (and confidence bands as well), significant deviations from red noise detected with these spectral densities are essentially the same in the first two examples. However, the third example shows important differences between the two approaches. The question of how the proposed IR relates to the traditional AR(1) modeling is addressed now. Suppose we have a general linear stochastic process

$$X_t = \sum_{j=0}^{\infty} b_j e_{t-j} \tag{7}$$

with expectation zero (for simplicity), where e_t has expectation zero and variance σ_e^2, and e_t and e_s are uncorrelated for every $t \neq s$. Note that this class of processes is a very general case in the spectral analysis (e.g., *Priestley*, 1981). It includes MA (moving average) and stationary ARMA (autoregressive-moving average) processes. Additionally, Eq. (7) can be rewritten under general conditions into an infinite AR process and preserving the first p number of autoregressive terms results in an AR(p) representation. The standard AR(1) approximation $X_t^{AR(1)} = a^{AR(1)} X_{t-1}^{AR(1)} + e_t^{AR(1)}$ to Eq. (7) is obtained with $a^{AR(1)} = R(1)$, where $R(1)$ is the one lag autocorrelation. Measuring the accuracy of an AR(1) approximation $X_t^{(a)} = aX_{t-1}^{(a)} + e_t^{(a)}$ to Eq. (7) with $\Delta = E\left[(X_t^{(a)} - X_t)^2\right]$, it can be shown after *Galbraith* and *Zinde-Walsh* (2002) that

$$\Delta = \sum_{j=0}^{\infty} (b_j - (1-a^2)^{1/2} \rho^{1/2} a^j)^2 \sigma_e^2,$$

where $\rho = \sum_{j=0}^{\infty} b_j^2$. In other words, the best AR(1) model is achieved with a that minimizes Δ, which, however, differs from $R(1)$. Hence, an AR(1) process with autoregressive coefficient $a^{AR(1)} = R(1)$ is not the best approximating model in the mean squared error sense.

Forgetting about this fact and just focusing on the question of how the spectral density of X_t is approximated with the spectral density of $X_t^{AR(1)}$, the following details can be provided. It is known that the spectral density Eq. (1) of an AR(1) process is consistently estimated when parameters a and σ_e^2 are substituted with their consistent estimates (*Mann* and *Wald*, 1943), but it is unrealistic that a time series comes from an AR(1) process. The spectral density of a linear process is consistently estimated by the spectral density of an AR(p) process when $p \to \infty, p^3 / n \to 0$ as $n \to \infty$ (*Berk*, 1974). However, fixing the value $p = 1$, nothing is known about the accuracy of such an estimate without knowing the true spectral density. Additionally, these results hold only for purely continuous spectra. For this latter reason, *Mann* and *Lee* (1996) proposed to fit AR(1) spectra to median smoothed periodogram elements. This is because median is robust against outliers of the periodogram, which might be present due to potentially existing discrete frequencies. But neither this approach quits the analytical form Eq. (1) of the spectral density, and hence we do not really know what the spectral density of the traditionally fitted AR(1) model represents. In contrast, the IR is a technique without any assumption on the analytical form of the spectral density. It is based on the least square (LS) estimation which is not too efficient for random variables far from Gaussian. However, the LS IR is identical with the maximum likelihood (ML) IR in some specific situations. This is the case for exponential distributions, and hence the LS IR represents the ML estimate of the spectral density under monotone decreasing constraint, because the periodogram elements have asymptotical exponential distributions.

A generalized method of IR (*Tibshirani et al.*, 2011), the so-called nearly-isotonic regression (NIR), permits the possibility of deviations from monotonicity when necessary. The necessity of monotonicity violations is controlled via a parameter that is estimated within the procedure. Adapting this technique to periodograms makes it possible to detect departures from red noise. Applying the NIR to SOI data clearly shows a local maximum of the spectral density between cycles of 3.4–7.5 years (*Fig. 7*). As the NIR is not a robust technique, the previously detected discrete frequencies were omitted. This may be done because the NIR can handle unevenly spaced data as well. *Fig. 8* shows the spectral density obtained with the NIR for NAO index time series. It can be concluded that annual and half annual cycles form a discrete spectrum, because so sharp spectral peaks should be due to discrete spectra. Additionally, the NIR spectrum is somewhat higher at low frequencies than the robust IR spectrum indicating that the 65.4-year cycle is an outlier in the robust IR, and hence the spectrum strongly deviates here from the red noise spectrum. The difference between spectral densities obtained with the robust IR and NIR is negligible for the third example (Northern Hemisphere temperature from proxy data, AD 200-1995). As the NIR makes it possible to detect departures from red noise, it seems that estimating red noise spectra either with AR(1) modeling or IR is unnecessary. Unfortunately, statistical properties of the NIR technique are not available, and hence the accuracy of this procedure is not known. Therefore, usage of the methodology based on the IR is advised as described in the paper.

Acknowledgement-The European Union and the European Social Fund provided financial support for the project under the grant agreement no. TÁMOP 4.2.1./B-09/KMR-2010-0003.

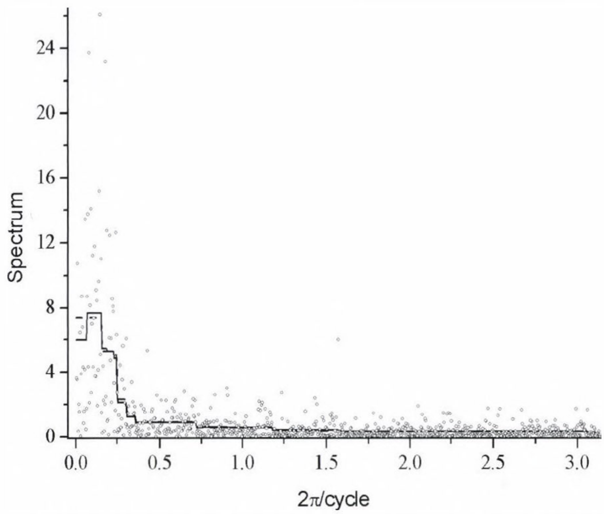

Fig. 7. Periodogram (dot) and spectral density of SOI (1866–2011) estimated by nearly isotonic regression (solid) and robust isotonic regression (dashed)

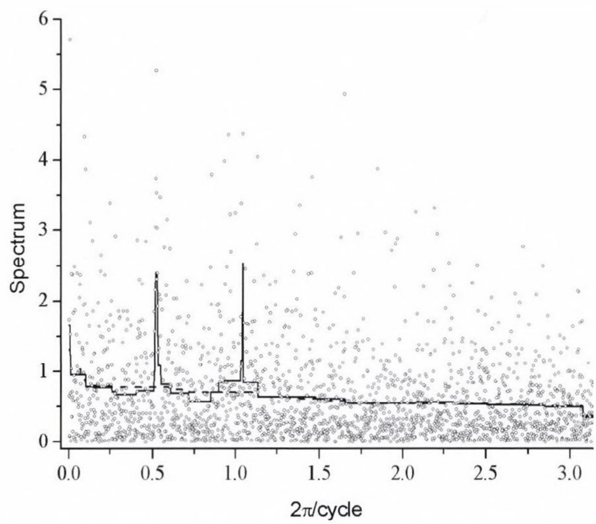

Fig. 8. Periodogram (dot) and spectral density of NAO index (1659-2000) estimated by nearly isotonic regression (solid) and robust isotonic regression (dashed)

References

Álvarez, E.E. and *Yohai, V.J.*, 2011: M-estimators for Isotonic Regression. arXiv: 1105.5065v1[stat.ME]

Berk, K.N., 1974: Consistent autoregressive spectral estimates. *Ann. Math. Stat. 2*, 489–502.

Box, J.E., 2002: Survey of Greenland instrumental temperature records: 1873–2001. *Int. J. Climatol. 22*, 1829–1847.

Chen, W.Y., 1982: Assessment of Southern Oscillation sea-level pressure indices. *Mon. Weather Rev. 113*, 1876–1888.

Chen, Z.G., *Wu, K.H.* and *Dahlhaus, R.*, 2000: Hidden frequency estimation with data tapers. *J. Time Ser. Anal. 21*, 113–142.

Damon. P.E. and Sonnett, C.P., 1991: Solar and terrestrial components of the atmospheric ^{14}C variation spectrum. In (Eds: *Sonnett, C.P., et al.*) The Sun in Time. University of Arizona Press, Tucson.

Galbraith, J.V. and *Zinde-Walsh, V.*, 2002: Autoregressive Approximation, with Econometric Applications, 401–421. In (Eds: *Ullah, A., et al.)* A Handbook of Applied Econometrics and Statistical Inference. Marcel Dekker, New York.

Gaucherel, C., 2010: Analysis of ENSO interannual oscillations using non-stationary quasi-periodic statistics: a study of ENSO memory. *Int. J. Climatol. 30*, 926–934.

Groeneboom, P. and *Wellner, J.A.*, 2001: Computing Chernoff's Distribution. *J. Comput. Graph. Stat. 10*, 388–400.

Huber, P.J., 1981: Robust statistics. Wiley, New York

Jones, P. D. and Mann, M.E., 2004: Climate over past millennia. *Rev. Geophys. 42*, RG2002.

Loehle, C. and *Scafetta, N.*, 2011: Climate Change Attribution Using Empirical Decomposition of Climatic Data. *Open Atm. Sci. J. 5*, 74–86.

Knight, J.R., *Allan, R.J.*, *Folland, C.K.*, *Vellinga, M.* and *Mann, M.E.*, 2005: A signature of persistent natural thermohaline circulation cycles in observed climate. *Geophys. Res. Lett. 32*, L20708.

Luterbacher, J., *Schmutz, C.*, *Gyalistras, D.*, *Xoplaki, E.* and *Wanner, H.*, 1999: Reconstruction of monthly NAO and EU indices back to AD 1675. *Geophys. Res. Lett. 26*, 2745–2748.

Luterbacher, J., *Xoplaki, E.*, *Dietrich, D.*, *Jones, P.D.*, *Davies, T.D.*, *Portis, D.*, *Gonzalez-Rouco, J.F.*, *von Storch, H.*, *Gyalistras, D.*, *Casty, C.* and *Wanner, H.*, 2002: Extending North Atlantic Oscillation Reconstructions Back to 1500. *Atmos. Sci. Lett.*, doi:10.1006/asle.2001.0044.

Mann, H.B. and *Wald, A.*, 1943: On the statistical treatment of stochastic difference equations. *Econometrica 11*, 173–220.

Mann, M.E. and *Lee, J.M.*, 1996: Robust estimation of background noise and signal detection in climatic time series. *Climatic Change 33*, 409–445.

Matyasovszky, I., 2010: Improving the methodology for spectral analysis of climatic time series. *Theor. Appl. Climatol. 101*, 281–287.

Mazzarella, A. and *Scafetta, N.*, 2012: Evidences for a quasi 60-year North Atlantic Oscillation since 1700 and its meaning for global climate change. *Theor. Appl. Climatol. 107*, 599-609.

Priestley, M.B., 1981: Spectral Analysis and Time Series. Academic Press, New York.

Simonoff, J.S., 1996: Smoothing Methods in Statistics. Springer Series in Statistics, Springer-Verlag, New York.

Tibshirani, R.J., *Hoefling, H.* and *Tibshirani, R.*, 2011: Nearly-Isotonic Regression. *Technometrics 53*, 54–61.

Zhao, O. and *Woodroofe, M.*, 2012: Estimating a monotone trend. *Stat. Sinica 22*, 359–378.

IDŐJÁRÁS

Quarterly Journal of the Hungarian Meteorological Service
Vol. 117, No. 2, April – June 2013, pp. 201–218

An IMEX scheme combined with Richardson extrapolation methods for some reaction-diffusion equations

István Faragó[1,2*], **Ferenc Izsák**[1], and **Tamás Szabó**[3,4]

[1] *Department of Applied Analysis and Computational Mathematics*
Eötvös Loránd University
H-1117, Budapest, Pázmány P. sétány 1/c. Hungary

[2] *HAS-ELTE Reserch Group "Numerical Analysis and Large Networks"*
H-1117, Budapest, Pázmány P. sétány 1/c. Hungary

[3] *BCAM Basque Center for Applied Mathematics*
Alameda Mazarredo, 14, E - 48009 Bilbao
Basque Country, Spain

[4] *CAE Engineering Kft.*
H-1122, Budapest, Ráth György u. 28. Hungary

e-mails: faragois@cs.elte.hu, izsakf@cs.elte.hu, szabot@cs.elte.hu

**Corresponding author*

(Manuscript received in final form March 3, 2013)

Abstract–An implicit-explicit (IMEX) method is combined with some so-called Richardson extrapolation (RiEx) methods for the numerical solution of reaction-diffusion equations with pure Neumann boundary conditions. The results are applied to a model for determining the overpotential in a Proton Exchange Membrane (PEM) fuel cell.

Key-words: IMEX, reaction-diffusion equations, Richardson extrapolation, fuel cell, PEM, numerical solution

1. *Introduction*

The numerical solution of advection-reaction-diffusion equations is a central problem in the numerical analysis. In practice, many important meteorological phenomena are modeled using reaction-diffusion equations (which are often supplemented with advection terms). Therefore, the efficient numerical solution of these equations is of central importance. The numerical treatment of the boundary layer effect and the possibly stiff terms lead to challenging problems. The importance of this topic lies in the applicability of the corresponding models in the natural sciences including atmospheric modeling.

A previously (*Faragó et al.*, 2013) presented implicit-explicit (IMEX) method of second order in space is supplemented with Richardson extrapolation methods (passive and active) in time. The new method is developed for the numerical solution of reaction-diffusion equations with pure Neumann boundary conditions in order to have a method of second order both in space and time. Richardson extrapolation is a very efficient method to increase the accuracy of many numerical methods. It consists of applying a given numerical scheme with different discretization parameters (in our case different time steps) and combining the obtained results with properly chosen weights (*Zlatev et al.*, 2010).

2. *Motivation*

The method which we start from is stable under very mild conditions. If we can enhance also its time accuracy, we can have an efficient algorithm. In the atmospheric modeling it is particularly useful, since a fast method leading to an up-to-date forecast needs relatively large time steps. At the same time, in real life situations we have to run the corresponding simulations over many time steps, so the stability of the method is of primary importance.

To get a complex one-dimensional reaction-diffusion problem we cite here an interesting electrochemical model. Nowadays, electrical energy is the cleanest and most versatile energy that can be used in almost all fields of life. Due to the technical improvements, the utilization and efficiency of producing electrical energy are increasingly growing.

In this section, we compute numerically the overpotential in PEM fuel cells. These kinds of fuel cells "burn" hydrogen fuel and oxygen to water, producing electrical energy at a high efficiency without air pollution. Their operation can be reversible: they can also convert electrical energy into chemical energy.

The electro-chemical reactions take place at the anode and cathode on the boundary of two phases (solid and solution phase), while the charge neutrality is macroscopically preserved.

Complex models (*Ziegler et al.*, 2005) are needed to solve different phenomenological equations such as the Nernst-Planck equation for multiple mass transport, the Stefan-Maxwell equation for heat transfer, Ohm's law for ionic migration and electron conductivity, and the equations of electrochemical kinetics. These models are usually solved by using only a single solver, e.g., Runge-Kutta, Newton, or Crank-Nicholson methods.

Subramanian et al. (2007) developed a method to reduce the number of the governing equations of Li-ion battery simulation by using different mathematical techniques. The original problem with a proper discretization has 4800 equations which can be reduced to 49, and finally, the simulation time of the discharge curve can be cut to 85 ms. However, in this model the double-layer capacitance was not included.

We focus here only on the evolution of the overpotential and we take into consideration both the inhomogeneity of the conducting media and the presence of the different phases in the cell. We perform the computations with realistic parameters.

2.1. Physical laws: homogeneous and heterogeneous models

In practice, a consumer (some kind of electric device) is inserted into an electrical circuit, which is feeded by the fuel cell. We assume that the current in the outer circuit is known ($I(t)$) and we can control it. The aim of the following investigation is to calculate the corresponding voltage, which is called the cell potential. This gives also the electric energy provided by the fuel cell, which is very important in the course of evaluating the performance of a fuel cell.

According to Kirchoff's law, the cell potential E_{cell} can be calculated by the following equation, see also *Litster* and *Djilali*, (2007):

$$E_{cell}(t) = E_{OC}(t) - \eta^{a}(t) - \frac{W_{mem}}{\kappa_{mem}} I(t) - V^{*}(t), \tag{1}$$

where $t \in (0, T)$ denotes time. Here $E_{OC}(t) \approx 1.23\text{V}$ denotes the open circuit potential, which is present between the anode and cathode without the presence of any consumer.

Considering the simplest form of Ohm's law, the term $\frac{W_{mem}}{\kappa_{mem}} I(t)$ means the potential loss at the membrane, the thickness and conductivity of which are denoted by W_{mem} and κ_{mem}, respectively.

The calculation of the last quantity on the right-hand side (V^{*}), which refers to the potential loss at the cathode, needs a detailed analysis. The interval $(0, L)$ refers to the thickness of the cathode, where two phases are distinguished:

- The solution phase, where the hydrogen ions are conducted according to the rate κ_{eff}. The potential and the current density in this phase are denoted by ϕ_2 and i_2, respectively.
- In the solid phase of the cathode, electrons are conducted according to the rate σ_{eff}. The potential and the current density here are denoted by ϕ_1 and i_1, respectively.

All of these quantities could be allowed to depend on time and space corresponding to the given assumptions and the structure of the fuel cell and the time evolution of the process.

Using the defined quantities, V^* in Eq. (1) can be given as

$$V^*(t) = \phi_1(t, L) - \phi_2(t, 0), t \in (0, T). \tag{2}$$

The quantity we investigate in the governing equations is the overpotential

$$\eta(t, x) = \phi_1(t, x) - \phi_2(t, x) \geq 0, x \in (0, L), t \in (0, T). \tag{3}$$

In the calculation of the potentials, we choose the reference level to be at the left end of the solution phase, i.e., we define $\phi_2(t, 0) = 0$. This is in a good accordance with the uniqueness of the solutions in the corresponding equations. As we will see, the governing equations depend only on the spatial derivatives of the potentials, such that the above assumption is necessary to determine both $\phi_2(t, x)$ and $\eta_2(t, x)$. Then an immediate consequence of (2) and (3) is that

$$V^*(t) = \phi_1(t, L) = \eta(t, L) + \phi_2(t, L). \tag{4}$$

Applying Ohm's law for both phases we obtain

$$\begin{aligned} i_1(t, x) &= -\sigma_{eff}(x) \partial_x \phi_1(t, x) \\ i_2(t, x) &= -\kappa_{eff}(x) \partial_x \phi_2(t, x) \end{aligned} \tag{5}$$

and the principle of electroneutrality gives

$$-\partial_x i_1(t, x) = \partial_x i_2(t, x). \tag{6}$$

The conservation law for the currents (see *Newman* and *Thomas-Alyea*, 2004) results in the formula

$$\partial_x \left(\kappa_{eff}(x)\partial_x \phi_2(t,x)\right) = \\ -a(x)C_{dl}(x)\partial_t \eta(t,x) - a(x)i_0(x)g\left(\alpha \frac{F}{RT}\eta(t,x)\right). \tag{7}$$

Here, the function $C_{dl}(x)$ gives the double-layer capacitance at the cathode side, and the last term yields the faradic current with $i_0(x)$, the exchange current density at the cathode. For the notations of the material coefficients we refer to the Appendix. The function $g : \mathbb{R} \to \mathbb{R}$ refers to the kinetics of the oxygen reduction reaction here. This should be an increasing function with $g(0) = 0$.

Remark 2.1: *Among the several approaches for the sake of simplicity we apply linear kinetics and, accordingly, we use*

$$g_L(u) = c(x)u, \tag{8}$$

where $c(x)$ is a given bounded non-negative function. Other possible choices are the following, which are going to be used in the course of the analysis and the numerical experiments (*Kriston et al.*, 2010).

- *Butler–Volmer kinetics*:

$$g_{BV}(u) = c(x)(\exp(u) - \exp(-u)), \tag{9}$$

- *diffusion kinetics*:

$$g_D(u) = j_D(x)\left(\frac{c(x)\exp(u)}{c(x)(\exp(u)+j_D(x)} - \frac{c(x)\exp(-u)}{c(x)\exp(-u)+j_D(x)}\right), \tag{10}$$

where $j_D(x)$ is the limiting current, which in this equation is acting as a diffusion coefficient. This choice provides the most accurate model of the cathode reaction.
In what follows the notation $g(u)$ stands for any of the above functions (g_L, g_{BV}, g_D).

At the left end of the cathode, only the protons can exit to the membrane and similarly, at the right end (at the current collector), only the electrons can leave the cathode. Therefore, $\partial_x \phi_1(t,0) = 0$ and $\partial_x \phi_2(t,L) = 0$ such that using Eq. (3) we have the following boundary conditions:

$$\partial_x \eta(t,0) = -\partial_x \phi_2(t,0) = -\frac{1}{\kappa_{eff}(0)} I(t),\ t \in (0, t_{max}),$$
$$\partial_x \eta(t,L) = \partial_x \phi_1(t,L) = \frac{1}{\sigma_{eff}(L)} I(t),\ t \in (0, t_{max}). \qquad (11)$$

Although we have listed all physical principles and the governing equations here, the corresponding equations are not yet ready for the solution, since Eq. (7) contains also the unknown term $\phi_2(t,x)$.

2.2. Governing equations in the heterogeneous case

In this section we will obtain an explicit equation for the overpotential $\eta(t,x)$ by eliminating the term $\phi_2(t,x)$ in Eq. (7) without assuming constant material and kinetic coefficients.

The physical laws in Eqs. (5), (6), (7), and (11) can be rewritten into a single reaction-diffusion equation of type Eq. (21) for the unknown function η:

$$\begin{aligned} aC_{dl}\partial_t \eta(t,x) &= \partial_x \left(\frac{\kappa_{eff}}{\kappa_{eff}+\sigma_{eff}}\right)\left(-I(t) + \sigma_{eff}\partial_x \eta(t,x)\right) \\ &+ \frac{\kappa_{eff}}{\kappa_{eff}+\sigma_{eff}} \partial_x \left(\sigma_{eff}\partial_x \eta(t,x)\right) - ai_0 g\left(\alpha \frac{F}{RT}\eta(t,x)\right) \\ &= \partial_x \left[\frac{\kappa_{eff}\sigma_{eff}}{\kappa_{eff}+\sigma_{eff}} \partial_x \eta(t,x)\right] - \partial_x \left(\frac{\kappa_{eff}}{\kappa_{eff}+\sigma_{eff}}\right) I(t) \\ &\quad -ai_0 g\left(\alpha \frac{F}{RT}\eta(t,x)\right) \end{aligned} \qquad (12)$$

For the corresponding initial-boundary value problem we use the initial value

$$\eta(0,x) = 0,\ x \in (0,L), \qquad (13)$$

and (12) is equipped with the Neumann type boundary conditions in Eq. (11).

Remark: We can express $\phi_2(t,x)$ as

$$\partial_x \phi_2(t,x) = \frac{1}{\kappa_{eff}(x)+\sigma_{eff}(x)}\Big(I(t) - \sigma_{eff}(x)\partial_x\,\eta(t,x)\Big), \tag{14}$$

and consequently, by the assumption $\phi_2(t,0) = 0$ (see the explanation after Eq. (3)) we have

$$\phi_2(t,x) = \int_0^x \left(-\frac{\sigma_{eff}(t,s)}{\kappa_{eff}(t,s)+\sigma_{eff}(t,s)}\partial_s\eta(t,s) + \frac{1}{\kappa_{eff}(t,s)+\sigma_{eff}(t,s)}I(t)\right)ds. \tag{15}$$

Therefore, according to (4) we can give the potential loss V^* at the anode as

$$V^*(t) = \eta(t,L) + \phi_2(t,L)$$

$$= \eta(t,L) + \int_0^L -\frac{\sigma_{eff}(t,s)}{\kappa_{eff}(t,s)+\sigma_{eff}(t,s)}\partial_s\eta(t,s) + \frac{1}{\kappa_{eff}(t,s)+\sigma_{eff}(t,s)}I(t)\,ds. \tag{16}$$

This completes the computation of the right-hand side of Eq. (1), and the desired quantity $E_{cell}(t)$ can be given.

Remark: According to the notations of the second section of this work, we have that

$$p = \frac{1}{aC_{dl}}, \qquad q = \frac{\kappa_{eff}\sigma_{eff}}{\kappa_{eff}+\sigma_{eff}}, \qquad \text{and}$$

$$F\big(t,x,\eta(t,x)\big) = -\frac{i_0}{C_{dl}}g\left(\alpha\frac{F}{RT}\eta(t,x)\right) - \frac{1}{aC_{dl}}\partial_x\left(\frac{\kappa_{eff}}{\kappa_{eff}+\sigma_{eff}}\right)I(t). \tag{17}$$

2.3. Model problem

For testing the method in the article, we investigate here a model problem. Based on real measurements we have $\kappa_{eff} \approx 0.002$ and $\sigma_{eff} \approx 1.8$, and accordingly, we define

$$\kappa_{eff}(t,x) \approx 0.002 - 0.001x \text{ and } \sigma_{eff}(t,x) \approx 1.8 + 0.001x. \tag{18}$$

Consequently,

$$\kappa_{eff} + \sigma_{eff} = 1.801 \quad \text{and} \quad \frac{\kappa_{eff}}{\sigma_{eff}+\kappa_{eff}}(t,x) = \frac{2-x}{1801} \ .$$

For simplicity, we did not incorporate time dependence yet, but our analysis extends also to the case of time dependent conductivity parameters. If the analytic solution of the governing equation Eq. (12) is

$$\eta(t,x) = \frac{t^2}{4} \cdot \left(1 + (x - \frac{1801}{1803})^2\right), \tag{19}$$

we can verify that the equalities

$$-\frac{1}{\kappa_{eff}(t,0)} I(t) = \partial_x \eta(t,0) = \frac{t^2}{2}\frac{1801}{1803} \ ,$$
$$\frac{1}{\sigma_{eff}(t,1)} I(t) = \partial_x \eta(t,1) = -\frac{t^2}{2}\left(1 - \frac{1801}{1803}\right) \tag{20}$$

hold true such that $\partial_x \eta(t,0)$ and $\partial_x \eta(t,1)$ correspond to u_l and u_r in Eq. (12), where $I(t) = 10^{-3} \cdot \frac{1801}{1803} t^2$. These show that the boundary conditions in Eq. (11) are satisfied.
Using all parameters we can give $C_{dl}(x)$ such that η in Eq. (19) is the solution of Eq. (12) with the boundary conditions in Eq. (11).

It is justified to use the numerical method in Section 4 to approximate u, since the Assumptions 1, 2, and 3 are satisfied:

- According to (17) and the choice of the linear kinetics,

$$\partial_3 F(t,x,u) = c(x)\alpha \frac{F}{RT},$$

which is bounded.

- The coefficient functions p and q given in Eq. (17) are obviously positive.
- The inequalities in Assumption 3 have been verified consecutively in the time steps during the simulations. These results are shown in *Fig. 1*. One can see that using a reasonably accurate space discretization, we can simulate the underlying process over sufficiently long time.

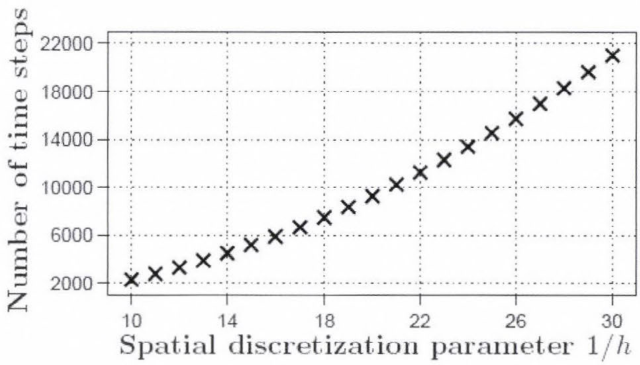

Fig. 1. Number of steps N with step length $\tau = 1$ s until Assumption 3 is satisfied vs. the number n of the grid points on the interval $I = 1$ cm.

3. *Finite difference approximation*

We use the following reaction-diffusion equation as a prototype to investigate some finite difference approximation:

$$\begin{cases} \partial_t u(t,x) = p(t,x)\partial_x\big(q(t,x)\partial_x u(t,x)\big) + F\big(t,x,u(t,x)\big), t \in (0,T), \quad x \in I \\ u(0,x) = u_0(x), \quad x \in I \\ \partial_x u(t,h_l) = u_l(t),\ \partial_x u(t,h_r) = u_r(t), \quad t \in (0,T), \end{cases} \tag{21}$$

for the unknown function u on the interval $I = (h_l, h_r) \subset \mathbb{R}$ over the time domain $[0,T)$, where the coefficient functions $p, q \in C^1([0,T] \times I)$, the reaction term $F \in C^1([0,T] \times I \times \mathbb{R})$, and the fluxes $u_l, u_r \in C^1[0,T]$ are given.

For the numerical approximation we use a staggered grid: I is divided into n uniform subintervals of length
$h = \frac{h_r - h_l}{n}$ such that

$$h_j := h_l + \frac{2j-1}{2|I|}, j = 1,2,\dots,n \text{ and } h_{j+\frac{1}{2}} := h_l + \frac{j}{|I|}, j = 0,1,\dots,n$$

denote the midpoints and the endpoints of the subintervals, respectively, as shown in the following figure:

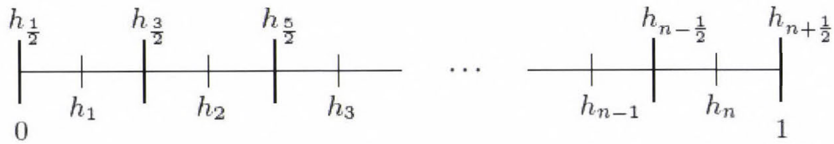

For the time discretization we use the time step $\tau = \frac{T}{N}$ and the notation $t_k := \tau \cdot k$.

We denote the vector of unknowns by

$$\boldsymbol{u}^k = (u_1^k, u_2^k, \dots, u_n^k),$$

where $u_j^k \approx u(t_k, h_j)$. The values of the coefficient function $p_j^k = p(t_k, h_j)$ are defined in the midpoints of the subintervals, i.e., $k = 0,1, \dots, N$ and $j = 1,2, \dots, n$. Accordingly, we use the notations

$$\boldsymbol{u}(k,\cdot) = (u(t_k, h_1), u(t_k, h_2), \dots, u(t_k, h_n))^T \quad ,$$

and

$$\boldsymbol{F}(t_{k+1}, h, \boldsymbol{u}^k) = (F(t_{k+1}, h_1, u_1^k), \dots, F(t_{k+1}, h_n, u_n^k))^T.$$

At the same time, the values of the coefficient function $q_{j+\frac{1}{2}}^k = q\left(t_k, h_{j+\frac{1}{2}}\right)$ are computed at the end points of the subintervals, i.e., $k = 0,1, \dots, N$ and $j = 0,1, \dots, n$.

4. *The IMEX scheme*

We developed a finite difference scheme reported in *Faragó et al.*, (2013). To discuss the corresponding extrapolation method, we summarize the notations and results in *Faragó et al.*, (2013). For the proof of the statements we refer to this work. We developed a finite difference scheme following the *method of lines*: the vector of unknowns at the $(k+1)$th time step is determined from that at the kth time step (*Faragó et al.*, 2013).
Using the notations in Section 3, we consider the following finite difference approximation of Eq. (21):

$$
\begin{cases}
u_j^0 = u_0(h_j),\ j = 1,2,3,\dots,n \\
\frac{u_j^{k+1}-u_j^k}{\tau} = \frac{1}{h} p_j^{k+1}\left(q_{j+\frac{1}{2}}^{k+1} \frac{u_{j+1}^{k+1}-u_j^{k+1}}{h} - q_{j-\frac{1}{2}}^{k+1} \frac{u_j^{k+1}-u_{j-1}^{k+1}}{h} \right) \\
+F\left(t_{k+1}, h_j, u_j^k\right),\ k = 0,1,\dots,N-1, j = 2,3,\dots,n-1 \\
\frac{u_1^{k+1}-u_1^k}{\tau} = \frac{1}{h} p_1^{k+1}\left(q_{\frac{3}{2}}^{k+1}\left(\frac{u_2^{k+1}-u_1^{k+1}}{h} + \frac{\frac{3}{23}u_2^{k+1}-\frac{2}{23}u_1^{k+1}-\frac{1}{23}u_3^{k+1}}{h} - \frac{1}{23}u_l(t_{k+1}) \right)\right. \\
\left. - q_{\frac{1}{2}}^{k+1} u_l(t_{k+1}) \right) + F\left(t_{k+1}, h_1, u_1^k\right),\ k = 0,1,\dots,N-1 \\
\frac{u_n^{k+1}-u_n^k}{\tau} = \frac{1}{h} p_n^{k+1}\left(-q_{n-\frac{1}{2}}^{k+1}\left(\frac{u_n^{k+1}-u_{n-1}^{k+1}}{h} - \frac{\frac{3}{23}u_{n-1}^{k+1}-\frac{1}{23}u_{n-2}^{k+1}-\frac{2}{23}u_n^{k+1}}{h} - \frac{1}{23}u_r(t_{k+1}) \right)\right. \\
\left. + q_{n+\frac{1}{2}}^{k+1} u_r(t_{k+1}) \right) + F\left(t_{k+1}, n, u_n^k\right),\ k = 0,1,\dots,N-1
\end{cases}
\tag{22}
$$

Under the following assumptions the consistency (of second order) and the convergence are proven in our previous work: *Faragó et al.*, (2013).

Assumption 1 *$\partial_3 F : \mathbb{R}^3 \to \mathbb{R}$ is bounded; $\partial_3 F \le F_{max} \in \mathbb{R}$.*
Note that a similar assumption is usual in the literature, (see, e.g., *Hoff*, 1978; *Koto*, 2008).
Assumption 2 *The coefficient functions p and q are nonnegative.*
Assumption 3 *For all $k = 1,2,\dots,N$ the following inequalities hold true:*

$$
s_1^k = \frac{25}{23} d_1^k - \frac{1}{23}\frac{d_1^k}{d_2^k} - \frac{1}{23}\frac{d_1^k c_2^k}{d_2^k} > 0
$$

$$
s_2^k = \frac{25}{23} c_n^k - \frac{1}{23}\frac{c_n^k}{c_{n-1}^k} - \frac{1}{23}\frac{c_n^k d_{n-1}^k}{c_{n-1}^k} > 0.
$$

Remark: The inequalities in Assumption 3 are equivalent with

$$
\boldsymbol{25 d_2^k > 1 + c_2^k \Leftrightarrow r p_2 \left(25 q_{\frac{5}{2}} - q_{\frac{3}{2}}\right) > 1}
$$

$$
25 c_{n-1}^k > 1 + d_{n-1}^k \Leftrightarrow r p_{n-1}\left(25 q_{n-\frac{1}{2}} - q_{n+\frac{1}{2}}\right) > \tag{23}
$$

Lemma 4.1 *The scheme Eq. (22) is consistent with the boundary value problem Eq. (21), and the corresponding order of consistency is* $\mathcal{O}(\tau) + \mathcal{O}(h^2)$.

To rewrite Eq. (22) into a more accessible form we introduce the notations for $j = 1, 2, \dots, n$:

$$rp_j^k q_{j-\frac{1}{2}}^k = c_j^k \quad \text{and} \quad rp_j^k q_{j+\frac{1}{2}}^k = d_j^k \quad \text{with} \quad r = \frac{\tau}{h^2}.$$

With these we define the matrix

$$\begin{pmatrix} 1+\frac{25}{23}d_1^k & -\frac{26}{23}d_1^k & \frac{1}{23}d_1^k & & 0 \;\; \dots \;\; 0 & \\ -c_2^k & 1+c_2^k+d_2^k & -d_2^k & & 0 \;\; \dots \;\; 0 & \\ 0 \quad -c_3^k & & 1+c_3^k+d_3^k & -d_3^k & \ddots & 0 \\ \vdots \quad \vdots & & \vdots & \vdots & & \vdots \\ & & & -c_{n-1}^k & 1+c_{n-1}^k+d_{n-1}^k & -d_{n-1}^k \\ 0 \quad \dots & & 0 & \frac{1}{23}c_n^k & -\frac{26}{23}c_n^k & 1+\frac{25}{23}c_n^k \\ 0 \quad \dots & & 0 & & & \end{pmatrix}$$

and the vector

$$\boldsymbol{v}^k = \left(\frac{\tau}{h}p_1^k\left(q_{\frac{3}{2}}^k \cdot \frac{1}{23} \cdot u_l(t_k) + q_{\frac{1}{2}}^k u_l(t_k)\right), 0, \dots, 0, -\frac{\tau}{h}p_n^k\left(q_{n-\frac{1}{2}}^k \cdot \frac{1}{23} \cdot u_r(t_k) + q_{n+\frac{1}{2}}^k u_r(t_k)\right)\right)^T.$$

The time stepping in Eq. (22) then can be given as

$$\boldsymbol{u}^k = A_{k+1,h}\boldsymbol{u}^{k+1} - \tau \boldsymbol{F}(t, h, \boldsymbol{u}^k) + \boldsymbol{v}^{k+1}. \tag{24}$$

The following property of $A_{k,h}$ is of central importance.

Lemma 4.2 *For all* $h > 0$ *and* $k = 0, 1, \dots, N$ *we have* $\left\|A_{k,h}^{-1}\right\|_\infty = 1$.

Theorem 4.1 *The finite difference method given by Eq. (22) converges to the solution of Eq. (21), and*

$$\max_{j \in \{1,2,\dots,n\}} \left\|u_j^N - u(T, h_j)\right\| = \mathcal{O}(\tau) + \mathcal{O}(h^2). \tag{25}$$

Proof: The error of the solution in the consecutive time steps is defined as

$$\left(e_1^k,\ e_2^k, \dots, e_n^k\right) = \boldsymbol{e}^k = u(k,\cdot) - u^k.$$

The consistency of the scheme implies that

$$\boldsymbol{u}(k,\cdot) = A_{k+1,h}\boldsymbol{u}(k+1,\cdot) - \ \tau\boldsymbol{F}\big(t,h,\boldsymbol{u}(k,\cdot)\big) + \boldsymbol{v}_{k+1} - \mathcal{R}^k,$$

where

$$\left\|\mathcal{R}^k\right\|_\infty = \ \tau(\mathcal{O}(\tau) + \mathcal{O}(h^2)). \tag{26}$$

This, together with Eq. (24) gives that

$$e^k = A_{k+1,h}e^{k+1} - \ \tau\left(\boldsymbol{F}(t,h,\boldsymbol{u}^k) - \ \boldsymbol{F}\big(t,h,\boldsymbol{u}(k,\cdot)\big)\right) + \mathcal{R}^k,$$

or in an equivalent form

$$\boldsymbol{u}^k - \boldsymbol{u}(k,\cdot) = e^{k+1} =$$
$$A_{k+1,h}^{-1}\, e^k + \ \tau A_{k+1,h}^{-1}\left(\boldsymbol{F}(t,h,\boldsymbol{u}^k) - \ \boldsymbol{F}\big(t,h,\boldsymbol{u}(k,\cdot)\big)\right) + \mathcal{R}^{k+1}.$$

Therefore, using the result in Lemma, the Lagrange inequality, and Assumption 3 we obtain

$$\left\|\boldsymbol{e}^{k+1}\right\|_\infty \leq \left\|\boldsymbol{e}^k\right\|_\infty + \ \tau\boldsymbol{F}_{max}\left\|\boldsymbol{e}^k\right\|_\infty + \left\|\mathcal{R}^{k+1}\right\|_\infty \tag{27}$$

for all $k = 1,2,\dots,N$. The consecutive application of Eq. (27) gives that

$$\|\boldsymbol{e}^N\|_\infty \leq \ (1+\ \tau\boldsymbol{F}_{max})^{N-1}\|\mathcal{R}^1\|_\infty + (1+\ \tau\boldsymbol{F}_{max})^{N-2}\|\mathcal{R}^2\|_\infty + \ \dots + \ \|\mathcal{R}^N\|_\infty$$
$$\leq \ N(1+\ \tau\boldsymbol{F}_{max})^N \max_{j\,\epsilon\,\{1,2,\dots,n\}}\left\|\mathcal{R}^j\right\|_\infty \leq Te^{T\cdot F_{max}}\frac{max_{j\,\epsilon\,\{1,2,\dots,n\}}\left\|\mathcal{R}^j\right\|_\infty}{\tau}$$

such that according to Eq. (26) we obtain the estimate in the theorem.

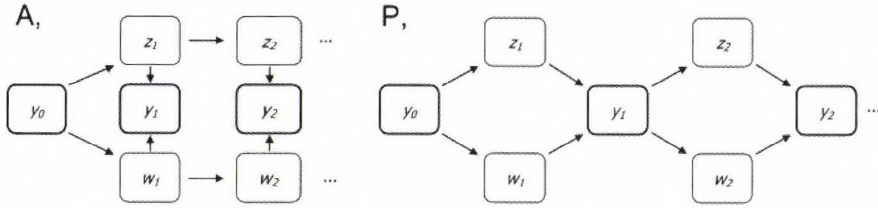

Fig. 2. Schematic comparison of the different Richardson extrapolation procedures: passive method (left) and active method (right)

5. *Richardson extrapolation*

According to Theorem 3, the previously presented numerical scheme provides us 2nd order of consistency in space, but not in time. We apply the Richardson extrapolation as a powerful device to increase the accuracy of the numerical method in *Richardson*, (1927). In general, it consists of the application of the given numerical scheme. In order to have a 2nd order scheme both in space and time, the application of another mathematical device is crucial.

Richardson extrapolation is a powerful device to increase the accuracy of some numerical method. It consists in applying the given numerical scheme with different discretization parameters (in our case, Δt and $\Delta t/2$) and combining the obtained numerical solutions by properly chosen weights. Namely, if p denotes the order of the chosen numerical method, w_n is the numerical solution obtained by $\Delta t/2$ and z_n that obtained by Δt, then the combined solution

$$y_n = \frac{2^p w_n - z_n}{2^p - 1}$$

has an accuracy of order $p + 1$. This method was first used by L. F. Richardson (*Richardson*, 1927) who called it "the deferred approach to the limit". The Richardson extrapolation is widely used especially for time integration schemes, where, as a rule, the results obtained by two different time-step sizes are combined.

The Richardson extrapolation can be implemented in two different ways when one attempts to increase the accuracy of a time integration method (see Figure 2), namely, passive and active Richardson extrapolations (*Zlatev*, 2010). These two versions of the Richardson extrapolation are also described in (*Botchev* and *Verwer*, 2009), where they are called global and local Richardson extrapolations. The main difference between these two methods is that in the case of passive extrapolation, the numerical solutions obtained with different step sizes are computed independently of the result of the extrapolation obtained at the previous time step, while in the active version, the result of the extrapolation is used as initial condition in each time step.

Remark 5.1 *It is not difficult to see that if the passive device is applied and the underlying method has some qualitative properties, then the combined method also possesses this property. However, if the active device is used, then this is not valid anymore: any property of the underlying method does not imply the same property of the combined method. Therefore, the active Richardson extrapolation requires further investigation when a given numerical method is applied.*

6. *Numerical results*

We present some numerical results here corresponding to the model problem discussed in Section 2.3. The analytic and numerical solution are compared at $T = 1$ in *Fig. 3* for a single parameter set.

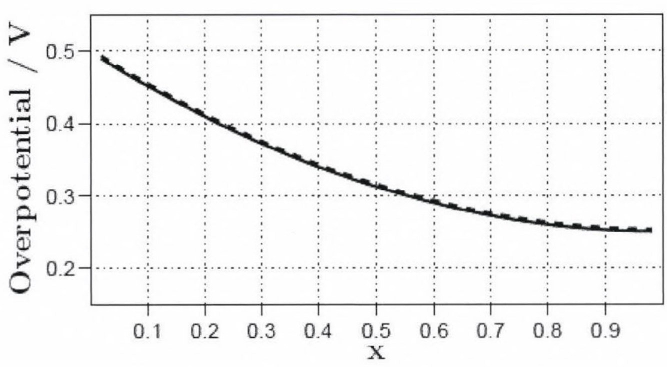

Fig. 3: Analytic solution Eq. (19) of Eq. (12) (continuous line) and the numerical approximation (dashed line) obtained by the method in Eq. (22) with $T = 1$, $N = 25$, and $\tau = 0.01$ for the test problem in Section 2.3. The remaining parameters are given in the Appendix.

We investigated the order of convergence in the $\|\cdot\|_\infty$ norm experimentally with respect to the spatial discretization. To this aim we consecutively refined the grid and the time step simultaneously such that the ratio $\frac{\tau}{h^2}$ is kept at constant level. Accordingly, in the figures we only investigate the dependence of the $\|\cdot\|_\infty$ -norm error on the number $\frac{1}{h}$ of the spatial grid points. The corresponding results are shown in *Fig. 4*. The numerical results confirm our expectation in Section 4: we can fit accurately a line of slope –2 to the log-log data, which shows a second order convergence with respect to the spatial discretization parameter, see *Fig. 4*.

In *Fig. 5* we illustrated the order of the convergence of the numerical models obtained by the application of the two types of Richardson extrapolation (active and passive) methods. Comparing this result to *Fig. 4*. (i.e., to the results obtained without Richardson extrapolation), one can easily see that the application of these methods led to lower approximation errors. Though, in the case of active Richardson extrapolation, the convergence becomes second order only in the limit $h \to 0$.

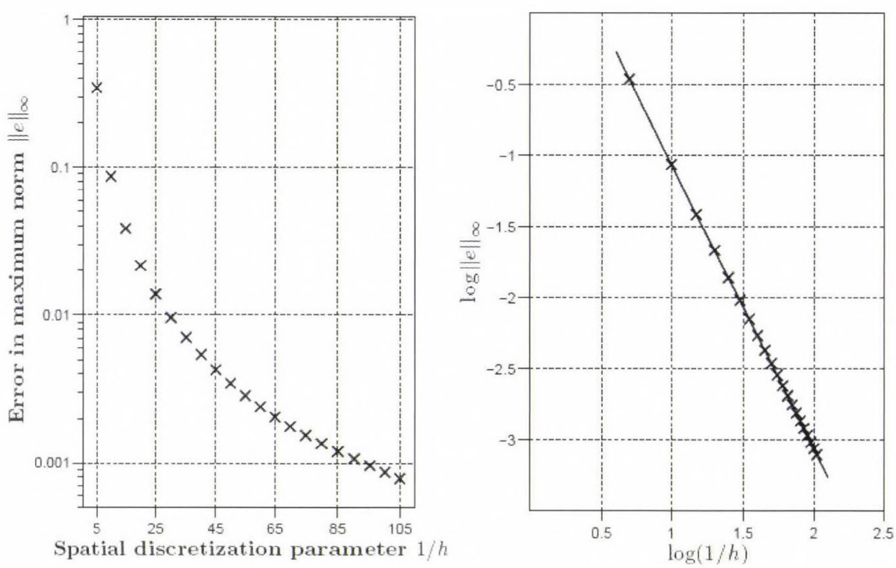

Fig. 4. $\|\cdot\|_\infty$ norm error in the numerical solution (obtained by the presented IMEX method) for the test problem in Section 2.3 vs. the spatial discretization parameter (left). Log-log plot of the error vs. the spatial discretization parameter and a fitted line with slope –2 (right).

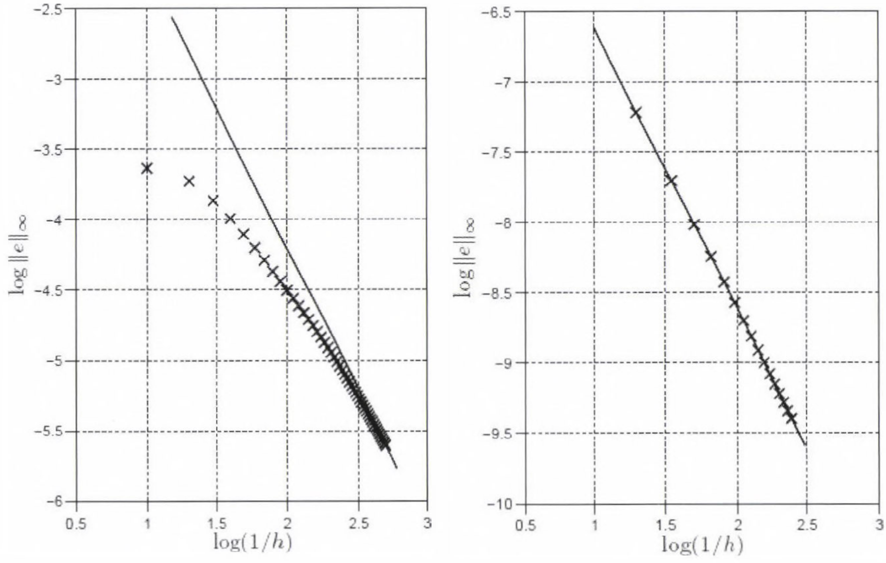

Fig. 5. Log-log plot of the $\|\cdot\|_\infty$ norm error vs. the spatial discretization parameter for the active Richardson extrapolation (left) and the passive Richardson extrapolation (right).

7. *Conclusions*

Our results have proven that the combination of the presented implicit-explicit method with some Richardson extrapolation methods can be a useful device for solving reaction-diffusion equations numerically. The numerical results in the previous section are also supporting our theoretical analysis.

Aknowledgements–The first author was supported by Hungarian National Research Fund OTKA No. K67819. All authors were supported by the European Union and co-financed by the European Social Fund (grant agreement no. TAMOP 4.2.1./B-09/1/KMR-2010-0003). The Financial support of the National Office of Research and Technology (OMFB-00121-00123/2008) is acknowledged by the authors.

References

Botchev, M.A. and *Verwer, J.G.*, 2009: Numerical integration of damped Maxwell equations. *SIAM J. Sci. Comput. 31(2),* 1322–1346.

Faragó, I.,Izsák, F., Szabó,T., and *Kriston, A.*, 2013: An IMEX scheme for reaction-diffusion equations: application for a PEM fuel cell model., *Cent. Eur. J. Math. 11*, 746–759.

Hoff, D., 1978: Stability and convergence of finite difference methods for systems of nonlinear reaction-diffusion equations. *SIAM J. Numer. Anal. 15*, 1161–1177.

Koto, T., 2008: IMEX Runge-Kutta schemes for reaction-diffusion equations. *J. Comput. Appl. Math., 215*, 182–195.

Kriston, A., Inzelt, G., Faragó, I., and *Szabó, T.*, 2010: Simulation of the transient behavior of fuel cells by using operator splitting techniques for real-time applications. *Comput. Chemical Eng. 34*, 339–348.

Litster, S. and *Djilali, N.*, 2007: Mathematical modelling of ambient air-breathing fuel cells for portable devices. *Electrochimica Acta, 52,* 3849–3862.

Newman, J. and *Thomas-Alyea, K.E.*, 2004: Electrochemical systems. John Wiley & Sons, Inc., Hoboken, New Yersey.

Richardson, L.F., 1927: The deferred approach to the limit, i-single lattice. *Philosophical Transactions of the Royal Society of London 226*, 299–349.

Subramanian, V.R., Boovaragavan, V., and *Diwakar. V.D.*, 2007: Toward real-time simulation of physics based lithium-ion battery models. *Electrochem. Solid-State Lett. 10,* A255–A260.

Ziegler, C., Yu, H.M., and *Schumacher, J.O.*, 2005: Two-phase dynamic modeling of pemfcs and simulation of cyclo-voltammograms. *J. Electrochem. Soc. 152*, A1555–A1567.

Zlatev, Z., Faragó, I., and *Havasi, A.*, 2010: Stability of the Richardson extrapolation applied together with the Θ-method. *J. Comput. Appl. Math. 235*, 507–517.

Appendix

Symbol	**Description**	**Unit**
a	Specific interfacial area	cm^{-1}
C_{dl}	Double-layer capacitance	F/cm^2
E_{cell}	Cell potential	V
E_{OC}	Open circuit potential	V
F	Faraday constant (96487)	C/mol
I	Total cell current density	A/cm^2
i_0	Exchange current density at the cathode	A/cm^2
i_0^a	Exchange current density at the anode	A/cm^2
i_1	Solid phase current density at the cathode	A/cm^2
i_2	Solution phase current density at the cathode	A/cm^2
i_f	Faradaic current density	A/cm^3
j_D	Limiting current at the cathode	A/cm^2
L	Thickness of the cathode	cm
R	Universal gas constant (8.3144)	J/molK
T	Cell temperature	K
V^*	Potential loss at the cathode	V
W_{mem}	Membrane thickness	cm
α	Transfer coefficient in the cathode	
α_a^a	Anodic transfer coefficient at the anode	
α_c^a	Cathodic transfer coefficient at the anode	
η	Overpotential at the cathode	V
η^a	Overpotential at the anode	V
ν^2	Dimensionless Exchange current density	
ϕ_1	Solid phase potential	V
ϕ_2	Solution phase potential	V
κ_{eff}	Effective solution phase conductivity	S/cm
σ_{eff}	Effective solid phase conductivity	S/cm
σ_{mem}	Membrane conductivity	S/cm

IDŐJÁRÁS

Quarterly Journal of the Hungarian Meteorological Service
Vol. 117, No. 2, April – June, 2013, pp. 219–237

Projected changes in the drought hazard in Hungary due to climate change

Viktória Blanka[1*], **Gábor Mezősi**[1*], and **Burghard Meyer**[2]

[1]*University of Szeged,*
Egyetem u. 2-6. H-6722 Szeged, Hungary

[2]*Universität Leipzig,*
Ritterstraße 26. DE-04109 Leipzig, Germany

**Corresponding authors E-mails: blankav@geo.u-szeged.hu, mezosi@geo.u-szeged.hu*

(Manuscript received in final form December 18, 2012)

Abstract–In the Carpathian Basin, drought is a severe natural hazard that causes extensive damage. Over the next century, drought is likely to remain one of the most serious natural hazards in the region. Motivated by this hazard, the analysis presented in this paper outlines the spatial and temporal changes of the drought hazard through the end of this century using the REMO and ALADIN regional climate model simulations.

The aim of this study was to indicate the magnitude of the drought hazard and the potentially vulnerable areas for the periods 2021–2050 and 2071–2100, assuming the A1B emission scenario. The magnitude of drought hazard was calculated by aridity (De Martonne) and drought indices (Pálfai drought index, standardised anomaly index). By highlighting critical drought hazard areas, the analysis can be applied in spatial planning to create more optimal land and water management to eliminate the increasing drought hazard and the related wind erosion hazard.

During the 21st century, the drought hazard is expected to increase in a spatially heterogeneous manner due to climate change. On the basis of temperature and precipitation data, the largest increase in the drought hazard by the end of the 21st century is simulated to occur in the Great Hungarian Plain. Moreover, the changes in the extreme indices (e.g., days with precipitation greater than 30 mm, heat waves, dry periods, wet periods) suggest that the frequency and duration of drought periods will increase. The drought hazard is projected to be lowest in the westernmost part of Hungary. This result is based on qualitative and quantitative analyses that showed the changes in precipitation, temperature, and extreme indices.

Key-words: regional climate change, ALADIN and REMO models, drought hazard, drought indices

1. Introduction

Drought is a severe natural phenomenon that occurs on most of the continents, and it causes extensive damage (*Kogan*, 1997). Drought is one of the most prevalent environmental hazards in parts of Europe and Russia (*Briffa et al.*, 1994, *Meshcherskaya* and *Blazhevich,* 1997). In the Carpathian Basin, drought is one of the most severe natural hazards, causing serious damage to the national economy, agriculture, and water resources. The lack of water during drought periods is harmful for all living organisms, including humans, and can result in social and economic consequences, such as drinking water shortages and reductions in agricultural yields.

Despite the seriousness of this phenomenon, drought is not a well-defined term, and the technical and colloquial uses of this term vary greatly. The absence of a precise and universally accepted definition of drought can lead to confusion concerning whether a drought exists and what the severity is. This imprecision causes considerable debate among meteorologists, farmers, and public officials. Researchers use the term "drought" to describe periods when precipitation is below average, leading to water shortages, and unmet demand for water (*Vermes et al.*, 2000). Drought is a creeping phenomenon. It is often difficult to ascertain when a drought begins, as the deficiency of moisture in a region takes time to emerge (*Changnon*, 1987), and when it ends (*Warrick et al.*, 1975). In addition to precipitation, a number of factors play a significant role in the evolution of a drought. These factors include evaporation, which is affected by temperature and wind, soil type and its ability to store water, the depth and presence of groundwater supplies, and vegetation. Accounting for these factors, three types of droughts are commonly noted: meteorological (*Palmer,* 1965, *Farago et al.,* 1989), agricultural (*Maracchi,* 2000), and hydrological (*Pálfai*, 2002a; *Hisdal* and *Tallaks*en, 2003). In addition, the terms "drought" and "aridification" are often confused. It is important that drought be distinguished from aridification. Generally, drought is described as a temporary phenomenon (*Dracup et al*., 1980), while aridification is described as the process of a region becoming increasingly dry.

Due to the discrepancies in describing these phenomena (differing definitions of event duration and numerous measurement methods – *Heim,* 2002), researchers often apply numerical methods or indices (e.g., the Palmer index, Standardised precipitation index (SPI), De Martonne index, and the Pálfai aridity index (PAI)) to define drought-affected areas (*Svoboda et al*., 2002; *Dunkel,* 2009). The application of these indices can eliminate the uncertainty of estimating the spatial and temporal extent and severity of a drought.

In the Carpathian Basin, drought is a severe natural hazard that causes extensive damage, and it is regarded as the most prominent natural hazard of the next century (*Bakonyi*, 2010). Therefore, the aim of this study was to outline the spatial and temporal changes in the drought hazard until 2100 by using experiments of the REMO and ALADIN regional climate models. These model simulations are suitable for this analysis because they use the A1B scenario (*Nakicenovic* and *Swart,* 2000), which represents intermediate estimations for the changes in greenhouse gas emissions over the next century, to model anthropogenic forcing. These model experiments have been used successfully in previous climate studies (*Szépszó* and *Horányi,* 2008; *Csima* and *Horányi,* 2008; *Pieczka et al.,* 2010; *Rannow et al.* 2010; *Mezősi et al.* 2012).

These models predicted a continuous, but not constant temperature increase in the Carpathian Basin, with the most intense increase occurring in the summer months (the rate of change is similar to that experienced between 1980 and 2010). The change in annual precipitation simulated by model experiments is not significant; however, the distribution of precipitation within a year is likely to change more significantly, the decreasing summer and increasing winter precipitation would result more homogenous distribution of the precipitation throughout the year (*Tables 1* and *2*) (*Bartholy et al.,* 2008; *Szabó et al.,* 2010; *Csorba et al.* 2012).

Table 1. Changes in the projected mean annual and seasonal temperature (°C) compared with the mean from the period of 1961–1990 based on the REMO and ALADIN model experiments (*Szabó et al.,* 2010)

Period	Year	Spring	Summer	Autumn	Winter
2021–2050	(+1.4)–(+1.9)	(+1.1)–(+1.6)	(+1.4)–(+2.6)	(+1.6)–(+2.0)	+1.3
2071–2100	+3.5	(+2.3)–(+3.1)	(+4.1)–(+4.9)	(+3.6)–(+3.8)	(+2.5)–(+3.9)

Table 2. Changes in the projected mean annual and seasonal precipitation (%) compared with the mean from the period of 1961-1990 based on the REMO and ALADIN model experiments (*Szabó et al.,* 2010)

Period	Year	Spring	Summer	Autumn	Winter
2021-2050	(–1)– 0	(–7)–(+3)	–5	(+ 3)–(+14)	(–10)–(+7)
2071–2100	(–5)–(+3)	(–2)–(+2)	(–26)–(–20)	(+10)–(+19)	(–3)–(+31)

Climate simulations show that extreme climate events may occur more frequently in the Carpathian Basin over the next century, and that more prolonged and severe hot and dry periods are projected. The number of frost days could decrease by 30 % by 2050 and by 50 % by the end of the 21st century, and the number of summer days (T_{max}>25 °C) could become double or even triple the present number (*Szépszó,* 2008). The projection for precipitation involves more uncertainty, in certain seasons even the tendency is contradictory in the REMO and ALADIN model simulations (*Szabó et al.,* 2010). Uncertainties in these long-term climate simulations arise from the nearly unpredictable social and economic changes that may occur over the next century and from the internal variability of the climate system (*Bartholy* and *Pongrácz,* 2010). However, despite the prediction limitations, this analysis can provide valuable information for future environmental and spatial planning (*Mezősi et al.*, 2012).

The aim of this study is to predict the magnitude of the drought hazard and the potentially vulnerable areas in Hungary for the periods 2021–2050 and 2071–2100, assuming the A1B emission scenario. This analysis can be used to highlight the critical drought areas. This information can be considered in spatial planning to create more optimal land and water management and to eliminate the increasing drought hazard and the related wind erosion hazard. These hazard projections can become an integral part of drought planning, preparedness, and mitigation efforts at the national, regional and local levels.

2. *Methods*

2.1. Determination of the landscape units

Due to the resolution of the climate data, an analysis of the 230 traditional, environmentally homogeneous micro-regions of Hungary were not possible; therefore, 18 larger landscape units were defined (*Fig. 1*). The areas of the defined units are better suited to the resolution of the climate data and the demands of spatial planning. The determination of the landscape units was based on the spatial diversity of landscape shaping factors (relief, soil, geology, vegetation, land use, and climate). The borders of the units were matched to the shapes of larger natural landscape units (e.g., micro-regions along the middle and lower sections of the Tisza River) and economic regions (e.g., central Hungary), where the border was justified by the climate dependence of the land use.

Due to their small areas, these landscape units are not substantive climatically. However, the physical parameters are relatively homogeneous in the units; therefore, any climate change affects the entire unit in the same way. An analysis on this scale can be important for the recognition of probable future climate effects and in the development of strategic spatial plans.

1 Little Hungarian Plain
2 Western part of the Carpathian Basin
3 Zala Hills
4 Marcal basin and Komárom Plain
5 Transdanubian Mountains
6 Hilly region of Inner Somogy
7 Transdanubian Hills
8 Dráva Plain and Mecsek Mountains
9 Mezőföld Plain
10 Danubian Plain
11 Danube-Tisza Interfluve
12 Gödöllő Hills
13 Western part of the North Hungarian Mountains
14 Eastern part of the North Hungarian Mountains
15 Plain of Upper Tisza
16 Plains of Nyírség and Hajdúság
17 Central part of the Great Hungarian Plain
18 Körös-Maros Interfluve

Fig. 1. The examined landscape units (after *Csorba et al.*, 2012)

2.2. Calculation of the climate data

The simulated future changes of the climate parameters were analyzed using two regional climate models, REMO and ALADIN. The models utilize the A1B scenario, which represents the average changes of greenhouse gas emissions, to model anthropogenic climate forcing. The A1B scenario describes an integrated world with rapid economic growth, slowing population increases, a quick spread of new and efficient technologies, and a balanced emphasis on all energy sources (*Nakicenovic* and *Swart,* 2000). The resolution of the climate data was 0.22 ° (approximately 25 km). The climate projections were generated by the Numerical Modelling and Climate Dynamics Division of the Hungarian Meteorological Service.

Daily temperature and precipitation data for the periods 2021–2050 and 2071–2100 were used in the calculations. The temperature and precipitation data changes are in °C and mm, respectively, with respect to the reference period of 1961–1990. The following changes in the extreme climate indices were also generated from the two models: frost days in days/year; summer days (T_{max}>25 °C) in days/year; extremely heavy precipitation days ($R_{day}\geq30$ mm), in days/year; and the simple daily intensity index (SDII), which is a measure of the precipitation amount per rainy day ($R_{day}\geq1$ mm), in mm/day. From all of these data, average yearly and monthly data were calculated and evaluated for the two study periods. Regional average values were calculated for the landscape units based on the climate parameters at each grid point.

2.3. Assessing the change in drought hazard

One method of evaluating drought hazard is calculating drought or aridity indices. Several indices use only precipitation and temperature data, while others evaluate the soil moisture condition or water budget and may be recursive (e.g., the widely known and frequently used Palmer index). All of these indices have advantages and disadvantages; therefore, comprehensive studies generally apply a number of indices to obtain a better result by eliminating the deficiencies of a single index (e.g., the US Drought Monitor uses seven different indices).

During this research, two different methods were applied to assess the future changes in the drought hazard and associated results. A qualitative analysis was applied to define the tendencies of the changes, and a quantitative analysis was used to provide numerical values for the changes.

In the qualitative analysis, the future climate change trends were assessed, and the current probability of drought occurrence in the landscape units was analyzed using the PAI (*Pálfai*, 1984, 1990, 2002b). The present-day conditions were compared with the tendencies due to climate change. The tendencies caused by climate change and the regions with similar characteristics were identified by cluster analysis. The temperature and precipitation data and 4 extreme climate indices (average number of summer days, average number of frost days, average number of heavy precipitation days - with precipitation above 20 mm, and the SDII precipitation index, describing number of precipitation days – above 1 mm rainfall) were used in the cluster analysis. After extracting the factor coefficients for the regions, hierarchical clustering applied, where natural groupings can be detected. Cluster analysis of the factors coefficients gave an alternative linkage approaches and metrics. The assessment identified the sensitivity of the landscape units and the vulnerable areas. This method did not provide information about the magnitude of the changes, but it took more parameters into account than did the aridity and drought indices. This result means that a more complex description of the changes can be provided that considers which extreme climate indices enhance or eliminate the effect of mean temperature and precipitation changes.

To evaluate the magnitude of the changes, aridity and drought indices were calculated. For the investigation, three indices with different temporal resolutions and that were determined through different calculation methods were selected. The indices were calculated by using observed meteorological data of the reference period (1961–1990) and the projected changes of the model simulations. This method of choosing indices reduced the errors from the models and allowed differences within a year to be estimated.

2.4. Aridity index: De Martonne (IDM)

To begin, an aridity index was calculated. Aridity indices primarily characterize the climate of a region rather than the drought hazard. However, as aridity increases, the occurrence of drought can become more frequent and the severity can grow, thereby increasing the drought hazard. From among several aridity indices, the De Martonne index was selected, which is based on annual temperature and precipitation data.

De Martonne index (*IDM*):

$$IDM = P/(T+10)\ ,$$

where P is the annual precipitation and T is the annual mean temperature. The temporal resolution of the input data is low, but this index is widely used (*Doerr,* 1963; *Botzan et al.,* 1998; *Grieser,* 2006; *Paltineanu et al.,* 2007; *Baltas,* 2007; *Livada* and *Assimakopoulos,* 2007; *Lungu et al.*, 2011). It was observed that the index properly demonstrates the spatial differences of drought.

The future drought hazard can be estimated by calculating drought indices. These indices were developed to describe the drought level on annual and sub-annual timescales. In this study, average values for the 30-year periods (2021–2050 and 2071–2100) was calculated, therefore, the drought levels in individual years could be notably different in the landscape units. Due to the uncertainties in the climate projections, it is not advisable to calculate the indices for shorter periods. In addition, a long-term average value showing the tendency of the change can be more applicable for spatial planning purposes.

2.5. Drought indices: $PaDI_0$ and the standardized anomaly index (SAI)

Two drought indices were calculated, the $PaDI_0$ index and the standardized anomaly index (*SAI*). The $PaDI_0$ index uses monthly temperature and precipitation data, and average monthly data were evaluated for the two study periods (*Pálfai* and *Herceg*, 2011). The $PaDI_0$ is based on the *PAI* and is used in Hungary, but its simplicity allows for wider use. Both $PaDI_0$ and *PAI* is a relative indicators that characterize the drought with one numerical value that is associated with one agricultural year.

$PaDI_0$ index:

$$PaDIo = \frac{\left[\sum_{i=apr}^{aug} Ti \right] \; / \; 5*100}{\sum_{i=oct}^{sept} (Pi * wi)} ,$$

where T_i is the mean monthly temperature from April to August, P_i is the monthly sum of precipitation from October to September, and w_i is a weighting factor (*Table 3*). The weighting factor expresses the importance of the months in the evolution of drought. The $PaDI_0$ index characterizes a drought with one numerical value for one agricultural year. The index focuses on the drought occurring in the vegetation period, as is indicated by the monthly weighting factors. The index was developed in Hungary, and it reveals the drought periods particularly well under the climatic conditions of the Carpathian Basin.

Table 3. Weighting factors w_i of monthly precipitation in $PaDI_0$ (*Pálfai* and *Herceg*, 2011)

Month	**Weight factor (w_i)**	**Month**	**Weight factor (w_i)**
October	0.1	April	0.5
November	0.4	May	0.8
December	0.4	June	1.2
January	0.5	July	1.6
February	0.5	August	0.9
March	0.5	September	0.1

To describe the role of precipitation changes in the changing drought hazard, an index was calculated using only precipitation data. The SAI was used to characterise the precipitation variability in a particular region. The main advantage of this index is the low data demand; however, in some situations, it does not indicate the drought level correctly (*Katz* and *Glantz,* 1986, *McKee et al*., 1993). Generally, the index is calculated for shorter periods (from 1 to 12 months), but it was computed for the two 30-year periods in this case. Even when calculated over longer periods, the SAI produces acceptable temporal and spatial differences in the drought hazard. For this evaluation, three-month SAI values were calculated for the most drought-prone and agriculturally important period, from June to August.

SAI:

$$SAI = \frac{P - m(P)}{d(P)},$$

where P is the precipitation amount, $m(P)$ is the average precipitation of the reference period, and $d(P)$ is the standard deviation of the precipitation in the reference period (1960–1990).

These indices provide numerical values of the changes in the drought hazard even though they analyse only a few parameters. These indices do not provide the most accurate value for the drought hazard because they use only the temperature and precipitation data (they do not even use evaporation or groundwater level data). However, all of the input data are extractable from the applied climate models. The aim of this study was not to give an accurate value of future changes in the drought hazard but to show the tendencies on the meso-scale.

3. *Results*

3.1. Qualitative analysis of the future drought hazard

The *PAI* (*Pálfai*, 2004) shows that the highest drought level was located in the landscape unit of the Great Hungarian Plain, and it decreased toward the north and west. The highest *PAI* values were in the central and southern part of the Great Hungarian Plain. The lowest values were in the higher elevations of the Alpokalja region and on the higher hills of the North Hungarian Mountains (*Fig. 2*).

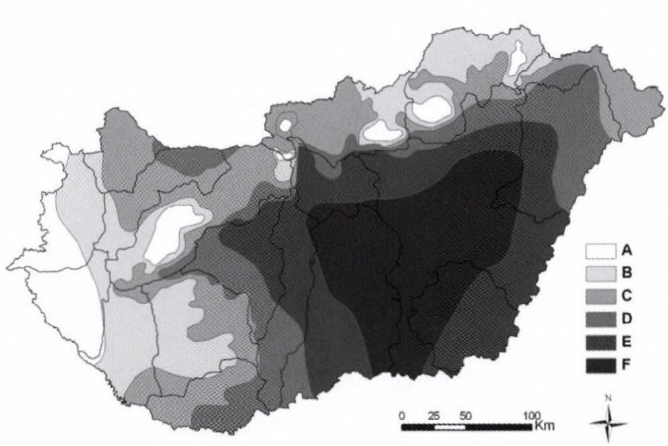

Fig. 2. Drought map of Hungary (*Pálfai*, 2004) (A: drought free; B: mild; C: moderate; D: medium; E: high; F: extremely high rate of exposure).

Despite the small area and the relatively low topographic diversity of the region, the two climate simulations showed spatial differences in the parameters. Four regions in Hungary with different climate change tendencies were defined by a cluster analysis based on the temperature, precipitation and extreme indices. In these regions, the climate change tendencies indicated diverse alterations of the social and ecological systems. The climate change in the 21st century affects the drought hazard differently in each of the four regions (*Mezősi et al.*, 2012).

The climate change tendencies in these regions have similar characteristics. The region type 1 is located along a west central corridor ranging from north to south. Moderate temperature increases and distinct changes in extreme temperature events are projected. Future precipitation is projected to increase with higher rates but moderate changes in extreme rainfall events. The region type 2 covers the northeastern regions along the Slovakian border. This region had the lowest annual mean temperatures and the highest intraregional temperature variation. Moderate future increases are simulated with moderate increases in the number of extreme event days. The region type 3 is essentially the Hungarian Great Plain, excluding the Plains of Nyírség and Hajdúság regions. This region has the highest temperatures and the lowest annual precipitation totals. The region is projected to experience the highest temperature increases, greatest changes in extreme temperature events (increases in summer days and decreases in frost days), highest precipitation decline ratios (or at least the lowest precipitation increase ratios), and an increase in the number of heavy rainfall days. The region type 4 covers only two landscape units in the western hilly area. This type is characterized by smaller temperature increases and smaller changes in temperature extremes. This region type is simulated to be more humid and have higher precipitation totals, smaller precipitation change ratios, and smaller change rates with regard to heavy rain events (*Fig. 3*).

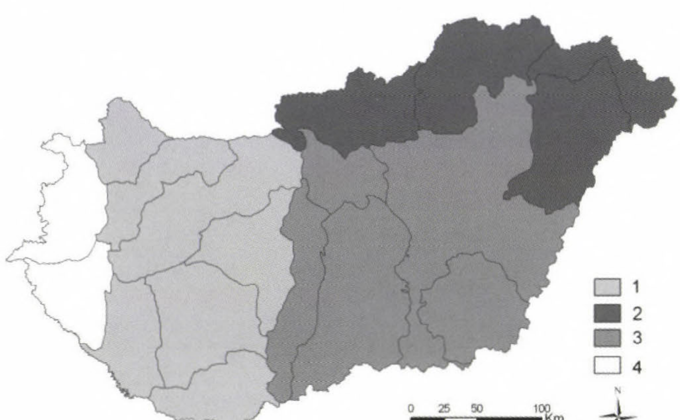

Fig. 3. Regional types of climate change exposure as a result of cluster analysis (*Mezősi et al.*, 2012).

The increase in the annual mean temperature affects the increase in the drought hazard in all regions. The largest increase in the drought hazard by the end of the 21st century is simulated in the third region type, because the increase in the annual mean temperature, increase in the number of summer days, and decrease in precipitation will all be the largest in this region type. Moreover, the increase in the number of extremely heavy precipitation days and the SDII indicated that the precipitation will fall in a more concentrated time period, which suggests that the frequency and duration of drought periods will increase. Additionally, this region already has the highest drought hazard.

In the first and second region types, the temperature increases are also projected to be significant, but the precipitation change will be slight, with a possible small increase. A moderate increase in the drought hazard is projected. The highest precipitation total and the lowest annual mean temperature currently occur in the fourth region, and future changes are projected to be moderate. The drought hazard will be the lowest in this region (*Fig. 4*).

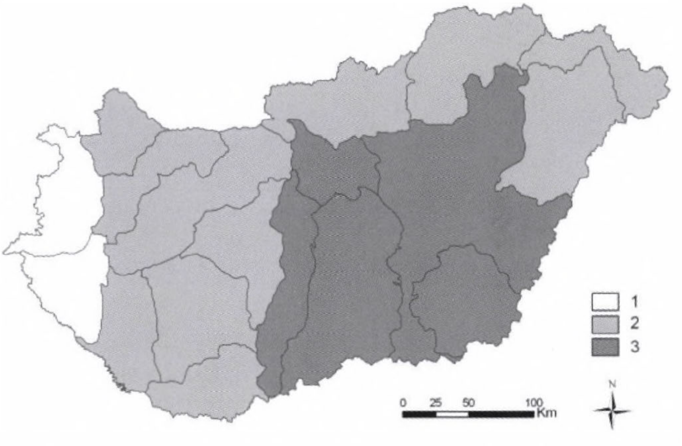

Fig. 4. Future changes in drought hazard due to climate change in the regions with similar characteristics (1. slight increase; 2. moderate increase; 3. major increase).

By using the regions defined by a cluster analysis as a basis for the analysis, the spatial differences and relations between the climate change tendencies and the changes in the drought hazard were revealed. Verification of the results is problematic, but the uncertainties can be reduced by using different calculation methods. Accordingly, the magnitude of the changes and the spatial differences were also analyzed by calculating the De Martonne index, $PaDI_0$ index, and SAI.

4. *Quantitative analysis of the future drought hazard*

4.1. Changes in the De Martonne index

In the reference period (1961–1990), the value of the De Martonne index varied between 23.7 mm/°C and 33.5 mm/°C in the landscape units on the basis of observed meteorological data. The lowest values, representing the highest aridity, were observed in the southeastern part of Hungary. The landscape units in that region of the country (the Danube-Tisza Interfluve and Körös-Maros Interfluve) were categorized as mediterranean (20 mm/°C $\leq$ IDM $\leq$ 24 mm/°C). The largest part of the country was categorized as semi-humid (24 mm/°C $\leq$ IDM $\leq$ 28 mm/°C), while some units along the northeastern and western borders were categorised as humid (28 mm/°C $\leq$ IDM $\leq$ 35 mm/°C).

Changes in the drought hazard can be analyzed with categories from the De Martonne index, which defines the drought hazard as low in humid regions, moderate in semi-humid regions, and high in mediterranean regions. Any future changes in the De Martonne index indicate changes in the drought hazard. For the period 2021–2050, the two model simulations showed similar changes; namely, the index values are likely to decrease to 20.7–31.4 mm/°C and 20.7–31.0 mm/°C using REMO and ALADIN outputs, respectively. In the southeastern and central regions of Hungary, four landscape units were transferred to the mediterranean category, and the Nyírség and Hajdúság units were transferred to the semi-humid category. For the period 2071–2100, the value of the index is projected to decrease in all of the units; however, the difference between the model experiments is larger in this period (19.6–28.8 mm/°C in case of REMO and 18.2–27.3 mm/°C in case of ALADIN). In the ALADIN model, the landscape unit of the Great Hungarian Plain, except for the Plains of Nyírség and Hajdúság portions, was transferred to the semi-dry (10 mm/°C $\leq$ IDM $\leq$ 20 mm/°C) category. When using outputs of REMO simulation, the spatial distribution of the changes was similar. However, this model indicated less significant changes, and only the Körös-Maros Interfluve unit was transferred to the semi-dry category. The index values also decreased in the humid-category landscape units in the two model simulations, and the units were transferred to the semi-humid category when using outputs of ALADIN simulation. Consequently, the De Martonne index indicates a future increase in the drought hazard over the entire country by 2100. The ALADIN model predicts that the changes will be more pronounced, and that all units will transfer at least one category to a more arid type by 2100. The REMO model showed less pronounced changes, and category changes were typical only in the northern part of the country and in the Hungarian Great Plain. In the Hungarian Great Plain, a new category is likely to appear, namely the semi-dry category, which indicates a very large drought hazard (*Fig. 5*).

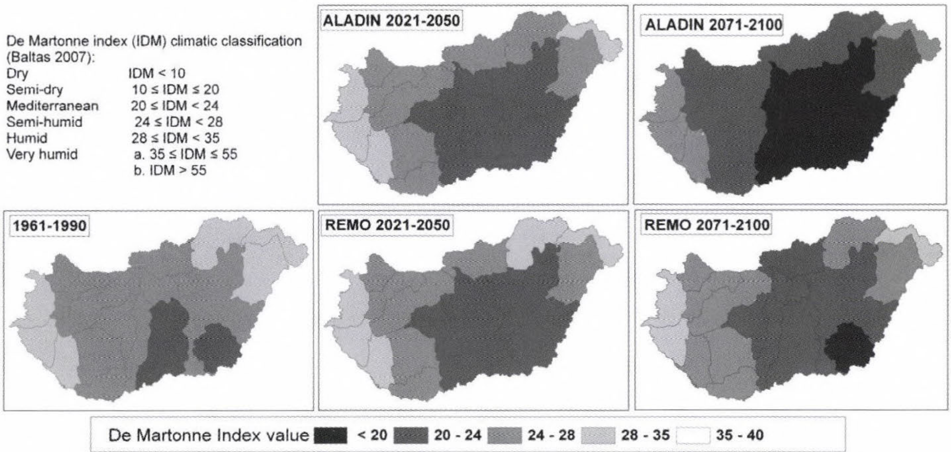

Fig. 5. Values of the De Martonne index in the periods of 1961–1990, 2021–2050, and 2071–2100.

4.2. Changes in the $PaDI_0$ index

The average value of the $PaDI_0$ index for the base period (1961–1990) varied between 3.5 and 5.3 °C/100 mm in the landscape units. These values are lower than those of the PAI (shown in *Fig. 2*). Because the calculation of the $PaDI_0$ was made for distinct years and averaged over 30 years, the extremes are hidden. Nevertheless, this result still correctly predicts the temporal changes. The maximum values of the index, which represent the highest drought hazard, were obtained in the landscape units in the central part of Hungary (the Gödöllő Hills, Danube-Tisza Interfluve, and the Danubian Plain). In contrast, the lowest values occurred in the western part of the country; therefore, the drought hazard was the lowest here.

The changes in the drought hazard can be analyzed using the changes in the drought-level categories of the $PaDI_0$ as a proxy. For the period 2021–2050, both model simulations indicated that the value of the index will increase, varying between 3.9 and 6.0 °C/100 mm (in case of REMO) and between 3.9 and 6.5 °C/100 mm (in case of ALADIN). The highest degree of change was indicated in the southeastern part of Hungary. Using REMO outputs, the maximum values are simulated in the Danube-Tisza Interfluve and Körös-Maros Interfluve units. Using ALADIN outputs, the maximum values are projected in the Körös-Maros Interfluve unit and in the central part of the Great Hungarian Plain unit (*Fig. 6*).

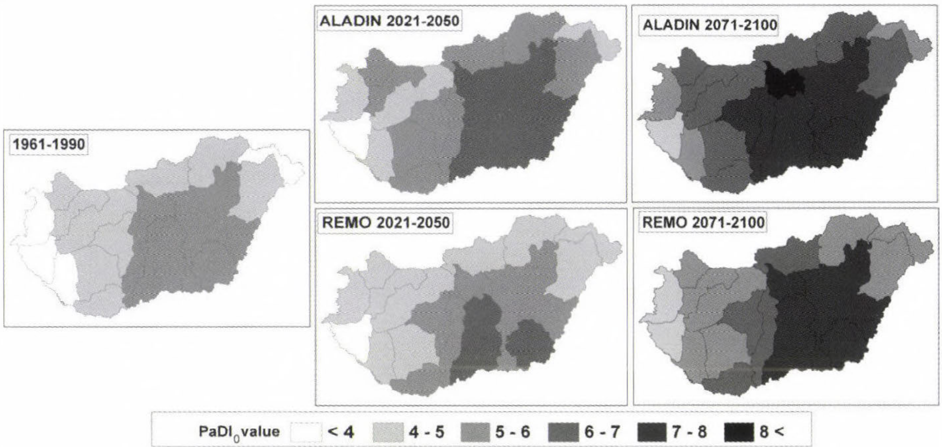

Fig. 6. Values of the PaDI$_0$ index in the periods of 1961-1990, 2021-2050, and 2071-2100.

For the period 2071–2100, the drought hazard is projected to increase, but significant differences were recognized between the model simulations (4.7–7.5 °C/100 mm and 4.8–8.4 °C/100 mm using REMO and ALADIN outputs, respectively). According to the REMO model, the maximum values are simulated in the Körös-Maros Interfluve unit and the central part of the Great Hungarian Plain unit. The predicted value of the index based on the ALADIN model is expected to exceed the highest values of the REMO model in the Gödöllő Hills unit.

4.3. Changes in the SAI

Changes in the precipitation were analyzed using the SAI for the three summer months (June to August), when the drought hazard is the highest.

According to the three-month SAI, the drought hazard is not projected to change significantly (the value varied between –1 and 1) until the 2021–2050 period, although there is notable uncertainty in these results considering the differences between the two model simulations. The model simulations indicate different rates of change, and in the northern and western parts of Hungary, the trend of the changes was different. A considerable increase in the drought hazard is simulated only in the southeastern part of Hungary, where both model simulations indicate the same tendency (*Fig. 7*).

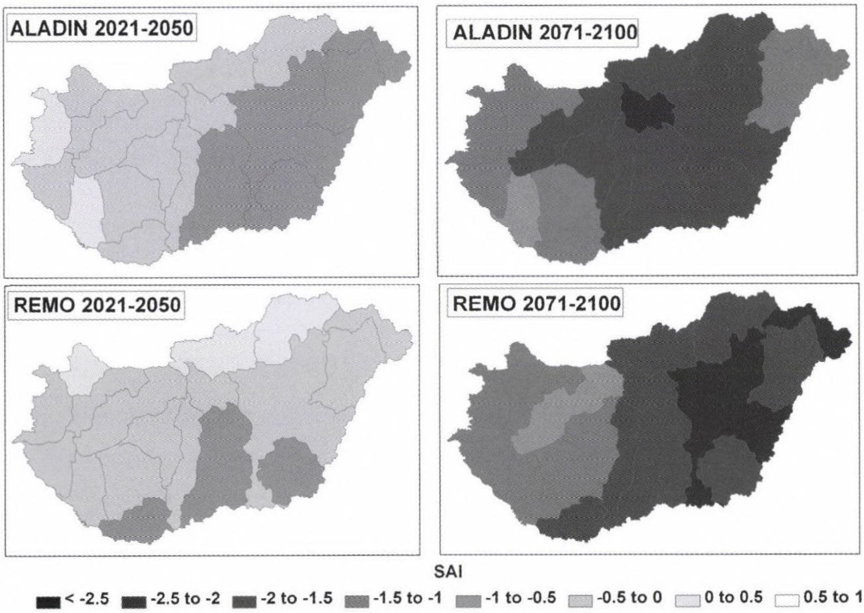

Fig. 7. Values of the SAI in the periods of 2021-2050 and 2071-2100

Both model simulations have clearly indicated an increase in the drought hazard in the summer months for the entire country by the end of the 21st century. Even despite the uncertainty of the precipitation projection, the value of the SAI varied between –0.5 and –2.5 in the period 2071–2100. The highest rate of precipitation decrease, with respect to the base period (1961–1990), is simulated in the northern part of the Great Hungarian Plain and the North Hungarian Mountains. However, due to the more favorable initial conditions in the North Hungarian Mountains, the drought hazard will be less serious even with large changes. The most critical drought hazard projected in all of the landscape units is in the north central part of the Great Hungarian Plain. The value of the SAI is below –2 in this unit, which indicates extreme dryness.

5. Conclusion

During the 21st century, the drought hazard in Hungary is likely to increase in a spatially heterogeneous manner due to climate change. The future changes in the drought hazard were assessed using two approaches, namely a qualitative and quantitative analysis. The two approaches provided similar results for the changes in the drought hazard. These assessments showed that the drought hazard is expected to increase throughout the country but with spatially different magnitudes. The maximum increase in the drought hazard is projected in the five landscape units of the Hungarian Great Plain. According to the qualitative analysis, the future tendency of the changes in the precipitation, temperature, and extreme indices is the most severe in terms of drought level in these units. The quantitative analysis confirmed these results. The most intensive changes in the calculated indices are likely to occur in the same landscape units. For these five units, the initial value and the amount of increase in the $PaDI_0$ were the highest, and the SAI value were the lowest in the country. The maximum change in the De Martonne index is likely to occur in these units, but, due to the initial conditions, the highest drought hazard is simulated in these units by the end of the 21st century.

By 2021–2050 period, the increase in the drought hazard is projected to be not significant. However, the results from the ALADIN simulations showed that the drought hazard is likely to increase in the landscape units of the Hungarian Great Plain, while the results from the REMO simulations indicated a significant increase only in the two southernmost units of the Hungarian Great Plain. These two landscape units currently have the highest drought hazard, causing climate change to generate severe drought problems in these units first. By 2071–2100 period, both model experiments indicated a significant drought hazard increase in all units of the Hungarian Great Plain. The results showed that the Körös-Maros Interfluve unit is projected to have the worst drought hazard. The De Martonne index was found to be highest on the basis of both model simulations for this unit, and the results from the REMO simulations showed that the $PaDI_0$ index was the highest. The *SAI*, based only on precipitation data, indicated that the most severe drought hazard is simulated in the Gödöllő Hills and the central part of the Great Hungarian Plain, but this index does not consider temperature changes. In the Gödöllő Hills, the results from the ALADIN simulations showed that the $PaDI_0$ index indicated the most intense drought hazard. This indicated that, despite the smaller temperature increases, the intense precipitation changes in the summer months are likely to cause severe water supply problems in this area.

According to the qualitative and quantitative analyses, the westernmost part of Hungary is likely to have the lowest drought hazard due to favorable changes in the precipitation, temperature, and extreme indices in this region.

This analysis, based on climate simulation data, suggests that the drought hazard will increase in the entire country, and that the most intense changes are simulated in the Hungarian Great Plain, which is currently the most drought-affected area. The Körös-Maros Interfluve and the Gödöllő Hills are particularly vulnerable. In these areas, more serious drought problems are projected to occur by the end of the 21st century than at present. The modification of drought hazards can be a slow process, but future strategies and landscape planning should include the development of mitigation strategies and preparations for environmental damage.

The drought hazard projections have several uncertainties. The most important uncertainties are the lack of verification and an accurate definition of the error. Further uncertainty is associated with the A1B scenario, as the projected data are only valid for a definite socio-economic development path. Despite these limitations, the present data set and analysis of the smaller units can provide valuable data for several sectors of society, including the economy, as the analysis can highlight the critical drought areas. This information can promote the development of optimal spatial planning strategies to create more optimal land and water management, which can mitigate the consequences of drought at national, regional and local levels. Preparing for prospective droughts by developing optimal land use and water management plans is a key objective of spatial planning to mitigate the damage caused by droughts

Additionally, these calculations consider only climate parameters, while other environmental parameters (e.g., the water-holding capacity of soils, groundwater depth and wind conditions) should be taken into consideration to obtain a more detailed and accurate definition of the drought hazard. The positive or negative characteristics of these parameters can locally modify the drought hazard.

The positive or negative characteristics of these parameters can locally modify the drought hazard. Therefore, further analysis is required to reveal how the drought hazard influences the complex interrelationship between the soil water, salinity of the soil and soil water, groundwater depth, land use, land cover, or local relief situation.

Acknowledgement–The research was funded by the „TÁMOP-4.2.1/B-09/1/KONV-2010-0005 – Creating the Center of Excellence at the University of Szeged" and the TÁMOP-4.2.2/B-10/1-2010-0012 – "Broadening the knowledge base and supporting the long-term professional sustainability of the Research University Centre of Excellence at the University of Szeged by ensuring the rising generation of excellent scientists" projects supported by the European Union and co-financed by the European Regional Fund.

References

Bakonyi, P., 2010: Flood and drought strategy of the Tisza river basin. VITUKI, Budapest, www.icpdr.org/icpdr-files/15494

Baltas, E., 2007: Spatial distribution of climatic indices in northern Greece. *Meteorol. Appl.14*, 69–78.

Bartholy, J. and *Pongrácz, R.*, 2010: Analysis of precipitation conditions for the Carpathian Basin based on extreme indices in the 20th century and climate simulations for the 21st century. *Phys. Chem. Earth 35*, 43–51.

Bartholy, J., Pongrácz, R., Gelybó, Gy., and *Szabó*, P., 2008: Analysis of expected climate change in the Carpathian Basin using the PRUDENCE results. *Időjárás 112*,249–264.

Botzan, M.A., Marino, M.A., and *Necula, A.I.*, 1998: Modified de Martonne aridity index: Application to the Napa Basin, California. *Phys. Geogr. 19*, 55–70.

Briffa, K.R., Jones, P.D., and *Hulme, M.*, 1994: Summer moisture variability across Europe, 1892–1991: an analysis based on the Palmer drought severity index. *Int. J. Climatol. 14*, 475–506.

Changnon, S.A., 1987: Detecting drought conditions in Illinois: Illinois State Water Survey, Champaign, Illinois, USA , Circular 169: 1–36.

Csima, G. and *Horányi, A.*, 2008: Validation of the ALADIN-Climate regional climate model at the Hungarian Meteorological Service. *Időjárás 112*, 155–177.
Csorba, P., Blanka, V., Vass, R., Nagy, R., Mezősi, G., and *Meyer, B.* 2012: A hazai tájak működésének veszélyeztetettsége új klímaváltozási előrejelzés alapján (Sensitivity of the Hungarian mesolandscapes according to the modelled climate change). *Földr. Közl.136*, 237–253.
Doerr, A.H., 1963: De Martonne's Index of Aridity and Oklahoma's Climate. *Proc. of the Oklahoma Academy of Science 43*, 211–213.
Dracup, J.A., Lee, K.S., and *Paulson, E.G.* 1980: 'On the definition of droughts', *Water Resour. Res. 16*, 297–302.
Dunkel, Z., 2009: Brief surveying and discussing of drought indices used in agricultural meteorology. *Időjárás 113*, 23–37.
Farago, T., Kozma, E., and *Nemes, Cs.*, 1989: Drought indices in meteorology. *Időjárás 93*, 45–59.
Grieser, J., Gommes, R., Cofield, S., and *Bernardi, M.* 2006: Data sources for FAO worldmaps of Koeppen climatologies and climatic net primary production FAO - The Agromet Group, SDRN. http://www.juergen-grieser.de/downloads/Koeppen-Climatology/CommonData/CommonData.pdf
Heim, R.R., 2002: A review of Twentieth-Century drought indices used in the United States. *B. Am. Meteorol. Soc. 83*, 1149–1165.
Hisdal, H. and *Tallaksen, L.M.*, 2003: Estimation of regional meteorological and hydrological drought characteristics. *J. Hydrol. 281*, 230–247.
Katz, R.W. and *Glantz, M.H.*, 1986: Anatomy of a rainfall index. *Mon. Weather Rev. 114*, 764–771.
Kogan, F.N., 1997: Global Drought Watch From Space. *B. Am. Meteorol. Soc. 78*, 621–636.
Livada, I. and *Assimakopoulos, V.D.*, 2007: Spatial and temporal analysis of drought in Greece using the Standardized Precipitation Index (SPI). *Theor. Appl. Climatol. 89*. 143–153.
Lungu, M., Panaitescu, L.., and *Niţă, S.* 2011: Aridity, climatic risk phenomenon in Dobrudja. *Pres. Environ. Sustain. Develop. 5*, 179–189.
Maracchi, G., 2000: Agricultural Drought – A practical approach to definition, assessment and mitigation strategies. In: *Vogt, J.V., Somma, F.*: Drought and Drought Mitigation in Europe. Advances in Natural and technological hazards Research, 14, Kluwer Academic Publisher Dordrecht, 63–78.
McKee, T.B, Doeskin, N.J., Kleist, J. 1993: The relationship of Drought Frequency and Duration to Time Scales. Proc. 8th Conf. on Applied Climatology. American Meteorological Society, Boston, 179–184.
Meshcherskaya, A.V. and *Blazhevich, V.G.*, 1997: The drought and excessive moisture indices in a historical perspective in the principal grain-producing regions of the Former Soviet Union. *J. Climate 10*, 2670–2682.
Mezősi, G., Meyer, B. C., Loibl, W., Aubrecht, C., Csorba, P., and *Bata, T.* 2012: Assessment of regional climate change impacts on Hungarian landscapes. *Reg. Environ. Change 17/4* online first (7 July 2012)
Nakicenovic, N. and *Swart, R., (eds.)*, 2000: Emissions Scenarios. A Special Report of IPCC Working Group III. Cambridge University Press, Cambridge, UK. 570p. Available at http://www.ipcc.ch/pdf/special-reports/emissions_scenarios.pdf
Pálfai, I. 1984: Az aszályossági index. Magyar Hidrológiai Társaság V. Országos Vándorgyűlés III. kötet 19–24. (In Hungarian)
Pálfai, I. 1990: Description and forecasting of droughts in Hungary. *Transactions of 14th Congress on Irrigation and Drainage. Rio de Janeiro ICID, 1-C*, 151–158.
Pálfai, I. 2002a: Probability of drought occurence in Hungary. *Időjárás 106*, 265–275.
Pálfai, I. 2002b: Magyarország aszályossági zónái. *Vízügyi Közl. 84*, 323-357.
Pálfai, I. 2004: Belvizek és aszályok Magyarországon. Köz Doc, Budapest.
Pálfai, I. and *Herceg, Á.*, 2011: Droughtness of Hungary and Balkan Peninsula. *Riscuri si Catastrofe, An X* 9, 145–154.
Palmer, W.C., 1965: Meteorological Drought. Research Paper No.45, U.S. Department of Commerce Weather Bureau, Washington, D.C., USA.
Paltineanu, C., Mihailescu, I .F., Seceleanu, I., Dragota, C., and *Vasenciuc F.* 2007: Using aridity indices to describe some climate and soil features in Eastern Europe: a Romanian case study. *Theor. Appl. Climatol. 90*, 263–274.

Pieczka, I., Pongrácz, R., Bartholy, J., Kis, A., and *Miklós, E.* 2010: A szélsőségek várható alakulása a Kárpát-medence térségében az ENSEMBLES projekt eredményei alapján. *36. Meteorológiai Tudományos Napok*, OMSZ, Budapest, 76–86. (in Hungarian)

Rannow, S., Loibl, W., Greiving, S., Gruehn, D., and *Meyer, B.C.*, 2010: Potential impacts of climate change in Germany – identifying regional priorities for adaptation activities in spatial planning. *Landscape Urban Plan. 98*,160–171.

Svoboda, M., LeComte, D., Hayes, M., Heim, R., Gleason, K., Angel, J., Rippey B., Tinker, R., Palecki, M., Stooksbury, D., Miskus, D., and *Stephens, S.*, 2002: The Drought Monitor. *B. Am. Meteorol. Soc. 83*, 1181–1190.

Szabó, P., Horányi, A., Krüzselyi, I., and *Szépszó, G.*, 2010: Az Országos Meteorológiai Szolgálat regionális klímamodellezési tevékenysége: ALADINClimate és REMO. *36. Meteorológiai Tudományos Napok*, OMSZ, Budapest, 87–101 (In Hungarian)

Szépszó, G. 2008: Regional change of extreme characteristics over Hungary based on different regional climate models of the PRUDENCE project. *Időjárás 112*, 265–284.

Szépszó, G. and *Horányi, A.*, 2008: Transient simulation of the REMO regional climate model and its evaluation over Hungary *Időjárás 112*, 203–231.

Vermes, L., Fésűs, I., Nemes, C., Pálfai, I., and *Szalai, S.*, 2000: Status and progress of the national drought mitigation strategy in Hungary. In (*Eds: Vermes, L., Szemessy, Á.*) Proceedings of the Central and Eastern European Workshop on Drought Mitigation 12-15 April, Budapest-Felsőgöd, Hungary, 55–64.

Warrick, R.A., Trainer, P.B., Baker, E.J., and *Brinkman, W.* 1975: Drought Hazard in the United States: A Research Assessment NSF Program on Technology, Environment and Man Monograph NSF-RA-E-75-004.

INSTRUCTIONS TO AUTHORS OF *IDŐJÁRÁS*

The purpose of the journal is to publish papers in any field of meteorology and atmosphere related scientific areas. These may be

- research papers on new results of scientific investigations,
- critical review articles summarizing the current state of art of a certain topic,
- short contributions dealing with a particular question.

Some issues contain "News" and "Book review", therefore, such contributions are also welcome. The papers must be in American English and should be checked by a native speaker if necessary.

Authors are requested to send their manuscripts to

Editor-in Chief of IDŐJÁRÁS
P.O. Box 38, H-1525 Budapest, Hungary
E-mail: journal.idojaras@met.hu

including all illustrations. MS Word format is preferred in electronic submission. Papers will then be reviewed normally by two independent referees, who remain unidentified for the author(s). The Editor-in-Chief will inform the author(s) whether or not the paper is acceptable for publication, and what modifications, if any, are necessary.

Please, follow the order given below when typing manuscripts.

Title page: should consist of the title, the name(s) of the author(s), their affiliation(s) including full postal and e-mail address(es). In case of more than one author, the corresponding author must be identified.

Abstract: should contain the purpose, the applied data and methods as well as the basic conclusion(s) of the paper.

Key-words: must be included (from 5 to 10) to help to classify the topic.

Text: has to be typed in single spacing on an A4 size paper using 14 pt Times New Roman font if possible. Use of S.I. units are expected, and the use of negative exponent is preferred to fractional sign. Mathematical formulae are expected to be as simple as possible and numbered in parentheses at the right margin.

All publications cited in the text should be presented in the *list of references*, arranged in alphabetical order. For an article: name(s) of author(s) in Italics, year, title of article, name of journal, volume, number (the latter two in Italics) and pages. E.g., *Nathan, K.K.*, 1986: A note on the relationship between photo-synthetically active radiation and cloud amount. *Időjárás 90,* 10-13. For a book: name(s) of author(s), year, title of the book (all in Italics except the year), publisher and place of publication. E.g., *Junge, C.E.*, 1963: *Air Chemistry and Radioactivity.* Academic Press, New York and London. Reference in the text should contain the name(s) of the author(s) in Italics and year of publication. E.g., in the case of one author: *Miller* (1989); in the case of two authors: *Gamov* and *Cleveland* (1973); and if there are more than two authors: *Smith et al.* (1990). If the name of the author cannot be fitted into the text: (*Miller,* 1989); etc. When referring papers published in the same year by the same author, letters a, b, c, etc. should follow the year of publication.

Tables should be marked by Arabic numbers and printed in separate sheets with their numbers and legends given below them. Avoid too lengthy or complicated tables, or tables duplicating results given in other form in the manuscript (e.g., graphs).

Figures should also be marked with Arabic numbers and printed in black and white or color (under special arrangement) in separate sheets with their numbers and captions given below them. JPG, TIF, GIF, BMP or PNG formats should be used for electronic artwork submission.

Reprints: authors receive 30 reprints free of charge. Additional reprints may be ordered at the authors' expense when sending back the proofs to the Editorial Office.

More information for authors is available: journal.idojaras@met.hu

Published by the Hungarian Meteorological Service

Budapest, Hungary

INDEX 26 361

HU ISSN 0324-6329

IDŐJÁRÁS

**QUARTERLY JOURNAL
OF THE HUNGARIAN METEOROLOGICAL SERVICE**

CONTENTS

Norbert Rácz, Gergely Kristóf, and *Tamás Weidinger:* Evaluation and validation of a CFD solver adapted to atmospheric flows: Simulation of topography-induced waves 239

Zorica Podrascanin and *Dragutin T. Mihailovic :* Performance of the Asymmetric Convective Model Version 2, in the Unified EMEP Model 277

Tsvetelina Dimitrova, Rumjana Mitzeva, Hans D. Betz,Hristo Zhelev, and *Sebastian Diebel:* Lightning behavior during the lifetime of severe hail-producing thunderstorms 295

Gábor Szász: Agrometeorological research and its results in Hungary (1870–2010) 315

****

http://www.met.hu/Journal-Idojaras.php

VOL. 117* NO. 3 * JULY – SEPTEMBER 2013

IDŐJÁRÁS

Quarterly Journal of the Hungarian Meteorological Service

Editorial Office: Kitaibel P.u. 1, H-1024 Budapest, Hungary
P.O. Box 38, H-1525 Budapest, Hungary
E-mail: journal.idojaras@met.hu
Fax: (36-1) 346-4669

Indexed and abstracted in Science Citation Index Expanded™ and Journal Citation Reports/Science Edition
Covered in the abstract and citation database SCOPUS®

Subscription by mail:
IDŐJÁRÁS, P.O. Box 38, H-1525 Budapest, Hungary
E-mail: journal.idojaras@met.hu

IDŐJÁRÁS

Quarterly Journal of the Hungarian Meteorological Service
Vol. 117, No. 3, July – September, 2013, pp. 239–275

Evaluation and validation of a CFD solver adapted to atmospheric flows: Simulation of topography-induced waves

Norbert Rácz[1*], **Gergely Kristóf**[1], and **Tamás Weidinger**[2]

[1]*Department of Fluid Mechanics, Budapest University of Technology and Economics (BME), Bertalan L. u. 4-6, H-1111 Budapest, Hungary*
E-mails: racz@ara.bme.hu; kristof@ara.bme.hu

[2]*Department of Meteorology, Eötvös Loránd University, P.O. Box 32, H-1518 Budapest, Hungary*
weidi@caesar.elte.hu

**Corresponding author*

(Manuscript received in final form December 15, 2012)

Abstract–Mountain wave phenomena have been simulated by using a well-known general purpose computational fluid dynamic (CFD) simulation system adapted to atmospheric flow modeling. Mesoscale effects have been taken into account with a novel approach based on a system of transformations and customized volume sources acting in the conservation and governing equations. Simulations of linear hydrostatic wave fields generated by a two-dimensional obstacle were carried out, and the resulting vertical velocity fields were compared against the corresponding analytic solution. Validation with laboratory experiments and full-scale atmospheric flows is a very important step toward the practical application of the method. Performance measures showed good correspondence with measured data concerning flow structures and wave pattern characteristics of non-hydrostatic and nonlinear mountain waves in low Reynolds number flows. For highly nonlinear atmospheric scale conditions, we reproduced the well-documented downslope windstorm at Boulder in January 1972, during which extreme weather conditions, with a wind speed of approximately 60 m s^{-1}, were measured close to the ground. The existence of the hydraulic jump, the strong descent of the stratospheric air, wave breaking regions, and the highly accelerated downslope wind were well reproduced by the model. Evaluation based on normalized mean square error (NMSE), fractional bias (FB), and predictions within a factor of two of observations (FAC2) show good model performance, however, due to the horizontal shift in the flow pattern, a less satisfactory hit rate and correlation value can be observed.

Key-words: complex terrain, gravity waves, CFD simulation, model validation, numerical weather prediction

1. Introduction

An extension of the physical model used in general purpose computational fluid dynamic (CFD) solvers has been developed recently in order to simulate mesoscale atmospheric flow phenomena in the same model with finely structured microscale flow around complex geometries (*Castro et al.*, 2008). We suggested a novel approach by utilizing a system of transformations and additional volume sources in the governing equations. Atmospheric stratification, adiabatic temperature change caused by vertical motion, baroclinicity, and Coriolis force are taken into account through this method (*Kristóf et al.,* 2009). The model uses only one single unstructured grid, and a uniform physical description for close- and far-field flow avoiding interpolation errors and model uncertainties due to model nesting. The authors intended purpose, furthermore, is to create a more general method, which is easy to implement in any CFD solver allowing programmable user defined volume sources in the governing equations. This new approach can be applied in several areas of practice, but before the application of the method, it is an important step to validate the model and to understand the capabilities of the technique.

In the early model validation steps (the implementation of the energy source term and the Coriolis force was investigated), large-eddy simulations (LES) of small scale thermal convection problems were carried out in order to simulate urban heat island circulation problem (*Noto,* 1996; *Lu et al.,* 1997; *Cenedese* and *Monti,* 2003). Good qualitative and quantitative agreement was found regarding the velocity and temperature profiles and the general flow pattern as well. Behavior of a spreading density current has also been simulated by solving the unsteady Reynolds averaged Navier-Stokes (URANS) equations, to study the behavior of the dynamical model core and compare the differences between the incompressible and compressible versions of the model (*Kristóf et al.,* 2009). The correct implementation of the Coriolis force was also tested in this work.

These validation cases have the advantage of that they have more control over the measured parameters due to the nature of the measuring device. However, they have low Reynolds number range, the cases are mainly hydrostatic, the vertical extent is limited to a certain height, and the density current study used a fixed turbulence viscosity model.

The purpose of the present paper is to further extend the validation cases characterized by non-hydrostatic and strong nonlinear situations. Further differences compared to previous validations (*Kristóf et al.,* 2009) are the complex topography, the extended simulation domain height incorporating the tropopause, and that all the source terms are activated (see Eqs.(30)–(35)). Results of gravity wave simulations compared against the corresponding analytic solution, small scale water-tank experiments (*Gyüre* and *Jánosi,* 2003), and full scale observations (*Lilly* and *Zipser,* 1972) will be presented. The simulation of such cases has been found to be ideal for testing and evaluating mesoscale numerical models due to the presence of complex flow patterns and wave breaking phenomena.

Atmospheric waves form when stable air flow passes over an obstacle. Fluid parcels tend to return into their original height due to the restoring forces caused by stratification. Various types of oscillatory flow responses occur depending on the state of stratification and geometric parameters (*Holton,* 2004) One can see two divisions of mountain waves, vertically propagating and trapped lee waves. Mountain waves vertically propagating over a barrier may have horizontal wavelengths of many tens of kilometers, even reaching the lower stratosphere (*Lin,* 2007). The vertical propagation of trapped lee waves is limited to a certain height due to the presence of a highly stable layer when waves can be reflected in such situations. In general, gravity waves can modify the local weather situation near mountains: they can create rotor motions, hydraulic jumps, and they have the capability of concentrating momentum on the lee slopes, or occasionally leading to violent downslope windstorms. (*Klemp* and *Lilly,* 1975; *Simon et al.,* 2006) Lee waves can be a potential hazard for wave gliders, by producing rotors or clear air turbulence. Flow beneath the wave crests can be extremely turbulent, thus causing a potential hazard for low-level aviation as well (National Research Council, 1983). The simulations of atmospheric scale flows around mountains can also have economical importance when the future location of a wind farm is to be estimated (*Montavon,* 1998; *Lopes da Costa et al.,* 2006; *Palma et al.,* 2008).

One can observe mountain waves (*Smith et al.,* 2002) with the help of various types of clouds, altocumulus or wave clouds at wave crests. Rotor clouds may dye some parts of the wave field if the appropriate amount of moisture is present. In some cases they are marked by regularly spaced clouds, and may be of great help to the flight of gliders (*Lesieur,* 2008).

Several researchers examined mountain waves and established theories to describe the basic phenomena (*Scorer,* 1949; *Long,* 1953; *Doyle and Durran,* 2002; *Smith,* 2002). One can also find experimental works dealing with the examination of flows around small scale, simplified, two-dimensional isolated obstacles (*Gyüre* and *Jánosi,* 2003). Gravity waves can be a good basis for the validation of atmospheric simulation models, as their structure strongly depends on the state of stratification. Indeed, one can see numerous works dealing with the validation of mesoscale models against mountain waves (*Durran* and *Klemp,* 1983; *Yang,* 1993; *Thunis* and *Clappier,* 2000; *Xue et al.,* 2000), such as the ones caused by a severe downslope windstorm event of Boulder. Similar events can occur in mountainous regions all over the world (*Colle and Mass,* 2000; *Belušič* and *Klai,* 2004). Postevent analysis of severe windstorms are often performed to study the future predictability of such events and also to test model performance and validity. A recent study dealt with the November 19, 2004 windstorm in the High Tatras in Slovakia (*Simon et al.,* 2006). The authors concluded that an increased 2.5 km resolution mesoscale model can forecast downslope windstorms.

In the following section the main aspects of numerical models used in meteorological codes and in engineering CFD will be compared together with a brief description of the model transformations (for the full description see *Kristóf et al.,* 2009). Simulation results will be shown in the third section in comparison with analytical solutions, water-tank experiments, and full scale downlsope windstorm observations. Conclusions and further investigations are outlined in Section 4.

2. *Model overview*

In this section a brief overview will be given on the governing equations, numerical methods, and parameterizations applied in numerical weather prediction (NWP) and CFD models in order to show the similarities and differences between the meteorological and engineering assumptions.

2.1. Meteorological outlook

The Navier-Stokes (N-S) equitation describes all types of fluid motion of our interest. It can be seen that today's NWP and CFD models are based on these equations of different forms.

2.1.1. Equations, numerical solution

Modern numerical forecast models are based on a formulation of the dynamical equations, which is essentially the formulation proposed by Richardson (*Lynch,* 2006):

$$\frac{d\mathbf{v}}{dt} = -2\mathbf{\Omega}\times\mathbf{v} - \frac{1}{\rho}\nabla p + \mathbf{g} + \mathbf{F_r} \ , \tag{1}$$

where $\mathbf{v}, \mathbf{\Omega}, \rho, p, \mathbf{g}\, and\, \mathbf{F_r}$ are the velocity vector, angular velocity of the Earth, air density, pressure, gravity term, and the frictional force, respectively. The centrifugal force is combined with gravitation in the gravity term $\mathbf{g}$. This form of the N-S equation is basic to most work in dynamic meteorology and solved together with the continuity and thermodynamic equations and the equation of state in NWP-s. After expanding the components of Eq. (1), one arrives to the eastward, northward, and vertical components in spherical coordinate system, respectively (*Holton,* 2004):

$$\frac{du}{dt}-\frac{uv\tan\varphi}{a}+\frac{uw}{a}=-\frac{1}{\rho}\frac{\partial p}{\partial x}+2\Omega v\sin\varphi-2\Omega w\cos\varphi+F_{rx}, \tag{2}$$

$$\frac{dv}{dt}-\frac{u^{2}\tan\varphi}{a}+\frac{vw}{a}=-\frac{1}{\rho}\frac{\partial p}{\partial y}-2\Omega u\sin\varphi+F_{ry}, \tag{3}$$

$$\frac{dw}{dt}-\frac{u^{2}+v^{2}}{a}=-\frac{1}{\rho}\frac{\partial p}{\partial z}-g+2\Omega u\cos\varphi+F_{rz}, \tag{4}$$

where u, v, w are the velocity components, a is the curvature of the Earth, φ is the latitude, and F_{ri} are the components of the frictional force. The terms standing with $1/a$ in Eqs. (2) – (4) are so-called curvature terms, and they arise due to the curvature of the Earth and often neglected in midlatitude synoptic scale motions.

The precise form of equations depends on the vertical coordinate system chosen as well, such as pressure coordinates, log pressure coordinates, sigma coordinates, hybrid coordinates, etc. (*Kasahara,* 1974; *Klemp et al.,* 2007; *Saito et al.,* 2007). Furthermore, the variables may be decomposed into mean and perturbation components. Equation systems using perturbation variables reduce the truncation errors in the horizontal pressure gradient calculations, in addition to reducing machine rounding errors in the vertical pressure gradient and buoyancy calculations. For this purpose, new variables are defined as perturbations from a hydrostatically-balanced reference state, and reference state variables are defined to satisfy the governing equations for an atmosphere at rest. (*Skamarock et al.,* 2005) As an example, in the hydrostatic model version of the Fifth-Generation Penn State/NCAR Mesoscale Model (MM5), the state variables are explicitly forecasted while in the non-hydrostatic model version (*Dudhia,* 1993) or in the more advanced Weather Research and Forecasting modeling system (WRF), pressure, temperature, and density are defined in terms of a reference state and perturbation components. When Reynolds averaging is applied, various covariance terms will appear in the system, representing turbulent fluxes. For many boundary layers, the magnitudes of the turbulent flux terms are of the same order as the other terms in Eqs. (2) – (4). In these cases one cannot neglect these fluxes even if it is not of direct interest.

There are tendencies towards higher spatial resolution models, but the resolution of most NWP models is yet too coarse to resolve boundary layer eddies, and parameterizations of them are usually necessary as the complete energy cascade cannot be resolved. (The High Resolution Limited Area models (HIRLAM), or ALADIN operate on horizontal grids in the range of 1–10 km.) Thus a number of turbulent mixing and filtering formulations were developed in the past. Some of these filters are for numerical reasons. For example, divergence damping filters acoustic modes from the solution. Other filters represent sub-grid processes that cannot be resolved on the given spatial resolution.

2.1.2. Filtering of acoustic modes

The complete equations of motion (Eqs. (2) – (4)) describes all types and scales of atmospheric motion. The elimination of terms on scaling considerations has an important advantage of simplified mathematics and filtering of a range of unwanted type of motions.

These high-frequency acoustic modes would limit the time step during the calculation. To circumvent, different time discretization techniques are developed, see, e.g., the Runge-Kutta time-split scheme in *Wicker* and *Skamarock* (2002) or *Almut* and *Herzog* (2007). The efficiency of the time-split scheme arises from that the large time step Δt is much larger than the acoustic time step $\Delta\tau$, so the most costly calculations are only done in the less-frequent large steps. There are less efficient methods than the leapfrog-based models (e.g. in MM5 or WRF) resulting typically a factor of two greater time step. In the non-hydrostatic model of MM5, a semi-implicit scheme based on *Wilhelmson* and *Klemp* (1978) is used to filter the acoustic waves, while in the hydrostatic model, a split-explicit scheme based on *Madala* (1981) is used to filter gravity waves from the solution. The time differencing in MM5 is extensively discussed in *Grell et al.* (1995). In highly complicated systems, also involving pollution transport and chemical reactions, efficient operator splitting methods are developed recently to reduce computational time. The method is well spread in related fields of applied mathematics (*Geiser,* 2008) and in circulation and pollution models (*Havasi et al.,* 2001; *Faragó,* 2006; *Kocsis et. al,* 2009)

2.1.3. Planetary boundary layer (PBL) and surface-layer schemes, turbulence, closure problem

NWP and air pollution models must contain proper treatment for the PBL since it couples energy, momentum, and mass transfer between the land and atmosphere. The importance of its modeling is increasing nowadays due to environmental requirements, including human health, urban air quality, local and global warming trends, or homeland security problems. The PBL parameterization is especially important for predicting pollutant transport and dispersion (*Lundquist* and *Chan,* 2006).

In order to solve the equations of motion (Eqs. (2)–(4)), closure assumptions must be made to approximate the unknown fluxes as a function of known quantities and parameters (*Holton,* 2004). Turbulent fluxes provide a lower boundary condition for the vertical transport done in the PBL schemes. The PBL schemes determine the flux profiles within the well-mixed boundary layer and the surface layer providing tendencies of temperature, moisture, and horizontal momentum in the entire column. Thus, when a PBL scheme is activated, explicit vertical diffusion is de-activated assuming that the PBL scheme will handle the process. Most PBL schemes apply dry mixing, but can also include moisture effects in the vertical stability that determines the mixing. The schemes are one-dimensional, since the horizontal large gradients cannot be resolved, and assume a clear scale separation between sub-grid eddies and resolved eddies. This assumption is less clear below a certain grid size, where boundary layer eddies may start to be resolved. In these situations the scheme is replaced by a fully three-dimensional local sub-grid turbulence scheme such as the turbulent kinetic energy (TKE) diffusion scheme (see in the WRF model: *Knievel et al.,* 2007; *Nagy,* 2010). Numerical simulations of PBL have been performed by many authors in the past resulting in different model complexity ranging from very simple zero dimensional parameterization to 3-D high resolution models. In the following sections a brief description will be given on the commonly used closure models.

2.1.3.1. First order closure

Operational NWP, emergency response, and air-quality models usually are of a RANS type (solving Reynolds averaged Navier-Stokes equations), and they employ first- or 1.5-order turbulence closures. The simplest turbulent transport parameterization is the first-order closure based on the K-theory (*Corrsin,* 1975; *Wyngaard* and *Brost,* 1984; *Holtslag* and *Moeng,* 1991; *Stull,* 1993). It is robust and requires low computational resources but gives poor approximation in the boundary layer, where the scale of typical turbulent eddies is strongly dependent on the distance to the surface and static stability. In many cases the most intense eddies have scales comparable to the boundary layer depth, and there the momentum and heat fluxes are not proportional to the local gradient of the mean. In much of the mixed layer, heat fluxes are positive even with neutral conditions.

To improve the model behavior, alternative approaches have been developed. An example is the modified first-order closure (*Townsend,* 1980; *Troen* and *Mahrt,* 1986; *Hong* and *Pan,* 1996). This scheme employs a counter-gradient flux for heat and moisture in unstable situations. It uses enhanced vertical flux coefficients in the PBL, and the PBL height is determined from a critical bulk Richardson number (Ri). It handles vertical diffusion with an implicit local scheme, and it is based on local Ri in the free atmosphere (Ri_{free}).

In spite of its drawbacks, the first-order closure based models remain the most popular parameterization for stable conditions, although alternative approaches have been used for the daytime convective period, e.g., the Blackadar (BK) non-local mixing scheme (*Blackadar,* 1976; *Zhang* and *Anthes,* 1982) and non-local K-theory (*Hong* and *Pan,* 1996). The BK scheme is a first-order hybrid local and nonlocal scheme in which eddy diffusivity, a function of the local Ri number, is applied to the stable and forced convective regimes, while nonlocal mixing is used for free convective cases. The BK scheme's closure is based on an expression for the mass that is exchanged between individual layers in the boundary layer.

Recent improvements of first order schemes include the Yonsei University model (YSU, *Hong et al.,* 2006) or the asymmetrical convective models ACM1 (*Pleim* and *Chang,* 1992) and ACM2 (*Pleim,* 2007). YSU is based on the K profile for the convective cases as a function of local wind shear and local Ri_{free}. It also considers non-local mixing by adding a non-local gradient adjustment term to the vertical diffusion equation. Moreover, it contains additional terms to describe entrainment at the top of PBL proportional to the surface flux. For stable cases, the original mixing coefficient (*Hong et al.,* 2006) is replaced by an enhanced diffusion based on the bulk Ri number between the surface and top layers (*Hong,* 2010). The ACM1 and ACM2 models are modifications of the BK scheme. In ACM1 the symmetrical downward transport of BK scheme is replaced by an asymmetrical layer-by-layer model. In order to produce more realistic vertical profiles, the ACM2 model, a combination of local and non-local closures, was introduced (*Pleim,* 2007), that adds an eddy diffusion component to the non-local transport. With this addition the ACM2 scheme can better represent the shape of the vertical profiles in the near surface region. Both ACM1 and ACM2 models are available in the MM5 and WRF solvers.

2.1.3.2. Higher order closures

Given the known drawbacks of these simpler models, new approaches are developed with increasing complexity of turbulence description. The Gayno–Seaman (GS) scheme is a 1.5-order local closure scheme that computes eddy diffusivities based on local vertical wind shear, stability, turbulent kinetic energy (TKE) predicted by a prognostic equation (*Shafran et al.,* 2000), and length scale. The Eta PBL scheme, also known as the Mellor-Yamada-Janjic (MYJ) scheme (*Janjic,* 1990; *Mellor* and *Yamada,* 1982, *Janjic,* 1996, 2002), is a level-1.5 local closure scheme that computes vertical eddy diffusivities based on TKE predicted by a prognostic equation as a function of local vertical wind shear, stability, and turbulence length scale. The effects of the viscous sub-layer are taken into account through variable roughness length for temperature and humidity (*Zilitinkevich,* 1995). Other more sophisticated schemes are based on ensemble-averaged turbulence models (*Xue et al.,* 1996) with varying orders of closure (e.g., *Mellor* and *Yamada,* 1974; *Wyngaard et al.,* 1974; *Andre et al.,* 1978). These schemes often perform remarkably well under horizontally homogeneous conditions in modeling the horizontally (ensemble) averaged profiles of quasi-conservative quantities. However, the 3-D structures of the boundary layer is not predicted well. They are more complicated, and require solving equations of higher order moments, limiting their practical application

(*Lee et al.,* 2006). Several researcher proposed modifications to the original MY model improving the master length scale equation (*Šušelj and Sood,* 2010) or the pressure-strain, pressure –temperature covariance closures (*Nakanishi* and *Niino,* 2009)

Other researchers, however, showed that there is little gain in accuracy with increasing scheme complexity using different turbulence parameterizations. Increasing the complexity of the turbulence parameterization not just increased the computational resources but did not show obvious improvement, sometimes producing equally poor, if not worse, predictions (*Zhong et al.,* 2007) of the simulated mean and turbulent properties in the boundary layer, even around complex regions (*Berg et al.,* 2005).

Traditional PBL schemes were adequate for flat, horizontally homogeneous surfaces under steady-state conditions with different stratification. They cannot cope, however, with increased-resolution models that require more detailed and accurate representations of physical processes (*Baklanov et al.,* 2011). Therefore, different approaches are developed where the calculation of eddies was done explicitly in the PBL using 3-D high resolution models. Since only a small portion of the turbulence is handled by the subgrid scale (SGS) scheme, the results are less sensitive to turbulence closure assumptions. The first LES models and work in this area was pioneered by *Deardorff* (1974a,b). For PBL applications, LES models typically require horizontal resolutions on the order of 100 m (see, e.g., ARPS, MESO-NH codes), and they are typically used for research applications (e.g., *Weigel et al.,* 2007). *Deardorff* (1980) designed a simplified 1.5-order closure scheme that requires the solution of only one additional prognostic equation for the SGS turbulent kinetic energy, where the eddy coefficient was assumed to be proportional to the square root of TKE. This scheme has been widely used by researchers (*Klemp* and *Wilhelmson,* 1978) to handle SGS turbulence in cloud-scale models. Such models have a horizontal resolution in the order of 1 km, and they are expected to resolve cloud structures and limited turbulent eddies.

2.2. Engineering outlook

CFD tools have been in use for decades with success for solving engineering related problems involving broad range of physics. Spatial scales are extended to urban scales to handle flows involving pollution dispersion and can be even extended to mesoscale problems by the presented transformation method. Therefore, it is interesting to show the main aspects and some of the current problems of CFD solvers in this field.

2.2.1. Governing equations, simulation of turbulent flows

In engineering CFD, continuity, momentum, and energy equations are usually solved based on the finite volume method in an unsteady conservative form.

Because of numerous advantages of the finite volume method, it is widely spread among commercial and open source fluid mechanical solvers. Although the instantaneous Navier–Stokes equations exactly define all fluid flow, it is essentially impossible to solve these equations for turbulent flows over domains of significant spatial scale. Therefore, the exact equations are often Reynolds averaged to create a set of equations that can be solved for the spatial scales of engineering interest. The current adaptation method was developed for the commercial fluid mechanical solver ANSYS-FLUENT, but it can be implemented in other solvers as well, having user defined function (UDF) capabilities such as the commercial codes ANSYS-CFX and StarCD or the open source solver Openfoam. Through UDF-s, the user can modify the governing equations of the CFD code by adding appropriate source/sink terms to the equations.

The governing equations (Eqs. (5) – (7)) are solved by using the Boussinesq approximation (Eq. (10)) for the density.

$$\nabla \cdot \tilde{\mathbf{v}} = 0, \tag{5}$$

$$\frac{\partial}{\partial t}(\rho_0 \tilde{\mathbf{v}}) + \nabla \cdot (\rho_0 \, \tilde{\mathbf{v}} \otimes \tilde{\mathbf{v}}) = -\nabla \tilde{p} + \nabla \cdot \boldsymbol{\tau} + (\tilde{\rho} - \rho_0)\mathbf{g} + \mathbf{F} \tag{6}$$

$$\frac{\partial}{\partial t}\left(\rho_0 c_p \tilde{T}\right) + \nabla \cdot \left(\tilde{\mathbf{v}} \, \rho_0 \, c_p \tilde{T}\right) = \nabla \cdot \left(K_t \nabla \tilde{T}\right) + S_T, \tag{7}$$

$$\frac{\partial}{\partial t}(\rho_0 \, k) + \nabla \cdot (\rho_0 \, \tilde{\mathbf{v}} \, k) = \nabla \cdot \left(\frac{\mu_t}{\sigma_k} \nabla k\right) + G_k + G_b - \rho_0 \, \varepsilon + S_k, \tag{8}$$

$$\frac{\partial}{\partial t}(\rho_0 \, \varepsilon) + \nabla \cdot (\rho_0 \, \tilde{\mathbf{v}} \, \varepsilon) =$$

$$= \nabla \cdot \left(\frac{\mu_t}{\sigma_\varepsilon} \nabla \varepsilon\right) + \rho_0 \, C_1 \, S \, \varepsilon - \rho_0 \, C_{2\varepsilon} \frac{\varepsilon^2}{k + \sqrt{\nu \, \varepsilon}} + C_{1\varepsilon} \frac{\varepsilon}{k} C_{3\varepsilon} G_b + S_\varepsilon, \tag{9}$$

$$\tilde{\rho} = \rho_0 - \rho_0 \, \beta\left(\tilde{T} - T_0\right). \tag{10}$$

In the equation system $\tilde{\mathbf{v}}, \tilde{p}, \tilde{\rho}, \tilde{T}$ are the transformed field variables of velocity, pressure, density, and temperature. c_p and β are the specific heat capacity of dry air at constant pressure and the thermal expansion coefficient.

From the velocity vector ($\tilde{\mathbf{v}} = u\,\mathbf{i} + v\,\mathbf{j} + \tilde{w}\,\mathbf{k}$) only the vertical component was affected by the transformation. $\boldsymbol{\tau}$ contains the viscous and turbulent stresses, $\mathbf{g} = -g\,\mathbf{k}$ is the gravitational force per unit mass, and g = 9.81[N kg^{-1}]. In the presented system the turbulent transport is modeled by the realizable k–ε turbulence model with full buoyancy effects (Eqs. (8) – (9)) developed by *Shih et al.* (1995). σ_k and σ_ε are the turbulent Prandtl numbers for k and ε , respectively. The turbulent viscosity μ_t and the turbulent heat conduction coefficient K_t are evaluated on the basis of turbulence kinetic energy (k) and dissipation rate (ε) fields (*Launder* and *Spalding,* 1972). The constant values of $C_{1\varepsilon}$, $C_{2\varepsilon}$, the expressions of C_1 and $C_{3\varepsilon}$, the turbulence production and buoyancy terms G_k and G_b, modulus of mean rate-of-strain tensor S can be referred either from CFD literature (*Shih et al.*, 1995) or from software documentation (*ANSYS Inc.,* 2012) of the applied simulation system. ρ_0 and T_0 are reference (sea level) values of density and temperature.

Volume sources S_T, S_k, and S_ε in Eqs. (7)–(9), as well as vector $\mathbf{F} = S_u\,\mathbf{i} + S_v\,\mathbf{j} + S_w\,\mathbf{k}$ in Eq. (6), are functions of local values of field (prognostic) variables, and used for adjusting the model to handle mesoscale effects. The components of the Coriolis force are included in **F** through S_u, S_v, and S_w.

Reynolds averaging introduces other unknowns into the equation system, the so-called Reynolds stresses. Since there is no existing general formula for the description of these stresses, large number of engineering turbulence models were developed applicable to certain flow features, but there are no turbulence models that would be generally applicable to all kind of turbulent flows. The modeling of these virtual stresses is still a major part of the today's turbulence modeling science. Different versions of two equation models are used in CFD for turbulence modeling. The most popular are versions of the k–ε model or other two equation models. These versions are denoted as linear eddy viscosity models, which adopt the Boussinesq approximation, implying an isotropic eddy viscosity. There were attempts using two equation models in NWP codes. An example is the implementation of a version of the k–ε model by *Hanjalic* and *Launder* (1972) in the MESO-NH meteorological code. It was not used extensively since, according to the authors, the current version did not give satisfactory results. The disadvantage of these eddy viscosity models is that they give an unrealistic representation of the normal turbulent stresses. This representation of the turbulent stresses produces fairly good results as long as only one of the turbulent stresses is dominant in the momentum equations. Further downside is that in more complicated flows, where more than one of the normal stresses is important, the ability of a turbulence model to predict normal stress anisotropy becomes significant. This motivates the development and application of nonlinear k–ε models (*Gatski* and *Jongen,* 2000) and other more advanced models, such as LES or hybrid RANS-LES models.

2.2.2. *Stratification and turbulence models*

One can find several works on the application of turbulence models in neutral conditions (*Richards and Hoxey,* 1993; *Blocken et al.,* 2007; *Hargreaves* and *Wright,* 2007). Stable stratification, however, causes drainage flows over uneven topography, intermittent turbulence, low-level jets, gravity waves, flow blocking, intrusions, and meandering, thus posing challenges in modeling of stable stratification (*Lee et al.,* 2006).

Several problems can be identified regarding the maintenance of turbulence profiles with distance (*Huser et al.,* 1997) dissipating turbulence early downstream of the obstacle (*Hanna et al.,* 2006). Treatment of these inconsistencies is the modification of the model constants of existing models (*Duynkerke,* 1988), adding source terms to the turbulent dissipation rate (TDR) equation for ε or a non-constant formulation for the $C_{1\varepsilon}$ parameter (*Freedman and Jacobson,* 2003; *Pontiggia et al.,* 2009). *Vendel et al.* (2010) proposed an inlet pressure profile and flux condition for the ground in order to define an appropriate downwind boundary condition for the stable or unstable cases.

Although CFD models are currently slow to be used for real-time emergency response, they can be used for planning purposes and to guide parameterizations of real-time wind flow models. A good example of a dispersion model that is parameterized based on the CFD results is the Quick Urban and Industrial Complex dispersion modeling system (*Williams et al.,* 2004). As computing power has become more affordable, CFD has become an increasingly valuable tool for studying urban flow. These models explicitly account for building geometry and require minimal parameterizations (*Balczó et al.,* 2011; *Balogh* and *Kristóf,* 2010). With the current model transformation, one can take into account mesoscale effects in the same numerical model with finely resolved topography.

2.2.3. *System of transformations*

The proper representation of Coriolis force, compressibility, and stratification effects is achieved by a system of transformations. These adjust the governing equations solved by the CFD solver through user defined volume source or sink terms. The CFD solver operates with transformed field variables (Eqs. (5)–(10)). Relations between untransformed physical quantities (T, p, ρ, z, w) and transformed ones $(\widetilde{T}, \widetilde{p}, \widetilde{\rho}, \widetilde{z}, \widetilde{w})$ are defined by Eqs. (11)–(15).

$$T = \widetilde{T} - T_0 + \overline{T}, \tag{11}$$

$$p = \frac{\overline{\rho}}{\rho_0}\, \widetilde{p} + \overline{p} = Ce^{-\zeta z}\, \widetilde{p} + \overline{p}, \tag{12}$$

$$\rho = \widetilde{\rho} - \rho_0 + \overline{\rho}, \tag{13}$$

$$z = -\frac{1}{\zeta} \ln\left(e^{-\zeta\, z_{ref}} - \frac{\zeta}{C}\left(\widetilde{z} - \widetilde{z}_{ref}\right)\right), \tag{14}$$

$$w = \frac{\rho_0}{\overline{\rho}}\, \widetilde{w} = \widetilde{w}\, C^{-1} e^{\zeta\, z}, \tag{15}$$

where ζ is the density parameter described by Eq. (18) and z_{ref} is a reference altitude (Eq. (20)). Zero subscipt denotes values at ground level. The vertical extent of the atmosphere is "compressed" below a well-defined bound (C/ζ) described by Eq. (14), thus $\widetilde{z} \to C/\zeta$, when $z \to \infty$, where C, described by Eq. (19), acts as a switch between the description of stratosphere and troposphere. The model utilizes an (x, y, z) Cartesian coordinate system. The Jacobian of the transformation of coordinate z can be calculated according to Eq. (16). $J \to 1$ when $\widetilde{z} \to 0$, and therefore the geometrical transformation has a negligible effect close to ground.

$$J = \frac{dz}{d\widetilde{z}} = C^{-1} \exp(\zeta\, z). \tag{16}$$

In this zone, the original form of the Cartesian equations existing in the CFD solver gives a good enough description for the flow close to the surface.

2.2.4. Reference profiles

The relationship between the absolute physical quantities and the field variables in the CFD solver are based on the reference profiles (distinguished by overbars) Eqs. (21)–(29). It can be optimized to have the least possible deviation from the hydrostatic equilibrium and can simplify the specification of the initial conditions. These terms depend only on the vertical coordinate using approximation of the polytrophic atmosphere, as according to Eqs. (21)–(29). The original transformation expressions (*Kristóf et al.,* 2009) that were valid below an altitude of 11 km have been extended to incorporate the tropopause and the lower stratosphere up to an altitude of 25 km. For simplicity, the following double valued constants are introduced to describe these layers:

$$\gamma = \begin{cases} \gamma_t \text{ , when } z < z_{tp} \\ 0 \text{ , when } z \geq z_{tp} \end{cases} , \tag{17}$$

$$\zeta = \begin{cases} \zeta_t \text{ , when } z < z_{tp} \\ \zeta_s \text{ , when } z \geq z_{tp} \end{cases} , \tag{18}$$

$$C = \begin{cases} 1 \text{ , } & \text{when } z < z_{tp} \\ e^{(\zeta_s - \zeta_t) z_{tp}} \text{ , } & \text{when } z \geq z_{tp} \end{cases} , \tag{19}$$

where subscripts t and s denote values for the troposphere and stratosphere, and z_{tp} is the tropopause altitude. In the stratospheric region we use z_{tp} as a reference altitude, therefore:

$$z_{ref} = \begin{cases} 0 \text{ , when } z < z_{tp} \\ z_{tp} \text{ , when } z \geq z_{tp} \end{cases} . \tag{20}$$

Using the above notations, the reference profiles for the troposphere will read as:

$$\overline{T_t} = T_0 - \gamma_t \, z , \tag{21}$$

$$\overline{p_t} = p_0 \left(\frac{T_0 - \gamma_t \, z}{T_0} \right)^{\frac{g}{R \, \gamma_t}} , \tag{22}$$

$$\overline{\rho_t} = \rho_0 \, e^{-\zeta_t \, z} , \tag{23}$$

$$\zeta_t = -\left(\frac{g - R\gamma_t}{z \, R \, \gamma_t} \right) \ln\left(1 - \frac{\gamma_t \, z}{T_0} \right) . \tag{24}$$

The reference profiles in the stratospheric region are based on an isothermal temperature profile, therefore:

$$\overline{T_s} = T_{tp}\,, \tag{25}$$

$$\overline{p_s} = p_{tp}\, e^{-\zeta_s\left(z - z_{tp}\right)}\,, \tag{26}$$

$$\overline{\rho_s} = \rho_{tp}\, e^{-\zeta_s\left(z - z_{tp}\right)}\,, \tag{27}$$

$$\zeta_s = \frac{g}{RT_{tp}}\,. \tag{28}$$

By using the above notations, the universal density profile reads:

$$\overline{\rho} = \rho_0 C\, e^{-\zeta\, z}\,. \tag{29}$$

The constant values in Eqs. (21) – (29) can be optimized for a given case, but the standard ICAO (*Manual of the ICAO Standard Atmosphere,* Doc 7488, 1993) temperature and pressure profiles, based on the following constants, have been found to be suitable references for simple applications: $\gamma_t = 0.0065\ ^{\circ}\mathrm{C\ m^{-1}}$, $T_0 = 15\ ^{\circ}\mathrm{C}$, $p_0 = 1.01325 \cdot 10^5$ Pa, $\rho_0 = 1.225\ \mathrm{kg\ m^{-3}}$, $R = 287.05\ \mathrm{J\ kg^{-1}\ K^{-1}}$, $\zeta_t = 10^{-4}$. $\mathrm{m^{-1}}$

2.2.5. Volume sources

The volume sources (Eqs. (30) – (35)) have been calculated according to Eqs. (20)–(25) by utilizing the UDF capability of the system.

$$S_u = \rho_0 fv - \rho_0 \ell\, \widetilde{w} J\,, \tag{30}$$

$$S_v = -\rho_0 fu\,, \tag{31}$$

$$S_w = \rho_0\left(J^2 - 1\right)\left(\ell\, u\, J^{-1} + \beta\left(\widetilde{T} - T_0\right)g\right) + \rho_0\, \ell\, u\, J^{-1} + \zeta\, J\left(\widetilde{p} - \rho_0 \widetilde{w}^2\right), \tag{32}$$

$$S_T = -\rho_0\, c_p\, \widetilde{w}(\Gamma - \gamma)\, J\,, \tag{33}$$

$$S_k = -\beta\, g \frac{\mu_t}{\mathrm{Pr}_t}(\Gamma - \gamma)\,, \tag{34}$$

$$S_\varepsilon = -C_{1\varepsilon}\, C_{3\varepsilon} \frac{\varepsilon}{k} \beta\, g \frac{\mu_t}{\mathrm{Pr}_t} (\Gamma - \gamma) \; . \tag{35}$$

In the above expressions, μ_t and Pr_t are the turbulent viscosity and turbulent Prandtl number, $f = 2\,\Omega \sin\varphi$ and $1 = 2\Omega \cos\varphi$ are the Coriolis parameters, φ is the average latitude, and Ω is the angular velocity of Earth. Moisture transport is not taken into account in the mathematical model, therefore the dry adiabatic temperature gradient Γ, appearing in Eqs. (19) – (21), is calculated according to the assumption of a dry adiabatic process: $\Gamma = g/c_p = 0.00976\ ^{\circ}\mathrm{C\ m}^{-1}$.

2.2.6. A simplified model version for water-tank experiments

Validation against small scale water tank experiments requires the adjustment of the transformation expressions. The working medium is liquid and the vertical extent of the device is small, therefore the atmospheric pressure variation with the vertical coordinate is negligible. Compressibility is not taken into account consequently ($\Gamma = 0, z = \tilde{z}$, and $\zeta_t = 0$). The vertical reference profiles for pressure and density are $\overline{\rho_t} = \rho_0, \overline{p_t} = p_0$. Due to the very weak turbulence characterizing these experiments, a laminar approach or LES method should be used instead of the k–ε model. The Coriolis force usually has a negligible effect in such experiments, and therefore, $\Omega = 0$ can be assumed.

These assumptions will simplify the source term acting on the energy equation:

$$S_{T,\,incomp.} = \rho_0\, c_p\, \widetilde{w}\, \gamma \,. \tag{36}$$

The values of $\gamma = -dT/dz$, c_p, β, and T_0 for water-tank simulations can be calculated according to the temperature or density gradient of the fluid, maintaining the same Brunt-Väisälä frequency and material properties of the experiment.

2.2.7. Nesting

In NWP models the simplest method is the "one-way" downward nesting, where the outer model provides 4D boundary conditions to the inner higher resolution domain. In some cases it can be provided, if the mesoscale model horizontal resolution is as fine as a few hundred meters. The one-way nesting technique, in the Advanced Regional Prediction System (ARPS), allows adjustments in vertical resolution between grids, which is important for LES mode, where the grid aspect ratio should be kept close to unity. In more advanced "two-way" nesting, the nested finer domain and the outer coarser domain interact at every time step of the outer coarse grid and, the microscale model provides lower boundary-condition to the outer domain. "With current computer capacities, this can be done within small parts of the mesoscale domain, which creates inconsistencies with the remaining parts of that domain." (*Baklanov et al.,* 2011) The current implementation of two-way nesting schemes in WRF or MM5 does not allow higher vertical resolution in the inner nesting levels, because the number of vertical levels must be the same for all levels (*Michioka* and *Chow,* 2008). Another problem that also exists in the CFD field is the velocity and length scale changes across the boundaries of nesting levels. This is especially important when the complex high resolution topography generates nonlinear motions close to these boundaries. One may also expect the damping of low frequency motions passing through the boundary and as a consequence providing an improper upstream turbulence field for the inner microscale model.

The advantage of the CFD approach is that it allows arbitrary mesh refinements in the simulation domain, resulting a continuous change of field variables around the finely resolved region. The possibility of nesting also exists in the CFD solver allowing different mesh resolution either horizontally or vertically on both sides of the domain interface, but one can avoid it with the existing mesh refinement options (*ANSYS Inc.,* 2012). In the following case studies, structured quad meshes can be used (without additional interfaces) due to the simplicity of the underlying geometries.

3. Results and discussion

The application of the model transformation will be presented in this section. Results will be compared against the analytical solution of linear, hydrostatic mountain wave field. Nonlinear and non-hydrostatic simulation cases are then compared to small scale water-tank experiments, and finally, a full scale nonlinear and non-hydrostatic downslope windstorm case will be shown against an inter-comparison study of NWP models and field measurements.

3.1. Verification with analytic solution

The simulations were compared with the analytic solution of a linear hydrostatic wave field. A Witch of Agnesi curve was used for the relief geometry,

$$z(x) = h \, \frac{a}{x^2 + a^2}, \tag{37}$$

where h and a are the obstacle height and half width, respectively. This geometry has been used extensively in the literature (*Wurtele et al.,* 1996), as an analytic solution can be derived for this shape. In order to obtain comparable results with water-tank experiments, the following material properties and working conditions were used:

$\rho_0 = 998$ kgm^{-3}, $T_0 = 27$ °C, $\beta = 0.000207$ K^{-1}, $-\gamma = 832$ K m^{-1}, U= 0.25 ms^{-1}.

The Reynolds number, based on the inlet flow speed (U) and the obstacle height (h), was about 2500; therefore a laminar model was used. Compressibility and the Coriolis force were not taken into account. Free-slip wall and symmetry boundary conditions were applied at the lower and upper boundaries. A constant velocity and static pressure profile were prescribed as inlet and outlet conditions. The model was initialized with constant $\widetilde{T} = T_0$, $\widetilde{p} = p_0$, and uniform horizontal velocity $\widetilde{U} = U_0$.

Based on the linear wave theory (Eq. (38)), an analytic solution can be found for hydrostatic problems with a constant Scorer parameter (l). The Scorer parameter is usually a function of the vertical coordinate, and it is derived from the wave equation for atmospheric gravity waves with an assumption of a two-dimensional, non-viscous, adiabatic flow (*Smith,* 1979; *Durran,* 1990). This parameter is most often used to forecast the existence of trapped lee waves, which can be expected when l decreases strongly with height. This is especially true if l decreases suddenly in the mid-troposphere due to the presence of a stable layer dividing the troposphere into a highly and a weekly stable layer. The square root of the parameter l (Eq. (40)) has units of wave number. The wave number of the lee wave (l) lies between l_{upper} of the upper layer and l_{lower} of the lower layer. Wide mountain ranges generate vertically propagating waves of wave numbers less than l_{upper}. Small obstacles, that force wave numbers greater than l_{lower}, produce waves that will vanish with height.

For hydrostatic problems, the development of the full analytic solution has been summarized by several researchers (*Alaka,* 1960; *Smith,* 1979). The combined governing equations were resulted in the deep Boussinesq equation (Eq. (38)) for w. The Scorer parameter l is defined by Eq. (38) and Eq. (39):

$$\frac{\partial^2\left(\sqrt{\frac{\rho_0(z)}{\rho_0(z=0)}}w\right)}{\partial x^2} + \frac{\partial^2\left(\sqrt{\frac{\rho_0(z)}{\rho_0(z=0)}}w\right)}{\partial z^2} - l^2(z)\left(\sqrt{\frac{\rho_0(z)}{\rho_0(z=0)}}w\right) = 0, \quad (38)$$

$$l^2(z) = \frac{N^2}{U^2} - \frac{1}{U}\frac{d^2U}{dz^2} - \frac{1}{U}\frac{d\ln\rho}{dz}\frac{dU}{dz} - \frac{1}{4}\left(\frac{d\ln\rho}{dz}\right)^2 - \frac{1}{2}\left(\frac{d^2\ln\rho}{dz^2}\right), \quad (39)$$

where w is the perturbation vertical velocity, $N=\sqrt{-\frac{g}{\rho_0}\frac{\partial\rho(z)}{\partial z}}$ is the Brunt-Väisälä frequency, U is the inlet flow speed, ρ is the fluid density, and z is the vertical coordinate, respectively. For incompressible flow only the first two terms remain.

$$l^2(z)=\frac{N^2}{U^2}-\frac{1}{U}\frac{d^2U}{dz^2}. \tag{40}$$

The first term on the right-hand side dominates in our case, and additionally, if a uniform velocity profile ($U = U_0$) and Brunt-Väisälä frequency (N) are used, Eq. (40) simplifies to:

$$l=\frac{N}{U}. \tag{41}$$

With the help of the Scorer formula, flows can be categorized on the basis of the following two dimensionless quantities:

$$F_x = a\,l,\quad F_z = h\,l. \tag{42}$$

When $F_x >> 1$, the flow is essentially hydrostatic, while non-hydrostatic effects become important when $F_x \sim 1$ (*Schumann et al.*, 1987). Regarding the linearity, when $F_z << 1$, the flow is linear and nonlinear effects dominate, when the value approaches to $F_z \sim 1$. The borders are, however, not well-defined, and that is why one can find test cases marked as moderately hydrostatic or moderately nonlinear (*Thunis* and *Clappier,* 2000). Calculating these parameters using $a = 2$ m and $h = 0.01$ m, one can find that our setup is linear and hydrostatic with $l = 5.32$ m^{-1}, $F_x = 10.64$, and $F_z = 0.0532$. In the case of hydrostatic flow, an analytic solution exists (Eq. (43)) for the vertical velocity field $w(x, z)$, based on Eq. (38):

$$w(x,z)=\sqrt{\frac{\rho_0(z=0)}{\rho_0(z)}}\;U\,h\,a\,\frac{(x^2-a^2)\sin(l\cdot z)-2\,x\,a\,\cos(l\cdot z)}{(a^2+x^2)^2}. \tag{43}$$

The vertical velocity contours have been plotted against the corresponding analytic solution on *Fig. 1*. The agreement between the two solutions is very good, with the magnitude of the vertical velocity in the numerical solution being only slightly smaller. The locations of velocity maxima, in the case of the CFD results, are shifted only moderately downward in the vertical direction.

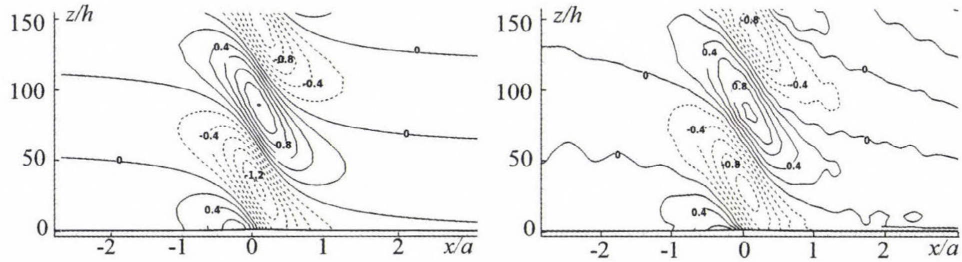

Fig. 1. Contour plots of the vertical velocity (w [mm s^{-1}]), obtained from the analytic solution based on Eq. (43) (left) and from CFD calculations (right). The solution is obtained for $U = 0.25$ m s^{-1}, $l = 5.32$ m^{-1}, $N = 1.3$ s^{-1}, $a = 2$ m, $h = 0.01$ m. The vertical and horizontal scales are normalized by the mountain height (h) and half width (a) respectively. Dashed lines represent negative values.

In the next section, a set of test cases have been prepared and the results are compared against experiments that cover a hydrostatic and nonlinear parameter range. The statistical performance measures applied for the comparison are also described briefly.

3.2. Statistical performance measures used during the evaluation

To quantitatively evaluate the output of the model with observations, *Hanna et al.* (1991, 1993) recommend the use of the following statistical performance measures (*Chang et al.,* 2005): the fractional bias (FB), the normalized mean-square error (NMSE), the fraction of predictions within a factor of 2 of observations (FAC2), and the hit rate (HR). *Chang* and *Hanna* (2004) suggest that a good model would be expected to have about 50% of the predictions within a factor of 2 of the observations (i.e., FAC2 > 0.5), a relative mean bias within 30% of the mean (i.e., –0.3 < FB < 0.3), a relative scatter of about a factor of 2 or 3 of the mean (i.e., NMSE < 4), and a hit rate above 66% (HR > 0.66) with an allowed deviation of D = 0.25. The absolute value of the model's fractional bias (FB) is reasonably good if it is less than 0.25. A tendency toward overprediction of wind speeds is seen, with the fractional bias regularly between 0 and –0.25 (*Lundquist* and *Chan,* 2006). The perfect model would have the following idealized performances: FAC2 = HR = 1 and FB = NMSE = 0. In air quality modeling, typical values of the above statistical measures have been defined as acceptable for model evaluation and also correspond to a model acceptance criterion (*Chang* and *Hanna,* 2004).

3.3. Numerical model results compared to small scale water-tank experiments

Among the experiments focused on topography-induced gravity waves, one can find investigations dealing with symmetric and asymmetric obstacles, looking at the effect of asymmetry (*Gyüre* and *Jánosi,* 2003), determining surface drag by numerical simulations (*Klemp* and *Lilly,* 1975) and numerically examining the wave breaking characteristics (*Doyle et al.,* 2000; *Afanasyev* and *Peltier,* 2001). The common feature of the former experiments is the experimental apparatus. They use mainly the water as working medium, since in water it is relatively easy to generate and maintain stable stratification for a longer period of time. Usually, this is done by using layered salt water. The achievable range of Reynolds number is limited to approximately 10^3. In spite of this fact, these methods are widely used, since there is more control on the parameters and conditions, than in real atmosphere.

Two-dimensional simulations of internal gravity waves have been carried out by using symmetric and asymmetric obstacles, in correspondence with the experiments performed by *Gyüre* and *Jánosi* (2003). Obstacle shapes have been characterized by the following function:

$$z(x) = a \exp(-b\,|\,x\,|\,2k) \tag{44}$$

where *a, b,* and *k* are shape parameters and *x* is the horizontal coordinate of the obstacle. Both the symmetric and asymmetric shapes can be described by Eq. (44), by prescribing different parameters for the upstream and downstream part of the mountain barrier. Measurements were performed in a narrow plexi glass tank of 2.4 m × 0.087 m × 0.4 m filled with linearly stratified salt water, by towing the obstacles along the bottom of the tank at a constant speed. The range of the experimental parameters (obstacle height h=0.02–0.04 m, towing velocity U=0.01–0.15 m s^{-1}, and Brunt-Väisälä frequency N=1.09–1.55 s^{-1}) corresponds to an atmospheric flow up to an elevation of 5–10 km for an obstacle height of 600 m and a wind speed of 10–70 m s^{-1} for a large range of hydrostatic state and linearity.

The flow was considered unsteady, incompressible, and two-dimensional in the simulation. Due to the low Reynolds number range, a laminar model was used. The domain was discretized with a structured quad grid, using 150 x 800 quad elements (*Fig. 2*). Second order time discretization, pressure staggering option (PRESTO) for pressure interpolation (*ANSYS Inc.,* 2012), and second order upwinding methods were used when solving the momentum and energy equations. Compressibility was turned off in this case by using the transformation described in Section 2.2.6.

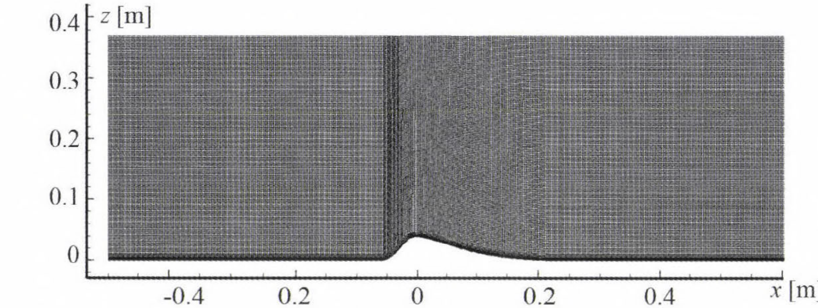

Fig. 2. Computational domain and numerical grid in the case of a gentle leeward side obstacle.

Typically for higher flow velocities, we observed flow separation during the simulation of symmetric steep lee-side obstacles. The separation induced bubble modified the shape of the leeward side in this case, quasi elongating the obstacle (*Fig. 3*), consequently changing the hydrodynamic characteristics of the barrier. Therefore, these cases were excluded from the comparison.

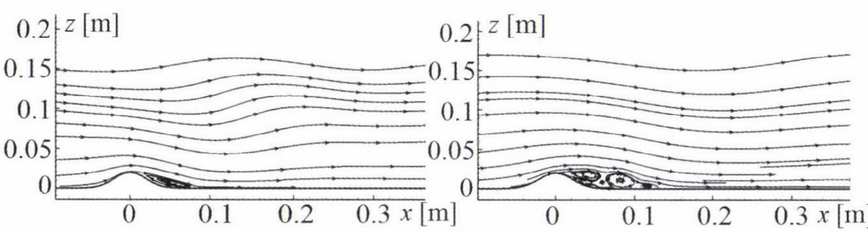

Fig. 3. Computed streamlines of the velocity field for $U/Nh = 0.7$ (left) and $U/Nh = 1$ (right) showing the elongation of the separation bubble and of the wave lengths for a symmetric obstacle.

In the numerical model, flow enters into the domain with a uniform inlet velocity profile. A moving bottom wall, for simulating the stationary bottom wall of the experiment was used. No visible disturbances were observed on the water surface, consequently a rigid lid (symmetry) with free slip boundary condition was applied in the simulation model. Avoiding the interaction between upward propagating and reflected wave fronts, data extraction was made after a short transient period, before interference could occur. This period was estimated from the vertical group velocity (*Gyüre* and *Jánosi,* 2003), which was proportional to the towing speed. In those cases where steepening and wave breaking occurred, samples were excluded from the averaging of amplitudes and wavelengths.

In *Table 1*, the simulations were categorized into four groups based on $F_x = Na/U$ and $F_z = Nh/U$ non-dimensional numbers as described by Eq. (42). These groups are nonlinear (NL), moderately nonlinear (M–NL), hydrostatic (H), and moderately non-hydrostatic (M–NH) cases. For all cases, the mountain height *h*, was 0.04 m, the leeward half width *a*, was 0.13 m, the Brunt-Väisälä frequency *N*, was 1.33 s^{-1} and *U* was the incoming flow velocity corresponding to the towing velocities of the obstacle in the survey.

Table 1. List of cases and parameters for the simulation of the gentle leeward side obstacle. Vertical structure and linearity categories are: H – hydrostatic, M-NH – moderately non-hydrostatic, NL – nonlinear, M–NL – moderately nonlinear

Case No.	U (m s^{-1})	*Na/U*	*Nh/U*	Vertical structure	Linearity
1	0.016	10.80	3.33	H	NL
2	0.032	5.31	1.64		
3	0.037	4.63	1.43		
4	0.041	4.15	1.28		
5	0.048	3.60	1.11		
6	0.053	3.24	1.00		
7	0.077	2.23	0.69	M–NH	M–NL
8	0.106	1.62	0.50		
9	0.160	1.08	0.33		

Wavelengths and amplitudes were measured in multiple positions above and downstream of the obstacle, by locating the wave fronts and measuring the distance between the fronts. The error bars in *Fig. 4* show the standard deviation of both the measured and simulated values. Circular wave fronts assumed in the case when lee waves are generated by a moving point source (*Voisin,* 1994). As shown from the upper part of *Fig. 5*, the shape of the wave fronts has been strongly affected by the obstacle shape, even in the M–NL cases. Here the centers of the wave fronts were gradually shifted toward negative coordinates, indicating strong wave dispersion. The large error bars of the measurements (*Fig. 4*) represent not only the limited resolution caused by the visualization technique (dying of different layers), but are also the consequence of the aforementioned strong dispersion of lee waves.

It was observed that our model performs well in the H–NL range for steeper lee-side obstacles, like the one presented in *Fig. 3*. However, close to the M–NH range with the same obstacle, results tend to differ from the experiments. This difference may be explained by boundary layer separation effects. At an increased velocity, the separation bubble that developed behind the obstacle elongated and caused the virtual mountain half width (mountain half width plus the horizontal size of the separation) and consequently the normalized wave length to almost double. (See the wave field in *Fig. 3*)

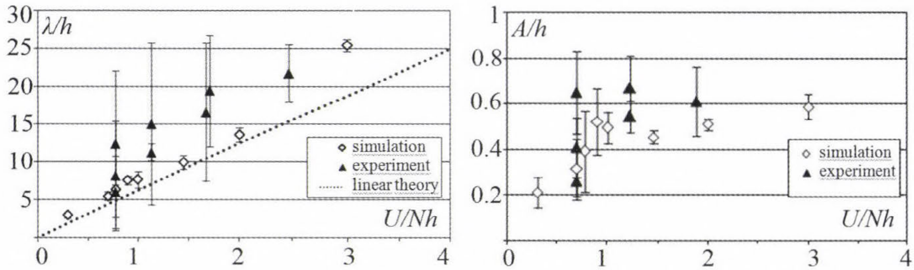

Fig. 4. Normalized averaged wave length (λ/h) (left) and normalized averaged wave amplitude (A/h) (right) as a function of non-dimensional horizontal flow velocity, in the case of the gentle leeward slope. The dotted line represents the wave length obtained from a linear theory, based on $\lambda = 2\pi U / N$ (*Scorer,* 1949). Filled symbols represent the measurements of *Gyüre* and *Jánosi* (2003). Error bars indicate the error originating from the data extraction technicque and wave dispersion.

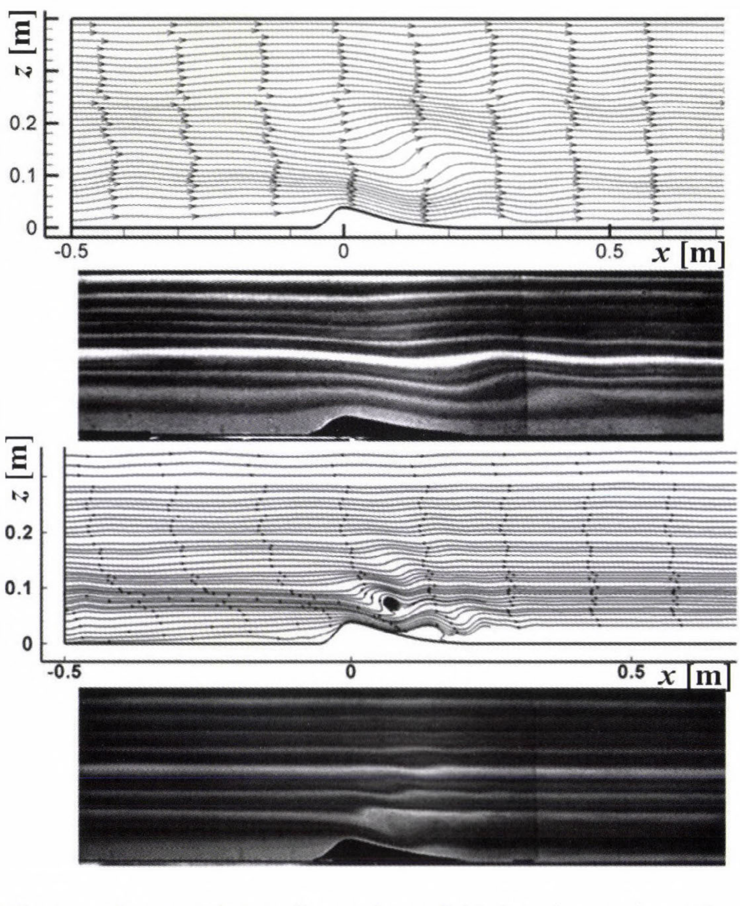

Fig. 5. Contours of computed streamlines and wave fields from the experiments (courtesy of *Gyüre* and *Jánosi,* 2003) at $Nh/U = 0.69$ (the upper two) and $Nh/U = 3.33$ (the lower two) non-dimensional flow velocities.

According to experimentalists (*Qiu* and *Xia,* 1998; *Gyüre* and *Jánosi,* 2003), the side walls have a negligible overall effect on the experimental results, however, the exact location and size of the separation were not captured properly, which can possibly be explained by the 3-D structure of the flow characterizing the laboratory experiments, due to the boundary layer on the side walls interacting with the separation bubble. In the case of a 3-D narrow obstacle, the separation bubbles were smaller, as the stratified flow tended to flow around the obstacle, instead of flowing over it. The prediction of the location of separation is currently a difficult topic, it requires the modeling of transitional turbulence and is beyond the scope of this investigation. Avoiding separation by using a gentle leeward side obstacle, however, gave both qualitative and quantitative agreements concerning the normalized amplitudes and wavelengths (*Fig. 4*). *Table 2* shows the performance measures, indicating good model performance. At low inlet velocities (bottom of *Fig. 5*), where wave breaking and rotors occurred, the flow structures, characterized by a high nonlinearity, were also captured properly.

Table 2. Statistic metrics of normalized wavelength *(λ/h)* and amplitude *(A/h)* for water-tank studies using CFD and experimental data of *Gyüre and Jánosi* (2003). Definition and the applied limits for the statistic metrics are described in *Chang et al.* (2005)

Validation metric	**Abbreviation**	**Limit**	***λ/h***	***A/h***	**Classification**
Correlation coefficient	R	>0.8	0.95	0.99	good
Fractional bias	FB	±0.3	0.317	0.21	good
Normalized mean square error	NMSE	0–4	0.12	0.05	good
Hit rate	HR	>0.66	0.75	1	good
Fraction of predictions within a factor of two of observations	FAC2	>0.5	1	1	good

3.4. Model comparison with a full scale event

3.4.1. Case study

A relatively well documented and studied event occurred during the winter of 1972 near Boulder, Colorado, where a severe wind storm, with a strong descent of air originating from the higher atmosphere, caused significant damage to the environment (*Lilly* and *Zipser,* 1972; *Brinkman,* 1974). The strong tropospheric descent is well reflected in the potential temperature contours in *Fig. 6a*, where the contours become denser close to the ground. The accompanying near ground downwind was also reported as being especially severe. A hydraulic jump and waves also developed behind the mountain (*Fig. 6a*).

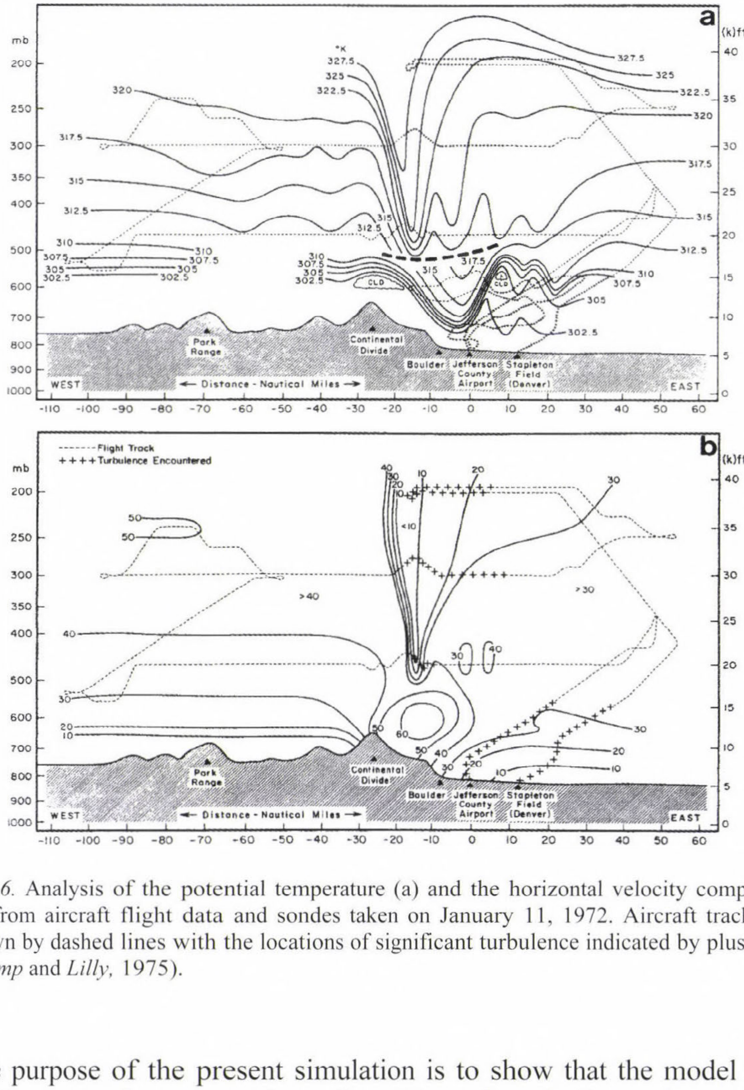

Fig. 6. Analysis of the potential temperature (a) and the horizontal velocity component (b) from aircraft flight data and sondes taken on January 11, 1972. Aircraft tracks are shown by dashed lines with the locations of significant turbulence indicated by plus signs (*Klemp* and *Lilly,* 1975).

The purpose of the present simulation is to show that the model is able to capture the main features and nonlinearities of such flows, for example the existence of the mentioned nonlinearities. This event became a standard test case of researchers (see ,e.g., *Xue et al.,* 2000) for developing simulation models, or to reproduce and understand the related mechanisms of such phenomena. A recent study dealt with the development of a severe thunderstorm in Budapest. With high resolution numerical modeling using MM5, they were able to reproduce the main features of the severe convective storm (*Horváth et al.,* 2007).

Different assumptions are made during similar case studies, in order to reduce computational cost, taking the advantage of the quasi two-dimensionality of the flow, or simply investigating each flow phenomena separately. Although mountain flows are generally three-dimensional, two-dimensionality can be a good assumption for the downslope windstorm case, as the continental divide is long compared to its cross section. This is acceptable only if the large scale flow is being investigated and the microstructure has only negligible influence on the main flow. In some cases these structures have an effect, e.g., by modifying the horizontal position of the hydraulic jump. This is due to the increased surface friction resulting from a non-slip boundary. In spite these differences in the treatment of the lower boundary, the main features of the flow will still remain.

The elevation of the realistic terrain of the E–W oriented section was derived from a 3 arc second resolution SRTM (Shuttle Radar Topographic Mission) database. The section was then interpolated for the latitude of 40.015 N. The longitudinal coordinates were between 107.100 W and 103.900 W, giving an approximately 270 km wide section. The new coordinates were transformed onto the Universal Transverse Mercator (UTM) coordinates and were interpolated onto an approximately 1.5 arc second grid using a bicubic spline method.

Test cases using an idealized geometry have also been examined, where a simplified two-dimensional model has been used. In spite of the fact, that the real mountain has a plateau-like shape, due to the upstream influence and partial blocking, the upstream mountain profile does not affect significantly the upstream flow. Due to this fact, a symmetric mountain profile was used in several works (*Klemp* and *Lilly,* 1975), as well as in this study. The profile described by Eq. (37) was used for modeling both the upstream and downstream sections of the geometry. Here $a = 10$ km and $h = 2$ km are the mountain half width and height, respectively. The initial temperature and velocity profiles were based on the intercomparison study of *Doyle et al.* (2000). They found that these initial conditions were more appropriate for wave breaking tests, and more realistic than the conditions used in earlier studies (*Peltier* and *Clark,* 1979). Conditions favorable for downslope windstorms are usually characterized by strong cross mountain winds, and by the presence of a stable layer at the appropriate height (*Durran,* 1986). Both of these conditions were present in the studied situation.

The solution was found to be sensitive to the grid resolution (*Doyle et al.* 2000), therefore, in this study a relatively higher resolution grid was used. An equidistant grid was applied with a size of 1000 m and adapted to 250 m in two steps in the vicinity of the mountain. In the vertical direction the mesh size decreased down to 10 m resolution close to the ground. The domain extended from 2 to 25 km in the vertical and – 115 to 120 km in the horizontal direction, with the mountain crest positioned at $x = 0$ km. The top boundary was defined as symmetry with zero normal velocity, and the bottom was defined as a free-slip wall. A standard non-reflective boundary condition (outflow) was applied as an outlet. This means that the internal pressure field has been extrapolated to the outlet surface, and therefore, no further information on the outlet velocity and pressure profiles were required by the system.

Second order time discretization, pressure staggering option (PRESTO) for pressure interpolation (*ANSYS Inc.*, 2012), and second order upwinding methods were used in the momentum and energy equations. Compressibility was introduced with the help of the transformation used for model adaption. Moist effect and the Coriolis force were not considered during the calculations.

By using the ANSYS–FLUENT 13 simulation system, the model was integrated for a non-dimensional period of time of $t^{*} = \overline{U}t / a = 43.2$, based on an average inlet flow speed of $30\ \mathrm{m\,s^{-1}}$, which corresponds to a 4-hour flow time. The results shown in this section are obtained at $t^{*} = 32.4$ time instant. Results were quantitatively compared to several mesoscale meteorological codes using statistical performance measures described in Section 3.2. The summary of the comparison can be seen in *Table 3.* Based on FB, NMSE, and FAC2, the idealized model can be considered acceptable. Negative FB values indicate lower predicted overall horizontal velocity. The correlation coefficient and hit rate, however, show values under the limit. The hit rate was calculated with $5\ \mathrm{m\,s^{-1}}$ absolute and 10% relative deviation for the velocity and 1 K and 5% for the temperature, respectively, since large deviations with a factor of 2 differences were realized among the different intercomparision cases presented by *Doyle et al.* (2000). *Chang* and *Hanna* (2004) suggest that the model performance should not be judged based only on the performance measures but together with the comparison of flow patterns or the time evolution of the flow field.

Table 3. Statistic metrics calculated for horizontal velocity (U) and potential temperature (Θ) for the Boulder windstorm case study comparing CFD and NWP (*Doyle et al.*, 2000) model results

Validation metric	**Abbreviation**	**Limit**	U	Θ	**Classification**
Correlation coefficient	R	>0.8	0.154	0.96	not sufficient
Fractional bias	FB	±0.3	−0.07	−0.056	good
Normalized mean square error	NMSE	0–4	0.396	0.01	good
Hit rate	HR	>0.66	0.29	0.56	not sufficient
Fraction of predictions within a factor of two of observations	FAC2	>0.5	0.7	1	good

According to the experiments of *Doyle et al.* (2000), the results were highly time dependent, and therefore, unsteady simulations were executed and time-averaging was applied on the results. An averaging interval varying from 10 to 60 minutes was applied during the simulation, and it was found that the value and location of the maximum velocity were not affected. The horizontal position of the upstream edge of the hydraulic jump however changed significantly. The lee-slope wind magnitude varied considerably among the model simulations presented by *Doyle et al.* (2000), and these differences were also reflected in the horizontal position of the hydraulic jump. The location of the upstream edge in some models, e.g., the *Durran* and *Klemp* (1983) model (DK83) or the Eulerian/semi-Lagrangian model (EULAG) was positioned immediately after the lee slope, similarly to our results, while in other cases it was positioned 10 – 25 km downstream of that (e.g., MESONH, RAMS, or RIMS models of the same intercomparison). This partially explains the lower HR and R values due to the horizontal shift in the flow pattern. Regarding the downslope wind, a higher value of maximum horizontal velocity was realized by the simulation than that of the onsite measurements. At $t^*=32.4$, the location of the maximum velocity peak was found at approximately 8.5 km downstream of the mountain crest at a height of 7 km (*Fig. 7*). With further integration, the locations of the maxima were shifted downstream to approximately 16 km beyond the crest and to a lower height of 4 km (bottom of *Fig. 7*). The magnitudes were not changed considerably, stabilizing at around 66 m s^{-1}. Regarding the wind speed close to the ground, within the lowest 50 m, 51 – 59 m s^{-1} was realized, depending on the position along the mountain lee side. The near ground values of velocity magnitude were in fair agreement both with the observations and the meteorological models. The high instantaneous velocity peaks at higher altitudes obtained from the simulation could be partly caused by the lack of moisture transport and phase change processes. According to *Durran* and *Klemp* (1983), the wave response could be even 50% lower if a proper treatment for moist air flow is applied. This could significantly affect the properties of wave breaking, and consequently the development of a low level jet.

Several mesoscale codes simulated multiple breaking regions with the strongest ones located above the hydraulic jump at an altitude of 12 km and above (see the model results of RAMS, MESONH models presented by *Doyle et al.* (2000)). Wave steepening regions were obtained by CFD for the ideal and real mountain profiles at a similar altitude (between 10 and 15 km). Using the idealized geometry (*Fig. 7*), this region was weaker. The altitude of the maximum steepness above the hydraulic jump in the breaking region was at about 12 km with the highest amplitude waves being of 2–2.5 km.

The present results show smooth downstream isolines. In some of the cases of *Doyle et al.* (2000), the downstream part of the hydraulic jump was oscillatory, while in other cases the isolines were smooth. Among the results of different mesoscale meteorological solvers, depending on the amount of applied eddy diffusivity (K_d), different flow structures were obtained. Smaller K_d values usually resulted in smaller wave structures.

The stratospheric air descent reached the altitude of 5–6 km using the real topography which correlates well with the non-hydrostatic mesoscale vorticity (TVM) model solution of *Thunis* and *Clappier* (2000), or the model comparisons presented by *Doyle et al.* (2000) (CUMM, RAMS, RIMS). The descent was even stronger and propagated to lower altitudes in the case of the simplified geometry accompanied by high TKE values (see *Fig. 7*) . The highest peaks, even reaching 117 m^2 s^{-2}, can be found around the upstream edge of the hydraulic jump and at the wave steepening regions at higher altitudes. The maximum value of TKE is reported approximately 15–20 m^2 s^{-2} in atmospheric rotors (*Doyle et al.,* 2002) and even reaches higher values in the case of extremely severe turbulence.

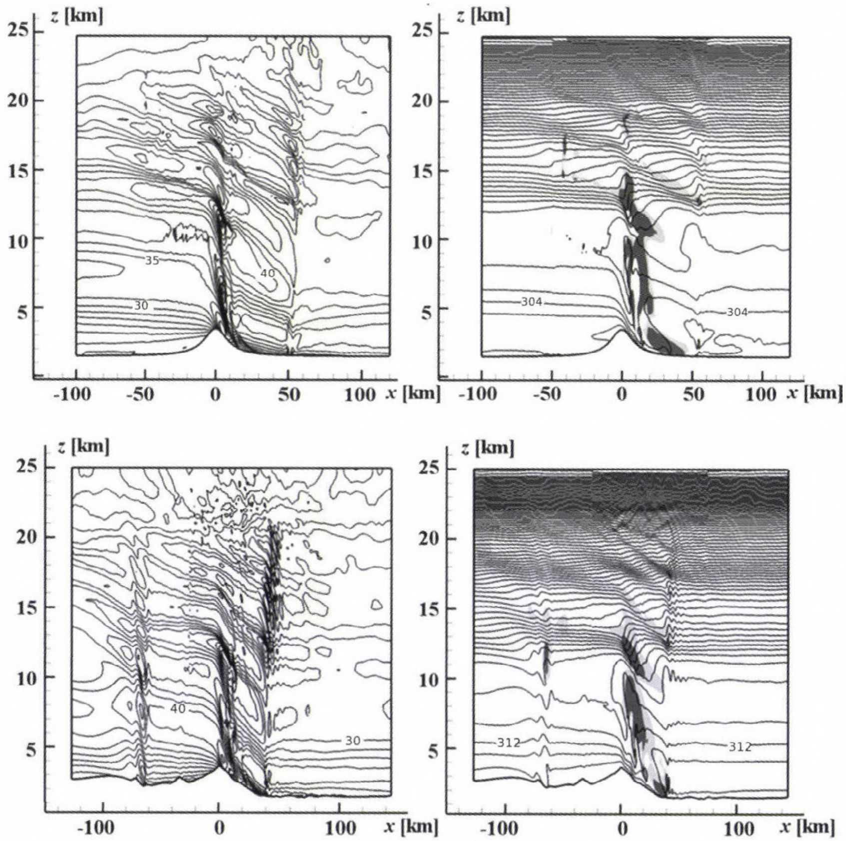

Fig. 7. Contours of horizontal velocity component (left panel) and potential temperature (right panel) for an idealized (top) and a real (bottom) mountain shape. The pictures show the results at $t^* = 32.4$ non-dimensional flow time. Vertical coordinates were magnified by a factor of 12 for better visualization. Potential temperature and velocity contour intervals are 8°C and 5 m s^{-1}, respectively. Light and dark grey areas indicate regions characterized by turbulent kinetic energy higher than 5 m^2 s^{-2} and between 5–25 m^2 s^{-2}.

Differences in the magnitude of the horizontal velocity may also be related to the two-dimensional treatment of the topography if compared to the real situation. In three spatial dimensions, the flow can pass around the obstacle, while in 2-D it is forced over it. The test results of *Doyle et al.* (2000) confirmed that a significant reduction in wave breaking could be found for the 3-D case. Some of the studies dealing with gravity wave evolution used a frictionless lower boundary (*Richard et al.,* 1989). Concerning the bottom boundary condition, a more realistic treatment of the ground surface could result in a slower movement and different horizontal location of the hydraulic jump.

4. Summary and conclusions

We briefly presented an adaptation method applicable to general purpose CFD solvers for atmospheric flow simulations, which was based on the application of an incompressible fluid model. Mesoscale effects, such as thermal stratification, adiabatic cooling caused by hydrostatic pressure driven expansion, compressibility, and Coriolis force were taken into account with the help of a transformation system and customized volume sources.

In this paper, simulations were presented around more complex geometrical features, idealized barriers, and real terrain, demonstrating the capabilities of the CFD based approach.

Simulations of linear hydrostatic waves were compared to an analytical solution, and it was stated that for this regime the code behaved well, and an excellent agreement was found.

Secondly, the simulation results were compared to water-tank experiments of two-dimensional mountain waves with different degrees of nonlinearity and hydrostacity. A good agreement was found based on the statistical performance measures and flow pattern comparison concerning the measured and simulated wavelengths and amplitudes. The model evaluation for λ/h gave a correlation coefficient of 0.95, fractional bias 0.317, normalized mean square error of 0.12, a hitrate value of 0.75 and 100% of predictions within a factor of two of observations. The equivalent results for A/h were 0.99 (R), 0.21 (FB), 0.05 (NMSE), 1 (HR), and 100% (FAC2). The model was also able to capture well the location and size of the appearing nonlinear structures, such as the rotor that was formed behind the obstacle.

Simulation of the Boulder windstorm case is ideal for testing and evaluating mesoscale numerical models, therefore it was chosen as the third object of analysis. The simulation results were compared to the on-site observations and a series of modeling experiments that were presented by *Doyle et al.* (2000). Model evaluation has demonstrated reasonable agreement with measurements for potential temperature (Θ). The model evaluation statistics gave a correlation coefficient of 0.96 and fractional bias –0.056, normalized mean square error of 0.01, a hit rate value of 0.56, and 100% of predictions within a factor of two of observations. The equivalent results for horizontal velocity (U) were 0.154 (R), –0.07 (FB), 0.396 (NMSE), 0.29 (HR) and

0.7 (FAC2). Results obtained from our simulations are encouraging with regard to the predictability of a low level, highly accelerated channel flow, and upper level wave breaking. Close to the ground a very strong lee-side wind was realized, accompanied by a well-defined hydraulic jump downstream.

Using only one single unstructured grid and a uniform physical description for close- and far-field flow, one can take the advantage of the model adaption in the simulation of mesoscale atmospheric phenomena. In the same model, one can investigate the finely structured microscale flow around complex geometrical features, such as flow around buildings with pollution dispersion or to study the close- and far-field of cooling towers and its effects to the environment.

The implementation and evaluation of non-reflective boundaries is planned through a 3-D mountain wave and associated downslope windstorm case study and the inclusion of moisture transport and phase change processes is also an important further step towards the practical application of the method.

Acknowledgments–This work has been supported by the Hungarian Research Fund under contract number OTKA T049573, the National Research and Development Program under contract number NKFP 3A/088/2004, and the TÁMOP-4.2.1.B-11/2/KMR-2011-0001 program. The authors are thankful for the data support from the SRTM.

References

Afanasyev, Y.D. and *Peltier, W.R.*, 2001: Numerical simulations of internal gravity wave breaking in the middle atmosphere: the influence of dispersion and three-dimensionalization. *J. Atmos. Sci. 58*, 132–153.

Alaka, M.A., Ed., 1960: The airflow over mountains. *WMO Tech. Note* 34, [Available from World Meteorological Organization, Case Postale 2300, CH-1211 Geneva 2, Switzerland.]

Almut, G. and *Herzog, H.J.*, 2007: A consistent time-split numerical scheme applied to the nonhydrostatic compressible equations. *Mon. Weather Rev. 135*, 20–36.

Andre, J.C., DeMoor, G., Lacarrere, P., Therry, G., and *Du Vachat, R.*, 1978: Modelling the 24-hour evolution of the mean and turbulent structures of the planetary boundary layer. *J Atmos Sci 35*, 1861–1883.

ANSYS Inc., 2012: FLUENT 13 documentation. In: Fluent User Services Center. [Available online at http://www.fluentusers.com/fluent/doc/doc_f.htm., Cited 26. September 2012.]

Baklanov, A.A., Grisogono, B., Bornstein, R., Mahrt, L., Zilitinkevich, S.S., Taylor, P., Larsen, S.E., Rotach, M.W., and *Fernando, H.J.S.*, 2011: The nature, theory, and modeling of atmospheric planetary boundary layers. *B. Am. Meteorol. Soc. 92*, 123–128.

Balczó, M., Balogh, M., Goricsán, I., Nagel, T., Suda, J.M., and *Lajos, T.*, 2011: Air quality around motorway tunnels in complex terrain - Computational Fluid Dynamics modeling and comparison to wind tunnel data. *Időjárás 115*, 179–204.

Balogh, M. and Krisróf, G., 2010: Fine scale simulation of turbulent flows in urban canopy layers. *Időjárás 114*, 135–148.

Belušič, D. and *Klaič, Z.B.*, 2004: Estimation of bora wind gusts using a limited area model. *Tellus A 56*, 296–307.

Berg, L.K. and *Zhong, S.*, 2005: Sensitivity of MM5-Simulated Boundary Layer Characteristics to Turbulence Parameterizations. *J. Appl. Meteorol.* 44, 1467–1483.

Blackadar, A.K., 1976: Modeling the nocturnal boundary layer. Preprints of the Third Symposium on Atmospheric Turbulence and Air Quality, Rayleigh, NC, 19–22 October 1976, Amer. Meteor. Soc., Boston, 46–49.

Blocken, B., Stathopoulos, T. and *Carmeliet, J.,* 2007: CFD simulation of the atmospheric boundary layer: wall function problems. *Atmos. Environ. 41*, 238–252.

Brinkman, W.A.R., 1974: Strong downslope winds at Boulder, Colorado. *Mon. Weather Rev. 102*, 592–602.

Castro, F.A., Santos, C.S. and *Palma, J.M.L.M.,* 2008: Parallelisation of the CFD Code of a CFD-NWP Coupled System for the Simulation of Atmospheric Flows over Complex Terrain. *High Performance Computing for Computational Science - VECPAR* 2008, 27–38.

Cenedese, A. and *Monti, P.,* 2003: Interaction between an urban heat island and a sea-breeze flow. A laboratory study. *J. Appl. Meteorol. 42*, 1569–1583.

Chang, J.C. and *Hanna, S.R.,* 2004: Air quality model performance evaluation. *Meteorol. Atmos. Phys. 87*, 167–196.

Chang, J.C., Hanna, S.R., Boybeyi, Z. and *Franzese, P.,* 2005: Use of Salt Lake City URBAN 2000 Field Data to Evaluate the Urban Hazard Prediction Assessment Capability (HPAC) Dispersion Model. *J. Appl. Meteorol. 44*, 485–501.

Colle, B.A. and *Mass, C.F.,* 2000: High resolution observation and numerical simulation of easterly gap flow through the strait of Juan de Fuca on 9–10 December 1995. *Mon. Weather Rev. 128*, 2398–2422.

Corrsin, S., 1975: Limitation of gradient transport models in random walks and in turbulence. *Adv. Geophys. 18A*, 25–60.

Deardorff, J.W., 1974a: Three-dimensional numerical study of the height and mean structure of a heated planetary boundary layer. *Bound.-Lay. Meteorol. 7*, 81–106.

Deardorff, J.W., 1974b: Three-dimensional numerical study of turbulence in an entraining mixed layer. *Bound.-Lay. Meteorol.* 7, 199–226.

Deardorff, J.W., 1980: Stratocumulus-capped mixed layers derived from a three-dimensional model. *Bound.-Lay. Meteorol.* 18, 495–527.

Doyle, J.D., Durran, D.R., Chen, C., Colle, B.A., Georgelin, M., Grubisic, V., Hsu, W.R., Huang ,C.Y., Landau, D., Lin, Y.L., Poulus, G.S., Sun, W.Y., Weber, D.B., Wurtele, M.G., and *Xue, M.,* 2000: An intercomparison of model-predicted wave breaking for the 11 January 1972 boulder windstorm. *Mon. Weather. Rev. 128*, 901–914.

Doyle, J.D. and *Durran, D.R.,* 2002: The Dynamics of mountain–wave induced rotors. *J. Atmos. Sci. 59,* 186–201.

Dudhia, J., 1993: A nonhydrostatic version of the Penn State / NCAR mesoscale model: Validation tests and simulations of an Atlantic cyclone and cold front. *Mon. Weather Rev. 121*, 1493–1513.

Durran, D.R. and *Klemp, J.B.,* 1983: A Compressible model for the simulation of moist mountain waves. *Mon. Weather. Rev 111*, 2341–2361.

Durran, D.R., 1986: Another look at downslope windstorms. Part I: The development of analogs to supercritical flow in an infinitely deep, continuously stratified fluid. *J. Atmos. Sci.* 43, 2527–2543.

Durran, D.R., 1990: Mountain waves and downslope winds. Atmospheric Processes over Complex Terrain. *Meteorol. Monog. 45*, 59–81.

Duynkerke, P.G., 1988: Application of the E–ε turbulence closure model to the neutral and stable atmospheric boundary layer. *J. Atmos. Sci. 45*, 865–880.

Faragó, I., 2006: Application of the operator splitting method for real-life problems. *Időjárás 110*, 379-395.

Freedman, F.R. and Jacobson, M.Z., 2003: Modification of the Standard ε equation for the stable ABL through enforced consistency with Monin-Obukhov similarity theory. *Bound-Lay Meteorol* 106, 384–410.

Gatski, T.B. and *Jongen, T.,* 2000: Nonlinear eddy viscosity and algebraic stress models for solving complex turbulent flows. *Prog. Aerosp. Sci. 36*, 655–682.

Geiser, J., 2008: Iterative operator-splitting methods with higher-order time integration methods and applications for parabolic partial differential equations. *J. Comput. Appl. Math. 217*, 227–242.

Grell, G.A., Dudhia, J. and *Stauffier, D.R.,* 1995: A description of the fifth-generation Penn State/NCAR mesoscale model. *NCAR Tech. Note, NCAR/TN-398-398+ST.*

Gyüre, B. and *Jánosi, I.M.*, 2003: Stratified flow over asymmetric and double bell-shaped obstacles. *Dynam. Atmo.s Oceans 37*, 155–170.
Hanjalic, K. and *Launder, B.E.*, 1972: A Reynolds stress model of turbulence and its application to thin shear flows. *J. Fluid Mech. 52*, 609–638.
Hanna, S.R., Strimaitis, D.G. and *Chang, J.C.*, 1991: Evaluation of commonly-used hazardous gas dispersion models. Vol. II, Hazard Response Modeling Uncertainty (A Quantitative Method). *Rep. A119/A120 prepared by Earth Tech, Inc., for Engineering and Services Laboratory, Air Force Engineering and Services Center, and for the American Petroleum Institute,* 334 pp.
Hanna, S.R., Chang, J.C. and *Strimaitis, D.G.*, 1993: Hazardous gas model evaluation with field observations. *Atmos. Environ.* 27A, 2265–2285.
Hanna, S.R., Brown, M.J., Camelli, F.E., Chan, S.T., Coirier, W.J., Kim, S. and *Reynolds, R.M.*, 2006: Detailed Simulations of Atmospheric Flow and Dispersion in Downtown Manhattan: An Application of Five Computational Fluid Dynamics Models. *B. Am. Meteorol. Soc. 87*, 1713–1726.
Hargreaves, D.M. and *Wright, N.G.*, 2007: On the use of the k–ε model in commercial CFD software to model the neutral atmospheric boundary layer. *J. Wind Eng. Ind. Aerod. 95*, 355–369.
Havasi, Á., Bartholy, J., and *Faragó, I.*, 2001: Splitting method and its application in air pollution modeling. *Időjárás 105*, 39–58.
Holton, J.R., 2004: An Introduction to Dynamic Meteorology. 4th Edition, Academic Press, 192–212
Holtslag, A.A.M. and *Moeng, C.-H.*, 1991: Eddy diffusivity and countergradient transport in the convective atmospheric boundary layer. *J. Atmos. Sci. 48*, 1690–1698.
Hong, S.-Y., 2010: A new stable boundary-layer mixing scheme and its impact on the simulated East Asian summer monsoon. *Q. J. Roy. Meteorol. Soc. 136*, 1481–1496.
Hong, S.-Y. and *Pan, H.-L.*, 1996: Nonlocal boundary layer vertical diffusion in a medium-range forecast model. *Mon. Weather Rev. 124*, 2322–2339.
Hong, S.-Y., Noh, Y, and *Dudhia, J.*, 2006: A new vertical diffusion package with an explicit treatment of entrainment processes. *Mon. Weather Rev. 134*, 2318–2341.
Horváth, Á., Geresdi, I., Németh, P. and *Dombai, F.*, 2007: The Constitution Day storm in Budapest: Case study of the August 20, 2006 severe storm. *Időjárás 111*, 41–63.
Huser, A., Nilsen, P.J. and *Skatun, H.*, 1997: Application of k-ε model to the stable ABL: pollution in complex terrain. *J. Wind Eng. Ind. Aerod. 67–68*, 425–436.
Janjic, Z.I., 1990: The step–mountain coordinates: physical package. *Mon. Weather Rev. 118*, 1429–1443.
Janjic, Z.I., 1996: The Mellor-Yamada level 2.5 scheme in the NCEP Eta Model. 11th Conference on Numerical Weather Prediction, Norfolk, VA, 19-23 August 1996; Amer Meteor Soc, Boston, MA, 333–334.
Janjic, Z.I., 2002: Nonsingular Implementation of the Mellor-Yamada Level 2.5 Scheme in the NCEP Meso model. *NCEP Office Note 437*.
Kasahara, A., 1974: Various vertical coordinate systems used for numerical weather prediction. *Mon. Weather Rev. 102*, 509–522.
Klemp, J.B. and *Lilly, D.K.*, 1975: The dynamics of wave-induced downslope winds. *J. Atmos. Sci. 32*, 320–339.
Klemp, J.B. and *Wilhelmson, R.B.*, 1978: The simulation of three-dimensional convective storm dynamics. *J. Atmos. Sci. 35*, 1070–1096.
Klemp, J.B., Skamarock, W.C., and *Dudhia, J.*, 2007: Conservative Split-Explicit Time Integration Methods for the Compressible Nonhydrostatic Equations. *Mon. Weather Rev. 135*, 2897–2913.
Knievel, J.C., Bryan, G.H. and *Hacker, J.P.*, 2007: Explicit Numerical Diffusion in the WRF Model. *Mon. Weather Rev. 135*, 3808–3824.
Kristóf, G., Rácz, N., and *Balogh, M.*, 2009: Adaptation of Pressure Based CFD Solvers for Mesoscale Atmospheric Problems. *Bound.-Lay. Meteorol. 131*, 85–103.
Launder, B.E. and *Spalding, D.B.*, 1972: Lectures in mathematical models of turbulence. Academic Press, London, England 1972. 169 pp.
Lee, S.-M., Giori, W., Princevac, M., and *Fernando, H.J.S.*, 2006: Implementation of a Stable PBL Turbulence Parameterization for the Mesoscale Model MM5: Nocturnal Flow in Complex Terrain. *Bound.-Lay. Meteorol. 119*, 109–134.
Lesieur, M., 2008: Turbulence in Fluids. Fourth edition, Springer, ISBN: 9781402064340.

Lilly, D.K. and *Zipser, E.J.*, 1972: The front range windstorm of 11 January 1972 – a meteorological narrative. *Weatherwise 25*, 56–63.
Lin, Y-L., 2007: Mesoscale dynamics. Cambridge University Press, ISBN 9780521808750.
Long, R.R., 1953: Some aspects of the flow of stratified fluids. I. A theoretical investigation. *Tellus 5*, 42–58.
Lopes da Costa, J.C., *Castro, F.A.*, *Palma, J.M.L.M.*, and *Stuart, P.*, 2006: Computer simulation of atmospheric flows over real forests for wind energy resource evaluation. *J. Wind Eng. Ind. Aerod.* 94, 603–620.
Lu, J., *Arya, S.P.*, *Snyder, W.H.* and *Lawson Jr., R.E.*, 1997: A laboratory study of the urban heat island in a calm and stably stratified environment. Part I: Temperature field. *J. Appl. Meteorol. 36*, 1377–1391.
Lundquist, J.K. and *Chan, S.T.*, 2006: Consequences of urban stability conditions for computational fluid dynamics simulations of urban dispersion. *J. Appl. Meteorol. Clim. 46*, 1080–1097.
Lynch, P., 2006: The Emergence of Numerical Weather Prediction: Richardson's Dream. Cambridge University Press, Cambridge, ISBN: 0521857295.
Madala, R.V., 1981: Efficient time integration schemes for atmosphere and ocean models. In (Book, D.L. Ed.) Fine-difference techniques for vectorized fluid dynamics calculations. Springer-Verlag, New York, 56–74.
Manual of the ICAO Standard Atmosphere, 1993: Doc 7488-CD, Third Edition, ISBN: 92-9194-004-6.
Mellor, G.L. and *Yamada, T.*, 1974: A hierarchy of turbulence closure models for planetary boundary layers. *J. Atmos. Sci. 31*, 1791–1806.
Mellor, G.L. and *Yamada, T.*, 1982: Development of a turbulence closure model for geophysical fluid problems. *Rev. Geophys. 20*, 851–875.
Michioka, T. and *Chow, F.K.*, 2008: High-resolution large-eddy simulations of scalar transport in atmospheric boundary layer flow over complex terrain. *J. Appl. Meteorol. Climatol. 47*, 3150–3169.
Montavon C., 1998: Simulation of atmospheric flow over complex terrain for wind power potential assessment. Doctoral thesis, EPFL, Lausanne, doi: 10.5075/epfl-thesis-1855.
Nagy, A., 2010: Application of WRF model for the meso-g scale processes. MSc Thesis Eötvös Loránd University, Departmernt of Meteorology. (In Hungarian)
Nakanishi, M. and *Niino, H.*, 2009: Development of an Improved Turbulence Closure Model
for the Atmospheric Boundary Layer. *J. Meteorol. Soc. JPN* 87, 895–912.
National Research Council, 1983. Low-Altitude Wind Shear and Its Hazard to Aviation. Washington, DC: The National Academies Press, Washington, DC, 1. Print.
Noto, K., 1996: Dependence of heat-island phenomena on stable stratification and heat quantity in a calm environment. *Atmos. Environ. 30*, 475–485.
Palma, J.M.L.M., *Castro, F.A.*, *Ribeiro, L.F.*, *Rodrigues, A.H.*. and *Pintod, A.P.*, 2008: Linear and nonlinear models in wind resource assessment and wind turbine micro-siting in complex terrain. *J. Wind Eng. Ind. Aerod. 96*, 2308–2326.
Peltier, W.R. and *Clark, T.L.*, 1979: The evolution and stability of finite-amplitude mountain waves. Part II: Surface wave drag and severe downslope windstorms. *J. Atmos. Sci. 36*, 1498–1529.
Pleim, J.E., 2007: A combined local and nonlocal closure model for the atmospheric boundary layer. Part II: Application and evaluation in a mesoscale meteorological model. *J. Appl. Meteorol. Climatol. 46*, 1396–1409.
Pleim, J.E. and *Chang, J.S.*, 1992: A non-local closure model for vertical mixing in the convective boundary layer. *Atmos. Environ. 26A*, 965–981.
Pontiggia, M., *Derudi, M.*, *Busini, V.*, and *Rota, R.*, 2009: Hazardous gas dispersion: A CFD model accounting for atmospheric stability classes. *J. Hazard Mater. 171*, 739–747.
Qiu, X.-L. and Xia, K.-Q., 1998: Viscous boundary layers at the sidewall of a convection cell. *Phys. Rev. E 58*, 486–491.
Richard, E., *Mascart, P.* and *Nickerson, E.C.*, 1989: The role of surface friction in downslope wind storms. *J. Appl. Meteorol. 28*, 241–251.
Richards, P.J. and *Hoxey, R.P.*, 1993: Appropriate boundary conditions for computational wind engineering models using the k–ε turbulence model. *J. Wind Eng. Ind. Aerod. 46–47*, 145–153.

Saito, K., Ishida, J., Aranami, K., Hara, T., Segawa, T., Narita, M., and *Honda, Y.,* 2007: Nonhydrostatic atmospheric models and operational development at JMA. *J. Meteorol. Soc. JPN 85B*, 271–304.
Schumann, U., Hauf, T., Holler, H., Schmidt, H,. and *Volkert, H.,* 1987: A mesoscale model for the simulation of turbulence, clouds and flow over mountains: Formulation and validation examples. *Beitr. Phys. Atmos. 60*, 413–446.
Scorer, R.S., 1949: Theory of waves in the lee of mountains. *Q. J. Roy. Meteor. Soc.* 75, 41–56.
Shafran, P.C., Seaman, N.L., and *Gayno, G.A.,* 2000: Evaluation of numerical predictions of boundary layer structure during the Lake Michigan Ozone Study (LMOS). *J. Appl. Meteorol. 39* 412–426.
Shih, T.-H., Liou, W.W., Shabbir, A., Yang, Z., and *Zhu, J.,* 1995: A new k–ε eddy-viscosity model for high Reynolds number turbulent flows – model development and validation. *Comput. Fluids 24*, 227–238.
Simon, A., Horváth, Á., and *Vivoda, J.,* 2006: Case study and numerical simulations of the November 19, 2004 severe windstorm in central Europe. *Időjárás 110*, 91–123.
Skamarock, W.C., Klemp, J.B., Dudhia, J., Gill, D.O., Barker, D.M., Wang, W., and *Powers, J.G.,* 2005: A Description of the Advanced Research WRF Version 2. *NCAR/TN–468+STR NCAR Technical Note.*
Smith, R.B., 1979: The influence of mountains on the atmosphere. Adv Geophys, Academic Press 21, 87–230.
Smith, R.B., 2002: Stratified airflow over mountains. In (Grimshaw, R., Ed.) Environmental Stratified Flows, Kluwer Publishing, 119–159.
Smith, R.B., Skubis, S., Doyle, J.D., Broad, A.S., Kiemle, C. and *Volkert, H.,* 2002: Mountain waves over Mont Blanc: Influence of stagnant boundary layer. *J. Atmos. Sci. 59*, 2073–2092.
Stull, R.B., 1993: Review of non-local mixing in turbulent atmospheres: Transilient turbulence theory. *Bound.-Lay. Meteorol. 62*, 21–96.
Šušelj, K. and *Sood, A,* 2010: Improving the Mellor–Yamada–Janjic parameterization for wind conditions in the marine planetary boundary layer. *Bound.-Lay. Meteorol. 136*, 301–324
Thunis, P. and *Clappier, A.,* 2000: Formulation and evaluation of a Nonhydrostatic Mesoscale Vorticity Model (TVM). *Mon. Weather Rev. 128*, 3236–3251.
Townsend, A.A., 1980: The response of sheared turbulence to additional distortion. *J. Fluid. Mech. 98*, 171–191.
Troen, I. and *Mahrt, L.,* 1986: A simple model of the atmospheric boundary layer; sensitivity to surface evaporation. *Bound.-Lay. Meteorol. 37*, 129–148.
Vendel, F., Lamaison, G., Soulhac, L., Volta, P., Donnat, L., Duclaux, O., and *Puel, C.,* 2010: Modelling diabatic atmospheric boundary layer using a RANS CFD code with k-epsilon turbulence closure. *HARMO13 – 1–4 June 2010, Paris, France – 13th Conference on Harmonisation within Atmospheric Dispersion Modelling for Regulatory Purposes* H13-124, 652–656.
Voisin, B., 1994: Internal wave generation in uniformly stratified fluids. Part 2. Moving point sources. *J. Fluid. Mech. 261*, 333–374.
Weigel, A.P., Chow, F.K., and *Rotach, M.W.,* 2007: On the nature of turbulent kinetic energy in a steep and narrow Alpine valley. *Bound.-Lay. Meteorol. 123*, 177–199.
Wicker, L.J. and *Skamarock, W.C.,* 2002: Time splitting methods for elastic models using forward time schemes. *Mon. Weather Rev. 130*, 2088–2097.
Wilhelmson, R. and *Klemp, J.B.,* 1978: A numerical study of storm splitting that leads to long-lived storms. *J. Atmos. Sci. 35*, 1974–1986.
Williams, M.D., Brown, M.J., Singh, B., and *Boswell, D.,* 2004: QUIC-Plume Theory Guide. LANL Report: LA-UR-04-0561.
Wyngaard, J.C., Cote, O.R., and *Rao, K.S.,* 1974: Modeling of the atmospheric boundary layer. *Adv. Geophys. 18(A)*, 193–212.
Wyngaard, J.C. and *Brost, R.A.,* 1984: Top-down and bottom-up diffusion of a scalar in the convective boundary layer. *J. Atmos. Sci. 41*, 102–112.
Wurtele, M.G., Sharman, R.D., and *Datta, A.,* 1996: Atmospheric lee waves. *Annu. Rev. Fluid. Mech. 28*, 429–476.

Xue, M., Zong, J., and *Drogemeier, K.K.,* 1996: Parameterization of PBL turbulence in a multi-scale nonhydrostatic model. Preprints, 11th Conf. on Numerical Weather Prediction, Norfolk, VA, Amer Meteor Soc, P2.5.

Xue, M., Droegemeier, K.K., and *Wong, V.,* 2000: The Advanced Regional Prediction System (ARPS). A multi-scale nonhydrostatic atmospheric simulation and prediction model. Part I: Model dynamics and verification. *Meteorol. Atmos. Phys. 75*, 161–193.

Yang, X., 1993: A nonhydrostatic model for simulation of airflow over mesoscale bell-shaped ridges. *Bound.-Lay. Meteorol.* 65, 401–424.

Zhang, D.-L. and *Anthes, R.A.,* 1982: A high-resolution model of the planetary boundary layer-sensitivity tests and comparisons with SESAME-79 data. *J. Appl. Meteorol.* 21, 1594–1609.

Zhong, S., In, H., and *Clements, C.,* 2007: Impact of turbulence, land surface, and radiation parameterizations on simulated boundary layer properties in a coastal environment. *J. Geophys. Res. 112*, D13110, doi:10.1029/2006JD008274.

Zilitinkevich, S.S., 1995: Non-local turbulent transport: pollution dispersion aspects of coherent structure of convective flows. In (Power, H., Moussiopoulos, N., and Brebbia, C.A., Eds.) Air Pollution III—Volume I. Air Pollution Theory and Simulation, Computational Mechanics Publications, Southampton Boston, 53–60.

IDŐJÁRÁS
Quarterly Journal of the Hungarian Meteorological Service
Vol. 117, No. 31, July–September 2013, pp. 277–294

Performance of the Asymmetric Convective Model Version 2, in the Unified EMEP Model

Zorica Podrascanin[1]* and **Dragutin T. Mihailovic**[2]

[1]*Faculty of Sciences, Department of Physics, University of Novi Sad, Dositej Obradovic Sq. 4, 21000 Novi Sad, Serbia*

[2]*Faculty of Agriculture, Department of Field and Vegetable Crops, University of Novi Sad, Dositej Obradovic Sq. 8, 21000 Novi Sad, Serbia, guto@polj.uns.ac.rs*

**Corresponding author E-mail: zorica.podrascanin@gmail.com*

(Manuscript received in final form March 6, 2013)

Abstract–We have investigated the performance of the Asymmetric Convective Model Version 2 (ACM2), a planetary boundary layer (PBL) vertical turbulent mixing scheme, that is a combination of local and non-local closures, in a complex system such as a chemical transport model, the Unified EMEP (European Monitoring and Evaluation Program) Model. For this purpose, we modified the local part of the ACM2 scheme to take into account the level of turbulent kinetic energy, and then incorporated this scheme in the Unified EMEP model. After incorporation, the scheme was validated under all stability conditions and for several compounds. Comparisons were made against the K-scheme currently used in the Unified EMEP model, and surface nitrogen dioxide (NO_2), sulfur dioxide (SO_2), and sulphate (SO_4^{2-}) concentrations were observed at different EMEP stations during the year 2005. In most cases, the model better simulated the NO_2, SO_2, and SO_4^{2-} concentrations when the ACM2 scheme was used, especially for NO_2 during the summer months, when the non-local mixing is presumably dominant.

Key-words: non-local convective mixing, local scheme, turbulent kinetic energy, chemical modeling, vertical turbulent mixing

1. Introduction

The Unified EMEP model (*Simpson et al.,* 2003) was developed as a part of the European Monitoring and Evaluation Programme (EMEP) under the Convention on Long-Range Transboundary Air Pollution (LRTAP). This and previous versions of this model have been used over the last 30 years to simulate the transboundary transport of air pollution on the European scale. The surface concentrations of pollutants are strongly related to the turbulent vertical mixing, and thus, a good representation of vertical mixing in the planetary boundary layer (PBL) is very important for every chemical transport model, including the Unified EMEP model. During the past 30–50 years, various turbulent vertical mixing schemes for use in the PBL were developed and tested in 1D and 3D simulations in both meteorological and air quality models. All of the suggested vertical mixing schemes can be categorized as diffusion schemes, K-schemes (e.g., *O'Brien*, 1970; *Deardorff*, 1972; *Louis,* 1979; *Holtslag* and *Moeng*, 1991; *Holtslag* and *Boville*, 1993; *Alapaty* and *Alapaty*, 2001), second and higher-order closure models (e.g., *Mellor* and *Yamada*, 1974; *Janjic*, 1990, 1994, etc.), non-local schemes (e.g., *Blackadar*, 1976; *Stull,* 1984; *Pleim* and *Chang*, 1992; *Hong* and *Pan*, 1996), and combinations of local (diffusion) and non-local schemes (e.g., *Pleim*, 2007a). Most of these schemes have been intensively tested and compared with each other and against measurements in many studies (e.g., *Zhang* and *Zheng*, 2004; *Berg* and *Zhong*, 2005; *Hu et al.*, 2010). The most important conclusions from those studies are as follows: 1) the model is sensitive to the turbulent vertical mixing scheme in the PBL; 2) the non-local aspect of these schemes is important for realistically representing the convective boundary layer (CBL); and 3) the realistic apportionment of fluxes between local and non-local components is critical for satisfactorily representing the mixing in a CBL.

The Unified EMEP model is an off-line chemical transport model, which means that the model is driven with outputs from meteorological weather prediction models without feedback between chemical and meteorological models. The advantage of this approach is the possibility of independent parameterizations, a more flexible grid construction, and that it is easier to use for the inverse modeling, among others (*Baklanov* and *Korsholm,* 2007). The Unified EMEP model uses K-schemes for parameterizing the vertical mixing: the O'Brien (*O'Brien*, 1970) scheme is used in the CBL, and the Blackadar scheme (*Blackadar*, 1979) is used in the stable boundary layer (SBL). During the past several years, some other vertical mixing schemes have been proposed for use in this model. *Mihailovic* and *Alapaty* (2007) proposed a closure based on turbulent kinetic energy (TKE) as an improvement of the vertical diffusion scheme by *Alapaty* (2003). They examined the performance of the scheme comparing simulated and measured NO_2 gas concentrations for the years 1999, 2001, and 2002. In 2008, the non-local convective mixing scheme with varying upward mixing rates (VUR) was proposed for use in the Unified EMEP model (*Mihailovic et al.*, 2008) and was later combined with TKE vertical diffusion scheme (*Mihailovic et al.*, 2009). This combination of the two previous schemes uses the VUR scheme for convective conditions and the TKE scheme for stable conditions. The disadvantage of this approach is an abrupt change from one scheme to another in the transition from convective to stable conditions. Additionally, in the VUR schemes, bottom-up fluxes originated in the first layer are distributed to the layers above; this is not realistic, because there is clearly an additional mixing between adjacent layers. The scheme that avoids the aforementioned drawback of the previous schemes used in the EMEP model has a realistic apportionment of fluxes between the local and non-local components as a result of combined local and non-local closures; this scheme is called the Asymmetric Convective Model Version 2 (ACM2) (*Pleim*, 2007a). The ACM2 scheme is built on the original Asymmetric Convective Model (ACM) (*Pleim* and *Chang*, 1992), a non-local convective mixing scheme, by adding an eddy diffusion component. The main advantage of this scheme in comparison to the ACM scheme (which is applicable only in convective conditions) is its applicability for all stability conditions. Mixing between a non-local and local diffusion scheme, in the case of convection, is governed by a pre-specified weighting factor that depends on the PBL height and Monin-Obukhov length. In stable conditions, stratification mixing is reduced to local diffusion. The ACM2 scheme has been tested in its 1D form against large-eddy simulations (LES) (*Pleim*, 2007a) and has been implemented in the meteorological model (fifth-generation Pennsylvania State University–NCAR Mesoscale Model (MM5)) (*Pleim*, 2007b). The profiles obtained with the ACM2 scheme in the 1D test have shapes that are more similar to the shapes of the LES profiles than those obtained with the ACM scheme. The MM5 model with the ACM2 scheme is evaluated with surface meteorological measurements, rawinsonde profile measurements, and the observed PBL height. The MM5 model with ACM2 performed as well or better than similar MM5 model studies.

We have incorporated the ACM2 scheme into the Unified EMEP model because of its previously mentioned properties to test its ability to work in a complex system that depends on a large number of processes: horizontal advection, emissions, vertical mixing, chemical reactions, dry and wet deposition, among others. For this purpose, we modified the local part of ACM2 to account for the level of turbulent kinetic energy and then incorporated it in the Unified EMEP model. The goal of this study was to demonstrate the possibility of applying the ACM2 scheme in the Unified EMEP model on the most important air pollutants from an environmental standpoint: NO_2, SO_2, and SO_4^{2-} (*Jericevic et al.*, 2010). The validation has been performed for all stability conditions, and the modeled surface nitrogen dioxide (NO_2), sulfur dioxide (SO_2), and sulphate (SO_4^{2-}) concentrations were compared with observations at different EMEP measurement stations during the year 2005. Descriptions of the standard Unified EMEP schemes and the ACM2 scheme are given in Section 2. The comparison results between the currently used scheme in the Unified EMEP model, the ACM2 scheme, and the measured concentrations are given in Section 3, while Section 4 summarizes the study and presents the concluding remarks.

2. *Materials and methods*

2.1. *Formulation of the vertical diffusion currently used in the Unified EMEP chemical model*

The vertical sub-grid transport is modeled using the K-scheme in the Unified EMEP chemical model as well as in many other chemical transport models. K is determined in the unstable conditions as

$$K(z)=\begin{cases} K(h)+\left(\dfrac{h-z}{h-h_s}\right)^2\Big\{\big[K(h_s)-K(h)\big]+ \\ \qquad (z-h_s)\left[\dfrac{\delta}{\delta_s}K(h_s)+2\dfrac{K(h_s)-K(h)}{h-h_s}\right]\Big\}, & h_s\le z<h \\ \dfrac{u_* kz}{\phi\left(\dfrac{z}{L}\right)}, & z<h_s \end{cases} \tag{1}$$

where z is the model layer height, h is the PBL height, h_s is the surface boundary layer height, u_* is friction velocity, ϕ is the atmospheric stability function for temperature, and k is the von Karman constant. In the model calculation, h_s is equal to 4% of the PBL height (*O'Brien*, 1970). The atmospheric stability function for temperature in convective conditions is

$$\phi=\left(1-16\frac{z}{L}\right) \tag{2}$$

and for stable conditions is

$$\phi=1+5\frac{z}{L}. \tag{3}$$

Accordingly, K is calculated in stable conditions and above the PBL (*Blackadar*, 1979) as

$$K(z)=\begin{cases}0.001 & R_i > R_{ic} \\ 1.1(R_{ic}-R_i)l^2\left|\Delta V_H/\Delta z\right| R_{ic} & R_i \le R_{ic}\end{cases}, \tag{4}$$

where l is the turbulent mixing length, ΔV_H represents the difference in wind-speed between two grid-cell centers separated by distance Δz, R_i is the Richardson number and R_{ic} is the critical Richardson number. The turbulent mixing length is parameterized according to:

$$\begin{aligned} l &= kz, \quad z \le z_m \\ l &= kz_m, \quad z > z_m \end{aligned} \tag{5}$$

where k is the von Karman constant, z is the height above the ground, and $z_m = 200$ m. Hereafter, the currently used scheme in the Unified EMEP model will be called the OLD scheme.

2.2. *Formulation of the ACM2 scheme for use in the Unified EMEP model*

According to the ACM2 scheme, the quantity φ in the model layer i is calculated as

$$\frac{\partial \varphi_i}{\partial t} = Mu'\varphi_1 - Md'_i\varphi_i + Md'_{i+1}\varphi_{i+1}\frac{\Delta z_{i+1}}{\Delta z_i} + \frac{1}{\Delta z_i}\left[\frac{K'_{i+1/2}\left(\varphi_{i+1}-\varphi_i\right)}{\Delta z_{i+1/2}} - \frac{K'_{i-1/2}\left(\varphi_i-\varphi_{i-1}\right)}{\Delta z_{i-1/2}}\right], \tag{6}$$

where Mu' and K' are the upward convective mixing rate and a diffusion coefficient, respectively, weighted by the factor f_{conv}, and Δz_i is the thickness of layer i. This factor f_{conv} controls the degree of local versus non-local behavior. The scheme reverts to either the non-local or local scheme for $f_{conv}=1$ or $f_{conv}=0$, respectively. The f_{conv} is estimated as

$$f_{conv} = \left[1 + \frac{k^{-2/3}}{0.1a}\left(-\frac{h}{L}\right)^{-1/3}\right]^{-1}, \tag{7}$$

where k is the von Karman constant, h is the PBL height, L is the Monin-Obukhov length, and a is set to 7.2. The Mu', Md' and K' were calculated as

$$Mu' = \frac{f_{conv}K(z_{1+1/2})}{\Delta z_{1+1/2}\left(h - z_{1+1/2}\right)}, \tag{8}$$

$$Md_i' = \frac{Mu'(h - z_{i-1/2})}{\Delta z_i} \tag{9}$$

and

$$K'(z) = K(z)(1 - f_{conv}), \tag{10}$$

where z is the height of the model layer and h is the PBL height. The diffusion coefficient K is calculated as in *Mihailovic* and *Alapaty* (2007). This method was chosen because it takes into account the level of TKE, which is a decisive parameter in the vertical mixing within the PBL. In the PBL, K is calculated as

$$K(z) = \frac{\overline{e}_* kz \left(1 - \frac{z}{h}\right)^2}{\phi}, \tag{11}$$

where $\overline{e}_*$ is the mean turbulent velocity scale within the PBL, k is the von Karman constant, z is the vertical coordinate, h is the PBL height, and ϕ is the atmospheric stability function for temperature (Eqs. (2-3)). The mean turbulent velocity scale within the PBL is calculated as

$$\overline{e_*} = \frac{1}{h} \int_0^h \sqrt{e(z)} \Psi(z) dz, \tag{12}$$

where Ψ is the vertical profile function (see *Mihailovic* and *Alapaty* (2007) for details about this function) and e is TKE.

The TKE vertical profile, $e(z)$, for near neutral to free convection conditions (*Zhang et al.*, 1996) is expressed as

$$e(z) = \frac{1}{2} \left(\frac{L_E}{h}\right)^{\frac{2}{3}} \left(0.4 w_*^3 + u_*^3 (h - z) \frac{\phi}{kz}\right)^{\frac{2}{3}}, \tag{13}$$

where h is the PBL height, $L_E = 2.6h$, w_* is the convective velocity scale, u_* is the friction velocity scale, k is the von Karman constant, and ϕ is a non-dimensional function of heat. For the stable atmospheric boundary layer, we modeled the TKE profile using an empirical function (*Lenschow et al.*, 1988) based on aircraft observations:

$$e(z) = 6u_* \left(1 - \frac{z}{h}\right)^{1.75}, \tag{14}$$

where h is the PBL height, z is the height of the model layer, and u_* is the friction velocity scale. Above the PBL, the diffusion coefficient K is calculated using Eq. (4).

2.3. Short description and model setups

The EMEP chemical model is designed to describe the transboundary acidification, eutrophication, and ground level ozone in Europe and has influenced European air quality policies since the late 1970s. Since the 1990s, this model has provided the reference inputs for the integrated assessment modeling atmospheric dispersion calculations. The Unified EMEP chemical model was developed at the Norwegian Meteorological Institute. In this work, tests were performed using the rv3.0 version of this model (*Simpson et al.*, 2003). The model advection is designed using a scheme by *Bott* (1989a, 1989b); the diffusion scheme, which is described in Section 2.1, is used for the turbulent vertical mixing. The Unified EMEP chemical model emissions inputs are provided for 10 anthropogenic source sectors and consist of gridded annual national emissions of sulfur dioxide (SO2), nitrogen oxides (NOx= NO + NO2), ammonia (NH3), non-ethane volatile organic compounds (NMVOC), carbon monoxide (CO), and particulates (PM2.5, PM10). The meteorological fields used in the model are provided every 3 hours from PARLAM-PS, which is a dedicated version of the HIRLAM (High Resolution Limited Area Model) Numerical Weather Prediction (NWP) model with parallel architecture (*Bjorge* and *Skalin*, 1995; *Berge* and *Jakobsen*, 1998; *Lenschow* and *Tsyro*, 2000). The linearly interpolated 3-hour meteorological fields, wind components, temperature and humidity, cloudiness, precipitation, and momentum and energy fluxes between the surface and atmosphere are then used to calculate the velocity scales, PBL height, and Monin-Obukhov length in every model time step. Note that we calculate new mixing levels using meteorological parameters from the meteorological model that has its own mixing. The parameters imported from PARLAM-PC are the friction velocity and energy fluxes. These parameters come from the Monin-Obukhov theory, that has been widely accepted as the best theory for the surface layer with the implicit assumption that the rest of the PBL mixing should be improved. The Unified EMEP model uses a polar-stereographic projection, true at 60° N, with a grid size of $50 \times 50\ km^2$ and a vertical σ coordinate with 20 levels. The horizontal grid of the model is the Arakawa C grid. All other model details can be found in *Simpson et al.* (2003). The domain with (131, 100) points is used in the simulations with a 1200 s time step and with the 3-hour resolution meteorological data from the PARLAM-PS model.

2.4. EMEP measurement network

The EMEP measurement network was one of the first international environmental measurement networks established in Europe. The data sets from that network are well documented, quality controlled, and suitable for comparing with model results. All details on measurement techniques, location of stations, and data sets can be found at http://www.nilu.no/projects/ccc/emepdata.html. The observed values from the EMEP measurement network have already been used in many papers for testing various mixing schemes as well as for other chemical transport studies (*Topçu et al.*, 2002; *Mihailovic* and *Alapaty*, 2007; *Mihailovic et al.*, 2009; *Calvo et al.*, 2010). In this study, we analyze the influence of the ACM2 scheme for vertical mixing in the PBL on the quality of the model's performance. For comparison, we have chosen the year 2005 and compared our results against surface concentration measurements of NO_2 ($\mu g\, N\, m^{-3}$), SO_2 ($\mu g\, S\, m^{-3}$), and SO_4^{2-} ($\mu g\, S\, m^{-3}$) from the EMEP stations because of their good spatial and temporal resolutions. Furthermore, these three compounds were chosen because they are important acidifying and atrophying pollutants and play a significant role in air pollution in Europe. Nitrogen contributes to the formation of photochemical smog, which can have significant impacts on human health. Sulphate, an oxidant of SO_2, is a secondary pollutant that contributes to acid rain formation. Mixing in the lower part of the PBL will influence mostly those tracers that have sources on the ground. This is not the case with ozone, the daytime concentration of which is primarily controlled by photochemistry and transport rather than the vertical mixing; therefore, the interpretation of the influence of vertical mixing on ozone concentrations is much more difficult (*Pleim*, 1992). Note that the Unified EMEP chemical model outputs cannot be always compared with observations in this network because of the coarse horizontal model resolution, which is especially pronounced at high altitudes. Additionally, a problem is encountered with the shipping emission path, because the high concentrations are horizontally diffused over a large area. The differences between the observed and modeled concentrations might be due to other reasons, such as stations can be affected by local sources, emissions, meteorology, and chemistry, among others. Some mountain stations (e.g., SK002R, DE003R, PL003R, and DE008) and some stations in the North Sea shipping area (e.g., DK005R, DE008R, and EE011R) with the highest discrepancies were excluded from the comparison (*Jericevic et al.*, 2010).

3. *The results and discussion*

The Unified EMEP model Version rv3.0 was first run with the OLD scheme with the setup described in Section 2.3. Whenever a new scheme is introduced into a model, the first step in the analysis usually concerns the differences between the new and the old vertical mixing schemes, especially for the chemical species that originate in the ground. At this moment, the full importance of comparing with the OLD scheme becomes evident. If just one aspect of the model is changed and the result improves, then it is very likely that the introduced change was the reason for the improvement. Clearly, this may not be always true in a complex meteorological-chemistry model. Then, if there is some sensitivity to introducing a new scheme, the model results are compared with the measurements if they are available. Eventually, better results with the new scheme suggest that it should be used in the Unified EMEP model. In our analysis, we will concentrate on the monthly averaged value of concentrations for the four aforementioned compounds. However, to be absolutely sure that a scheme is stable and that the monthly averaged value of concentrations is not a consequence of very low or very high peaks in daily concentrations, it is necessary to evaluate the daily concentrations in this scheme.

In addition to monthly averages, we will also present some diurnal variations as well as annual averages. For that purpose, we will use a few stations from the EMEP measurement network that are at different locations and altitudes. Station AT0002R is a measurement site located in Illmitz, Austria, at 47° 46'N, 16° 46'E and at an altitude of 117 m above sea level; station DE0001R is a measurement site located in Westerland, Germany, at 54° 56'N, 08° 19'E and at an altitude of 10 m above sea level; the station CZ0001R is a measurement site located in Svratouch, Czech Republic, at 49° 44'N, 16° 02'E and at an altitude of 737 m above sea level; station FR0012R is a measurement site located in Iraty, France, at 43° 02'N, 01° 05'W and at an altitude of 1300 m above sea level; and station DE0007R is a measurement site located in Neuglobsow, Germany, at 53° 09'N, 13° 02'E and at an altitude of 62 m above sea level. The annual time series of daily NO_2 and SO_2 concentrations at the stations AT0002R, DE0001R, and CZ0001R are depicted in *Fig. 1* and *2*, respectively, while the daily SO_4^{2-} concentrations at the stations FR0012R, DE0007R, and CZ0001R are shown in *Fig. 3*. The surface concentrations of NO_2 obtained by the ACM2 scheme at all stations are higher than those obtained with the OLD scheme. The differences between the concentrations of SO_2 and SO_4^{2-} obtained with the ACM2 and OLD schemes are not as pronounced as with the NO_2 concentrations. The root mean square error (RMSE) and mean annual concentration (MAC) for the above-mentioned stations are shown in *Tables 1-3* for the concentrations of NO_2, SO_2, and SO_4^{2-}, respectively. The RMSE values for the NO_2 concentrations are lower when the ACM2 scheme was used at the stations AT0002R and CZ0001R and higher for station DE0001R. The mean annual concentrations of NO_2 obtained by the ACM2 scheme at all stations are closer to the measured mean annual concentrations. The RMSE and MAC values obtained with the OLD and ACM2 schemes are very similar for the concentrations of SO_2 and SO_4^{2-}. The scatter plot diagrams with coefficient of determination (R^2) between measured and modeled concentrations with the OLD and ACM2 schemes for NO_2, SO_2, and SO_4^{2-} at mentioned stations are showed in *Fig. 4*. The R^2 between daily measured and modeled data is slightly higher when the ACM2 scheme is used than the OLD scheme for the concentrations of NO_2 and SO_2 and opposite for the concentration of SO_4^{2-}.

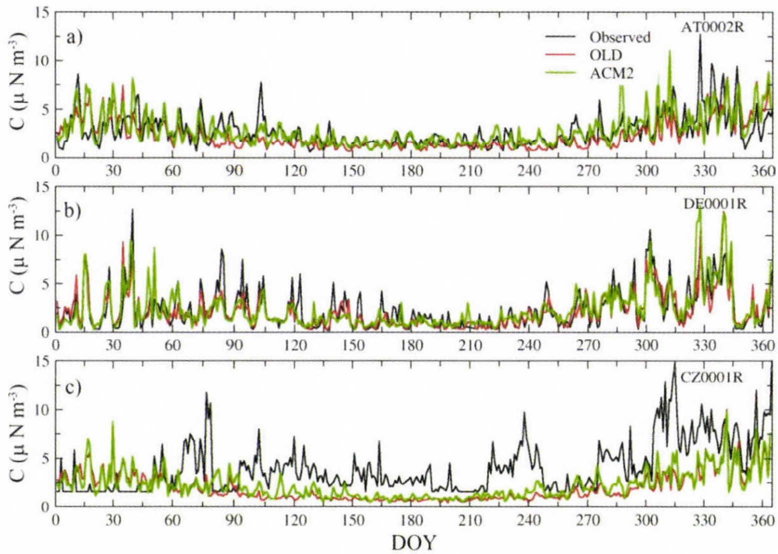

Fig. 1. Time series of the measured and modeled daily surface NO2 concentrations for a) AT0002R, b) DE0001R, and c) CZ0001R in the year 2005. Modeled results are obtained with two vertical diffusion schemes: OLD and ACM2. The time is shown on the x-axis as the day of the year (DOY).

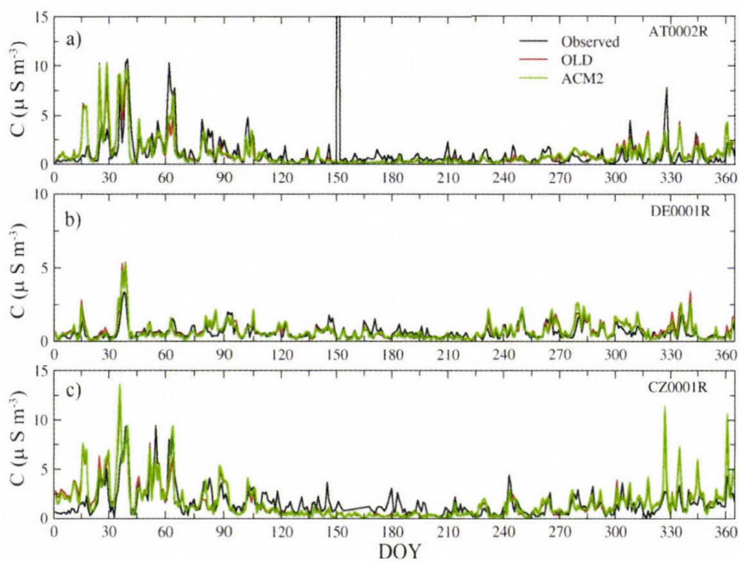

Fig. 2. Time series of the measured and modeled daily surface SO2 concentrations for a) AT0002R, b) DE0001R, and c) CZ0001R in the year 2005. The modeled results are obtained with two vertical diffusion schemes: OLD and ACM2. The time is shown on the x-axis as the day of the year (DOY).

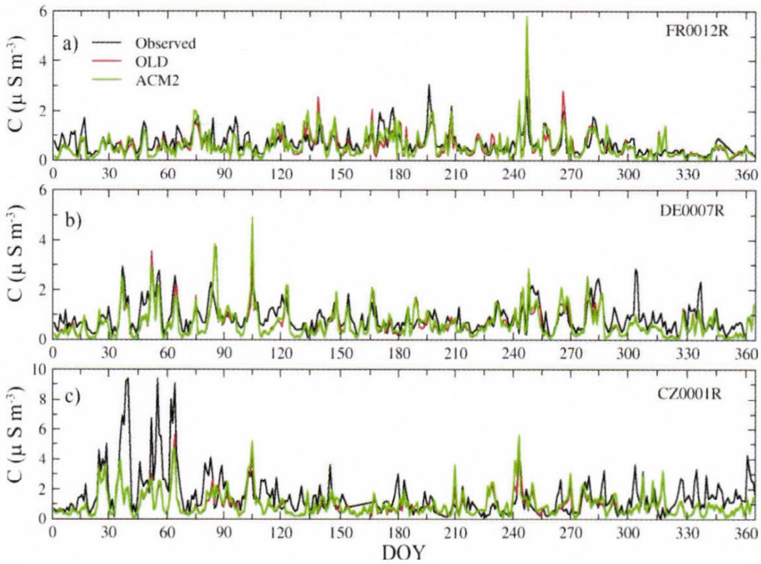

Fig. 3. Time series of the measured and modeled daily surface SO_4^{2-} concentrations for a) FR0012R, b) DE0007R, and c) CZ0001R in the year 2005. Modeled results are obtained with two different vertical diffusion schemes: OLD and ACM2. The time is shown on the x-axis as the day of the year (DOY).

Table 1. RMSE and mean annual concentration of NO_2

Station	**RMSE (OLD)**	**RMSE (ACM2)**	**MAC(OLD) (μg N m^{-3})**	**MAC(ACM2) (μg N m^{-3})**	**MAC (observed) (μg N m^{-3})**
AT0002R	1.66	1.59	2.26	2.82	2.69
DE0001R	1.30	1.52	2.16	2.33	2.33
CZ0001R	3.21	2.96	1.91	2.23	4.00

Table 2. RMSE and mean annual concentration of SO_2

Station	**RMSE (OLD)**	**RMSE (ACM2)**	**MAC(OLD) (μg S m^{-3})**	**MAC(ACM2) (μg S m^{-3})**	**MAC(observed) (μg S m^{-3})**
AT0002R	3.45	3.45	1.05	1.09	1.25
DE0001R	0.45	0.44	0.70	0.67	0.59
CZ0001R	1.43	1.47	1.56	1.67	1.72

Table 3. RMSE and mean annual concentration of SO_4^{2-}

Station	RMSE (OLD)	RMSE (ACM2)	MAC(OLD) ($\mu g\ S\ m^{-3}$)	MAC(ACM2) ($\mu g\ S\ m^{-3}$)	MAC (observed) ($\mu g\ S\ m^{-3}$)
FR0012R	0.43	0.43	0.56	0.58	0.70
DE0007R	0.49	0.52	0.62	0.63	0.88
CZ0001R	1.37	1.39	0.92	1.00	1.56

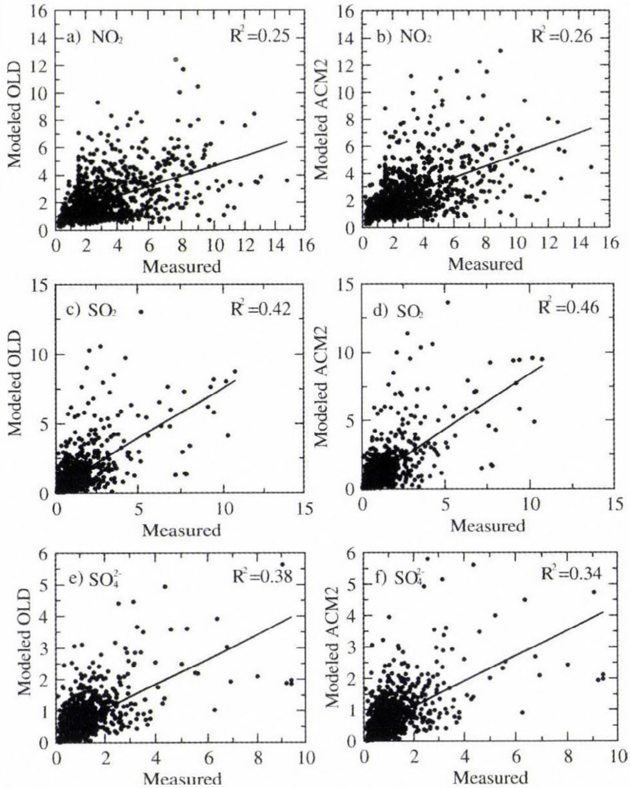

Fig. 4. Scatter plot diagrams of modeled against measured daily concentrations with corresponding coefficients of determination. Panels are: concentration of NO2 modeled by a) OLD and b) ACM2; concentration of SO2 modeled by c) OLD and d) ACM2, and concentration of SO_4^{2-} modeled by e) OLD and f) ACM2.

After the analysis of the daily concentrations showed that there are no peaks in this concentration, we compared the average monthly concentrations at the stations from the EMEP network, except those mentioned in Section 2.4 with the model results obtained using the OLD and ACM2 schemes. The scatter plot diagrams with R^2 between monthly concentrations of NO_2, SO_2, and SO_4^{2-} calculated using the OLD and ACM2 scheme and corresponding measured concentrations are depicted in *Fig. 5*. The R^2 between monthly measured and modeled data using the OLD and ACM2 scheme are very similar for all compounds. To compare the results, we calculated the following statistical quantities: (i) RMSE, (ii) BIAS, and (iii) standard deviations of the simulations (SDS) and observations (SDO). These quantities are given by the following equations:

$$\mathrm{RMSE} = [\sum_{i=1}^{N_s} (M_i - O_i)^2 / N_s]^{1/2}, \tag{15}$$

$$\mathrm{BIAS} = \left(\frac{\overline{M} - \overline{O}}{\overline{O}} \right) \cdot 100\%, \tag{16}$$

$$\mathrm{SDS} = [\sum_{i=1}^{N_s} (M_i - \overline{M})^2 / N_s]^{1/2}, \tag{17}$$

$$\mathrm{SDO} = [\sum_{i=1}^{N_s} (O_i - \overline{O})^2 / N_s]^{1/2}, \tag{18}$$

where M_i and O_i denote the modeled and observed average monthly concentrations, respectively, and N_s is the number of stations, while an over bar indicates an average monthly concentration for all stations.

Biases for the measured and modeled average monthly NO_2, SO_2, and SO_4^{2-} concentrations for both schemes are shown in *Fig. 6*. In the upper panel of this figure, the BIAS of the ACM2 scheme is observed to be lower than that of the OLD scheme. Both schemes underestimate the observations during the warmer months, but the ACM2 scheme overestimates the observed NO_2 concentration in the colder months. Inspecting the BIAS for SO_2 (middle panels of the same figure) does not show larger differences in the BIAS for the OLD and ACM2 schemes. Both schemes underestimate the SO_2 observations during the warmer months and overestimate them during the colder months. The BIAS of the ACM2 scheme for SO_4^{2-} (lower panels of the same figure) is lower than for the OLD schemes. Both schemes underestimate the SO_4^{2-} observations except for September, when the ACM2 scheme overestimates the observations. The higher BIAS obtained for SO_4^{2-} may be due to many complicated processes, including microphysics and aqueous phase reactions, connected with this particular compound. Our understanding of *Fig. 6* is as follows: in the colder part of the year, the atmosphere is basically stable; therefore, the diffusive part of the ACM2 scheme has a greater contribution to its performance. In contrast to the colder months, the warmer months are more influenced by the non-local part of the ACM2 scheme. The smaller BIAS between the modeled and observed concentrations for the ACM2 scheme indicates that the average estimated concentrations are closer to the average observed concentrations.

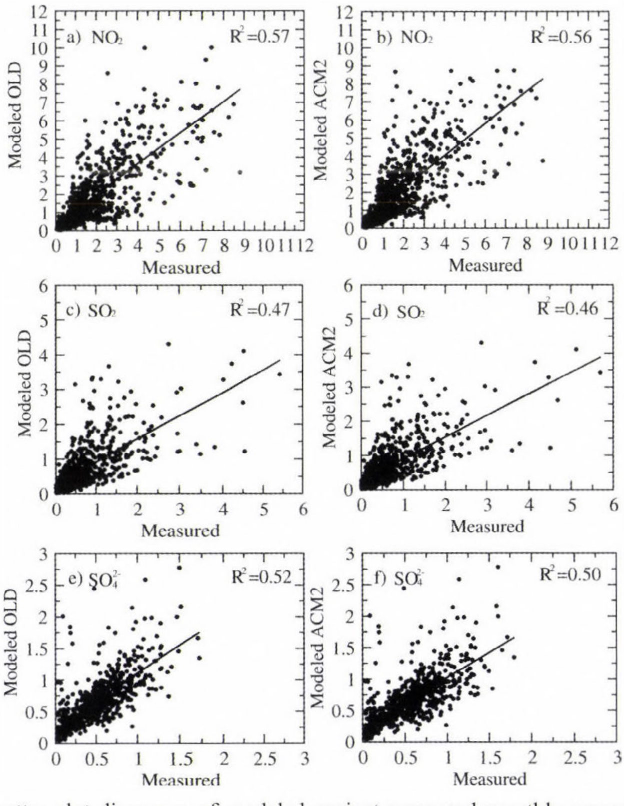

Fig. 5. Scatter plot diagrams of modeled against measured monthly concentrations with corresponding coefficients of determination. Panels are: concentration of NO2 modeled by a) OLD and b) ACM2; concentration of SO2 modeled by c) OLD and d) ACM2, and concentration of SO_4^{2-} modeled by e) OLD and f) ACM2.

The RMSE is a good measure in this type of comparison, and *Fig. 7* shows the RMSE for the measured and modeled average monthly NO_2, SO_2, and SO_4^{2-} concentrations for both schemes. In the upper panel of this figure, the RMSE of the ACM2 scheme is shown to be slightly lower than that for the OLD scheme, except January and December. A further inspection of the RMSE for SO_2 and SO_4^{2-} (middle and lower panels of the same figure) shows that the non-local scheme and the OLD scheme show similar behavior, i.e., SO_2 and SO_4^{2-} are very similar.

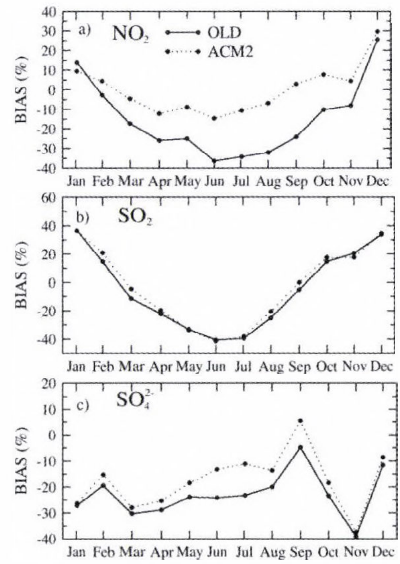

Fig. 6. Average monthly BIAS (%) for the observed and modeled (a) NO_2, (b) SO_2 and (c) SO_4^{2-} concentrations for the ACM2 and OLD schemes used in the Unified EMEP chemical model for 2005.

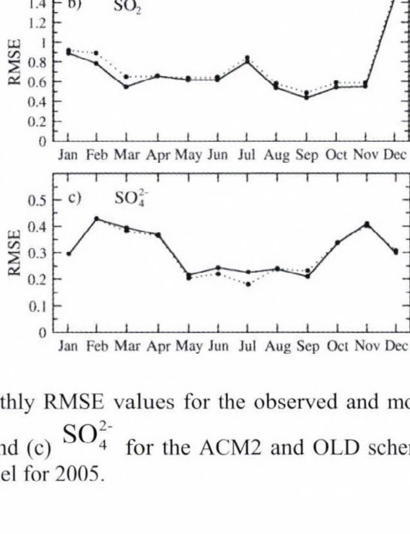

Fig. 7. Average monthly RMSE values for the observed and modeled concentrations of (a) NO2, (b) SO2, and (c) SO_4^{2-} for the ACM2 and OLD schemes used in the Unified EMEP chemical model for 2005.

The final statistics compared are the standard deviations of the observed and modeled concentrations. The standard deviations of the average monthly observed and modeled concentrations (SDS and SDO), given by Eqs. (17)–(18), are depicted in *Fig. 8*. The scheme is considered to give better results if its SDS is closer to its SDO. It can be concluded from this figure that (i) the SDS for both schemes are higher for colder months except for SO_4^{2-}, and that (ii) the SDS for the ACM2 scheme is much closer to the SO_4^{2-} SDO. For both schemes, the SDS values are similar for some months, indicating that they have the same yearly pattern.

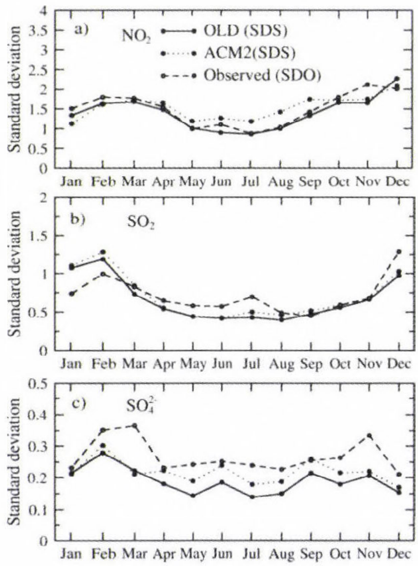

Fig. 8. Average monthly SDO and SDS values of (a) NO_2, (b) SO_2, and (c) SO_4^{2-} for the ACM2 and OLD schemes used in the Unified EMEP chemical model for 2005.

4. Conclusions

The ACM2 scheme was incorporated into a Unified EMEP model. Comparisons between the already present scheme and the new one were made, and sensitivity was demonstrated. Furthermore, the outputs of NO_2, SO_2, and SO_4^{2-} surface concentrations for both schemes were compared with the measured values. In most cases, it was shown that the Unified EMEP chemical model slightly better simulates the concentrations of NO_2, SO_2, and SO_4^{2-} when the ACM2 scheme is used. The sensitivity of the NO_2 concentrations to the choice of vertical scheme is much higher than for the other analyzed compounds. The lifetime of NO_2 in troposphere is short and has a seasonal variability. It is the shortest during the summer months. Additionally, during the summer months the mixing driven by bouncy is fast. Those are the reasons why the sensitivity of the NO_2 concentrations to the choice of vertical scheme is much higher than for the other analyzed compounds, and it is particularly emphasized for their concentrations during the summer months. Let us note that the lifetime of both compounds, SO_2 and SO_4^{2-} is longer than that of NO_2, so it is more influenced by the horizontal advection than by vertical mixing. Overall, the agreement with the measured values is reasonably good, such that the ACM2 scheme could be used in the Unified EMEP model. Furthermore, as the ACM2 scheme possesses a higher level of sophistication, it is expected that its influence will be higher with the increased horizontal resolution of the Unified EMEP model.

Acknowledgements–This paper was realized as a part of the project "Studying climate change and its influence on the environment: impacts, adaptation and mitigation" (No. III43007), which is financed by the Ministry of Education and Science of the Republic of Serbia within the framework of integrated and interdisciplinary research over the period 2011-2014. The authors would like to thank the Norwegian Meteorological Institute for giving us the meteorology inputs for the Unified EMEP chemical model for 2005.

References

Alapaty, K., 2003: Development of two CBL schemes using the turbulence velocity scale. Proceedings of 4thWRF Users' workshop, Boulder (http://www.wrf-model.org/wrfadmin/presentations.php).

Alapaty, K. and *Alapaty, M.*, 2001: Evaluation of a nonlocal-closure K-scheme using the MM5. Workshop Program for the Eleventh PSU/NCAR MM5 Users' Workshop, Foothills Laboratory, NCAR (http://www.mmm.ucar.edu/mm5/workshop/).

Baklanov, A. and *Korsholm, U.*, 2007: On-line integrated meteorological and chemical transport modeling: Advantages and Prospectives. In (Eds.: *Borrego, C.* and *Miranda, A.I.*) Proceedings of the 29th NATO/CCMS International Technical Meeting on Air pollution Modelling and its Application, 24–28 September 2007, Aveiro.

Berg, L.K. and *Zhong, S.*, 2005: Sensitivity of MM5-simulated boundary layer characteristics to turbulence parameterizations. *J. Appl. Meteor. 44*, 1467–1483.

Berge, E. and *Jakobsen, H.A.*, 1998: A regional scale multi-layer model for the calculation of long-term transport and deposition of air pollution in Europe. *Tellus 50*, 205–223.

Bjorge, D. and *Skalin, R.*, 1995: PARLAM – the parallel HIRLAM version at DNMI. Research Report, No.27, Norwegian Meteorological Institute, Oslo.

Blackadar, A.K., 1976: Modeling the nocturnal boundary layer. Preprints, 3rd Symposium on Atmospheric Turbulence, Diffusion and Air Quality, Raleigh, NC, 19–22 October 1976, *Amer. Meteor. Soc.*, 46–49.

Blackadar, A.K., 1979: High resolution models of the planetary boundary layer. In (Eds. Pfaffin, J.R., and Ziegler, E.N.) Advances in environment and scientific engineering, Vol. 1, Gordon and Breach, Newark, 50–85.

Bott, A., 1989a: A positive definite advection scheme obtained by non-linear re-normalization of the advection uses. *Mon. Weather Rev. 117*, 1006–1015.

Bott, A., 1989b: Reply. *Mon. Weather Rev. 117*, 2633–2636.

Calvo, A.I., Olmo, F.J., Lyamani, H., Alados-Arboledas, L., Castro, A., Fernández-Raga, M., and *Fraile, R.*, 2010: Chemical composition of wet precipitation at the background EMEP station in Víznar (Granada, Spain) (2002–2006). *Atmos. Res. 96*, 408–420.

Deardorff, J.W., 1972: Theoretical expression for the countergradient vertical heat flux, *J. Geophys. Res. 77(30)*, 5900–5904.

Holtslag, A.A.M., and *Boville, B.A.*, 1993: Local versus nonlocal boundary-layer diffusion in a global climate model. *J. Climate 6*, 1825–1842.

Holtslag, A.A.M., and *Moeng, C.-H.*, 1991: Eddy diffusivity and countergradient transport in the convective atmospheric boundary layer. *J. Atmos. Sci. 48*, 1690–1698.

Hong, S.Y., and *Pan, H.L.*, 1996: Nonlocal boundary layer vertical diffusion in a Medium-Range Forecast model. *Mon. Weather Rev. 124*, 2322–2339.

Hu, X.-M., Nielsen-Gammon, J.W., and *Zhang, F.*, 2010: Evaluation of three planetary boundary layer schemes in the WRF model. *J. Appl. Meteor. Climatol. 49*, 1831–1844.

Janjic, Z.I., 1990: The step-mountain coordinate: Physical package. *Mon. Weather Rev. 118*, 1429–1443.

Janjic, Z.I., 1994: The step-mountain Eta coordinate model: Further development of the convection, viscous sublayer and turbulent closure schemes. *Mon. Weather Rev. 122*, 927–945.

Jericevic, A., Kraljevic, L., Grisogono, B., Fagerli, H., and *Vecenaj, Z.*, 2010: Parameterization of vertical diffusion and the atmospheric boundary layer height determination in the EMEP model. *Atmos. Chem. Phy. 10*, 341–364.

Lenschow, D.H., Li, X.S., and *Zhu, C.J.*, 1988: Stably stratified boundary layer over the Great Plains. Part I: Mean and turbulent structure. *Bound.-Layer Meteor. 42*, 95–121.

Lenschow, S., and *Tsyro, S.*, 2000: Meteorological input data for EMEP/MSC-W air pollution models. EMEP MSC-W Note 2/2000.

Louis, J., 1979: A parametric model of vertical eddy fluxes in the atmosphere. *Bound.-Layer Meteor. 17*, 187–202.

Mellor, G.L., and *Yamada, T.*, 1974: A hierarchy of turbulence closure models for planetary boundary layers. *J. Atmos. Sci. 31*, 1791–1806.

Mihailovic, D.T., and *Alapaty, K.*, 2007: Intercomparison of two K-schemes: local versus non-local in calculating concentrations of pollutants in chemical and air-quality models. *Environ. Model. Softw. 22*, 1685–1689

Mihailovic, D.T., Alalapaty, K., and *Sakradzija, M.*, 2008: Development of a non-local convective mixing scheme with varying upward mixing rates for use in air quality and chemical transport models. *Environ. Sci. Pollut. Res. 15*, 296–302.

Mihailovic, D.T., Alapaty, K., and *Podrascanin, Z.*, 2009: The combined non-local diffusion and mixing schemes, and calculation of in-canopy resistance for dry deposition fluxes. *Environ. Sci. Pollut. Res. 16*, 144–151.

O'Brien, J.J., 1970: A note on the vertical structure of the eddy exchange coefficient in the planetary boundary layer. *J. Atmos. Sci. 27*, 1213–1215.

Pleim, J.E., and *Chang, J.S.*, 1992: A non-local closure model for vertical mixing in the convective boundary layer. *Atmos. Environ. 26A*, 965–981.

Pleim, J.E., 2007a: A combined local and nonlocal closure model for the atmospheric boundary layer. Part I: Model description and testing. *J. Appl. Meteorol. Clim. 46*, 1383–1395.

Pleim, J.E., 2007b: A combined local and non-local closure model for the atmospheric boundary layer. Part 2: Application and evaluation in a mesoscale model, *J. Appl. Meteor. Clim. 46*, 1396–1409.

Simpson, D., Fagerli, H., Jonson, J.E., Tsyro, S., Wind, P., and *Tuovinen, J.-P.*, 2003: Transboundary acidification and eutrophication and ground level ozone in Europe: Unified EMEP Model Description, EMEP Status Report 1/2003 Part I, EMEP/MSC-W Report, The Norwegian Meteorological Institute, Oslo.

Stull, R.B., 1984: Transilient turbulence theory. Part I: The concept of eddy mixing across finite distances. *J. Atmos. Sci. 41*, 3351–3367.

Topçu, S., Incecik, S., and *Atimtay, A.T.*, 2002: Chemical composition of rainwater at EMEP station in Ankara, Turkey. *Atmos. Res. 65*, 77–92.

Zhang, D.L., and *Zheng, W.Z.*, 2004: Diurnal cycles of surface winds and temperatures as simulated by five boundary layer parameterizations. *J. Appl. Meteor. 43*, 157–169.

Zhang, C., Randall, D.A., Moeng, C.-H., Branson, M., Moyer, M., and *Wang, Q.*, 1996: A surface parameterization based on vertically averaged turbulence kinetic energy. *Mon. Weather Rev. 124*, 2521–2536.

IDŐJÁRÁS
Quarterly Journal of the Hungarian Meteorological Service
Vol. 117, No. 3, July–September 2013, pp. 295–314

Lightning behavior during the lifetime of severe hail-producing thunderstorms

Tsvetelina Dimitrova [1], **Rumjana Mitzeva** [2*], **Hans D. Betz**[3, 4], **Hristo Zhelev**[1, 2], and **Sebastian Diebel**[4]

[1]*Agency Hail Suppression, 17 Hristo Botev Blvd., 1606 Sofia, Bulgaria,*
E-mail: dimitrova_tsvetelina@abv.com

[2] *Faculty of Physics, University of Sofia, 5 J. Bourchier Blvd.1164 Sofia, Bulgaria,*

[3] *University of Munich, Department of Physics, D-85748 Garching Germany,*
E-mail:hans-dieter.betz@physik.uni-muenchen.de

[4] *Nowcast GmbH, Sauerbruchstraße 48, 81377 Munich, Germany,*
E-mail: sebastian.diebel@nowcast.de

**Corresponding author; E-mail address: rumypm@phys.uni-sofia.bg*

(Manuscript received in final form November 6, 2012)

Abstract– Results from an analysis of total lightning (cloud-to-ground and intracloud) behavior during the lifetime of severe hail-producing thunderstorms are presented. The analysis was carried out for different types of storms: multicell, supercell, and multicell which evolved into supercell storms. The study reveals: (1) There is a positive time lag between the jumps of both multiplicity and flash rate and the beginning of large hail in the three analyzed thunderstorms. (2) The mean and maximum values of total flash rate, as well as the multiplicity of negative total strokes in the multicell and supercell storms are remarkably lower than for the multicell that became supercell storm. (3) Significant numbers of positive total strokes are detected in both supercell and multicell which evolved into supercell storms. The highest percentage of positive strokes is observed during the period of large hail falls on the ground. (4) The jump of lightning density is observed before large hail fall in the three storms, following a dramatic decrease of the lightning rate during the beginning of the hail fall. In the supercell storm the lightning "hole" occurred, associated with an existence of bounded weak-echo region of the cell.

Key-words: total lightning; flash rate; multiplicity; lightning density; hail; radar reflectivity

1. Introduction

The relationship between lightning and thunderstorm severity (large hail, heavy rain leading to flash flooding, strong wind, and tornado) has been subject of studies for more than 50 years. One of the purposes of these studies has been to evaluate whether lightning characteristics could be used to improve nowcasting of severe thunderstorm events. However, the results related to lightning characteristics during the lifetime of severe thunderstorms are often contradictory in the numerous studies.

In previous studies it is noted that severe storms are characterized by higher total flash rates than ordinary non-severe storms. The more intense the storm the more lightning is produced (*Maier* and *Krider*, 1982; *Taylor*, 1973; *Turman* and *Tettelbach*, 1980). *Williams* (1985) explained this link with the intensification of the updrafts. The correlation between updraft and flash rate is also established by *Deierling* and *Petersen* (2008), *Goodman et al.* (2005), and *Wiens et al.* (2005).

However, there are severe storms that are characterized by low cloud-to-ground flash rates. Low CG flash rates are observed when hail was produced in two thunderstorms studied by *Lang et al.* (2000). In both studied storms, radar reflectivity and the production of hail were anti-correlated with the production of significant negative cloud-to-ground lightning. The authors explained this with the elevation charge hypothesis (*MacGorman et al.*, 1989) and suggested that low production of negative CGs can be explained by the production of significant quantities of hail, high IC flash rates, and strong updrafts. In hail - bearing storms, studied by *Soula et al.* (2004), the CG rate does not exceed 2 min^{-1} when the cells produce hail, while it can reach up to 12 min^{-1} for heavy precipitating storms.

According to some studies, the cloud-to-ground (CG) lightning frequency decreases when hail forms in the cloud (*Lang et al.*, 2000; *Soula et al.*, 2004). *Williams et al.* (1999) found that peak flash rate precedes severe weather at the ground by 5–20 min. Their analysis showed that "A distinguished feature of severe storms is the presence of lightning "jumps"– abrupt increases in flash rate in advance of the maximum rate for the storm". *Kane* (1991) obtained similar results – tornadoes and large hail occurred about 10–15 min after the peak of the 5-min cloud-to-ground lightning rate.

Additionally, a change in the polarity ratio is apparent in cases of severe weather: positive CGs are more prevalent than negative ones, resulting in a decrease of negative CG lightning frequency. Some authors (e.g., *Carey* and *Rutledge*, 1998; *Lang et al.*, 2004; *Reap* and *MacGorman*, 1989; *Seimon*, 1993; *Stolzenburg*, 1994; *Wiens et al.*, 2005) reported a relationship between large hail and positive CG lightning. They showed that hailstorms usually produce large hailstones in the active period of positive CG flashes. For example, *MacGorman* and *Burgess* (1994) analyzed the characteristics of CG flashes in 15 severe storms with large hailstones or tornadoes and found that the large hail occurred during the period when positive ground flashes dominated. In 11 tornadic storms, tornadoes occurred either during or after the period when positive ground flashes dominated. The strongest tornado usually begins after the positive ground flash rate decreases from its maximum value. *Montanya et al.* (2007, 2009) and *Soula et al.* (2004) revealed a reversal of the dominant polarity of the CG flashes from negative to positive during the period when cells produced hail.

Other studies showed that severe weather often occurs without dominating positive strokes. *Bluestein* and *MacGorman* (1998) and *Curran* and *Rust* (1992) reported that within the hailstorms they had studied, the negative cloud-to-ground flashes dominated.

Carey et al. (2003) analyzed severe storms for a period of 10 years (1989–1998) and came to the conclusion that there was a significant regional variability in the percentage of positive CG lightning produced by severe storms during the warm season. It is assumed that the geographical preference of positive storms is linked to specific meteorological conditions of the region. For this reason, some authors (*Gilmore* and *Wicker*, 2002; *MacGorman* and *Burgess*, 1994; *Smith et al., 2000*; *Williams et al.*, 2005) explored the relationships between the environmental conditions and CG lightning. Based on the hypothesis that mesoscale environment indirectly influences lightning polarity of the storms by directly controlling storm structure, dynamics, and microphysics which in turn control storm electrification, the analysis of *Carey* and *Buffalo* (2007) demonstrated significant and systematic differences in environmental conditions of positive and negative storms.

Lang and *Rutledge* (2002) analyzing 11 thunderstorms came to the conclusion that "The only significant differences between intense storms that produced predominately positive cloud-to-ground (CG) lightning for a significant portion of their lifetimes (PPCG storms) and intense storms that produced little CG lightning of any polarity (low-CG storms) was that PPCG storms featured much larger volumes of significant updrafts and produced greater amounts of precipitation (both rain and hail)".

Different authors reported various values of multiplicity. For example: *Soula et al.* (2004) obtained values from 1.9 to 2.6 for the negative CG flashes and from 1.0 to 1.2 for the positive ones, while *Carey et al.* (2003) obtained similar values of mean positive and negative CG multiplicity (1.2 and 1.1, respectively) for the analyzed supercell.

The interesting feature of lightning behavior during the lifetime of a severe storm is the presence of a lightning "hole" (areas of week or even zero total lightning density surrounded by larger values). The existence of a hole is reported by many authors (*Goodman et al.*, 2005; *Lang et al.*, 2004; *MacGorman et al.*, 2005; *McKinney et al.*, 2008; *Murphy* and *Demetriades*, 2005; *Steiger et al.*, 2007; *Wiens et al.*, 2005). *Lang et al.* (2004) found that the lightning hole is associated with extremely strong updrafts in the bounded weak echo region of the supercell. This hypothesis is supported by different observations (for example, *Goodman et al.*, 2005; *Steiger et al.*, 2007). However, *Murphy* and *Demetriades* (2005) analyzing two hail-producing supercells reported that the lightning "hole" was not linked to the bounded weak echo region but rather was a manifestation of a more complicated radar structure.

It is clear that conclusions based on the investigations conducted in different geographical regions are often contradictory, because the variability of lightning parameters is linked to several factors, especially latitude, season, location, and climatic conditions (e.g., *Orville*, 2002; *Sheridan*, 1997; *Soriano et al.*, 2001; *Soula et al.*, 2004;). Different types of thunderstorms were studied by *Lang et al.* (2000) and *Ray et al.* (1987) in order to analyze the reasons for the differences in lightning behavior.

Bulgaria is situated in southeast Europe. Within a relatively small area (111 000 km^2), the Bulgarian landscape exhibits a striking topographic variety – large plains and lowlands, valleys and gorges, low and high mountains (up to 2–3 km). The mountains are important factor for the intensification of convection.

From April to September the frequency of thunderstorms in Bulgaria is high. In more than 60% of the days there are thunderstorms and half of them produce hail.

The analyses in *Dimitrova et al.,* (2009) revealed that most of lightning features of the studied severe and non-severe thunderstorms developed over Bulgaria were similar to those in other geographical regions. However, there are some differences in lightning behavior in severe storms that stimulated the analysis of lightning characteristics in different types of severe storms.

The goal of the present paper is to study the lightning behavior in three different types of severe storms produced large hail (diameter more than 2 cm) over Bulgaria. The evolution of lightning characteristics of a multicell, a supercell, and a multicell that evolved into a supercell storm is analyzed together with the radar characteristics.

2. Data

The lightning and volume radar data over the territory of Bulgaria have been available since 2008. Lightning data are taken from the LINET network (*Betz et al.*, 2008). Radar information is obtained from radar network of Hail Suppression Agency in Bulgaria.

The main information about the hail precipitation is regularly obtained using data from the rain gauge network with distance between the gauges of about 10–12 km. Additional information is given by voluntary observers in towns and villages situated between the rain gauges.

2.1. *Radar data*

Data from two S-band Doppler radars were used (*Fig. 1*). The one is in North Bulgaria (Bardarski geran village, Vratsa district) and the other is in South Bulgaria (Golyam Chardak village, Plovdiv district).

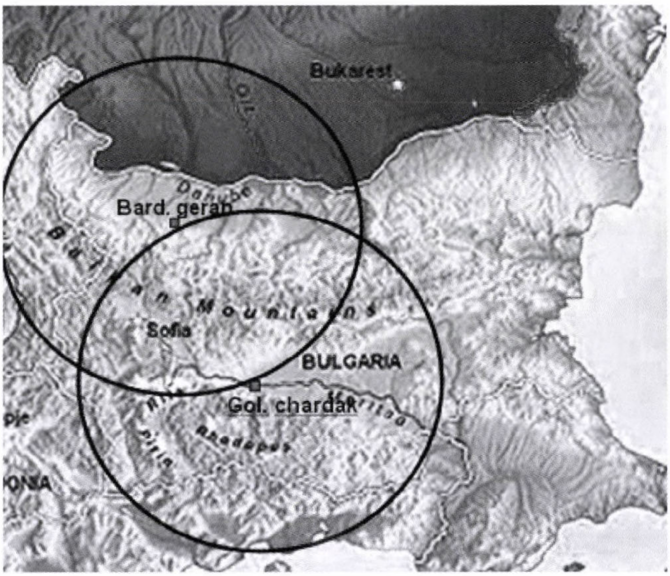

Fig. 1. Range of radar observation. Both radar stations (in Bardarski geran village – North Bulgaria and Golyam Chardak – South Bulgaria) are part of radar network of Hail Suppression Agency in Bulgaria.

Radar data were used to produce horizontal and vertical cross sections of thunderstorm cell structures. These profiles are estimated from volumetric data generated by an automatic scanning at 14 elevation angles. The elevation of the successive scan was increased from 0.2° to 85° with an irregular step while spinning around 360° of azimuth. The full volume scan was performed for 4 minutes in a range of 150 km. IRIS (Interactive Radar Information System) generates products based on this volume scan.

Data for the vertical profile of reflectivity for the storms' cells - maximum reflectivity, height of maximum reflectivity, Hzmax, maximum heights of 15 dBZ, and 45 dBZ contour (H15 and H45 respectively) were analyzed to investigate storm's structure and evolutions.

2.2. *Lightning data*

The analyzed information for lightning characteristics was taken from the European LINET (Betz et al., 2008).

LINET is a VLF/LF lightning detection network developed at the University of Munich, which provides continuous data for both research and operational purposes. During international co-operations, LINET has been deployed in four continents. LINET covers a wide area approximately from a longitude of -10° to 25° and from latitude of 35° to 66° (*Betz et al.*, 2009). The LINET data set provides information on stroke time, geographical location, height of intra-cloud (IC) events, peak current (PC), and polarity. The discrimination between CG and IC lightning in LINET relies on a TOA (times of arrival) analysis. The corresponding differences in travel time from high- and low-lying emission centers are exploited within the TOA locating algorithm (*Betz et al.*, 2004; *Betz at al.*, 2009). This 3D discrimination method is reliable when the sensor baseline does not exceed ~250 km. Thus, while the sensor geometry in the central part of the network allows locating very weak lightning events with the inclusion of large numbers of IC and reliable discrimination between CG and IC, in the surrounding areas the network reports predominantly the stronger events, which are mainly return strokes (CG) (*Betz et al.*, 2009). Bulgaria is in the edge of the LINET network geometry. To avoid inaccuracies in the separation of IC and CG strokes, total lightning is studied in the present paper.

The lightning characteristics – flash rate (FR), peak current (PC), multiplicity (number of strokes in one flash) Mn, and polarity of total lightning (intra-cloud and cloud-to-ground) were analyzed. The flash rate was calculated per 4 minutes in accordance with the period of radar volume scan.

3. *Case studies*

Three severe thunderstorms with a different development were studied. One of them was a multi-cellular storm (MC) which developed on August 8, 2010 (*Fig. 2a*). The other one occurred on May 30, 2009 and was an isolated developed supercell (SC) (*Fig. 2c*), while the third one, developed on August 6, 2010, was multicellular and evolved into a supercell storm (MSC) (*Fig. 2b*).

Maximum values of some radar characteristics together with the corresponding temperature given in *Table 1* show that the three thunderstorms had a strong vertical development (the top echo, H15 of thunderstorms reached at altitude of 16–17 km) and intense radar reflectivity echo – 60–65 dBZ. The other similarity between the studied thunderstorms is the long life time (longer than 2 hours) and the registration of large hail (diameter larger than 2 cm) at the ground.

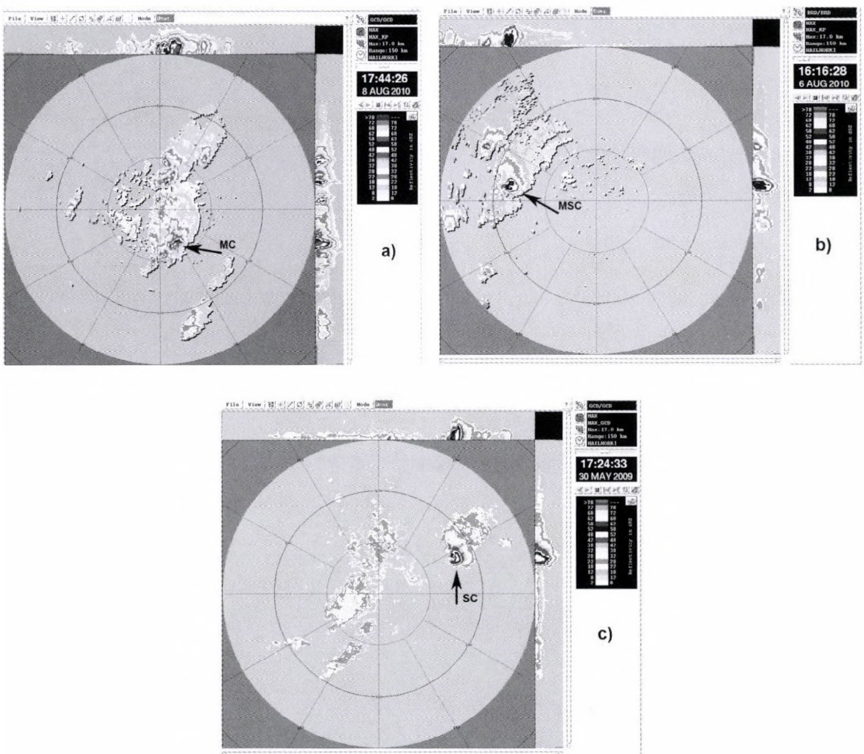

Fig. 2. Radar display of the maximum radar reflectivity [dBZ] obtained by S-band radar in the moment of maximum development of: a) multicell thunderstorm, MC on August 8, 2010 at 1444 UTC (1744 local time); b) multicell evolving into a supercell thunderstorm, MSC on August 6, 2010 at 1316 UTC (16:16 local time); c) supercell storm, SC on May 30, 2009 at 1424 UTC (1724 local time). The range markers identify 50 km separations.

Table 1. Maximum values of some radar characteristics and corresponding temperature in the three studied thunderstorms: multicell thunderstorm, MC; evolved from multicell into supercell thunderstorm, MSC; supercell storm, SC

Max values	**MC**	**MSC**	**SC**
H15 [km]	16.1	16.5	16.9
T_{H15} [°C]	–60.7	–59.2	–60.1
H45 [km]	11.8	13.5	10.9
T_{H45} [°C]	–42.2	–51.0	–54.3
Zmax [dBZ]	65.0	60.0	63.5
Hzmax [km]	8.8	7.9	8.0
T_{Hzmax} [°C]	–28.4	–24.6	–33.1

However, the studied storms had differences in the development and radar structure. From the beginning the SC storm developed as an individual super cell with a rapid vertical development. In 10 minutes the height of 15 dBZ radar echo increased from 7.6 km to 10 km and the maximum reflectivity increased from 35 dBZ to 53.5 dBZ. In the next 10 minutes the maximum reflectivity reached 60 dBZ keeping up these high values (60–65 dBZ) during the next 90 min.

Unlike this storm, both MSC and MC storms started as ordinary non-severe multicell storms. MSC storm underwent a transition from a weak multicellular storm into an intense supercellular storm in the period 1236 UTC – 1300 UTC. The development of MC storm intensified after 1416 UTC. The maximum measured radar reflectivity in MSC storm was 60 dBZ and in MC storm – 65 dBZ.

There is a well pronounced pulse in the vertical development of MC storm and two pulses in MSC storm. These pulses are associated with a sharp increase of H15 and H45 centered around 1416 UTC in the MC storm and around 1236 UTC and 1304 UTC in the MSC storm. The maximum values of H45 in the three studied storms are significantly different (Table 1). In MSC storm, H45 reached 13.5 km and in SC and MC storms – 10.9 and 11.8 km, respectively. Another significant difference between MSC storm and MC and SC storms is the location of region with high radar reflectivity $\geq$ 60 dBZ. The duration of an existence of high radar reflectivity above zero isotherm, H0, in MC storm and in SC storm was about 3 times longer than for MSC storm. (*Fig. 3a, b, c*)

The MC and SC thunderstorms produced hailstones with diameter up to 3 cm and MSC storm up to 6 cm. There is also a significant difference in the duration of large hail falling on the ground from the three thunderstorms – 60 min from MC storm (with interruptions due to the multi-cellular development), 15 min from SC storm, and 26 min from MSC storm.

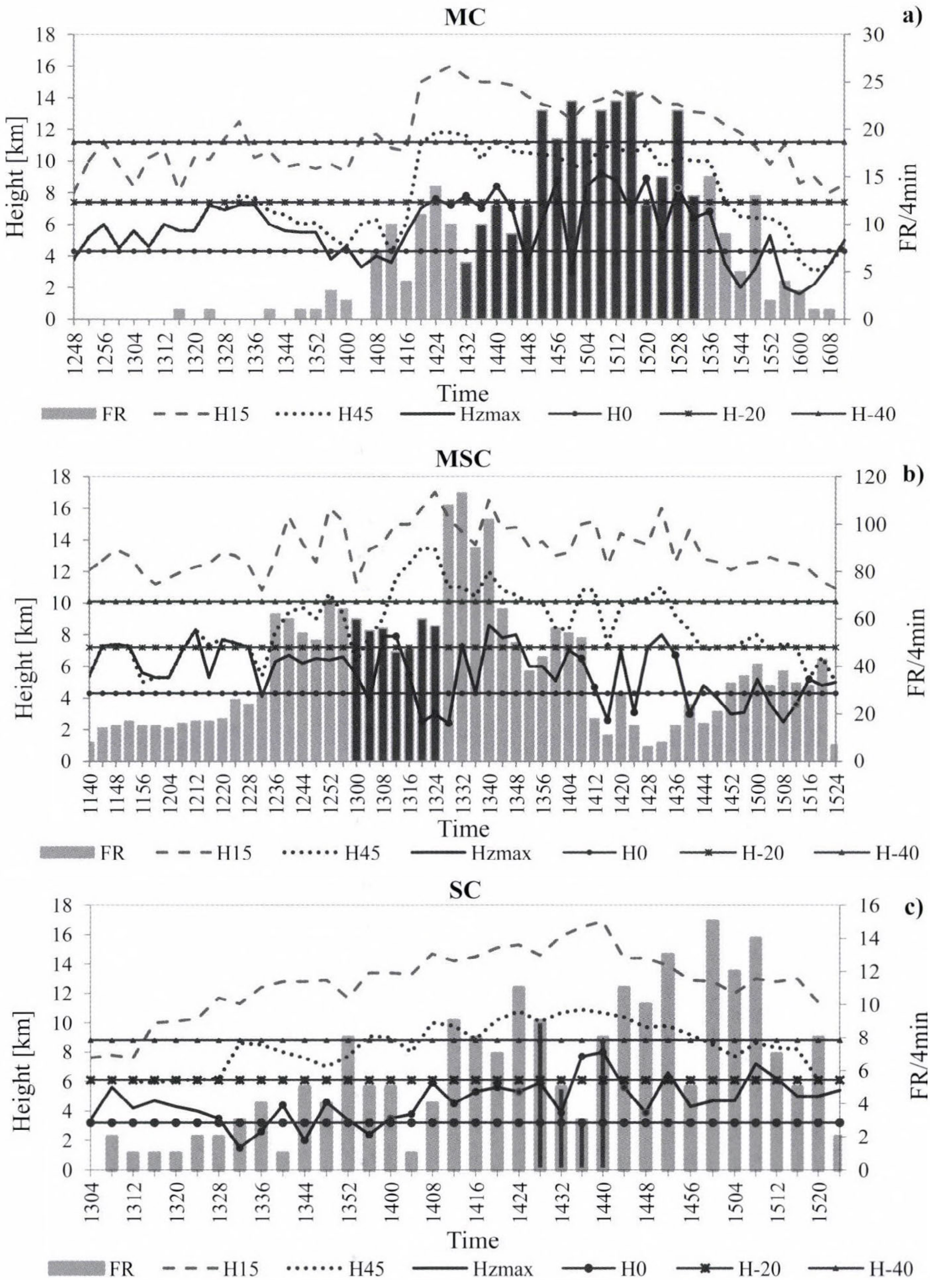

Fig. 3. Number of total flashes per 4 min, FR and radar information, as a function of time for the studied thunderstorms: a) multicell thunderstorm, MC; b) multicell evolving into a supercell thunderstorm, MSC; c) supercell storm, SC

4. Lightning behavior

Evolution of flash rate (FR), polarity, peak current (PC), and multiplicity (Mn), during the lifetime of the three severe storms were analyzed together with radar characteristics of the storms.

The flash rate of total lightning in MSC storm (*Fig. 3b*) is remarkably higher than in MC and SC storms (*Fig. 3a* and *Fig. 3c*, correspondingly). The mean and maximum values of both negative and positive flash rates in the MSC storm are also considerably higher than the corresponding characteristics in MC and SC storms (*Table 2*).

Table 2. Mean and maximum values of flash rate per 4 minutes during the lifetime of studied thunderstorms: multicell thunderstorm, MC; evolved from multicell into supercell thunderstorm, MSC; supercell storm, SC

	Flash rate per 4 minutes					
	Positive		**Negative**		**Total**	
	mean	**max**	**mean**	**max**	**mean**	**max**
MC	1.2	2	9.9	23	10.1	24
SC	2.1	5	4.9	15	6.0	15
MSC	11.2	38	27.8	80	38.8	113

During the non-severe stage of MC storm (from 1248 UTC till 1412 UTC) and MSC storm (from 1140 UTC till 1232 UTC), the flash rate is significantly lower in comparison with the severe stage (see *Fig. 3a*, *Fig. 3b*). In the non-severe stage, the time duration of H15 and H45 above –40 °C and –20 °C isotherms, respectively, is longer for MSC storm in comparison with MC storm. Thus, the vertical profile of radar reflectivity indicates that MSC storm has a stronger updraft than MC storm. One can speculate (see *Carey* and *Rutledge*, 1996) that the stronger updraft in MSC storm is responsible for the greater number of graupel than in MC storm and thus for higher flash rate via the non-inductive mechanism of thunderstorm electrification (*Saunders et al.*, 1991).

In the three thunderstorms there is a jump in the flash rate before the occurrence of large hail on the ground. The flash rate FR$\geq$1 min^{-1} sharply increases more than 2 times 12 min before the hail fall in MC storm, 20 min in SC storm, and 24 min in the MSC storm (see *Fig.3a, b, c*). The increase is more pronounced in MSC and MC storms. It is just before the transition of non-severe to severe stage of both thunderstorms, when a pulse in the vertical development of the cells (sharp increase of H15 and H45) is abrupt.

The maximum values of flash rate in the three storms are detected after the maximum vertical development of the storms (see *Fig 3*). In MC and MSC storms these values are reached after a second jump of flash rate, which occurs after the lowering of the height of radar reflectivity ≥ 60 dBZ below the 0°C isotherm.

A small decrease of the flash rate is observed in MSC storm during the large hail falls, while the corresponding decrease by a factor of 4 is significant in SC storm. However, the flash rate reached maximum values in MC storm during the occurrence of large hail.

The plot of lightning density (number of strokes for 10 minutes in a grid cell 5 km × 5 km) is shown in *Fig. 4*. The lightning density reached its maximum values before the falling of large hail on the ground and decreased in the beginning of this period in all three thunderstorms. While the lightning density reached its maximum, there was a convective vertical development, when a reflectivity of 45 dBZ extended up to –40°C isotherm and the maximum radar reflectivity ($\geq$60 dBZ) – extended up to the –20 °C isotherm.

During the large hail fall (the period of time is denoted by red color in *Fig. 4*), the decrease of lightning density was observed, although the radar reflectivity was very high. The lower panel in *Fig. 4* shows that a lightning "hole" is observed in SC storm during the hail fall (from 1430 UTC till 1440 UTC). The more detailed analysis revealed that the presence of a lightning "hole" is accompanied by an occurrence of bounded weak-echo region (BWER) of the SC storm (*Fig. 5*).

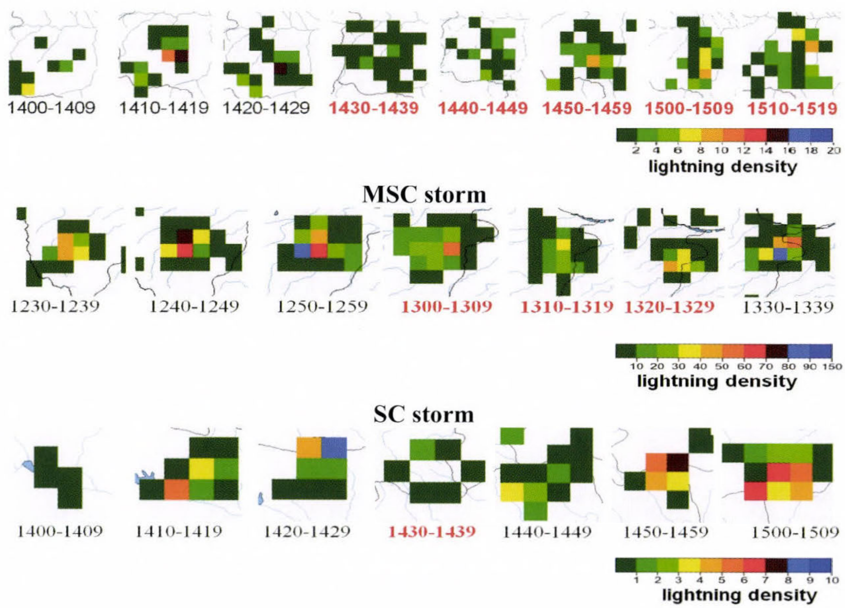

Fig. 4. Lightning density (number of strokes for 10 minutes in a grid cell 5 km x 5 km) during the part of lifetime of a multicell thunderstorm, MC (upper panel); multicell evolving into supercell thunderstorm, MSC (middle panel); a supercell storm, SC (lower panel). The period of large hail is denoted in red.

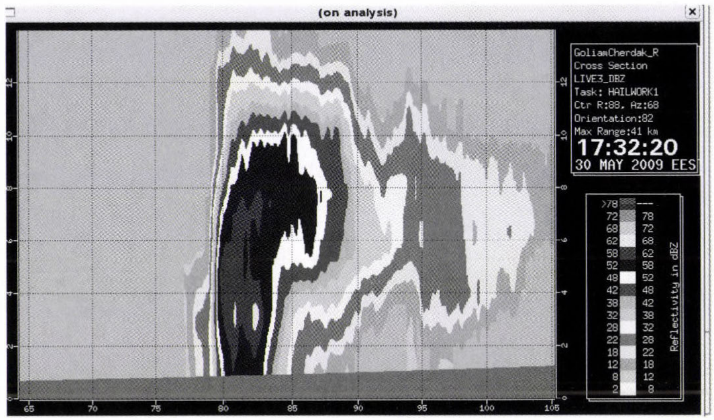

Fig. 5. Vertical cross-section of the supercell storm, SC on May 30, 2009 at 1432 UTC (17:32 in local time).

There is no direct correlation between flash rate, FR, and radar characteristics. However, a statistically significant (α=0.05) correlation is established between H45 and FR averaged in 1 km bin (see *Fig. 6*). Based on the assumption that the radar volume fraction for graupel correlates with the volume with reflectivity of 45 dBZ, one can speculate that these results are consistent with the non-inductive charging mechanism (*Saunders et al.*, 1991; *Sanders*, 1993), which relies on the rebounding collisions between graupel and ice crystals in the presence of the super-cooled liquid water.

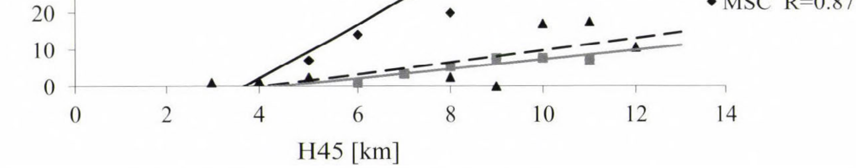

Fig. 6. Flash rate FR (averaged in 1 km bin), as a function of H45.

The analysis of strokes polarity showed that positive strokes were detected in all three studied cases (*Fig. 7*). However, the percentage in MC storm is very low (≈1%), while in SC and MSC storms it is approximately 20%. The number of positive strokes is highest during the period of large hail detected on the ground (*Fig. 8*). In SC storm, the FR of positive flashes predominated and was 2.5 times higher than FR of negative ones 8 minutes before large hail on the ground (*Fig. 7c*).

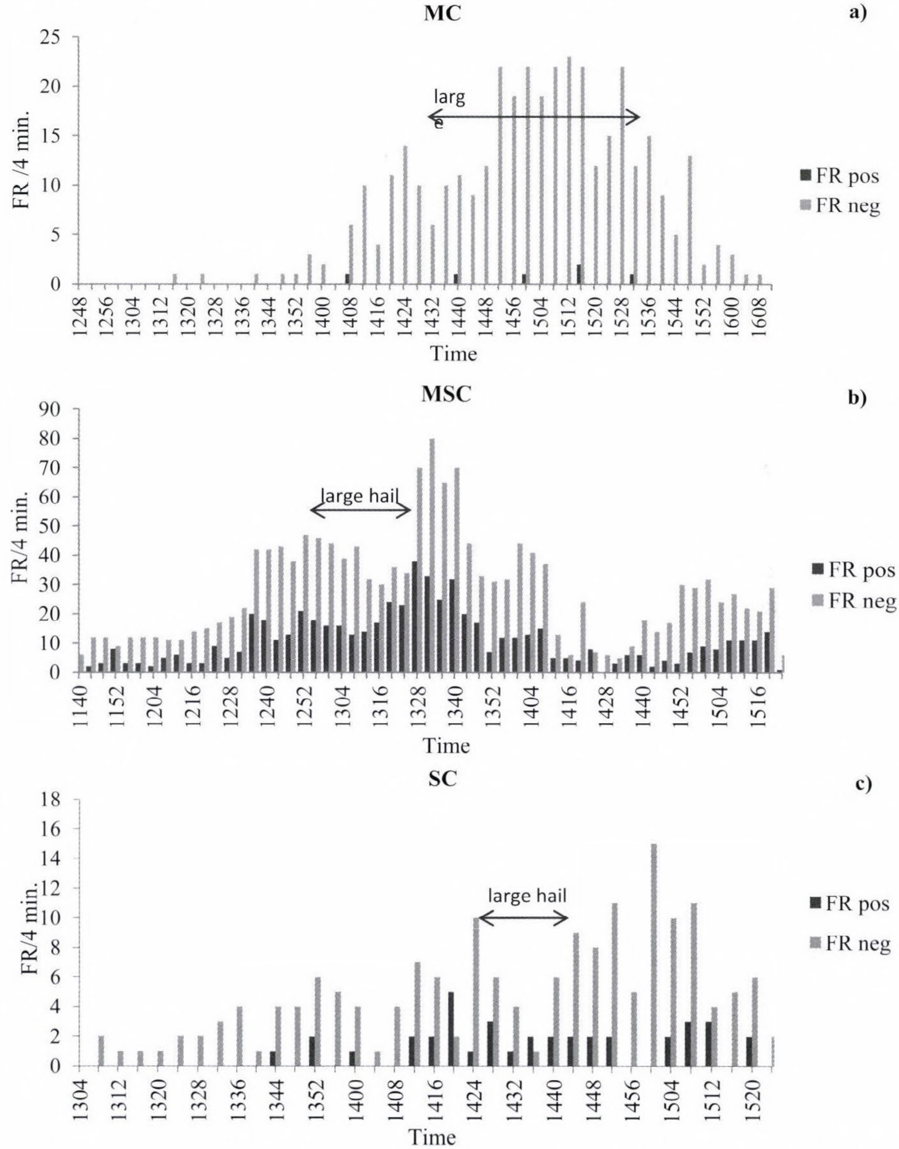

Fig. 7. Number of total negative and positive flashes per 4 min. as a function of time for the studied thunderstorms: a) multicell thunderstorm, MC; b) multicell that evolved into a supercell thunderstorm, MSC; c) supercell storm, SC.

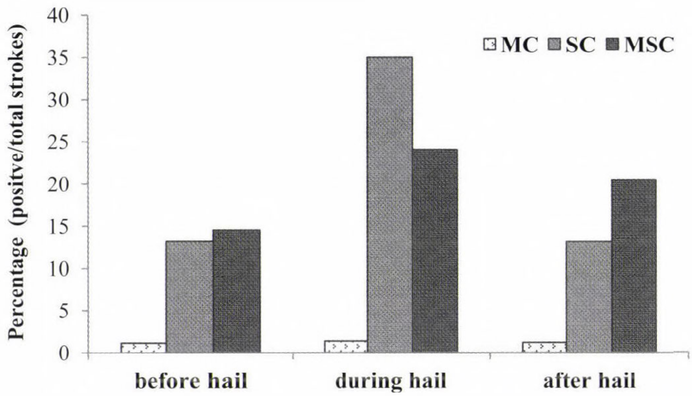

Fig. 8. Percentage of positive strokes before, during, and after large hail falling on the ground.

The mean and maximum values of multiplicity of negative flashes in MC and SC storms are similar (*Table 3*). Their maximum values are significantly lower than the ones in MSC storm.The maximum values of multiplicity in the three storms were before the falling of large hail on the ground (*Table 4*).The highest value of 16 is registered in MSC storm, while maximum values in MC and SC storms are 6 and 7, respectively. In the three thunderstorms, there is a pronounced jump in multiplicity before the time of detection of large hail on the ground – 18 min in MC storm, 8 min in SC storm, and 68 min in MSC storm (*Fig. 9 a, b, c*).

Table 3. Mean and maximum values of multiplicity and peak current (absolute value), PC, of the studied thunderstorms

	Multiplicity				PC			
	Positive		Negative		Positive		Negative (absolute values)	
	mean	max	mean	max	mean	max	mean	max
MC	1.0	1.0	1.2	6.0	22.8	48.2	21.4	67.6
SC	1.0	1.0	1.3	7.0	21.2	70.3	17.4	64.5
MSC	1.1	3.0	1.8	16.0	10.8	37.3	16.4	104.7

Table 4. Mean and max values of multiplicity, Mn during different periods of the studied thunderstorms development: before the first severe hail fall on the ground; during a severe hail fall on the ground; after the last registration of severe hail on the ground

	MC				MSC				SC			
	mean		max		mean		max		mean		max	
	Neg	Pos	Neg	Pos	Neg	Pos	Neg	Pos	Neg	Pos	Neg	Pos
before	1.4	1.0	6.0	1.0	2.3	1.1	16	2.0	1.3	1.0	7.0	1.0
during	1.2	1.0	4.0	1.0	2.0	1.1	11	2.0	1.1	1.0	2.0	1.0
after	1.2	1.0	3.0	1.0	1.5	1.1	10	3.0	1.3	1.0	5.0	1.0

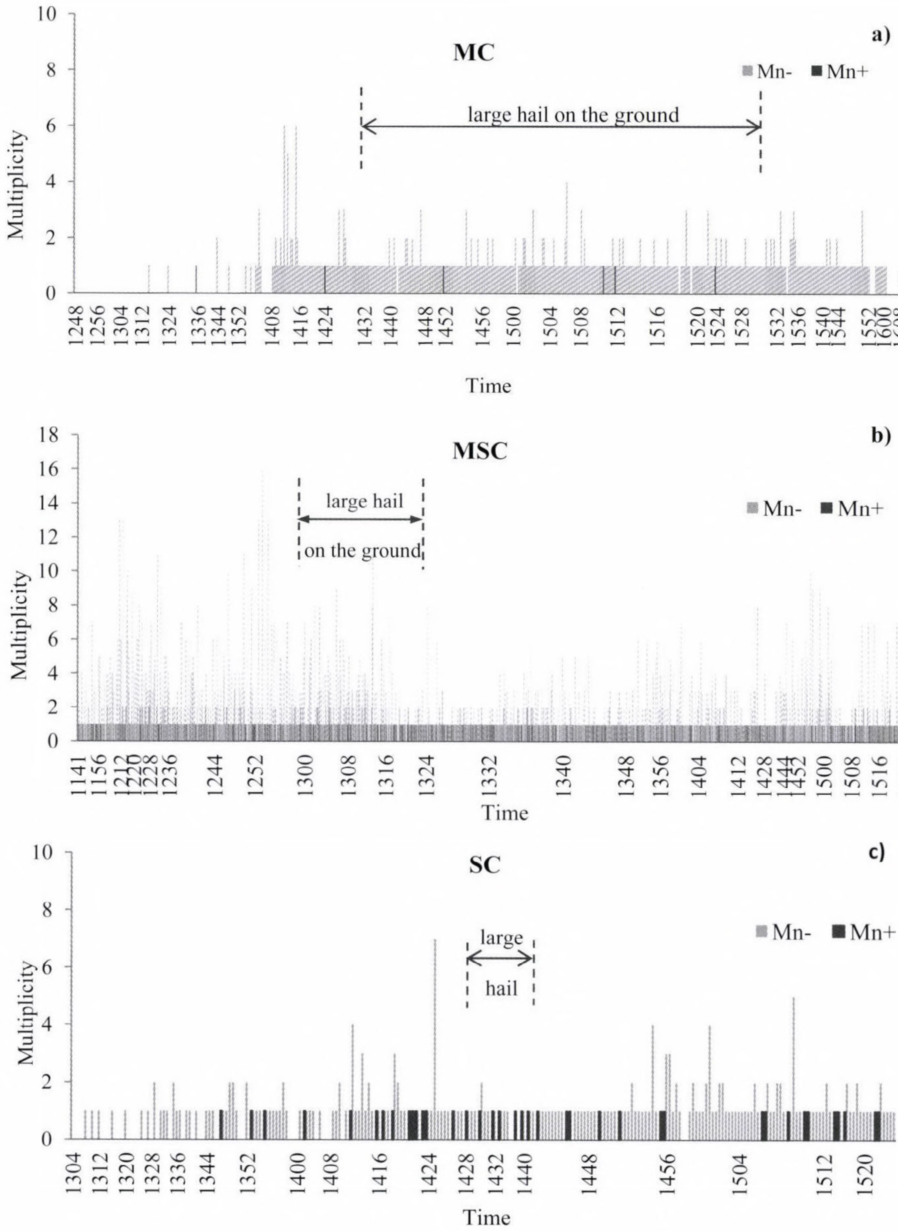

Fig. 9. Multiplicity of positive flashes, Mn+ and negative flashes, Mn−, as a function of time for a) multicell thunderstorm, MC; b) multicell that evolved into a supercell thunderstorm, MSC; c) supercell storm, SC.

The analysis of negative peak current shows that there are no significant differences in their mean absolute values for the three storms (*Table 3*). The mean values of positive peak current in MC and SC storms are 2 times higher than in MSC storm, and the highest value of 70.3 kA was registered in SC, while the highest absolute values of negative peak current was detected in MSC (105 kA). Additional analyses showed that in MC and SC storms all detected strokes had absolute values of peak current above 10 kA, and in MSC storms there was a great number of strokes (14% for negative and 46% for positive) with absolute values of peak currents less than 10 kA.

5. *Discussion and conclusion*

An analysis was carried out on total lightning behavior during the lifetime of different types of severe thunderstorms (a multicell, a supercell, and a multicell that evolved into a supercell) producing large hail over Bulgaria.

Significant number of positive strokes was detected in both supercell SC and MSC storms with the highest percentage during the period of large hail falls on the ground. In the supercell of the SC storm, the positive strokes even dominated over negative ones 8 minutes before the beginning of large hail fall. The detected significant number of positive strokes is in agreement with the results obtained by other authors (e.g., *Carey* and *Rutledge*, 1998; *Lang et al.*, 2004; *MacGorman* and *Burgess*, 1994; *Stolzenburg*, 1994; *Wiens et al.*, 2005). There are two "main" hypotheses for explaining the large number of positive CG lightning in some thunderstorms – the tilted-dipole charge structure or the formation of inverted dipole (*MacGorman* and *Nielsen,* 1991, *MacGorman* and *Burgess,* 1994). Since a high number of negative flashes together with the positive ones were detected in SC and MSC, one can assume that tilted dipole structure of supercell storm can explain the high number of positive CG flashed. The analyses reveal that the top of the updraft core in SC and MSC is displaced sufficiently far horizontally from the reflectivity core, which supports the assumption that the tilted dipole structure is responsible for the large positive flashes in SC and MSC.

The jump of lightning density is observed before large hail fall in the three thunderstorms, associated with a dramatic decrease in the beginning of the hail fall. There is a positive time lag between the jumps of both multiplicity and flash rate and start of large hail falls in the three studied thunderstorms. The established jump in the flash rate before the large hail fall corresponds to the results reported by *Kane* (1991), *Soula et al.* (2004), and *Williams et al.* (1999). Laboratory results in *Brooks et al.*, 1997 show that the magnitude of separated charge is higher at higher liquid water content and velocity of interacting particles. Based on that one can assume that the flash rate increases sharply at the increase of supercooled water and updraft velocity which also lead to the growth of large hail. Thus, an increase in the CG lightning rate may consider as an indication of the subsequent falling of damage hail on the grounds. One possible reason for the decrease of flash rate at the beginning of intensive hail fall is the diminution of charge density due to the fall out of charged particles from thunderstorm cloud.

The mean and maximum values of total flash rate, as well as of the multiplicity of negative strokes in MC and SC storms are remarkably lower than in MSC storm. In the frame of the present study, the reason for the dramatically higher values of flash rates in MSC storm in comparison to those for MC and SC storms is not clear. One can speculate that this results from the more intensive vertical development during the severe stage of MC and SC storms in comparison with MSC storm. *Lang et al.*, 2000, obtained similar results and suggested that a possible explanation could be the elevation charge hypothesis (*MacGorman et al.*, 1989), namely that strong updraft prevents the formation of dipole structure due to the elevation of interacting ice particles (ice crystals and graupel) at higher level. In the supercell storm, SC, the lightning "hole" in the flash density is observed. The hole is associated with a bounded weak-echo region (BWER) of the cell, respectively with a strong updraft in this region (*Lang et al.*, 2000, *MacGorman et al.,* 2005, 2008, *Wiens,* 2005). We supposed that two processes are responsible for the lack of lightning in this region – the elevation of the interacting ice particles by very strong updraft (*MacGorman et al.,* 2005, 2008) and reduction of the amount of charge separation by rebounding collisions of ice particles in regions where hail is in a regime of wet growth (*MacGorman* et al., 2012; *Murphy* and *Demetriades,* 2005).

The present study reveals that most of the lightning signatures in the studied severe thunderstorms developed over Bulgaria are similar to those in other geographical regions, and the results are promising that lightning activity information can be used as an indicator for the occurrence of large hail on the ground over Bulgaria. One can speculate that the significant difference in some lightning characteristics of the three types of thunderstorms supports the conclusion by *Fehr et al.* (2005) that the convective organization plays a crucial role in lightning development. Due to the limited number of the studied cases, the results presented here have to be considered only as a first step to the study of lightning behavior from severe thunderstorms over Bulgaria. For firm conclusions, the analysis of lightning characteristics of more severe thunderstorms producing damaging hail has to be carried out in order to establish a broader statistical basis.

Acknowledgements–The authors are grateful to Hail Suppression Agency in Bulgaria for radar information and LINET for reliable lightning data. The present work is partially supported by the Science Foundation of Sofia University (Grant 170/2011)

References

Betz, H.-D., Schmidt, K., and *Oettinger, W.P.,* 2008: LINET – An International VLF/LF Lightning Detection Network in Europe. In (Eds. *H.-D. Betz, U. Schumann, and P. Laroche*) Lightning: Principles, Instruments and Applications, ch. 5, Dordrecht (NL), Springer.

Betz, H.-D., Schmidt, K., Oettinger, P., and *Wirz, M.,* 2004: Lightning detection with 3D-discrimination of intracloud and cloud-to-ground discharges. *J.Geophys. Res. Lett. 31*, L11108. doi:10.1029/2004GL019821.

Betz, H.D., Schmidt, K., Laroche, P., Blanchet, P., Oettinger, W.P., Defer, E., Dziewit, Z., and *Konarski, J.,* 2009: LINET— An international lightning detection network in Europe. *Atmos. Res. 91*, 564–573.

Bluestein, H.B. and *MacGorman, D.R.,* 1998: Evolution of cloud-to-ground lightning characteristics and storm structure in Spearman, Texas, tornadic supercells of 31 May 1990. *Mon. Weather Rev. 126*, 1451–1467.

Brooks, M., Saunders, C.P.R., Mitzeva, R., and *Peck, S.L.,* 1997: The effect on thunderstorm charging of the rate of rime accretion by graupel. *J. Atmos. Res. 43*, 277–295.

Carey, L.D. and *Buffalo, K.M.,* 2007: Environmental control of cloud-to ground lightning polarity in severe storm. *Mon. Weather. Rev. 135*, 1327–1353.

Carey, L.D. and *Rutledge, S.A.,* 1996: A multiparameter radar case study of the microphysical and kinematic evolution of a lightning producing storm. *Meteor. Atmos. Phys. 59*, 33–64.

Carey, L.D. and *Rutledge, S.A.,* 1998: Electrical and multiparameter radar observations of a severe hailstorm. *J. Geophys. Res. 103*, 13979–14000.

Carey, L.D., Rutledge, S.A., and *Petersen, W.A.,* 2003: The Relationship between Severe Storm Reports and Cloud-to-Ground Lightning Polarity in the Contiguous United States from 1989 to 1998. *Mon. Weather Rev. 131*, 1211–1228.

Curran, E.B., and *Rust, W.D.,* 1992: Positive ground flashes produced by low-precipitation thunderstorms in Oklahoma on 26 April 1984. *Mon. Weather. Rev. 120*, 544–553.

Deierling, W. and *Petersen W.,* 2008: Total lightning activity as an indicator of updraft characteristics. J. *Geophys. Res. 113*, D16210, doi: 10.1029/2007JD009598.

Dimitrova, Ts., Mitzeva, R., and *Todorova, A.,* 2009: Lightning activity in rain and hail bearing thunderstorms over Bulgaria. Preprints 5th European Conference on Severe Storms, Landshut, Germany, 12–16 October 2009, 239–240

*Fehr, Th., Dotzek, N.,*and *Höller, H.,* 2005: Comparison of lightning activity and radar-retrieved microphysical properties in EULINOX storms. *Atmos. Res. 76*, 167–189.

Gilmore, M.S. and *Wicker, L.J.,* 2002: Influences of the local environment of supercell cloud-to-ground lightning, radar characteristics, and severe weather on 2 June 1995. *Mon. Weather. Rev. 130*, 2349–2372.

Goodman, S.J. , Blakeslee T.R., Christian, H., Koshak, W., Bailey, J., Hall, J., McCaul, E., Buechler, D., Darden, C., Burks, J., Bradshaw, T., and *Gatlin, P.,*2005: The North Alabama Lightning Mapping Array: Recent severe storm observations and future prospects. *Atmos. Res. 76*, 423–437

Kane, R.J., 1991: Correlating lightning to severe local storms in the northeastern United States. *Weather Forecast. 6*, 3–12.

Lang, T.J. and *Rutledge, S.A.,* 2002: Relationships between convective storm kinematics, precipitation, and lightning. *Mon. Weather. Rev. 130*, 2492–2506.

Lang, T.J., Rutledge, S.A., Dye, J., Venticinque, M., Laroche, P., and *Defer, E.,* 2000: Anomalously low negative Cloud-to-ground lightning flash rates in intense convective storms observed during STERAO-A. *Mon. Weather Rev. 128*, 160–173.

Lang, T.J, Miller, L.J, Weissman, M., Rutledge S.A., Barker III, L.J., Chandrasekar, V., Detwiler, A., Doesken, N., Helsdon, J., Knight, C., Krehbe, P, Lyons, W.A., MacGorman, D., Rasmussen, E., Rison, W., Rust, W., and *Thomas, R. J.,* 2004: The severe thunderstorm electrification and precipitation study. *B. Am. Meteorol. Soc. 85*, 1107–1125.

MacGorman, D.R. and *Burgess, D. W.,* 1994: Positive cloud-to-ground lightning in tornadic storms and hailstorms. *Mon. Weather Rev. 122*, 1671–1697.

MacGorman, D. R., and *Nielsen, K. E.*, 1991: Cloud-to-ground lightning in a tornadic storm on 8 May 1986. *Mon. Weather Rev. 119*, 1557–1574.

MacGorman, D.R., Emerisc, C., and *Heinselman P.L.*, 2012: Lightning activity in a hail-producing storm observed with phased-array radar. 22nd International lightning detection conference, Broomfield Colorado, USA, 2–3 April 2012.

MacGorman, D.R., Burgess, D.W., Mazur, V., Rust, W.D., Taylor, W.L., and *Johnson, B.C.*, 1989: Lightning rates relative to tornadic storm evolution on 22 May 1981. *J. Atmos. Sci. 46*, 221–250.

MacGorman D.R., Rust, W.D., Krehbiel, P., Rison, W., Bruning, E., and *Wiens, K.*, 2005: The electrical structure of two supercell storms during STEPS. *Mon. Weather Rev. 133*, 2583–2607.

MacGorman, D.R., Rust, W.D., Schuur, T.J., Biggerstaff, M.I., Straka, J.M., Ziegler, C.L., Mansell, E.R., Bruning, E.C., Kuhlman, K. ., Lund, N.R., Biermann, N.S., Payne, C., Carey, L.D., Krehbiel, P.R., Rison, W., Eack, K.B., and *Beasley, W.H.*, 2008: TELEX: The Thunderstorm Electrification and Lightning Experiment. *B. Am. Meteor. Soc. 89*, 997–1013.

Maier, M. W., Krider, E. P., 1982: A comparative study of cloud-to-ground lightning characteristics in Florida and Oklahoma thunderstorms. Twelfth Conference on Severe Local Storms, San Antonio, *Am. Meteor. Soc*, 363–367.

McKinney, C.M., Carey, L.D., and *Patrick, G.R.*, 2008: Total lightning observations of supercells over north central Texas. *Electron. J. Severe Storms Meteor. 4(2)*, 1–25.

Montanya, J., Soula, S., and *Pineda, N.*, 2007: A study of the total lightning activity in two hailstorms. *J. Geophys. Res. 112(D13)118*, doi:10.1029/2006JD007203.

Montanya, J., Soula, S., Pineda, N., Van der Velde, O., Clapers, P., Sola, G., Bech, J., and *Romero, D.*, 2009: A study of the total lightning activity in a hailstorm. *Atmos. Res. 91*, 430–437.

Murphy, M. J. and *Demetriades, N.W.S.*, 2005: An analysis of lightning holes in a DFW supercell storm using total lightning and radar information. Extended Abstracts, Conf. on Meteorological Applications of Lightning Data, San Diego, CA, Amer. Meteor. Soc.

Orville, R. E., Huffines, G. R., Burrows, W. R., Holle, R. L., and *Cummins, K.*, 2002: The North American Lightning Detection Network (NALDN)- First results: 1998–2000. *Mon. Weather Rev. 130*, 2098–2109.

Ray, P.S., MacGorman, D.R., Rust, W.D., Taylor, W.L., and *Rasmussen, L.W.*, 1987: Lightning location relative to storm structure in a supercell storm and a multicell storm. *J. Geophys. Res. 92*, 5713–5724.

Reap, R.M. and *MacGorman, D.R.*, 1989: Cloud-to-ground lightning: Climatological characteristics and relationships to model fields, radar observations, and severe local storms, *Mon. Weather Rev. 117*, 518–535.

Saunders, C.P.R., 1993: A review of thunderstorm electrification processes. *J. Appl. Meteorol. 32*, 642–655.

Saunders, C.P.R., Keith, W.D., and *Mitzeva, R.P.*, 1991: The effect of liquid water on thunderstorm charging. *J. Geophys. Res. 96*, 11007–11017.

Seimon, A., 1993: Anomalous cloud-to-ground lightning in an F5-tornado producing supercell thunderstorm on 28 August 1990. *B. Am. Meteor. Soc. 74*, 189–203.

Sheridan, S.C., Griffiths, J.H., and *Orville, R.E.*, 1997: Warm season cloud-to-ground lightning – precipitation relationship in the South-Central United States. *Weather Forecast. 12*, 449–458.

Smith, S.B., LaDue, J.G., and *MacGorman, D.R.*, 2000: The relationship between cloud-to-ground lightning polarity and surface equivalent potential temperature during three tornadic outbreaks. *Mon. Weather Rev. 128*, 3320–3328.

Sorriano, L.R., De Pablo, F., and *Diez, E.G.*, 2001: Relationship between convective precipitation and cloud-to-ground lightning in the Iberian Peninsula. *Mon. Weather. Rev. 129*, 2998–3003.

Soula, S., Seity, Y., Feral, L., and *Sauvageot, H.*, 2004: Cloud-to-ground lightning activity in hail-bearing storms. *J. Geophys. Res. 109*, D02101, 1–13.

Steiger, S.M., Orville, R., and *Carey, L.D*, 2007: Total lightning signatures of thunderstorm intensity over North Texas, Part I: Supercell. *Mon. Weather Rev. 135*, 3281–3302.

Stolzenburg, M., 1994: Observations of high ground flash densities of positive lightning in summertime thunderstorms. *Mon. Weather Rev. 122*, 1740–1750.

Taylor, W.L., 1973: Electromagnetic radiation from severe storms in Oklahoma during April 29–30 1970. *J. Geophys. Res. 78*, 8761–8777.

Turman, B.N. and *Tettelbach, R.J.*, 1980: Synoptic-scale satellite lightning observations in conjunction with tornadoes. *Mon. Weather Rev.108*, 1878–1882.

Wiens, K.C., Rutledge S.A., and *Tessendorf, S.A.*, 2005: The 29 June 2000 supercell observed during the STEPS. Part II: Lightning and charge structure, *J. Atmos. Sci. 62*, 4151–4177.

Williams, E.R., 1985: Large-scale charge separation in thundercloud, *J. Geophys. Res. 90*, 6013–6025.

Williams, E.R., Boldi, B., Matlin, A., Weber, M., Hodanish, S., Sharp, D., Goodman, S., Raghavan, R., and *Buechler, D.*, 1999: The behavior of total lightning activity in severe Florida thunderstorms. *Atmos. Res. 51*, 245–265.

Williams, E.R., Mushtak, V., Rosenfeld, D., Goodman, S., and *Boccippio, D.*, 2005: Thermodynamic conditions favorable to superlative thunderstorm updraft, mixed phase microphysics and lightning flash rate. *Atmos. Res. 76*, 288–306.

IDŐJÁRÁS
Quarterly Journal of the Hungarian Meteorological Service
Vol. 117, No. 3, July – September, 2013, pp. 315–358

Agrometeorological research and its results in Hungary (1870–2010)

Gábor Szász

University of Debrecen, Centre for Agricultural and Applied Economic Sciences, Institute for Land Utilisation, Technology and Regional Development, Agrometeorological Observatory, Böszörményi út 138, H-4032 Debrecen, gszasz@agr.unideb.hu

(Manuscript received in final form June 12, 2012)

Abstract—Agrometeorology is the branch of atmospheric sciences. Lately, modern agrometeorology has been based on exact principles and its findings are of interdisciplinary nature. The focal questions of agrometeorology are determined by the climate of large regions; therefore, its material division is specified by the local nature of the climate system and its methods are systematized by macro- and micrometeorology. Agrometeorology can be regarded as a group of determinant aspects of economic decisions. This publication summarizes the 150 years of development of agrometeorology in Hungary.

Key-words: history of agriculture in Hungary, agrometeorology, climatology, agroclimatology, productivity, weather sensitivity, hazards, water supply of crop canopy, evaporation, production, fertility, actual and potential production

1. Introduction

The ancient cultures had been continuously extending due to the knowledge created by the accumulation of observations. The specialization of this knowledge base created the fundamentals of specialized sciences as a result of the integration of sciences. Of these, the production activity dealing with the issues of human nourishment was developed, as well as the range of consumers which stems from human needs and these two were equally regulated by the climatic endowments of the environment whose risky significance has a global effect even nowadays. Through the centuries, agricultural production and social consumption, as well as the risk range of these two got into an increasingly close connection with each other which resulted in the forceful development of interests of connections towards each other and the deepening of these interests. During the modernization of agriculture, the climatic risk has been continuously increasing with the development of the consumer society. As a result, an increasingly complex connection has been developed between the agriculture and the climatic environment. The research area of agrometeorology arose from this field, as agrometeorology is meant to explain the causal chain of the biological consequences triggered by the physical effects of the atmosphere with the consideration of the causal order. It follows from this statement that the database of agrometeorology and the nature of its treatment methods is such a partial complex of the meteorological bases that concludes to the physical explanation and consequences of the effects elicited by the atmosphere.

2. *Preliminaries of agrometeorological research in Hungary (1850-1950)*

Temperate zone modern agriculture roots back into the 13th–16th century in England and the Netherlands. By this time, the history-forming period of great European migrations was over and a seemingly more permanent agriculture unfolded which rooted in the ancient fundamentals and which also provided the basis for modern agriculture that developed in the subsequent centuries. In the centuries after the millennium, there was no agriculture in a sense of that is called agriculture today. The increased population in the mentioned areas demanded an extremely intensive grazing animal husbandry whose environmental conditions were mainly provided by the favorable climatic endowments. This development resulted in severe natural consequences and they are regarded as the first revolution of agriculture in history. As a result of the heavy use, soils gradually lost their fertility. The soil degradation caused by soil use strongly deteriorated the ecological balance (*Overton* and *Campbell,* 1996; *Allen,* 1999; *Campbell,* 2010). The dilemma of losing the ecological balance resulted in an episode of developing agriculture which was regarded as an imperative condition in relation to the elimination of the crisis. Following the abolition of the aggravating circumstances, a more modern agriculture was developed in a few centuries, involving closed-loop animal husbandry, while crop rotations also became widely used and various methods of cultivation were also becoming increasingly widespread. This modernization became a general characteristic of agriculture inside the continent in a few centuries.

By the middle of the second millennium and the subsequent centuries, the production techniques applied for various climatic characteristics penetrated the Carpathian Basin. The production of western European, relatively more water demanding crops increased, the problems of water management regularly causing mediterranean droughts in the summer became more frequent, new plant species and varieties appeared, and these all contributed to the modernization of the Hungarian agriculture.

The region of Central European agriculture was the meeting point of the effects coming from these three directions, and the simultaneous benefits and complexity could be detected in the history of the past of Hungarian agriculture. *Fig. 1* shows the direction of the peculiarities characterizing the agriculture which evolved as a result of the mentioned climatic effects and the various large territorial differences.

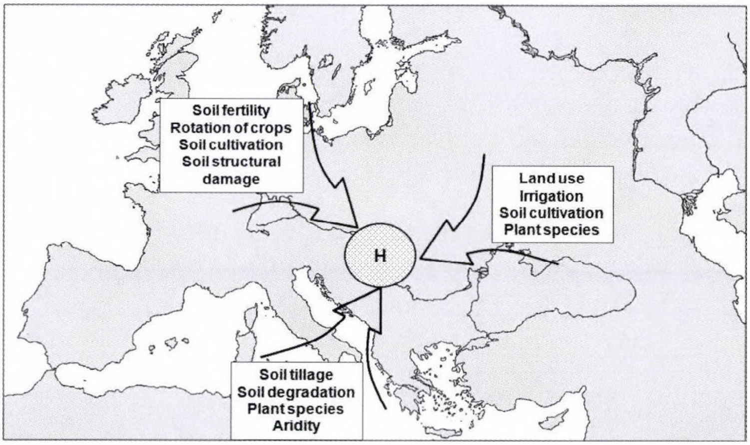

Fig. 1. Development dynamics of modern agriculture in Central Europe (1200-1600)

The conservative layer which is not adjusted to the given climate was struck by the extending cropping area of *newly produced plants* and the lack of *professional knowledge*. Simultaneously with the increasing change and modernization of the production structure, the processing industry was forcibly developed, resulting in what is called technical development.

The growth of agricultural production of this period was characterized by a less powerful prosperity and issues, in which the strong consequences of climatic effects were obvious developed and the dependence on these effects was also necessary. Since agriculture was based solely on natural resources at this time, the various soil characteristics and the consequence of the correlation between climate and soil also had an essential role in addition to climatic factors. The differences in the environment of the areas of the Carpathian Basin which are suitable for agricultural production played a very important role not only in the climate, but also in the soil characteristics. This role provided the basis for getting to know the empirical correlations and phenomena of subsequent agrometeorological knowledge.

There was limited receptiveness concerning development opportunities in the 18th century, mainly due to the social structure. The elements of production modernization were created almost only by the so-called allodial plot system. The smaller feudal farms represented the less favored social class.

In the 19th century, natural sciences developed sharply, resulting in the further intensification of agriculture. As a result of the increasing demand for new knowledge in the 1800s, agricultural higher education institutions were established which prepared professionals who constituted the intellectual basis of development. These were the institutions (Keszthely 1797, Magyaróvár 1850, Debrecen 1867) where agricultural climatology evolved in Hungary, as "Climatology" was an obligatory subject in the education program. Also, the outstanding teachers of these institutions provided the intellectual basis that was able to accept various forms of modernization. Simultaneously with the scientific basic education, field experiments were launched in a relatively narrow framework. In these trials, the determinant role of climatic effects which regulate yield were of chief importance in addition to cultivation and nutrient management. These issues necessitated the increasing range of research complexity.

The establishment of the National Meteorological and Earth Magnetic Science Institute (1870) was a significant event. Within this institution, an agrometeorological department was also established in addition to the more special data and knowledge collection activities, although it stopped working in the subsequent decades. The station network of the former meteorological institute published climatic data in various forms still used by educated agriculturalists and researchers with significant efficiency. The so-called agricultural experimental stations were also established in this period. In these stations, the climatic information was of significant scientific value.

Mention has to be made of the results of technical development launched in the second half of the 1800s. During the targeted planning processes, this development always considered the climatic parameters that provide information to build various constructions. Last but not least, it has to be noted that agrometeorology is a field of climatology which makes it possible to consider the efficiency of an agricultural technological system. From this viewpoint, Hungarian agrometeorological research left room for development for the succeeding generations.

In the first half of the 1900s, the agricultural use of meteorological information significantly served the research of climatic examination results which cannot be missing from agricultural development. Therefore, the publication of the standard time series of various weather elements was of primary importance. Based on these results, it was possible to launch agroclimatological research subsequently (*Smith*, 1915; *Cserháti*, 1905; *Gyárfás*, 1922; *Kreybig*, 1953; *Boncz*, 1992; *Nyíri*, 1993; *Kemenessy*, 1964; *Birkás*, 2006; *Györffy*, 1990).

The increasing development resulted in a production increase that created the basis of the economic crisis by the first half of the 1800s. As a result, the evaluation and thorough research of climatic effects was done rather slowly. In this period, the main tasks of the National Meteorological Institute were the gradual extension of climatic data collection, the improvement of its system, their collection in a few decades, the publication of the several year averages of the main elements, as well as the performance of technically limited forecasts.

The activity of the institute resulted in the simple information basis on which agrometeorology was built up.

In this period, no specific agrometeorological research was launched, but some researchers were already dealing with climate effect issues that affect agriculture, mainly with the aim to determine the extent of climate damages. The observation series performed between 1901–1930 made it possible to estimate the climate effects based on several decades, but these data were still mainly in connection with climatic extremities, and no more detailed statistical analysis was performed. The basis of examinations was the determination of the climatic differences between low and high yields concerning not more than a few smaller regions. In the subsequent decades of the millennium, there were yield series which provided an opportunity to analyze and explain the fluctuation of yields due to climatic reasons.

The reason for the late launching of agrometeorological research was not the lack of interest, but the simultaneous lack of knowledge about crop production and climate, although this issue arose as a problem independent of historical influences in an agriculturally significant country.

In the first decades of the 1900s, the preparation for war, the difficult economic circumstances caused by the First and Second World Wars, and the subsequent social change did not make it possible to further improve the related research. Despite the fact that the already traditional climatic observations coupled with the poor and significantly mutilated education system became incapable of functioning, tasks driven by new goals and the launching of these tasks became necessary.

3. Expansion of agrometeorological research (1950-2010)

In Hungary, the economic change after the Second World War took nearly ten years. The new fundamentals of the agricultural area and the change of farming methods root back to 1960. Also, this period marks the beginning of the modernization of agriculture. The reorganization of crop production was started, mainly by the replacement of crop species, partially the increasing use of *fertilizers* due to the lack of organic manure and further improvement of soil fertility. Within the *more modern agriculture*, the sensitivity to weather increased in crop production, also resulting in the growing production risk. This large change increased the demand for climatological information. This need was expressed in numerous forms, several different agricultural service research institutes were formed, some of which also performing various meteorological observations, measurements, and research activities that served agriculture directly (see later).

The manifold development elicited the fundamental change of the *agroecological approach* and a change of direction: research built on various natural science bases was becoming wider and the integrated system of knowledge was also extending. In the initial phase of development, the opportunities of intervention were gradually increasing with the extension of technological elements, but the long-term consequences of the interventions, their mechanisms, and the correlations of these remained unknown for the most part. Practically, the complex representation and mapping of the dynamics which can be observed in the field could not be done. The main question was posed: what could be the most important new method and system which can help in directly exploring the efficiency of interventions? It could be regarded as a historical point when the idea of launching complex *long-term experiments* was conceived.

The examinations covered not only the plant, but also the environmental factors which directly or indirectly affect the vital functions of the plant. These examinations are mainly built on biological, chemical, and physical rules. Only a narrow range of empirical methods can be observed in the basic concept of these examinations. Instead, the system of parameters which can be described in an exact way by explaining the causal conditions became more extended.

The agroecological systems have a specific energy and material flow. The factors governing the whole system are

- created by humans,
- driven by solar energy,
- maintained by the energy and material source and of the environment, as well as its flow,
- regulated by humans.

Therefore, the aim of natural science examinations is not to question the correctness of observations, but to get to know and describe exactly the assumed consequence. The dynamic approach built on the principle of causality lays the main emphasis on the importance of getting to know the processes. While the static approach is condition-focused, the dynamic approach focuses on the process. In addition to climate, soil can also be regarded as an environmental factor, although its characteristics are totally different than those of the atmosphere. Still, its conditions can greatly vary between crop years and the reason of this phenomenon is partly the climate effects, but also the use and effect of technological factors which are adjusted to the climatic conditions, too. Therefore, the effect of climate affects the physical condition of the air space close to the surface, and it has an indirect and altering effect through the soil as well. By doing so, the air, soil, and plants form a specific system in a physical sense, which is basically an ecological system of the nature (*Szász*, 1987; *Petrasovits* and *Balogh*, 1974).

The process-focused analysis of each question of modern crop production can only be performed if their basis is constituted by a scientific information system in which the criteria that meet the hierarchic principles are strictly met. This new approach set an ideal aim to perform the integrity role of cooperating branches of science; therefore, to be a cooperating research partner of meteorological research (*Monteith*, 1975; *Várallyay*, 2008).

As a matter of course, the development of the approach of agrometeorology cannot neglect climatological and meteorological measurements and the development of a database derived from their data, on which the narrowly interpreted agrometeorology is built. In other words, no agrometeorological examinations can be performed without climatological bases, since these areas of science systematize the effects which act on agriculture over time, and agrometeorology works out the explanation of the responses to these effects. Therefore, this is the reason why the main activity of agrometeorology cannot be observed without knowing the climatic examination of the country which is described by the section about the main characteristics of the climate of Hungary (*Várallyay et al.*, 1980).

4. Climatic description of the flat regions of the Carpathian Basin

The climatological information on which agrometeorological examinations are built could be summarized as follows. It has to be emphasized that these data mainly refer to the relatively flat areas where the widely interpreted crop production has been carried out for centuries.

4.1. Radiation

The measurement of the energy of radiation was started after the 1900s, instruments were used to perform these measurements only on a few stations guided by the National Meteorological and Earth Magnetic Science Institute (OMFI) in the 1930s. Simultaneously with the network measurements, statistical analyses were also performed with the aim to determine the correlation between the measured sunshine duration and the daily duration of relative radiation. The aim was to get to know the average regional distribution of the radiation energy calculated on the basis of the sunshine duration measurements performed at 30-40 stations. In the 1950s, based on the research done by *Dobosi* and *Takács* (1959), the radiation balance could be determined on the basis of calculation. The first measurements aimed at determining the radiation balance were launched by the OMFI and the Agrometeorological Observatory of the former Agricultural Academy of Debrecen, which carried out regular measurements and energy flow examinations.

Radiation measurements were integrated into micrometeorological measurement programs (Berényi-Hesse, Hortobágy, 1962, OMFI-Balaton program 1958-1962, etc.), while some radiation measurements were carried out on demand at various agricultural research institutes (crop production, horticultural, agroecological research programs at Matronvásár MTA, University of Gödöllő, Debrecen, Keszthely, Szarvas, etc.)

The first step towards working out the method of estimating the photosynthetic proportion of radiation in Hungary was made by *Felméry* (1974).

By the millennium, the database of agrometeorological research needs was provided by a network which consisted of around 40 stations. This network helped to establish the research school whose leaders (*Takács,* 1972; *Dobosi,* 1972; *Major,* 1985) laid down the basis of the research and analysis of radiation measurements in Hungary. Furthermore, this network also provided other research locations (universities, research institutes, around 10 stations) with radiation data.

Based on the published measurement results related to the radiation energy supply of the agricultural area and the collected and organized measurements of the components of radiation flow, it can be stated that the energy supply of the Carpathian Basin significantly exceeds that of the agricultural areas at the same latitude.

Radiation is a meteorological element with two components, as the duration of radiation which is generally characterized by sunshine duration and the characteristics of the temporal and spatial features of radiation energy can be used both in theoretical and practical terms.

The temporal and spatial values of *sunshine duration* can be determined on the basis of the following important information:

- astronomic sunshine duration,
- temporal and spatial distribution of the quantity of radiation energy.

The *astronomic sunshine duration* is determined by the position of the Sun and the Earth to each other, and its value is referred to the solid angle of 180° if expressed in hours. The published possible sunshine duration values refer to the latitudinal degree of the country, whose monthly values are summarized in *Table 1*. The extreme values of the yearly solar cycle of the potential sunshine duration refer to the lowest and highest sun height days, expressed in hours/month and hours/day. The monthly and yearly sums (in geographical terms) of the potential sunshine duration slightly differ from each other due to the small range of the related surface. The yearly average sum of the potential sunshine duration is 4450 hours. The daily, monthly, and yearly sums of the actual sunshine duration are determined by geographical and climatological factors, of which the most important are the relief (due to the difference in the reference solid angle) and the clouds (due to climatological reasons). The monthly sums of the potential sunshine duration are shown in *Table 1*, where the actual monthly sunshine duration values are expressed in hours.

Despite the relatively small area of the country, there are average differences in the regional distribution of the sunshine duration mainly due to climatic reasons (clouds, fog). The regional difference of the average yearly sums exceeds 350 hours annually even in flat areas. According to the detailed examinations of *Takács*, the lowest yearly sums develop around the western and southwestern bordering areas of the Transdanubian region, where the yearly sum does not exceed 1700 hours. The area which is the richest in sunshine is the southern Danube-Tisza mid-region and the southern areas of the Trans-Tisza region, whose regional proportion is shown in *Fig. 2*.

Table 1. Monthly actual, possible and relative sunshine duration in Hungary

Month	**Actual**	**Possible**	**Relative**
	Sunshine duration		
Januar	2.0	8.9	0.22
February	3.0	10.2	0.29
March	4.5	11.8	0.38
April	6.1	13.5	0.45
May	7.8	15.0	0.52
Juny	8.5	15.7	0.54
July	9.2	15.4	0.60
August	8.5	14.2	0.60
September	6.4	12.6	0.51
October	4.3	10.9	0.39
November	2.3	9.3	0.25
December	1.5	8.3	0.18

Based on the research done by *Takács* and *Major*, as well as *Dobosi*, the temporal and spatial distribution of global solar radiation was processed by *Dávid et al.,* (1990), using the data of the period between 1951–1980 (*Distribution of the radiation balance in Hungary based on the data between 1951-1980, 1990.*). This work gives information concerning the monthly energy sums of the global radiation related to 44 polygons of the country, as well as the average values which determine the radiation balance.

4.2. Temperature

Air temperature values determined in accordance with climatological averages provide a wide range of information and they are published to a detailed extent. The agricultural consequences of the variability of temperature are commonly known. Nevertheless, the response reactions of the effect of different variability cannot be neglected either, as the reactive heat demand of the plants are constantly changing. It is one of the tasks of the modernization of agroecological research to analyze the climate sensitivity of various culture plants. While the determination of optimal heat demand was in focus in the past decades, manifold consequences of the effects of tolerance to extremities and heat stress had to be taken into consideration in the recent decades. The system of related agrometeorological knowledge is still incomplete. The traditional methods of temperature observations and the demand-focused information system of agriculture only partially satisfy this need (*Bacsó*, 1952, 1959).

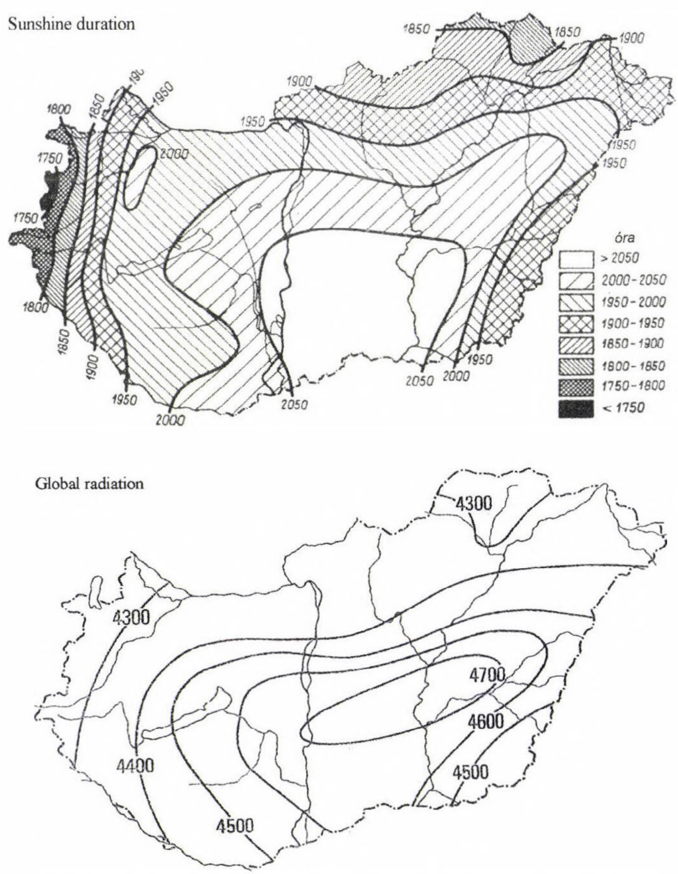

Fig. 2. Annual average of sunshine duration and the sum of global radiation (MJ m^{-2} $year^{-1}$) in Hungary (*Takács*, 1972; *Major*, 1985).

The agroclimatological characterization of temperature could be summarized on the basis of means, standard deviations, and the coefficient of variance. *Table 1* shows monthly mean temperatures of 100 years and the related statistical parameters of the 5 stations. Based on the multiple year mean values of this table, significant difference is shown between the various areas of the country. The yearly mean temperature is between 9–11 °C in Hungary. The yearly fluctuation is characterized by the difference between the mean temperature in July and January, and the extent of fluctuation continuously decreases from eastern Hungary to the west, whose value is around 20–21 °C. Typically, the interim seasons are long from agricultural aspect and this phenomenon lengthens the vegetation period (*Aujeszky et al.*, 1951).

The 50–50 and 100-year monthly mean values shown in *Table 2* are rather close to each other, but it can only partially be accepted in view of the standard deviation values; therefore, longer periods need to be considered in order to determine the statistical probability of the variability. Nevertheless, these differences are significant from climate statistical aspect, and they do not have any fundamental importance from the viewpoint of agroclimatology. The referred values clearly show the great variability of the winter period. The lowest variability evolves in the second part of summer ($s<1.5$). This statistical parameter is further increasing in the spring and autumn months ($s=1.5$–2.5), which is then finally expressed in the value of coefficient variability (CV) (*Szász,* 1981, 2005).

In field crop production, the cumulated sum of daily mean temperature values is frequently used. This topic cannot be dealt with in detail in this study, since these values represent environmental physical effect and consequence for plants which have different heat demand.

The most perfect and detailed information about the variability of temperature and the probability of its values are provided by the distribution analyses. No such analyzed research results are available from agrometeorological measurements. In order to fill this gap, *Fig. 3* shows the distributions based on daily observations of 100 years in Debrecen, showing the daily mean temperature. The distribution curves of the three summer months make it possible to gain information mainly on the probability of the extremely high or low value ranges which cannot be related to any given day, but they serve the purpose of getting to know the lower and upper limits of the tolerance of plants' needs (*Fig. 4*).

The daily fluctuation of air temperature has a practical significance in agriculture, the extent of its value is shown below:

Season	**Winter**	**Spring**	**Summer**	**Autumn**
Daily average range (°C)	4,2–7,5	7.5–13.0	11.0–14.0	5.0–13.0

The minimum and maximum values of the daily fluctuations can cause irreversible damages to various extents. In the interim seasons, the critical extreme temperature is the minimum value, while it is the maximum value that could cause stress in the summer from the aspect of the heat demand of plants (*Kakas*, 1960).

Table 2. Monthly means, standard deviation, and coefficient variation of temperature (1901–1950, 1951–2000)

Mean temperature (°C)														
Station		**I.**	**II.**	**III.**	**IV.**	**V.**	**VI.**	**VII.**	**VIII.**	**IX.**	**X.**	**XI.**	**XII.**	**Year**
Zalaegerszeg	1901–1950	–1.2	0.7	5.8	10.8	15.8	18.9	20.9	19.9	15.8	10.4	5.0	1.0	10.3
	1951–2000	–1.2	0.7	4.9	9.9	14.6	18.0	19.5	19.1	15.2	9.9	4.6	0.4	9.6
Magyaróvár	1901–1950	–1.4	0.7	5.1	10.2	15.4	18.4	20.3	19.4	15.6	10.1	4.6	0.7	9.9
	1951–2000	–1.2	0.7	5.0	10.3	15.2	18.4	20.1	19.5	15.4	10.1	4.6	0.7	9.9
Túrkeve	1901–1950	–2.3	–0.3	5.3	10.9	16.6	19.7	22.0	21.1	16.7	10.8	4.8	0.3	10.5
	1951–2000	–1.8	0.4	5.3	11.1	16.4	19.9	21.6	21.1	16.7	10.9	4.9	0.5	10.6
Szeged	1901–1950	–1.0	0.8	6.5	11.7	17.2	20.4	22.7	21.7	17.7	12.1	6.1	1.6	11.5
	1951–2000	–1.3	0.8	5.4	11.1	16.2	19.6	21.2	20.8	16.6	11.0	5.2	0.8	10.6
Debrecen	1901–1950	–2.3	–0.5	4.9	10.8	16.4	19.5	21.5	20.5	16.1	10.4	4.7	0.3	10.2
	1951–2000	–2.1	0.0	4.9	10.7	15.9	19.1	20.8	20.2	16.0	10.5	4.7	0.1	10.1

Standard deviation (S)													
Station		**I.**	**II.**	**III.**	**IV.**	**V.**	**VI.**	**VII.**	**VIII.**	**IX.**	**X.**	**XI.**	**XII.**
Zalaegerszeg	1901–1950	3.2	3.5	2.4	1.8	1.7	1.4	1.5	1.3	1.4	1.6	2.0	2.3
	1951–2000	2.6	2.7	2.2	1.6	1.6	1.3	1.5	1.6	1.5	1.6	1.9	1.8
Magyaróvár	1901–1950	3.1	3.4	2.2	1.7	1.7	1.5	1.2	1.2	1.5	1.6	1.9	2.3
	1951–2000	2.7	2.6	2.2	1.4	1.6	1.4	1.4	1.5	1.5	1.7	1.8	1.8
Túrkeve	1901–1950	3.5	3.4	2.3	1.9	1.8	1.4	1.3	1.5	1.6	1.8	2.2	2.6
	1951–2000	2.7	3.0	2.4	1.6	1.6	1.4	1.4	1.7	1.7	1.5	2.0	2.3
Szeged	1901–1950	3.5	3.5	2.5	1.9	1.8	1.5	1.5	1.7	1.7	1.7	2.0	2.5
	1951–2000	2.6	3.0	2.2	1.6	1.5	1.3	1.4	1.5	1.6	1.6	2.1	2.3
Debrecen	1901–1950	3.4	3.2	2.3	2.0	1.8	1.5	1.2	1.4	1.6	1.8	2.2	2.5
	1951–2000	2.7	2.9	2.3	1.6	1.6	1.3	1.3	1.5	1.6	1.4	2.0	2.3

Coefficient of variation (CV)													
Station		**I.**	**II.**	**III.**	**IV.**	**V.**	**VI.**	**VII.**	**VIII.**	**IX.**	**X.**	**XI.**	**XII.**
Zalaegerszeg	1901–1950	–269.4	540.8	41.0	16.4	10.7	7.3	7.3	6.6	9.2	15.8	40.1	223.5
	1951–2000	–217.9	381.9	44.5	15.7	11.0	7.5	7.5	8.4	10.1	16.4	41.2	415.2
Magyaróvár	1901–1950	–221.3	520.4	43.9	16.6	10.7	8.0	5.8	6.4	9.7	15.5	40.7	343.0
	1951–2000	–221.1	371.8	44.0	13.9	10.8	7.8	7.1	7.5	9.7	16.6	38.8	243.9
Túrkeve	1901–1950	–153.4	–1031.5	43.5	17.4	10.9	7.4	5.9	7.0	9.7	16.8	44.7	877.7
	1951–2000	–146.8	720.4	44.5	14.4	9.8	7.2	6.4	8.2	10.0	13.4	40.8	510.0
Szeged	1901–1950	–336.6	448.1	38.6	16.1	10.5	7.6	6.6	7.8	9.7	14.0	33.5	156.1
	1951–2000	–209.1	391.4	39.9	14.1	9.3	6.7	6.5	7.3	9.6	14.3	40.1	278.0
Deebrecen	1901–1950	–150.3	–660.1	47.5	18.3	10.7	7.6	5.7	6.9	9.8	17.6	47.4	727.9
	1951–2000	–133.5	6405.0	47.4	14.7	10.0	6.8	6.3	7.6	9.9	13.1	42.5	1679.5

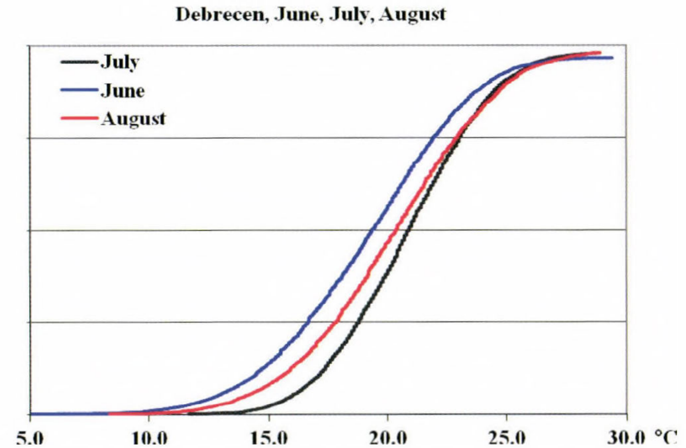

Fig. 3. Probable distribution of the daily average temperatures in summer months (Debrecen, 1901–2000).

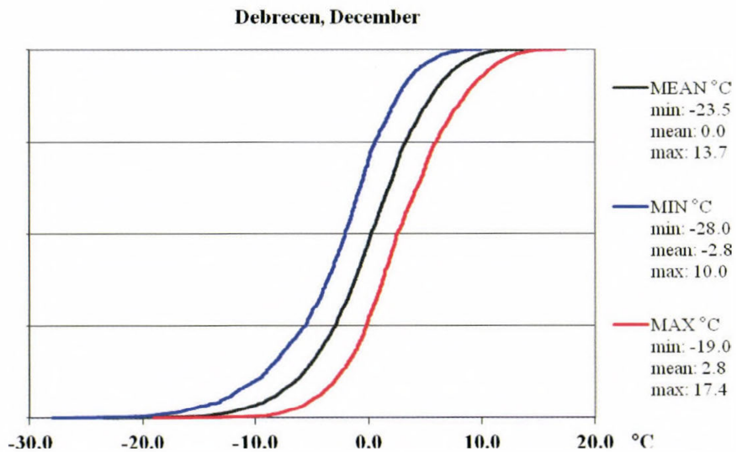

Fig. 4. Frequency distribution of the daily average and extreme temperatures in December with absolute maximun and minimum values (1901–2000).

The spring and partially the autumn temperature damages are mostly caused by radiation frosts which are developed in accordance with local conditions, such as micro relief, heat capacity of soils, etc.

There has been no frost statistical frequency analysis related to a short period of time which is based on several years of observations because of the spatial and temporal heterogeneity of frost sensitivity. *Table 3.* provides information about the frequency of frost of various strength in the region of Nyíregyháza and Kecskemét broken down to 5-day periods and expressed in a percentage which represents the duration of frost in days (*Szász,* 1988). This table shows the values calculated on the basis of the minimum temperatures measured at 200 cm height, which cannot be regarded as typical values in the lower soil layers.

Table 3. Frequency of five–day minimum temperature (Kecskemét, Nyíregyháza, 1931–1970)

Relativ frequency of different frosts, 1931–1970. Kecskemét											
	III.				**IV.**						**V.**
day	**12–16**	**17–21**	**22–26**	**27–31**	**1–5**	**6–10**	**11–15**	**16–20**	**21–25**	**26–30**	**1–5**
Frost days %	49.20	48.20	36.40	25.10	15.90	8.20	10.75	5.75	3.40	1.025	2.05
0 -(–0.9)	17.16	24.50	35.21	32.67	45.15	68.80	66.70	36.40	16.75	50.00	25.00
(–1)-(–1.9)	15.60	19.15	15.50	24.50	35.50	6.20	19.05	45.40	66.60		25.00
(–2)-(–2.9)	16.66	16.00	21.10	12.25	6.45	18.80	4.76	9.10	16.65	50.00	50.00
(–3)-(–3.9)	13.55	8.50	14.10	8.16	12.90	6.30	4.76				
(–4)-(–4.9)	11.45	11.70	5.64	16.30			4.73	9.10			
(–5)-(–5.9)	10.40	9.57	8.45	4.08							
(–6)-(–6.9)	5.21	5.32		2.04							
(–7)-(–7.9)	5.21	2.13									
(–8)-(–8.9)	3.12										
(–9)-(–9.9)	1.04	2.13									
(–10)-(–10.9)		1.00									

Relativ frequency of different frosts, 1931–1970, Nyíregyháza																
	III.				**IV.**						**V.**					
day	**11-15**	**16-20**	**21-25**	**26-31**	**1-5**	**6-10**	**11-15**	**16-20**	**21-25**	**26-30**	**1-5**	**6-10**	**11-15**	**16-20**	**21-25**	**26-31**
Frost days %	62.0	56.5	44.0	32.5	22.5	22.0	12.5	10.0	5.0	4.0	2.0	0.0	0.5	0.5	0.5	
0-(–0.9)	20.2	20.4	26.2	32.3	35.6	47.7	28.0	40.0	50.0	50.0	50.0		100.0		100.0	
(–1)-(–1.9)	22.6	23.0	25.0	30.8	22.2	31.8	40.0	10.0	30.0	25.0	50.0			100.0		
(–2)-(–2.9)	12.9	11.5	23.8	15.4	22.2	9.1	20.0	25.0	0.0							
(–3)-(–3.9)	13.7	11.5	10.2	6.2	15.6	6.8	4.0	15.0	10.0	25.0						
(–4)-(–4.9)	4.8	9.8	8.0	7.8	2.2	2.3		5.0	10.0							
(–5)-(–5.9)	10.5	5.2	6.8			2.3		5.0								
(–6)-(–6.9)	7.3	7.1		1.5			8.0									
(–7)-(–7.9)	4.0	3.5		1.5	2.2											
(–8)-(–8.9)	0.8	6.2		1.5												
(–9)-(–9.9)	0.8	0.9		1.5												
(-10)-(-10.9)	0.8	0.8														
(-11)-(-11.9)	0.8															
(-12)-(-12.9)				1.5												
(-13)-(-13.9)	0.7															

4.3. Precipitation

One of the main elements of agricultural production is precipitation, since the water supply of plants produced in Hungary is provided by natural precipitation with few exceptions. Precipitation is one of the most important aspects which determine yield. It has to be emphasized also because of the fact that the amount of precipitation in Hungary usually does not satisfy the demand posed by plants.

The level of precipitation supply is usually characterized by average sums. Temperate zone areas with continental climate usually have their maximum precipitation in the summer and the minimum precipitation in the winter. In mediterranean areas, this relation of precipitation during the year is the opposite. Since climate borders are rather variable, the different climatic characters are present in a mixed form in the Carpathian Basin (*Berényi*, 1943, 1945). From year to year, precipitation shows a rhapsodic yearly course in comparison with temperature that can be explained by the high variability of this element. Similarly to the description of temperature, the multiple-year mean values of precipitation, as well as its statistical parameters related to the 5 stations are summarized by *Table 4*. One of the most suitable statistical parameter of the variability of precipitation is the coefficient of variation (CV = standard deviation / mean). The coefficients of variation show a specific and strict yearly course in Hungary: the CV values reach their maximum (57–79%) at the beginning of spring – usually in March – and then they decrease until May and June. The minimum values fall around the time of precipitation maximum (44–63%), then they increase again until the end of summer or the first month of autumn to reach a secondary maximum (55–75%); by the winter months, the values will decrease again, but the monthly values will stay between 50 and 70%. CV values calculated for various points of the country are summarized in *Table 4*.

If the distribution of the precipitation sum of the growing season is shown on a similar scale, it can be seen that there is still a difference between the precipitation supply of the eastern and western part of the country. However, the difference between the yearly mean values of the driest and wettest areas is 300 mm per year, and the same difference in the growing season is still 300 mm, but this value refers to a significantly shorter period of time. As a consequence, the difference in the summer precipitation supply has a much stronger effect mainly on crop production, more specifically on the water balance of soils than before and after the vegetation period (*Bacsó,* 1952; *Szepesiné,* 1966).

As a matter of course, the extremes of the yearly precipitation sum take place in the southwestern areas of the Transdanubian region, which can be explained partially by relief-related reasons and partially by the current circulation status. In these areas, the range of fluctuation of the yearly sum significantly exceeds 900 mm, but the minimum amount is below 400 mm. The fluctuation range of the yearly sums of the Great Plain areas, where the usual amount of precipitation is low, is near 650 mm (*Hajósy*, 1952; *Kéri* and *Kulin,* 1953; *Szász,* 2005; *Goda*, 1966; *Péczely*, 1963, 1968).

Table 4. Sum, standard deviation, and variation coefficient of the monthly precipitation (1901–1950, 1951–2000)

		Precipition (mm)												
Station		**I.**	**II.**	**III.**	**IV.**	**V.**	**VI.**	**VII.**	**VIII.**	**IX.**	**X.**	**XI.**	**XII.**	**Year**
Zalaegerszeg	1901–1950	39	38	43	62	74	81	87	81	70	65	59	49	748
	1951–2000	31	31	42	52	72	86	84	74	64	54	63	45	698
Magyaóvár	1901–1950	37	34	38	43	66	58	65	59	52	49	52	49	602
	1951–2000	33	33	36	43	54	66	69	57	45	43	53	44	576
Túrkeve	1901–1950	27	29	33	45	56	68	55	53	44	49	48	38	545
	1951–2000	33	32	30	41	60	71	55	49	41	32	48	46	536
Szeged	1901–1950	32	34	38	49	60	67	50	48	46	51	50	40	565
	1951–2000	28	27	28	40	52	66	53	51	37	31	43	43	497
Debrecen	1901–1950	32	32	34	45	59	69	61	60	46	53	51	41	583
	1951–2000	33	32	29	44	59	77	60	58	38	33	45	45	554
		Standard deviation (S)												
Station		**I.**	**II.**	**III.**	**IV.**	**V.**	**VI.**	**VII.**	**VIII.**	**IX.**	**X.**	**XI.**	**XII.**	
Zalaegerszeg	1901–1950	23.0	28.6	30.5	33.3	42.6	35.7	53.7	49.3	42.0	42.6	40.9	29.2	
	1951–2000	20.2	21.5	22.1	29.8	32.6	45.3	43.5	42.1	34.7	41.9	34.4	26.4	
Magyaróvár	1901–1950	19.5	20.3	28.8	25.8	39.1	29.5	37.2	38.3	37.0	34.3	35.0	24.6	
	1951–2000	19.9	22.2	19.9	26.0	30.0	36.3	44.4	32.2	29.4	30.2	30.6	22.9	
Túrkeve	1901–1950	14.3	20.3	22.8	25.1	33.0	32.8	35.9	34.6	30.7	35.5	28.0	25.6	
	1951–2000	20.9	19.7	19.5	20.2	35.8	36.7	33.2	33.2	30.0	29.9	35.2	26.3	
Szeged	1901–1950	18.6	26.1	24.4	28.3	34.2	31.6	31.0	28.8	29.1	36.2	30.9	22.9	
	1951–2000	17.9	19.7	18.0	18.8	33.4	36.3	32.9	31.4	25.7	27.7	29.7	27.8	
Debrecen	1901–1950	19.0	21.6	25.5	27.4	29.8	33.3	38.1	38.5	30.5	33.7	29.8	27.6	
	1951–2000	18.4	19.0	18.5	19.4	34.9	40.0	33.5	37.8	28.9	30.0	27.5	22.9	
		Coefficient of variation (CV)												
Station		**I.**	**II.**	**III.**	**IV.**	**V.**	**VI.**	**VII.**	**VIII.**	**IX.**	**X.**	**XI.**	**XII.**	
Zalaegerszeg	1901–1950	59	75	71	54	58	44	62	61	60	65	69	60	
	1951–2000	66	70	53	57	45	53	52	57	54	78	55	58	
Magyaróvár	1901–1950	53	60	76	60	59	51	57	65	71	70	67	50	
	1951–2000	60	68	55	61	56	55	64	56	65	71	58	52	
Túrkeve	1901–1950	53	70	69	56	59	48	65	65	70	72	58	67	
	1951–2000	64	63	65	49	60	52	61	67	72	94	73	58	
Szeged	1901–1950	58	77	64	58	57	47	62	60	63	71	62	47	
	1951–2000	64	72	65	47	64	55	63	62	70	90	69	65	
Debrecen	1901–1950	59	68	75	61	51	48	62	64	66	64	58	67	
	1951–2000	56	60	63	44	59	52	56	66	75	90	61	51	

Due to the variable nature of precipitation, exact precipitation maps can only be prepared with lots of imperfections, since the areas bordered by isohyets could also form patches of different variability. Apart from a few exceptions, a precipitation map is drawn on the basis of a *linear scale*, in accordance with the arbitrarily chosen value ranges of the so-called isohyets. Drawing up such a map is a relatively simple task, but the role of isohyets to function as borders is questionable. In reality, the difference in precipitation supply in the mentioned range has more or less similar variability. If high standard deviation is associated with the nearly identical mean values, it is possible to lose the reality of the map, since the difference between the areas limited by the isohyets which have the same values could show different probability. In order to prevent this error, the extent of distinction can be modified in accordance with the principles of statistical probability. If these principles are taken into consideration, a parting line can only be drawn between two stations if not only the mean, but also the standard deviation values of the related precipitation sums differ (*Szász*, 1968). If the standard deviations are considered, the *limit of the probability significance* can be calculated that will not necessarily be different from the averages, but the standard deviations from the mean values. The statistical precipitation map of Hungary shown in *Fig. 5* was prepared by *Szász* (1971). The precipitation sums of the areas delineated by the isohyets significantly differ from each other, while the sums did not significantly differ in the related period within the areas. Therefore, areas with homogeneous precipitation supply can be separated by using this principle. The advantage of this method can be reached by determining the number of precipitation measurement stations. Within the homogeneous fields, nearly exact precipitation sums can be determined at each optional point in the area delineated by the isohyets, even at the point where the standard deviation of the line, which is in accordance with the measurement location, is accepted. In other words, the mean values do not necessary mean identity or difference in themselves, but the standard deviation values of the two locations to be compared need to be considered in order make a decision. The determination of the difference in supply based on the statistical probabilities is necessary mainly in the areas where the mean precipitation and the related standard deviations are close to each other. The editing of homogeneous fields is by all means a complicated task, but the computerized processing removes this difficulty.

Considering the fact that the analysis of the precipitation in the country is rather manifold and numerous bibliographical sources were published in the last 50 years, we do not wish to describe any further matter of detail (*Péczely*, 1963, 1968; *Goda,* 1966; *Bacsó,* 1967; *Schirokné*, 1983).

4.4. Air humidity, evaporation

As a result of the radiation energy, significant amount of water gets into the air from wet surfaces by means of evaporation. Evaporation is a process which uses heat energy: its approximate value is 2500 kJ g^{-1}. Although the *quantity of water vapor in the air* is negligible in comparison with the mass of the atmosphere, its physical significance is rather great. The commonly known greenhouse gas effect is mostly created by water vapor. The highest possible quantity of water vapor in the air depends on temperature. The saturated vapor pressure (mbar) is the highest vapor pressure which is determined by temperature; the difference between the saturated and the actual vapor pressure is the saturation gap, a value very often used mainly during practical calculations. The ratio of the current and possible vapor pressure at a given temperature is the relative humidity, which serves the quantified expression of saturation. It has to be emphasized that the amount of water vapor present in the air space of the Carpathian Basin varies in a rather wide range (*Száva-Kováts*, 1937), which is mainly caused by the large differences in water vapor content of the air masses arriving from areas which have rather different climate.

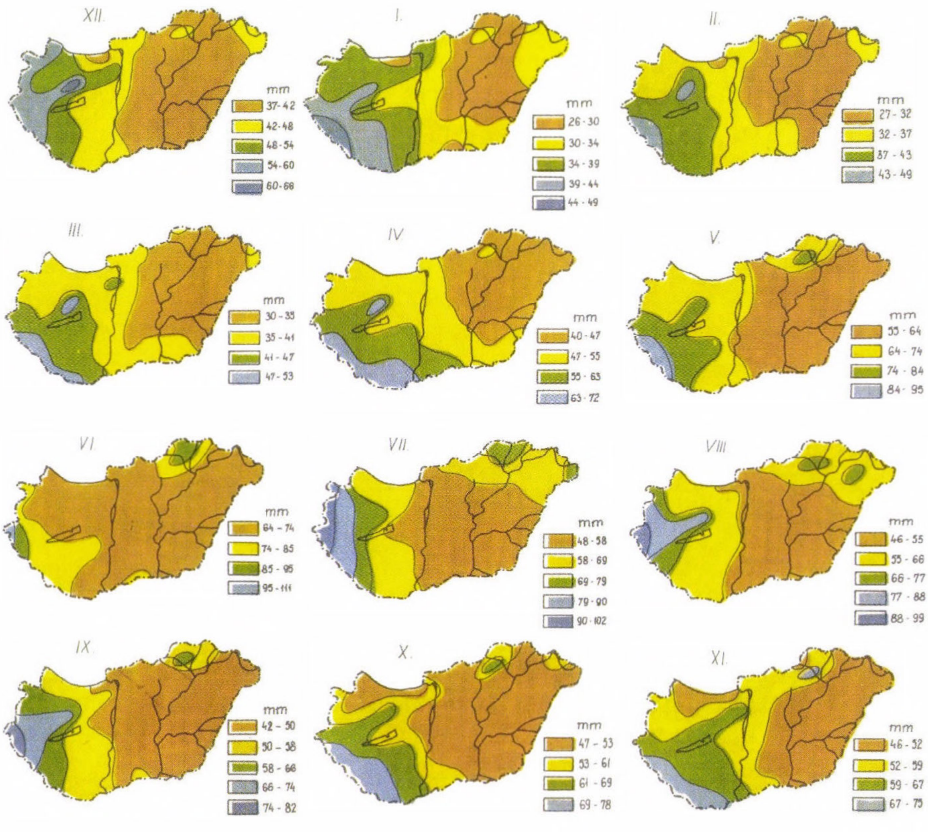

Fig. 5. Significant probable heterogeneity of monthly average precipitations in Hungary (1901–60) (*Szász*, 1971).

Nearly every meteorological element has a role in forming the conditions of *evaporation* to a different extent. The strongest regulatory factor is the incoming energy on the surface that is the absolute value of the radiation balance per unit of time. A high percentage of this energy can be used for evaporation above wet and water surfaces. The saturation deficit or the relative humidity define the intensity of the evaporation process, similarly to the increase of wind speed, which makes the *process of evaporation* more intensive with the increase of turbulence.

Evaporation is the meteorological element which cannot be measured directly; therefore, the mentioned significant factors determine the actual evaporation in a ratio which is in accordance with their importance. The actual evaporation can be estimated with various physical correlations. The amount of water which gets into the air in the form of water vapor in the case of the given physical condition of the atmosphere is called potential evaporation (P_0) (*Thornthwaite*, 1948). As a matter of fact, potential evaporation is a physical constraint, and it expresses the highest evaporation ability if the lack of water hinders evaporation. Measurements show that the evaporation of the open water surface is close to the potential evaporation. Instead of the rather complicated but reliable findings, various empirical formulae are used generally. The high number of these formulae makes it necessary to use them with precaution, because the weights of the various factors are different in areas with different climate. Theoretically, without the certification of the empirical formulae, the mentioned correlations cannot be appropriate and usable (*Fisher* and *Yates*, 1957).

Various formulae become popular in Hungary, of which the research considers the following to be worth mentioning:

Antal's method (1968): $P_0 = 0{,}74 \cdot (E-e)^{0{,}7}(1+\alpha T)^{4{,}8} \quad \left[mm\ day^{-1}\right]$,

Szász' method (1973): $P_0 = \beta\left[0{,}0056(T-21)^2(1-RN_a)^{2/3} f(v)\right] \quad \left[mm\ day^{-1}\right]$,

Varga-Haszonits' method (1977): $P_0 = \dfrac{1-RN_a}{1+RN_a} \cdot T_k$,

where T_k is the temperature, RN is the relative humidity, v is the wind speed, $(E–e)$ is the saturation deficit.

By using the empirical formulae, it is possible to determine the evaporation ability of the air (P_0), thereby providing the temporal and spatial change of the P_0 values in a wide range. Independently of climatic conditions, the extent of potential evaporation cannot exceed the equivalent of the radiation energy balance (expressed in mm) if rigorous physical criteria are considered. This form of evaporation is usually called balanced evaporation.

In order to determine the evaporation ability of the air, the evaporation-related water loss of different-sized, but standard water-filled tubs is determined.

Based on the water level differences measured in these tubs, the sum of evaporation in a day or in several days can be observed. For agricultural purposes, the evaporation loss of natural water surfaces is usually compared to this value. The examination of evaporation is almost indispensable from the practical aspect during the examination of the climatic characteristics of the country, since this is one of the strongest limiting factors in the development of crop production. In this relation, the climatic analysis of water supply problems have to be performed in order to work out the practical solutions (*Szász*, 1973a,b).

The Hungarian agrometeorological research has reached significant achievements in examining the potential evaporation in the country. Altogether, these results are suitable for the competent authorities to take the steps which are essential to implement developments such as water replenishment, irrigation, and drainage (*Kéri* and *Kulin,* 1953; *Péczely,* 1963; *Pálfai,* 2004).

The regional distribution of potential evaporation in Hungary is between 120–150 mm in the summer months. In the interim seasons, the monthly values range between 60–90 mm, while they are between 10–12 mm in the winter months. In the northern half of the Great Hungarian Plain, the value of P_0 ranges between 660–680 mm, while it reaches 800 mm in the southeastern areas of the Great Plain (*Antal*, 1968; *Szász,* 1973a,b).

The difference between the actual and potential evapotranspiration is the highest in the summer period, its regional distribution is shown in *Fig. 6*. Based on the curves in this figure, the lack of water and the difference between the actual and potential evaporation can be quantified (*Berkes,* 1946; *Antal,* 1966, 1987; *Füri* and *Kozma,* 1972, 1975, 1978; *Posza* and *Stollár*, 1983; *Dunkel et al.,* 1990; *Ács et al.,* 2007).

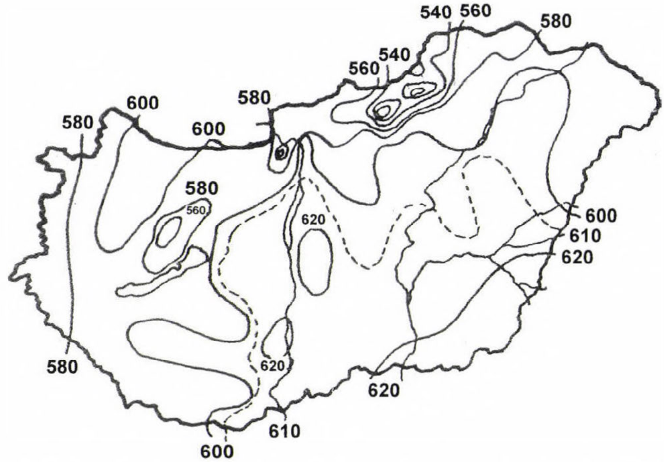

Fig. 6. Areal distribution of potential evapotranspiration in the summer half-year (1901–60).

Due to the high complexity of the problem to be solved, no numerical empirical formulae were prepared to estimate the actual evaporation, and the result of the estimation could contain non-negligible errors. The actual evaporation is significantly modified not only by the amount of available water, but also the speed differences between the water transfer of the soil and plants (*Szász,* 1988; *Ács,* 2004).

4.5. Wind

The interest of modern analyzing agrometeorology in wind speed became extraordinarily wide and deep in the last decades. The motion of air can have different direction and speed. As a matter of fact, wind is only one specific form of this motion system, representing the horizontal component of the motion of the air. The vertical movement is an especially important component of agrometeorology in the existing motion system. Wind speed increases with height, maintaining the process of energy and material transport which is directed towards the heights. The transport processes (sensible and latent heat, CO_2, pollutants, etc.) towards high levels are maintained by the air motion which has a turbulent structure, in which its vertical component plays a very important role.

In Hungary, high energy winds are relatively infrequent, the average wind speed is 2–3 m/s above flat regions. The maximum wind speed can be observed in one of the spring months and the minimum occurs usually in October. The highest wind speed values in the spring could reach 8–10 m/s and the rarely forming tornado-like speed is close to or even exceeds 20 m/s. The change of wind speed is characterized by strengthening during the day and lower values at dawn (1984).

High wind speed results in strong pressure of air. Wind pressure is proportional to the squared wind speed in reference to the surface perpendicular to the motion. These motions can cause significant mechanical damages mainly in forests or in large-leaved herbaceous plants (*Wágner* and *Papp,* 1984; *Papp,* 1974; *Tar,* 1991).

5. Climatic effects in crop production

The physical and dynamic effects on different branches of agriculture can be derived from the database of the climatological information system, and they could be either favorable or unfavorable in a differentiated way. Based on these effects, the responses or reactions whose theoretical and practical significance constitutes the basis of scientific advancement became known, and the system of effects and responses increases the concept range of agrometeorology.

We have a rather wide range of information about climate which provides the increase of knowledge with the accelerating technical development. Also, the increasing amount of information makes it more difficult to interpret research findings. Considering the fact that the information need is becoming increasingly manifold, a differentiated information system needs to be worked out. Crop production constitutes one component in the science which demands agricultural information. This means that crop production is not satisfied anymore by the traditionally processed climatic data, but it became necessary to get to know the consequences of their effects so that decisions can be made in relation to the introduction of yield-increasing technologies. The research of climate is the concern of meteorologists, but the effect of climate is a social concern. It is necessary to search for the opportunity for sciences dealing with the effect of climate to get to know the complex physical system of processes which is commonly known as agrometeorology.

The summarized findings in this area refer to the crop production-related framework of climate while looking for the opportunity of regional distinguishability in a geographical sense. These research projects could be regarded as agroecological examinations which cover the climatic factor group of the condition system of agriculture, more specifically crop production. This area of research restricts itself to the quantified determination of productivity also in relation to the approach to and the solution of modeling analyses while trying to explore the climatically potential production size in a quantified way for each region of the country based on the climatic *"constraint"* acting on various plants. The model which was worked out on the basis of this concept assumes certain simplified limit conditions, but this fact does not exclude the possibility of development. The most important objective is that the findings should well represent the role of climate in altering productivity; therefore, the climatically potential production expresses the size of climatic value (*Antal*, 1978; *Györffy*, 1976; *Hunkár*, 1990; *Jolánkai*, 1993).

For this reason, the following section provides the partial results which became commonly known as the findings of the main foreign and Hungarian research projects. All these results aimed at the quantified expression of climate as a factor which determines yield. The basis of the characterization of agrometeorology is the collection of climatic elements, which make it possible to describe the effects in an exact way in order to be able to quantify them. The brief overview of the climate of the examined area is done from this aspect.

5.1. Crop development and production

The quantified description of crop development is possible with using various models. Usually, an empirical correlation related to an impact factor in a certain form is used as a basis in an analytical form, which can be theoretically substantiated and it can be easily handled. The change of crop mass, height, its other organs over time describes the rate of development in which mass growth, development phases and the calendar dates of these phases can be determined in an exact way. The related field of science is called phenology, in which not only crop production but also genetics are significantly interested. Despite the fact that a non-linear process needs to be described, it still has to be expressed in the form of higher level functions in a mathematic form based on the temporal change of usually one climatic element (*Berzsenyi*, 2000). The use of non-recent formulae is significant and the most commonly used ones are worth mentioning here:

$$w/dt = k_1 \cdot m^{c1} - k_2 \cdot m^{c2} \qquad (Bertalanffy,\ 1941),$$

$$w = A\left(1 - b \cdot e^{-kt}\right) \qquad (Mitscherlich,\ 1909),$$

$$w = A\left(\frac{1}{1 + b \cdot e^{-kt}}\right) \qquad (Verhulst, 1838),$$

$$w = w_0 \cdot e^{kt} \qquad (Blackman,\ 1919),$$

$$w = w_0\ exp\left(\frac{\mu_0\left(1 - e^{Dt}\right)}{D}\right) \qquad (Gompertz,\ 1825),$$

$$w = w_0\ exp\left(a_1 t - a_2 t^2\right) \qquad (Richards),$$

$$\frac{dw}{dt} = \mu w\left(1 - \frac{w}{B}\right)e^{-Dt} \qquad (Chanter,\ 1976),$$

where w is the growth, k_x is a coefficient, t is the time, D is the coefficient of integration, μ is the coefficient of growth rate.

The number of optional functions is high, but the change of ontogenesis mass over time is different in the case of each species and crop year; therefore, the mentioned correlations and analyses provide a good opportunity to fulfil the target task (*Ábrányi,* 1978; *Berzsenyi*, 2000; *Szász,* 1988; etc.). According to Hungarian observations, growth curves can be effectively used in distinguishing crop year effects. Due to the changing distribution types of the parameters of multivariate functions, the extent of their usability is much lower. The growth curves are mainly realized with the use of continuous climatic elements, considering the fact that these functions describe a certain cumulative curve on various mathematical bases which necessitates the equidistant value series of the independent variable. The temporal distribution of the partial crop mass often becomes necessary to be used, e.g., stem mass, leaf mass, root mass, etc. Processing of the phenological and phenometric values in the mentioned form becomes valuable information, because the character of the curve describes the correlation between both the genetic and climatic effects. This latter question becomes useful information, because the parameters of these functions could be used to express the quantified values of the climatic reactions. For the sake of completeness, it has to be noted that the accumulation of the active temperature values above the basis temperature is a widespread method to classify the environmental conditions of several plants and also in phenological forecasts in other cases (*Berzsenyi*, 1993).

In the case of any functions which are used to describe growth, it has to be emphasized that the results do not refer to the whole vegetation period, but they mostly express the period between sprouting and flowering; therefore, they can be used for the vegetative development phase. The description of the generative phase is a more complex task, since the inner physiological processes regulate the yield increase and ripening instead of the environmental factors.

5.2. Correlation between weather and yield

This topic looks for an answer to the most important question of meteorology and crop production: in what way and to what extent do different elements regulate yield and yield quality in a separated form or together? This question is rather complex, and although we do not have universal and general equations, it is still worth summing up the currently reliable correlations, which were developed into what they are now.

The simplest correlation is the empirical one which usually verbally refers to the correlation between precipitation, temperature, and yield. Their time-enduring character is questioned and it is only rarely proven. *Bauman* (1949) worked out an empirical correlation used in crop production research by separating the crop years of high and low yields after classifying yields based on their extent. Bauman had the assumption that the best and most unfavorable weather type prevailed in these two categories. This procedure was also used in Hungary by *Berényi* in 1952 (*Berényi* 1945, 1954; *Berényi et al.,* 1959) who also analyzed the significance of the statistical difference of results. Later it was proved that Bauman's method can only be used if the weather effect is parabolic. In these cases, the optimal condition (temperature and precipitation) can be found at the intersection of two lines and its direct statistical surrounding (*Bocz* and *Szász*, 1962).

In the 1900s, correlation and regression analysis became widely used in agricultural research based on the method of *Smith* (1915). This method became common in the first half of the past century in Europe (*Holdefleiss,* 1930; *Smith,* 1915). In parallel with this, the method based on the examination of standard deviation was most commonly used in England (*Fischer* and *Yates,* 1957).

In the Hungarian agrometeorological research, the correlation methods were used in uni- and multivariate forms in order to determine the temperature and precipitation need of the main produced plants as well as their role in regulating yield (*Aujeszky, et.al.,* 1951). With this work, Berényi laid the foundations of one of the most important agrometeorological topic; therefore, several followers used this method within the framework of the yield analysis of plants (*Kerék,* 1934; *Szász,* 1955; *Justyák,* 1989; *Erdős* and *Lambert,* 1987; etc.). The correlation analysis was further developed, and the path analysis became widespread for the purpose of expressing the modification of the weight of different variables during the plant development process (*Botos* and *Varga-Haszonits,* 1974).

In the last 50 years, standard deviation analysis was used as a multifactor analytical method which can be applied to several purposes as a result of the extraordinary mathematical advancement. Its mathematical-statistical one-sidedness is shown by the fact that it is mainly widespread in the field of technical development. One of its main products is factor analysis which is only used by high-level mathematical analysts, and it is only applied in computerized model-based examinations.

Apart from these, further modern methods became very widely used which can be applied in the form of procedures built into complex systems based on probability-focused principles.

The analytical form of the correlation between weather elements and yield built on physical bases was first used in the 1950s with the following physical concept: the development of the organism of plants happens by taking up organic and inorganic substances from the soil in a chemical way, as well as by absorbing solar energy through plant vital processes and by incorporating this energy in the presence of water. This recognition immediately shows that the atmosphere has an almost exclusive role in this process, since the solar and soil surface sources of energy and water get to plants in the form of precipitation by means of meteorological processes. If the active role of solar energy is clarified, we can conclude that, through CO_2 and water – the constituents of the atmosphere –, plant life is not possible without development, growth, energy, water, and nutrients taken up from the soil. In other words, this means that the maximum mass of plant organism developed through vital processes is clearly determined by energy and water supply; that is the generator of production is energy and the fuels are CO_2 and water. The task of agriculture is to achieve the highest genetically possible vegetable production in a given place using the energy, and material stock provided by nature. The physical condition of nature is constant, while the genetic potential is changing and it can be altered by humans; therefore, only these two climatic factors form the basis upon which the mentioned criterion is expected to be realized in the form of organic matter in the future.

Temporal characterization of growth and development can be done with biophysical and chemical methods by describing photosynthesis in detail. The dry matter to be formed can be estimated on the basis of the rules of gross net assimilation and carbohydrate production. From the agrometeorological aspect, it is a fundamental question how actual and potential photosynthesis is going on and what is the ratio of the dry matter which was formed. The answer for this question is known in agrometeorology, although this ratio also involves the effect of other, non-meteorological roles of the production site, i.e., nutrient supply, soil effect, etc. This explains why the potential production can be estimated in the mentioned form since the 1950s (*de Wit*, 1954). Although the first analyses were done mainly in a global or climatic zone-focused relation

(*Lieth,* 1976), the aim of these examinations was primarily vegetation research. Also, one of the energetic research projects was launched by the author (*Szász*, 1981), who determined the energetically potential production size on the basis of the water analogue of Penman and the PAR values with 0.03 energy efficiency. In the following decades, the further developed form of this work also incorporated the effect of temperature and water supply, and an attempt was made to analyze the typical climatic potential of production sites by considering the proportion of the role of the level of plants' nutrient supply. It has to be noted that *Antal* (1978) and *Varga-Haszonits* (1987b) defined the size of climatic potential, but they used the proportion of the energy balance and water balance to characterize the climatic potential of various regions, that is the size of the dry matter mass which was approximated from the values of energy and water balance that were incorporated in the examination. *Szász* (1981) wished to determine the size of the actual production from the value of climatic potential. The basic correlations of this method could be summarized as follows:

$$EP_0 = \varepsilon(1-a)\,PAR/\eta,$$
$$KP_k = \varepsilon[(1-a)PAR/\eta]f(T,W)^{-1},$$
$$KP_{k\cdot N} = \varepsilon[(1-a)PAR/\eta]f(T,W)^{-1},$$
$$KP_{k\cdot N}/EP_0,\ \ PAR = G/2,$$

where η is the coefficient of conversion (15.7 MJ/kg), KP_{kN} is the plant factor referring to productivity, W is the humidity, G is the global radiation, KP_k is the sensitivity factor referring to temperature and humidity.

Based on these latter, the method was used on the yield series from 23 regions of the county with typically different climatic and soil endowments. As a result of the analyses, the following parameters were arrived at:

energetic potential $\approx$ EP_0 (t/ha),

climatic potential $\approx$ KP_k (t/ha),

genetic potential $\approx$ $KP_{k\cdot N}$ (t/ha),

proportion $\approx$ $KP_{k.N}/KP_0$.

The correlation system shown above constituted the basis of examinations whose database was the 30-year average yields from 23 production regions and the related meteorological database. The author used the method for agricultural purposes by means of estimating the role of genetic potential for various plant species as a parameter of determination. As a matter of fact, the genetic potential, i.e., productivity is a mobilizing factor which could be made usable to express maximum climate effects. A part of this correlation is shown in *Fig. 7* which demonstrates the energetically and climatically potential average yields, as well as the actual average yield and the level of production which can be achieved from the genetic aspect. These results were used in Hungarian and also in foreign research.

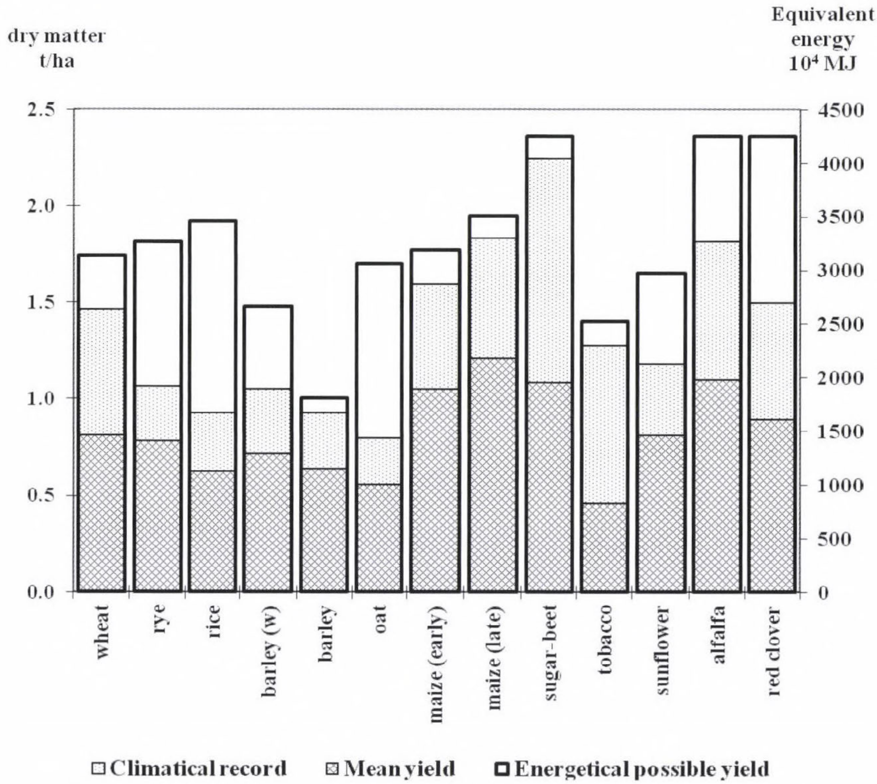

Fig. 7. Climatic records, energetically possible and mean yields of different plants.

It has to be emphasized that significant analyses were performed by the National Meteorological Service in the last 50 years in order to get to know the climate sensitivity of the main produced plants. Of these, the weather dependence findings of wheat (*Varga-Haszonits,* 1974), maize, and potato (*Berényi,* 1943, 1945, 1948;, *Szász,* 1961; *Ajtay,* 1979; *Hunkár,* 1990), paprika (*Erdős* and *Lambert*, 1987), barley (*Varga-Haszonits,* 1974), and various vegetable (*Cselőtei*, 1987) and fruit species are worth mentioning. Detailed and programmed examinations were performed in forests (*Justyák,* 1987). It also has to be mentioned that various governing authorities and ministries, such as the employees of the Agrometeorology and Forecast Department of the National Meteorological Service, cooperated in solving numerous agrometeorological problems by participating in various research programs directed by the government and professional departments.

The agrometeorological research turned into and have been going on in a rather manifold direction for decades, but two factors have especially important role due to the climatic endowments of the country. These are a) the natural water supply of agriculture and irrigation and b) the climatic effects of nutrient management. Details of these two topics still represent a current problem in guiding and developing agriculture on a country level.

5.3. The importance of water supply in crop production

The water cycle has one of the most important roles in the meeting point of the soil-plant-atmosphere system as the activity of all three spheres is peculiar at all times. The water cycle and the broadly meant balance-like record of water in the soil, i.e., *water balance* is an important natural phenomenon whose quantity can be detected by the form of the distinguished processes of the various production sites. The concept of *water cycle* can be approached in any possible ways, as it becomes clear that it refers to a specific motion system that is perpetuated by solar energy, and the transported material is water itself which is the main element of the material flow in plants. The limits of interpreting field crop production can be defined in physical terms; therefore, the limits of the atmospheric part and space of the water balance of various plant communities can be set, where certain physical parameters of the frictional boundary layer of the surface do not significantly change at a given distance from the surface. The lower boundary layer is located in the soil layer where the plant's root mass and the capillary boundary layer below the root mass meet.

The soil of the continent is a vast water reservoir also in global terms. Its upper layer contains all moisture, while its rhythmical change is regulated by the climate. The change is regulated by the simultaneous course of evaporation and precipitation. These two phenomena establish the water need of the plant cover in an optimal or – incidentally – extreme way. One of the main tasks of agrometeorology is to track the temporal change of soil moisture which originates from precipitation and to determine evaporation or evapotranspiration.

Nearly from the beginnings of the agrometeorological research, they tried to get to know the relative value of the available water stock. The numerical value of this stock is the water demand of plants which is the same as the measureable extent of the soil moisture content at all times (accessible soil moisture). The amount of precipitation only refers to the amount of water on the surface, while the water stock that can be stored is 30–40% of precipitation. This is the reason why the total amounts of precipitation and soil moisture are not in balance in the Carpathian Basin, depending on climate. In fact, their correlation is quite the opposite. Considering the physical characteristics of the most valuable soils from the agricultural aspects, the actual stored water stock and the monthly values of the balance components were the following:

- precipitation,
- stored water stock,
- evaporation.

These few data represent the yearly change of the cycle, the moisture content of the soil, and the values of the balance. As a matter of course, the variability of these values may greatly depend on the physical structure of the soil, the temporal distribution of precipitation, as well as the evaporation ability.

One of the most important ecological parameters of crop production is the water stock which can be taken up by plants, as well as its regional homogeneity. Since the physical heterogeneity of the soil is rather different along the profile, the change of the extent of moisture can hardly be determined from the quantities of the balance components. If the physical reality of the water balance equation is not harmed, it is possible to simplify the correlations of which several forms are known. There are no available long series (in climatic terms) of the soil moisture content, but *Varga-Haszonits* (1987a) estimated county mean values by means of calculation for the whole country. As a matter of course, this method has all those errors which could come from the inaccuracy of the equation used during the calculation. Based on a database which contains more than 30 years of measurement data, these components of the balance provided an opportunity to express the relative values of the water stock of the root zone related to a culture which has an average water need (grass). The relative value of crop water supply (*CWS*) can be estimated by using the following, seemingly simple equation:

$$CWS = \left[\frac{1}{F} \cdot R\left(XII - V\right) \cdot \frac{10 \cdot \sum R\left(VI - VIII\right)}{0.2 \cdot \sum T_d\left(VI - VIII\right)} \right] \cdot \frac{\left(e/E\right)_a}{\left(e/E\right)_m},$$

where (R) in the numerator is the amount of precipitation, the value in the denominator is the potential evapotranspiration, while $(e/E)_a$ represents the actual ratio of vapor pressure and saturation vapor pressure, and $(e/E)_m$ means the average ratio of vapor pressure and saturation vapor pressure for the same period, and T_d is the mean air temperature. The first member of the equation on the right is the value which depends on the physical condition of the soil, and it can be used to express the after-effect of soil moisture before the period of examination. Therefore, the equation expresses a recursive estimation. The value of water supply can be used to characterize the soil endowments, while it can also be interpreted from the climatic aspect; therefore, it can be regarded as a pedoclimatic correlation.

The regional distribution of the water supply (CWS) value – if the summer period is considered to be determinant – is the following: If the CWS value is <20, the region can be considered dry, CWS = 20–40 shows favorable water supply, while CWS > 40 is abundant and overabundant water supply. Due to the simplicity of the map, no extra explanation is needed.

5.4. Correlation between weather and agrotechnical effects

So far, the main characteristics of the range of findings were covered by the correlation between the climate and plants. With the advancement of agriculture, more specifically, modern crop production, the interest in various agrotechnical procedures got into focus. The main reasons for this phenomenon are the increase of soil fertility, the substantial unfolding of genetic potentials, and the protection of the physical condition and the living resources of the soil.

The organic medium of the soil and its health status makes it possible for plant nutrients to form continuously as a result of microbial activity. While the physical structure of the soil is a constant characteristic, the microbial processes in the soil greatly depend on its physical and chemical conditions. Significant research was carried out on the dependence of the nitrogen supply ability of soils on weather (*Szász* and *Lakatos*, 1991; *Nagy,* 2007). The nutrient stock of soil is an important component of the mentioned factor, since the dimension of the conceptual level of soil fertility mainly depends on this aspect. The determination of actual fertility is even more difficult, because the yield of plants cannot be increased without changing the actual fertility. Also, *Kreybig* (1953), *Sipos* (1979), and *Nagy* (1995, 2007) had a similar viewpoint as they emphasized that soil fertility is a dynamic characteristic and it significantly changes even within one crop year. Atmospheric effects play an important role in the change of soil fertility between seasons. The extent of soil fertility can be expressed by the collective of the chemical elements (e.g., mass fraction, etc.) that regulate the nutrient content of plants. In these series of factors, the available nitrogen forms develop in the phases of the C and N cycles. The activity of the microbial system which maintains this process depends on the quantity of bacteria at a given pH value, as well as the temperature and moisture content of the soil. The microbial activity, therefore, the dependence of the nitrate-nitrogen development on temperature is regulated by the Arrhenius equation concerning the value of the daily temperature fluctuation of soil:

$$v_M = K(\Delta T_{min})exp(-E/RT),$$

where K is the dimensionless adjusting factor of living resources (currently referring to the bacteria sustaining nitrification) and T_{min} is the environmental temperature at which production is zero. This temperature can be considered to be nearly linear in the T_{min}–T_{max} range.

In addition to the theoretical statements, it is also necessary to talk about its significant role in practice. The amount of NO_3-N in 100 g soil (mg) is determined by soil temperature and its water content simultaneously: it is rapidly increasing with temperature in the case of average spring moisture, reaching its maximum at 15–20 mg/100 g in May at the time of the maximum precipitation. By the end of summer and in the early spring, the extent of forming drops back to a low level as a result of dried out soil, and then a secondary maximum develops by the end of autumn after the increase of moisture when the frequency of NO_3 decreases to about half of its highest possible value.

The dependence of the mentioned nitrification process on weather can be increased with favorable cultivation; therefore, it is worth maintaining a proper soil moisture content (water preservation, irrigation) and developing adequate soil moisture by loosening and compacting to be able to regulate the temperature. Most importantly, these tasks call for different cultivation methods on different soils in order to increase or maintain the level of soil fertility.

The natural soil fertility is not enough for the abundant nutrient supply of plants; therefore, its artificial increase became necessary by adding organic and mineral fertilizers into the soil. In relation to this procedure, the previously mentioned rule is applied again, since sustaining of the power of the soil is nothing else than the increase of the intensity of nitrification processes which is the consequence of microbial activity. The regulation of the extent of nitrification is done in an experimental way by artificially applied fertilizers. Usually, the yearly dose of nitrogen replenishment of soils with high fertility amounts to 120–150 kg/ha nitrogen fertilizers that are applied together with potassium and phosphorus (NPK) in order to increase efficiency. The effectiveness of fertilizers can be assured mainly by keeping the moisture content of the soil on the proper level. In other words, this means that the efficiency of fertilization is low in drought, and this effect reaches its maximum with maintaining around 70% of the relative moisture content of soils. Water abundance reduces efficiency in the form of leaching. Since each crop year has different characteristics, the efficiency is always different, too. *Fig. 8* shows the change of yield against different precipitation supplies depending on different NPK fertilizer doses in maize (*Rácz* and *Nagy,* 2011; Nagy, 2007). Providing fertilizer has an extraordinary importance in modern crop production, as if adequate soil moisture and fertilizer quantity is provided, 10–15% or even higher yield surplus can be reached in the case of water-demanding crops, while the lack of precipitation or the overdose of fertilizers could result in yield depression. In addition to the above, it has to be emphasised that the theoretical basis and the practical implementation of yield regulation in the mentioned form of fertilization calls for wide climatological knowledge, since economical yield increase with high efficiency can only be reached this way or by knowing how to conform to the climatic conditions.

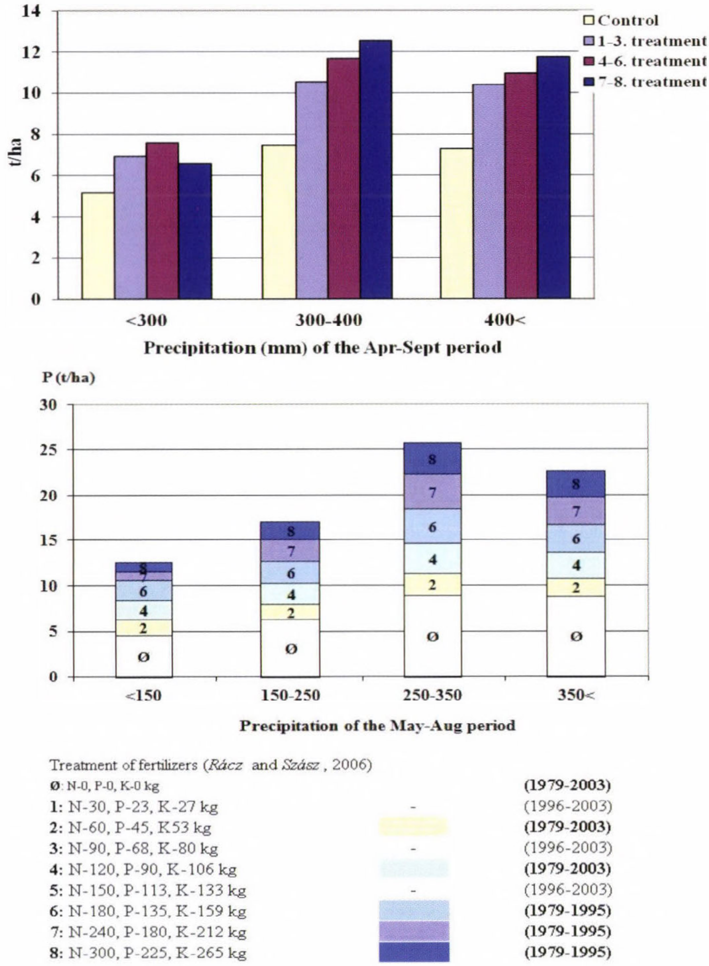

Fig. 8. Effects of mineral-fertility on corn yield by different natural water supply.

Fig. 8 shows the time series of the average yield of maize with different fertilization. On the horizontal axis the amount of precipitation are shown for the given period. Based on these time series, it can be established that the same fertilizer quantity provides significant yield surplus in the case of better precipitation supply. This statement shows that the nutrient effect will only unfold if the increased water demand is satisfied. These data were taken from a long-term field experiment carried out at the Hajdúság loess ridge (*Nagy*, 2007).

The effect of nutrient supply on water need was a generally researched topic. This issue was analyzed within the framework of numerous agrometeorological experiments (Keszthely, Szarvas, National Meteorological Service). As a general observation, it is known that if the average amount of precipitation is supplemented with around 50 mm irrigation water, the efficiency of fertilization increases significantly (*Antal,* 1968; *Posza* and *Tóth,* 1975; *Antal et al.,* 1977; *Tóth,* 1978; *Dávid,* 1981).

The two mentioned agrotechnical interventions: irrigation + fertilizer effects are the most influential factors concerning the efficiency of crop production; therefore, the research of these factors is among the most important topics even today. One should not neglect the fact that these two agrotechnical effects amount to 30–40% of the prime production costs in crop production. This high amount of costs makes it important to explore the correlations of this topic to an even deeper extent, since they could contribute to the reduction of production risk.

In addition to field experiments, the joint examination of water and nutrient supply is also carried out in so-called evapotranspiration model experiments in a rather manifold way in two locations (Szarvas, Keszthely). The model experiments clearly show that this bifactoral experiment makes it possible to determine the optimal ratio of interaction between water and nutrients which can have a significant role from the aspect of producing crops with average and high water needs. Solving this problem would not only have professional significance, but it could also satisfy an economic requirement.

In addition to the above, it has to be emphasized that these sections summarize only the historical framework of the Hungarian agrometeorological research. There were numerous research results in various topics – mainly in relation to issues close to agriculture – which constitute the problems of various long-term experiments. As a matter of fact, these and similar cooperations should be regarded praiseworthy, due to their successfulness (*Dávid*, 1981, *Berényi*, 1945).

In the agricultural crop production in Hungary, there was a significant change in the modernization of the nutrient management of soils in the 1950s in addition to numerous other processes. In the early fifties, the once traditional organic manure use was switched by the widespread use of mineral fertilizers. The new technology raised new problems, one of which is the determination of the quantity and proportion of mineral fertilizer supply in the case of crops with various nutrient needs. As a matter of fact, Hungarian soils have rather heterogeneous structure and this characteristic is also shown by their nutrient supply. By properly building up the nutrient balance of soils, the specific fertility of soils can be improved which can mainly be expressed in yields. There are numerous well known approaches which say that increasing nutrient supply could moderate yield reduction (*Bocz* and *Szász*, 1962). According to other examinations, the yield fluctuation of different crops is still significant, even though it has changed – some decreased, others increased – for other reasons not mentioned here. From this aspect, the reason of fluctuation is mainly the climatic endowments. In order to clarify this issue, there was a wide survey in the eighties in Hungary to find an explanation to this phenomenon. Although the ratio of the variability of yield and each weather element did not change substantially, the dependence of plants on weather; therefore, their climate sensitivity still existed as shown by standard deviation analyses. It seems that this question is still not fully answered, as further examinations are necessary to explore the causal correlation between weather variability and the standard deviation of yield. *Table 5* shows the 30-year-long time series of wheat and maize which are the two main crops in Hungary. During the analysis of these series, it was established that the correlations between the two phenomena did not change substantially – $r=0.6-0.8$ – which shows that there was no significant change in the ratio of standard deviations, only the yield level increased. In other words, the relative yield fluctuation really decreased with the increase of yields, but its absolute value did not increase. Based on this, it can be stated that the average yield of crops moderately increase as a result of yield level increase in the case of the same climatic effect. This issue is one of the fundamental points of the modernization of crop production.

Table 5. Average corn and wheat yield, standard deviation (S) and coefficient of variation (CV)

Soil region	Corn yields (t/ha)			Wheat yields (t/ha)		
	Mean 1961-90	**S**	**CV**	**Mean 1961-90**	**S**	**CV**
Szeghalom	3.04	0.79	25.80	2.13	0.78	36.52
Edelény+Encs	3.19	1.25	39.15	2.73	1.01	36.94
Kiskőrös	3.19	1.25	39.31	2.79	0.95	34.20
Fehérgyarmat	3.26	1.03	31.57	2.81	0.94	33.46
Nyírbátor	3.38	1.06	31.29	2.88	1.03	35.76
Gyöngyös	3.64	1.37	37.56	3.10	1.06	34.34
Gödöllő	4.05	1.48	36.64	3.16	1.03	32.63
Pápa	4.08	1.26	30.93	3.16	1.15	36.43
Barcs	4.17	1.23	29.45	3.22	1.06	33.04
Vas	4.19	1.44	34.33	3.29	1.08	32.86
Zalaegerszeg	4.22	1.40	33.04	3.30	1.24	37.69
Siófok	4.28	1.29	30.14	3.47	1.20	34.73
Kunszentmárton+Szentes	4.56	1.58	34.63	3.47	1.27	36.52
Siklós	4.57	1.52	33.30	3.57	1.35	37.94
Csorna	4.60	1.40	30.52	3.58	1.33	37.28
Komárom	4.66	1.66	35.74	3.62	1.32	36.57
Szolnok	4.73	1.70	35.89	3.80	1.26	33.21
Baja	4.86	1.48	30.39	3.83	1.22	31.92
Sárbogárd	5.04	1.69	33.56	3.90	1.22	31.29
Hódmezővásárhely	5.31	1.94	36.57	4.08	1.51	36.88
Szekszárd	5.35	1.78	33.27	4.19	1.63	38.84
Mezőkovácsháza	5.54	1.56	28.14	4.25	1.35	31.75
Hajdúhát	6.49	1.98	30.49	4.62	1.45	31.47

Fig. 9 shows yearly yield of wheat and corn in different growing regions between 1961–90 in Hungary. The increase of nutrient supply results in the increasing water demand of crops. Since the variability of precipitation supply did not decrease, the increased yields could react more powerfully to the extent of water supply. The reaction to water supply is increased by the increased water need, although the amount of precipitation showed a decreasing tendency over the past decade. As a result, drought periods and crop years are becoming more frequent. (*Ruzsányi,* 1974, 1992)

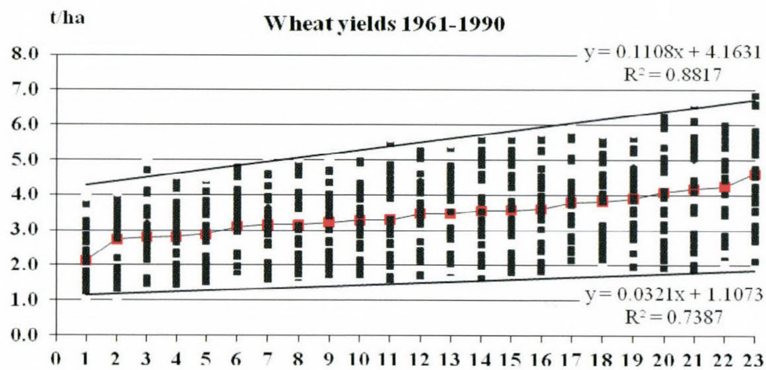

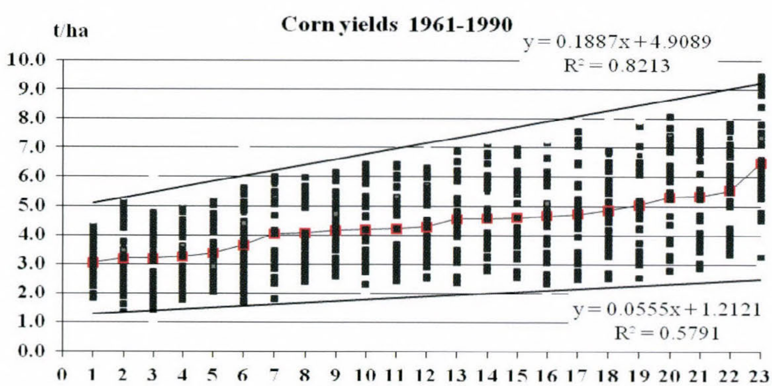

Fig. 9. Yearly yield of wheat and corn indifferent growing region between 1961–90 in Hungary.

Explanation of numbers on horizontal axis is given below in details.

Soil type	Nr.
Low-fertility soils (skeletal soils, bog soils, salt-affected soils)	1, 3-5
Brown forest soils	2, 6-11
Meadow soils, alluvial and sedimentary soils	13, 17, 22
Chernozem soils	15, 18-21, 23

The increase of nutrients and the associated yield increase reach its maximum if the nutrient effect unfolds in the case of favorable water supply. It is an undisputed fact that the extent natural water utilization became more favorable with the increase of yield, while this phenomenon is further intensified by the modest natural water supply level. This latter is favorable until a certain critical value, but the stronger unfolding of water shortage reduces the extent of water utilisation and develops disorders in crop growth, finally resulting in yield decrease.

5.5. Micrometeorology in agrometeorology

Within the framework of complex meteorological research, the physical problems of meteorology are often raised from theoretical and practical aspects in various areas of meteorological practice. As a matter of fact, this phenomenon is ordinary, since it represents two sides of a problem. The predecessor of agrometeorology is the complex and complication of empiricism, physics, micrometeorology, and energetic and aerodynamic processes in the frictional space of the surface. Agrometeorology gets increasingly involved in the interpretation of various parts of agriculture, but its methods are based on physical principles, and it mainly uses the direct physical findings of the surface boundary layer while interpreting biological processes. Today, this phenomenon is clearly shown by the fact that well known international journals feature lots of practically usable findings of agrometeorological research which are based on physical principles among studies that show the aims of nearly sterile meteorological examinations. Despite the fact that agrometeorology and micrometeorology are only narrow branches of science, neither of them can exist without the other concerning the issues they are dealing with; therefore, disciplinarity can be clearly recognized from both sides. In Hungary, agrometeorology originated from empiricism and it also took elements from climatology in order to survey meteorological impacts. From this position, agrometeorology builds a more detailed physical basis while gradually leaving climatology behind in order to provide solution to various problems. Based on this path, it can be established that agrometeorology was not separated from meteorology. On the contrary, it increasingly utilizes the new physical knowledge that formed in the field of micrometeorology. However, agrometeorology attempts to show them "in different clothes" in the area of a more practical science. This process was clearly expressed in the past 50 years in Hungary.

At the beginning, the process described above was shown in the instructions of the former German "Geiger" school, which described the phenomena in the air space close to the surface in a descriptive way under the summarizing name of microclimate and it also attached a speculative explanation to the description of these phenomena, assuming the causal aspect of their background. Microclimatology was widespread mostly in European countries; therefore, there is a large number of related case studies among Hungarian micrometeorological publications, especially from the previous decades.

Agricultural microclimatology observes the yearly and daily cyclic condition changes triggered by plants, the change of temperature and moisture profiles in plant populations and the difference from the profiles above the flat surface and grasslands free from plants. In Hungary, agricultural microclimatology was known as "population climate" both in agriculture and meteorology. At the beginning, the research dealing with this branch of science did not aim at finding the physical explanation for the development of profiles. Instead, the goal was to explore the relationship between the developed profile and some physiological processes of the plant. Therefore, the population climate, or, in other words, vegetable microclimate did not consider the difference between the profiles to be the production of a dynamic process, but mainly of its biological consequence (*Endrődi,* 1967, 1974; *Hunkár,* 1985; *Justyák,* 1989). According to this point of view, the plant population does not intend to explain the quantified evaluation of the physical processes going on in the air space. Instead, the primary subject of interest was the impact of the air condition on plants in high detail. It is not a coincidence that the erroneous nature of this approach did not provide the importance of the new knowledge from the physical aspect from which it could have been the initiator of various biophysical conclusions. It is an undoubted fact that the correlation between the air space of the canopy and the physiological processes of the plant can be considered an especially important knowledge, but the new observations provided usable scientific information mostly in the field of plant biophysics (*Dunkel,* 1984; *Cselőtei,* 1987; *Varga-Haszonits,* 1987b; *Anda* and *Lőke,* 2005).

Canopy climate research was launched in the decades after the turn of the century in Hungary and abroad. In Hungary, *Kálmán Kerpely* performed various population climate-related examinations with the aim to determine the resulting impact between temperature, moisture and evaporation ability in various grown crop populations. The mentioned examinations were carried out in the field experiments established at the Debrecen Agricultural Academy with notable results. The main findings of these examinations referred to the exploration of the joint efficiency of the nutrient and water supply. The work performed in the mentioned field is still significant today.

Later, German researcher *Geiger* organized highly detailed canopy climate research projects in the populations of field crops and forests. The aim of this research was to emphasize the population climate modification role of water supply. *Berényi* extended the population climate research while also considering the microclimate modification impact of the relief in addition to the biological need of plants (*Berényi,* 1954, 1958; *Justyák,* 1960; *Borhidi* and *Dobosi,* 1967; *Szász,* 1973a,b, 1988).

While we acknowledge the agrometeorological significance of population climate research findings, it can be established that the static-focused work needs to be renewed, which was first recognized in foreign research stations. The meteorological use of the physical examination results of the boundary layer – Prandtl's layer – provided an extensive space for evolving new directions while accepting the findings of the previous population climatological research. The modernization was founded by the general use of energetic measurements, as well as the detailed exploration of the aerodynamic rules of energy and material transfer, further extending the possibilities of complex agro- and biophysical research which justified and explained the previously observed change of conditions with proper physical reality. The simpler energy balances and the implementation of the quantified analysis of turbulent sensible and latent heat transfer provided new bases for a significant part of agrometeorology both in macro- and microclimatic senses. This way, agrometeorology became an interdisciplinary science which made use of atmospheric physical and agricultural knowledge jointly. The theoretical cognition and methodical use of turbulent transport processes made it possible to describe the processes with mathematical correlations based on physical principles – an opportunity that had only been a desire until this point. Furthermore, based on these correlations, a phase of processes can be built up bases on which model-based research findings can be obtained.

Today, modeling can be considered a reachable goal in agrometeorology, despite the fact that gathering and arranging theoretical knowledge still calls for numerous tasks to be done. It is possible to describe the processes which will serve the purpose of the basic model of scientific life by building together separate processes later, based on the results of measurement systems built on digital bases. It has to be emphasized that the most critical point of this problem is the development of the right algorithms that could be regarded as bricks in the building of science (*Ábrányi,* 1978; *Hunkár,* 1984, 1986, 1990; *Szász,* 1987; *Dunkel et al.*, 1987, 1989; *Szabó,* 1988, 1989; *Justyák,* 1989; *Ács,* 2004).

From this viewpoint, the Hungarian agrometeorological research is successful, since numerous research findings were obtained which provided model-based results in order to make progress. The modeling activity that is becoming increasingly accurate is a hopeful tendency that has enormous progress today in international relations. It has to be emphasized that the professional representatives of this tendency do not only increase the values of the agrometeorological research in a narrow sense, but they have high significance in developing practical agriculture both from theoretical and practical points of view. The high level economic utilization of the model system of agricultural activities is recognized in a definite form today, but it can only be hoped to become more extensive if the branches of science associated with agriculture, e.g., agrometeorology will contribute actively to this joint activity. In this field, the Hungarian agrometeorological research calls for further development in order to carry out joint development. The sum and collective of partial potentials represent the level of total active potential concerning all areas. In other words, this means that without the cooperation of the related branches of knowledge, it could become doubtful to reach the potential borders; therefore, the performance level of the scientific society stays under the potential borders.

In addition to the above, it has to be emphasized that these sections summarize only the historical framework of the Hungarian agrometeorological research. There were numerous research results in various topics – mainly in relation to issues close to agriculture – which constitute the problems of various long-term experiments. As a matter of fact, these and similar cooperations should be regarded praiseworthy, due to their successfulness.

6. Conclusions and results

The Hungarian events and findings of the more than one and half-century-long history of agrometeorology could be summarized as follows:

1. Modernization of agriculture in Hungary was extended in the second half of the 1800s, mostly due to Western European impacts.
2. Around the middle of that century, agricultural higher education institutions were established, providing a professionally educated expert basis for the subsequent periods.
3. In the years between 1850–2000, research institutes were established which helped Hungary becoming increasingly effective in launching international agricultural research.
4. The National Institute of Meteorology and Geomagnetics started to work in 1870 and launched organized and controlled climatological observations at its stations while connected to the international network.
5. At the beginning of the 20th century, the first standard climate elements appeared in the form of 30-year averages (1870–1900).
6. Empirical climate-based agrometeorological research was launched, dealing mostly with the issues of successful prevention of damages caused by weather (e.g., frost, drought, water logging, wind).
7. There was a restructuring in the Hungarian climate network at the time of the World War II.
8. Effect functions, indexes and statistical indexes in accordance with the empirical or physical correlations serving the characterization of the climate and the temporal and spatial change of agrometeorological processes were worked out.
9. By the middle of the 20th century, a national climatic database was established as a result of the joint work of the Hungarian Meteorological Service and the main research institutes. This database made it possible to

establish an agrometeorological information system.

10. The research order of agrometeorological research started to unfold characteristically in the 1960s:
    a. statistical agrometeorology,
    b. agrometeorology built on biophysical bases,
    c. model-based agrometeorology.

    The interpretation range of all specialized branches was continuously becoming increasingly widespread, thereby establishing theoretical bases in a way that they could finally be clustered into a complex research system.
11. For today, the findings of this branch of science which is built on climatic and micrometeorological bases contribute to the development of agriculture in a manifold way. Therefore, the requirements of increasing the natural energies by man also increased.
12. The need for the cooperation between meteorology and agriculture resulted in the further increase and efficiency growth of both fields of science.

References

Ábrányi, A., 1978: Matematikai modell az őszi búza termésének időjárás okozta ingadozásaira. *OMSZ. Hiv. Kiadv. XLVI.* 157–163. (In Hungarian)

Ács, F., 2004: A talaj-növény-légkör rendszer modellezése a meteorológiában. ELTE TTK, Budapest. (In Hungarian)

Ács, F., Breuer, H. and *Szász, G.*, 2007: A tényleges párolgás és a talajvízkészlet becslése egy módosított Thornthwaite-féle modell alapján. *Agrokémia és Talajtan 56*, 217–236. (In Hungarian)

Ajtay, Á., 1979: A burgonya terméshozamának előrejelzése meteorológiai paraméterek segítségével. In (Szerk: *Lőrincz J.*) A burgonya termesztése. Mezőgazdasági Kiadó, Budapest. (In Hungarian)

Allen, R.E., 1999: Tracking the agricultural revolution in England. *Ec. History Rev., LII.*, 209–235.

Anda, A. and *Lőke, Zs.*, 2005: Microclimate simulation in maize with two watering levels. *Időjárás 109*, 21–37.

Antal, E. 1965: Öntözés és meteorológia. *Időjárás 69*, 248–256. (In Hungarian)

Antal, E., 1966: Egyes mezőgazdasági növényállományok potenciális evapotranszspirációja. *Öntözéses Gazd. 4*, 69–86. (In Hungarian)

Antal, E., 1968: Az öntözés előrejelzése meteorológiai adatok alapján. Kandidátusi értekezés, (In Hungarian).

Antal, E., 1978: A növénytermesztés felső határát meghatározó éghajlati potenciál. *OMSZ. Hiv. Kiadv. XLVI*, 164–170. (In Hungarian)

Antal, E., 1987: Agrometeorológiai kutatások az Országos Meteorológiai Szolgálat keretében. *Időjárás 91*, 68–79. (In Hungarian)

Antal, E., Posza, I. and *Tóth, E.*, 1977: Az időjárás és éghajlat hatása a műtrágya érvényesülésére. *Időjárás, 79*, 95–104. (In Hungarian)

Aujeszky, L., Berényi, D., and *Béll B.*, 1951: Mezőgazdasági meteorológia. Akadémiai Kiadó, Budapest. (In Hungarian)

Bacsó, N., 1952: A hőmérséklet szélsőértékei Magyarországon. *OMSZ Hiv.Kiadv. XV*, 8–26. (In Hungarian)

Bacsó, N., 1955: Az egyórás csapadékok gyakorisága és hozama. *Időjárás 59*, 13–28. (In Hungarian)
Bacsó, N., 1959: Magyarország éghajlata. Akadémia Kiadó, Budapest. (In Hungarian)
Bacsó, N., 1967: A mikroklíma fizikai szemlélete. Tudományos értekezés, Gödöllő. (In Hungarian)
Baumann, H., 1949: Wetter und Ernteertrag. Dtsch. Bauernverlag, Berlin.
Berényi, D., 1943: Magyarország Thornthwaite-rendszerű éghajlati térképe és az éghajlati térképek növényföldrajzi vonatkozásai. *Időjárás 47*, 81–90. (In Hungarian)
Berényi, D., 1945: A kukorica termelése és összefüggése az időjárással. Tiszántúli Mezőgazd. Kamara, Debrecen. (In Hungarian)
Berényi D. 1948: A növényklíma fogalmi elhatárolása. *Időjárás 52*, 175–176. (In Hungarian)
Berényi, D., 1954: Az időjárási elemek és a terméseredmények közötti összefüggések kutatásának eredményei. *KLTE Meteorol. Int. Közl. 10*, 193–204. (In Hungarian)
Berényi, D., 1958: Az állományklímát alakító tényezők. *MTA Agr. Tud. Oszt. Közl. XIV*, 155–193. (In Hungarian)
Berényi, D., Nagy, L., and *Szász, G.*, 1959: A talajművelés hatása a talaj hő- és vízgazdálkodására. *KLTE Meteorol. Int. Tud. Közl. 15*, 311–328. (In Hungarian)
Berkes, Z., 1946: A Kárpát-medence vízháztartása. *Időjárás 96*, 5–13. (In Hungarian)
Berzsenyi, Z., 1993: A N-műtrágyázás és az évjárat harása a kukoricahibridek (Zea mays L.) szemtermésére és N-műtrágyareakciója tartamkísérletekben az 1970-1991 években. *Növénytermelés* 49–63. (In Hungarian)
Berzsenyi, Z., 2000: Növekedésanalízis a növénytermesztésben. Veszprémi Egyetem, Georgikon Mezőgazdaség. Tud. Kar, Veszprém. (In Hungarian)
Birkás, M., 2006: Földművelés és földhasználat. Mezőgazdasági Kiadó, Budapest. (In Hungarian)
Bocz, E., 1992: Szántóföldi növénytermesztés. Mezőgazda Kisdó, Budapest. (In Hungarian)
Bocz, E. and *Szász, G.*, 1962: A műtrágya szerepe a kiegyenlítetten nagy termések elérésében. *MTA Agr. Tud. Oszt. Közl. XX*. 109-123. (In Hungarian)
Borhidi, A. and *Dobosi, Z.*, 1967: A felszíni albedó területi eloszlása Magyarországon. *Időjárás 71*, 150–159. (In Hungarian)
Botos, L. and *Varga-Haszonits, Z.*, 1974: Agroklimatológia és növénytermesztés. MÉM, Budapest. (In Hungarian)
Campbell, B.M.C., 2010: Agriculture and national incomes in Europe, c 1300–1850., Univ. Belfast 29.
Cseháti, S., 1905: Általános és különleges növénytermelés. Nirtsmann József Könyvkiadója, Győr. (In Hungarian)
Cselőtei, L., 1987: A meteorológia szerepe a mezőgazdaságban. *Időjárás 91*, 60–67. (In Hungarian)
Dávid, A., 1981: Összefüggés az időjárás, a műtrágyázás és a kukorica fejlődésének jellemzői között. *Időjárás 85*, 103–111. (In Hungarian)
Dávid, A., Takács, O. and *Tiringer, Cs.*, 1990: A sugárzási egyenleg eloszlása Magyarországon az 1951–80-as időszak adatai alapján. *OMSZ Kisebb kiadv. 66*. (In Hungarian)
Dobosi, Z., 1972: A sugárzási egyenleg területi eloszlása Magyarországon. Doktori Értekezés Budapest. (In Hungarian)
Dobosi, Z. and *Takács, L.*, 1959: A globális sugárzás területi eloszlása Magyarországon. *Időjárás 63*, 82–84. (In Hungarian)
Dunkel, Z., 1984: Szántóföldi növények fejlődésének (tömeggyarapodásának) dinamikus (szimulációs) modellezése. *OMSZ Beszámolók, 1981*. 269–284. (In Hungarian)
Dunkel, Z., Hunkár, M., and *Zárbok, Zs.*,1987: A kukorica fejlődésének leírása dinamikus-szimulációs növénynövekedési modell segítségével. *Időjárás 91*, 197–208. (In Hungarian)
Dunkel, Z., Stollár, A., Szabó, T., and *Tiringer, Cs.*, 1990: A területi párolgás meghatározása Magyarországon. *Időjárás 94*, 149–155. (In Hungarian)
Dunkel, Z., Bozó, P., Szabó, T., and *Vadász, V.*, 1989: Application of Thermal Infrared Remote Sensing to the Estimation of regional Evapotranspiration. *Adv. Space Res. 9*, 255–258.
Endrődi, G., 1967: A növényállomány hatása a talaj felmelegedésére. *Időjárás 71*, 39–43. (In Hungarian)
Endrődi, G., 1974: A cukorrépa vízszükségletének és öntözővíz-igényének agrometeorológiai alapjai. *OMSZ Beszámolók 1971*. 186–199. (In Hungarian)
Erdős, L. and *Lambert, K.*.,1987: Modellek a fűszerpaprika festéktartalmának és termésátlagának előrejelzésére. *Időjárás 91*, 187–196. (In Hungarian)

Felméry, L., 1974: A fotoszintézisben aktív sugárzás mennyisége a tenyészidőszakban. *Időjárás 78*, 235–239. (In Hungarian)
Fischer, R.A. and *Yates, F.*, 1957: Stastistical tables or biological, agricultural, and medical research. Oliver & Boyd. London.
Füri, J. and *Kozma, F.*, 1972: Az öntözés hatása a szőlőállomány energiafogalmára. *Szőlő- és gyümölcstermesztés 8*, 61–73. (In Hungarian)
Füri, J. and *Kozma, F.*, 1975: A szőlő evapotranspirációja. *Időjárás 79*, 112–120. (In Hungarian)
Füri, J. and *Kozma, F.*, 1978: A szőlő tényleges evapotranspirációja és öntözővíz szükséglete. *OMSZ Beszámolók 1975*. 181–194. (In Hungarian)
Goda, L., 1966: A többnapos nagy csapadékok gyakorisága. *VITUKI Tanulmányok és kutatási eredmények XX*. 1–15. (In Hungarian)
Gyárfás, J., 1922: Sikeres gazdálkodás szárazságban. Magyar Dry Farming. Mezőgazdasági Kiadó, Budapest. (In Hungarian)
Győrffy, B., 1990: Tartamkisérletek Martonvásáron. In (Ed.: *Kovács, I.*)Martonvásár második húsz éve. Martonvásár. 114–118. (In Hungarian)
Győrffy, B., 1976: A kukorica termelésére ható növénytermesztési rényezők értékelése. *Agrártudományi közlemények 35*, 239–266. (In Hungarian)
Hajósy, F., 1952: Magyarország csapadékviszonyai 1901–40. OMSZ, Budapest. (In Hungarian)
Holdefleiss, P., 1930: Agrometeorologie. Verl. P. Parey. Berlin.
Hunkár, M., 1984: A simle calculation of the vertical profile of average PAR flux density within a maize stand. *Időjárás 88*, 139–153.
Hunkár, M., 1985: A fotoszintetikusan aktív sugárzás vertikális profilja kukoricaállományban. *OMSZ Beszámolók 1982*, 125–139. (In Hungarian)
Hunkár M., 1986: A növényfejlődés dinamikus modelljében alkalmazott növekedési függvények. *OMSZ Beszámolók 1983*, 111–120. p. (In Hungarian)
Hunkár, M., 1990: Kukoricaállomány mikroklímájának szimulációja. *Időjárás 94*, 221–229. (In Hungarian)
Jolánkai, M., 1993:A búzatermesztés egyes meghatározó tényezői. Akadémiai doktori értekezés, Martonvásár. (In Hungarian)
Justyák, J., 1960: A művelésmódok hatása a szőlő állományklímájára Tokaj-Hegyalján. Kandidátusi értekezés. (In Hungarian)
Justyák, J., 1987: Energiaháztartás-mérések tölgyerdőben. *Időjárás 91*, 131–146. (In Hungarian)
Justyák, J., 1989: A tokaj-hegyaljai szőlőültetvények mezo- és mikroklimatikus jellemzői. Akadémiai doktori értekezés. (In Hungarian)
Kakas, J. (ed.),1960: Magyarország Éghajlati Atlasza. II. kötet. Országos Meteorológiai Intézet, Akadémiai Kiadó, Budapest. (In Hungarian)
Kemenessy, E., 1964: Talajművelés. Mezőgazdasági kiadó, Budapest. (In Hungarian)
Kerék, J., 1934: Az időjárás befolyása az Alföldön a termés mennyiségére és minőségére. Budapest. (In Hungarian)
Kéri, M. and *Kulin, M.*, 1953: Csapadékösszegek gyakorisága Magyarországon 1901–50. *OMSZ Hiv. Kiadv. XVI*. (In Hungarian)
Kreybig, L., 1953: Az agrotechnika tényezői és irányelvei. Akadémiai Kiadó, Budapest. (In Hungarian)
Lieth, H., 1976: The use of correlation models to predict primary productivity from precipitation or evapotranspiration. In *Lange et al.* Water and Plant Life. Berlin. 392–407.
Major Gy., 1976: A napsütés Magyarországon 1958–1972. *OMSZ Magyarország éghajlata 10.* (In Hungarian)
Major, Gy., 1985: A napenergia-hasznosítás meteorológiai megalapozása Magyarországon. OMSZ, Budapest.
Major, Gy., 2002: Magyarországi éghajlat-energetikai tanulmányok. BKAE, MTA. Budapest. (In Hungarian)
Montheith, J.L., (ed.) 1975: Vegetation and the atmosphere. Academic Press, London, New York, San Francisco.
Nagy, J., 1995: A talajművelés, a műtrágyázás, a növényszám és az öntözés hatásának értékelése a kukorica termésére . *Növénytermelés 44*, 252–260. (In Hungarian)

Nagy, J., 2006: A debreceni kukorica tartamkísérlet kutatási eredményei. Debreceni Egyetem Agrártudományi Centrum. Debrecen. (In Hungarian)
Nagy, J., 2007: Kukoricatermesztés. Akadémiai Kiadó, Budapest. (In Hungarian)
Nyíri, L., 1993: Földműveléstan. Mezőgyzdasági Kiadó, Budapest. (In Hungarian)
Overton, M., and *Campbell B.M.S.*, 1996: Production and productivity in English agriculture, 1086–1871. *Econ. History Rev.*, *Historie et Messure, 1996*, 255–297.
Pálfai I., 2004: Belvizek és aszályok Magyarországon. Hidrológiai Tanulmányok. Közl. Dok. Budapest. (In Hungarian)
Papp, É., 1974: A szélsebesség–óraátlagok gyakorisági eloszlásának sajátosságai. *Időjárás 78,* 342–347. (In Hungarian)
Péczely, Gy., 1963: Csapadékmentes időszakok tartamvalószínűsége Magyarországon. *Időjárás 67*, 33–38. (In Hungarian)
Péczely, Gy., 1968: A szárazsági hajlam évi járása és szingularitásai. *Időjárás 62*, 294–297. (In Hungarian)
Petrasovits, I. and *Balogh, J.*, 1974:Az evapotranspirációs kutatása, magyarországi helyzete és nemzetközi vonatkozásai. MTA Vízgazd. TB – Műsz. TB Kiadv., Budapest. (In Hungarian)
Posza, I. and *Stollár, A.*, 1983: A tényleges párolgás számításához használt növénykonstansok értékei többévi mérés alapján. *Időjárás 87*,170–177. (In Hungarian)
Posza, I. and *Tóth, E.*, 1975: A kukorica vízigényének alakulása az időjárási viszonyok és az NPK szintek függvényében. *OMSZ Beszámolók 1972*, 298–305. (In Hungarian)
Rácz, Cs., and *Nagy, J.*, 2011: A víz- és tápanyagellátottság illetve -hasznosulás megítélésének kérdései kukorica terméseredmények vonatkozásában. *Növénytermelés 60*, 94–117. (In Hungarian)
Ruzsányi, L., 1974: A műtrágyázás hatása egyes szántóföldi növényállományok vízfogyasztására és vízhasznosítására. *Növénytermelés 23*, 249–258. (In Hungarian)
Ruzsányi, L., 1992: Főbb növénytermesztési tényezők és a vízellátás kölcsönhatásai, Akadémiai doktori értekezés tézisei, Debrecen. (In Hungarian)
Schirokné, Kriszton I., 1983: A nagycsapadékok gyakorisági analízise és valószínű legnagyobb csapadékbecslése. *Vízügyi Közlemények LXV*. 167–187. (In Hungarian)
Sipos, S., 1979: Talajművelési kísérletek eredményei réti talajon. In *Bajai, J.* (szek.) Kukoricatermesztési kísérletek 1968–1974. Akadémia Kiadó, Budapest, 213–221. (In Hungarian)
Smith, J.W., 1915: Agricultural meteorology. *Proc. Ohio Acad. Sci. 6*, 239–264.
Szabó, T., 1988: A felszínhőmérséklet, mint agrometeorológiai információhordozó. Kandidátusi értekezés. (In Hungarian)
Szabó, T., 1989: Inverz módszer az aktív felszín hőmérsékletén alapuló energiaháztartási egyenlet megoldására. *Időjárás 93*, 115–120. (In Hungarian)
Szász, G., 1955: A rozs termesztésének összefüggése az időjárással és az éghajlattal. MTA Értekezés. Debrecen. (In Hungarian)
Szász, G., 1961: A rizs termesztésének időjárási feltételei a fő termőtájakon. *Növénytermelés 35*, (In Hungarian)
Szász, G., 1968: A csapadékösszegek szórásának vizsgálata Magyarországon (1901–50). *DATE, Tud. Közl.*, 185–210. (In Hungarian)
Szász, G., 1971: Untersuchungen der räumbichen Homogenität von Niederschlagssummen. *Acta Georg. Debrecina XV-XVI*, 225–237.
Szász, G., 1973a: A potenciális párolgás meghatározásának új módszere. *Hidrológiai Közlöny*, 435–442. (In Hungarian)
Szász, G., 1973b: A termesztett növények vízigényének és az öntözés gyakoriságának meteorológiai vizsgálata. *Növénytermelés 22*, 241–258. (In Hungarian)
Szász, G., 1981: Az időjárási folyamatok és a termelés közötti kapcsolat modellezésének alapjai. *Időjárás 85*, 334–345. (In Hungarian)
Szász, G., 1987: A mezőgazdasági célú távérzékelés jelentősége az agrometeorológiában. *Időjárás 91*, 88–103. (In Hungarian)
Szász, G., 1988: Agrometeorológia – általános és speciális. Mezőgazd. Kiadó, Bp. (In Hungarian)

Szász, G., 2005: Termésingadozás és éghajlati változékonyság a Kárpát-medencében. *„Agro-21" Füzetek 40,* 33–69. (In Hungarian)
Szász, G. and *Lakatos, L.*, 1991: A légköri hatások szerepe a talajok N-szolgáltató képességének alakulásában. *Időjárás 95.* 289–300. (In Hungarian)
Száva-Kováts, J., 1937: A légnedvesség évi ingadozása Európában. *Időjárás 68,* 2–16. (In Hungarian)
Szepesiné Lőrincz, A., 1966: A Kárpát-medence hidroklímájának jellemzői. *OMSZ Hiv. Kiadv. XXIX.*, 86–114. (In Hungarian)
Takács, O., 1972: A teljes besugárzás függőleges felületeken. *OMSZ Beszámolók 1969,* 231–238. (In Hungarian)
Tar, K., 1991: Magyarország szélklímájának komplex statisztikai elemzése. *OMSZ Kisebb kiadv. 67.* (In Hungarian)
Thornthwaite, C.W., 1948: An approach toward a rational classification of climate. *Geogr. Rev. 38,* 55–94.
Tóth, E., 1978: A kukorica evapotranspirációja, terméshozama és vízhasznosítása különböző tápanyag és vízellátás mellett. *OMSZ Beszámolók 1975*, 241–255. (In Hungarian)
Wágner, R. and *Papp, É.*, 1984: A szél néhány statisztikai jellemzője. *OMSZ. Hiv. Kiadv. LVII.* 108–117. (In Hungarian)
Várallyay, G., 2008: Extreme soil moisture regime as limiting factor of plants' water uptake. *Cereal Res. Commun. 36 Suppl.*, 3–6.
Várallyay, G.,Szűcs, L., Rajkai, K., Zilahy, P., and *Murányi, A.*, 1980: Magyarországi talajok vízgazdálkodási tulajdonságainak kategóriarendszere és 1:100000 méretarányú térképe. *Agrokémia és Talajtan 29*, 77–112. (In Hungarian)
Varga-Haszonits, Z., 1974: A meteorológiai elemek hatása az őszi árpa fejlődésére. *OMSZ Beszámolók 1971*, 72–77. (In Hungarian)
Varga-Haszonits, Z., 1987a: Agrometeorológiai információk és hasznosításuk. Mezőgazd. Kiadó. Budapest. (In Hungarian)
Varga-Haszonits, Z., 1987b: Az időjárás-növény modellek elvi-módszertani kérdései. *Időjárás 91*, 176–186. (In Hungarian)
Wit, C.T. de, 1954: Photosynthesis of leaf canopies. Centre f. *Agricult. Publ. Doc. Wageningen*, 1–57.

INSTRUCTIONS TO AUTHORS OF *IDŐJÁRÁS*

The purpose of the journal is to publish papers in any field of meteorology and atmosphere related scientific areas. These may be

- research papers on new results of scientific investigations,
- critical review articles summarizing the current state of art of a certain topic,
- short contributions dealing with a particular question.

Some issues contain "News" and "Book review", therefore, such contributions are also welcome. The papers must be in American English and should be checked by a native speaker if necessary.

Authors are requested to send their manuscripts to

Editor-in Chief of IDŐJÁRÁS
P.O. Box 38, H-1525 Budapest, Hungary
E-mail: journal.idojaras@met.hu

including all illustrations. MS Word format is preferred in electronic submission. Papers will then be reviewed normally by two independent referees, who remain unidentified for the author(s). The Editor-in-Chief will inform the author(s) whether or not the paper is acceptable for publication, and what modifications, if any, are necessary.

Please, follow the order given below when typing manuscripts.

Title page: should consist of the title, the name(s) of the author(s), their affiliation(s) including full postal and e-mail address(es). In case of more than one author, the corresponding author must be identified.

Abstract: should contain the purpose, the applied data and methods as well as the basic conclusion(s) of the paper.

Key-words: must be included (from 5 to 10) to help to classify the topic.

Text: has to be typed in single spacing on an A4 size paper using 14 pt Times New Roman font if possible. Use of S.I. units are expected, and the use of negative exponent is preferred to fractional sign. Mathematical formulae are expected to be as simple as possible and numbered in parentheses at the right margin.

All publications cited in the text should be presented in the *list of references*, arranged in alphabetical order. For an article: name(s) of author(s) in Italics, year, title of article, name of journal, volume, number (the latter two in Italics) and pages. E.g., *Nathan, K.K.*, 1986: A note on the relationship between photo-synthetically active radiation and cloud amount. *Időjárás 90,* 10-13. For a book: name(s) of author(s), year, title of the book (all in Italics except the year), publisher and place of publication. E.g., *Junge, C.E.*, 1963: *Air Chemistry and Radioactivity*. Academic Press, New York and London. Reference in the text should contain the name(s) of the author(s) in Italics and year of publication. E.g., in the case of one author: *Miller* (1989); in the case of two authors: *Gamov* and *Cleveland* (1973); and if there are more than two authors: *Smith et al.* (1990). If the name of the author cannot be fitted into the text: (*Miller,* 1989); etc. When referring papers published in the same year by the same author, letters a, b, c, etc. should follow the year of publication.

Tables should be marked by Arabic numbers and printed in separate sheets with their numbers and legends given below them. Avoid too lengthy or complicated tables, or tables duplicating results given in other form in the manuscript (e.g., graphs).

Figures should also be marked with Arabic numbers and printed in black and white or color (under special arrangement) in separate sheets with their numbers and captions given below them. JPG, TIF, GIF, BMP or PNG formats should be used for electronic artwork submission.

Reprints: authors receive 30 reprints free of charge. Additional reprints may be ordered at the authors' expense when sending back the proofs to the Editorial Office.

More information for authors is available: journal.idojaras@met.hu

Published by the Hungarian Meteorological Service

Budapest, Hungary

INDEX 26 361

HU ISSN 0324-6329

IDŐJÁRÁS

QUARTERLY JOURNAL
OF THE HUNGARIAN METEOROLOGICAL SERVICE

Special Issue: Atmospheric Physics and chemistry in modern meteorology
Guest Editors: **István Geresdi**

CONTENTS

Editorial I

Zita Ferenczi: Predictability analysis of the $PM_{2.5}$ and PM_{10} concentration in Budapest 359

Eszter Lábó and *István Geresdi:* Application of a Detailed Bin Scheme in Longwave Radiation Transfer Modeling 377

Zoltán Tóth: High resolution solar spectrophotometry and narrow spectral range solar radiation measurements at the Hungarian Meteorological Service 403

Ádám Leelőssy, Erika Lilla Ludányi, Márk Kohlmann, István Lagzi, and *Róbert Mészáros*: Comparison of two Lagrangian dispersion models: a case study for the chemical accident in Rouen, 21–22 January 2013 435

****

http://www.met.hu/Journal-Idojaras.php

VOL. 117* NO. 4 * OCTOBER – DECEMBER 2013

IDŐJÁRÁS

Quarterly Journal of the Hungarian Meteorological Service

Editor-in-Chief
LÁSZLÓ BOZÓ

Executive Editor
MÁRTA T. PUSKÁS

Editorial Office: Kitaibel P.u. 1, H-1024 Budapest, Hungary
P.O. Box 38, H-1525 Budapest, Hungary
E-mail: journal.idojaras@met.hu
Fax: (36-1) 346-4669

Indexed and abstracted in Science Citation Index Expanded™ and Journal Citation Reports/Science Edition
Covered in the abstract and citation database SCOPUS®

Subscription by mail:
IDŐJÁRÁS, P.O. Box 38, H-1525 Budapest, Hungary
E-mail: journal.idojaras@met.hu

Editorial

Special Issue: Physics and chemistry in modern meteorology

The theme of the 38th Meteorological Scientific Days was the atmospheric physics and atmospheric chemistry. They are relatively new research fields of the meteorology. The first research about the cloud physics was initiated by weather modification programs in the late fifties and early sixties. The era of modern atmospheric chemistry began also in the fifties of last century, and research activity in this field became important as air pollution turned into an inevitable problem in the seventies. The importance of atmospheric physics and chemistry and their direct and indirect effects on both the short and long term atmospheric processes became obvious at about the middle of the last century. Due to the small size scale of physical and chemical processes, the laboratory observations gave a good opportunity to get the first results in the early sixties. The fast improvement of computer technology has allowed us both to apply the numerical simulation as a new research tool and to take into consideration the wide scale of physical and chemical processes in the weather forecast models and in the climate research as well. Since the interaction between the small scale physical and chemical processes and the large scale dynamics are rather strong, taking observation out of the laboratories became rather urgent by the eighties. Direct observations by aircrafts and application of satellites and radars have got essential role in the research and in the day-to-day operational works, as well.

The intention of the organizing committee was to get a comprehensive presentation of research activities and applications accomplished and developed by different research groups in Hungary. Eighteen oral presentations showed our knowledge in the fields of aerosol chemistry, transport of pollution in the atmosphere, radiation, and furthermore atmospheric electricity and cloud physics. The oral presentations were delivered by researchers and PhD students from Eötvös Loránd Univeristy, Hungarian Meteorological Service, University of Pannonia, and University of Pécs.

Four papers are presented in this special issue about different topics of the conference. In two papers the authors publish their result about the application of numerical models for investigation of the long-range transport of air pollution. In one paper the results about the state-of-the-art numerical simulation of the effect of clouds on the long-wave radiation are presented. One paper gives a detailed analysis about the solar radiation measurement carried out at the Hungarian Meteorological Service.

István Geresdi
Guest Editor

IDŐJÁRÁS
Quarterly Journal of the Hungarian Meteorological Service
Vol. 117, No. 4, October–December, 2013, pp. 359–375

Predictability analysis of the $PM_{2.5}$ and PM_{10} concentration in Budapest

Zita Ferenczi

Division for Analysis of Atmospheric Environment,
Hungarian Meteorological Service,
H-1675 Budapest, P.O.Box 39.
ferenczi.z@met.hu

(Manuscript received in final form July 29, 2013)

Abstract—The harmful effect of air pollution on human health have raised a series of concerns in recent years and imposed needs for accurate descriptions of air pollution levels in urban areas. This implies that tools supporting national pollution control and planning need to be developed including public web sites or other media, where citizens exposed to the air pollutants can catch urban background concentration data, predicted concentrations, or alerts. In recent years, PM_{10} episodes caused the most critical air quality problems in Budapest. Before the development of air quality forecasting systems, which help to predict the high PM_{10} concentration episodes, the main determinants have to be identified. In this work, the effect of long-range transport and meteorological conditions on PM_{10} concentration in Budapest was analyzed in detail, as well as the results of an existing air quality forecasting systems were evaluated in case of PM_{10}.

Key-words: air quality forecast, monitoring network, urban environment, emissions, meteorological parameters

1. Introduction

Climate, weather, and air quality have harmful effects on human health and environment. For centuries, people have selected their home where they could experience the most favorable environmental conditions. The Industrial Revolution brought great changes in energy usage and technological development. People moved in the cities in the hope of a better life, where the air was contaminated with different pollutants, depending on the current level of development of technology. The first big problem was the sulphur dioxide pollution, which was caused by the burning of coal. A few hundred years later, the widespread use of cars resulted in the increase of nitrogen oxides and tropospheric ozone concentrations in the atmosphere. Nowadays, the high level of airborne particles concentration is considered seriously *(WHO,* 2011), especially in the winter season in Hungary.

Over the past few hundred years, we had to face also the changes in climate in parallel with the changes in air quality. The observed changes in climate, weather, and air quality continuously interact with each other: the pollutants are changing the climate, thus changing the weather, but also the climate impacts on air quality (*Bernard et al.,* 2001). The increasing number of extreme weather situations can occur as a result of climate change, which could create favorable conditions for rising of PM pollutant concentrations. In recent years, the PM_{10} episodes, which in many cases are associated with extreme weather situations, caused the most critical air quality problems in Budapest. The first step before developing a successful air quality forecast system is a detailed analysis of the meteorological background of the PM_{10} high-level situations (*Demuzere et al.,* 2009). Our investigation will focus on those episodes, which are caused by this pollutant, and on the long-range transport of the aerosol particles, which have also essential role in the formation of PM situation in Budapest.

The sum of all particles suspended in the atmosphere is referred to as PM (particulate matter). The particulates are classified according to their size and their capacity of penetrating the respiratory tract, causing harmful effects on people. The source of the particulate matter can be anthropogenic or natural. In urban environment, the most important causes of high PM_{10} concentration are traffic emissions, and in particular the use of diesel engines and motorcycles (*Sillanpää et al.,* 2006). Notable proportion is due to old tires and car brakes. During winter, emissions from domestic heating are added to the PM_{10} in larger amounts due to materials such as coal and wood.

Before developing an air quality forecasting system, which helps to predict the high PM_{10} concentration episodes, the main determinants (emission, meteorological conditions, and long-range transport) have to be identified. In this work, the effect of long-range transport and meteorological conditions on particulate matter in Budapest and Hungary was analyzed in detail.

Finally, the first results of the validation of the air quality prediction system of the Hungarian Meteorological Service are presented. In the evaluation work, the PM_{10} data detected by the air quality monitoring network of Budapest, as well as the forecasted air pollutant concentration values of the air quality prediction model system are used.

2. Analysis of the most important effects on PM concentration

Air quality of Budapest is determined by domestic and traffic emissions combined with the meteorological conditions. The effect of the long-range transport could also be essential. In this paragraph, the effect of emission, long-range transport, and meteorological conditions will be analyzed in detail.

2.1. Emission

The emission of PM_{10}, which has essential effect on the air quality of Budapest is determined by the industrial, traffic, and domestic heating activity in the area of Budapest. While the yearly variability of the industrial and traffic emissions are not significant, the domestic emissions increase in the winter season. All the mentioned emissions have weekly, daily and, especially for the traffic hourly variabilities. The different time variabilities of these emission sectors are reflected in the daily and yearly variability of concentration values of the PM_{10}.

2.2. Effect of the long-range transport on PM concentration

Effect of the long-range transport on the PM_{10} concentration was determined by the EMEP chemical transport model (*Simpson et al.,* 2012). With this examination only the yearly average of this effect could be analyzed. Sometimes the impact of the long-range transport can be negligible and sometimes it can be responsible for the episode situation. In this paragraph the effect of long-range transport on the PM_{10} and $PM_{2.5}$ in Budapest and Hungary will be analyzed in detail. The results will show how important this effect is and how we will able to put this information into an air quality forecasting system.

2.2.1. Short description of the EMEP model

Many types of air pollutants have been observed to travel far from their sources causing air quality problems (*EMEP Status Report,* 2012). Therefore, it is very important to begin the development of chemical transport models with investigating the long-range transport of the air pollutants. A representative of these types of models is the EMEP Eulerian long-range transport model (*Simpson et al.,* 2012). The model is an important tool to analyze both acidification and photo-oxidant activities in the air. The current version of the model working on a polar-stereographic projection, true at 60 N, has commonly been used, with grid-size of 50 km×50 km at 60 N. The standard domain has changed somewhat over the years, and was enlarged towards Eurasia in 2007. The model currently uses 20 vertical levels from the surface to the top of the model domain (currently: 100 hPa, 15 km). The 15 km high air column is divided into 20 levels in a form that the lower layer (3 km), which is relevant in the mixture of air pollutants, includes 10 levels, allowing the detailed examination of this air layer. The EMEP model uses a chemical pre-processor to convert lists of input chemical species and reactions to differential equations in Fortran code. The default chemical scheme, which is used in the open source version of the EMEP model, is the

EmChem09. This chemical scheme describes 137 reactions and 26 photochemical reactions between 72 chemical species. The model calculates the dry and wet deposition of the chemistry substances. The dry deposition flux is determined by using the deposition velocity, while the wet deposition processes include both in-cloud and sub-cloud scavenging of gases and particles.

The standard emissions input required by EMEP model consists of gridded annual national emissions of sulphur dioxide (SO_2), nitrogen oxides (NO_x $=NO+NO_2$), ammonia (NH_3), non-methane volatile organic compounds (NMVOC), carbon monoxide (CO), and particulates ($PM_{2.5}$, and PM_c, the latter being the coarse aerosol fraction, PM_{10}-$PM_{2.5}$). The particulate matter categories can be further divided into elemental carbon, organic matter, and other compounds as required. Emissions can be from anthropogenic sources (burning of fossil and biomass based fuels, solvent release, etc.), or from natural sources such as foliar VOC emissions or volcanoes.

The EMEP model has been adapted to run with meteorological fields calculated by a number of numerical weather prediction models, like the ECMWF IFS. In 2013, the data of the ECMWF IFS are available for forecasts with $0.125° \times 0.125°$ horizontal grid length and 137 vertical levels, and this model became the default meteorological driver.

2.2.2. Calculation of the long-range transport of PM_{10} concentration

For determining the long-range transport of the PM (particulate matter), the effect of the national emission from all countries in the EMEP model calculation area and the natural resources in the region were taken into account (*Gauss et al.,* 2012). The most important natural sources are the sea and the volcano, which have effect on the PM air quality conditions.

Our study was carried out for five years (2006–2010) in order to filter the variability of the weather as much as possible. Since the emission values show considerable variability from year to year (not only in case of Hungary), it is difficult to separate the effects of the weather from the effect of the emissions in the results.

First the proportion of the effect of the long-range transport was determined on the PM_{10} concentration in Hungary for five years (2006–2010). The results are summarized in *Table 1*.

On the basis of model calculations it was found that in annual average the transboundary sources are responsible for the 80% of the PM_{10} pollution formation in Hungary. According to *Table 1*, it can be said that in the last 5 years in Hungary, the PM_{10} emissions are significantly changed, and it could cause the variability in the quantity of the long-range transport.

Table 1. Fraction of transboundary contributions to PM_{10} concentrations in Hungary (unit: %) and the PM_{10} emission from Hungary (unit: Gg)

Years	Fraction of transboundary contributions (%)	Emission from Hungary (Gg)
2006	79	48
2007	83	36
2008	80	38
2009	79	48
2010	79	46

During the studied five years, trend in the change of the impact of the long-range transport could not be observed, the difference between the years can be mainly explained by changes in the PM_{10} emission of Hungary. In the years when the emission of Hungary was decreased significantly, the proportion of the long-range transport increased slightly. *Fig. 1* shows the spatial variability of the impact of long-range transport in Hungary between the years 2006 and 2010.

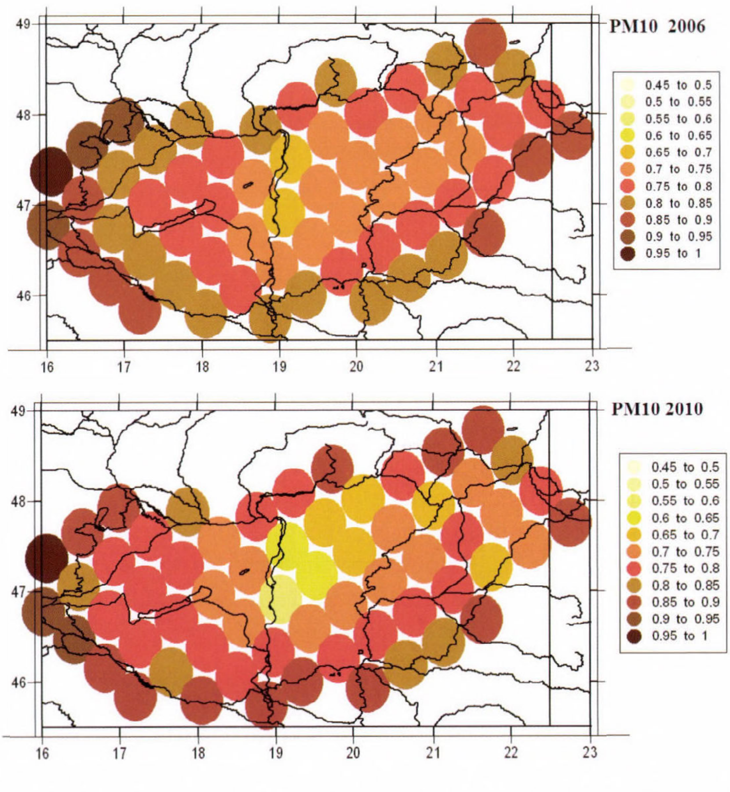

Fig. 1. Fraction of transboundary contributions to PM_{10} concentrations in Hungary in the years of 2006 and 2010 (unit: %).

In the second part of this study, the proportion of the long-range transport was determined on the PM_{10} pollution formation in the air quality zones of Hungary (*Table 2*). The definitions of the zones are:

1. Budapest and its surroundings
2. Győr - Mosonmagyaróvár
3. Komárom – Tatabánya - Esztergom
4. Székesfehérvár - Veszprém
5. Dunaújváros and its surroundings
6. Environs of Pécs
7. Sajó Valley
8. Debrecen and its surroundings

Table 2. Fraction of transboundary contributions to PM_{10} concentrations in the zones of Hungary in different years (unit:%)

Years	Zone 1	Zone 2	Zone 3	Zone 4	Zone 5	Zone 6	Zone 7	Zone 8
2006	69%	80%	78%	76%	68%	79%	72%	75%
2007	71%	86%	82%	80%	68%	84%	75%	77%
2008	68%	80%	76%	75%	65%	80%	71%	76%
2009	63%	76%	74%	73%	62%	80%	69%	77%
2010	65%	77%	74%	75%	58%	80%	67%	73%

According to *Table 2*, it can be said that the effect of the long-range transport on the PM_{10} concentration is the lowest in zone 1 (Budapest and its surroundings) and 5 (Dunaújváros and its surroundings), and the highest in zone 2 (Győr - Mosonmagyaróvár) and 6 (Environs of Pécs). Considering the country's size, this difference is mainly due to the significant spatial variability of the PM_{10} emission in Hungary. The largest industrial areas of Hungary located in zone 1 and zone 5 includes the area of our capital, where the combined effect of traffic and industries can cause high level PM_{10} emission.

2.2.3. Calculation of the long-range transport of $PM_{2.5}$ concentration

Further we determined the main contributor countries, which have significant effect on the $PM_{2.5}$ pollution formation in Hungary. *Table 3* summarizes the time variation of the national $PM_{2.5}$ emission of Hungary between 2006 and 2010.

Table 3. $PM_{2.5}$ emission from Hungary (unit: Gg).

Years	$PM_{2.5}$ emission from Hungary (Gg)
2006	29
2007	21
2008	23
2009	28
2010	32

Before preparing pie diagrams, the examined countries were placed into an order of magnitude based on how large the proportion of their contribution is to the $PM_{2.5}$ pollution of Hungary. The pie diagrams (*Fig. 2.*) show the proportion of the effect of Hungary and the 8 main contributor countries on the $PM_{2.5}$ concentration in the years of 2006 and 2010.

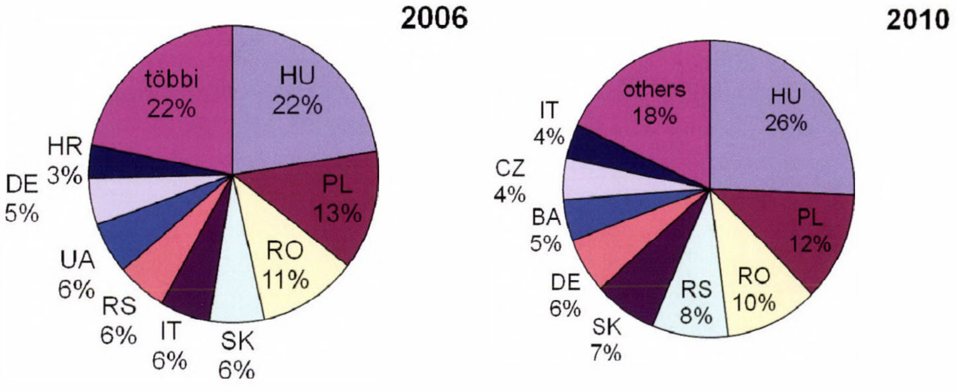

Fig. 2. Main contributors to concentrations of $PM_{2.5}$ in Hungary in the years of 2006 and 2010 (unit:%).

According to the pie charts, our homeland contributes to the $PM_{2.5}$ contamination in Hungary with 20–25%. It can be declared in general, that among the neighboring countries, the effect of Poland and Romania is considerable to the $PM_{2.5}$ contamination in Hungary, the combined effect of these two countries is comparable to the effect of Hungary. It can be said that the effect of Italy, Slovakia, Germany, and Serbia could also be considerable, but the contribution of these countries to the Hungarian $PM_{2.5}$ contamination are essentially affected by the atmospheric conditions.

Finally, the contribution of Hungary to the $PM_{2.5}$ contamination of the neighboring countries was examined. *Fig. 3* shows the results of this investigation.

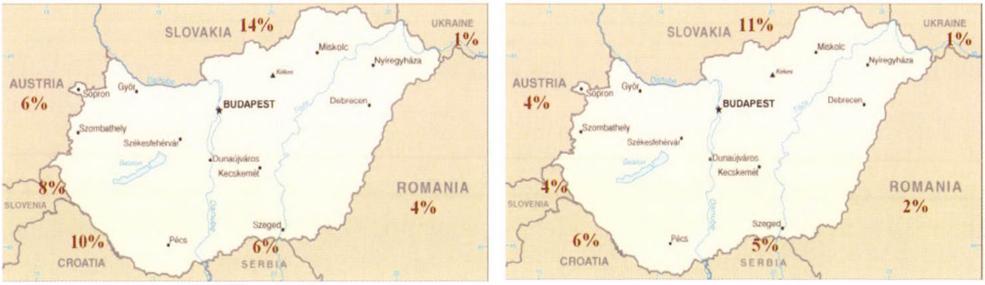

Fig. 3. Contribution of Hungary to the $PM_{2.5}$ contamination of the neighboring countries in the years of 2006 (left) and 2010 (right)(unit:%).

Comparing *Fig. 3* with the pie charts (*Fig. 2*), the amount of the contribution of the Hungarian $PM_{2.5}$ emission to the air pollution conditions in the neighboring countries is similar to their contribution to the Hungarian air pollution. The balance is positive only in the case of Romania, which means that Hungary receives much more particles from Romania than the amount was sent by Hungary to Romania. Hungary significantly pollutes the air of Slovakia, Croatia, and Serbia. Hungary contributes to the air pollution of these countries with 5–20%. The value of this rate depends on the meteorological conditions and the changes in the emission of these countries from year to year.

After specifying Hungary's contribution to the $PM_{2.5}$ air pollution in the surrounding states, it was possible to determine which countries are the net polluters of Hungary and, on the other hand, which countries are polluted by Hungary. The results of this investigation are summarized in *Table 4*.

According to *Table 4* it can be related, that Poland and Romania pollute Hungary much more, than Hungary pollutes these countries. In case of Slovakia the situation is inverse, because Hungary pollutes this country much more than Slovakia pollutes Hungary.

Finally, it was determined that from the particles emitted by Hungary 37 percent remain in the country and 63 percent cross the border of Hungary and increase the $PM_{2.5}$ contaminations of other countries. Considering the total emission of the modeling domain in case of Hungary the amount of aerosols particles arrive to the area of Hungary from outside sources are 30% more than those emitted by Hungary in all.

Table 4. The proportion of the received and sent polluted particles from the point of view of Hungary.

Year	Poland		Romania		Serbia		Slovakia	
	received	**sent**	**received**	**sent**	**received**	**sent**	**received**	**sent**
2006	13%	4%	11%	4%	6%	6%	6%	14%
2007	12%	2%	7%	4%	8%	5%	7%	9%
2008	7%	2%	10%	3%	8%	5%	6%	12%
2009	10%	3%	10%	3%	8%	5%	7%	11%
2010	12%	2%	11%	2%	8%	5%	7%	11%

The results of this investigation can be summarized as follows: the long-range transport is very determinant in Central Europe, and could not be neglected in the transport model calculations.

2.3. Effect of the weather conditions

PM_{10} concentrations exceed the threshold value mainly in winter and fall. In summer, high PM_{10} concentrations can be observed very rarely. We think, that the effect of special meteorological situations are determinant in the high level PM_{10} concentration formations (*Barmpadimos et al.,* 2011; *Mok* and *Hoi.,* 2005). In this paragraph we examine the effect of some meteorological parameters on the PM_{10} concentration. In Budapest, an air quality network of 10 stations detects the hourly concentration values of PM_{10}, we used this database.

2.3.1. Seasonal effects

Examining the past few years, it shows that high PM_{10} air quality conditions were observed especially in the winter semester. In order this statement could be supported by measurements we examined the PM_{10} data of the Gilice tér air quality monitoring station in Budapest. Those days were selected, when the daily average of the PM_{10} concentration values exceeded the limit value for the protection of human health (50 $\mu g/m^3$). The results of the study are shown in *Fig 4.*

Fig. 4 shows, that the exceedance of the limit values can be observed especially in fall and winter, in spring and summer this situation is very rare. The picture also shows a threshold value (red line) which means that the PM_{10} daily mean value may not exceed 50 $\mu g/m^3$ more than 35 times in a year. In the last years it was usual that the PM_{10} daily values exceeded the limit values for the protection of human health more than 35 times, except in 2009. *Fig 4* shows the result of the investigation only for the monitoring station „Gilice tér", but the situation is the same not only in Budapest, but in case of all of the Hungarian air quality monitoring stations. How can we explain that high PM_{10} concentration levels can be observed in Hungary especially in fall and winter in Hungary? Due to the fact that the emission and the weather situation determine the PM_{10} concentration together, the seasonal variability of these two effects has to be analyzed. In the case of PM_{10}, the most significant emissions originate from the traffic and residential wood and cool combustion. From the two factors, only the residential combustion has essential seasonal variability.

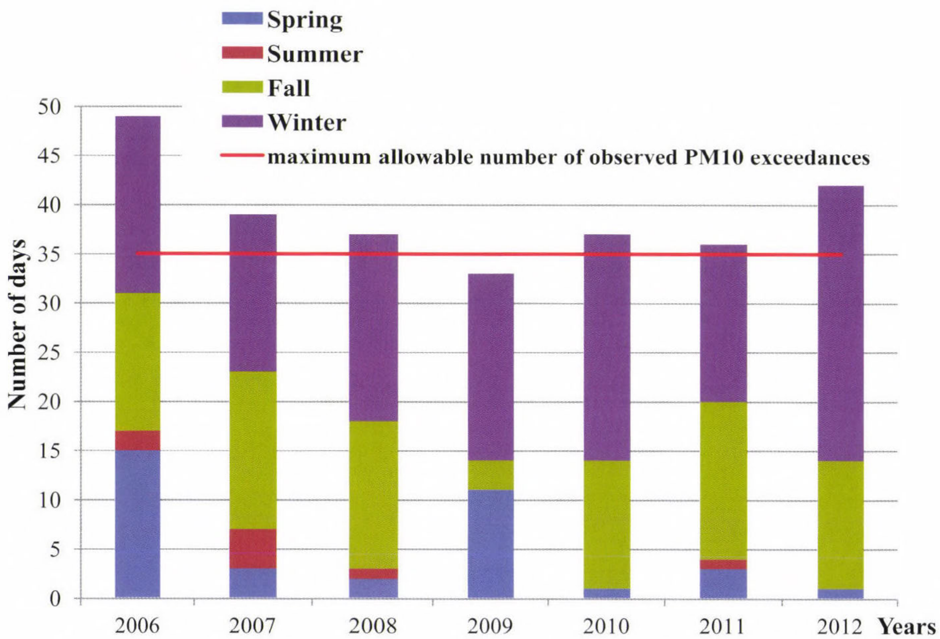

Fig. 4. Exceedance days of air quality threshold (health protection) values of PM_{10} (Budapest, Gilice tér, 2006–2010)

Beside the emission, weather situations also change from season to season in the Carpathian Basin. The typical weather situation, which favors the development of high PM_{10} concentration occurs primarily in the winter season. Furthermore, these weather situations, and meteorological parameters, which can be linked to these meteorological situations, will be examined in more detail.

Not the conventional meteorological measurements, but the grid point data of the numerical weather prediction models are used in the experiments, because we had to produce that type of parameters, which are not measurable or not possible to be calculated from the classical measurements. In this study we used the results of two different numerical weather prediction models to eliminate the differences in the parameterization methods of the two NWP models (finally, in the results, there was no significant difference).

The features of the two numerical weather prediction models used in the examination are as follows:

AROME (Applications of Research to Operations at MEsoscale) is an atmospheric non-hydrostatic modeling system, which includes a state-of-the-art numerical weather prediction model and a data assimilation system. The horizontal resolution of the model domain is 2.5 km with 60 vertical model levels. The model is used primarily for ultra-short-term forecasting and runs at the Hungarian Meteorological Service's supercomputer four times a day.

WRF (Weather Research and Forecasting) is a versatile numerical weather prediction model, which was developed at the National Center for Atmospheric Research (NCAR) and U.S. National Oceanic and Meteorological Service (NOAA) in cooperation with many research institutes and universities. Operational WRF model used by the Hungarian Meteorological Service with high resolution (2.6 km) and non-hydrostatic configuration. The service runs four times a day on a supercomputer.

2.3.2. Effect of the planetary boundary layer (PBL)

One of the most important parameter of the diffusion processes is the planetary boundary layer (PBL) height. The planetary boundary layer is defined as the part of the atmosphere that is strongly influenced directly by the presence of the surface of the earth, and responds to surface forcings with a timescale of about an hour or less (*Holton,* 1992). In the boundary layer the horizontal transport is dominated by the mean wind and the vertical by the turbulence. When pollutants are emitted into this layer, they dispersed horizontally and vertically because of the action of convection and mechanical turbulences until it becomes completely mixed.

The height of this layer cannot be measured directly, but many methods are known to determine it. In this work, two different numerical weather prediction models, AROME and WRF were applied to determine the PBL height values using different PBL parameterization schemes. In the Hungarian version of the WRF model, the BouLac PBL scheme (*Bougeault et al.,* 1989) was used to calculate the PBL height. The BouLac PBL scheme is classified as a one-and-a-half order turbulent kinetic energy (TKE) closure scheme, which determines the diffusion coefficients from the prognostically calculated TKE. In the Hungarian version of the AROME model, the top of the PBL height is determined by the momentum flux profile method (*Szintai* and *Kaufmann,* 2008). The top of the PBL is the height where the momentum flux value becomes less than 5 percent of the surface level momentum flux value.

Because the numerical weather prediction models determine the PBL height using different parameterization schemes, we determined the connection between the two differently determined PBL height, and the PM_{10} concentration values.

In our examination the hourly average PM_{10} concentration values were used, that are measured between October 27 and November 26, 2011 at the air quality monitoring station Gilice tér, and the hourly PBL height determined by the two mentioned numerical weather prediction models. The examined time period is the longest PM_{10} episode situation which has been detected since the PM_{10} measurements started in Budapest. *Fig 5* shows the relationship between the two parameters.

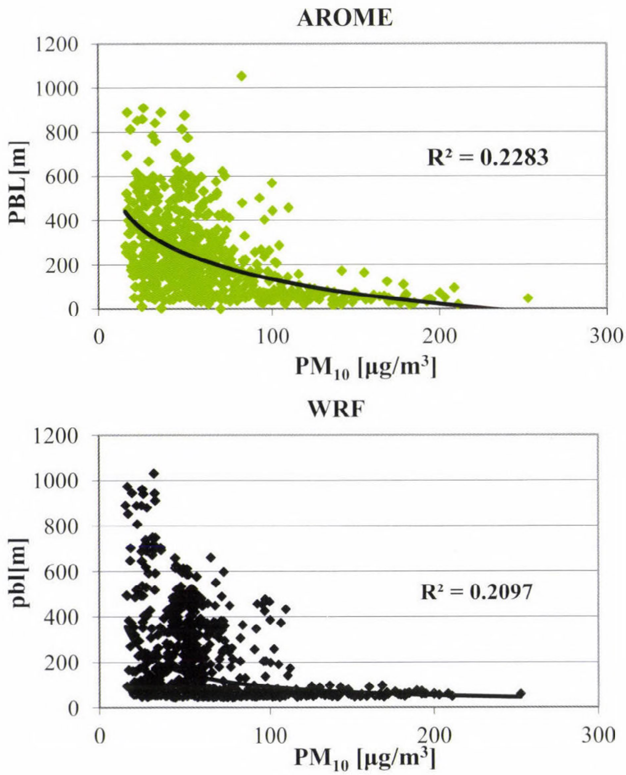

Fig. 5. The relationship between the height of the planetary boundary layer (PBL) and the PM_{10} concentrations (Budapest, Gilice tér).

According to *Fig. 5,* in case of high (>100 μg/m^3) PM_{10} concentration values the PBL heights were lower than 200m. Nevertheless, this statement is not true in another direction, because in case of low PBL height the PM_{10} concentration is not so high in every cases. Regression analysis was also performed to determine the connection between the PM_{10} concentration and PBL height hourly values. There is not big difference between the results of AROME and WRF models. The value of the regression is a little bit higher in case of AROME.

2.3.3. *Effect of the stagnation index (SI)*

Because the results of the analysis with the PBL height was not convincing to find the weather conditions resulting high PM_{10} concentration level, we took into the analysis other meteorological parameters. While the PBL height characterizes the intensity of the vertical diffusion in the atmosphere, the magnitude of wind speed and wind shear could be the index of the intensity of the horizontal diffusion. The SI index is the parameter (*Holst et al.* 2008), which characterizes the intensity of the horizontal and vertical diffusion in the lower layer of the atmosphere as it takes into account the height of the PBL and the wind speed in the surface layer. The SI index can be determined by this simple equation:

$$SI = \sqrt{\frac{10^6}{PBL \times v}}$$

Fig. 6 shows the relationship between the SI index and the PM_{10} concentration. According to *Fig. 6*, the relationship between the SI index and the PM_{10} concentration is slightly stronger, than the relationship between the PBL height and the PM_{10} concentration. Based on this study we can conclude that the weak mixing processes in the planetary boundary layer (low PBL heights and low wind speed) are responsible for the formation of high PM_{10} concentrations with 25%, and there is no big difference between the results, which was based on the WRF or AROME numerical weather prediction models.

2.3.4. *Effect of the wind speed*

The analysis so far basically studied the effect of the intensity of the atmospheric diffusion processes on the PM_{10} concentration. However, the atmospheric processes may be relevant in terms of the region from where the polluted air arrived to the area of the measuring point. In this respect, the effect of wind direction is essential. Using this analysis, clean and dirty sectors could be separated in the area of the monitoring station, and changes in the emission intensity and compositions could be inferred.

In this analysis, PM_{10} data detected by the air quality monitoring station Gilice tér, as well as the measured meteorological data between January 9, 2006 and February 14, 2012 are used. In case of this examination we halved the day to daytime and nighttime. *Fig. 7* shows the dependence of the PM_{10} concentrations on the wind direction in daytime and nighttime. The results are significantly different in the different parrt of the day. For daytime episode situation, the effect of traffic emission from the direction of M5 highway can be observed, while nighttime the effect of domestic heating from the direction of the residential district can be observed.

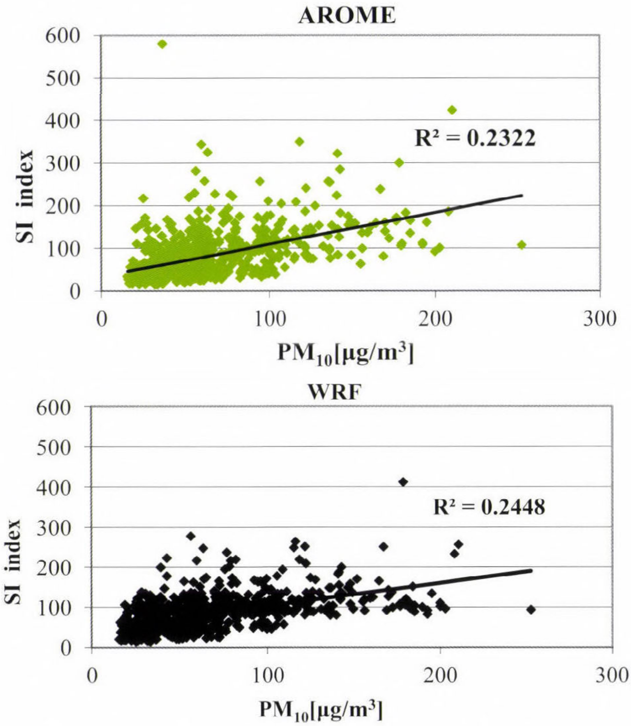

Fig. 6. The relationship between the SI index and the PM_{10} concentrations. (Budapest, Gilice tér).

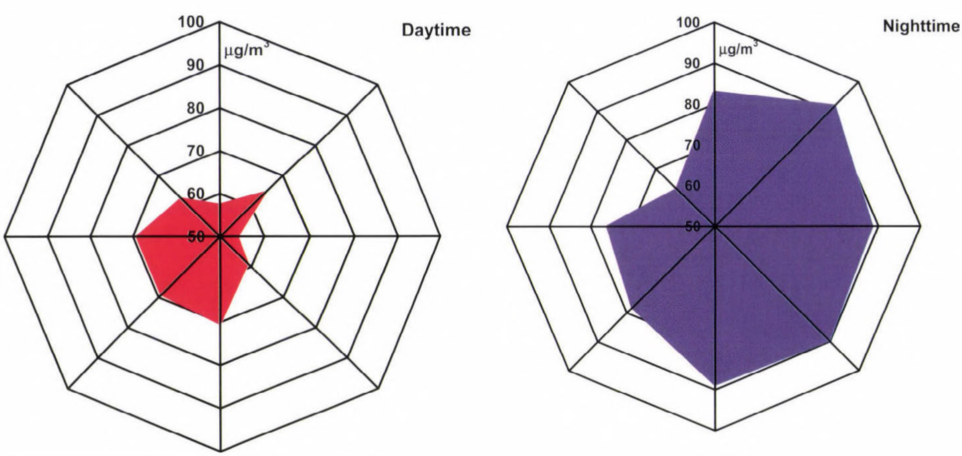

Fig. 7. Wind direction dependency of the PM_{10} concentrations in episode situations for daytime and nighttime. (Budapest, Gilice tér).

Based on *Fig. 7*, it is likely that during the day the traffic emission and during the night the domestic heating is the primary source of PM_{10} pollution in the area of Gilice tér station. It is worth to compare the highest average concentration values, which was detected in daytime and nighttime. During the day, the average hourly maximum concentration was 70 $\mu g/m^3$, while at night it was 90 $\mu g/m^3$, which could be explained with the low boundary layer at night, but it is possible that the level of emissions from residential combustion is greater than the traffic emission.

3. Validation of the PM_{10} forecast for Budapest

The Hungarian Meteorological Service adopted a chemical transport model to forecast the concentration values of the main pollutants. The forecasting tool is an integrated system of the WRF meteorological and CHIMERE chemical transport models. The air quality prediction system has been operating since June 1, 2010, which means, that there are longer than 2-year data sets to evaluate how it is working. In the validation work the PM_{10} data detected by the air quality monitoring network of Budapest, as well as the forecasted air pollutant concentration values of the air quality prediction model system are used. The values of NMSE (normalized mean square error) and correlation were determined for the PM_{10} pollutants and for the grid points, where the air quality monitoring stations are located. NMSE is a typical statistical indicator of the overall deviations between predicted and measured values. Low values mean, that the model is well performing both in space and time. The correlation coefficient is a measure of how well the predicted values from a forecast model "fit" the real-life data. The values indicate that the best forecast can be expected in the area of Honvéd utca monitoring station (the correlation value is 0.53) and the worst in the area of Pesthidegkút monitoring station (the correlation value is about 0.15) for PM_{10}. *Table 5* shows all the results of this examination.

The results of this evaluation work shows, that the PM_{10} concentration prediction is not so good. There is big lack in the emission input data base calculated for PM_{10}, mainly in the domestic heating, which is reflected in the case of Pesthidegkút monitoring station, for which the values of NMSE and correlation are very bad. Presumably there are some problems with our traffic emission data base, and sometimes the NWP model is not able to predict well the essential meteorological parameters, which have effect on the PM_{10} concentration (*Saide et al.,* 2011).

In the future we plan to develop our emission database, determine new boundary conditions. We hope, that this investigation will result in an improvement in the PM_{10} forecast.

Table 5. NMSE and correlation values of the PM_{10} prediction

Station	NMSE	Correlation
Csepel	0.97	0.39
Erzsébet tér	0.35	0.49
Gergely utca	0.40	0.45
Gilice tár	0.57	0.31
Honvéd	0.31	0.53
Kőrakás park	0.14	0.36
Kosztolányi tér	0.36	0.33
Pesthidegkút	0.88	0.15
Széna tér	0.50	0.35
Teleki tér	0.45	0.49
Tétényi út	0.64	0.19

4. Conclusion

In this study, we tried to determine the contribution of the effect of the long-range transport and meteorological conditions to the Hungarian PM_{10} and $PM_{2.5}$ air pollution. In case of the long-range transport, the study tool was the EMEP chemical transport model, and the results of this model calculations were the bases of examination.

The conclusions drawn from the calculations are:

- In Hungary, the contribution of the long-range transport to the PM air pollution is 70–80%.
- The effect of the long-range transport shows significant spatial variability, the most important part is the western frontier of Hungary, and the smallest is the central part of the country.
- Among the European states, Romania and Poland are the greatest polluters of Hungary's atmosphere.
- Particles emitted by Hungary contribute significantly to the PM pollution of Slovakia, Serbia, and Croatia.
- 37% of the particulate matters emitted by Hungary remain in the country, and 63% cross the border of Hungary and increase the PM contaminations of other countries.
- In case of Hungary, the aerosol particles arrive to the area of Hungary from outside sources are 30% more than the particles emitted by the country in all.
- The reasons of the formation of PM_{10} related to high air pollution situations are: unfavorable weather conditions and increasing emission of the domestic heating. Among the meteorological parameters, the effect of the SI index is the most significant.

A dispersion modeling system was developed by the Hungarian Meteorological Service to predict the air quality in Budapest for 48 hours. The core of this system is the CHIMERE chemical transport model. Beside the CHIMERE's built-in emission database, also own emission data (point sources, traffic count) for Budapest are used during modeling. It was shown that the quality of the results depends on the quality of the weather forecast, the long-range transport, and the emission database. It was also demonstrated that there is a lack in the emission input database calculated for PM_{10}. Long-term transport of the pollutants seems to play an important role during concentration calculations. Validation of the system also confirms these statements.

References

Barmpadimos, I., Hueglin, C., Keller, J., Henne, S., and. *Prévôt, A.S.H.,* 2011: Influence of meteorology on PM_{10} trends and variability in Switzerland from 1991 to 2008, *Atmos. Chem. Phys. 11*, 1813–1835.

Bernard, S.M., Samet, J.M., Grambsch, A., Ebi K.L., and *Romieu, I.,* 2001: The Potential Impacts of Climate Variability and Change on Air Pollution-Related Health Effects in the United States. *Environ.Health Perspect. 109*, 199–209.

Bougeault, P. and *Lacarrére, P.*, 1989: Parameterization of orography-induced turbulence in amesobeta-scale model. *Mon. Weather Rev. 117,* 1872–1890.

Demuzere, M., Trigo, R.M., de Arellano, J.V., and van *Lipzig, N.P.M.*, 2009: The impact of weather and atmospheric circulation on O_3 and PM_{10} levels at a rural mid-latitude site, *Atmos. Chem. Phys. 9*, 2695–2714.

EMEP Status Report 1, 2012: "Transboundary acidification, eutrophication and ground level ozone in Europe in 2010" Joint MSC-W & CCC & CEIP Report

Gauss, M., Nyíri, Á., Steensen, B.M., and *Klein, H.*, 2012: MSC-W Data Note 1: Transboundary data by main pollutants (S, N, O_3) and PM: Hungary. Oslo: Norwegian Meteorological Institute.

Holst, J., Mayer, H., and *Holst, T.,* 2008: Effect of meteorological exchange conditions on PM_{10} concentration. *Meteorol. Zeit. 17*, 273–282.

Holton, J.R., 1992: An Introduction to Dynamic Meteorology. *Academic Press*, New York.

Mok K.M. and *Hoi, K.I.*, 2005: Effects of meteorological conditions on PM10 concentrations - A study in Macau, *Environ. Monit. Assess. 102*, 201–223.

Saide, P.E; Carmichael, G.R; Spak, S.N; Gallardo, L., Osses, A.E., Mena-Carrasco, M.A., and *Pagowski, M.,* 2011: Forecasting urban PM_{10} and $PM_{2.5}$ pollution episodes in very stable nocturnal conditions and complex terrain using WRF–Chem CO tracer model. *Atmos. Environ. 45*, 2769–2780.

Sillanpää, M., Hillamo, R., Saarikoski, S., Frey, A., Pennanen, A., Makkonen, U., and *Salonen, R.O.,* 2006: Chemical composition and mass closure of particulate matter at six urban sites in Europe. *Atmos. Environ. 40*, 212–223.

Simpson, D., Benedictow, A., Berge, H., Bergström, R., Emberson, L.D., Fagerli, H., Flechard, C.R., Hayman, G.D., Gauss, M., Jonson, J.E., Jenkin, M.E., Nyíri, A., Richter, C., Semeena, V.S., Tsyro, S., Tuovinen, J.-P., Valdebenito, Á., and *Wind, P.*, 2012: The EMEP MSC-W chemical transport model – technical description. *Atmos. Chem. Phys., 12*, 7825–7865,

Szintai, B., and *Kaufmann, P.*, 2008: TKE as a measure of turbulence. *COSMO Newsletter 8*, 2–9.

WHO, 2011: Explosure to air pollution (Particulate Matter) in outdoor air (available at web site: http://www.euro.who.int/__data/assets/pdf_file/0018/97002/ENHIS_Factsheet_3.3_July_2011.pdf

IDŐJÁRÁS
Quarterly Journal of the Hungarian Meteorological Service
Vol. 117, No. 4, October–December, 2013, pp. 377–402

Application of a detailed bin scheme in longwave radiation transfer modeling

Eszter Lábó*[1] and **István Geresdi**[2]

[1]*Hungarian Meteorological Service, P.O. Box 38, H-1525 Budapest, Hungary*

[2]*Szentagothai Research Center, University of Pécs, Ifjúság útja 20, H-7624 Pécs, Hungary*

Corresponding author E-mail: labo.e@met.hu

(Manuscript received in final form October 15, 2013)

Abstract—Absorption and transfer of radiation in clouds are sensitive to size distribution of water drops. A new numerical scheme has been developed for calculating the extinction coefficients of water clouds in the longwave region. While the generally applied bulk schemes in numerical models characterize the whole size distribution of the water droplets with one parameter (effective radius), detailed models allow us to calculate the optical properties without any assumption about the size distribution of water drops. Our model uses a bin microphysical scheme which uses the number concentration and mixing ratios of water in 36 size intervals.

This paper describes the developed bin radiation scheme. The wavelength-dependence of extinction coefficients calculated by bin and bulk schemes is compared at different effective radius. It was also investigated how the number concentration of droplets and liquid water content affect the difference between the two schemes. The relative difference depends both on the effective radius and on the wavelength. If the effective radius is larger than 10 μm, the relative difference remains below 20%. It is higher in the case of smaller effective radius.

The bin scheme has also been implemented in the RRTM LW radiation transfer model code. Upward, downward, and net radiation profiles for four different cases were studied with the RRTM model. It was found that the outgoing longwave radiation is sensitive on the applied scheme when the cloud layer is thin. Significant differences were found between the gradients of the net longwave radiation profiles in all cases. These differences have significant impact on the evolution of the vertical temperature profiles, which affects both cloud dynamics and microphysics.

Key-words: longwave radiation, bin scheme, numerical modeling, cloud-radiation interaction, water clouds, cooling rate

1. Introduction

The large impact of clouds on the temperature profiles and radiation budget stirs the need for a more accurate modeling of cloud-radiation interactions (*Ramanathan* and *Inamdar,* 2006; *Corti* and *Peter,* 2009). Recent research focuses on the development of more precise calculation methods of radiative cloud forcing (*Liu et al.,* 2009). Besides models, measurement campaigns have been launched to determine the effect of cloud radiative forcing on the Earth's atmosphere (*Arking,* 1991, *Chen et al,.* 2000). It is widely accepted that the clouds decrease the shortwave radiative flux at the surface by 40–50 Wm–2 , and they also decrease the outgoing longwave radiative flux by around 30 Wm–2 (*Ramanathan et al.,* 1989; *Wielicki et al.,* 1996; *Rossow* and *Duenas,* 2004). These effects result in a net diminution of 10–20 Wm–2 (*Chen* and *Rossow,* 2002; *Oreopoulos* and *Rossow,* 2011). However, the determination of the radiative forcing for each cloud and cloud type requires exact numerical models including accurate parameterization of cloud physical processes.

The necessity of a more detailed cloud radiation schemes in the modeling of cloud-radiation interactions has been permanently suggested during the last 30 years. It has been asserted by *Kunkel* (1984) and later by *Fouquart et al.* (1990) that a more accurate parameterization of cloud-radiation interactions is essential. *Buriez et al.* (1988) stated that until the '90s, optical characteristics had been tuned in the atmospheric models by arbitrary diagnostic cloud schemes to fit the results to the observations. *Harrington* (1997) showed that the applied parameterization technique in models strongly affects the optical properties of the simulated clouds. *Stephens* (2004) proved that the cloud properties such as optical depth, liquid and ice water contents, and particle size distribution significantly affect the radiation budget of Earth. Lack of correct data about optical properties of clouds is one of the major obstacles in determining the radiation budgets both of atmosphere and surface. According to *Stephens* (2004), the effect of clouds on heating and cooling of the atmosphere is a substantial feedback mechanism that had not been adequately investigated. Improvement in the numerical forecasting capacities of a weather forecasting model has been demonstrated in *Liu et al.* (2009). They have included detailed radiation scheme with microphysical size dependence in the U.S. Navy's Coupled Ocean-Atmosphere Mesoscale Prediction System (COAMPS) model. It has ultimately reduced the model's systematic warm bias, and overestimation of humidity in the upper troposphere. Comparing with measurements, the root mean square error of LW downward flux has changed from 17.67 Wm–2 to 9.44 Wm–2 in the case of standard model, and that of improved radiation model, respectively. *Petters et al.* (2012) highlighted that cloud radiative heating, and its feedback on cloud dynamics is largely sensitive to the number concentration of water droplets in stratiform clouds.

In numerical models, optical properties of warm clouds such as single scattering albedo and extinction coefficient are generally calculated by using a characteristic size of cloud droplets (*Lindner* and *Li,* 2000; *Ebert* and *Curry,* 1992). In these bulk schemes the size distribution of the droplets is generally given by an idealized gamma function with one or two independent parameters (*Ritter* and *Geleyn,* 1992; *Walko et al.*, 1995; *Straka et al.,* 2007; *Tompkins* and *Di Giuseppe,* 2009). The bulk models use the effective radius of cloud droplets and liquid water content to determine the optical properties (*Fu et al.,* 1998; *Hong et al.,* 2009, *Gettelman et al.,* 2008). Contrary to bulk schemes, bin microphysical schemes are capable to describe arbitrary size distribution of cloud droplets. In the case of bin schemes no assumption is needed on the droplet size distribution. While the bin schemes for the numerical simulation of cloud microphysical processes has been widely used since the early nineties, the application of this technique to calculate the optical properties of the clouds has become in the focus of researches in the last ten years. The advantage of the application of bin schemes for the calculation of cloud optical properties was proved by *Harrington* and *Olsson* (2001). They showed that the longwave radiation budget at the surface can be altered by 40 Wm^{-2} depending on how the effective radius of cloud droplets was calculated. The impact of using bin models on the cloud microphysical structure has been examined in *Harrington et al.* (2000). He has evaluated the effect of radiative cooling on the growth of water droplets. He showed that larger drops were growing faster than smaller drops. Drizzle-sized drops could be produced from 20 to 50 min earlier through the inclusion of the radiative term, which leads to a higher potential for enhancing drop collection and precipitation formation.

In this paper results about a new bin radiation scheme are presented. This technique was developed to calculate the extinction coefficients of water droplets in the infrared region. The impact of application of this new scheme on the longwave radiation budget is presented. The next section contains the description of the scheme. The results about the comparison with a bulk scheme are presented in Section 3. In Section 3.1, the changes in the extinction coefficients are presented. In Section 3.2, the change in the intensity of longwave radiation due to the application of bin scheme compared to the bulk scheme is studied. Section 3.3 examines the changes in the radiation profile with the help of the RRTM radiative transfer model, caused by the difference in the extinction coefficients. The conclusions are given in Section 4.

2. *Description of the model*

2.1. Description of the bin scheme

The optical parameters describing scattering, extinction, and absorption of radiation in clouds are: the extinction and scattering coefficients (β_{ext} and β_{sca});

the single scatter albedo (ω), which is the ratio of scattering in total extinction; and the asymmetry parameter (g), which characterizes the angle-dependence of the scattering (*Roach* and *Slingo,* 1979; *Stephens,* 1984; *Hu* and *Stamnes,* 1993). The definitions of these parameters for a given wavelength, in the case of water droplets assumed to be spherical are given in Eq. (1) – (4).

$$\beta_{ext}=\int_0^\infty A(D)Q_{ext}(D,m,\lambda)n(M)dM \quad , \tag{1}$$

$$\beta_{sca}=\int_0^\infty A(D)Q_{sca}(D,m,\lambda)n(M)dM \quad , \tag{2}$$

$$\omega=\frac{\beta_{sca}}{\beta_{ext}} \quad , \tag{3}$$

$$g=\frac{1}{2}\int_{-1}^{1} p(\mu)\mu\, d\mu \quad , \tag{4}$$

where D is the droplet diameter, M is the mass of the droplet, λ is the wavelength, $n(M)$ is the droplet size distribution as a function of M, Q_{ext} is the extinction efficiency, Q_{sca} is the scattering efficiency, μ is the cosine of the scattering angle, and $p(\mu)$ is the phase function. m is the refraction index, $A(D)$ is the cross section.

The radiation transfer models and numerical models calculate the radiative transfer over radiation bands instead of calculating it at single wavelengths. For this purpose, a so-called broadband extinction coefficient is defined for an arbitrary wavelength interval of $\Delta\lambda$ (*Slingo* and *Schrecker* (1982)):

$$\beta_{ext}=\left(\int_{\Delta\lambda} E_\lambda \int_0^\infty A(D)Q_{ext}(D,m,\lambda)n(M)dM\, d\lambda\right)/\int_{\Delta\lambda} E_\lambda d\lambda \quad , \tag{5}$$

where E_λ is the Planck-function at a reference temperature (usually at 273 K). Bin scheme presented in details in *Rasmussen et al.,* (2002) is used to calculate the above integrals. The size range from 1.5625 μm to 5.07968 mm is divided into 36 bins with doubling the mass at the bin edges. The applied moment conserving technique allows us to describe the size distribution of water drops in every bin:

$$n_k(M)=A_k+M\cdot B_k\,. \tag{6}$$

The coefficients A_k and B_k are calculated from the number concentrations and mixing ratios in the kth bin (see more details in *Tzivion et al.*, 1987). Using the bin scheme the Eq. (5) can be approximated by the following equation:

$$\beta_{ext} = \sum_{k=2}^{N_{bins}} \left[\int_{\Delta\lambda} \left(E_\lambda \int_{M_{k-1}}^{M_k} A(D) Q_{ext}(D,m,\lambda) n_k(M) dM\, d\lambda \right) / \int_{\Delta\lambda} E_\lambda d\lambda \right] , \quad (7)$$

where N is the number of the bins, furthermore, M_{k-1} and M_k are the mass of the water drops at the edges of the kth bin.

The extinction coefficients can be calculated in every bin over any arbitrary wavelengths interval of $\Delta\lambda$. E_λ was calculated at T=273 K in this research. Sensitivity of the extinction coefficients on the temperature was investigated by calculating the above integral at T_1=303 K and T_2=243 K. Differences were found to be insignificant for the extinction coefficients for the whole infrared spectra. Comparing to the case of T=273 K, in the case of T_1 a little bit smaller value was calculated (the maximum difference was 0.17%), and in the case of T_2 a slightly larger value was calculated (maximum difference was 0.29%). Thus, the temperature dependence of extinction coefficients is neglected in this study.

The Q_{ext} extinction efficiency can be evaluated on the base of the Lorentz-Mie theory; however, it cannot be analytically calculated even in the case of spherical water drops. Instead of using time consuming numerical methods, the modified anomalous diffraction theory (MADT) was applied to describe the optical properties of water drops. *Mitchell* (2000) proved that application of this theory results in small errors comparing to the Lorentz-Mie theory. According to MADT, the extinction efficiency can be defined as a sum of two different components: the corrected Q_{ext}, and Q_{edge}:

$$Q_{ext,m}(D,\lambda,m) = \left(1 + \frac{C_{res}}{2}\right) Q_{ext} + Q_{edge} . \quad (8)$$

The details about calculation of C_{res}, Q_{ext}, and Q_{edge} variables can be found in Appendix A.

As the $Q_{ext}(D,\lambda,m)$ function has been given in explicit form, the integrals in Eq. (7) can be calculated by taking into consideration the $n_k(M)$ size distribution given by Eq. (6). The evaluation of the integrals in Eq. (7) can be made to be very fast, if two two-dimensional kernels were precalculated over the two-dimensional grid defined by both mass intervals and wavelength intervals of the radiative transfer model described in Section 2.3.

The details about the calculation of $K_{Akj}(M_{k-1},M_k,\Delta\lambda_j)$ and $K_{Bkj}(M_{k-1},M_k,\Delta\lambda_j)$ are given in Appendix B. These coefficients can be implemented in the radiative transfer model afterwards, to yield extinction coefficients for the new bin method.

2.2. Description of the bulk scheme

Because the computational cost of the bin scheme is high, it is important to investigate whether the optical parameters defined by the Eqs. (1) – (4) are sensitive on the method they are calculated. In this study, extinction coefficients (Eq. (1)) obtained by bin scheme are compared to the extinction coefficients obtained by a bulk scheme method (*Hu* and *Stamnes,* 1993). This parameterization is currently used to calculate extinction coefficients in the RRTM LW radiation transfer model. More details about this model are given in Section 2.3.
The method developed by *Hu* and *Stamnes* (1993) is a frequently applied bulk parameterization scheme, which uses the effective radius and the liquid water content (*LWC*) as input parameters:

$$\beta_{ext}/LWC = a\,r_e^b + c \tag{9}$$

The *a, b, c* coefficients are defined for the following three intervals of the effective radius: 2.5 – 12 μm; 12 – 30 μm; and 30 – 60 μm, and for 50 wavelength bands in the infrared spectrum. This scheme is based on Mie-scattering calculations, which is appropriate method to determine the Q_{ext} (D,m,λ) extinction efficiency, at any wavelengths and droplet diameters. The $n(M)$ droplet size distribution was assumed to be a gamma-size distribution:

$$n^*(r) = \frac{N_0}{\Gamma(\gamma)\,r_m}\left(\frac{r}{r_m}\right)^{\gamma-1}\exp^{-r/r_m} , \tag{10}$$

where N_0 is the total (volume) number concentration, Γ is the gamma function, r_m is the characteristic radius of the size distribution, and γ is a constant, that defines the shape of the distribution (*Stephens et al.*, 1990).

The *a, b, c* coefficients were calculated by least-square fitting of Eq. (9) on the set of extinction coefficients related to data pairs of effective radius and liquid water content. The effective radii and liquid water content were calculated by using different shape parameters (γ), characteristic sizes (r_m), and total number concentrations (N_0) in Eq. (10). This group of data was set up for 50 predefined wavelengths, ranging from 3.9 μm to 150 μm (*Hu* and *Stamnes,* 1993).

2.3. Description of the radiative transfer model

The RRTMG LW (rapid radiative transfer model for the longwave radiation) (*Clough et al.*, 2005) radiation model is used in our studies to calculate the longwave fluxes in the case of different clouds. It has been developed for the calculation of longwave atmospheric fluxes and cooling rates in atmospheric radiative transfer studies, as well as for implementation in numerical weather prediction and climate models.

The longwave spectrum is divided into 16 bands in the RRTM, from 3.33 μm to 1000 μm, according to the main absorption bands of the atmospheric gases at different wavelengths (*Table 1*). These bands have been determined to have maximum two main absorbing compounds in each band; to limit the variation of the Planck function within the bands; and to keep the number of bands minimized as possible while keeping the previous two conditions. The model is capable to take into account the radiative effects of water vapor, carbon dioxide, ozone, nitrous oxide, methane, oxygen, nitrogen, and halocarbons. The two main compounds (water vapor, carbon dioxide) were taken into consideration in present calculations.

Table 1. Wavelengths intervals of the RRTM model

Band	**Wavelength (μm)**	**1050–96 (hPa)**	**96–0.01 (hPa)**
16	40.00 – 1000.00	H_2O	H_2O
15	20.00 – 40.00	H_2O	H_2O
14	15.90 – 20.00	H_2O, CO_2	H_2O, CO_2
13	14.30 – 15.90	H_2O, CO_2	CO_2, O_3
12	12.20 – 14.30	H_2O, CO_2	CO_2, O_3
11	10.20 – 12.20	H_2O	–
10	9.26 – 10.20	H_2O, O_3	O_3
9	8.47 – 9.26	H_2O	O_3
8	7.19 – 8.47	H_2O, CH_4	CH_4
7	6.76 – 7.19	H_2O	H_2O
6	5.55 – 6.76	H_2O	H_2O
5	4.81 – 5.55	H_2O, CO_2	–
4	4.44 – 4.81	H_2O, N_2O	–
3	4.20 – 4.44	CO_2	CO_2
2	3.85 – 4.20	N_2O, CO_2	–
1	3.33 – 3.85	H_2O, CH_4	–

The development of RRTM has been based on the calculations made by the line-by-line radiative transfer model (LBLRTM) (*Mlawer et al.*, 1997). The absorption coefficients for different temperatures, pressures, and relative amount of the absorption gases have been determined by this model. These constants are imported as look-up-tables into the RRTM model, and linear interpolation is used to calculate the absorption coefficients at the actual temperature, pressure, and gas concentration.

The radiative transfer is calculated in the RRTM model for all of the 16 spectral bands, as if it was a single spectral wavelength. In the case of vertically inhomogeneous layers, it uses the Pade's approximation to calculate effective Planck function for each layer, by using the temperatures at boundaries of layers, and mean layer temperatures (*Clough et al.,* 1992; *Mlawer et al.,* 1995). The variation of the Planck function in a band according to the wavelength is taken into account by weighting according to the abundance of main gas compounds related to the band. (*Mlawer et al.*, 1995).

In RRTM the correlated-k method is used to describe the wavelength-dependency of the absorption coefficients in the radiative transfer equations. The correlated k-technique is an approximation method with high accuracy. It is frequently applied for the calculation of radiative transfer radiances by transforming the integral over wavelength into integral over a cumulative probabilistic function. This function is determined by rearranging the absorption coefficient values in ascending order according to the fraction of the given value in the actual wavelength band (*Mlawer et al.,* 1997). This generates a new order of the absorption coefficients according to their probability. A characteristic average value of the absorption coefficient in a given probability-interval is then defined, and used in the radiative transfer equations to calculate the radiances.

The values of the probability function at given pressure and temperature are calculated beforehand by a line-by-line radiative transfer model. In the RRTM, they are interpolated linearly between the logarithm of temperature and pressure values. Also, linear weighting of the absorption coefficients is done according to their integrated line strengths and column amount, when two different species are dominant in the same spectral band. These simplifications make this method computationally fast, meanwhile keeping the needed accuracy.

Validation of the RRTM model shows that RRTM results agree with those computed by the line-by-line model within 1.0 Wm^{-2} at all levels, and the computed cooling rates agree to within 0.1 K/day in the troposphere and 0.3 K/day in the stratosphere (*Clough et al.,* 2005). The RRTM model has been implemented as the operational code for longwave radiation at the European Center for Medium-Range Weather Forecasts (ECMWF) and in the Global Forecast System (GFS) of the National Centers for Environmental Prediction (NCEP). It is also implemented as one option in the National Center for Atmospheric Research (NCAR) Weather Research and Forecasting (WRF) model.

3. Results

3.1. Comparison of the extinction coefficients calculated by bin and bulk schemes

Extinction coefficients calculated by bin and bulk schemes are compared in this section. The investigated cases are described in *Table 2.* The first column gives the number concentration, the second, third, and fourth ones show the effective radii if $LWC_1 = 10^{-3}\,\mathrm{kg\,m^{-3}}$, $LWC_2 = 10^{-4}\,\mathrm{kg\,m^{-3}}$ and $LWC_3 = 10^{-5}\,\mathrm{kg\,m^{-3}}$, respectively. The size distributions of the water drops were given by Eq. (10), and the value of γ parameter was chosen to be equal to 3.

Table 2. Effective radius for gamma-distributions for different number of concentration and LWC values

	LWC_1=10^{-3} kg m^{-3}	LWC_2= 10^{-4} kg m^{-3}	LWC_3= 10^{-5} kg m^{-3}
N_i (*10^6) 1/m^3	r_{eff} (*10^{-6}) m	r_{eff} (*10^{-6}) m	r_{eff} (*10^{-6}) m
1000	7.92	3.68	–
250	12.57	5.84	2.71
100	17.07	7.92	3.67
50	21.50	9.98	4.63
20	29.18	13.55	6.29

It has been found that the changes in the difference between the extinction coefficients calculated by the bin and by the bulk scheme depends mostly on the value of the effective radius of the size distribution, regardless of the values of the LWC and the number concentration of water droplet. E.g., the differences between the bin scheme and the bulk scheme were very similar in the following two cases: $LWC_2 = 10^{-4}\,\mathrm{kg\,m^{-3}}$, $N = 1000 \cdot 10^6\,\mathrm{m^{-3}}$ and $LWC_3 = 10^{-5}\,\mathrm{kg\,m^{-3}}$, $N = 100 \cdot 10^6\,\mathrm{m^{-3}}$.

Fig. 1 summarizes the results obtained at $LWC_1 = 10^{-3}\,\mathrm{kg\,m^{-3}}$ at two different concentrations of the droplets, and *Fig. 2* summarizes the results obtained at $LWC_2 = 10^{-4}\,\mathrm{kg\,m^{-3}}$, at two different number concentrations.

Fig. 1 and *Fig. 2* show that the difference between the extinction coefficients depends both on the wavelength and on the effective radius. Because the surface and the atmosphere emit most of the energy in the wavelength interval of 5–20 μm, the difference between the results of the schemes will be analyzed in this interval. The relative difference can be higher than 20% if the effective radius is lower than 10 μm. There is no significant (maximum 4%) difference between the calculated extinction coefficients if the effective radius is higher than about 10 μm, and the wavelength is less than about 8.0 μm. Although the local minimum values at near to the wavelength of 10 μm given by the different schemes are very similar, the application of the bulk scheme results in much sharper decrease and increase of the extinction coefficients in the wavelength interval of 10–15 μm.

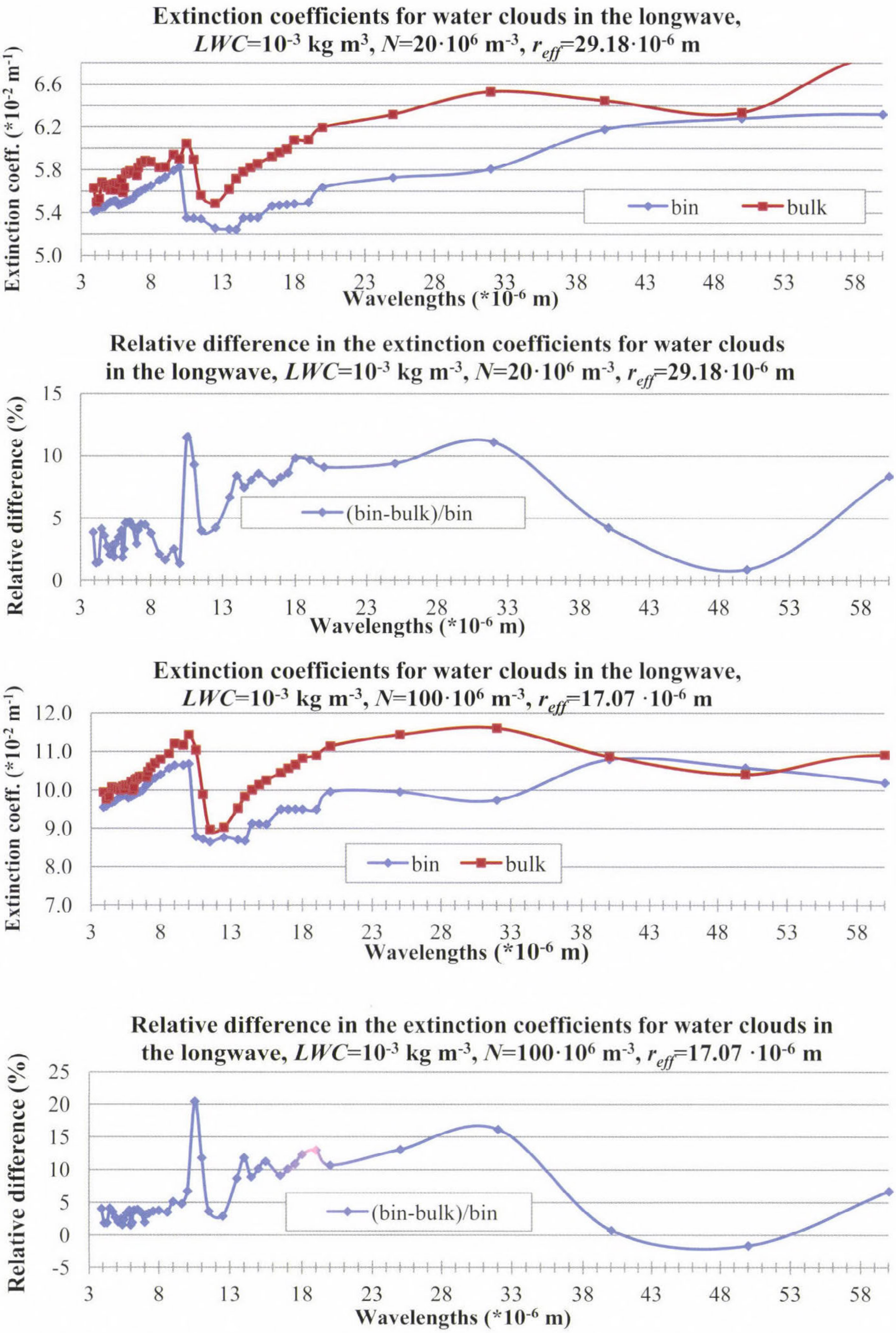

Fig. 1. Extinction coefficients and relative differences calculated for two different gamma-size distributions (N=20, and $100 \cdot 10^6$ m^{-3}, $LWC=10^{-4}$ kg m^{-3}).

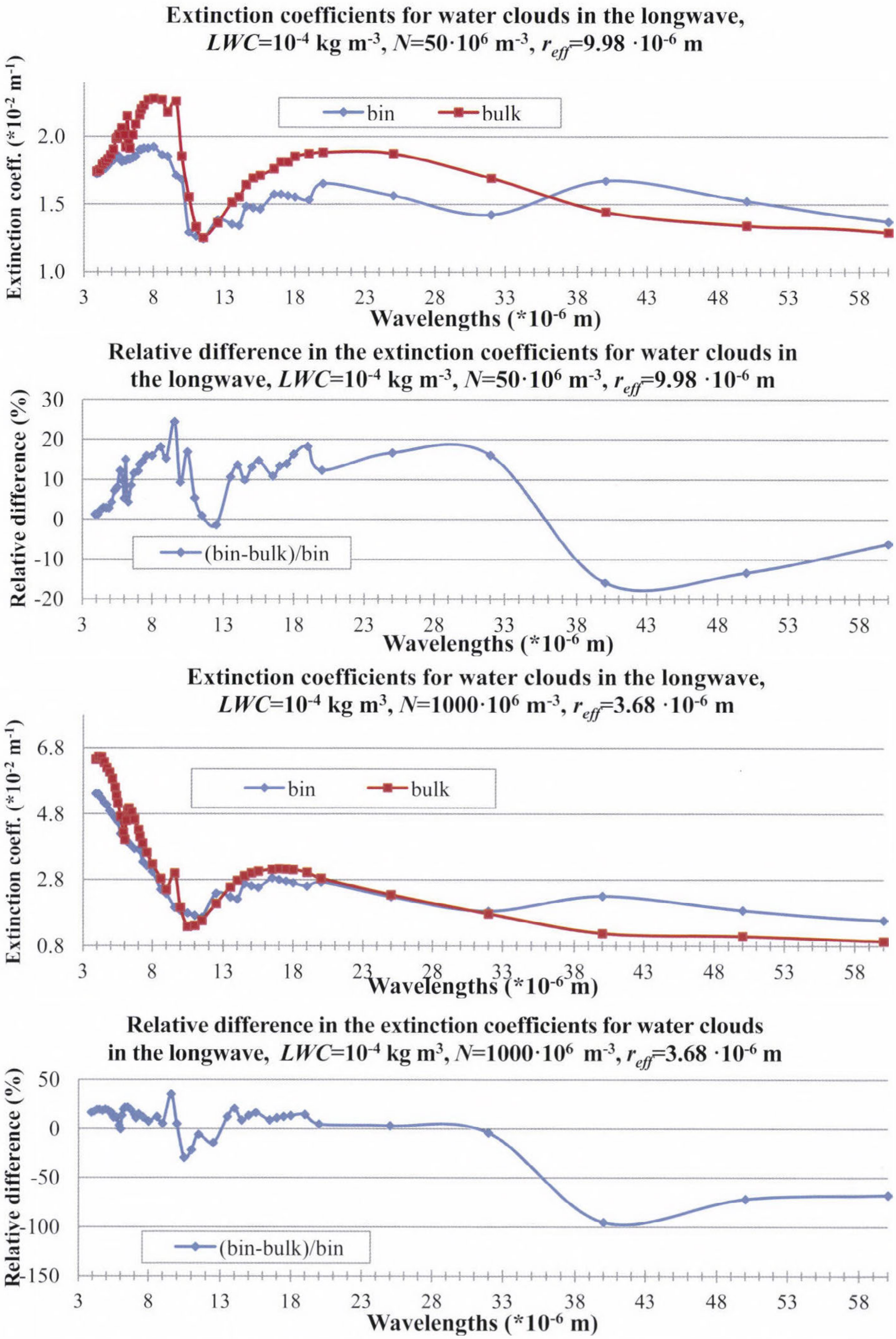

Fig. 2. Extinction coefficients and relative differences calculated for two different gamma-size distributions (N=50, and 1000 10^6 m^{-3}, $LWC=10^{-4}$ kg m^{-3}).

In the critical wavelength interval near to the wavelength of 10 μm – where the absorption of both vapor and CO_2 is relatively small and the absorption of the water drops can be dominant –, significant difference can be found between the results of bulk and that of bin scheme if the effective radius is between 3–15 μm. In this size range, significant positive difference (larger than 10%) can be observed in the whole spectra, except at a narrow wavelength interval of 10–13 μm, where at 9.6 μm wavelength, the difference is much higher for all effective radius values. In case of larger effective radius (>10 μm), the difference is getting smaller, and is getting more emphasized above the wavelength of 10 μm.

It has to be noted that the comparison was made by using idealized gamma size distribution in the case of bin scheme as well. In the real clouds the size distribution of the water drops can significantly differ from the gamma size distribution. The difference between the two schemes shows that the application of effective radius and the liquid water for evaluating the optical properties may results in overestimation of the extinction coefficient mostly in the case of relatively high concentration of the larger water droplets..

It can be established that the bin scheme gives generally smaller value than the bulk scheme does, except at large wavelengths (λ>33 μm), and except at wavelength interval of 10–13 μm in the cases of smaller effective radii. If r_{eff}>20μm, the bulk scheme gives always higher value than the bin scheme does.

From *Figs. 1* and *2*, it can be concluded that the curves related to the extinction coefficients calculated by the bin scheme are smoother; they do not fluctuate by the wavelength as sharply as it can be observed in case of a bulk scheme. The reason for this is that bulk scheme uses only the r_{eff} drop size, and radius much different from this characteristic size are not represented in calculation; whereas the bin scheme allows us to take into account the extinction caused by any drop sizes.

3.2. Comparison of the longwave outgoing radiations at top of cloud layer

In this section results about the longwave outgoing radiation at the top of a cloud layer are presented. The calculations were made for 100 m deep cloud layers with different liquid water contents and drop concentrations. To focus on the effect of water drops, the absorption of the vapor and that of CO_2 was not taken into consideration in the radiative transfer model in this section. It was assumed that the cloud base temperature is 293 K and the vertical temperature gradient is wet adiabatic. The emitted thermal radiation goes through the 100 m thick cloud characterized by different microphysical parameters. The number concentration and *LWC* values of these clouds are given in *Table 1*. The cases presented in *Figs. 3* and *4* are the same cases as in *Figs. 1* and *2*.

The RRTM model described in Section 2.3 was used for calculating the radiation transfer. The new bin scheme has been implemented into the RRTM model. The two dimensional arrays of K_{Akj} $(M_{k-1},M_k,\Delta\lambda_j)$ and K_{Bkj} $(M_{k-1},M_k,\Delta\lambda_j)$ were precalculated, and were used during the simulations.

This development is a novel one, as the RRTM model has been capable to use only the bulk scheme described in Section 2.2. In the case of bulk scheme, the input parameters for the cloud profiles are the effective radius and the cloud water path (which is the LWC multiplied by cloud thickness). Now RRTM can be coupled to a detailed microphysical model, which gives the thickness of the cloud layer, and A_k and B_k coefficients (defined in Section 2.1) for each bin as input data.

The results are summarized in *Table 3*. The first column gives the number concentrations, the second, third, and fourth ones give the difference between the intensities calculated by bin and bulk schemes at different liquid water contents.

Table 3. Difference of the radiation intensity (bin-bulk) at different number of concentration and *LWC* in the case of 100-m-thick cloudy layer, water vapor and CO_2 is not included

	LWC_1=10^{-3} kg m^{-3}	LWC_2= 10^{-4} kg m^{-3}	LWC_3= 10^{-5} kg m^{-3}
N_i (*E+06) 1/m^3	r_{eff} (*10^{-6}) m	r_{eff} (*10^{-6}) m	r_{eff} (*10^{-6}) m
1000	10.70	10.28	–
250	11.35	10.83	–
100	11.77	11.18	4.37
50	12.07	11.35	4.17

The data in *Table 3* show that the application of bin scheme results in about 11 Wm–2 larger outgoing energy in a second at the top of a 100-m-thick cloud when the amount of liquid water content is about 10^{-4} kg m^{-3}, and no significant increase between the differences can be observed if the liquid water content was increased by one order. In the case of LWC_3 =10^{-5} kg m^{-3}, the difference is about a factor of 2. This decrease of difference between the outgoing radiations corresponds with results of pervious Section. This shows that although the relative difference between the extinction coefficients calculated by different schemes depends mostly on the effective radius, the difference between the calculated intensities of radiation depends on the absolute value of the extinction coefficient, which is higher in the case of higher LWC values. It also stems from data in *Table 3* that the extinction becomes saturated in the clouds with increasing *LWC*. This is the reason why there is no further significant change in the difference of the calculated intensities as the liquid water content increases from 10^{-4} kg m^{-3} to 10^{-3} kg m^{-3}.

The differences between the two schemes at the cloud top in each band have been plotted in *Figs. 3* and *4* for the four cases presented in *Figs. 1* and *2*. It can be seen that the majority of the differences appears in the bands of 1–12, which corresponds with the wavelengths interval of 3.3–14.3 μm. It means that the main difference comes from this wavelengths band, as already stated in Section 3.1. The highest difference for all cases is in band 6. The peak of the Planck function at T=293 K is at 9.88 μm (band 10 of RRTM), so the wavelengths band with the maximum change between the two schemes is not correlated with the maximum of the Planck function. It can be due to the different methods that the bulk scheme and the bin scheme uses for calculating averaged extinction coefficients for the wavelengths bands.

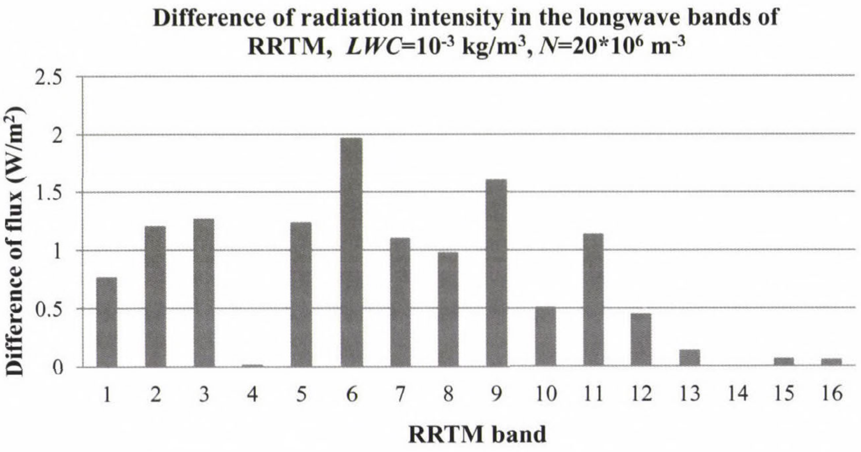

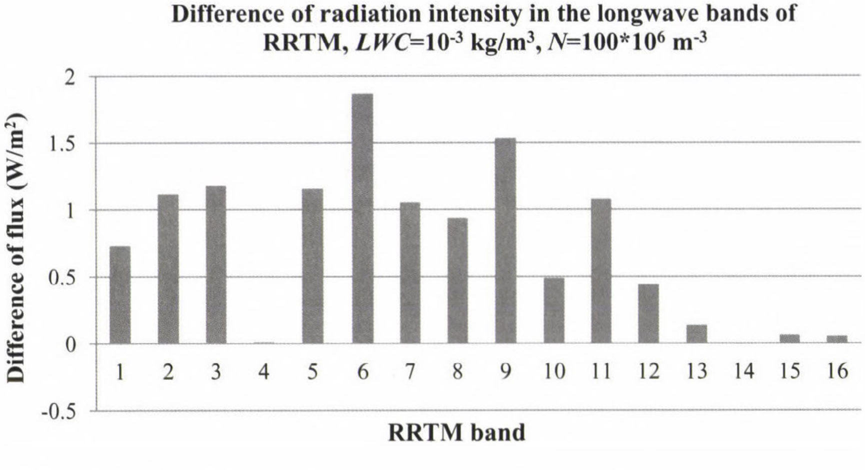

Fig. 3. Differences between the two schemes (bin-bulk) at different bands. $LWC=10^{-3}$ kg m^{-3}, the values of N are given at the top of the figures.

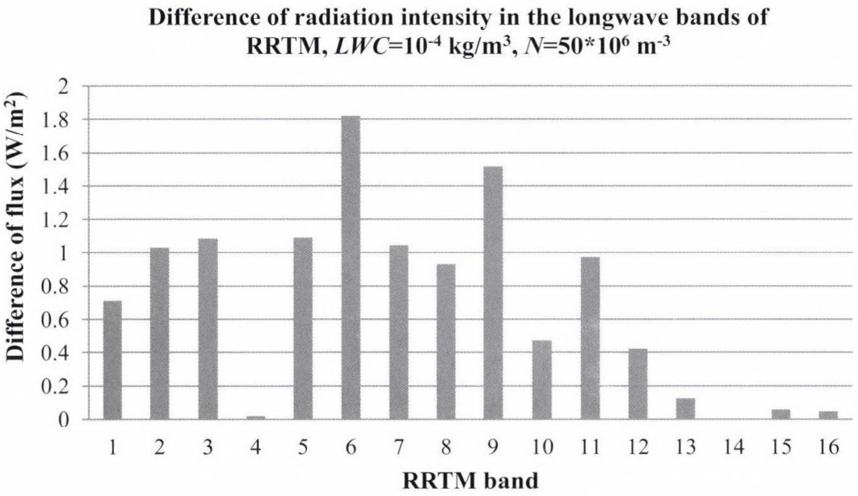

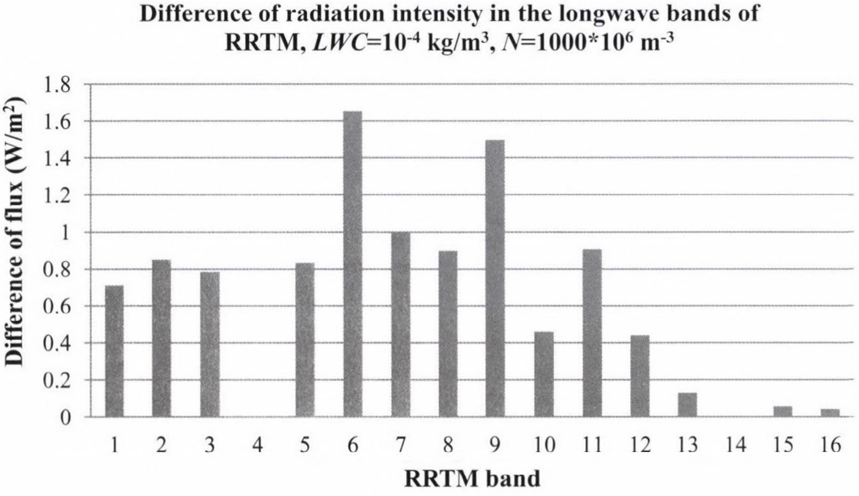

Fig. 4. Differences between the two schemes (bin-bulk) at different bands. $LWC=10^{-4}$ kg/m^3, the values of N are given at the top of the figures.

Control calculations show that presence of vapor and CO_2 reduces the difference between the schemes by a factor of two. The largest difference was found to be 6.11 W m^{-2} at N =20·m^{-3} and LWC = 10^{-3} kg m^{-3}. In the presence of vapor and CO_2, no significant difference is shown in channels 1–4, difference is significant in channels 5–9 where the Planck energy is relatively high.

3.3. Results of the application of bin scheme in RRTM model

In this section the results about the upward and downward radiation profiles are presented. The atmospheric radiation profiles with the RRTM model for four different clouds were calculated. The thickness of the clouds, the number concentration of cloud droplets, and the liquid water content in the clouds are summarized in *Table 4*. In the case of fog the base was at the surface, and LWC was constant. In the case of the cloud the cloud base was at 400 m, and the LWC linearly increased until 625 m (where LWC=5·10^{-4}kg m^{-3}), and above this height it linearly decreased. The size distribution of the water drops was given by Eq. (10) in both schemes.

Table 4. The summary of the investigated cases. * indicates mean value in the cloud layer.

Abbr.	Thickness (m)	N (*10^6 1/m^3)	LWC (10^{-3} kg m^{-3})
fog50	100	50	1
fog100	100	100	1
cloud100	300	100	2.5
cloud500	300	500	2.5

The water vapor and temperature profiles used for the calculation are plotted in *Figs. 5 and 6.* The temperature gradient was 0.976 K/m below the cloud, and it was 0.7 K/m above the fog and the cloud, and the temperature was constant above 12 km. In the cloud wet adiabatic temperature profile was supposed. The water vapor mixing ratio was equal to the saturation values within the clouds, and it decreased linearly above the cloud (and the fog) top until the height of 9 km, where it became equal to zero.

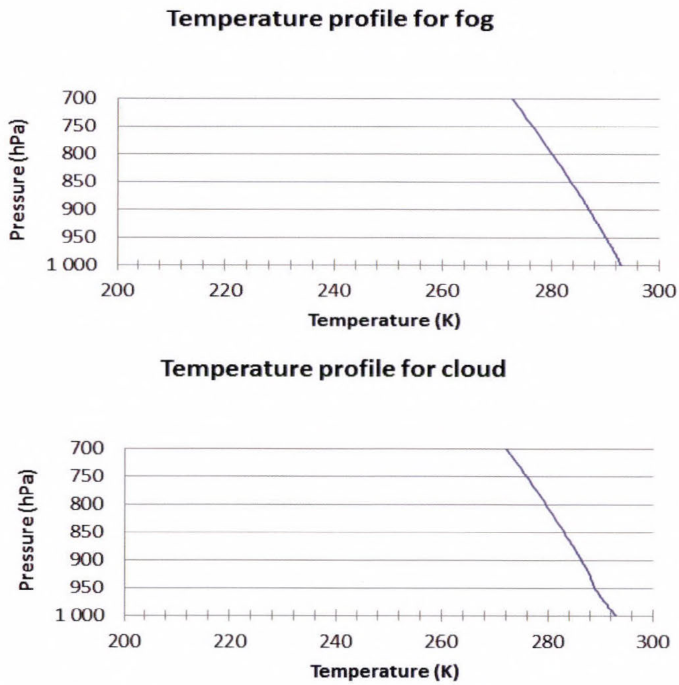

Fig. 5. Temperature profiles for the cloud and fog cases.

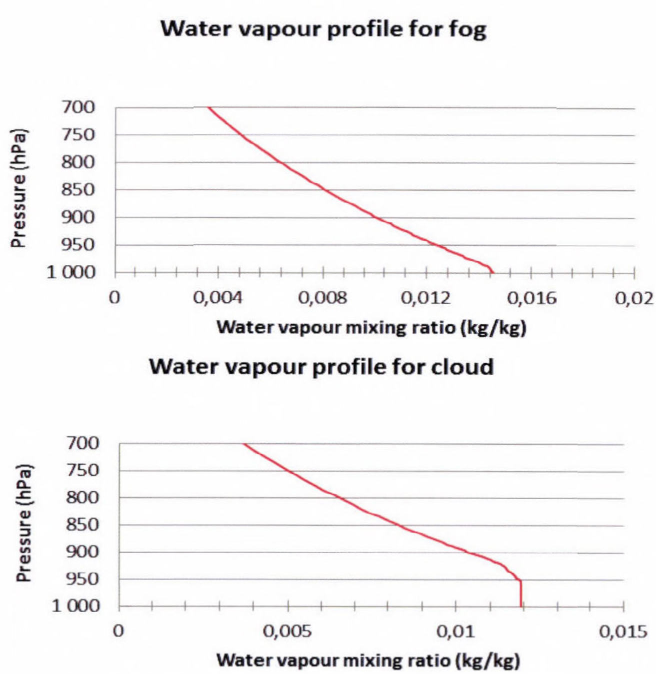

Fig. 6. Water vapor profiles for the cloud and fog cases.

The results of the RRTM calculations are shown in *Figs. 7–10*. While the upward radiation profiles were hardly affected by modification of scheme, the downward profiles were more significantly sensitive on the applied scheme. In the case of the fog, the difference between the intensity of the downward radiations at the surface is about 20 Wm^{-2}. In the case of the cloud, similar difference can be observed at about 100 m below of the cloud top. More absorption is observed in the case of the bin scheme (when absorption is closer to 1, the net flux is closer to 0). Comparison of fog50 and fog100 cases shows that the difference between the two schemes is hardly affected by the number concentration of the water droplets.

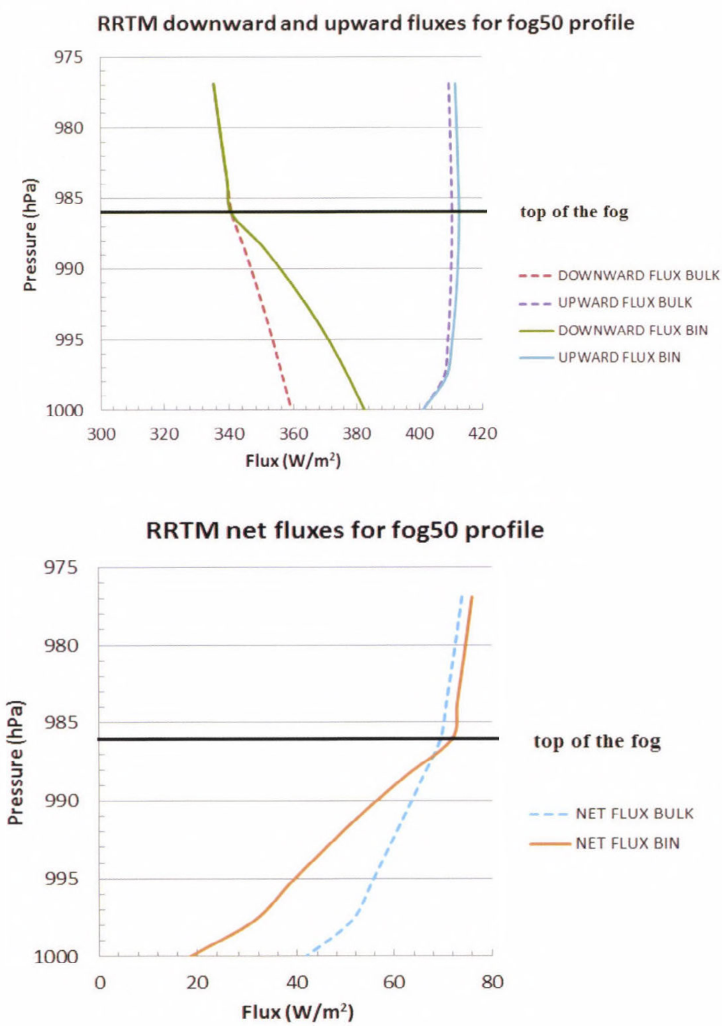

Fig. 7. Upward, downward, and net radiation flux profiles in fog50.

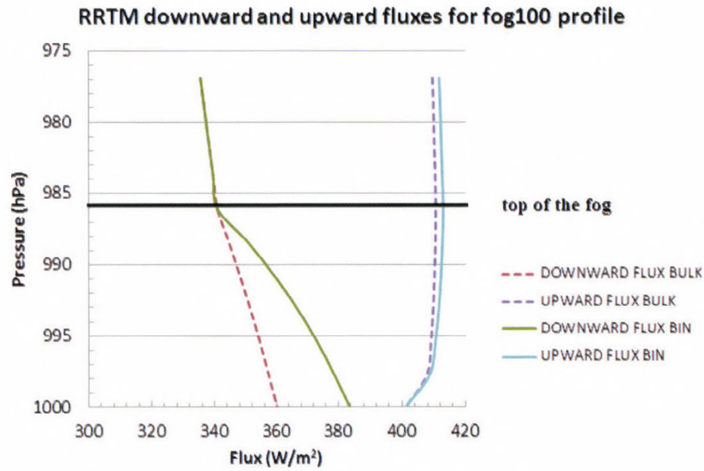

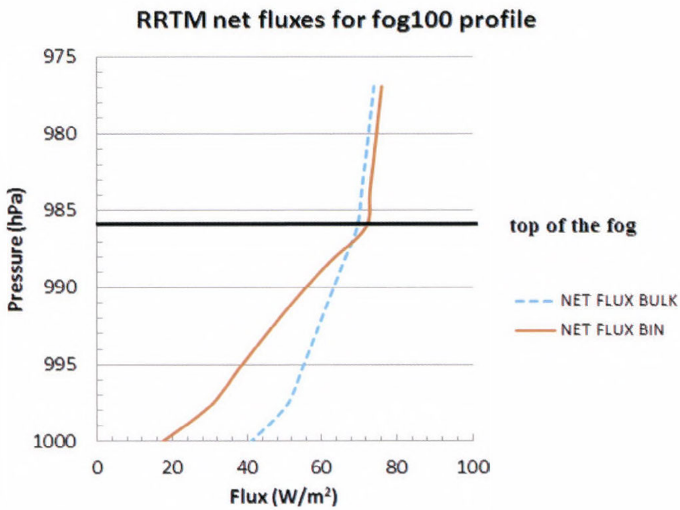

Fig. 8. Upward, downward, and net radiation flux profiles in fog100.

It can be also noted in *Figs. 9* and *10* that the absorption of the downward radiation is more intense in case of the bin scheme than in the bulk scheme. In the cloud layer the net radiation (the difference between the downward and upward radiation) is close to zero in the case of the bin scheme and slightly larger than zero in the case of bulk scheme. This means that the absorption within the cloud is almost 1. Considering the net fluxes, the maximum difference between the two profiles is around 30 Wm^{-2} in case of clouds and 20 Wm^{-2} in the case of the fog. As the gradient of the net flux is different within the cloud layer, the heating/cooling rate is larger in case of the bin scheme, because the flux is changing more sharply. Thus, difference between the schemes can impact both the cloud dynamics and cloud microphysics.

The different schemes give significantly different gradients of the net radiation in both cloud100 and cloud500 cases. The difference between the schemes is more significant in the case of cloud500, both at the cloud base and at the cloud top. So it can be concluded that the number of concentration of the droplets affect the gradient of the net fluxes, and subsequently the cooling rate at the cloud edges. The maximum cooling rate at the top of the layer in case of fog50 was 34.5 K/day in the bin scheme; whereas in the bulk scheme, it was only 12.9 K/day.

It can be seen from *Figs. 9* and *10* that if the cloud layer is thinner (100 m in case of the fog), the difference in the net outgoing radiation between the two schemes is much higher than in case of the 300-m-thick cloud.

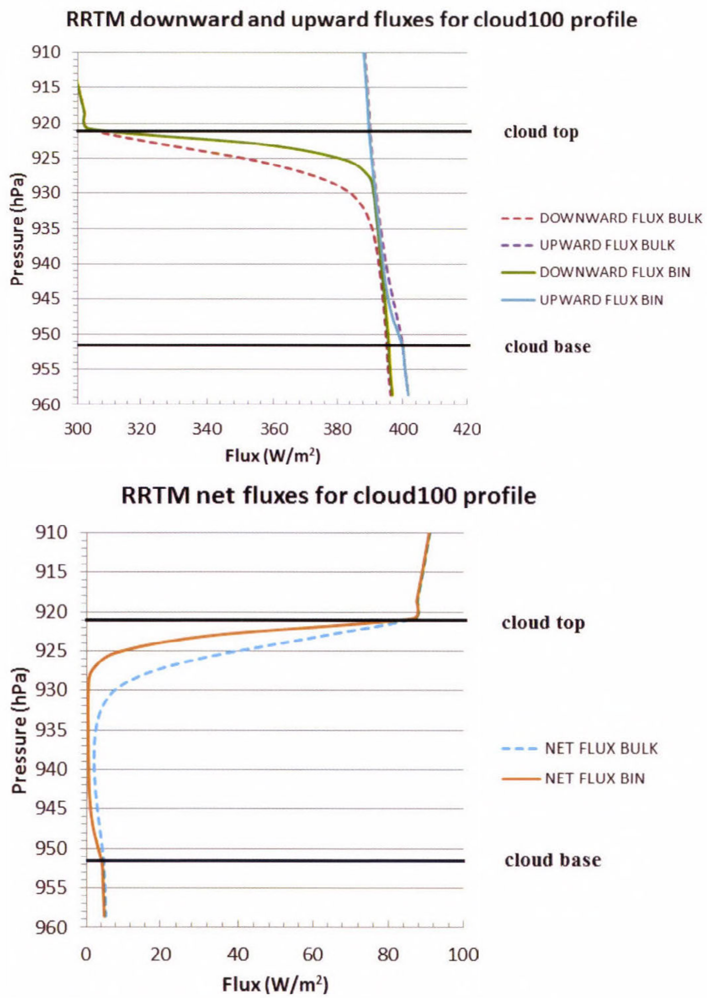

Fig. 9. Upward, downward, and net radiation flux profiles in cloud100.

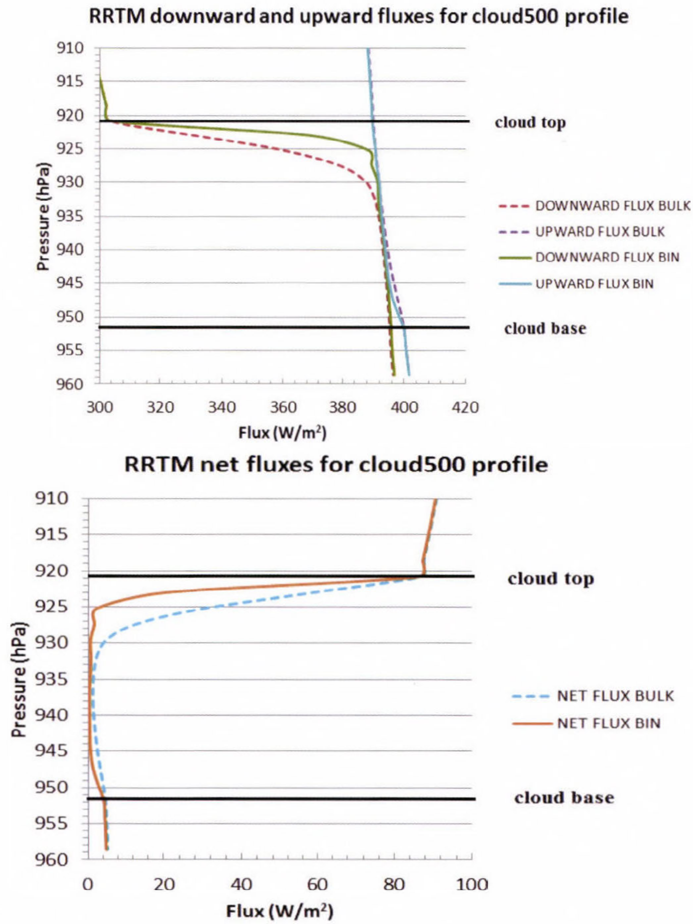

Fig. 10. Upward, downward, and net radiation flux profiles in cloud500.

4. *Conclusion*

Cloud-radiation interactions are essential to be understood and modeled correctly. The evolving radiation profile affects temperature and microphysical processes in micro-scale, and atmospheric motions in larger scales. Weather events and climatic patterns strongly depend on the radiation budget. More accurate description of cloud optical properties can significantly improve numerical weather forecasts.

In this study it was investigated how evaluation of the extinction coefficients affects longwave radiation budget, and longwave heating/cooling rates in the atmosphere. A new bin radiation scheme was developed, and the results of bin scheme were compared to that of a currently applied bulk scheme, which is widely used in operational numerical weather prediction models.

The results are summarized in the following points:

(1) The extinction coefficient calculated by the bin scheme was generally smaller than that calculated by the bulk scheme. The difference between the extinction coefficients calculated by the two different ways depends on the effective radius and the wavelength. The two curves fit well in the whole spectrum if the effective radius is higher than 10 μm, and the wavelength is less than about 8.0 μm. In the case of the smaller effective radius, or higher wavelengths, significant difference was found in the wavelength interval of 5–20 μm (around 10%), and even higher at the wavelengths of 9.6 μm for all effective radii.

(2) The variations of the extinction coefficients in the bin scheme are smoother than in the bulk scheme, due to the fact that the bin scheme represents a broad size of droplet spectra, compared to the bulk scheme which is represented by a single effective radius.

(3) The two different methods for the calculation of the extinction coefficients result in an increase of about 10 Wm^{-2} in the outgoing longwave radiation in case of a 100-m-thick cloud layer when the effect of the water vapor and CO_2 is not taken into account. The change in the intensity was two times smaller if the *LWC* was reduced to 10^{-5} kg m^{-3}within the cloud. The main difference comes from the wavelengths bands below 14 μm, where the majority of the Planck energy is. The presence of the vapor reduces the difference between the two schemes.

(4) The number of concentration in the cloudy layer does not affect considerably the resulting difference between the outgoing radiations calculated by the two schemes. However, the value of *LWC* and the cloud thickness have larger impact: the lower the *LWC*, and the higher the cloud thickness is, the smaller the difference between the two schemes.

(5) Large uncertainty of net radiation at surface can result in significant error in the forecast of the surface temperature. Supposing steady state conditions, the difference of 20 Wm^{-2} can results in about 3 C differences in surface temperature after 6 hours.

(6) Large difference (30 Wm^{-2}) between the two schemes was found within the simulated cloud layer near to the cloud tops. 20 Wm^{-2} difference between the net longwave radiations was found at the surface in case of fog.

(7) The bin scheme produced profiles with higher gradient at the edges of the cloud layer, which results in higher cooling rate as well both at the cloud top and cloud base. In the case of the bulk scheme, temperature hardly changes at the cloud base, which results in negligible warming. The consequence of different temperature profiles given by the two schemes can be significantly different cloud microphysics and cloud dynamics.

At the next phase of the research, the RRTM model will be coupled with a two-dimensional cloud model. The model uses bin microphysics, which allows us to give an appropriate input for the recently developed bin radiation scheme.

References

Arking, A., 1991:_The Radiative Effects of Clouds and their Impact on Climate. *B. Am. Meteorol. Soc. 72*, 795–953.

Buriez, J.C., Bonnel, B., Fouquart, Y., Geleyn, J.F., and *Morcrette, J.J.,* 1988: Comparison of model-generated and satellite- derived cloud cover and radiation budget. *J. Geophys. Res. 93*, 3705–3719.

Chen, T., Rossow, and *W.B., Zhang, Y.*, 2000: Radiative Effects of Cloud-Type Variations. *J. Climate*, *13*, 264–286.

Chen, T., and *Rossow, W.B.*, 2002: Determination of top-of-atmosphere longwave radiative fluxes: A comparison between two approaches using ScaRaB data. *J. Geophys. Res., 107(D8)*. ACL 6-1–ACL 6-13.

Cough, S.A., Iacono, M.J., and *Moncet, J.L.,* 1992: .Line-by-line calculations of atmospheric fluxes and cooling rates: Application to water vapor. *J. Geophys. Res. 97*, 15761–15785.

Clough, S.A., Shephard, M.W., Mlawer, E.J., Delamere, J.S., Iacono, M.J., Cady-Pereira, K., Boukabara, S., and Brown, P.D., 2005: Atmospheric radiative transfer modeling: a summary of the AER codes, Short Communication. *J. Quant. Spectrosc. RA 91*, 233–244.

Corti, T. and *Peter, T.*, 2009: A simple model for cloud radiative forcing. *Atmos. Chem. Phys. Discuss. 9*, 8541–8560.

Ebert, E.E. and *Curry, J.A.*, 1992: A parameterization of ice cloud optical properties for climate models. *J. Geophys. Res. 97(D4),* 3831–3836.

Fouquart, Y., Buriez, J.C., Herman, M., and *Kandel, R.S.*, 1990: The Influence of Clouds on Radiation: A Climate-Modeling Perspective. *Rev. Geophys. 28*, 145–166.

Fu, Q., Ping, Y., and *Sun, W.B.*, 1998: An Accurate Parameterization of the Infrared Radiative Properties of Cirrus Clouds for Climate Models. *J. Climate 11*, 2223–2237.

Geresdi, I., 1998: Idealized simulation of the Colorado hailstorm case: comparison of bulk and detailed microphysics. *Atmos. Res. 45,* 237–252.

Gettelman, A., Morrison, H., and *Ghan, S.J.,* 2008: A New Two-Moment Bulk Stratiform Cloud Microphysics Scheme in the Community Atmosphere Model, Version 3 (CAM3). Part II: Single-Column and Global Results. *J. Climate 21*, 3660–3679.

Harrington, J.Y., 1997: The Effects of Radiative and Microphysical Processes on Simulated Warm and Transition Season Arctic Stratus. Ph.D. Thesis, Colorado State University, Ft. Collins, CO. 298.

Harrington, J.Y., Feingold, G., and *Cotton, W.R.*, 2000: Radiative Impacts on the Growth of a Population of Drops within Simulated Summertime Arctic Stratus. *J. Atmos. Sci. 57*, 766–785.

Harrington, J. and *Olsson, P.Q.*, 2001: A method for the parameterization of cloud optical properties in bulk and bin microphysical models. Implications for arctic cloudy boundary layers. *Atmos. Res. 57,* 51–80.

Hong, G., Yang, P., Baum, B.A., Heymsfield, A.J., and *Xu, K-M.,* 2009: Parameterization of Shortwave and Longwave Radiative Properties of Ice Clouds for Use in Climate Models. *J. Climate 22*, 6287–6312.

Hongqi W. and *Gaoxiang, Z.,* 2002: Parameterization of longwave optical properties for water clouds. *Adv. Atmos. Sci. 19*, 25–34.

Hu, Y. X. and *Stamnes, K.*, 1993: An accurate parameterization of the radiative properties of water clouds suitable for use in climate models. *J. Climate 6*, 728–742.

Kunkel, B.A., 1984: Parameterization of Droplet Terminal Velocity and Extinction Coefficient in Fog Models. *J. Climate Appl. Meteorol. 23*, 34–41.

Lindner, T.H. and *Li, J.,* 2000: Parameterization of the Optical Properties for Water Clouds in the *Infrared J. Climate 13*, 1797–1805.

Liu, M., Nachamkin, J.E., and *Westphal, D.L.*, 2009: On the Improvement of COAMPS Weather Forecasts Using an Advanced Radiative Transfer Model. *Wea. Forecast 24*, 286–306.

Lynn, B.H., Khain, A.P., Dudhia, Rosenfeld, D.J., Pokrovsky, A., and *Seifert, A.*, 2005: Spectral (Bin) Microphysics Coupled with a Mesoscale Model (MM5). Part I: Model Description and First Results. *Mon. Weather Rev. 133*, 44–58.

Lynn, B. and *Khain, A.*, 2007: Utilization of spectral bin microphysics and bulk parameterization schemes to simulate the cloud structure and precipitation in a mesoscale rain event. *J. Geophys. Res. 112*, D22205.

Mitchell, D.L., 2000. Parameterization of the Mie extinction and absorption coefficients for water clouds. *J. Atmos. Sci. 57*, 1311–1326.

Mlawer, E.J., Taubman, S.J., and *Clough, S.A.*, 1995: RRTM: A Rapid Radiative Transfer Model, Fifth Atmospheric Radiation Measurement (ARM) Science Team Meeting http://www.arm.gov/publications/proceedings/conf05/extended_abs/mlawer_ej.pdf

Mlawer, E.J., Taubman, S.J., Brown, P.D., Iacono, M.J., and *Clough, S.A.*, 1997: Radiative transfer for inhomogeneous atmospheres: RRTM, a validated correlated-k model for the longwave, *J. Geophys. Res. 102(D14)*, 16663–16682.

Oreopoulos, and *L., Rossow, W.*, 2011: The cloud radiative effects of International Satellite Cloud Climatology Project weather states. *J. Geophys. Res. 116(D12202).*

Petters, J.L., Harrington, J.Y., and *Clothiaux, E.E.*, 2012: Radiative–Dynamical Feedbacks in Low Liquid Water Path Stratiform Clouds. *J. Atmos. Sci. 69*, 1498–1512.

Ramaswamy, V., Boucher, O., Haigh, J., Hauglustine, D., Haywood, J., Myhre, G., and *Solomon, S.*, 2001: Radiative forcing of climate. In *Climate Change 2001: The Scientific Basis. Contribution of Working Group I to the Third Assessment Report of the Intergovernmental Panel on Climate Change*. Cambridge, U.K.: Cambridge University Press, 349–416.

*Ramanathan, V., Cess, R.D., Harrison, E.F., Minnis, P., Barkstrom, B.R., Ahmad, E.,*and *Hartmann, D.*, 1989: Cloud-Radiative Forcing and Climate: Results from the Earth Radiation Budget Experiment. *Science, New Series 243*, 4887, 57–63.

Ramanathan, V., Inamdar, A., 2006: The radiative forcing due to clouds and water vapor. Cambridge University Press.

Rasmussen, R.M., Geresdi, I., Thompson, G., Manning, K., Karplus, E., 2002: Freezing Drizzle Formation in Stably Stratified Layer Clouds: The Role of Radiative Cooling of Cloud Droplets, Cloud Condensation Nuclei, and Ice Initiation. *J. Atmos. Sci. 59*, 837–860.

Ritter, B., Geleyn, J.F., 1992: A Comprehensive Radiation Scheme for Numerical Weather Prediction Models with Potential Applications in Climate Simulations, *Mon. Wea. Rev. 120*, 303–325.

Roach, W.T., Slingo, A., 1979: A high resolution infrared radiative transfer scheme to study the interaction of radiation with cloud, *Q..J.Roy.Meteor.Soc. 105*, 603–614.

Rossow, W. B., Duenas, E.N., 2004: The international satellite cloud climatology project (ISCCP) web site: An online resource for research. *Bull. Amer. Meteor. Soc. 85*, 167–172.

Slingo, A., Schrecker, H.M., 1982. On the shortwave properties of stratiform water clouds. *Q. J. Roy. Meteorol. Soc. 108*, 407–426.

Stephens, G.L. 1984: The parameterization of radiation for numerical weather prediction and climate models, *Mon. Wea. Rev. 112*, 826-867.

Stephens, G.L., Tsay, S-C., Stackhouse, P.W., Flatau, P.J., 1990: The Relevance of the Microphysical and Radiative Properties of Cirrus Clouds to Climate and Climatic Feedback. *J. Atmos. Sci. 47*, 1742–1754.

Stephens, G.L.,, 2004: Cloud Feedbacks in the Climate System: A Critical Review. *Climate 18*, 237–273.

Straka, J.M., Kanak, K.M., and *Gilmore, M.S.*, 2007: The behavior o f number concentration tendencies for the continuous collection growth equation using one- and two-moment bulk parameterization schemes. *J. Appl. Meteorol. Climatol. 46*, 1264–1274.
Tompkins, A.M. and *Di Giuseppe, F.*, 2009: Cloud radiative interactions and their uncertainty in climate models, in P. Williams and T. Palmer, eds., Stochastic Physics and Climate Models, *Cambridge University Press, UK*
Tzivion, S., Feingold, G. Levin, Z., 1987: An efficient numerical solution to stochastic collection eqation, *J. Atmos. Sci. 44*, 3139–3149.
Walko, R.L., Cotton, W.R., Meyers, M.P., Harrington, J.Y., 1995: New RAMS cloud microphysics parameterization: Part I. The single moment scheme. *Atmos. Res.* 38, 29–62.
Wielicki, B.A., Barkstrom, B.R., Harrison, E.F., Lee, R.B., Smith, G.L., and *Cooper, J.E.*, 1996: Clouds and the earth's radiant energy system (CERES): An earth observing system experiment. *B. Am. Meteorol. Soc. 77*, 853–868.

Appendix A

Q_{ext} depends on the droplet diameter (D), wavelength (λ), and index of refraction (m), with the imaginary component n_i and real component n_r:

$$Q_{ext}(D, \lambda, m) = 2K(tD), \tag{A1}$$

where $t = \frac{2\pi}{\lambda}[n_i + i(n_r - 1)]$, $m = n_r - i \times n_i$, and $K(x) = 1 + 2\mathrm{Re}[\frac{e^{-x}}{x} + \frac{e^{-x} - 1}{x^2}]$.
The correction parameter C_{res} is a rather complicated function of the drop size and the refraction index:

$$C_{res} = r_a \frac{k^m e^{-\varepsilon k}}{k_{max}^m e^{-m}}, \tag{A2}$$

where

$$r_a = 0.7393 n_r - 0.6069, \tag{A3}$$

and

$$m = \frac{1}{2}, \quad k = \frac{D}{\lambda}, \quad k_{max} = \frac{m}{\varepsilon}, \text{ and } \quad \varepsilon = \frac{1}{4} + 0.6\{1 - \exp[-\frac{8\pi n_i}{3}]\}^2. \tag{A4}$$

The Q_{edge} term in Eq.(1) is given by:

$$Q_{edge} = 2(\pi k)^{-2/3}[1 - \exp(-0.06\pi k)]. \tag{A5}$$

After substituting Eqs. (A1)–(A5) into Eq. (1) or Eq. (7), we can evaluate the extinction efficiency as a function of droplet diameter, wavelength, and refraction index (which is the $Q_{ext}(D,\lambda,m)$ function in explicit form).

Appendix B

Using the MADT method Eq. (8), the integral in Eq. (7) can be divided in three parts:

$$\beta_{ext,i}=\sum_{j=1}^{16}\sum_{k=2}^{N_{bins}}[\int_{\Delta\lambda_j}(E_\lambda\int_{M_{k-1}}^{M_k}A(D)Q_{ext,i}(D,m,\lambda)n_k(M)dM\,d\lambda)/\int_{\Delta\lambda_j}E_\lambda d\lambda] \quad ,\text{(B1)}$$

where

$Q_{ext,1}(D,\lambda,m)=Q_{ext}$, $Q_{ext,2}(D,\lambda,m)=\frac{C_{res}}{2}\times Q_{ext}$, and $Q_{ext,3}(D,\lambda,m)=Q_{edge}$,

and *j* is the number of band in *Table 1*. Using the appropriate equations from the Appendix A, the above integral can be written as the sum of the next three equations. After substitution of Eq. (6) in (B1), the integrals can be evaluated analytically.

$$\beta_{ext,1}=\sum_{j=1}^{16}\sum_{k=2}^{N_{bins}}[\int_{\Delta\lambda_j}(E_\lambda\int_{M_{k-1}}^{M_k}(\frac{\pi}{4}\times D^2(1+2\mathrm{Re}[\frac{e^{-tD}}{tD}+\frac{e^{-tD}-1}{t^2D^2}])(A_k+M\times B_k)dM\,d\lambda)/\int_{\Delta\lambda_j}E_\lambda d\lambda]=$$

$$=\sum_{k=2}^{N_{bins}}A_k\times\sum_{j=1}^{16}K_{A1kj}(M_{k-1},M_k,\Delta\lambda_j)+\sum_{k=2}^{N_{bins}}B_k\times\sum_{j=1}^{16}K_{B1kj}(M_{k-1},M_k,\Delta\lambda_j).$$

$$\beta_{ext,2}=\sum_{j=1}^{16}\sum_{k=2}^{N_{bins}}[\int_{\Delta\lambda_j}(E_\lambda\int_{M_{k-1}}^{M_k}(\frac{\pi}{4}\times D^2(1+2\mathrm{Re}[\frac{e^{-tD}}{tD}+\frac{e^{-tD}-1}{t^2D^2}])\times\frac{C_{res}}{2}\times(A_k+M\times B_k)dM\,d\lambda)/\int_{\Delta\lambda_j}E_\lambda d\lambda]=$$

$$=\sum_{k=2}^{N_{bins}}A_k\times\sum_{j=1}^{16}K_{A2kj}(M_{k-1},M_k,\Delta\lambda_j)+\sum_{k=2}^{N_{bins}}B_k\times\sum_{j=1}^{16}K_{B2kj}(M_{k-1},M_k,\Delta\lambda_j).$$

$$\beta_{ext,3}=\sum_{j=1}^{16}\sum_{k=2}^{N_{bins}}[\int_{\Delta\lambda_j}(E_\lambda\int_{M_{k-1}}^{M_k}(\frac{\pi}{4}\times D^2\times 2(\pi\frac{D}{\lambda})^{-\frac{2}{3}}[1-e^{-0.06\pi\frac{D}{\lambda}}](A_k+M\times B_k)dM\,d\lambda)/\int_{\Delta\lambda_j}E_\lambda d\lambda]=$$

$$=\sum_{k=2}^{N_{bins}}A_k\times\sum_{j=1}^{16}K_{A3kj}(M_{k-1},M_k,\Delta\lambda_j)+\sum_{k=2}^{N_{bins}}B_k\times\sum_{j=1}^{16}K_{B3kj}(M_{k-1},M_k,\Delta\lambda_j).$$

The final K_{Akj} and K_{Bkj} kernels are the sum of the K_{ikj} constants in the three parts (i=1,2,3).

IDŐJÁRÁS

Quarterly Journal of the Hungarian Meteorological Service
Vol. 117, No. 4, October–December, 2013, pp. 403–433

High resolution solar spectrophotometry and narrow spectral range solar radiation measurements at the Hungarian Meteorological Service

Zoltán Tóth

Atmospheric Physics and Measurement Technics Division
Hungarian Meteorological Service
P.O.Box 39, H-1675 Budapest, Hungary

(Manuscript received in final form June 17, 2013)

Abstract— Aims of the spectral radiation measurements can be devided to two wider areas: one is to get information about the radiation source, and the other is to get information about the properties of the space between the radiation source and the detector if output signal from the radiation source is known. In the latter case either the optical properties of the certain space or some optical parameter of an object placed in there is to be studied. The sun can be the object of the study or it can be used as natural radiation source to investigate some important properties of the atmosphere. The term 'solar spectrophotometry' refers to this.

Although detection of spectral distribution of the solar radiation is considered a special area that is relatively rarely used even today in atmospheric physical measurements, it still has big significance. In addition to the 'mere' knowledge of spectal solar irradiance, the measured data can be used in a considerably wide range. In special cases, the narrow spectral range informations about the radiation can be very useful. Typical example is the erythemally weighted UV radiation. Though it does not give spectral information, the spectral range that is characterized by it, is considerably narrower than that of the classical radiation components. So this type of measurements is also discussed here.

Main applied physical and technical principles of solar spectrophotometry, as well as spectrophotometers working in the UV, visible, and near infrared spectral range used at the Hungarian Meteorological Service (HMS), are shown in this paper. Measurement results and results from studies and researches using these data are also shown and analyzed. Also some special studies performed occasionally are shown.

Today the primary base for operation of high accuracy measurement systems is the calibration. Since we have reference instruments, QA/QC procedures are of crucial importance in our measuring practice. Our activitiy as we operate WMO Regional Center for Solar Radiation in Region VI gives even bigger emphasis to that.

Key-words: solar radiation, measurement technics, spectrophotometry, optical depth, total ozone, UV radiation, calibration

1. Introduction

Solar radiation measurements in a station mean, in most cases of solar radiation practice of meterorological observations, the measurement of components of classical radiation budget of the atmosphere. Use of narrow spectral range or high resolution spectral solar radiation measurements can be considered relatively rare even today, despite the fact that it is not a brand new technique. The main reason is that it requires suitable special expertancy and special, rather expensive equipments that cannot be provided easily by institutions.

Narrow range and high resolution measurements of solar radiation have started at the Hungarian Meteorological Service (HMS) in the early nineties of the previous century by installation of ultraviolet detectors measuring erythemally weighted UV radiation and continued with installation of two high resolution spectrophotometers, then later by sunphotometers. It is important to note that primary acitvity of the HMS is to operate monitoring networks and establishing quality controlled databases. Consequently, the studies or researches concern different processing of data and analysis of processed data mostly and, only in a few case, some other 'more scientific' job in area of solar radiation measurements also.

The operation, and physical and technical background of the aforementioned systems, as well as some results from studies and researches based on their data are also shown in this paper. To detailedly describe the operation and technical background cannot be object of this paper, so they are concerned very briefly only.

2. Background physics

The background physics is not discussed in details because it can be found in numerous books and articles concerning theoretical and applied physics. The basic physics is the theoretical and experimental approaches of radiative transfer that can be performed in many ways depending on the type of the problem to be solved. It is, by all means, to be noted that the basic terms and definitions concern monochromatic radiation. It is, however, to be stressed that when monochromatic flux is mentioned in measurement technics, it means a flux belonging to very narrow, but finite range, because finite quantity cannot belong to a zero interval in reality. So the monochromatic quantities are only quasi-monochromatic ones, actually. Consequently, if the wavelength of a spectral irradiance is given, the irradiance refers to a spectral band whose center is at the wavelength in question. Mathematically it can be expressed as follows:

$$I_\lambda^q = \int_{\lambda-d\lambda}^{\lambda+d\lambda} I_\lambda d\lambda \ , \tag{1}$$

where

I_λ^q is the quasi-monochromatic flux,
I_λ is the theoretical monochromatic flux,
λ is the wavelength of the center of the spectral band,
$\Delta\lambda$ is the half-width of the spectral band.

The narrower the band, the more accurate the flux referring to the given wavelength.

If the aim of the measurement is to get information about the space or, in atmospheric physics practically, a medium, or any component in the atmosphere, also the spectral flux at the top of the atmosphere (the so-called extraterrestrial flux) should be known. Considering the extraterrestrial flux and the flux measured at the surface, the total amount of a given component can be determined, obviously in the case when values of other physical quantities are known from measurement or calculation.

2.1. Determination of total columnar amount of atmospheric gaseous components

The calculation methods are well and fully described in several books and guide-books, so they are mentioned here very briefly, and also some special physical quantities or methods are explained in more details. Determination of gaseous components using solar spectrophotometry is performed by the method of relative intensities (*Dobson,* 1957). The main principle is described here very briefly only, without quantification. This main principle is that the irradiance is measured at several wavelength pairs so that one of the pairs is at a wavelength where the absorption coefficient of the gas is considerably high and the other one is at a wavelength where the absorption coefficient is as low as it can be taken as zero. An important criterium is that the two wavelengths have to be very close to each other, so a spectral interval is needed where the absorption coefficient varies by high rate. The reason is that the properties of the aerosol being present in the atmospheric column between the solar disc and the detector at the time of the observation is not known. It is well-known, however, that the variation of the aerosol optical depth with wavelength can be described in each case by a smooth and non-rapidly changing function. Consequently, its effect on the calculated value of optical depth of the gaseous component, whose total columnar amount is to be determined, can be neglected (it means mathematically that the aerosol optical depth, as variable, is eliminated from the equation).

2.2. Determination of aerosol optical depth

Calculation of aerosol optical depth (AOD) is also a well-known standard method and described in several publications (*Alföldy et al.,* 2007), so the reduction of the formula by which it is calculated is not shown here. The AOD is calculated by the equation as follows:

$$\delta_{A\lambda} = \frac{1}{M} ln \frac{I_{0\lambda}}{I_{\lambda} S} \left(\frac{P}{P_0} \delta_{R\lambda} + \delta_{O\lambda} \right), \quad (2)$$

where:

$\delta_{A\lambda}$ is the aerosol optical depth at wavelength λ;

$I_{0\lambda}$ is the extraterrestrial irradiance;

I_{λ} is the irradiance at the observational point;

S is the correction factor for the Earth-Sun distance (ratio of Earth-Sun distance at the time of the measurement to the mean value);

M is the relative optical airmass;

$\delta_{R\lambda}$ is the optical depth of Rayleigh scattering from atmospheric molecules;

$\delta_{O\lambda}$ is the optical depth of ozone absorption: $\delta_{O\lambda} = \alpha_{O\lambda}\eta$;
where $\alpha_{O\lambda}$ is the ozone absorption coefficient and η is the total ozone content of the air column between the solar disc and the detector;

P, P_0 are the surface pressure and at the time of the observation and standard sea level pressures.

To obtain $\delta_{A\lambda}$, value of I_{λ} is measured by solar spectrophotometer and P is known by measurement also. Total ozone content η either can be observed at the given site or known from satellite observations. Values of both $I_{0\lambda}$ and S are known.

Since high accuracy spectrophotometric total ozone content data are available at the Marczell György Main Observatory, accurate estimation of AOD is possible to perform. The standard wavelengths are used to estimate AOD are 368, 380, 412, 450, 500, 610, 675, 778, 862, and 1024 nm, and since the autocorrelation of AOD values estimated for these 10 wavelengths is very high, AOD for 500 nm is used generally for studies and in models.

2.3. Determination of graybody (broad band) optical depth

Graybody (broad band) optical depth (GBOD) can be determined if definition of monochromatic optical depth is extended to a wider spectral range if irradiances measured at the surface are available (*Németh et al.,* 1996). Consequently, the GBOD will then be determined in the following way. If $I_{\lambda 0}$ is the irradiance coming onto the top of the atmosphere at wavelength λ and I_{λ} is the irradiance measured at the surface by a pyrheliometer in case of relative optical air mass m, then:

$$\int_{S_{PYR}} I_{\lambda} d\lambda = \left(\int_{S_{PYR}} I_{\lambda 0} d\lambda \right) e^{-m\delta_{GB}}, \quad (3)$$

where δ_{GB} is the GBOD and S_{PYR} is the sensitivity range of the pyrheliometer.

Thus GBOD is given by the following equation if direct irradiance (denominator of the fractional) is measured:

$$\delta_{GB} = \frac{1}{m} ln \frac{\int_{S_{PYR}} I_{\lambda 0} d\lambda}{\int_{S_{PYR}} I_{\lambda} d\lambda}. \tag{4}$$

Though graybody optical depth is not a spectral quantity, as it is evident from its definition, results from studies concerning it are important to include here due to, on the one hand, its very close connection with spectral aerosol optical properties and on the other, its good usability to characterize short-wave radiation transmission of the atmosphere.

2.4. Ångström exponent

The Ångström exponent α characterizes the particle size distribution in the aerosol being present in the air column over the measuting site at the time of the observation. Value of α is approximetaly 1.3 for average normal size distribution. Values higher than 1.3 are resulted in by the relatively higher frequency of smaller particles as compared with the large particles having a radius greater than 0.5 μm. Values lower than 1.3 mean the relatively higher frequency of large particles (*Ångström*, 1929). α exceeds 2 considerably, or it does not reach 0.4 or 0.5 only in extreme situations.

α is determined by the following equation (*Alföldy et al.*, 2007):

$$ln\,\delta_{A\lambda} = ln\,\beta - \alpha\, ln\,\lambda, \tag{5}$$

where:

$\delta_{A\lambda}$ is the aerosol optical depth at the wavelength λ,

β is the Ångström turbidity coefficient,

α is the Ångström exponent.

This practically means that considering ln $\delta_{A\lambda}$ as a function of ln λ, α is the steepness of the curve. α can then be determined by a reasonable linear fitting in that regression.

3. *Narrow spectral range measurements*

3.1. Biologically effective UV radiaton

Due to the global ozone depletion, accurate monitoring of biologically effective UV radiation has become stressedly important in the last decades, and after the atmospheric ozone has started to recover, it has remained important due to the fact that UV irradiation is not decreasing despite the ozone increase.

If one wants to know the exact biological effect of an irradiation on a biological system, the response of the biological system in question to the irradation is needed to know. It means, practically, the spectral sensitivity of the biological system. The function describing the wavelength dependence of the sensitivity is called action spectrum and it is consequently a weighting function. The biological irradiance for a given wavelength can be obtained if the measured spectral irradiance is multiplied by the value of the action spectrum for the wavelength in question. The biological effective dose, I_{eff}, can be obtained by the following equation:

$$I_{eff} = \int_{\lambda_L}^{\lambda_U} I_\lambda A_\lambda d\lambda \ , \qquad (6)$$

where

λ_L and λ_U are the lower and upper limit of the spectral range where values of the action spectrum are used,

I_λ is the irradiance at the wavelength λ,

A_λ is the value of the action spectrum for the wavelength λ.

If a high resolution spectrophotometer is available for the observations, the biologically effective radiation is determined by Eq. (6). However, there are broad band UV detectors, the so-called UV Biometers, whose output is the biologically effective dose. Spectral response of the human skin to the UV radiation is called Erythema, so the biologically effective radiation in case of human skin is called generally erythemally weighted radiation. The biophysical background of these processes is not object of this paper, so it is not discussed in details. *Fig. 1* shows the meaning of the aforementioned facts in reality. A physical spectrum (red line) and the corresponding erythemally weighted spectrum (blue line) can be seen in the figure. The spectrum is from our database of high-resolution UV spectra recorded by Brewer spectrophotometer at the Marczell György Main Observatory of HMS in Budapest. The importance of use of the response function in case when biological effect of a radiation is studied is clear based on the figure. Due to the very rapid variation of the Erythema function, the biological spectrum considerably differs from the physical one.

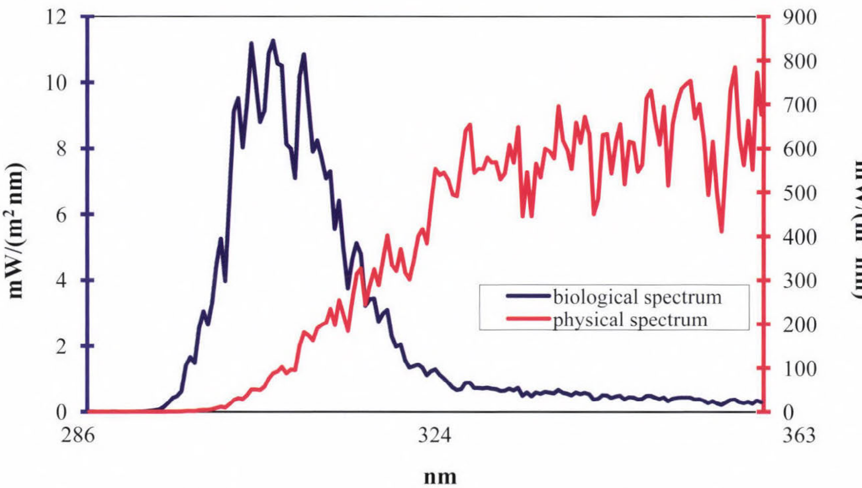

Fig. 1. Physical UV spectrum measured by Brewer MKIII spectrophotometer and the calculated corresponding erythemally weighted (biological) spectrum.

3.2. Photosynthetically Active Radiation (PAR)

PAR is a special quantity that means the biological effectiveness of visible radiation on photosynthesis of plants. Consequently, nature of PAR is the same like any other action spectrum weighted radiations, but it is expressed in a special unit.

4. Measuring equipments at the HMS

The equipments that are used for high resolution spectral measurements and special narrow range measurements at the Hungarian Meteorological Service are shown very briefly in this section. To describe their technical details and specifications, as well as principles of their operation cannot be object of this paper. Their instrument manuals include detailed informations about them (see references).

4.1. Brewer MKIII double monochrometer spectrophotometer

This instrument is a high accuracy spectrophotometer that is the most accurate and most reliable spectral equipment in the UV region today. Its sensitivity range is from 286.5 nm to 363 nm with a spectral resolution of 0.5 nm. It is equipped with a double monochrometer to increase the effectiveness of filtering of stray light that is very important due to the low irradiances to detect. A photomultiplier is used as detector to produce suitably high signal-to-noise ratio.

The equipment measures the total air columnar ozone and sulphur-dioxide content and records global UV spectrum in the range and with the parameters mentioned above (for any other details, see *Brewer MKIII Spectrophotometer Operator's Manual,* 1998).

In our operational measurement practice, it observes total ozone and sulphur-dioxide, as well as records UV spectra by approximately 15–20 minutes (the reason why the mesurement frequency varies a bit is that the observations are carried out at fixed solar zenith angles, and it, in addition to the observations in question, performs several tests concerning its optics, electronics, and mechanics to provide the possible highest quality data).

The Brewer spectrophotometer was installed in 1998, but the high accuracy total ozone observations have been started at the HMS in 1969 with the manually controlled Dobson spectrophotometer, that has been the highest quality instrument to observe total ozone then.

The two spectrophotometers worked simultaneously for one and a half year until terminating observations with Dobson spectrophotometer due to lack of manpower. These observations are carried out the Marczell György Main Obervatory in Budapest.

4.2. LI-1800 spectroradiometer / spectrophotometer

This high accuracy instrument is constructed to record electromagnetic spectra in the spectral range from 300 nm to 1100 nm with a spectral resolution of 1 nm. The diffraction spectra are produced by a monochrometer. The instrument is basically designed as spectroradiometer, namely to measure global (full-sky) irradiance, but, by using a suitably designed pipe with diaphragms, it has been made to be suitable to measure direct irradiance. It can thus work as both spectroradiometer and spectrophotometer.

In our operational measurement practice, LI-1800 records spectra by 15 minutes or 30 minutes normally according to the schedule set by us. Measurements are carried out only in cases when solar disc is not covered by cloud because the aim of the measurements with LI-1800 is to calculate aerosol optical depth and Ångström exponent characterizing size distribution of the aerosol. AOD values are archieved for all standard wavelenghts, though generally AOD at 500 nm is used for studies due to the very high autocorrelation of AOD values in a certain spectrum.

LI-1800 has options to measure PAR and illuminance, and very special quantities like leave transmissivity, leave reflectivity, etc. These quantities are not measured operationally but occasionally in special campaigns or for orders. LI-1800 is installed at the Budapest observatory also (for more technical details see: *LI-1800 Portable Spectroradiometer Instruction Manual,* 1989).

4.3. Sunphotometer SP02

Sunphotometers are special devices that are designed to measure one of the physical quantities characterizing the radiation transmissivity of the atmosphere.

The early sunphotometers measured turbidity, but the recent models masures rather aerosol optical depth. Filters are used in sunphotometers to select the required wavelengths, so their accuracy is considerably lower than that of the insturments having monochrometers. Their considerably less complicated construction and, as a consequence, their far lower prices makes them, however, practical to use in monitoring networks.

Sunphotometer SP02 is a relatively accuate and reliable device in its category. Two are operated by the HMS, one is at the Marczell György Main Observatory in Budapest and the other is at the Kékestető Observatory that is situated on the highest peak of Hungary called Kékesető.

SP02 has four channels to measure aerosol optical depth that are as follows: 412, 500, 675, and 862 nm. In case of SP02, the aerosol optical depth should not be calculated from measured irradiance, because its output is the aerosol optical depth itself (namely, the voltage output corresponds to aerosol optical depth value).

4.4. UV Biometer

UV Biometers are special broad band detectors and can be considered not so old type of detectors, since the first experimental copies started to work in the seventies, their use started to spread in monitoring networks in the late eighties and mainly in the early and mid-nineties, so most of the national networks are not older than 15 years. The UV Biometers output erythemally weighted irradiance.

Measurement of UV radiaton has not been an important task in meteorological and atmospheric physical observations in the previous decades, because its flux density is neglectably low as compared with that of the visible and infrared ranges, so consequently it has no important role in radiation budget of the atmosphere. Its crucial role in production of vitamin D in human body and its harmful effect on biological systems, however, has motivated some scientists or institutes to establish sporadic campaigns to measure UV spectrally or in broad band way. But no any long term UV monitoring network has been operated until discovering atmspheric ozone depletion. The number of national networks has increased rapidly since then. Due to their simple construction and, consequently, their considerably lower price, use of broad band UV detectors are far more practical in networks than use of higher accuracy spectral equipments.

UV monitoring network of the HMS includes five sites that are as follows: Budapest, Kékestető, Kecskemét, Sármellék, and Siófok. The former four stations have started to operate in 1994, while in Siófok, the measurements have been started in 2009.

5. Quality assurance and quality control

QA/QC procedures are of crucial importance nowadays in operating high accuracy networks. The calibrations, routine checkings and tests are performed in the measuring practice of the HMS in the ways and with the frequencies that are recommended by the manufacturers of the equipments. Each procedure for the different instruments are performed by following the working instructions of the HMS. To descript the details would not be reasonable in this paper, but it is still to be noted that to follow the given instructions is of stressed importance for us, we operate a regional center for solar radiation.

6. Operation of regional center for solar radiation, WMO Region VI, Budapest

The HMS has been operating the regional center for solar radiation since 1980. The solar radiation regional centers of WMO are operated to represent the World Radiation Reference (WRR) of the World Radiation Center, Davos, Switzerland, for the instruments of the countries of the given region. The absolute cavity pyrheliometer that represents the WRR in our regional center is the HF 19746 instrument. It participate in each international pyrheliometer comparisons held in the World Radiation Center in every fifth year. The imortance of our activity as regional center has decreased a bit during the decades since 1980, as more and more countries have started to operate absolute cavity pyrheliometers. The spectrum of our activity has, in the same time, widened by installing high resolution spectral instruments, narrow spectral range detectors, and sunphotometers. Currently we have reference to calibrate instruments as follows: spectrophotometers, spectroradiometers, filterradiometers, sunphotometers, UV Biometers, and special spectral devices including PAR meters, illuminance meters, personal UV dosimeters, filters, or other special radiometers.

As concerns the future of the operation of the regional center, it is to be noted that though its significance as representing world reference pyrheliometric scale had a bit decreased in the previous years, increasing interest appeared from other scientific areas, such as biology, agronomy, daylighting, etc. Particularly, the inclusion of UV radiation-related studies and experiments started to be more frequent in the last decade in the scientific areas mentoned above.

Another task that will probably be more and more important even in the near future is the testing of diode array spectroradiometers. This is a brand new technology and its three main advantages are the very high speed, the high spectral resolution, and the fact that the diode array spectrometers do not include moving parts. Nowadays, however, several problems are still unsolved, so the accuracy and reliability is considerably lower than that of traditional monochrometer spectrometers. Results of calibration of some of these instruments that we have made confirmed the fact mentioned above.

7. *Selected results*

Selected results from studies and researches based on the data coming from the activities shown in the previous sections are shown here. The results shown are a small part of the entire set of results. Detailed analyzis of the results is not discussed here, because it would be the aim of separate papers. Thus, in addition to very brief analyzes, the references where the details can be found are given instead.

7.1. Total ozone

Total ozone measurements have been carried out at the HMS since 1969. *Fig. 2* shows the long term variation of total ozone for Budapest for the period 1969–2012. The percentage deviations of yearly means from the mean of many years are shown in the figure. The mean of many years have been calculated for the period 1969–1980 to eliminate the effect of the stronger ozone decrease of the later decades on the estimated mean that characterizes a quasi-unperturbated condition.

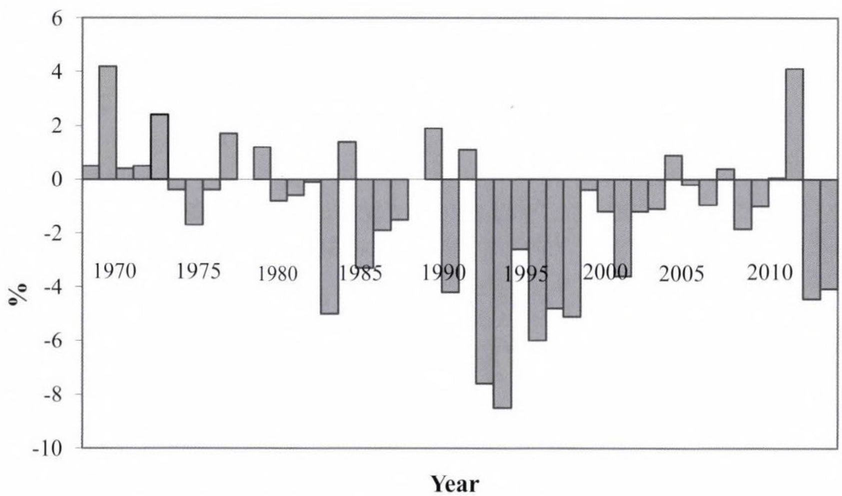

Fig. 2. Percentage deviations of yearly means of total ozone content from the mean of many years for Budapest, 1969–2012.

It is well-known that total ozone has a yearly course in the midlatitudes that is more and more stressed from the equator towards the poles. *Fig. 3* shows the calculated average (smoothed) yearly course for Budapest with the upper and lower limits of natural variability (defined as two times of the standard deviation).

It is to be noted that despite the ozone recovery, considerable ozone losses were found for most of the summers of the last decade. The summer ozone losses in the last decade were significant even considering all 43 summers despite the increasing trend in the yearly averages. It is difficult to answer the question today whether it is a consequence of some variations in the circumastances influencing ozone concentration that are of climatic scale or they were incident events.

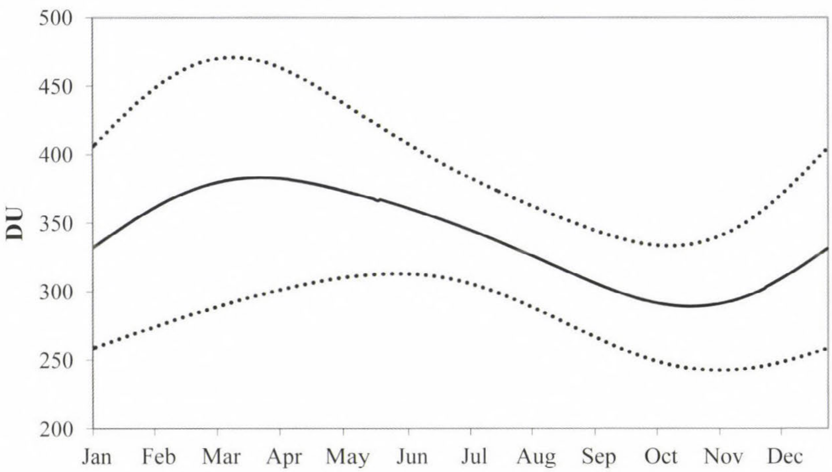

Fig. 3. Average yearly course of total ozone for Budapest.

7.2. Short-wave radiation transmission of the atmosphere

7.2.1. Graybody optical depth and the scattering parameter

Some results concerning the behavior of transparency of the atmosphere are shown in this section.

Fig. 4 shows the long term variation of graybody optical depth for Budapest for the period 1967–2011 that is demonstrated by the yearly means. The values are increasing up to 1994 and decreasing from then (similar behavior was found for each monthly trends), thus a sectioned trend analysis was performed as an experiment for the period 1967–1994 and for 1995–2011. Considering the different months, based on the trend analysis for the period 1967–1994, the only month was December for which significant increase was not found. It is to be noted, that reason for no yearly averages are shown in the figure for 2008 and 2009 is that no sufficient number of measured data were available for the correct calculation for both years due to susbequent failures of the solar tracking system. It has unfortunately taken for a long time while the manufacturer's trouble-shooting trials has become succesful.

Yearly course of GBOD is shown in *Fig. 5.* It is clear, based on the figure, that transparency of the atmosphere is higher in winter than in summer, as it has been expected otherwise.

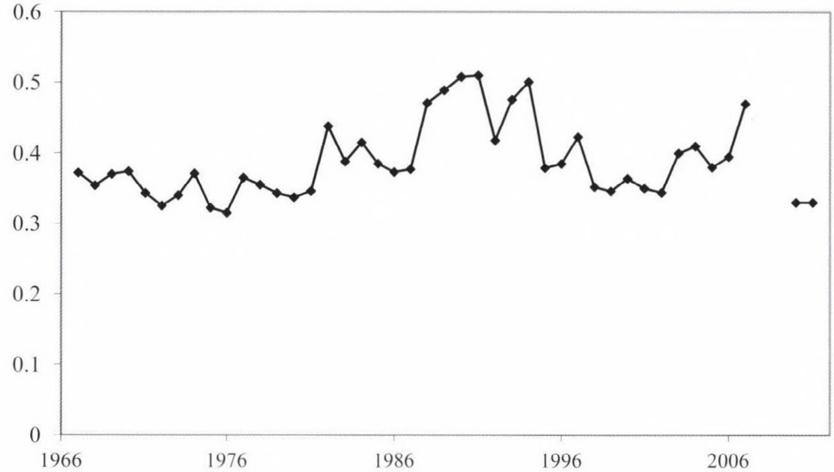

Fig. 4. Yearly means of graybody optical depth for Budapest for the period 1967–2011.

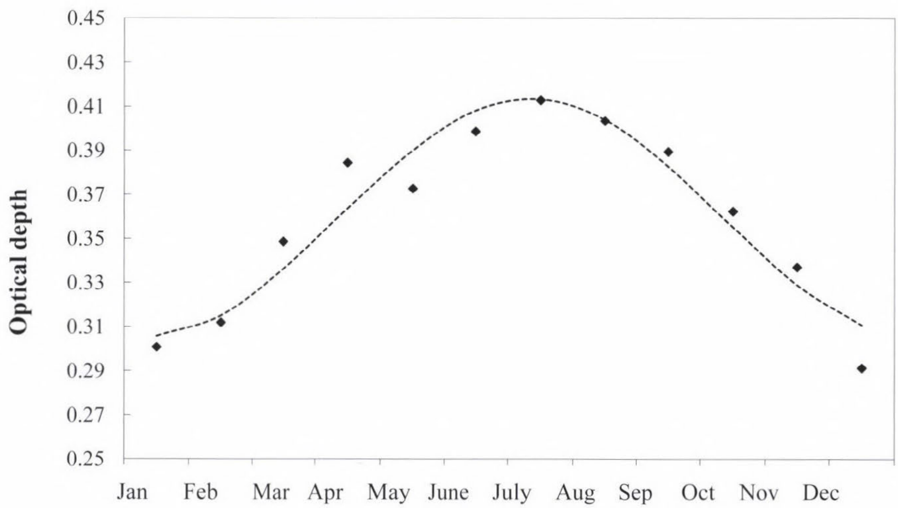

Fig. 5. Average yearly course of graybody optical depth for Budapest.

These studies were performed for another special quantity called scattering parameter (Θ). It is an indicator of ratio of diffuse irradiance to the total global irradiance in the way that measured diffuse-to-global ratio is normalized by the diffuse-to-global ratio theoretically calculated for the Rayleigh-atmosphere, and it is in high correlation with turbidity (*Kaskaoutis et al.*, 2007) Thus it is expressed in the following way:

$$\Theta = \frac{D/G}{D_R/G_R},$$

where D and G are the diffuse and global irradiances, respectively, measured on a horizontal surface, D_R and G_R are the diffuse and global irradiances calculated for Rayleigh-atmosphere for the time of the observation, respectively.

Long term variation (1967–2002) and average yearly course were also determined for scattering parameter, and the results are very similar that those obtained for graybody optical depth.

Scattering parameter is a useful quantity to examine how close, in respect of transparency, the real atmosphere can be to the Rayleigh atmopshere in the clearest cases (least polluted cases, actually). In order to perform this, the lowest D/G values (occurred during the experimental period) were to determine. A reference can be the minimum value of a month (monthly absolute minimum value) from the long-term database. *Fig. 6* shows the yearly course of absolute minimum values of D/G (solid line) and values of D/G calculated for Rayleigh-atmosphere (D_R / G_R) for the middle of the hour intervals used for the study (dashed line). The important message of *Fig. 6* is that in the clearest (least polluted) cases the atmosphere above the observatory almost equalled to the Rayleigh-atmosphere.

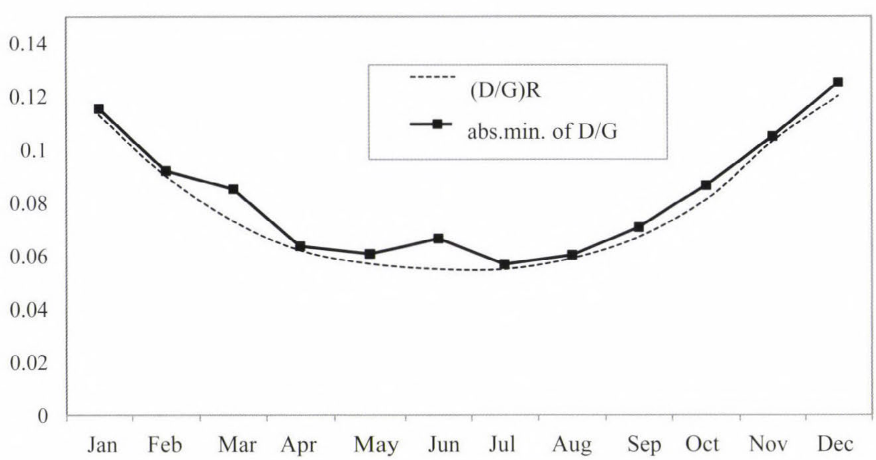

Fig. 6. Yearly course of monthly absolute minimum values of D/G and calculated values of D/G for Rayleigh-atmosphere.

7.2.2. Optical properties of the aerosol

Optical properties of aerosols were studied by using AOD and Ångström exponent. Due to the consequentially very high autocorrelation between the AOD values calculated for the different standard wavelengths from the same spectrum, AOD for 500 nm (AOD_{500}) was used for each study. To determine long term variation of AOD_{500} was not possible because of the insufficient number of observations (that is a consequence of the fact that AOD, due to its definition, can be estimated when solar disc is not covered by any clouds).

However, a mean value (a quasi-mean of many years, actually) of AOD for Budapest was determined. The value obtained, of course, is not too reliable due to the abovementioned insufficiency. However its estimation, in contrast with the trend analysis, has reasonability due to the fact that for this estimation all data together are needed. The same can be stated for the mean of many years for the Ångström exponent.

Aerosol optical depth values are available for the period 1996–2011, so the mean of many years is valid for a period of 16 years. Since the results obtained for GBOD, that should relatively be in close connection with AOD, show that the transparency of the atmosphere has started to incease from the mid-nineties, the obtained mean for AOD_{500} will then underestimate a mean of many years concerning a longer period. A value of 0.28 was found as mean of many years for AOD_{500}. A general experience for values of AOD at 500 nm is well-known as a result of numerous previous studies. It says that urban and industrial areas are characterized by values higher than 0.3, while rural areas are characterized by values lower than 0.2. Values between 0.2 and 0.3 characterize areas polluted on the average. Though the obtained value seems to be indicative of the suburban situation of the observatory, where there is no considerable industrial pollution, but traffic, it is to be noted that the correct value supposed to be some tenth higher due to the expected underestimation of AOD_{500} due to the aforementioned reasons.

The obtained mean of many years for wavelength exponent is 1.31. Considering the facts about different values of α written in 2.4., this value can be called usual value. It shows that the usual particle size is the dominant in the aerosols being present in the air colum above the observatory.

Dependence of Ångström exponent on AOD_{500} was also studied and the result is shown in *Fig. 7.* It was found that despite the considerably high dispersion of the set of dots, the two quantities are inversely proportional to each other, namely the dominant particle size increases with the increasing aerosol content of the air column. This fact has an important message to us: it means that there is a weak tendency showing bigger aerosol masses tend to be composed by larger particles with higher likelihood, statistically, and conversely: lower aerosol optical depths are, with higher statistical likelihood, produced by aerosols including smaller particles.

A parameterization technique was developed to estimate AOD data from GBOD data (*Tóth,* 2008). In principle, GBOD and AOD values calculated from irradiances that were measured at the same time, differ only due to GBOD, which is influenced by total vapor and ozone absorption (as main absorbers that can considerably vary), while AOD is not. Dependence of AOD at 500 nm on GBOD is shown in *Fig. 8.* If the aforementioned facts are accepted, the dispersion of GBOD values that belong to a given value of AOD_{500} is caused by effect of total water vapor content and total ozone content on GBOD. Consequently, if total water vapor content and total ozone content dependence of the residuals are determined, a correction can be computed by which the relationship between the two optical depths can be improved. It means that AOD values can be computed from GBOD values by considering total precipitable water and ozone.

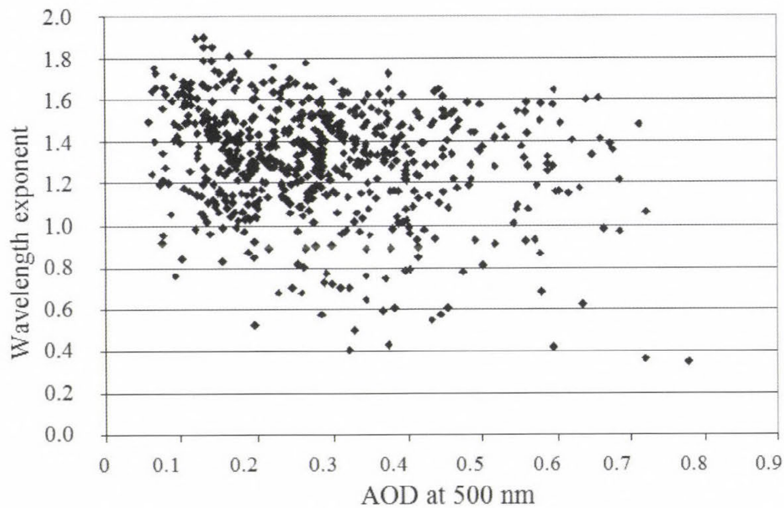

Fig. 7. Relationship between AOD_{500} and Ångström exponent.

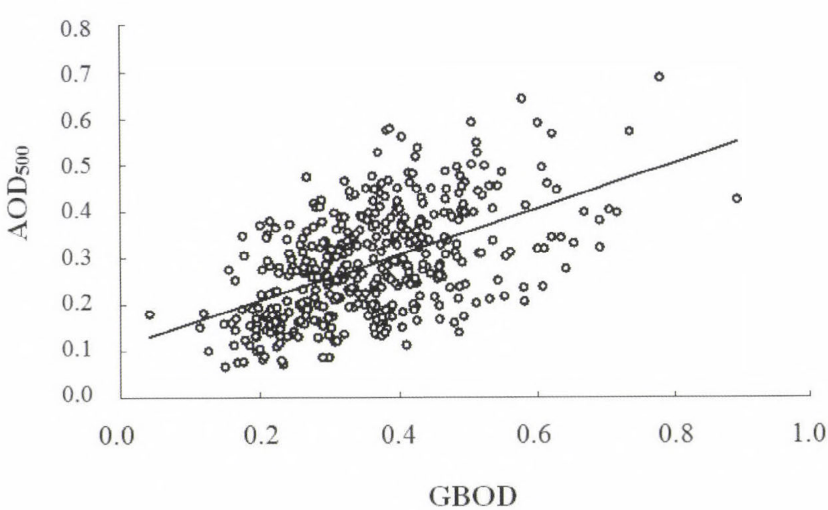

Fig. 8. Relationship between GBOD and AOD_{500}.

Total precipitable water data calculated from rawinsound observations regularly performed in the observatory and total ozone data coming from ozone measurements carried out also operationally at the observatory by the Brewer spectrophotometer were used for the parametrization, so the parametrization equation was as follows:

$$\delta_{A\lambda} = C_{0\lambda}\delta_{GB} - C_{1\lambda}X_{TPW} - C_{2\lambda}X_{O3} + C_{3\lambda}, \tag{7}$$

where

$\delta A\lambda$ is the aerosol optical depth at wavelength λ,

δGB is the graybody optical depth,

X_{TPW} is the total precipitable water,

X_{O3} is the total air columnar ozone content,

$C0\lambda$, $C1\lambda$, $C2\lambda$, $C3\lambda$ are the conctants to determine.

The wavelength used for the study was 500 nm.This parameterization resulted in an approximately 30% increase in correlation coefficient. It means that a method is available to calculate aerosol optical depth from graybody optical depth if total precipitable water and ozone contents are known.

The discussion of the methods used for the study and detailed analysis of the results has been published in a conference proceedings (*Tóth*, 2008).

7.2.3. Relationship between aerosol size distributions and aerosol optical depth spectra

In a study, the size distribution of aerosol and its relationship with wavelength exponent was investigated. The size distribution was estimated by a mathematical inversion method developed by King et al. (*King et al.,* 1978). The size distribution can be deterined from aerosol optical depth spectrum by using this method.

It was found that the obtained size distributions are in good connection with the wavelength exponent. Though they are not independent from each other due to the fact that the aerosol optical depth spectrum is the base for both, to analyze their relationship is still reasonable, because they are very different quantities. While the wavelength exponent is one number that characterizes the fequency of larger particles, and the dominant particle size can be estimated from it by using an empirical equation determined by Ångström (*Ångström,* 1929), the size distribution determined by King's method is a function estimating a realistic size distribution of the particles being present in the aerosol at the time of the recording of the spectrum. So we had to find a property of the function that could be brought into relationship with a number. The shape of the function was found to be suitable to compare. It was found that the shape of the size distribution changes with the value of α. Results are shown in *Fig 9*. To make details more easily visualizable, size distributions are graphed for 5 different values of α, but the effect found is the same if all size distributions is involved.

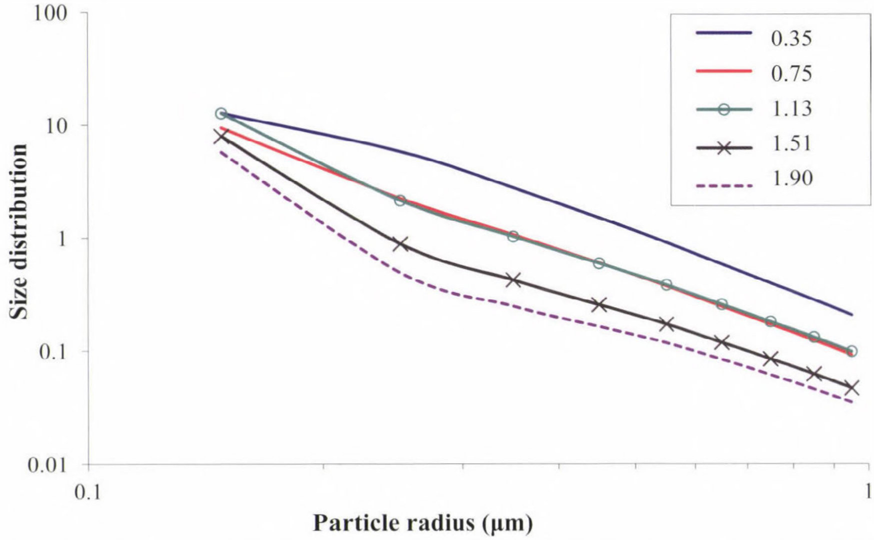

Fig. 9. Shapes of computed aerosol particle size distributions for different values of Ångström exponent.

The size distribution function for the lower values of α has a typical shape that is decreasing slowly for the shortest particle radii (approx. 0.3 μm – 0.4 μm) and from that value it is decreasing by a bit higher rate. This shape tends to be quasi-linear and then tends to be inflectious from about 0.6 μm, but oppositely to the shortest radii: first it is decreasing a bit rapidly, then slowly, and the inflection point is at about 0.25 μm that remains almost unvariable along the studied radius range (a bit shifted to the longest radii, but even the maximum shift is only some hundredth μm). The another inflection point was found somewhere between 0.6 μm and 0.7 μm. *Fig. 10a, b,* and *c* show that differences between the shape of the size distributions are very small for a given value of α.

7.2.4. Dependence of spectral diffuse-to-direct irradiance on the atmospheric turbidity

A special investigation was performed previously concerning dependence of spectral diffuse-to-direct beam irradiance ratio on the atmospheric turbidity and solar zenith angle for the wavelength range from 300 nm to 1100 nm *(Kaskaoutis et al,* 2007). It was performed by modeling based on measured data. Since the detailed analyzes cannot be discussed in this paper, only two of the several results are shown here. *Fig. 11* shows the spectral ratios for AOD_{500} = 0.3, α = 1.3, and solar zenith angle of 20°, for three different values of single cattering ratio.

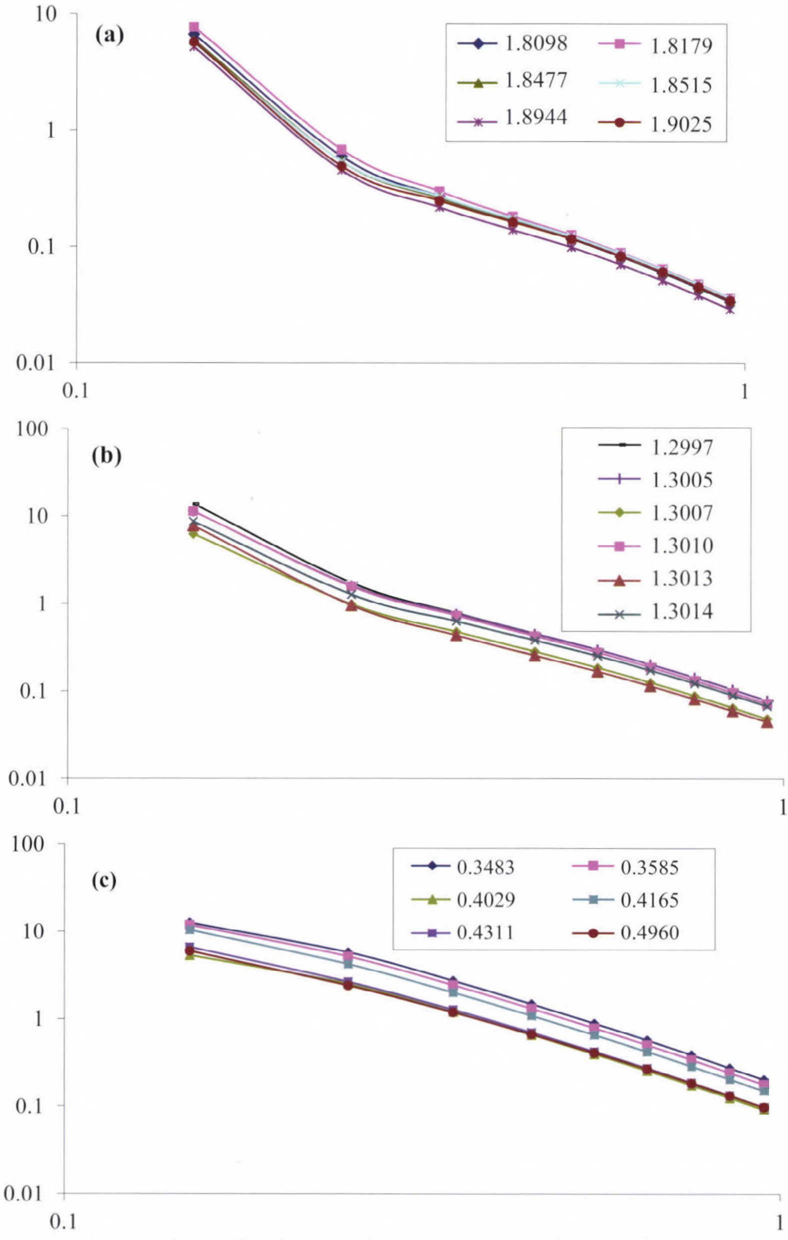

Fig. 10. Computed aerosol size distributions for high (a), normal (b), and low (c) values of Ångström exponent.

Fig. 12 shows the ratios for AOD = 0.3, single scattering ratio = 0.9, and solar zenith anlge = 60°, for three different values of α. It can be seen from both figures that the ratio increases moderately towards the shorter wavelength in most part of the visible range, then this increase becomes very rapid in the shortest part of the visible range, and the rate of increase is considerably sharper in the ultraviolet range. The increase rate increases with increasing single scattering albeldo, as it has been expected. At the same time, the increase rate increases as wavelength exponent increases (the dominant particle size decreases). Detailed analysis of all results can be found in the paper referred.

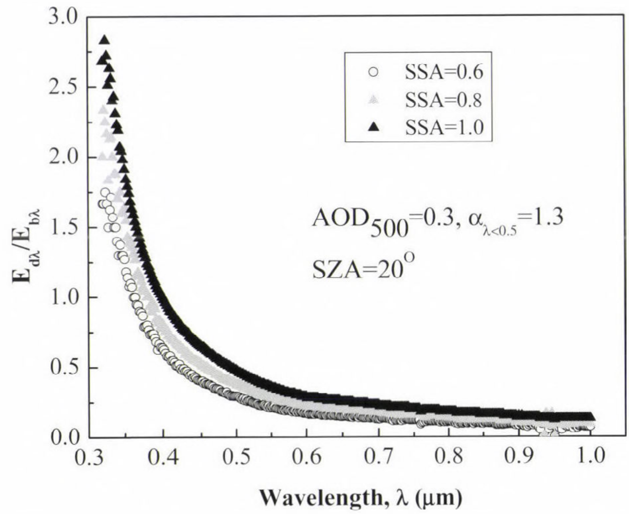

Fig. 11. Spectral diffuse-to-direct beam ratios for AOD_{500} = 0.3, α = 1.3, and solar zenith angle of 20°.

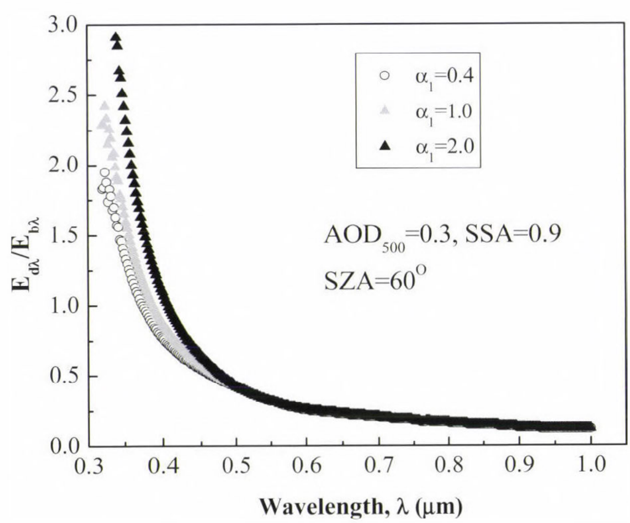

Fig. 12. Spectral diffuse-to-direct beam ratios for AOD = 0.3, single scattering ratio = 0.9, and solar zenith anlge = 60°.

7.3. UV radiation

Some results concerning UV radiation are shown in this section.

Fig. 13 shows the characteristic maximum spectra for the different months for Budapest. It is clear from the figure that no considerable UV irradiance is received by the Earth's surface below 296 nm in Budapest even in case of the summer months. Despite this fact, measuring biologically effective UV radiation at the shorter wavelengths is reasonable, because the biophysical effects of the shortest wavelengths that yet reaching the Earth's surface are not known exactly today.

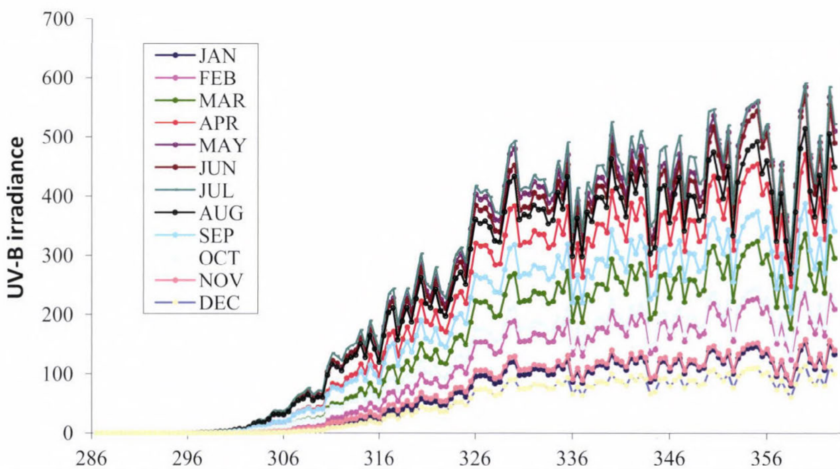

Fig. 13. Characteristic maximum UV spectra for the different months for Budapest coming from observations by Brewer MKIII spectrophotometer

The yearly totals and summer season totals of the biologically effective UV dose are shown in *Fig. 14* and *Fig. 15,* respectively, for the period 1995–2012. It is to be noted that despite the UV monitoring network of HMS includes five stations, only four were used for studying long term variations of UV. The reason is that one of the stations, Siófok, has started to operate in 2009, as it was mentioned in Section 4.4, so its inclusion in this study was not reasonable. An increasing trend of 3–6%/10 years was found for the different stations for both quantities. The obtained value fits the world-wide tendencies and the values computed from models for these areas (*Lytinska et al.,* 2009). The reason for the UV increase is that the increase of atmospheric transparency presumably compensates the UV reducing effect of the total ozone increase.

7.4. Effects of atmospheric circumstances on UV radiation reaching the Earth's surface

It is very important to know how atmospheric circumstances affect UV irradiances reaching the Earth's surface. Some results concerning this are shown in this section.

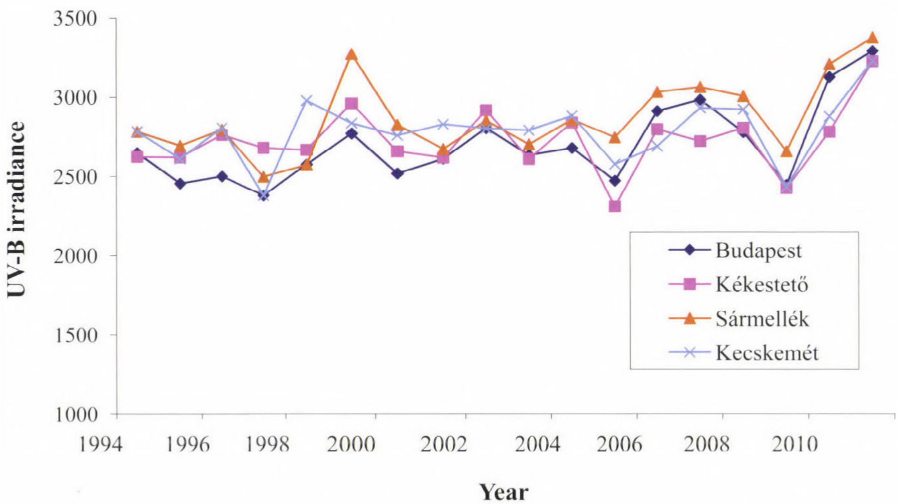

Fig. 14. Yearly totals of erythemally weighted UV irradiances for 4 sites of Hungary.

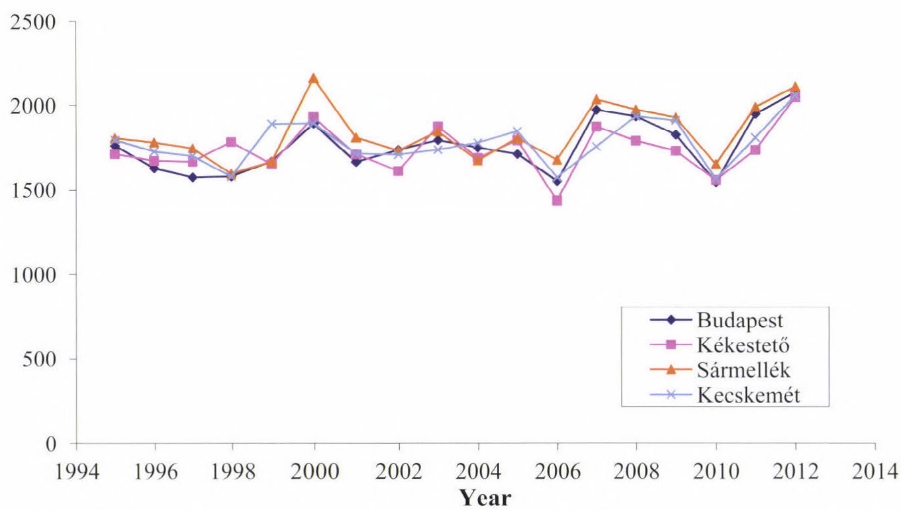

Fig. 15. Summer season totals of erythemally weighted UV irradiances for 4 sites of Hungary.

Fig. 16 shows the relationship between total ozone content and UV radiation reaching the Earth's surface. Theoretically well-known that, as a consequence of strong ozone absorption in the UV-B range, the UV irradiance measured at the surface should be in inverse relationship with total ozone: the higher the total ozone content, the lower the UV irradiance. This fact can be seen well in *Fig. 14,* where the daily course of erythemally weighted UV radiation is shown for two days for which total ozone has considerably differed.

This dependence well-traced exactly for our total ozone and UV radiation dataset.

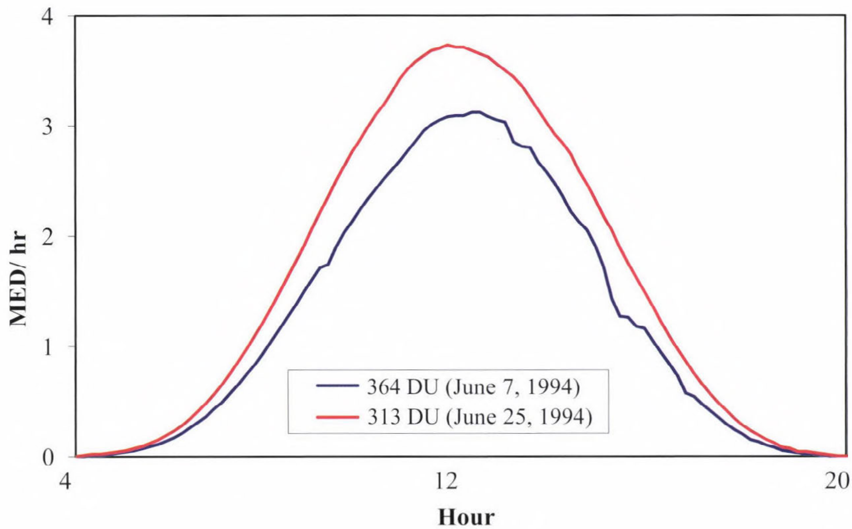

Fig. 16. Daily course of erythemally weighted UV irradiance for two days with different total ozone content.

A relatively frequently used quantity is the RAF (Radiation Amplification Factor) that is a practical indicator of the principle mentioned above. RAF shows the percentage increase in erythemally weighted UV irradiance that is resulted in an effect of 1% decrease in total ozone content. Value of RAF was determined by us by using spectrophotometric total ozone data and measured broad band UV data. The RAF obtained by us was in Section 1.17 (*Németh et al.*, 1996) that is in good agreement with values obtained by other authors. Though not being used generally, to determine a special spectral RAF (SRAF) seemed to be very informative (it can be called the 'monochromatic version' of the aforementioned broad band RAF). SRAF was determined from data coming from Brewer measurements. *Fig. 17* shows the dependence of SRAF on the wavelength. The slope sharply incresases towards the shorter wavelengths. The very important medical conclusion from the figure is that relatively smaller ozone losses can have dangerous effects, mainly for persons having extremely sensitive skin, because the pattern suggests that considerable amount of photons can appear at the very short wavelengths where the human skin is not prepared for their effect. Though it is not clear if it can be more dangerous either on short time scale or on longer time scale, it seems to be sure that the effect is considerably dangerous on longer scale. Furthermore, considering the significant ozone deficits in the last 6–7 summers, this result warns us to be very careful with sunbathing.

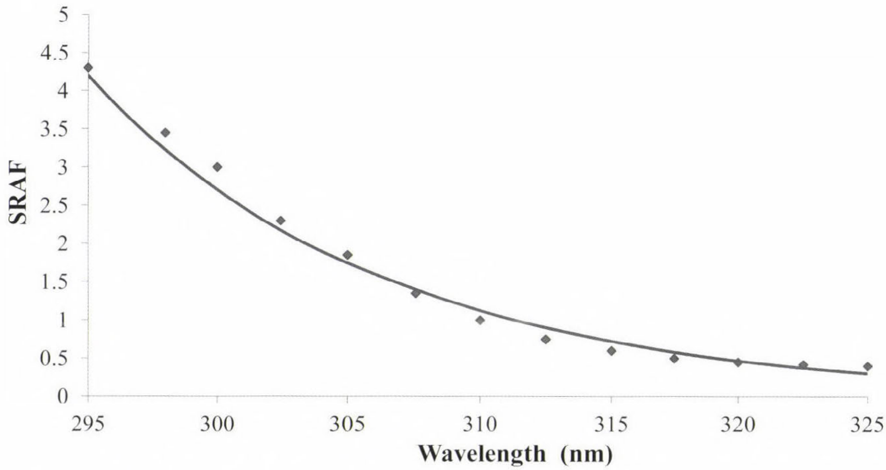

Fig. 17. Dependence of SRAF on the wavelength.

The effect of cloudiness on the UV irradiance received by the Earth's surface is an important parameter. The results have been published by us previously (*Németh et al.,* 1996), so they are discussed here only very briefly. Though radiative transfer is known exactly in theory and can be modeled with relatively good reliability, in very practical tasks, for example in case of UV forecast, a reliable empirical relationship can solely be used due to the fact that numerous parameters of the cloud influencing radiative transfer in the cloud is not known exactly at the time of the given observation. A non-heigth-dependence CMF (Clud Modification Factor) was determined by us, which means that only the percentage cloudiness was considered in the study. All data were used for the study with no any filtering that depends on atmospheric circumstances. The results are shown in *Figs. 18a* and *b* for solar elevations higher than 30° and lower than 30°, respectively. The non-linear dependence is clear from the figures, but a peculiar behaviour is revealed from *Fig. 16b:* UV irradiances can, with high statistical likeliohood, be higher in case of 10–40% cloud coverage than irradiances detected for clear sky conditions. The explanation for this unexpected behavior is the very effective radiation scattering towards the Earth's surface on the edges of the clouds. Cloud coverages between 10 and 40% can be produced by mainly cumuli with relatively high probability and, due to their ragged, fragmented structure, the scattering on the cloud edges can thus be considerable.

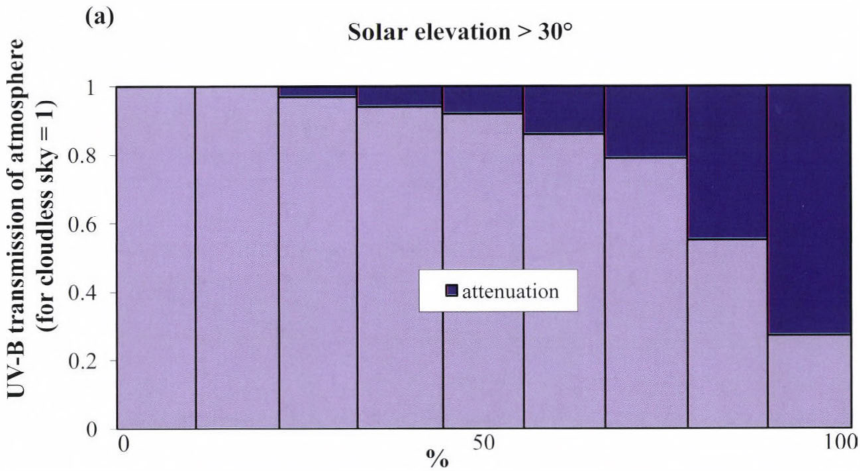

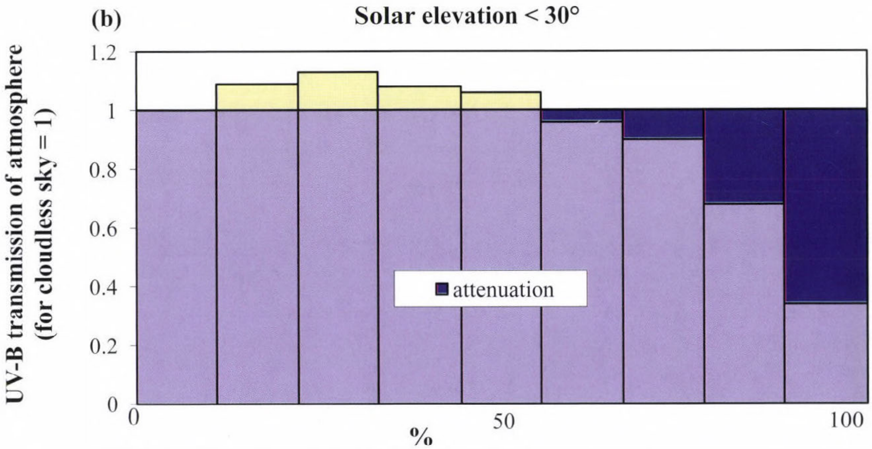

Fig. 18. Dependence of UV transmission on cloudiness in the atmosphere in Budapest of solar elevations higher (a) and lower (b) than 30°.

7.5. Verification of surface solar radiation outputs predicted by ALADIN model

Verification of predicted solar radiation data from ALADIN weather forecast model was carried out in 2001 (*Tóth,* 2002). Not the results of the verification themselves are that are shown here, because on the one hand, it cannot be aim of this paper and on the other, several improvements have been made on the model since the time of the verification in question. The aim is to show how high resolution spectral data can be useful for and can contribute to the verification by pointing out the strongnesses and weaknesses of the concerned module of the model. The verification was performed for total global fluxes for three stations and direct as well as diffuse fluxes for one station, because direct and diffuse radiation measurements have been carried out at only one station (Budapest) then. The predicted data for both the subsequent day and the day after subsequent day were verified.

Two main factors affect solar radiation flux reaching the Earth's surface in case of wider energy range radiation: total water vapor content and total aerosol content of the air column. A study was still invented to find out how ALADIN would be able to estimate surface solar radiaton fluxes in cloudless cases or in other words: how it would be able to estimate atmospheric radiation transmission. Implicitly, the data were used for this study that has been produced at cloudless situation. The detailed description of filtering that was made in order to select data meeting with the criteria given by us, see the paper referred. To represent radiation transmission condition of the atmosphere, aerosol optical depth at 500 nm (AOD_{500}) was selected.

The aim of the study was to obtain any information on reliability of ALADIN-made surface solar radiation forecasts concerning different atmospheric radiation transmission conditions. It is very important, since considerable radiation extinction can in many cases occur even when sky is cloudless.

Relationship between AOD_{500} and difference of observed and predicted solar irradiances (DIF_DIR, DIF_DIF, and DIF_GL in the figures) was studied for all three radiation parameters. Results are shown in *Figs. 19, 20,* and *21.* AOD_{500} is represented on horizontal axis and differences between observed and forecasted irradiances are represented on vertical axis in each figure.

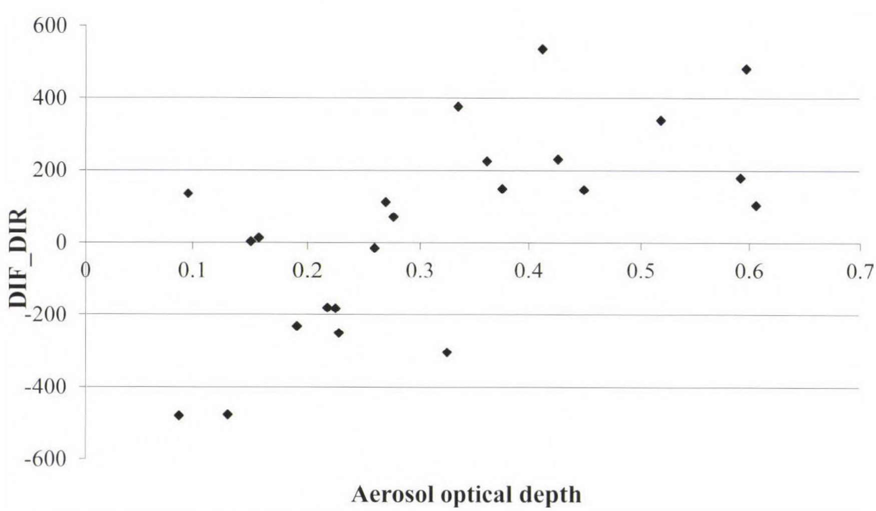

Fig. 19. Dependence of DIF_DIR on AOD_{500}.

Results for direct irradiance is shown in *Fig. 19.* Based on our five-year-long aerosol optical depth data series, it was known that average value for the

Marcell György Main Observatory in Budapest was approximately 0.3 for 500 nm. It is clear from *Fig. 19* that for the most part, overestimations are found for values of AOD_{500} lower than 0.3 and underestimations are found for τ_{500} values higher than 0.3. It means that the model underestimates direct irradiance reaching the surface in cases when atmospheric radiation transmission is high, namely when very small amount of pollutant is present and overestimates it in cases when atmosphere is considerably polluted. Based on it one can conclude, that atmospheric radiation conditions predicted by the model are generally approaching average conditions due to that the model draftly handles parameters influencing radiation transmission, namely its variability is lower than that of the corresponding true parameters. The model predicts more polluted atmosphere compared with reality in very clear cases being close to Rayleigh atmosphere. These findings are confirmed by results of the same study made for diffuse irradiance (*Fig. 20*). Pollutants and water vapor intensively scatter radiation, consequently diffuse (scattered) irradiance observed at Earth's surface increases as larger amount of them is present in the atmosphere. It can be seen in *Fig. 20* that in case of diffuse irradiance, inverse effect was found as compared to that found for direct component: the model overestimates diffuse irradiance in cases of high transmission (AOD_{500} < 0.3), namely it forecasts more polluted conditions than the true state of atmosphere and, at the same time, it underestimates in cases of lower transmission, namely it forecasts lower pollution than that appearing in true atmosphere. The same effect lies behind this phenomena like in case of direct fluxes so the explanation is the same: the model tends to produce such physical conditions of atmosphere that result in more average atmospheric transmission than those occurring in reality. Those mentioned above are valid for global radiation also (see *Fig. 21*), but the effect is relatively less evident due to the fact that global irradiance is the sum of the previous two parameters so the effect in queston decreases.

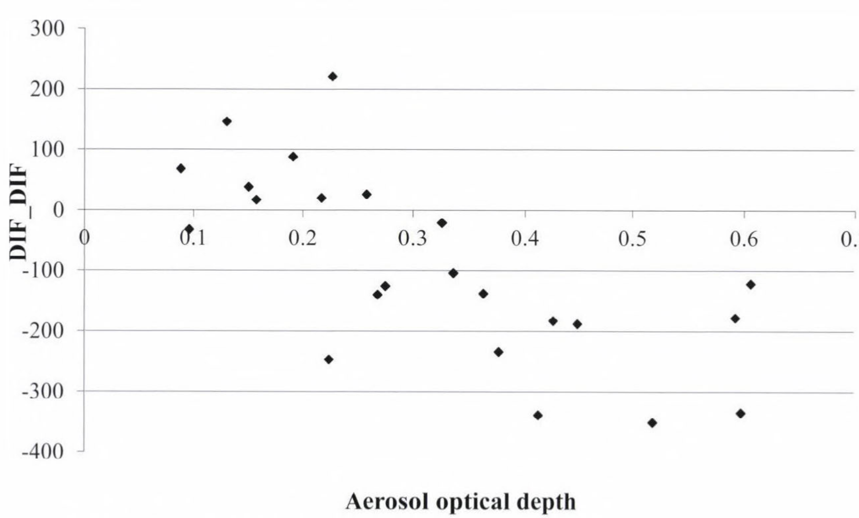

Fig. 20. Dependence of DIF_DIF on AOD_{500}.

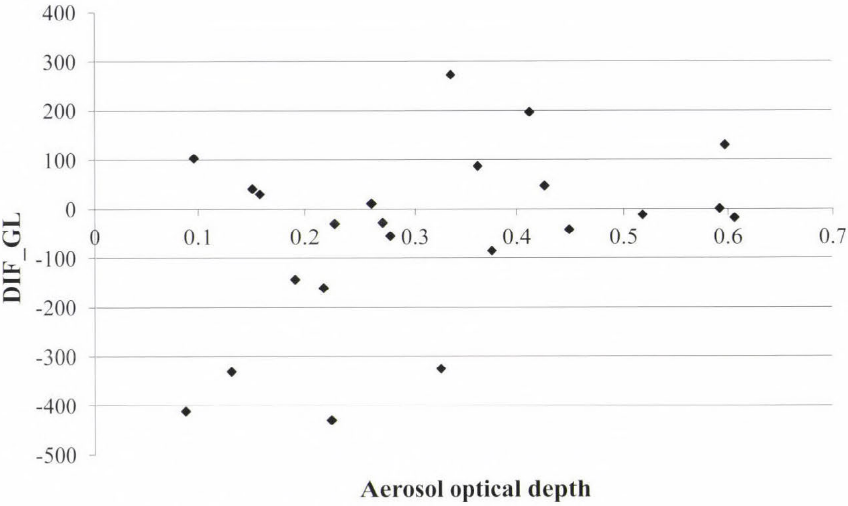

Fig. 21. Dependence of DIF_GL on AOD_{500}.

8. *Other special studies*

Special individual studies occur with variable frequency in our activities and concern wide area in solar radiation measurements. They concern radiation transmission of given materials, or variation of their radiation transmission due to longer exposure to solar radiation (mainly UV), or spatial distribution of radiation source's emitted radiation, etc. Amongst these studies, results for only one are shown that are very useful and instructive. Several experiments concerning UV radiation transmission change of UV blocking plastic foils used in agriculture and special seed holding materials used in agriculture. The plastic foils have been exposed to UV radiation in the whole vegetation period (from May to October), and the change both in their special mechanical parameters and in their radiation transmission was investigated. The latter was performed by us, but measured data were provided to the former also by the Hungarian Meteorological Service. The experiment were supported by Hungarian Institute for Agrucultural Engineering (for other details, see *Csatár* and *Fenyvesi,* 2008).

Five kinds of foils were examined: 1) a plastic foil that included no UV filtering material was for control, 2) white-colored foil including 5% UV filtering metarial, 3) white-colored foil including 20% UV filtering material, 4) violet-colored foil including 5% UV filtering material, 5) violet-colored foil including 20% UV filtering material. Only a brief summary is discussed here to concern the most important results that are shown in *Figs. 22a, b, c.*

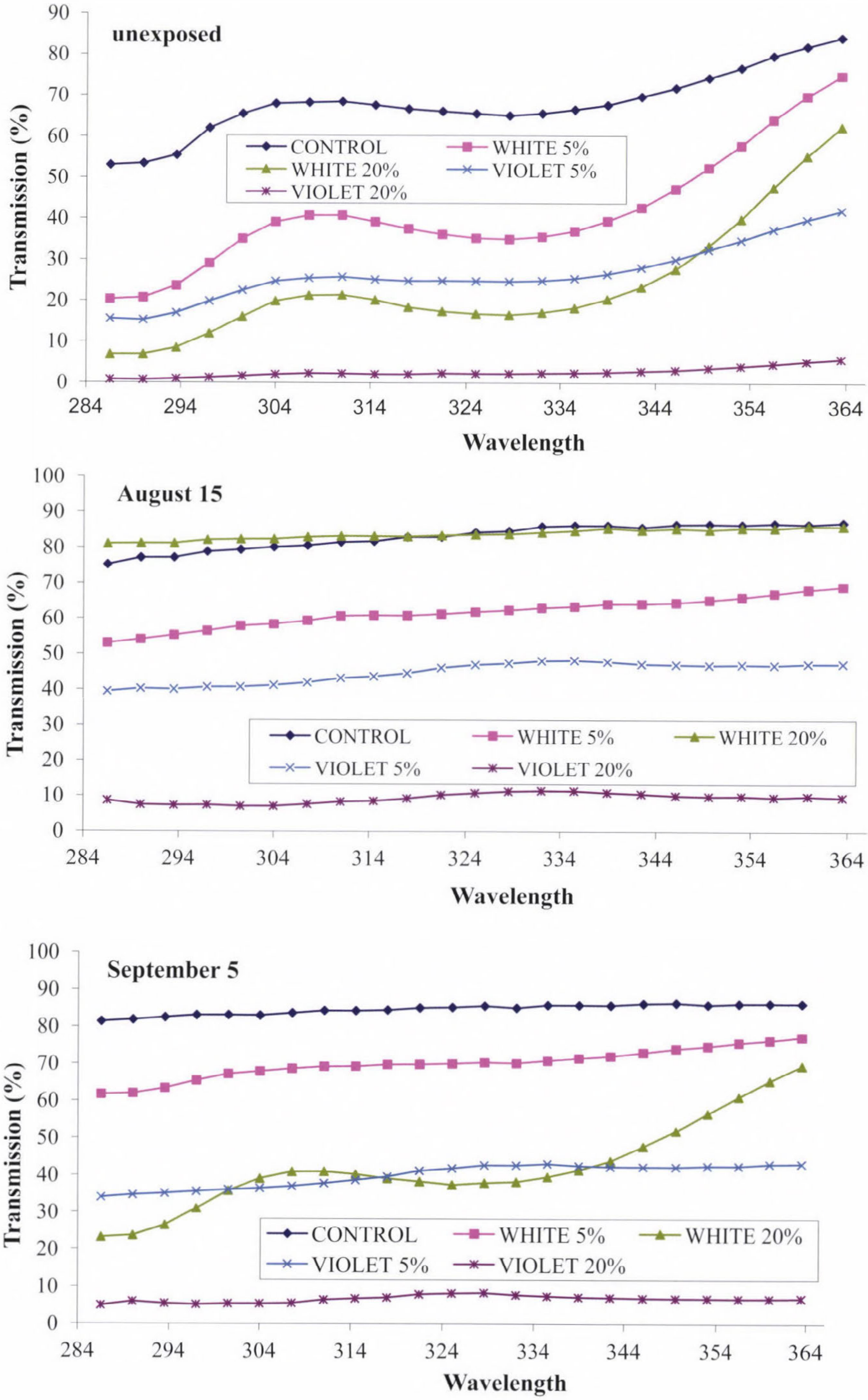

Fig. 22. UV transmission spectra of the examined plastics for three different sampling dates during the experiment (unexposed, Aug 15, Sep 5)

The plastics have been installed at the end of May in the garden of the Marczell György Main Observatory of the HMS and have thus been exposed to solar radiation until the beginning of October covering the entire vegetation period. Samples have been taken out from them by two weeks and their mechanical parameters and UV radiation transmission spectra have been examined to study variations in them. UV transmission spectra for three selected sampling dates for the spectral range from 286.5 nm to 363 nm for five selected sampling dates are shown in the figure. The behavior of the plastics are very similar and difference was found only quantitatively. It is evident that the UV blocking effect starts to loose partly soon after the installation, namely their increasing UV transmission increases and become considerable for the white foils and increases by a low rate for the violet foils for the second half of the examined period. It is also clear that at the end of the period, a chemical recovery starts up because the UV trasmission decreases a bit. Also a smoothing effect can be seen in the fine structure of each of the transmission spectra, but one type (white 20 %) retrieves partly its original shape. One can conclude that the destructive effect of UV radiation on the UV blocking material is not entirely irreversible. These results have stressed importance for the agriculture in application of the foils in UV protection of plants.

9. *Conclusions*

Due to the nature of this paper, conclusions cannot be made in the usual way. A special measurement technique and its theoretical background, covering, at the same time, a wide scale of measurement types were shown that is operationally run at the Hungarian Meteorological Service. Results coming from studies and investigations concerning very considerably different areas were shown, so their detailed analyzes were not possible, though some conclusions was made straight after showing the given results.

It is, however, still to be noted that use of high resolution spectrophotometry and spectroradiometry in atmospheric physical observations and investigations is very useful for numerous purposes, and it has reason for existence both in operational measurements and special experiments. It should be clear based on the studies and results showed that modern solar radiation measurements require its inclusion to an increasing degree.

Acknowledgements—Since high number of very different studies was shown in this paper, numerous domestic and foreign colleagues have contributed to them, so to list them is on the one hand, unreasonable and on the other, impossible due to the fact that contribution or significance of contribution of given persons cannot be estimated correctly. Still, one person is to be mentioned by name, because he is the author's long term colleague in the solar radiation area and his work on most part of the aforementioned studies is of primary importance. He is *Zoltan Nagy*, who is currently the head of the Atmospheric Physics and Measurement Technics Division of the HMS where all activities on solar radiation belong to. Nevertheless, the author thankfully acknowledges every international and domestic project that has founded or contributes by any way to the tasks shown, as well as also thankfully acknowledges all persons who have contributed to them in any degree.

References

Alföldy B., Osán, J., Tóth, Z., Török, Sz., Harbusch, A., Jahn, C., Emeis, S. and *Schäfer*, K., 2007: Aerosol optical depth, aerosol composition and air pollution during summer and winter conditions in Budapest. *Sci. Total Environ. 383,* 141–163.

Ångström, A., 1929: On the atmospheric transmission of sun radiation and on dust in the air. *Geogr. Anna. 11*, 156–166.

Brewer MKIII Spectrophotometer (Double Spectrometer) Operator's Manual, 1998: SCI-TEC Instruments Inc.

Csatár, A. and *Fenyvesi, L.*, 2008: Effect of UV radiation and temperature on rheological features of multi-layer agricultural packaginig foils. *Prog. Agricult. Engin. Sci. 4,* 27.

Dobson, G.M.B., 1957: Observer's handbook for the ozone spectrophotometer (on behalf of the International Ozone Commission (I.M.A.) in conjunction with Messrs. R. & J. Beck Ltd.). *Pergamon Press*.

Kaskaoutis, D.G., Kambezidis, H.D. and *Tóth, Z.*, 2007: Investigation about the dependence of spectral diffuse-to-direct-beam irradiance ratio on atmospheric turbidity and solar zenith angle. *Theor. Appl. Climatol. 89,* 245–256.

King, M.D., Byrne, D.M., Herman, B.M, and *Reagan, J.A.*, 1978: Aerosol side distributions obtained by inversion of spectral optical depth measurements. *J. Atmos. Sci. 21,* 2153–2167.

LI-1800, Portable Spectroradiometer Instruction Manual, 1989: Publication No. 8210-0030, LI-COR, inc.

Lytinska, Z., Koepke, P., De Backer, H., Groebner, J., Schmalwieser, A. and *Vuilleumier, L.*, 2009: Long term changes and climatology of UV radiation over Europe. *Final Sci. Report, COST Action 726.*

Németh, P., Tóth, Z. and *Nagy, Z.*, 1996: Effect of weather conditions on UV-B radiation reaching the earth´s surface. *J. Photochem. Photobiol. B 32*, 177–181.

Tóth, Z, 2002: Verification of surface solar radiation fluxes predicted by ALADIN. *ALADIN Newsl. 21,* 80–92.

Tóth, Z, 2008: Long-term variation of atmospheric shortwave radiation transmission above Budapest, Hungary. *Proceedings of the 4th International Conference on Solar Radiation & Daylighting SOLARIS 2008, Hong Kong, China,* 27–35.

IDŐJÁRÁS

Quarterly Journal of the Hungarian Meteorological Service
Vol. 117, No. 4, October–December, 2013, pp. 435–450

Comparison of two Lagrangian dispersion models: a case study for the chemical accident in Rouen, January 21-22, 2013

Ádám Leelőssy[1], **Erika Lilla Ludányi**[1], **Márk Kohlmann**[1], **István Lagzi**[2], and **Róbert Mészáros**[1,*]

[1]*Department of Meteorology, Eötvös Loránd University, P.O. Box 32, H-1518 Budapest, Hungary*
[2] *Department of Physics, Budapest University of Technology and Economics, Budafoki út 8, H-1111 Budapest, Hungary*

**Corresponding author E-mail: mrobi@nimbus.elte.hu*

(Manuscript received in final form July 10, 2013)

Abstract—Industrial accidents have been a serious environmental and public health issue for the last decades. Although the development of atmospheric dispersion models was largely motivated by the notorious nuclear catastrophes, simulations are now mostly used in cases of chemical accidents that regularly occur in all parts of the world. In an accidental situation, the accuracy of the results is primarily important for risk management and decision making strategies. However, it largely depends on the meteorological conditions and the quality of input data. A chemical accident happened in a factory in Rouen, France on January 21, 2013. The emitted methyl mercaptan gas caused odor and sickness in densely populated areas, including Paris. The meteorological conditions were rapidly changing in both space and time during the release period, thus the case is particularly challenging for dispersion models and provides a good basis for testing them.

Dispersion of the released methyl mercaptan gas was estimated using the PyTREX trajectory model, developed at the Eötvös Loránd University, and NOAA's HYSPLIT model. The simulation results are in a good agreement with media reports of the polluted areas, and lead to a better understanding of the complex synoptic situation at the time of the accident. Comparison of the results of two models also provided information about the uncertainty of the predictions and pointed out the most important directions for further development of the PyTREX model.

Key-words: atmospheric dispersion, accidental release, HYSPLIT, industrial accident, air pollution, Lagrangian model

1. *Introduction*

In case of an accidental release of toxic material into the atmosphere, dispersion models provide valuable information for risk management and decision support. In most cases, simulation of the dispersion of pollutants released during an accident is a difficult task because of the complex physical processes occurring in the atmosphere, the importance of fast response, and the lack of information about the details of the release. Computer simulations, based on either Eulerian or Lagrangian (trajectory) approaches are now able to provide fast and accurate estimation about the concentration patterns after an accident.

In the past years, PyTREX, a Lagrangian trajectory model has been developed for regional to continental scale simulation of dispersion of passive pollutants. In this work, we present the PyTREX results for the case of the Lubrizol accident in Rouen, compared against HYSPLIT, a state-of-the-art software, to estimate the uncertainty and show the strengths and weaknesses of our model. The Rouen accident happened under complex meteorological conditions where dispersion models are less reliable and depend largely on the accuracy of their host numerical weather prediction model.

This work aims to provide a case study of the Rouen accident, involving its synoptic meteorological conditions and the consequent dispersion patterns. On January 21, 2013, a gas leak caused a significant release of methyl mercaptan from the Lubrizol factory. Although methyl mercaptan had no health risks, its intense odor could cause nausea and headache. As the dispersion plume crossed densely populated areas, many complaints arrived from the public, and numerous media announcements and reports have been published. Despite the fact that methyl mercaptan gas measurements are not available, these media reports provide information about the affected areas and the intensity of the odor in a particular location, thus the dispersion of the plume can be qualitatively verified.

2. *Overview of atmospheric dispersion modeling*

Atmospheric dispersion involves multiscale air pollution problems that are treated using different mathematical approaches and modeling tools. Computer simulations have to take into account the horizontal advection of the released pollutant by the mean wind, the horizontal and vertical mixing caused by turbulent diffusion, chemical reactions, wet and dry deposition, sedimentation, and radioactive decay. The wide range of scales and physical processes led to the development of several atmospheric dispersion models that are specialized to the simulation of certain types of air pollution situations.

Microscale models, often referred to as street canyon simulations use a computational fluid dynamics (CFD) approach to solve the governing equations as well as the dispersion equation on a very fine grid around a complex geometry like a city, a tunnel or an industrial site (*Balczó et al.*, 2011; *Di Sabatino et al.*, 2008). Sophisticated CFD models like Ansys or OpenFOAM are able to take into account microscale phenomena, the effect of buildings, and turbulence generation on the walls (*Cheng* and *Liu*, 2011; *Yamada*, 2004). This approach provides valuable information about urban air quality (*Vardoulakis et al.*, 2003), however, it is not applicable on larger scales due to its large computational cost and the unrepresented physical processes like atmospheric stability and mesoscale wind patterns (*Baklanov*, 2000).

On meso- to macroscale, atmospheric dispersion simulations are based on the output data of numerical weather prediction (NWP) models. Besides the three-dimensional wind field, atmospheric stability characteristics, planetary boundary layer height, and surface parameters are also obtained from NWP results (*Stohl et al.*, 2005). Regional and continental scale dispersion models often use the same grid as the host NWP to solve the transport equation. This Eulerian approach has the advantage that meteorological data is obtained without interpolation, complex chemical reactions can be easily taken into account, and the output concentration and deposition fields are directly computed by the model (*Simpson et al.*, 2012).

Lagrangian simulations avoid the costly partial differential equation solvers and compute tracer trajectories using the NWP-provided wind field. As the calculation of a few trajectories is very fast, Lagrangian models are able to provide immediate information about the dispersion's direction without calculating concentrations. However, with thousands of trajectories, cluster analyses can be carried out to obtain the concentration field. Turbulent mixing is taken into account with a stochastic random walk method (*Stohl et al.*, 2005). Although Lagrangian models require costly interpolation of meteorological data, this approach is particularly suitable for near-source simulations, where numerical diffusion introduces a large error in Eulerian models. This error can be largely reduced by using adaptive gridding that refines the resolution if large gradients are present (*Lagzi et al.*, 2009). Coupled modeling systems have also been introduced that use a near-source Lagrangian treatment within a large-scale Eulerian model (*Brandt et al.*, 1996).

Lagrangian approach is used in state-of-the-art atmospheric dispersion software like the NAME, HYSPLIT, and FLEXPART models (*Draxler* and *Hess*, 1998; *Stohl et al.*, 2005). Besides their worldwide application for environmental studies and risk management, these models provided valuable and accurate information during recent air pollution episodes like the Fukushima accident in 2011 or the eruption of Eyjafjallajökull volcano in 2010 (*Dacre et al.*, 2011; *Long et al.*, 2012; *Srinivas et al.*, 2012; *Stohl et al.*, 2011).

The simulation of long-term average air pollution patterns caused by continuous release is a challenge for most atmospheric models. EMEP's Eulerian model provides continental scale forecasts and archive data for most air pollutants' concentration with a special attention on acidic compounds (*Simpson* *et al.*, 2012). The online coupled dispersion and mesoscale weather prediction model WRF-Chem is a powerful tool for atmospheric dispersion modeling: its Eulerian approach allows the simulation of complex chemical reaction systems, meanwhile, the integrity with an NWP model makes it easy to run detailed simulations in any meteorological situations (*Huh et al.*, 2012).

On regional scale, plume models like AERMOD or ADMS are often used to calculate long-term average concentrations caused by a continuous pollutant source (*Holmes* and *Morawska,* 2006; *Silverman et al.*, 2007). Plume models assume straight downwind dispersion from the source point and a concentration field with Gaussian distribution in crosswind and vertical direction (*Cimorelli et al.*, 2005). Although these models are not reliable in complex weather situations and terrain, their fast runtime makes them optimal for long-term statistical air quality investigations for both normal (*Righi et al.*, 2009) and accidental (*Leelőssy et al.*, 2011) continuous releases.

In Hungary, an integrated atmospheric dispersion modeling system (AERMOD) and a trajectory and particle dispersion model (FLEXTRA-FLEXPART) are used by the Hungarian Meteorological Service for environmental monitoring and risk management (*Kocsis et al.*, 2009; *Steib* and *Labancz*, 2005). The CHIMERE model was also adapted at the Hungarian Meteorological Service for operative mesoscale air quality forecast in Budapest (*Baranka* and *Labancz*, 2009). At the Paks Nuclear Power Plant, the RODOS decision support system provides a Lagrangian trajectory model for regional to continental scale simulations. The SINAC program system was developed to follow the consequences of radioactive releases of a hypothetical nuclear accident (*Földi et al.*, 2010). A multiscale Lagrangian and Eulerian dispersion model, TREX has also been developed at the Eötvös Loránd University for the area within 30–500 km from the power plant (*Mészáros et al.*, 2010). For larger scales, the extended PyTREX trajectory model has been developed. Local scale CFD simulations are carried out at Budapest Technical University and Eötvös Loránd University using Fluent, Miskam, and OpenFOAM models (*Balczó et al.*, 2011; *Goricsán et al.*, 2004).

3. Model description

3.1. The HYSPLIT model

In the present work, we used HYSPLIT and PyTREX models to simulate the consequences of the industrial accident in Rouen. HYSPLIT is a widely used Lagrangian dispersion model developed by the National Oceanic and Atmospheric Administration Air Resources Laboratory (NOAA ARL). Its worldwide applications cover various forward and backward simulations from meso- to continental scale (*Challa et al.*, 2008; *Koracin et al.*, 2011; *Long et al.*, 2012; *McGowan* and *Clark*, 2008; *Shan et al.*, 2009). HYSPLIT calculates single trajectories based on meteorological fields provided by the Global Data Assimilation System (GDAS) database. Particle motion in each timestep is defined as a sum of an advective and a turbulent component (*Draxler* and *Hess*, 1998). The advective motion is obtained directly from the wind field, however, vertical turbulent wind fluctuations are computed using Hanna's parameterization based on stability characteristics defined by the Monin–Obukhov length (*Draxler* and *Hess*, 1998; *Moreira et al.*, 2011). While large scale turbulence is estimated with a random walk method, small scale turbulent diffusion is calculated with a puff approach: each particle has a horizontal extent with a Gaussian concentration distribution, which broadens according to the local turbulence intensity. Concentration field is given as the superposition of concentration fields of all particles.

3.2. The PyTREX model

PyTREX is a continental scale trajectory model developed at the Eötvös Loránd University. It computes single particle trajectories based on meteorological data provided by short-range forecasts of the Global Forecast System (GFS). GFS is initialized in every 6 hours and provides output fields for every 3 hours, thus the first and second timestep of each model run was used to create a continuous 3-hourly forecast database for archive situations. Forecast outputs were preferred against analyses in order to gain advantage of GFS parameterizations that provide derived quantities such as turbulent surface fluxes or precipitation patterns. GFS grid has 0.5-degree spatial resolution from which data is obtained for any point with linear interpolation in both space and time. For compatibility with the GFS outputs, PyTREX uses spherical coordinate system in horizontal and pressure system in vertical direction. Meteorological and user-defined input data of PyTREX are presented in *Table 1*.

Table 1. Input data requirements of the PyTREX trajectory model

Release data and simulation setup	**Meteorological data (GFS)**
Release location(s)	Geopotential on main pressure levels
Release height(s)	Wind components on main pressure and near-surface levels
Release time(s) and length(s)	Temperature on main pressure and near-surface levels
Simulation duration	Surface pressure, temperature
Total released mass from each location	Surface height above ground level
Number of trajectories from each location	Planetary boundary layer height
Minimum computational timestep	Surface momentum and heat flux
Halftime of radioactive decay	Mixing ratio on main pressure and near-surface levels

PyTREX trajectories are calculated using a linear scheme from the superposition of advective and turbulent motions:

$$\frac{d\underline{r}}{dt} = \underline{v} + \underline{v}_t, \tag{1}$$

where $\underline{v}$ is the vectorial sum of the horizontal wind and the vertical motion, $\underline{v}_t$ is the vector of turbulent fluctuations, and $\underline{r}$ is the position of the particle. While $\underline{v}$ is directly obtained from GFS outputs, $\underline{v}_t$ is calculated using the Langevin equation (*Stohl et al.*, 2005):

$$dv_{t,i} = -v_{t,i}\frac{dt}{T_{Li}} + \sigma_i\sqrt{\frac{2dt}{T_{Li}}}\zeta(0{,}1), \tag{2}$$

where $v_{t,i}$ is the ith component of the turbulent velocity vector, T_{Li} is the Lagrangian timescale representative for the ith direction, σ_i is the turbulent fluctuation of the ith component of the wind vector, and $\zeta(0{,}1)$ is a random number from a standard normal distribution, generated with the Mersenne Twister algorithm of Python's *random* module.

The TLi Lagrangian timescales and σ_i turbulent wind fluctuations are estimated using the Monin–Obukhov theory, thus we need to compute the atmospheric stability parameter z/L (*Draxler* and *Hess*, 1998):

$$\frac{z}{L} = \frac{z_1 \cdot k \cdot g \cdot T^*}{T_1 \cdot u^{*2}}, \tag{3}$$

where z is the height above ground, L is the Monin–Obukhov length, k is the von-Kármán constant, and g is the gravitational acceleration. Besides constants and surface parameters, PyTREX uses the temperature data T_1 of z_1 height, the first level above ground in the meteorological dataset (80 m for GFS data).

Friction temperature T^* and friction velocity u^* are calculated from surface heat and momentum fluxes:

$$u^* = \left(\frac{\sqrt{\overline{\rho u'w'}^2 + \overline{\rho v'w'}^2}}{\rho}\right)^{0{,}5}, \tag{4}$$

$$T^* = -\frac{H}{\rho_f c_p u^*}, \tag{5}$$

where $\overline{\rho u' w'}$ and $\overline{\rho v' w'}$ are surface momentum fluxes and H is the surface heat flux. Both momentum and heat flux data is directly obtained from GFS outputs. The air density ρ and air density on surface ρ_f are calculated from the temperature field using dry air assumption. Accordingly, c_p is the specific heat of dry air.

Based on the stability characteristics presented in Eqs. (3–5) and the planetary boundary layer height provided by GFS, the velocity fluctuations and Lagrangian timescales are obtained through Taylor's parametrization, which was set up in a way presented by *Moreira et al.* (2011). The computational timestep dt is defined as the tenth of the minimum of Lagrangian timescales (*Stohl et al.*, 2005). However, in order to reduce the computational cost for near-surface trajectories, a minimum timestep can be defined that also gives a lower boundary for Lagrangian timescales.

Besides drawing single trajectories, PyTREX calculates concentration field on a three-dimensional rectangular grid based on the density of trajectories crossing the specified grid cell during a certain time period.

4. Synoptic situation during the Rouen incident

On January 21, 2013, a chemical accident happened in a factory of the Lubrizol company located in Rouen, northwestern France. The firm announced that a significant amount of non-toxic methyl mercaptan gas had been released from approximately 07 UTC (http://www.paris-normandie.fr/article/actualites/en-direct-fuite-de-mercaptan-chez-lubrizol). Although no health risk was identified, an unpleasant smell spread across northwestern France after the accident, reaching Paris at the following night. Media announcements reported serious complaints of odor from several districts of the capital. Odor caused by methyl mercaptan gas was also reported from Normandy and Southeastern England (*Fig. 1*) (http://www.bbc.co.uk/news/world-europe-21147361).

Looking at the map of northwestern France (*Fig. 1*), it might be confusing that odor was reported within 24 hours from largely different directions from Rouen, including Paris, which is located to the southeast from the location of the accident, and also from England, to the northwest of the factory. Furthermore, despite that the accident happened only 120 km away from the capital, it took more than 12 hours for the plume to reach Paris. These unusual dispersion patterns were caused by a complex synoptic situation involving a significant shift in the wind direction within a short time period.

On January 20, 2013, two dominant processes were detectable that would determine the spreading of the emitted material. The first synoptic object was a mature trough above the Mediterranean – North African region, with a corresponding low pressure system above the western basin of the Mediterranean Sea (*Fig. 2* (a)-(d)). This low pressure system was severed off into a bi-central system by the inertia of the cold air arriving at the rear of the trough, along the western coastlines of France (*Fig. 2* (a)). The primary low remained above the Mediterranean, and was being advected eastward with the rest of the trough, while the secondary low (object A), gaining enhanced circulation by baroclinity was advected towards Northern France.

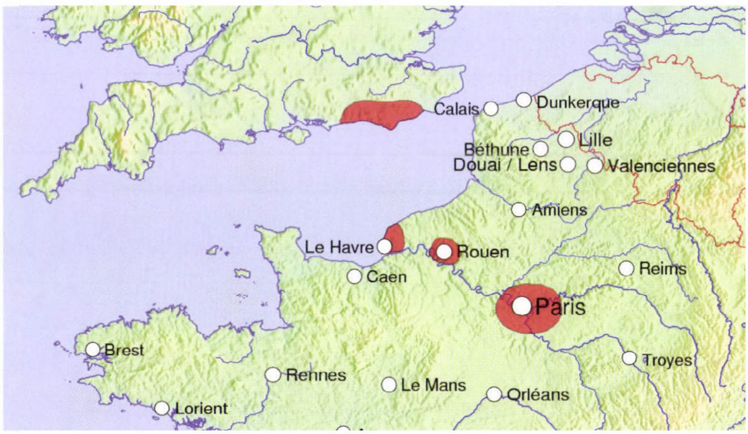

Fig. 1. The most affected areas based on media coverage after the Lubrizol chemical accident in Rouen, January 21-22, 2013.

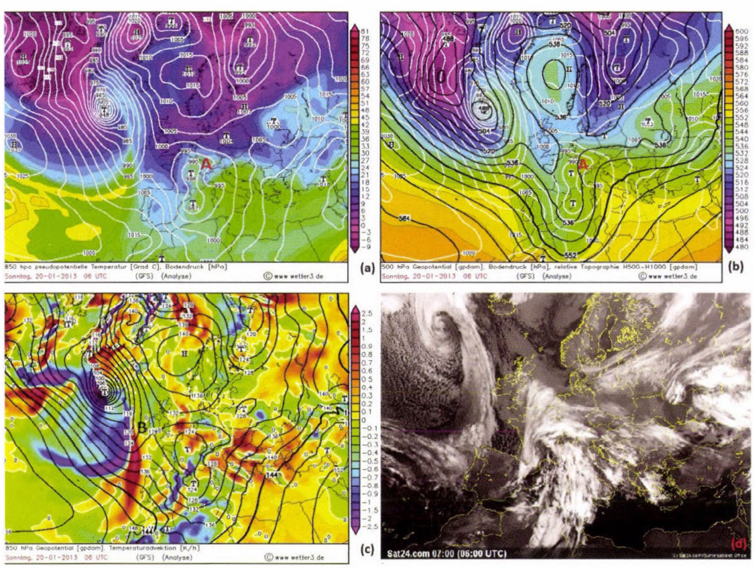

Fig. 2. GFS output (a)-(c) and infrared satellite image (d) at 06 UTC, January 20, 2013. (a) Equivalent potential temperature and MSLP (EPT850) (b) 500 hPa height (gpdam), MSLP and 500/1000 ReTop, (c) Height (gpdam) and TA at 850 hPa. Courtesy of wetter3.de and sat24.com, respectively.

The second main synoptic process was a rapidly deepening trough above the Atlantic, characterized by strong winds and cold advection on lower levels (*Fig. 2* (c)). The leading edge of this trough reached the Rouen region with a cutoff low on the ground level (object B) (*Fig. 3*). Between 18 UTC, January 20, and 12 UTC, January 21, the two low pressure systems started merging in a circular motion (Fig. 3) with the first system (object A) following the streamlines of the second low (object B). At 06 UTC, January 21, the two main lows could be located at Bretagne and Southern England creating the rotating flow that would spread the emitted material southeast and northwest of the facility at the lower levels of the troposphere (*Fig. 4*, *Fig. 5*).

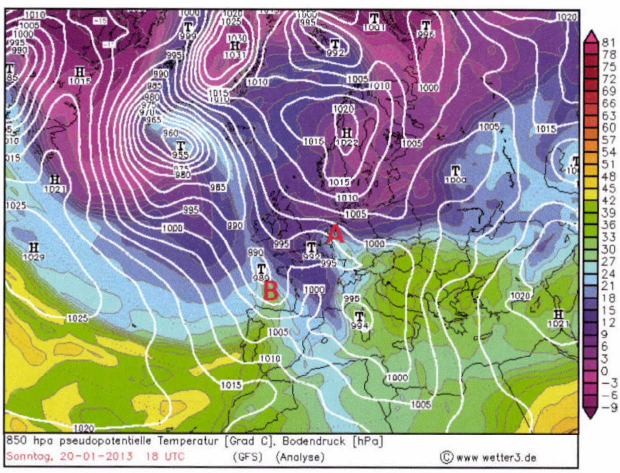

Fig. 3. GFS output on 18 UTC, January 20, 2013, EPT 850. The two stream defining lows begin to merge above the Channel. Courtesy of wetter3.de.

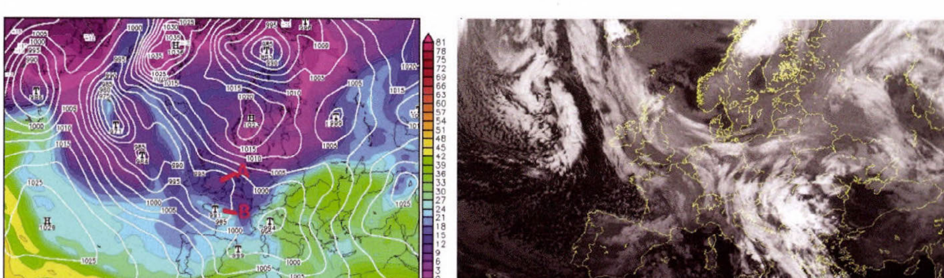

Fig. 4. GFS output (a) EPT850 and infrared satellite image (b) at 06 UTC, January 21, 2013 depicting the synoptic setup shortly before the accident. The two merging lows are clearly visible on (a), above Bretagne and Southern England. On (b), only the rotating field of the southern system is visible. Courtesy of wetter3.de and sat24.com, respectively.

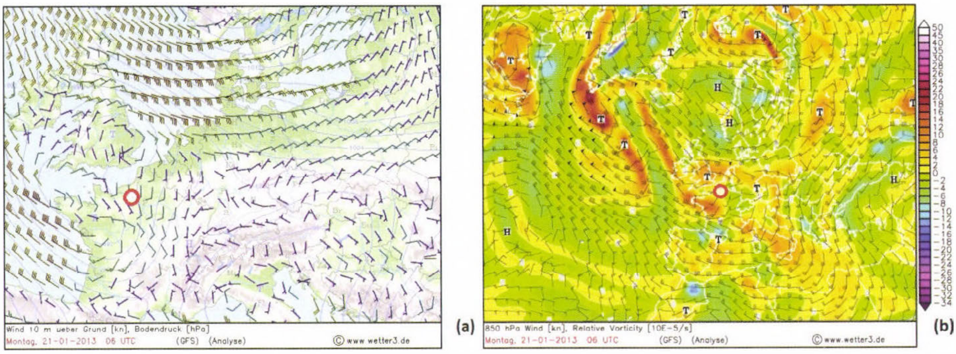

Fig. 5. GFS output at 06 UTC, January 21, 2013. Wind at 10 m (a), wind and vorticity at 850 hPa (b), depicting the bi-central rotating flow at the marked location of the accident. Courtesy of wetter3.de.

Synop reports also show a gradual shifting of the mean wind from northwesterly (18 UTC, January 21) to southeasterly direction indicating the presence of the rotating flow on the ground level. The temperature field did not significantly change due to the overcast nocturnal sky.

5. Dispersion model results

Two trajectory models, HYSPLIT and PyTREX were used to simulate the dispersion of the plume released from the Lubrizol factory during the incident. Besides understanding the pollution patterns reported in the media, our investigation aimed to compare the model results in this complex synoptic situation in order to estimate the uncertainty of trajectories and the concentration field.

The same release data was used for both model runs. Assuming a 24-hour long continuous release from 50 m height, 20 400 trajectories were calculated with evenly distributed starting time during the release period. The number of trajectories was given by default in HYSPLIT, and the same value was used in PyTREX for comparable results. As the exact quantity of the released material was not known, unity total released mass was assumed for the simulation. No wet and dry deposition was taken into account, which is a good assumption for mercaptans. In PyTREX, output concentration map was produced with a 0.25 degrees horizontal and 100 m vertical resolution. Both model calculated one-hour average concentrations for each location.

HYSPLIT results clearly show the wind shift during the release period: in the first 7 hours of the accident, the plume is advected by weak southern wind over the La Manche channel (*Fig. 6*). Between the 7th and 15th hour of the incident, the wind became stronger and changed to northwesterly direction, which forced the plume back to Northwestern France, reaching again the source region and also Paris. The weak dispersion towards England during the first hours explains the delay between the accident and the pollution reports in Paris, as well as the fairly high intensity of the odor that reached the capital. After the 15th hour of the accident, the wind turned to southeasterly again, and the plume spread towards Southern England, reaching the country approximately 24 hours after the beginning of the release.

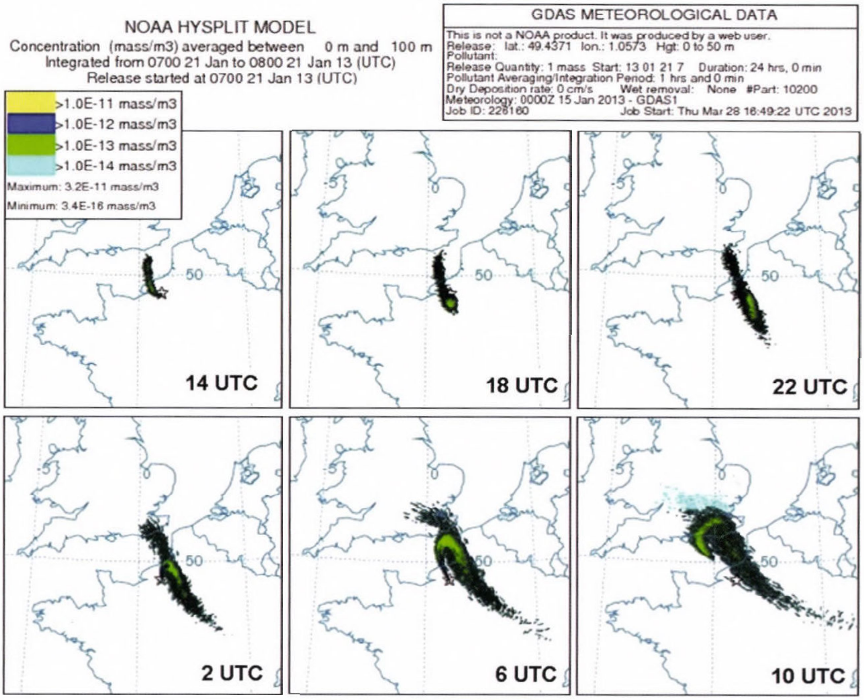

Fig. 6. HYSPLIT surface concentration field between 14 UTC, January 21 and 10 UTC, January 22, 2013. A 24 hours long continuous release was started at 07 UTC, January21. 360° change of wind direction is observable that allowed the plume to reach Central France.

The PyTREX results also well demonstrate the rapid wind shift (*Fig. 7*). The affected areas by the plume are in good qualitative agreement with HYSPLIT's results despite the different meteorological data and physical parameterizations of the models. We note that 27 hours after the beginning of the accident, both models expected that the plume would reach London. In fact, there are a few reports about odor complaints in London, thus the diluted pollutant could reach the city in a fairly high concentration (http://www.dailymail.co.uk/news/article-2266383/Smelly-gas-cloud-factory-Rouen-travels-Channel-France-Kent.html).

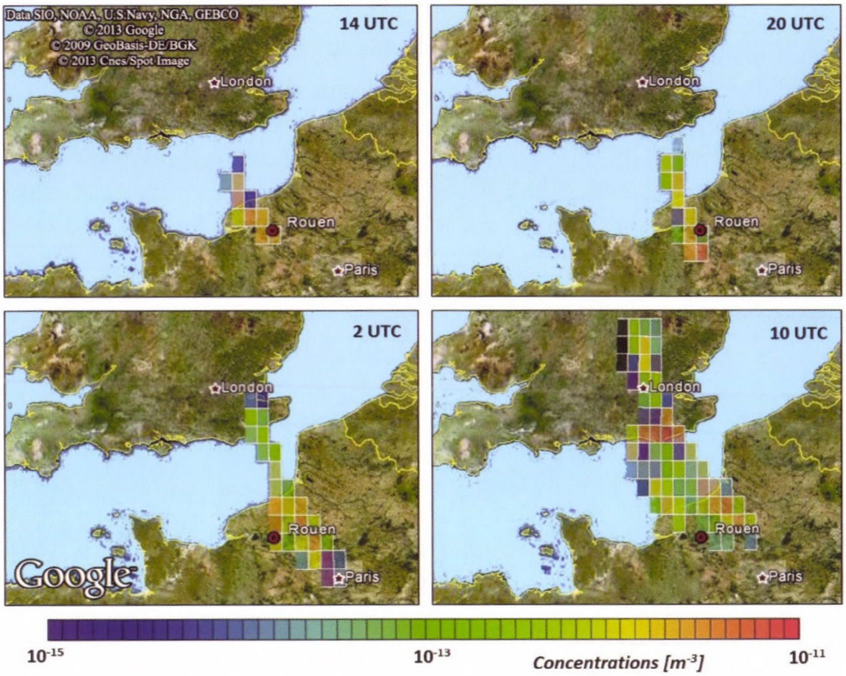

Fig. 7. PyTREX surface concentration field between 14 UTC, January 21 and 10 UTC, January 22, 2013. A 24-hour long continuous release was started at 7 UTC, January 21. Results show a good agreement with HYSPLIT's output.

In *Fig. 8*, three trajectories are presented, started in the 1st, 6th, and 16th hours of the accident. It can be seen that the pollutants spread towards Paris only within a few-hour long time period, before and after which the wind forced the plume to northern, northwestern direction.

Fig. 8. PyTREX trajectories started from Rouen at 07 (red), 13 (yellow), and 22:30 (green) UTC, January 21, 2013. Meteorological conditions allowed the plume to spread towards Paris only within a few-hour long time period.

In order to compare the concentration estimates provided by the two models, the maximum one-hour average concentration was obtained for six locations (*Table 2*). It can be seen that the values are largely different, but remain within the same magnitude for most of the locations, however, close to the source, one magnitude difference is present.

Table 2. Maximum concentration in selected locations based on two models' simulations

Location	Coordinates		Max. concentration [$10^{-13}/m^3$]	
	Latitude [°]	**Longitude [°]**	**HYSPLIT**	**PyTREX**
Rouen	49.375	1.125	149.50	34.30
Gaillon	49.125	1.375	3.31	24.70
Dieppe	49.875	1.125	8.02	8.88
Paris	48.875	2.375	1.50	6.76
London	51.375	–0.125	1.39	2.93
Bristol	51.376	–2.625	0.82	1.39

It can be concluded that the models are in a good agreement in determining the direction of the dispersion and the affected areas by the plume. The high uncertainty in concentration values might occur from the largely different turbulence treatment of the models: while HYSPLIT uses a mixture of random walk and Gaussian turbulence models, PyTREX performs a 3D random walk turbulence simulation. Based on this knowledge, PyTREX probably underestimates the near-source concentration, because it averages the density of trajectories for a 0.25×0.25 degree cell. Although no measurements are available for methyl mercaptan gas, public complaints of odor can be used to verify the models (http://www.lemonde.fr/planete/article/2013/01/22/fuite-de-gaz-a-lubrizol-mobilisation-maximale-mais-prevention-floue_1820793_3244.html). While Paris was largely affected by the plume, only a few complaints are known from London. HYSPLIT expected a similar concentration value in both cities, which is unlikely.

The uncertainty of the results might also be caused by different meteorological data: while HYSPLIT uses analyses fields, PyTREX is based on short-range forecast files with derived surface parameters.

6. Conclusion

The chemical accident in Rouen on January 21–22, 2013 happened in a complex synoptic situation with rapidly changing wind direction. Two trajectory models were used for the simulation of the dispersion in order to understand the effect of an interplay of complex meteorological conditions, as well as to compare the model results. The results of PyTREX, a three-dimensional trajectory model developed at the Eötvös Loránd University were compared against the output of HYSPLIT, a widely used atmospheric dispersion model developed by NOAA.

The pollution affected areas in largely different directions because of the rapidly changing wind governed by a multi-centered low pressure system located above Northern France and Southern England. During the release period, a 360° turn of the wind direction was observable, as the dominant southerly wind turned into northwestern direction for a few hours, which allowed the plume to return above Northwestern France and reach Paris. Later, as the wind turned back to southerly direction, the plume crossed the Channel and affected Southern England and London.

Despite the complex synoptic situation, the different meteorological input data, and the fast changing conditions, HYSPLIT and PyTREX results were in a good agreement regarding the dispersion and the polluted areas. Concentration values in selected locations showed large differences, but remained within the same order of magnitude in most cases. PyTREX largely underestimated the near-source concentrations, while HYSPLIT provided unlikely similar results for Paris and London. Uncertainty between models is probably caused by their different turbulence treatment, which requires more sophisticated investigation and verification against measurement data.

The case study of the Rouen incident showed that PyTREX provides reliable results of dispersion patterns even in a complex synoptic situation, however, concentration values have one order of magnitude of uncertainty between the two tested software. Parallel usage of the two models, as well as adjusting parameterizations based on measurement data can largely improve atmospheric dispersion simulations to provide valuable information for risk management in a case like the Lubrizol incident in Rouen.

Acknowledgements–Authors acknowledge the financial support of the Hungarian Research Found (OTKA K81933, K81975, K104666, K109109, and K109361), the *Zoltán Magyary* Postdoctoral Fellowship, the European Union, and the European Social Fund (TÁMOP 4.2.4.A-1).

References

Baklanov, A., 2000: Application of CFD Methods for Modelling in Air Pollution Problems: Possibilities and Gaps. *Environ. Monit. Assess. 65*, 181–189.

Balczó, M., Balogh, M., Goricsán, I., Nagel, T., Suda, J.M., and *Lajos, T.*, 2011: Air quality around motorway tunnels in complex terrain: computational fluid dynamics modeling and comparison to wind tunnel data. *Időjárás 115*, 179–204.

Baranka, G. and *Labancz, K.*, 2009: Urban air quality forecast for the city of Budapest, Hungary. *EMS Annual Meeting Abstracts 6*, EMS2009-403.

Brandt, J., Mikkelsen, T., Thykier-Nielsen, S., and *Zlatev, Z.*, 1996: Using a combination of two models in tracer simulations. *Math. Comput. Model. 23*, 99–115.

Challa, V.S., Indrcanti, J., Baham, J.M., Patrick, C., Rabarison, M.K., Young, J.H., Hughes, R., Swanier, S.J., Hardy, M.G., and *Yerramilli, A.*, 2008: Sensitivity of atmospheric dispersion simulations by HYSPLIT to the meteorological predictions from a meso-scale model. *Environ. Fluid Mech. 8,* 367–387.

Cheng, W.C. and *Liu, C-H.*, 2011: Large-Eddy Simulation of Flow and Pollutant Transports in and Above Two-Dimensional Idealized Street Canyons. *Bound.-Lay. Meteorol. 139*, 411–437.

Cimorelli, A.J., Perry, S.G., Venkatram, A., Weil, J.C., Paine, R.J., Wilson, R.B., Lee, R.F., Peters, W.D,. and *Brode, R.W.*, 2005: AERMOD: A dispersion model for industrial source applications. Part I: General model formulation and boundary layer characterization. *J. Appl. Meteorol. 44,* 682–693.

Dacre, H.F., Grant, A.L.M., Hogan, R.J., Belcher, S.E., Thomson, D.J., Devenish, B.J., Marenco, F., Hort, M.C., Haywood, J.M., Ansmann, A., Mattis, I., and *Clarisse, L.*, 2011: Evaluating the structure and magnitude of the ash plume during the initial phase of the 2010 Eyjafjallajökull eruption using lidar observations and NAME simulations. *J. Geophys. Res. 116,* D00U03.

Di Sabatino, S., Buccolieri, R., Pulvirenti, B., and *Britter, R.E.*, 2008: Flow and Pollutant Dispersion in Street Canyons using FLUENT and ADMS-Urban. *Environ. Model. Assess. 13*, 369–381.

Draxler, R.R. and *Hess, G.D.*, 1998: An Overview of HYSPLIT_4 Modelling System for Trajectories, Dispersion and Deposition. *Australian Meteorol. Mag. 47,* 295–308.

Földi, A., Mészáros, M., Sági, L., Deme, S., Dombovári, P., Szántó, A., Tóth, K., and *Petőfi-Tóth, K.*, 2010: Légköri terjedésszámító szoftverek összehasonlítása. *Sugárvédelem 3(1),* 33–41. (In Hungarian)

Goricsán, I., Balczó, M., Régert, T., and *Suda, J.M.*, 2004: Comparison of Wind Tunnel Measurement and Numerical Simulation of Dispersion of Pollutants in Urban Environment. In Impact of Wind and Storm on City Life and Built Environment. *COST C14 International Conference on Urban Wind Engineering and Buildings Aerodynamics,* D.6.1-D.6.10.

Holmes, N.S. and *Morawska, L.*, 2006: A review of dispersion modelling and its application to the dispersion of particles: An overview of different dispersion models available. *Atmos. Environ. 40,* 5902–5928.

Huh, C-A., Hsu, S-C., and *Lin, C-Y.*, 2012: Fukushima-derived fission nuclides monitored around Taiwan: Free tropospheric versus boundary layer transport. *Earth Planet. Sci. Lett. 319–320,* 9–14.

Kocsis, Zs., Ferenczi, Z., Havasi, Á., and *Faragó, I.*, 2009: Operator splitting in the Lagrangian air pollution transport model FLEXPART. *Időjárás 113,* 189–202.

Koracin, D., Vellore, R., Lowenthal, D.H., Watson, J.G., Koracin, J., McCord, T., DuBois, D.W., Chen, L-W.A., Kumar, N., Knipping, E.M., Wheeler, N.J.M., Craig, K., and *Reid, S.*, 2011: Regional Source Identification Using Lagrangian Stochastic Particle Dispersion and HYSPLIT Backward-Trajectory Models. *J. Air Waste Manage. Assoc. 61*, 660–672.

Lagzi, I., Tomlin, S.A., Turányi, T., and *Haszpra, L.*, 2009: Modelling photochemical air pollutant formation in Hungary using an adaptive grid technique. *Int. J. Environ. Poll. 36*, 44–58.

Leelőssy, Á., Mészáros, R., and *Lagzi, I.*, 2011: Short and long term dispersion patterns of radionuclides in the atmosphere around the Fukushima Nuclear Power Plant. *J. Environ. Radioactiv. 102,* 1117–1121.

Long, N.Q., Truong, Y., Hien, P.D., Binh, N.T., Sieu, L.N., Giap, T.V., and *Phan, N.T.*, 2012: Atmospheric radionuclides from the Fukushima Dai-ichi nuclear reactor accident observed in Vietnam. *J. Environ. Radioactiv. 111*, 53–58.

McGowan, H. and *Clark, A.*, 2008: Identification of dust transport pathways from Lake Eyre, Australia using HYSPLIT. *Atmos. Environ. 42,* 6915–6925.

Mészáros, R., Vincze, Cs., and *Lagzi, I.*, 2010: Simulation of accidental release using a coupled transport (TREX) and numerical weather prediction (ALADIN) model. *Időjárás, 114*, 101–120.

Moreira, V.S., Degrazia, G.A., Roberti, D.R., Timm, A.U., and *Carvalho, J.C.*, 2011: Employing a Lagrangian stochastic dispersion model and classical diffusion experiments to evaluate two turbulence parametrization schemes. *Atmos. Poll. Res. 2,* 384–393.

Righi, S., Lucialli, P., and *Pollini, E.*, 2009: Statistical and diagnostic evaluation of the ADMS-Urban model compared with an urban air quality monitoring network. *Atmos. Environ. 43*, 3850–3857.

Shan, W., Yin, Y., Lu, H., and *Liang, S.*, 2009: A meteorological analysis of ozone episodes using HYSPLIT model and surface data. *Atmos. Res. 93,* 767–776.

Silverman, K.C., Tell, J.G., Sargent, E.V., and *Qiu, Z.*, 2007: Comparison of the Industrial Source Complex and AERMOD Dispersion Models: Case Study for Human Health Risk Assessment. *J. Air Waste Manag. Assoc. 57,* 1439–1446.

Simpson, D., Benedictow, A., Berge, H., Bergström, R., Emberson, L.D., Fagerli, H., Hayman, G.D., Gauss,M., Jonson, J.E., Jenkin, M.E., Nyíri, A., Richter, C., Semeena, V.S., Tsyro, S., Tuovinen, J.-P., Valdebenito, Á., and *Wind, P.*, 2012: The EMEP MSC-W chemical transport model – Part 1: Model description. *Atmos. Chem. Phys. Discuss. 12,* 3781–3874.

Srinivas, C.V., Venkatesan, R., Baskaran, R., Rajagopal, V., and *Venkatraman, B.*, 2012: Regional scale atmospheric dispersion simulation of accidental releases of radionuclides from Fukushima Dai-ichi reactor. *Atmos. Environ. 61,* 66–84.

Steib, R. and *Labancz, K.*, 2005: Regulatory modeling in Hungary – the AERMOD model. PART I. Description and application. *Időjárás 109,* 157–172.

Stohl, A., Forster, C., Frank, A., Seibert, P., and *Wotawa, G.*, 2005: Technical note: The Lagrangian particle dispersion model FLEXPART version 6.2. *Atmos. Chem. Phys. 5,* 4739–4799.

Stohl, A., Seibert, P., Wotawa, G., Arnold, D., Burkhart, J.F., Eckhardt, S., Tapia, C., Vargas, A., and *Yasunari, T.J.*, 2011: Xenon-133 and caesium-137 releases into the atmosphere from the Fukushima Dai-ichi nuclear power plant: determination of source term, atmospheric dispersion, and deposition. *Atmos. Chemis. Phys. 11,* 28319–28394.

Yamada, T., 2004: Merging CFD and atmospheric modeling capabilities to simulate airflows and dispersion in urban areas. *Comput. Fluid Dynam. J. 13(2), 47,* 329–341.

Vardoulakis, S., Fisher, B.E.A., Pericleous, K., and *Gonzalez-Flesca, N.*, 2003: Modelling air quality in street canyons: a review. *Atmos. Environ. 37,* 155–182.

IDŐJÁRÁS

VOLUME 117 * 2013

BUDAPEST, HUNGARY

AUTHOR INDEX

Aguilar, E. (Tarragona, Spain) 47
Auer, I. (Wien, Austria) 47
Betz, H.D. (Garching,Germany) 295
Bihari, Z. (Budapest, Hungary) 143
Blanka, V. (Szeged, Hungary) 219
Bobvos, J. (Budapest, Hungary) 175
Böhm, R. (Wien, Austria) 47
Caramelo, L. (Vila Real, Portugal) 69
Diebel, S. (Munich, Germany) 295
Dimitrova, T. (Sofia, Bulgaria) 295
Domonkos, P. (Tortosa, Spain) 47, 91
Dubuisson, B. (Toulouse, France) 47
Faragó, I. (Budapest, Hungary) 201
Farda, A. (Brno, Czech Republic) 123
Ferenczi, Z. (Budapest, Hungary) 359
Freitas, L. (Vila Real, Portugal) 69
Führer, E. (Sopron, Hungary) 159
Geresdi, I. (Pécs, Hungary) 377
Guijarro, J.A. (Palma di Mallorca, Spain) 35, 47
Horváth, L. (Budapest, Hungary) 159
Izsák, F. (Budapest, Hungary) 201
Jagodics, A. (Budapest, Hungary) 159
Juhász, I. (Budapest, Hungary) 159
Klancar, M. (Ljubljana, Slovenia) 47
Kohlmann, M. (Budapest, Hungary) 4.4
Kristóf, G. (Budapest, Hungary) 239
Krisztalovics, K. (Budapest, Hungary) 175
Lábó, E. (Budapest, Hungary) 377
Lagzi, I. (Budapest, Hungary) 4.4
Lakatos, M. (Budapest, Hungary) 143
Lebarbier, E. (Paris, France) 47
Leelőssy, Á. (Budapest, Hungary) 4.4
Ludányi, E.L. (Budapest, Hungary) 4.4
Lindau, R. (Bonn, Germany) 1
Marosi, Gy. (Sopron, Hungary) 159
Matyasovszky, I. (Budapest, Hungary) 187
Mendes, M. (Lisboa, Portugal) 69
Mestre, O. (Toulouse, France) 47
Mészáros, R. (Budapest, Hungary) 4.4
Meyer, B. (Leipzig, Germany) 219
Mezősi, G. (Szeged, Hungary) 219
Mihailovic, D.T. (Novi Sad, Serbia) 277
Mitzeva, R. (Sofia, Bulgaria) 295
Nunes, L.F. (Lisboa, Portugal) 69
Páldy, A. (Budapest, Hungary) 175
Pereira, M.G. (Lisboa, Portugal) 69
Picard, F. (Villeurbanne, France) 47
Podrascanin, Z. (Novi Sad, Serbia) 277
Rácz, N. (Budapest, Hungary) 239
Robin, S. (Paris, France) 47
Štěpánek, P. (Brno, Czech Republic) 47, 123
Szabó, T. (Basque Country, Spain) 201
Szalai, S. (Gödöllő, Hungary) 143
Szász, G. (Debrecen, Hungary) 315
Szentimrey, T. (Budapest, Hungary) 113, 143
Trájer, A. (Budapest, Hungary) 175
Tóth, Z. (Budapest, Hungary) 4.3
Venema, V. (Bonn, Germany) 1
Vertachnik, G. (Ljubljana, Slovenia) 47
Weidinger, T. (Budapest, Hungary) 239
Zahradníček, P. (Brno, Czech Republic) 123
Zhelev, H. (Sofia, Bulgaria) 295

TABLE OF CONTENTS
I. Papers

Blanka, V., Mezősi, G., and *Meyer, B.*: Projected changes in the drought hazard in Hungary due to climate change 219

Dimitrova, T., Mitzeva, R., Betz, H.D., Zhelev, H., and *Diebel, S.*: Lightning behavior during the lifetime of severe hail-producing thunderstorms 295

Domonkos, P.: Measuring performances of homogenization methods 91

Faragó, I., Izsák, F., and *Szabó, T.*: An IMEX scheme combined with Richardson extrapolation methods for some reaction-diffusion equations 201

Ferenczi, Z.: Predictability analysis of the $PM_{2.5}$ and PM_{10} concentration in Budapest 359

Freitas, L., Pereira, M.G., Caramelo, L., Mendes, M., and Nunes, L.F.: Homogeneity of monthly air temperature in Portugal with HOMER and MASH 69

Führer, E., Jagodics, A., Juhász, I., Marosi, Gy., and *Horváth, L.*: Ecological and economical impacts of climate change on Hungarian forestry practice 159

Guijarro, J. A.: Climatological series shift test comparison on running windows 35

Lábó, E. and *Geresdi, I.*: Application of a Detailed Bin Scheme in Longwave Radiation Transfer Modeling 377

*Lakatos, M., Szentimrey, T., Bihari, Z.,*and *Szalai, S.*: Creation of a homogenized climate database for the Carpathian region by applying the MASH procedure and the preliminary analysis of the data 143

Leelőssy, Á., Ludányi, E.L., Kohlmann, M., Lagzi, I., and *Mészáros, R.,*: Comparison of two Lagrangian dispersion models: a case study for the chemical accident in Rouen, 21–22 January 2013 .... 4.4

Lindau, R. and *Venema, V.*: On the multiple breakpoint problem and the number of significant breaks in homogenization of climate records 1

Matyasovszky, I.: Estimating red noise spectra of climatological time series 187

Mestre, O., Domonkos, P., Picard, F., Auer, I., Robin, S., Lebarbier, E., Böhm, R., Aguilar, E., Guijarro, J., Vertachnik, G., Klancar, M., Dubuisson, B., and *Štěpánek, P.*: HOMER: a homogenization software – methods and applications 47

Podrascanin, Z. and *Mihailovic, D.T.*: Performance of the Asymmetric Convective Model Version 2, in the Unified EMEP Model 277

Rácz, N., Kristóf, G., and *Weidinger, T.*: Evaluation and validation of a CFD solver adapted to atmospheric flows: Simulation of topography-induced waves 239

Štěpánek, P., Zahradníček, P., and *Farda, A.*: Experiences with data quality control and homogenization of daily records of various meteorological elements in the Czech Republic in the period 1961–2010 123

Szász, G.: Agrometeorological research and its results in Hungary (1870–2010) 315

Szentimrey, T.: Theoretical questions of daily data homogenization 113

Trájer, A., Bobvos, J., Krisztalovics, K., and *Páldy, A.*: Regional differences between ambient temperature and incidence of Lyme disease in Hungary 175

Tóth, Z.: High resolution solar spectrophotometry and narrow spectral range solar radiation measurements at the Hungarian Meteorological Service .. 4.3

SUBJECT INDEX

A

accidental release 435
agriculture, history 315
agroclimatology 315
agrometeorology 315
air quality
- forecast 359

- of Budapest 359
- of Hungary 359
- monitoring 359
air pollution modeling 359, 435
ALADIN regional climate model 219
atmospheric dispersion 359, 435
Austria 47
autoregressive model 187

B

bin scheme 377
break point detection 1
Bulgaria 295
bulk scheme 377

C

calibration 403
Carpathian Region Project 143
climate
- Carpathian Region Project 143
- change 159, 175, 219
- extremes 113
- indices 143
- regional change 219
- series 1, 35, 47, 69, 91, 113, 123, 143, 159, 187
- stations 1
- variations 35
climatological
- regional differences 175
- series inhomogeneity 1, 35, 47, 69, 91, 113, 123, 143
- surface observations 91, 113, 123, 143
- upper air observations 91
climatology 315
cloud microphysics 377
cloud-radiation interaction 377
comparison, shift tests 35
complex terrain 239
computational fluid dynamics 239
convective mixing, non-local 277
cooling rate 377
COST Action ES0601 – HOME 1, 35, 47, 91, 143
crop canopy 315
Czech Republic 123

D

data
- quality control 123
- processing 123
daily data
- processing 123
- series 113
diesase, vector-borne 175
diffusion equations 201, 359
dispersion modeling 359, 435
distribution 113
drought
- hazard 219
- indices 219
dynamic programing 1

E

EMEP
- long-range transport model 359
- unified model 277
emissions 359
environment, urban 359
equation
- reaction-diffusion 201
evaporation 315
extrapolation, Richardson 201

F

fertility 315
finite difference approximation 201
flash rate 295
forest
- annual revenues 159
- ecosystem 159
- yield classes 159
fluid dynamics 239
fuel cell 201

G

Germany 1, 219, 295
gravity waves 239

H

hail 295
hazard
- drought 219, 315
- environmental 219
higher order moments 113
history of Hungarian agrometeorology 315
HOMER homogenization software 47, 69
homogenization 1, 35, 47, 69, 91, 143
homogenization methods 47, 69, 91, 113, 143
homogenized climate database 143
Hungary 113, 143, 159, 175, 187, 201, 219, 239, 315, 435, 377, 403

I

IMEX – implicit-explicit method 201
indice
- climate 143
- hazard 219
industrial accident 435
inhomogeneity
- in climate series1, 35, 47, 69, 91. 113, 123
- in monthly mean temperature series 69
- statistical correction 1, 35, 47, 69, 91, 113, 123
indicator species 175
interaction between cloud and radiation 377
isotonic regression 187
Ixodes ricinus 175

J

joint segmentation 47

K

kinetic energy, turbulent 277

L

Lagrangian dispersion model 435
lightning
- density 295
- total 295
longwave radiation transfer 377
Lyme borreliosis 175

M

MASH homogenization method 47, 69, 113
mathematical formulation 113
measurements
- air pollution 359
- climate datasets 1, 47, 69, 91
- radiation 403
- technics 403
meteorological parameters 359
method
- implicit-explicit 201
microphysics of clouds 377
mixing
- non-local convective 277
- vertical turbulent 277
model
- air quality forecast 359
- ALADIN regional climate 219
- autoregressive 187
- CFD (compuational fluid dynamics) 239
- chemical 277, 359
- dynamic programing 1
- dispersion 435
- EMEP long-range transport 359
- EMEP unified 277
- emission modul 359
- HYSPLIT Lagrangian dispersion 435
- PyTREX continental trajectory 435
- REMO regional climate 219
- RRTM RW radiation transfer 377
- validation 239
monitoring network 359
multiple break point detection 1
multiplicity 295

N

non-local convective mixing 277
numerical
- solution 201
- weather prediction 239

O

observations
- surface climatic 1, 47, 69, 91
- upper air climatic 91

optical depth 403
optimal segmentation 47
ozone
- total 403
- tropospheric 359

P

parameters, meteorological 359, 435
particulate matter 359
PEM – proton exchange membrane 201
penalty term 1
Portugal 69
precipitation
- series 47, 113, 123, 159

prediction, numerical weather 239
production
- actual 315
- capacity 159
- potential 315

productivity 315
programing, multiple 1
PyTREX trajectory model 435

R

radar reflectivity 295
radiation
- longwave 377
- modeling 377
- solar 403
- UV 403

reaction-diffusion equations 201
red noise spectra 187
reflectivity, radar 295
regional climate change 219
regional climatic differences 175
regression
- isotonic 187
- robust 187

REMO regional climate model 219
Richardson extrapolation 201
robust regression 187

S

search algorithm 1
segmentation
- joint 47
- optimal 47

Serbia 277
shift tests comparison 35
solar radiation 403
Spain 35
species
- indicator 175
- tree 159

spectra 187
spectrophotometry 403
statistical correction of inhomogeneities 123
stop criterion for search algorithms 1
surface climatic observations 91

T

temperature
- daily data series 113, 159
- Portugal monthly mean 69
- series homogenization 47, 69, 91
- urban series (UBRIS) 47

terrain, complex 239
time series, climatological 1, 35, 47, 69, 91, 113, 123, 143, 159, 187
total lightning 295
tree species 159
trend bias 47
turbulent
- kinetic energy 277
- vertical mixing 277

U

upper air climatic observations 91
urban
- environment 359
- trend bias 47

UV radiation 403

V

validation, numerical model 239
vector-borne disease 175
vertical turbulent mixing 277

W

water clouds 377
water supply of crop canopy 315
waves, gravity 239
weather prediction, numerical 239

Y

yield
- forest yield classes 159

INSTRUCTIONS TO AUTHORS OF *IDŐJÁRÁS*

The purpose of the journal is to publish papers in any field of meteorology and atmosphere related scientific areas. These may be

- research papers on new results of scientific investigations,
- critical review articles summarizing the current state of art of a certain topic,
- short contributions dealing with a particular question.

Some issues contain "News" and "Book review", therefore, such contributions are also welcome. The papers must be in American English and should be checked by a native speaker if necessary.

Authors are requested to send their manuscripts to

Editor-in Chief of IDŐJÁRÁS
P.O. Box 38, H-1525 Budapest, Hungary
E-mail: journal.idojaras@met.hu

including all illustrations. MS Word format is preferred in electronic submission. Papers will then be reviewed normally by two independent referees, who remain unidentified for the author(s). The Editor-in-Chief will inform the author(s) whether or not the paper is acceptable for publication, and what modifications, if any, are necessary.

Please, follow the order given below when typing manuscripts.

Title page: should consist of the title, the name(s) of the author(s), their affiliation(s) including full postal and e-mail address(es). In case of more than one author, the corresponding author must be identified.

Abstract: should contain the purpose, the applied data and methods as well as the basic conclusion(s) of the paper.

Key-words: must be included (from 5 to 10) to help to classify the topic.

Text: has to be typed in single spacing on an A4 size paper using 14 pt Times New Roman font if possible. Use of S.I. units are expected, and the use of negative exponent is preferred to fractional sign. Mathematical formulae are expected to be as simple as possible and numbered in parentheses at the right margin.

All publications cited in the text should be presented in the *list of references*, arranged in alphabetical order. For an article: name(s) of author(s) in Italics, year, title of article, name of journal, volume, number (the latter two in Italics) and pages. E.g., *Nathan, K.K.*, 1986: A note on the relationship between photo-synthetically active radiation and cloud amount. *Időjárás 90,* 10-13. For a book: name(s) of author(s), year, title of the book (all in Italics except the year), publisher and place of publication. E.g., *Junge, C.E.,* 1963: *Air Chemistry and Radioactivity.* Academic Press, New York and London. Reference in the text should contain the name(s) of the author(s) in Italics and year of publication. E.g., in the case of one author: *Miller* (1989); in the case of two authors: *Gamov* and *Cleveland* (1973); and if there are more than two authors: *Smith et al.* (1990). If the name of the author cannot be fitted into the text: (*Miller,* 1989); etc. When referring papers published in the same year by the same author, letters a, b, c, etc. should follow the year of publication.

Tables should be marked by Arabic numbers and printed in separate sheets with their numbers and legends given below them. Avoid too lengthy or complicated tables, or tables duplicating results given in other form in the manuscript (e.g., graphs).

Figures should also be marked with Arabic numbers and printed in black and white or color (under special arrangement) in separate sheets with their numbers and captions given below them. JPG, TIF, GIF, BMP or PNG formats should be used for electronic artwork submission.

Reprints: authors receive 30 reprints free of charge. Additional reprints may be ordered at the authors' expense when sending back the proofs to the Editorial Office.

More information for authors is available: journal.idojaras@met.hu

Published by the Hungarian Meteorological Service

Budapest, Hungary

INDEX 26 361

HU ISSN 0324-6329